SYNTHESIS, CHARACTERIZATION AND CATALYTIC APPLICATIONS OF METAL OXIDE BASED NANOPHOTOCATALYSTS

Thesis submitted to the
Bharathidasan University, Tiruchirappalli
in partial fulfilment of the requirements
for the award of the degree of
DOCTOR OF PHILOSOPHY IN CHEMISTRY

by PREEJA. P. THATTIL

(Ref. No.16509/Ph.D.K2/Chemistry/Full-Time/October-2017)

Under the Guidance of

Dr. A. LEEMA ROSE
Associate Professor of Chemistry



PG & RESEARCH DEPARTMENT OF CHEMISTRY

HOLY CROSS COLLEGE (Autonomous)

Affiliated to Bharathidasan University, Tiruchirappalli
Nationally Accredited (4th Cycle) with 'A++' Grade (CGPA 3.75/4) by NAAC
College with Potential for Excellence by UGC

TIRUCHIRAPPALLI - 620 002, INDIA

MAY 2022

Dr. A. LEEMA ROSE

Associate Professor,

PG & Research Department of Chemistry, Holy Cross College (Autonomous),

Tiruchirappalli-620 002, Tamil Nadu, India.

CERTIFICATE

I hereby certify that the thesis entitled "SYNTHESIS, CHARACTERIZATION

CATALYTIC APPLICATIONS AND METAL **OXIDE**

NANOPHOTOCATALYSTS" submitted to the Bharathidasan University, Tiruchirappalli

for the award of the degree of Doctor of Philosophy in Chemistry, embodies the

results of bonafide research work carried out by PREEJA. P. THATTIL

Ref. No.16509/Ph.D.K2/Chemistry/Full-Time/ October-2017) under my guidance

and supervision in the PG & Research Department of Chemistry, Holy Cross College

(Autonomous), Tiruchirappalli, Tamil Nadu, India. I further certify that no part of this

thesis has previously formed the basis for the award of any degree, diploma,

associateship, fellowship or other similar title of this to any other University.

Place: Tiruchirappalli

Dr. A. LEEMA ROSE

Date:

Research Advisor

PREEJA. P. THATTIL

Research Scholar,
PG & Research Department of Chemistry,
Holy Cross College (Autonomous),
Tiruchirappalli - 620 002, Tamil Nadu, India.



DECLARATION

I hereby declare that the work embodied in this thesis entitled "SYNTHESIS,

CHARACTERIZATION AND CATALYTIC APPLICATIONS OF METAL

OXIDE BASED NANOPHOTOCATALYSTS" has been originally carried out

by me under the guidance and supervision of Dr. A. LEEMA ROSE

Associate Professor, PG & Research Department of Chemistry, Holy Cross College

(Autonomous), Tiruchirappalli, Tamil Nadu, India. I further declare that this work

either in whole or part has not been submitted for the award of any degree or diploma

to any other University.

Place: Tiruchirappalli

(PREEJA. P. THATTIL)

Date:

Research Scholar



PG & RESEARCH DEPARTMENT OF CHEMISTRY HOLY CROSS COLLEGE (AUTONOMOUS)

Affiliated to Bharathidasan University, Tiruchirappalli
College with Potential for Excellence by UGC
Nationally Accredited (4th Cycle) with 'A++' Grade (CGPA 3.75/4) by NAAC
TIRUCHIRAPPALLI - 620 002, INDIA

CERTIFICATE OF PLAGIARISM CHECK

1	Name of the Research Scholar	PREEJA. P. THATTIL
2	Course of Study	Ph.D., Chemistry
3	Title of the thesis/ Dissertation	SYNTHESIS, CHARACTERIZATION AND CATALYTIC APPLICATIONS OF METAL OXIDE BASED NANOPHOTOCATALYSTS
4	Name of the Research Supervisor	Dr. A. LEEMA ROSE
5	Department/Institute/ Research Centre	PG & Research Department of Chemistry, Holy Cross College (Autonomous), Tiruchirappalli-620 002.
6	Acceptable Maximum Limit	10%
7	Percentage of Similarity of Content Identified	1%
8	Software Used	Ouriginal
9	Date of Verification	29.03.2022

Report on plagiarism check, item with % of similarity is attached

Signature of the Research Scholar

Signature of the Research Advisor



Document Information

Analyzed document PREEJA plagiarism check.docx (D131880319)

Submitted 2022-03-29T08:35:00.0000000

Submitted by Crossianplagiarism

Submitter email crossianplagiarism@gmail.com

Similarity 1%

Analysis address crossian plagiarism. holy@analysis.urkund.com

Sources included in the report

W	URL: https://www.orientjchem.org/vol37no4/high-photocatalytic-performance-of-modified-bismuth-oxychloride-semiconductor-under-sunlight/ Fetched: 2022-02-19T10:04:42.0630000	88	28
W	URL: https://www.mdpi.com/2673-7256/1/3/24/pdf Fetched: 2021-11-12T05:33:18.4100000	88	4
w	URL: https://www.researchgate.net/publication/330891858_Photocatalytic_degradation_of_organic_dyes_using_WO3-doped_ZnO_Nanoparticles_fixed_on_a_glass_surface_in_aqueous_solution Fetched: 2021-09-18T15:04:41.9000000	88	1
W	URL: https://link.springer.com/article/10.1007/s13204-014-0337-y Fetched: 2020-03-27T08:02:55.3200000	88	1
W	URL: https://www.degruyter.com/document/doi/10.1515/secm-2019-0017/pdf Fetched: 2021-10-06T06:07:30.5970000	88	1
W	URL: https://www.mdpi.com/2073-4441/11/2/373/pdf Fetched: 2019-12-10T10:34:17.9300000	88	1

Dedicated to my Dear Parents

ACKNOWLEDGEMENTS

First of all, I thank the **God Almighty** for showering his abundant blessings upon me and giving me good health, strength and courage in every endeavor of my research work.

I feel immense pleasure to express my deep sense of gratitude to my Research Advisor **Dr. A. Leema Rose**, Associate Professor and Head, PG and Research Department of Chemistry, Holy Cross College (Autonomous), Tiruchirappalli, for her invaluable guidance. I specially thank her for leading me in a cordial atmosphere, giving constant encouragement, positive criticism and also for spending her valuable time and energy in my research activity and for rendering all possible support in publishing our research findings.

I am thankful to **Rev.** (**Sr**). **Dr. A.** Christina Bridget, Principal and the Management of Holy Cross College (Autonomous), Tiruchirappalli, for providing all necessary facilities during the entire tenure of my research work.

I thank the Doctoral Committee Members **Dr. S. Joseph Selvaraj**, Associate Professor and Head, Department of Chemistry, St. Josephs College (Autonomous), Tiruchirappalli and **Dr. M. Purushothaman**, Assistant Professor, Department of Chemistry, Jamal Mohamed College (Autonomous), Tiruchirappalli for their helpful suggestions and encouragement during the course of this research work.

I sincerely thank **Dr. S. Thennarasu**, Senior Principal Scientist, Organic Chemistry Lab, Central Leather Research Institute, Chennai for useful discussions and constant encouragement to carry out the research work.

I would like to express my gratitude to **Dr. Felicia Rajammal Selvarani**Former Head and Associate Professor (Retd.) of the Department of Chemistry,

Holy Cross College (Autonomous), Tiruchirappalli for the moral support and encouragement to complete my research work.

My special thanks to **Dr. S. Vidhya** and **Dr. F. Janeeta Priya**, Assistant Professors and other faculty members, Department of Chemistry, Holy Cross College (Autonomous), Tiruchirappalli for their constant encouragement and words of motivation to complete my research work.

I am highly thankful to **Dr. Cheryl Antonette Dumenil**, Assistant Professor of English, Holy Cross College (Autonomous), Tiruchirappalli for helping me in correcting the thesis.

In a special way I would like to acknowledge **Dr. A. Senthamil Selvi**, Librarian of Holy Cross College (Autonomous), Tiruchirappalli, for introducing the new E-Resources that were highly useful for the expediting my research work.

In a very special way, I thank the **Research Scholars** in the Department of Chemistry, Holy Cross College (Autonomous), Tiruchirappalli for all the support to carry out my research work with more enthusiasm.

I wish to thank all the **non-teaching staff members** in the Department of Chemistry, Holy Cross College (Autonomous), Tiruchirappalli for the timely help rendered in the most needed hours of my research work.

I express my heartfelt thanks to **Director G. Selvaraj** for giving me an opportunity to visit the dyeing industry, Tiruppur, Tamil Nadu. I am extremely thankful to **Mr. Ravichandran** for spending his valuable time for me in explaining the processes involved in the effluent treatment.

I am highly grateful to the authors of various research articles and books whose work have been referred, utilized and cited in my thesis.

Above all without my parents nothing would have been possible in my life, especially in this pandemic period. I thank my most affectionate father Mr. T. O. Poly and my caring mother Mrs. Jaya Poly for their unconditional love, moral and financial support throughout my life. Their confidence in my determination, ability and capability motivated me to a great extent. I owe a special deal of thanks to my beloved sister Ms. Preethi. P. Thattil for supporting me, being asides me and cheering me up to overcome the obstacles during this course of my research work. My special thanks to Mr. Chandrasekaran for giving me strong motivation, constant support and encouragement throughout my academics. Also I wish to thank my grandparents, relatives and especially my Aunties Rev. Sr. Naveena and Rev. Sr. Anitha for their prayers, constant encouragement and support which kept me going ahead with a positive attitude in life.

Finally, I would like to thank each and everyone who wished me well during this important phase of my academic career.

Preeja. P. Thattil

CONTENTS

Chapter No		Title	Page No
	List of	Tables	
	List of	Figures	
	List of	Abbreviations	
	Abstra	ct	
I	INTR	ODUCTION	1
	1.1	Water Pollution	1
	1.2	Water Pollution from Dyeing Industries	2
	1.3	Dyes and their Classification	2
	1.4	Water consumption in Textile Dyeing Industries	4
	1.5	Harmful Effects of Water Pollution to the Environment	6
	1.6	Various Treatment technologies Adopted for the Remediation of Wastewater	7
	1.7	Limitations of Previously Adopted Wastewater Treatment Technologies	12
	1.8	Advanced Oxidation Processes	14
	1.9	Semiconductor Photocatalysts	26
	Bibliog	graphy	36
II	REVI	EW OF LITERATURE	46
	2.1	Heterogeneous Semiconductor Photocatalysis	46
	2.2	Semiconductor Photocatalysts for Degradation of Dyes	47
	2.3	Coupling of semiconductor Photocatalysts	52
	2.4	Metal doped semiconductor photocatalysts	57
	2.5	Codoped and Tridoped semiconductor photocatalysts	63
	2.6	Dye sensitized semiconductor photocatalysts	73
	2.7	Supported semiconductor photocatalysts	76
	Bibliog	graphy	82
III	AIM A	AND SCOPE	97
	3.1	Need for the Present Investigation	97
	3.2	Aim and Scope of the Present Research Work	101
	3.3	Objectives of the Present work	102
	Bibliog	graphy	105
IV	MATE	ERIALS AND METHODS	107
	4.1	Dyes Chosen for the Study	107
	4.2	Chemicals Required	112
	4.3	Synthesis of Photocatalysts	113
	4.3.1	Synthesis of Aluminum fluoride doped ZnO and Strontium silicate doped ZnO Photocatalysts	113

	4.3.2	Synthesis of Aluminium fluoride doped TiO ₂ and Strontium silicate doped TiO ₂ Photocatalysts	114
	4.3.3	Synthesis of Aluminium fluoride doped BiOCl and Strontium silicate doped BiOCl Photocatalysts	115
	4.4	Characterization Techniques	116
	4.4.1	X-Ray Diffraction Studies	116
	4.4.2	Field Emission-Scanning Electron Microscopic Analysis	117
	4.4.3	Energy Dispersive X-Ray Analysis	117
	4.4.4	Transmission Electron Microscopic Analysis	118
	4.4.5	UV-Diffuse Reflectance Spectrum	118
	4.4.6	Fourier Transform Infra Red Spectroscopy Studies	118
	4.4.7	BET-Surface area Analysis	119
	4.4.8	Double Beam UV-Visible spectrophotometer	119
	4.4.9	Total Organic Carbon Analyzer	119
	4.4.9	Photocatalytic studies	120
	4.6	Collection and storage of the Dye effluent	120
	4.0	Antimicrobial studies	121
			124
V	Bibliog	LTS AND DISCUSSION	124
<u> </u>	-		
	5.1	Characterization and Photocatalytic Studies of Zinc Oxide, Aluminium Fluoride Doped Zinc Oxide and Strontium Silicate Doped Zinc Oxide	125
	5.1.1	X-Ray Diffraction Studies	125
	5.1.2	HR-SEM Analysis	127
	5.1.3	Energy Dispersive X-Ray Analysis	128
	5.1.4	Transmission Electron Microscopic Analysis	129
	5.1.5	UV-Visible Diffuse Reflectance Spectroscopy Studies	133
	5.1.6	Fourier Transform Infra-Red Spectroscopy Studies	134
	5.1.7	BET Surface Area Analysis	136
	5.1.8	Photocatalytic Studies	139
	5.1.9	Effect of pH on the photocatalytic dye decolourization process	142
	5.1.10	Effect of Catalyst Concentration	145
	5.1.10	Effect of Initial Dye Concentration	147
	5.1.12	Effect of Addition of Aluminium Fluoride and Strontium Silicate to ZnO Photocatalyst	150
	5.1.13	Kinetic Studies	155
	5.1.13	UV-Visible Spectroscopic Analysis	159
	5.1.14	Comparison of the Degradation Efficiencies of the	
	3.1.13	Photocatalysts	162
	5.1.16	Effect of Radical Quenchers	164

5.1.17	Mineralization Studies	167
5.1.18	Reusability Studies	168
5.1.19	Proposed Mechanism	170
5.2	Characterization and Photocatalytic Studies of Titanium Dioxide, Aluminium Fluoride Doped Titanium Dioxide	173
5.2.1	and Strontium Silicate Doped Titanium Dioxide X-Ray Diffraction Studies	173
5.2.2	HR-SEM Analysis	175
5.2.3	Energy Dispersive X-Ray Analysis	177
5.2.4	Transmission Electron Microscopic Analysis	179
5.2.5	UV-Visible Diffuse Reflectance Spectroscopy Studies	183
5.2.6	Fourier Transform Infra-Red Spectroscopy Studies	184
5.2.7	BET Surface Area Analysis	186
5.2.8	Photocatalytic Studies	
5.2.9	· ·	187 189
3.2.9	Effect of pH on the photocatalytic dye decolourization process	189
5.2.10	Effect of Catalyst Concentration	192
5.2.11	Effect of Initial dye concentration	194
5.2.12	Effect of Addition of Aluminium Fluoride and Strontium Silicate to TiO ₂ Photocatalyst	197
5.2.13	Kinetic Studies	202
5.2.14	UV-Visible Spectroscopic Analysis	206
5.2.15	Comparison of the Efficiencies of Different Photocatalysts	209
5.2.16	Effect of Free radical scavenging activity	211
5.2.17	Mineralization Studies	214
5.2.18	Reusability Studies	215
5.2.19	Proposed Mechanism	216
5.3	Characterization and Photocatalytic Studies of Bismuth Oxychloride, Aluminium Fluoride Doped Bismuth Oxychloride and Strontium Silicate Doped Bismuth Oxychloride Catalysts	219
5.3.1	X-Ray Diffraction Studies	219
5.3.2	HR-SEM Analysis	221
5.3.3	Energy Dispersive X-Ray Analysis	222
5.3.4	Transmission Electron Microscopic Analysis	223
5.3.5	UV-Visible Diffuse Reflectance Spectroscopy Studies	227
5.3.6	Fourier Transform Infra-Red Spectroscopy Studies	228
5.3.7	BET Surface Area Analysis	230
5.3.8	Photocatalytic Studies	232
5.3.9	Effect of pH on the photocatalytic dye decolourization process	233

	5.3.10	Effect of Catalyst Concentration	234
	5.3.11	Effect of Initial dye concentration	236
	5.3.12	Effect of Addition of Aluminium Fluoride and Strontium silicate to BiOCl photocatalyst	237
	5.3.13	Kinetic Studies	241
	5.3.14	UV-Visible Spectroscopic Analysis	242
	5.3.15	Comparison of the Efficiencies of Different Photocatalysts	243
	5.3.16	Effect of Free radical scavenging activity	245
	5.3.17	Mineralization Studies	246
	5.3.18	Reusability Studies	247
	5.3.19	Proposed Mechanism	248
	5.4	Effluent treatment and Antimicrobial activity of 2% AlF ₃ -ZnO/1% AlF ₃ -TiO ₂ /3% AlF ₃ -BiOCl photocatalyst	252
	5.4.1	Effluent Treatment	252
	5.4.2	Analysis of the physico-chemical parameters of the Effluent	256
	5.4.3	In Vitro Antimicrobial Assay of the synthesized 2 wt %AlF ₃ -ZnO/1 wt % AlF ₃ -TiO ₂ / 3 wt % AlF ₃ -BiOCl composite	262
	5.4.4	Antimicrobial activity of nanocomposites	262
	5.4.5	Antibacterial studies of 2 wt % AlF ₃ -ZnO/ 1 wt % AlF ₃ -TiO ₂ / 3 wt % AlF ₃ -BiOCl photocatalyst	263
	5.4.6	Antifungal studies of 2 wt % AlF ₃ -ZnO/ 1 wt % AlF ₃ -TiO ₂ / 3 wt % AlF ₃ -BiOCl photocatalyst	265
	5.4.7	Mechanism of antimicrobial activity	267
	Bibliog	raphy	270
VI	SUMM	IARY AND CONCLUSION	277
	SCOPI	E FOR FURTHER STUDY	282
	LIST C	OF PUBLICATIONS	
	LIST C	OF PAPER PRESENTATIONS	

LIST OF TABLES

Table No.	Title	Page No.
1.1	Water requirement (L/per Kg) for dyeing of different types of fabrics	5
5.1.7	Surface area, Pore volume and Pore radius of bare-ZnO, AlF ₃ -ZnO and SrSiO ₃ -ZnO photocatalysts	138
5.1.15	Comparison of the efficiencies (in terms of % decolourization) of doped and undoped zinc oxide photocatalysts towards methylene blue, indigo carmine and crystal violet	163
5.2.7	Surface area, Pore volume and Pore radius of bare-TiO ₂ , AlF ₃ -TiO ₂ and SrSiO ₃ -TiO ₂ , photocatalysts	187
5.2.15	Comparison of the efficiencies (in terms of % decolourization) of doped and undoped titanium dioxide photocatalysts towards basic yellow 2, acid red 94 and congo red	210
5.3.7	Surface area, pore volume and pore radius of bare-BiOCl, AlF ₃ -BiOCl and SrSiO ₃ -BiOCl photocatalysts	231
5.3.15	Comparison of the efficiencies (in terms of % decolourization) of doped and undoped bismuth oxychloride oxide photocatalysts towards acid green1	244
5.4.1	Permissible limits for the discharge of wastewaters according to Indian Standards	253
5.4.2	Results of the Physico-chemical analysis of the effluent before and after the photocatalytic treatment	261
5.4.5	Results of <i>in vitro</i> Antibacterial activity of 2 wt % AlF ₃ -ZnO/ 1 wt % AlF ₃ -TiO ₂ / 3 wt % AlF ₃ -BiOCl catalyst	264
5.4.6	Results of <i>in vitro</i> Antifungal activity of 2 wt % AlF ₃ -ZnO/ 1 wt % AlF ₃ -TiO ₂ / 3 wt % AlF ₃ -BiOCl catalyst	266

LIST OF FIGURES

Figure No.	Title	Page No.
1.1	Various stages of textile processing	4
1.2	Photocatalytic mechanism involved with bare semiconductors	21
1.3	Photocatalytic mechanism operating in heterojunction type semiconductors	23
1.4	Photocatalytic mechanism operating in p-n heterojunction and z-scheme photocatalysis	25
5.1.1A	X-Ray diffraction pattern of the synthesized undoped zinc oxide photocatalyst	126
5.1.1B	X-Ray diffraction pattern of the synthesized 2 wt% AlF ₃ doped zinc oxide photocatalyst	126
5.1.1C	X-Ray diffraction pattern of the synthesized 2wt% SrSiO ₃ doped zinc oxide photocatalyst	126
5.1.2A	HR-SEM image of bare zinc oxide photocatalyst	127
5.1.2B	HR-SEM image of 2 wt% AlF ₃ doped zinc oxide photocatalyst	127
5.1.2C	HR-SEM image of 2 wt% SrSiO ₃ doped zinc oxide photocatalyst	127
5.1.3A	EDAX image of bare zinc oxide photocatalyst	128
5.1.3B	EDAX image of 2 wt% aluminium fluoride doped zinc oxide photocatalyst	129
5.1.3C	EDAX image of 2 wt% strontium silicate doped zinc oxide photocatalyst	129
5.1.4 A,B,C	HR-TEM images and SAED pattern of the undoped ZnO photocatalyst	130
5.1.4 D,E,F	HR-TEM images and SAED pattern of the 2 wt% AlF ₃ doped ZnO photocatalyst	130
5.1.4 G,H,I	HR-TEM images and SAED pattern of the 2 wt% SrSiO ₃ doped ZnO photocatalyst	130
5.1.5A	DRS-UV-Visible absorption spectra for bare ZnO photocatalyst	131

DRS-UV-Visible absorption spectra for 2 wt% AlF ₃ doped ZnO photocatalyst	131
DRS-UV-Visible absorption spectra for 2 wt% SrSiO ₃ doped ZnO photocatalyst	131
FTIR spectrum of the synthesized bare Zinc Oxide photocatalyst	135
FTIR spectrum of the synthesized 2 wt% AlF ₃ doped Zinc Oxide photocatalyst	135
FTIR spectrum of the synthesized 2 wt% SrSiO ₃ doped zinc oxide photocatalyst	136
N ₂ adsorption-desorption isotherms of the synthesized undoped ZnO photocatalyst	138
N ₂ adsorption-desorption isotherms of the 2 wt% AlF ₃ doped ZnO photocatalyst	138
N ₂ adsorption-desorption isotherms of the 2 wt% SrSiO ₃ doped ZnO photocatalyst	138
Primary analysis of methylene blue dye solution using zinc oxide photocatalyst	140
Primary analysis of indigo carmine dye solution using zinc oxide photocatalyst	141
Primary analysis of crystal violet dye solution using zinc oxide photocatalyst	141
Effect of pH on the photocatalytic decolourization of methylene blue dye using zinc oxide catalyst	143
Effect of pH on the photocatalytic decolourization of indigo carmine dye using zinc oxide catalyst	144
Effect of pH on the photocatalytic decolourization of crystal violet dye using zinc oxide catalyst	144
Effect of zinc oxide catalyst concentration on the photocatalytic decolourization of methylene blue dye	146
Effect of zinc oxide catalyst concentration on the photocatalytic decolourization of indigo carmine dye	146
Effect of zinc oxide catalyst concentration on the photocatalytic decolourization of crystal violet dye	147
Effect of initial concentration of methylene blue on photocatalytic decolourization using ZnO catalyst	148
	ZnO photocatalyst DRS-UV-Visible absorption spectra for 2 wt% SrSiO ₃ doped ZnO photocatalyst FTIR spectrum of the synthesized bare Zinc Oxide photocatalyst FTIR spectrum of the synthesized 2 wt% AIF ₃ doped Zinc Oxide photocatalyst FTIR spectrum of the synthesized 2 wt% SrSiO ₃ doped zinc oxide photocatalyst N ₂ adsorption-desorption isotherms of the synthesized undoped ZnO photocatalyst N ₂ adsorption-desorption isotherms of the 2 wt% AIF ₃ doped ZnO photocatalyst N ₂ adsorption-desorption isotherms of the 2 wt% SrSiO ₃ doped ZnO photocatalyst Primary analysis of methylene blue dye solution using zinc oxide photocatalyst Primary analysis of indigo carmine dye solution using zinc oxide photocatalyst Primary analysis of crystal violet dye solution using zinc oxide photocatalyst Effect of pH on the photocatalytic decolourization of methylene blue dye using zinc oxide catalyst Effect of pH on the photocatalytic decolourization of indigo carmine dye using zinc oxide catalyst Effect of zinc oxide catalyst concentration on the photocatalytic decolourization of methylene blue dye Effect of zinc oxide catalyst concentration on the photocatalytic decolourization of indigo carmine dye Effect of zinc oxide catalyst concentration on the photocatalytic decolourization of indigo carmine dye Effect of zinc oxide catalyst concentration on the photocatalytic decolourization of crystal violet dye Effect of initial concentration of methylene blue on

5.1.11B	Effect of initial concentration of indigo carmine on	149
	photocatalytic decolourization using ZnO catalyst	
5.1.11C	Effect of initial concentration of crystal violet on the photocatalytic decolourization using ZnO catalyst	149
5.1.12A	Photocatalytic decolourization of methylene blue using different weight percents of aluminium fluoride doped ZnO catalyst	152
5.1.12B	Photocatalytic decolourization of methylene blue using different weight percents of strontium silicate doped ZnO catalyst	152
5.1.12C	Photocatalytic decolourization of indigo carmine using different weight percents of aluminium fluoride doped ZnO catalyst	153
5.1.12D	Photocatalytic decolourization of indigo carmine dye using different weight percents of strontium silicate doped ZnO catalyst	153
5.1.12E	Photocatalytic decolourization of crystal violet using different weight percents of aluminium fluoride doped ZnO catalyst	154
5.1.12F	Photocatalytic decolourization of crystal violet using different weight percents of strontium silicate doped ZnO catalyst	154
5.1.13.1A	Plot of $\ln C_0/C \ vs$ 't' for the photocatalytic decolourization of methylene blue using undoped ZnO and (0.5-3 wt%) AlF ₃ doped ZnO	158
5.1.13.1B	Plot of ln C ₀ /C vs't' for the photocatalytic decolourization of methylene blue using (0.5-3 wt %) SrSiO ₃ doped ZnO photocatalyst.	158
5.1.13.2A	Plot of $\ln C_0/C \ vs$ 't' for the photocatalytic decolourization of indigo carmine using undoped ZnO and (0.5-3 wt%) AlF ₃ doped ZnO	158
5.1.13.2B	Plot of ln C ₀ /C vs't' for the photocatalytic decolourization of indigo carmine using (0.5-3 wt %) SrSiO ₃ doped ZnO photocatalyst.	158
5.1.13.3A	Plot of ln C ₀ /C vs't' for the photocatalytic decolourization of crystal violet using undoped ZnO and (0.5-3 wt%) AlF ₃ doped ZnO	158
5.1.13.3B	Plot of ln C ₀ /C vs't' for the photocatalytic decolourization of crystal violet using (0.5-3 wt %) SrSiO ₃ doped ZnO photocatalyst.	158

5.1.14.1A	UV-Visible absorption spectra showing the decolourization of methylene blue in the presence of AlF ₃ /ZnO photocatalyst	161
5.1.14.1B	UV-Visible absorption spectra showing the decolourization of methylene blue in the presence of SrSiO ₃ /ZnO photocatalyst	161
5.1.14.2A	UV-Visible absorption spectra showing the decolourization of indigo carmine in the presence of AlF ₃ /ZnO	161
5.1.14.2B	UV-Visible absorption spectra showing the decolourization of indigo carmine in the presence of SrSiO ₃ /ZnO photocatalyst	161
5.1.14.3A	UV-Visible absorption spectra showing the decolourization of crystal violet in the presence of AlF ₃ /ZnO photocatalyst	161
5.1.14.3B	UV-Visible absorption spectra showing the decolourization of crystal violet in the presence of SrSiO ₃ /ZnO photocatalyst	161
5.1.16.1	Effect of radical scavengers on the photocatalytic degradation of methylene blue using 2wt% AlF ₃ /ZnO photocatalyst under optimized conditions	165
5.1.16.2	Effect of radical scavengers on the photocatalytic degradation of indigo carmine using 2 wt% AlF ₃ /ZnO photocatalyst under optimized conditions	166
5.1.16.3	Effect of radical scavengers on the photocatalytic degradation of crystal violet using 2wt% AlF ₃ /ZnO photocatalyst under optimized conditions	166
5.1.17	Percentage removal of total organic carbon in the aqueous solution of methylene blue, indigo carmine and crystal violet using 2wt% AlF ₃ /ZnO photocatalyst under optimized conditions	168
5.1.18A	Reusability of the most active 2wt% AlF ₃ /ZnO catalyst for the photocatalytic degradation of methylene blue	169
5.1.18B	Reusability of the most active 2wt% AlF ₃ /ZnO catalyst for the photocatalytic degradation of indigo carmine	169
5.1.18C	Reusability of the most active 2wt% AlF ₃ /ZnO catalyst for the photocatalytic degradation of crystal violet dyes	169
5.1.19	Perspective mechanism for the degradation of dyes mediated by AlF ₃ /ZnO catalyst under sunlight	172
5.2.1A	X-Ray diffraction pattern of the synthesized undoped Titanium dioxide photocatalyst	175
3.2.111		175

5.2.1B	X-Ray diffraction pattern of the synthesized 1 wt% AlF ₃ doped Titanium dioxide photocatalyst	175
5.2.1C	X-Ray diffraction pattern of the synthesized 1wt% SrSiO ₃ doped Titanium dioxide photocatalyst	175
5.2.2A	HR-SEM image of the synthesized undoped titanium dioxide photocatalyst	176
5.2.2B	HR-SEM image of the synthesized 1 wt% AlF ₃ doped titanium dioxide photocatalyst	176
5.2.2C	HR-SEM image of the synthesized 1 wt% SrSiO ₃ doped titanium dioxide photocatalyst	176
5.2.3A	EDAX image of the synthesized undoped Titanium dioxide photocatalyst	178
5.2.3B	EDAX image of the synthesized 1 wt% Aluminium fluoride doped Titanium dioxide photocatalyst	178
5.2.3C	EDAX image of the synthesized 1 wt% Strontium silicate doped Titanium dioxide photocatalyst	178
5.2.4A,B,C	HR-TEM images and SAED Pattern of the undoped TiO ₂ photocatalyst	180
5.2.4D,E,F	HR-TEM images and shows the SAED Pattern of the 1% AlF ₃ doped TiO ₂ photocatalyst	181
5.2.4G,H,I	HR-TEM images and shows the SAED Pattern of the 2% SrSiO ₃ doped TiO ₂ photocatalyst	182
5.2.5A	DRS-UV-Visible absorption spectra for undoped TiO ₂ photocatalyst	183
5.2.5B	DRS-UV-Visible absorption spectra for 1 % AlF ₃ doped TiO ₂ photocatalyst	183
5.2.5C	DRS-UV-Visible absorption spectra for 1% SrSiO ₃ doped TiO ₂ photocatalyst	183
5.2.6A	FTIR spectrum of the synthesized bare Titanium dioxide photocatalyst	185
5.2.6B	FTIR spectrum of the synthesized 1 % AlF ₃ doped Titanium dioxide photocatalyst	185
5.2.6C	FTIR spectrum of the synthesized 1 % SrSiO ₃ doped Titanium dioxide photocatalyst	185
5.2.7A	N_2 adsorption-desorption isotherm of the synthesized TiO_2 photocatalyst	186

5.2.7B	N ₂ adsorption-desorption isotherm of the synthesized 1% AlF ₃ doped TiO ₂ photocatalyst	186
5.2.7C	N ₂ adsorption-desorption isotherm of the synthesized 1% SrSiO ₃ doped TiO ₂ photocatalyst	186
5.2.8A	Primary analysis of basic yellow 2 dye solution using titanium dioxide photocatalyst	
5.2.8B	Primary analysis of congo red dye solution using titanium dioxide photocatalyst	188
5.2.8C	Primary analysis of acid red 94 dye solution using titanium dioxide photocatalyst	
5.2.9A	Effect of pH on the photocatalytic decolourization of basic yellow 2 using titanium dioxide catalyst	190
5.2.9B	Effect of pH on the photocatalytic decolourization of congo red dye using titanium dioxide catalyst	191
5.2.9C	Effect of pH on the photocatalytic decolourization of acid red 94 dye using titanium dioxide catalyst	191
5.2.10A	Effect of Titanium dioxide catalyst concentration on the photocatalytic decolourization of Basic yellow 2 dye	193
5.2.10B	Effect of titanium dioxide catalyst concentration on the photocatalytic decolourization of congo red dye	193
5.2.10C	Effect of titanium dioxide catalyst concentration on the photocatalytic decolourization of acid red 94 dye	194
5.2.11A	Effect of initial concentration of basic yellow 2 on the photocatalytic decolourization using ZnO catalyst	195
5.2.11B	Effect of initial concentration of acid Red 94 on the photocatalytic decolourization using TiO ₂ catalyst	196
5.2.11C	Effect of initial concentration of congo red on the photocatalytic decolourization using TiO ₂ catalyst	196
5.2.12A	Photocatalytic decolourization of basic yellow 2 using different weight percents of aluminium fluoride doped TiO ₂ catalyst	199
5.2.12B	Photocatalytic decolourization of basic yellow 2 using different weight percents of strontium silicate doped TiO ₂ catalyst	200
5.2.12C	Photocatalytic decolourization of acid red 94 using different weight percents of aluminium fluoride doped TiO ₂ catalyst	200

r		
5.2.12D	Photocatalytic decolourization of acid red 94 using different weight percents of strontium silicate doped TiO ₂ catalyst	201
5.2.12E	Photocatalytic decolourization of congo red using different weight percents of aluminium fluoride doped TiO ₂ catalyst	201
5.2.12F	Photocatalytic decolourization of congo red using different weight percents of strontium silicate doped TiO ₂ catalyst	
5.2.13.1A	Plot of ln C ₀ /C vs't' for the photocatalytic decolourization of basic yellow 2 using TiO ₂ and (0.5-3 wt%) AlF ₃ doped TiO ₂ photocatalysts	205
5.2.13.1B	Plot of ln C ₀ /C vs't' for the photocatalytic decolourization of basic yellow 2 using (0.5-3 wt %) SrSiO ₃ doped TiO ₂ photocatalyst	205
5.2.13.2A	Plot of ln C ₀ /C vs't' for the photocatalytic decolourization of acid red 94 using undoped TiO ₂ and (0.5-3 wt%) AlF ₃ doped TiO ₂	205
5.2.13.2B	Plot of ln C ₀ /C vs't' for the photocatalytic decolourization of acid red 94 using using (0.5-3 wt %) SrSiO ₃ doped TiO ₂ photocatalyst.	205
5.2.13.3A	Plot of ln C ₀ /C vs't' for the photocatalytic decolourization of congo red using undoped TiO ₂ and (0.5-3 wt%) AlF ₃ doped TiO ₂	205
5.2.13.3B	Plot of ln C ₀ /C vs't' for the photocatalytic decolourization of congo red using using (0.5-3 wt %) SrSiO ₃ doped TiO ₂ photocatalyst.	205
5.2.14.1A	UV-Visible absorption spectra showing the decolourization of basic yellow 2 in the presence of AlF ₃ /TiO ₂	208
5.2.14.1B	UV-Visible absorption spectra showing the decolourization of basic yellow 2 in the presence of SrSiO ₃ /TiO ₂ photocatalysts	208
5.2.14.2A	UV-Visible absorption spectra showing the decolourization of acid red 94 in the presence of AlF ₃ /TiO ₂	208
5.2.14.2B	UV-Visible absorption spectra showing the decolourization of acid red 94 in the presence of SrSiO ₃ /TiO ₂ photocatalysts	208
5.2.14.3A	UV-Visible absorption spectra showing the decolourization of congo red in the presence of AlF ₃ /TiO ₂	208
5.2.14.3B	UV-Visible absorption spectra showing the decolourization of congo red in the presence of SrSiO ₃ /TiO ₂ photocatalysts	208
5.2.16.1	Effect of radical scavengers on the photocatalytic degradation of basic yellow 2 using 1wt% AlF ₃ /TiO ₂ photocatalyst under optimized conditions	212

5.2.16.2	Effect of radical scavengers on the photocatalytic degradation of acid red 94 using 1wt% AlF ₃ /TiO ₂ photocatalyst under optimized conditions	213
5.2.16.3	Effect of radical scavengers on the photocatalytic degradation of congo red using 1wt% AlF ₃ /TiO ₂ photocatalyst under optimized conditions	213
5.2.17	Percentage removal of total organic carbon in the aqueous solution of basic yellow 2, acid red 94 and congo red dyes using 1wt% AlF ₃ /TiO ₂ photocatalyst under optimized conditions	214
5.2.18A	Reusability of the most active (1wt%) AlF ₃ /TiO ₂ catalyst for the photocatalytic degradation of basic yellow 2	216
5.2.18B	Reusability of the most active 1wt% AlF ₃ /TiO ₂ catalyst for the photocatalytic degradation of acid red 94	216
5.2.18C	Reusability of the most active 1wt% AlF ₃ /TiO ₂ catalyst for the photocatalytic degradation of congo red dyes	216
5.2.19	Perspective mechanism for the degradation of dyes mediated by 1 wt % AlF ₃ /TiO ₂ catalyst under sunlight	219
5.3.1A	X-Ray diffraction pattern of the synthesized undoped bismuth oxychloride photocatalyst	220
5.3.1B	X-Ray diffraction pattern of the synthesized 3 wt% AlF ₃ doped bismuth oxychloride photocatalyst	220
5.3.1C	X-Ray diffraction pattern of the synthesized 3 wt% SrSiO ₃ doped bismuth oxychloride photocatalyst	220
5.3.2A	HR-SEM image of the synthesized bare bismuth oxychloride photocatalyst	221
5.3.2B	HR-SEM image of the synthesized 3 wt% AlF ₃ doped bismuth oxychloride photocatalyst	221
5.3.2C	HR-SEM image of the synthesized 3 wt% SrSiO ₃ doped bismuth oxychloride photocatalyst	221
5.3.3A	EDAX image of the synthesized undoped bismuth oxychloride photocatalyst	222
5.3.3B	EDAX image of the synthesized 3 wt% aluminium fluoride doped bismuth oxychloride photocatalyst	223
5.3.3C	EDAX image of the synthesized 3 wt% strontium silicate doped bismuth oxychloride photocatalyst	223
5.3.4A,B,C	HR-TEM images and SAED pattern of the undoped Bismuth oxychloride photocatalyst	224

5.3.4D,E,F	HR-TEM images and shows the SAED pattern of the AlF ₃ (3%) doped BiOCl photocatalyst	225
5.3.4G,H,I	HR-TEM images and shows the SAED pattern of the SrSiO ₃ (3%) doped BiOCl photocatalyst	
5.3.5A	DRS-UV-Visible absorption spectra for bare BiOCl photocatalyst	
5.3.5B	DRS-UV-Visible absorption spectra for 3 wt% AlF ₃ doped BiOCl photocatalyst	
5.3.5C	DRS-UV-Visible absorption spectra for 3 wt% SrSiO ₃ doped BiOCl photocatalyst	
5.3.6A	FTIR spectrum of the synthesized bare bismuth oxychloride photocatalyst	229
5.3.6B	FTIR spectrum of the synthesized 3wt% AlF ₃ /BiOCl photocatalyst	229
5.3.6C	FTIR spectrum of the synthesized 3wt% SrSiO ₃ /BiOCl photocatalyst	
5.3.7A	N_2 adsorption-desorption isotherm of the synthesized BiOCl photocatalyst	231
5.3.7B	N_2 adsorption-desorption isotherm of the synthesized 3 wt% AlF3 doped BiOCl photocatalyst	231
5.3.7C	N ₂ adsorption-desorption isotherm of the synthesized 3 wt% SrSiO ₃ doped BiOCl photocatalyst	
5.3.8	Primary analysis of acid green 1 dye solution using bismuth oxychloride photocatalyst	232
5.3.9	Effect of pH on the photocatalytic decolourization of acid green 1 using bismuth oxychloride catalyst	234
5.3.10	Effect of bismuth oxychloride catalyst concentration on the photocatalytic decolourization of acid green 1 dye	235
5.3.11	Effect of initial concentration of acid green 1 on photocatalytic decolourization using BiOCl catalyst	
5.3.12A	Photocatalytic decolourization of acid green 1 dye using different weight percent of aluminium fluoride doped BiOCl catalyst	240
5.3.12B	Photocatalytic decolourization of acid green 1 dye using different weight percent of Strontium silicate doped BiOCl catalyst	240

5.3.13A	Plot of ln C ₀ /C vs't' for the photocatalytic decolourization of acid green 1 using undoped BiOCl and (0.5-4 wt%) AlF ₃ doped BiOCl	242
5.3.13B	Plot of ln C ₀ /C vs't' for the photocatalytic decolourization of acid green 1 using using (0.5-4 wt %) SrSiO ₃ doped BiOCl photocatalyst	242
5.3.14A	UV-Visible absorption spectra showing the decolourization of acid green 1 in the presence of AlF ₃ /BiOCl	243
5.3.14B	UV-Visible absorption spectra showing the decolourization of acid green 1 in the presence of SrSiO ₃ /BiOCl photocatalysts	243
5.3.16	Effect of radical scavengers for the photocatalytic degradation of acid green 1 dye using 3wt % AlF ₃ /BiOCl photocatalyst under optimized conditions	246
5.3.17	Percentage removal of total organic carbon in the aqueous solution of acid green 1 dye using 3wt% AlF ₃ /BiOCl photocatalyst under optimized conditions	247
5.3.18	Reusability of the most active 3 wt % AlF ₃ /BiOCl catalyst for the photocatalytic degradation of acid green 1 dye	248
5.3.19	Perspective mechanism for the degradation of dye mediated by AlF ₃ /BiOCl catalyst under sunlight	251
5.4.1A	UV-Visible absorption spectrum of the diluted effluent before the photocatalytic tretament	255
5.4.1B	UV-Visible absorption spectrum of the effluent after the photocatalytic tretament	255
5.4.5	Antibacterial disc diffusion assay of 2 wt % AlF ₃ -ZnO/ 1 wt % AlF ₃ -TiO ₂ / 3 wt % AlF ₃ -BiOCl composite towards <i>Staphylococcus aureus, Pseudomonas aeruginosa</i> and <i>Escherichia coli</i>	265
5.4.6	Antifungal disc diffusion assay of 2 wt % AlF ₃ -ZnO/ 1 wt % AlF ₃ -TiO ₂ / 3 wt % AlF ₃ -BiOCl composite towards Aspergillus flavus, Candida vulgaris and Candida albicans	267

LIST OF ABBREVIATIONS

L/per Kg Litre per kilogram

hv Photon

g L⁻¹ Gram per Litre

°C Degree Centigrade

UV Ultra Violet

VB Valence Band

CB Conduction Band

ZnO Zinc Oxide

TiO₂ Titanium dioxide

BiOCl Bismuth oxychloride

eV Electron Volt

AOP Advanced Oxidation Process

nm Nanometer

kHz Kilo Hertz

MHz Mega Hertz

GHz Giga Hertz

K Kelvin

Atm Atmosphere

W Watt

CVD Chemical Vapour Deposition

PVD Physical Vapour Deposition

m²/g Meter Square per Gram

MRI Magnetic Resonance Imaging

NIR Near Infra Red

g-C₃N₄ Graphitic Carbon Nitride

ppm Parts Per Million

% Percentage

mM Milli Molar

min Minutes

g/L Gram per Litre

BET Brunauer Emmett Teller

COD Chemical Oxygen Demand

BOD Biological Oxygen Demand

TOC Total Organic Carbon

TDS Total Dissolved Solids

TSS Total Suspended Solids

LED Lead Emitting Diode

mg Milligram

M Molarity

AlF₃ Aluminium Trifluoride

SrSiO₃ Strontium Silicate

MB Methylene Blue

IC Indigo Carmine

CV Crystal Violet

BY2 Basic Yellow 2

AR94 Acid Red 94

CR Congo Red

AG1 Acid Green 1

C.I. No. Color Index Number

mL Millilitre

kV Kilo Volt

mA Milli Ampere

s Seconds

Theta

μm Micrometer

cm Centimeter

μl Microlitre

hrs Hours

APHA American Public Health Association

 λ Lamda

~ Approximately

ln Logarithm

wt% Weight Percentage

EDTA Ethylene Diammine Tetra Acetic Acid

ROS Reactive Oxygen Species

OH Hydroxyl Radical

 h^{+} Holes

e Electrons

O₂. Superoxide anion Radical

cc/g Cubic Centimeter per Gram

NTU Nephelometric Turbidity Units

ABSTRACT

The present work focuses on the synthesis of low cost, environment-friendly and reusable metal oxide photocatalysts. Till date the most widely exploited photocatalysts for the degradation of pollutants are zinc oxide and titanium dioxide photocatalysts due to their ever fascinating optoelectronic properties and non-toxic nature. Recently bismuth based materials are also tested for their photocatalytic applications due to their environmentally benign nature and tunable band gap properties. Understanding the everlasting potential of utilizing natural sunlight as a source for the excitation of the electrons from the semiconductor metal oxides to initiate the redox reactions, the present study is concentrated towards the effective utilization of sunlight for photocatalytic destruction of the dyes. Although the zinc, titanium and bismuth semiconductors show catalytic activity under direct sunlight, the wide bandgap of these materials (~ 3.2eV) causes some drawbacks such as small amount of photon absorption and fast recombination of the photogenerated charge carriers which restricts the large scale practical applicability of these semiconductor photocatalysts. So to overcome these limitations and increase the photocatalytic response of the metal oxides used in the study under direct sunlight modification of the ZnO, TiO₂ and BiOCl catalysts are done by doping aluminium fluoride and strontium silicate salts. Further in order to understand the structural and morphological characteristics of synthesized photocatalysts different analytical techniques such as X-ray diffraction analysis, field emission scanning electron microscopy analysis, energy dispersive X-ray analysis and high resolution transmission electron microscopy analysis are employed. The presence of metaloxygen bonds, bandgap values and surface area of the photocatalysts are determined

from the fourier transform infra-red spectroscopy analysis, UV diffuse reflectance spectroscopy analysis and nitrogen adsorption-desorption isotherm analysis.

The Hexagonal wurtzite phase of the ZnO catalyst, anatase, rutile and brookite phases of TiO₂ and tetragonal phase of BiOCl and crystallinity of the synthesized materials were established from the XRD patterns. The morphology of the synthesized photocatalysts were recognized from the FE SEM and TEM images and the SAED pattern confirmed the crystallinity of the materials which further supported the XRD data. The presence of major elements in the synthesized photocatalysts was observed in the EDAX spectra and the formation of metal-oxygen bonds in all the photocatalysts were confirmed from the FTIR spectra. An increase in the surface area and a decrease in the bandgap values of the photocatalysts were evidenced after the process of doping which resulted in the improvement in the catalytic performance of the modified photocatalysts.

Seven synthetic organic dyes such as methylene blue, indigo carmine, crystal violet, basic yellow 2, acid red 94, congo red and acid green 1 are chosen for the study based on their applicability and chemical structure. The preliminary photocatalytic studies showed that sunlight, effective purging and the use of a photocatalyst is essential for the degradation of the dyes. The parameters such as pH, catalyst weight and dye concentration are optimized to achieve maximum photocatalytic degradation of the dyes. Different weight percent of aluminium fluoride and strontium silicate salts incorporated to ZnO, TiO₂ and BiOC1 photocatalysts showed that the photocatalytic degradation of the dyes can be achieved with less time compared to that obtained with bare photocatalysts. The photocatalytic degradation of dyes followed pseudo-first order kinetics by obeying Langmuir-Hinshelwood kinetic

model. The active participation of all the reactive species such as electrons, holes, hydroxyl and superoxide anion radicals are evaluated using suitable scavengers. The destruction of the chromophoric groups in the dyes are confirmed from the UV-Visible spectroscopic studies and the extent of mineralization of the dyes are understood from total organic carbon content analysis of the dye solution before and after the photocatalytic treatment. Among the aluminium fluoride and strontium silicate modified ZnO, TiO₂ and BiOCl photocatalysts, the AlF₃ modified photocatalysts showed faster degradation for all the dyes. The reusability of the AlF₃ modified ZnO, TiO2 and BiOCl semiconductors confirmed the photostability of the catalysts and hence a composite of AlF3 modified ZnO, TiO2 and BiOCl photocatalysts is prepared and utilized for the photocatalytic treatment of the effluent. The physico-chemical analysis of the effluent before and after the photocatalytic treatment showed that the composite photocatalyst is effective in the removal of colour as well as a significant reduction in the level of contamination is also analyzed. Further the antimicrobial studies carried out with the 2wt%AlF₃-ZnO/1wt%AlF₃-TiO₂/3wt%AlF₃-BiOCl photocatalyst against various microorganisms revealed that the composite has potential photocatalytic disinfection properties.

CHAPTER - I

Introduction

CHAPTER - I

INTRODUCTION

1.1. WATER POLLUTION

Access to clean and safe drinking water is one of the prime necessities in our day to day life. Even though there are many sources of water bodies, the percentage of freshwater available on the earth is only 2.5%, and the remaining 97.5% is saline water^{1, 2}. Due to the overgrowth in population and the industrial revolution, a large amount of water is being utilized from rivers, lakes and underground reservoirs to meet the demands of common people. Apart from this, the dumping of garbage, sewage and liquid wastes from households, industrial sectors and agricultural fields pollutes the water bodies. This water pollution affects the life of aquatic plants and animals and is also the primary reason for several health issues for people across the globe. The World Health Organization and United Nations Department of Economic and Social Affairs report says, that around 900 million people do not have access to clean drinking water and about 2.6 billion, almost half the population of the developing world do not have access to adequate sanitation^{3,4}. Due to the consumption of contaminated waters and seafood, around 1.8 million people die annually from diarrheal diseases^{5,6}. A significant impact of water-borne diseases is on child mortality. Around 105 million children under 5 years die each year due to water-borne diseases resulting in the loss of two hundred million man-hours a day every year^{7,8}. Hence, freshwater is one of the critical resources in the world which should be managed appropriately, efficiently utilized and recycled for the sustainability of human life.

1.2. WATER POLLUTION FROM DYEING INDUSTRIES

The use of synthetic chemical dyes in various industrial processes, including paper and pulp manufacturing, plastics, cloth dyeing, leather treatment and printing, has increased considerably over the last few decades. It is estimated that over 10,000 different dyes and pigments are used industrially, and over 7×10^5 tons of synthetic dyes are annually produced worldwide⁹. In addition, the increased demand for textile products, the proportional increase in their production, and the use of synthetic dyes have contributed to dye wastewater becoming one of the substantial sources of severe water pollution problems in current times.

1.3. DYES AND THEIR CLASSIFICATION

A dye is usually a coloured organic compound used to impart colour to a substrate, but all the coloured substances are not dyes. According to Witt's theory, a dye is made up of two parts, namely chromophores and auxochromes. The colour usually appears in an organic compound if it possesses certain unsaturated groups (such as -N=N, C=S, C=C, C=O, N=O, etc.) called chromophores. Auxochromes are specific groups (such as -NH₂, -COOH, -OH, SO₃H, Cl, -CN, -OCH₃, -CONH₂ etc.) that increase the intensity of the colour of an organic compound and make this organic compound a dye by fixing it to the fabric of the material to be dyed either by association or salt formation. The fixing of the dye to the fibre is generally due to the formation of a chemical bond between the fibre and the auxochrome¹⁰.

The dyeing method varies depending upon the structure of dyes, nature of fibres, and physical properties such as solubility; and hence, one single fabrication method cannot be adopted for all the classes of dyes. Thus, dyes can be classified based on the mode of application.

Many of the dyes are prepared well in advance, after which they can be applied to the fibres, whereas some of them can be prepared in the fibre itself. The dyes developed on the cellulosic material itself are called developed or ingrain dyes. Some dyes can be made readily available for use. They may be either water-soluble or water-insoluble dyes.

The water-insoluble dyes are the ones that cannot be directly applied to the cellulosic fibres. These dyes are first reduced in an alkaline medium. On reduction, they split into simpler molecules that are water-soluble and then the cellulosic fibres are impregnated in the solution for which they show affinity. These types of dyes are mainly used for cotton and cellulosic fibres; they cannot be applied to wool and silk because the fibres get damaged in an alkaline medium. Some of the water-insoluble dyes are Vat dyes, Solubilized vat dyes, Sulphur dyes and Sulphurised vat dyes.

Disperse dyes are another class of water-insoluble dyes that are finely grounded and dispersed in water using the suitable dispersing agent. The micro-fine dispersions are applied to the fibres either by using organic carriers or by high temperature and pressure. The nitro, azo, and anthraquinone dyes are the predominantly used disperse dyes.

The following are some of the water-soluble dyes which can be directly used for dyeing purposes.

Direct dyes- These dyes are generally soluble in water due to sulphonic acid groups. They are attached to the cellulosic fibres by hydrogen bonding.

Acid dyes- These dyes have some acidic groups like –SO₃H and phenolic – OH. These dyes are easily attached to protein fibres like wool and silk by ionic forces but have no affinity for cotton.

Basic dyes- These dyes are cationic in nature containing some basic groups like $-NH_2$, $-NR_2$ etc in their colour base. Like acid dyes, they also have a strong affinity towards protein fibres like silk and wool but have less affinity towards cellulosic fibres.

Reactive dyes- These dyes generally have a heterocyclic system containing – Cl, --NH₂, which chemically react with the hydroxyl groups of cellulose fibres by covalent bonds. Hence, these dyes are mainly used for cotton and cellulosic fibres^{11, 12}.

1.4. WATER CONSUMPTION IN TEXTILE DYEING INDUSTRIES

More than eighty per cent of the synthetic dyestuffs in India are used in the textile industry due to the high demand for polyester and cotton clothes¹³. The textile industry ranks among the top ten water-consuming industries globally. Large quantities of water are used in different stages of textile processing operations. The various stages of textile processes are shown below in a flow chart.

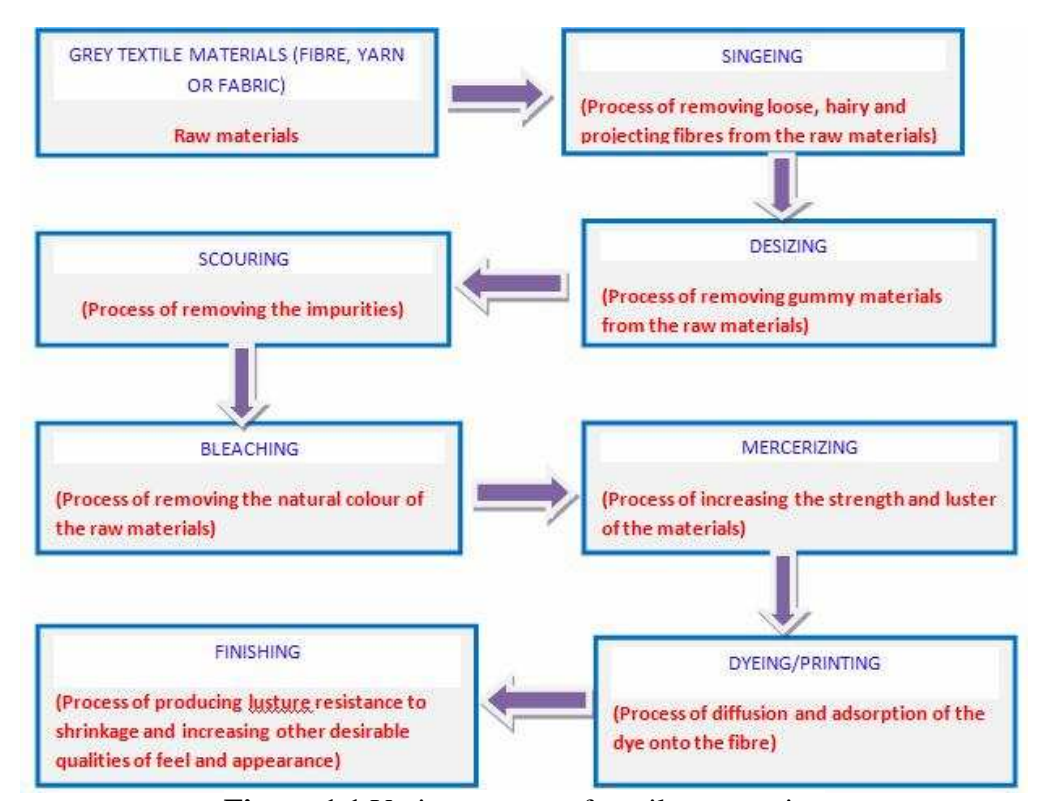


Figure 1.1 Various stages of textile processing

Water plays a significant role in almost all industrial sectors. A large amount of water is used in the pre-treatment processes of the textile dyeing industry, such as singeing, desizing, scouring, bleaching and mercerizing. Almost all the dyes and chemicals are applied to the fabrics from the water bath. Depending upon the type of the fabric, nature of the dyes, finishing agents, and the type of processing machinery used, the amount of water consumption also varies. The average quantity of water required for dyeing various types of fabrics is shown in the following table.

Table 1.1 Water requirement (L/per Kg) for dyeing of different types of fabrics

TYPES OF FABRICS	AVERAGE AMOUNT OF WATER REQUIRED FOR DYEING PROCESS (L/PER KG OF FABRIC)
Cotton	10,000-30,000
Wool	16,000-22,000
Rayon	17,000-34,000
Acetate	34,000-50,000
Nylon	17,000-34,000
Acrylic	17,000-34,000

In the 1980s, the water required for processing one kilogram of cloth was 226.5 litres, and in 2000, it was around 145 litres, respectively. For dyeing purposes, the average water requirement was 175 litres per kilogram of cloth in a small to medium industry, and it was around 120 litres per kilogram of cloth in large industries; this is attributed to the advancement in technology¹⁴. However, due to the inefficient dyeing process, the loss of dyes to the environment is around 10-50% and

each litre of wastewater generated further pollutes around 5-8 litres of freshwater sources, and this polluted water is very rarely used by the industries¹⁵⁻¹⁷. Due to this environmental impact, the textile dyeing industry is estimated to consume more water than any other industry globally.

1.5. HARMFUL EFFECTS OF WATER POLLUTION TO THE ENVIRONMENT

The major problem in releasing the effluents into our environment is that they are highly carcinogenic in nature. These effluents contain dyes and other recalcitrant organic chemicals, metal salts, surfactants, chlorinated compounds, high fluctuating pH levels, and high chemical oxygen demand with suspended solids. This effluent discharge seriously affects the aesthetic quality and the transparency of the water bodies, decreasing the sunlight penetration and disturbing the photosynthetic activity of the aquatic plants¹⁸⁻²⁰. Further, the decrease in the photosynthetic activity may also lead to a reduced level of dissolved oxygen content, leading to a septic condition characterized by a foul odour and suspended solids. This pollution caused in the environment discourages camping, boating, and fishing, retards the development of a locality²¹⁻²³.

The disposal of the effluents into the nearby water bodies is undesirable, not only because of their colour but also because of the breakdown products that persist in the environment for an extended period. For example, the hydrolyzed reactive blue 19 dye has a half-life of approximately forty-six years^{24, 25}. Similarly, azo dyes are produced worldwide due to their cost-effectiveness and ease of synthesis. However, these azo dyes on reduction form 2-benzotriazole derivatives and aromatic amines, which are highly mutagenic in nature than the original dye²⁶⁻²⁹. Due to the toxic nature of the dyes and their reactive intermediates formed, the usual functioning of the

cells gets disturbed, which alters the physiological and biochemical mechanisms of mammals. Further, the workers in the textile, dyeing, printing, leather and food industries face several health issues such as asthma, nasal problems, rhinitis, allergic reactions and dermatitis^{30, 31}. The people living near the noyyal river basin in Tamil Nadu are highly affected due to the consumption of contaminated water³².

1.6. VARIOUS TREATMENT TECHNOLOGIES ADOPTED FOR THE REMEDIATION OF WASTEWATER

Due to the growth of industrialization, water scarcity problems are expected to grow, even in the regions now considered as water-rich areas. To address these issues, a tremendous amount of research is being conducted. Since the effluents released from the dyeing industries not only contain colorants but also a wide range of chemicals, a single water treatment technique may not be suitable to eliminate all the organic pollutants. The treatment of dyeing effluents is usually done in three stages the primary process, the secondary process, and then the tertiary treatment process is carried out.

1.6.1. Primary Treatment Process

In the primary treatment process larger suspended particles and coarse materials are removed by the following methods.

1.6.1.1. Equalization and Sedimentation

Different streams of effluents are collected in a holding tank and allowed to settle for a specific period of time. During this process of equalization majority of the solid particles settle down along with the heavy metals, and sedimentation is the process where the solid particles are allowed to settle by the force of gravity. Some amount of fibre and scum are also removed by this method.

1.6.1.2. Neutralization

During this process, the extreme pH values of the dye effluents are neutralized by adding lime. This process of neutralization is also carried out by mixing acidic waste with the alkaline waste generated in the treatment plant or from the nearby industries, which is considered the cheapest method.

1.6.1.3. Coagulation

Fine suspended impurities present in the textile effluent do not settle down quickly. Hence these particles are destabilized by the addition of chemicals. Then fine particles that are chemically coagulated tend to form more extensive floc-like materials removed by subsequent settling and filtrations. Most widely employed coagulants are potash alum, ferrous sulphate and ferrous chloride.

1.6.1.4. Floatation

In the floatation process, the fine suspended particles in the effluent are removed by applying air. The impurities are carried away by the air bubbles to the liquid surface, which are readily removed by the skimmers.

1.6.2. Secondary Treatment Processes

Soluble organic substances are removed only in the secondary treatment process, which employs microorganisms for the breakdown of complex organic molecules into simpler substances.

1.6.2.1. Activated sludge process

In the activated sludge process, the textile effluents after clarification are passed to the aeration tank where it is biodegraded with the help of microorganisms such as bacteria, fungi, protozoa, rotifers and sometimes nematodes.

1.6.2.2. Trickling filtration

In this process the organic compounds in the wastewater are oxidized to simpler substances by the metabolic activity of the bacterial slimes that are sprinkled over a bed of stones. After this filtration process the effluents are allowed to settle down and then it is discharged.

1.6.2.3. Aerated Lagoons

Aerated lagoons are the activated sludge units that operate without sludge return. Here, the microorganisms oxidise the organic compounds, and the floating aerators provide the necessary oxygen.

1.6.2.4. Oxidation ponds

The complex organic compounds in the wastewater are broken down into smaller substances with the help of microorganisms like bacteria. The algae release the oxygen required for the metabolic activity of the bacteria in the ponds, which, in turn, utilises the carbon dioxide supplied by the bacteria for its photosynthetic activity. Hence, a mutual symbiotic action is essential for the effective treatment of wastewater in the oxidation ponds.

1.6.2.5. Anaerobic digestion

Here, the liquid waste containing soluble organics is degraded to carbon dioxide, ammonia, methane, H_2S and organic acids by a combination of chemical precipitation and microbial treatment in the absence of air.

1.6.3. Tertiary Treatment Process

The aqueous salts, dissolved solids, metal ions and colourants from the textile wastewater are removed in the tertiary treatment processes.

1.6.3.1. Membrane Filtration

A membrane is usually a barrier that separates two phases from each other in a selective manner. The three basic principles of the membrane treatment process are adsorption, sieving and electrostatic phenomenon. The separation of the colloidal particles, dissolved salts and metal ions through the membrane depends upon the pore size. The movement of solid particles through the membrane is based upon different driving forces. There are equilibrium-based membrane processes such as (membrane distillation, forward osmosis, and liquid membranes) and non-equilibrium-based processes such as (microfiltration, ultrafiltration, nanofiltration, and reverse osmosis which is classified as a pressure-driven process) and electrodialysis (non-pressure driven process). The pressure-driven membranes that rely on the hydraulic pressure to achieve separation are most widely employed to treat wastewater³³⁻³⁶.

1.6.3.2. Ion Exchange Processes

An ion exchange membrane is a polymeric matrix with the ionic groups fixed to its polymeric backbone. The three different ionic exchange membranes are anionic, cationic, and bipolar ion-exchange membranes. The anionic exchange membranes are the ones that have positively charged groups such as $-NH^{3+}$, $-NRH^{2+}$, $-NR^2H^+$ and $-NR^{3+}$ attached to them, which allows the transport of anions through the membranes and rejects the cations. The cationic exchange membranes are the ones that have negatively charged groups such as $-SO^{3-}$, $-COO^-$ and $-PO_3^{2-}$ attached to them, which allows the transport of cations and rejects the anions. The combination of cationic and anionic exchange membranes is known as bipolar ion-exchange membranes. The process of selectively transferring cations and anions through the membranes upon applying an external electric current is the basis of electrodialysis. Desalination of

brackish water by electrodialysis and electrolytic production of chlorine and caustic soda are the two main processes where ion exchange membranes are made use^{37, 38}.

1.6.3.3. Adsorption process

Adsorption is a surface phenomenon; it refers to the accumulation of a substance at the interface between the two phases (solid-liquid interface or gas-solid interface) ³⁹. Activated carbons show great adsorption capacity in the treatment of polluted wastewater due to their unique characteristic features such as highly developed porosity and large surface area^{40, 41}. Powdered activated carbon is found to be an effective adsorbent in the treatment of polluted wastewater. However, the commercially available activated carbon's high cost and low regeneration have limited its use as an adsorbent⁴². In recent years much research has been focused onto the production of activated carbon from low cost and renewable precursors such as sugarcane bagasse⁴³, barley straw⁴⁴, cashew nut shell⁴⁵, potato peel⁴⁶, rice straw⁴⁷, coir pith⁴⁸, orange peel⁴⁹, sawdust ⁵⁰ and coconut shell⁵¹.

1.6.3.4. Electrolytic Process

Electrolysis is the process of breaking down the substances by applying an electric current. The chemical reaction takes place in an electrolytic bath which allows the transfer of ions between the electrodes; at the electrode, the cations are reduced, and the anions are oxidized⁵². Electrocoagulation/Flocculation is one of the electrolytic processes that involve the application of electric current to the electrodes. The electrolytic oxidation of the sacrificial electrode generates coagulating agents that neutralize the surface charge, destabilize the colloidal particles and break down the emulsion. The oxygen generated at the anode and the hydrogen generated at the

cathode gets adsorbed on colliding with the flakes, carrying the impurities in suspension to the top and thereby promoting the clarification of the effluents⁵³. Some of the metals that have been employed as electrodes include aluminium, iron, stainless steel and platinum^{54,55}. According to Xuejun et al., about 89.8% reduction in the chemical oxygen demand by electrochemical oxidation was achieved however; the cost of electricity consumption and the scarification of the electrodes were considered to be significant concerns throughout the study⁵⁶.

1.7. LIMITATIONS OF PREVIOUSLY ADOPTED WASTEWATER TREATMENT TECHNOLOGIES

In general, a combination of physical, chemical and biological methods is employed to treat the polluted wastewater. Each method has its own advantages and constraints regarding cost, efficiency and feasibility. Some of these limitations are discussed below.

The coagulation and flocculation process, which uses inorganic coagulants such as aluminium chloride, aluminium sulphate, and ferric sulphate, are found to be effective in treating textile effluents. However, the high residual aluminium concentration in the sludge can lead to the development of Alzheimer's disease and senile dementia⁵⁷. It is also difficult to control the rate of precipitation and the size of the floc that is affected by the impurities such as non-ionic detergents, and the higher concentration of oxidizing or reducing agents disturbs the flocculation process further; these chemicals need to be neutralized before discharge⁵⁸. The membrane bioreactors, which are a combination of the membrane and biological processes, have wide applications in the treatment of polluted water. The main advantage of membrane processes is that it does not involve the use of any chemicals. However, the dissolved solids cannot be

separated by this method, and after prolonged exposures, fouling occurs with the clogging of the pores of the membranes; therefore, the quality of discharge water from the membrane also decreases, leading to high running costs and maintenances⁵⁹. The application of microorganisms for the biodegradation of organic pollutants is found to be simple, attractive and well accepted by the public. However, proper maintenance and management of the microorganism remain a time consuming and cost-intensive process. The biological treatment processes such as aerobic oxidation are found to be ineffective in degrading the azoic dyes.

In contrast, in the anaerobic treatment processes, the azo compounds get transformed into aromatic amines, which persist in the environment for an extended period of time. Thus, the incomplete destruction of organic compounds by the biological treatment process has led to the idea of transferring the pollutants onto the biomass-derived carbon by the adsorption process⁶⁰⁻⁶². The powdered activated carbon, which acts as an efficient adsorbent for removing a wide range of environmental pollutants, also has certain disadvantages. It causes turbidity in the treated water, difficult separation, cost-intensive regeneration, and secondary pollutants generation, which has limited its use⁶³. Thus, in most of the treatment methods adopted for wastewater remediation, the pollutants are not entirely eliminated from the effluents. They are either transferred from one phase to another and in many cases, the dyes are just adsorbed on the sludge and not degraded due to their recalcitrant nature, which is a source of secondary pollutants and requires further treatment. Hence, many researchers have concentrated on developing low-cost, robust and effective processes that could degrade the pollutants from the wastewater. In recent years, researchers have identified advanced oxidation processes as the most promising method for removing organic pollutants, which are bio-recalcitrant and are not treatable by conventional techniques.

1.8. ADVANCED OXIDATION PROCESSES

In the 1980s, advanced oxidation processes were first proposed only for the treatment of portable water⁶⁴ later; it was extended for the treatment of different wastewaters because the solid oxidising species such as hydroxyl radicals and superoxide anion radicals involved in the reaction were found to be capable of degrading the recalcitrant organic pollutants into more straightforward non-toxic end products. The efficiency of advanced oxidation processes depends on the generation of reactive free radicals such as hydroxyl radicals (OH), hydroperoxyl radicals (HO₂·), superoxide radicals (O₂··), alkoxyl radicals (RO·), among which the hydroxyl radicals play a vital role in the treatment of wastewater due to its high oxidation potential (2.8V versus standard hydrogen electrode), non-selective nature, highly reactive that it can oxidise and decompose various hazardous organic compounds into carbon dioxide and inorganic ions⁶⁵⁻⁶⁸. Some of the advanced oxidation processes are discussed below

1.8.1. Photochemical oxidation processes

In this photochemical oxidation process, the UV light (λ =254nm) is used as a source along with some oxidants such as hydrogen peroxide, ozone, a combination of hydrogen peroxide and ozone to initiate the generation of reactive free radicals to oxidize the organic pollutants⁶⁹. Some of the key reactions involved in these photo-oxidation processes are listed below

i. UV/ Ozone process:

$$O_3 + H_2O + hv \rightarrow O_2 + H_2O_2$$
 eq.(1.1)

ii. UV/H_2O_2 process:

$$H_2O_2 + hv \rightarrow 2HO$$
 eq.(1.2)

iii. UV/O₃/H₂O₂ process:

$$O_3 + H_2O + hv \rightarrow O_2 + H_2O_2$$
 eq.(1.3)

$$H_2O_2 + hv \rightarrow OH + OH$$
 eq.(1.4)

iv. UV/HOCl process:

$$HOCl + hv \rightarrow \cdot OH + Cl \cdot \dots eq.(1.5)$$

v. Photo-Fenton process:

$$H_2O_2 + Fe^{3+} \rightarrow Fe^{2+} + \cdot OH + OH^-$$
 eq.(1.6)

$$Fe^{2+} + H_2O + hv \rightarrow Fe^{3+} + \cdot OH + H^+$$
 eq.(1.7)

1.8.2. Wet Oxidation Processes

The wet oxidation processes are employed to treat wastewaters and sludge with a chemical oxygen demand level between 5-200 g L⁻¹. Typically, the wet oxidation processes operate at a temperature ranging between 90°C to even 600°C. The degree of oxidation depends on the temperature, pressure and operating time. Hence higher the operating temperature, the higher is the extent of oxidation achieved⁷⁰. Some of the wet oxidation processes and their operating conditions are discussed below.

1.8.2.1. Wet Peroxide Oxidation Process

Wet peroxide oxidation is similar to that of the fenton reaction, but the removal of total organic carbon can be achieved more efficiently due to the high operating temperature above 100°C with a pressure of 3-5 bars. The typical catalyst employed in the reaction is iron recently; copper⁷¹ and activated carbon⁷² are also found to be successful.

1.8.2.2. Wet Air Oxidation and Catalytic Wet Air Oxidation Process

The wet air oxidation process uses oxygen-containing gases such as air or molecular oxygen to oxidize the pollutants in the liquid phase operating at a temperature range between 125-320°C and pressure of 5-200 bars. In catalytic wet air oxidation, a homogenous or heterogeneous catalyst is employed to achieve the oxidation at much higher rates at lower temperatures (130-250°C) and with a pressure of 20-50 bars. Noble metal catalysts such as doped-ceria supported platinum and ruthenium are found to be more effective in oxidizing the organic pollutants⁷³.

1.8.2.3. Supercritical Wet Air Oxidation Process

Supercritical wet air oxidation process operates at a temperature above 374°C and at a pressure of 221bar which is the critical point of water, therefore above this temperature the oxidizable organic compounds and oxygen can be mixed in a single homogeneous phase ⁷⁴⁻⁷⁶. Most of the organic compounds can be destructed while operating at a temperature between 400-500°C.

1.8.3. Electrochemical and Photo-Electrocatalytic Oxidation Processes

The electrochemical method used in wastewater treatment mainly focuses on anodic oxidation. At the anode, the water molecules are oxidized, leading to the formation of free radicals, and at the cathode, hydrogen gas is evolved. Oxidation of water molecules leading to the generation of physisorbed active oxygen and adsorbed hydroxyl radicals are critical reactions. Electrochemical oxidation mediated by other electrogenerated oxidants such as S₂O₈²⁻, H₂O₂, Cl₂, HClO, ClO⁻, also leads to the decontamination of total organics. Similarly, photoelectrocatalysis is an emerging wastewater treatment technology in which titanium dioxide-based thin film anodes are irradiated under UV light. In this process, the photoinduced electrons are continuously

extracted from the anode by an external circuit, which causes the suppression of electron-hole recombination, and the photogenerated holes acquire a longer lifetime, promoting redox reactions. Chun et al⁷⁷ reported the photoelectrocatalytic degradation of formic acid using platinum doped titanium dioxide films. The experimental results revealed that 73.4% of COD removal of formic acid was achieved using Pt-TiO₂ photoanodes. This enhancement in the photoelectrocatalytic activity is due to the suppression of recombination of photogenerated charge carriers. However, low absorption coefficient, low incident photon to charge efficiency at lower potentials, poor photocurrent stability and self oxidative deactivation of some photoanodic materials are the key issues that need to be addressed in the photoelectrocatalytic processes.

1.8.4. Photocatalysis

Photocatalysis is when light and catalyst are used simultaneously to speed up a chemical reaction. On the other hand, it can also be defined as the "catalysis driven acceleration of a light-induced reaction." An Italian photochemist Giacomo Luigi Ciamician was the first person to conduct experimental studies to understand the fact that light and light alone would enable chemical reactions. Upon carrying out experiments under blue and red light, he found that the chemical effect took place only under the blue light, and he was also able to conclude that the acceleration of the reaction did not occur by thermal heating induced by light. The first occurance of the keyword "Photocatalysis" appeared in the scientific literature in the year 1911 when scientists discovered the bleaching of Prussian blue pigment by zinc oxide under illumination. Later on the researchers began to explore the potential use of zinc oxide as a photocatalyst and continuous efforts have been made by them wherein

the subsequent findings by the researchers such as reduction of $Ag^{\scriptscriptstyle +}$ to $Ag^{\scriptscriptstyle 80}$ in the year 1924, photocatalytic reduction of AuCl₃ to Au, AgNO₃ to Ag⁸¹ by TiO₂ and Nb₂O₅ in the year 1932, bleaching of dyes⁸² using TiO₂ as photosensitizer in the presence of O₂ in the year 1938, photo-oxidation of isopropanol⁸³ by zinc oxide and titanium dioxide was also reported in the year 1964. However, a breakthrough in the field of photocatalysis occurred in the year 1972 when Akira Fujishima and Kenichi Honda reported the remarkable discovery of photocatalytic water splitting reaction using TiO₂ electrodes under UV light irradiation⁸⁴ which later on paved an onset for the investigation of large number of photo-induced redox reactions on different semiconductor surfaces. In the year 1977, Frank and Bard experimented with the heterogeneous photocatalytic oxidation of cyanide and sulphate ions⁸⁵ using different semiconductor metal oxides and metal sulphide such as zinc oxide, titanium dioxide, iron oxide, cadmium sulphide and tungsten trioxide. Following this Ollis reported the TiO₂ catalyzed photodegradation of chlorinated organic compounds⁸⁶ and the photochemical sterilization of microorganism using platinum loaded titanium dioxide catalyst⁸⁷ was reported by Matsunaga et al., in the year 1985. Soon it was realized by scientists that such semiconductor mediated light induced reactions can be employed to solve environmental related issues such as photodegradation of toxic pollutants, microorganisms, CO₂ reduction, selective organic transformations etc. Thus, both the societal and technological importance of photocatalytic technology has increased over the past few decades.

1.8.4.1. Advantages and Disadvantages of photocatalysis

The release of the wide spectrum of pollutants into our environment by the growing industrial revolution has deteriorated the quality of water bodies and thereby

the health and living standards of the people. The need for environmental cleanup in order to maintain the earth's ecological balance has increased considerably over the past few decades. Among many advanced oxidation processes, heterogeneous photocatalysis is a unique process that has the potential to make use of the sunlight and semiconductor metal oxides to degrade the toxic organic pollutants and microorganisms from the contaminated water bodies. Some of the significant advantages⁸⁸ of the photocatalytic technology over other competing processes are as follows

- Complete mineralization of the toxic organic pollutants
- No harmful by-product generation and thus no waste disposal problems
- Cost-effectiveness
- Reactions can be performed at ambient temperature and pressure
- It is possible to reduce the concentration of the pollutants to ppm/ppb levels
- Utilizes the solar, visible and UV light as an economical source of energy
- The process does not require any expensive oxidizing chemicals
- The semiconductor photocatalysts can be recycled and reused

Though the photocatalytic process has several advantages over other advanced oxidation technologies, the full-scale commercialization of the technology for the environment-related issues is still underway due to some technical barriers⁸⁹ such as

- Post recovery of the semiconductor particles after the photocatalytic process is tedious.
- Low usage of visible light from the solar spectrum by the semiconductor materials.
- Fast charge recombination rates of photo-induced electrons and holes.

- The semiconductor photocatalysts with high band energy values require more energy to be absorbed to deliver charge carrier separation.
- The active surface sites of the photocatalyst may get deactivated or poisoned by interaction with the intermediate products.
- The presence of any natural scavengers can impair the photocatalytic efficiency by interactions with photogenerated reactive oxygen species.

Hence, in order to overcome these limitations various strategies have been designed by the researchers to obtain modified catalysts with high photocatalytic efficiencies.

1.8.4.2. General mechanism of semiconductor photocatalysis

Irradiation of a photocatalyst with a photon of energy greater than or equal to the band gap energy value promotes the electron from the valence band to the conduction band of the photocatalyst leaving behind the holes. The electrons and holes generated during the photo-excitation process undergoe numerous redox reactions, which are discussed below.

1. Excitation:

Semiconductor
$$\xrightarrow{h\nu} e^- + h^+$$
 eq.(1.8)

These generated electrons and holes migrate to the surface of the semiconductor photocatalyst and induce oxidation-reduction reactions.

2. Reduction of dissolved oxygen by photogenerated electrons leading to the formation of hydroxyl and superoxide anion radicals

$$O_2 + e^{-} \rightarrow O_2$$
 eq.(1.9)

$$O_2$$
 + $H^+ \rightarrow HO_2$ eq.(1.10)

 Oxidation of adsorbed water molecules by photogenerated holes leading to the formation of hydroxyl radicals.

$$H_2O \rightarrow H^+ + {}^-OH$$
 eq.(1.13)

$$h^{+} + OH \rightarrow OH$$
 eq.(1.14)

4. The generated hydroxyl radicals are highly reactive species which can oxidize most of the organic species in the water to form carbon-di-oxide, water and mineral acids.

$$R-H + OH \rightarrow R' + H_2$$
 eq.(1.15)

$$R^+ + h^+ \rightarrow R^{-+} \rightarrow \text{degraded products } (CO_2 + H_2O + \text{mineral acids}) \dots \text{ eq.} (1.16)$$

5. The photogenerated electrons and holes may undergo the recombination process and dissipate energy in the form of heat.

$$e^{-}+h^{+} \rightarrow Semiconductor + energy$$
 eq.(1.17)

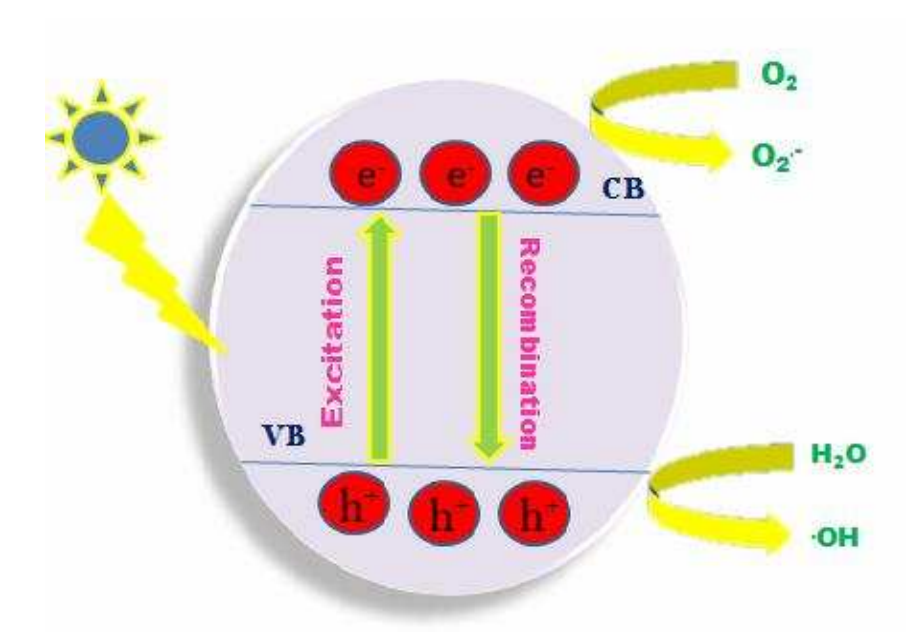


Figure 1.2 Photocatalytic mechanism involved with bare semiconductors

Hence, the general photocatalytic dye degradation mechanism using a single semiconductor photocatalyst involves five different steps such as (1) Diffusion of the organic pollutants from the bulk liquid phase to the surface of the semiconductor photocatalyst (2) Adsorption of the pollutants onto the surface of the photocatalyst (3) Generation of hydroxyl, superoxide anion radicals followed by redox reactions and degradation of the pollutants (4) Desorption of the intermediates or the mineralized products from the surface of the semiconductor photocatalyst (5) Diffusion of the end products to the bulk liquid phase. However, in a single semiconductor photocatalytic system, the recombination of the electron-hole pairs takes place at a faster rate such that the generation of the highly reactive species such as hydroxyl and superoxide anion radical generation is hindered. So, for an efficient photocatalytic dye degradation process, the recombination rate of the charge carriers must be suppressed, which can be achieved by either coupling two semiconductors, surface functionalization by metallic or non-metallic doping, modification of the photocatalyst dye sensitization and by preparing composites such as Carbon nanotube, carbon dots, graphene or clay loaded metal oxides.

The mechanism that operates for the modified catalysts is based on the construction of heterojunctions. A heterojunction is the interface formed between two semiconductors with unequal band structures which can form band alignments⁹⁰. The conventional heterojunction includes straddling bandgap structure, staggered bandgap structure and broken bandgap structure. In the straddling type heterojunction (type I), the energy band gap of semiconductor A is wider than that of semiconductor B thus the electron and holes get accumulated in the semiconductor B alone and hence there is a possibility of recombination of charge carriers resulting in a lower redox

potential. In staggered type heterojunction (type II), the valence band and conduction band of semiconductor A are higher and lower than that semiconductor B. Thus, the photogenerated electrons will migrate from the conduction band of semiconductor A to that of B and the photogenerated holes will migrate from the valence band of semiconductor B to that of semiconductor A. Thus, spatial separation of the charge carriers occurs making the redox reactions possible. However, in type(III) broken band gap heterojunction, the gap between the two semiconductors A and B is so wide in such a way that the overlapping of the two semiconductors become impossible and hence the transfer or migration of the charge carriers from one semiconductor to another is not possible. In an overall view, the type (II) heterojunction is more effective compared to type(I) and type (III) heterojunctions for improving the photocatalysis performance of the photocatalysts.

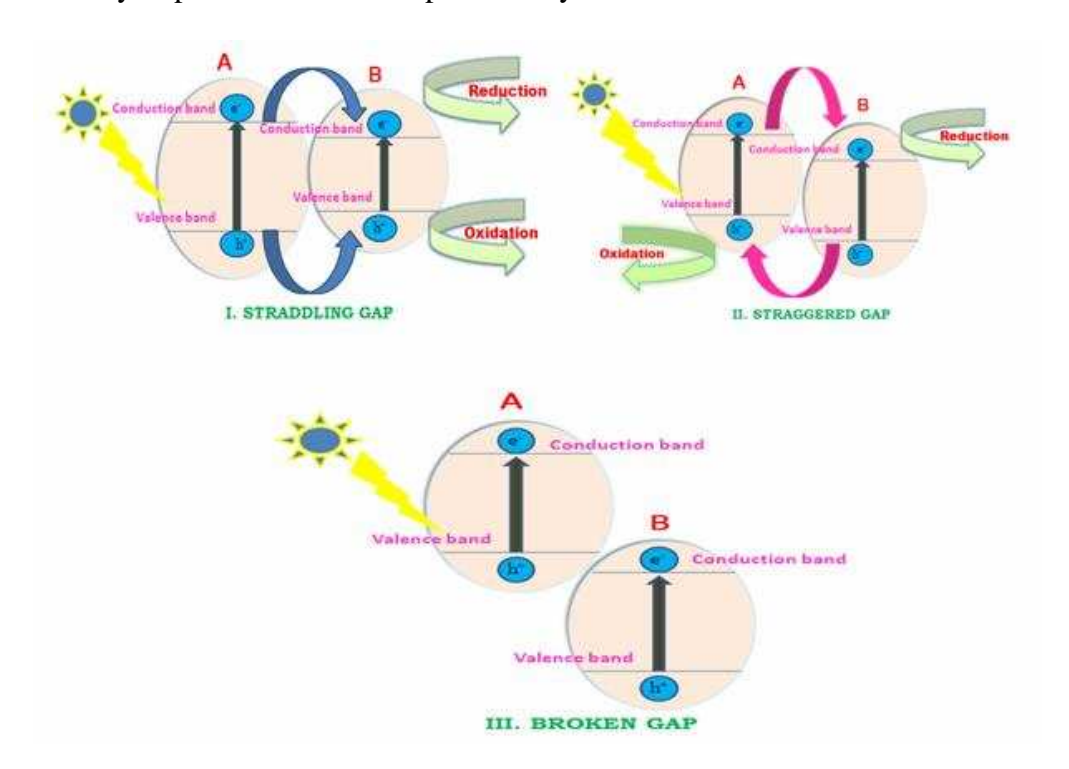


Figure 1.3 Photocatalytic mechanism operating in heterojunction type semiconductors

Although spatial separation of electron-hole pairs is possible in the staggered (type II) heterojunction, there are some limitations that hinder the photocatalytic ability, such as the suppression of the electron-hole migration by electrostatic repulsion and a relatively weaker redox ability is observed due to the lower oxidation and reduction potentials. In order to overcome these limitations, many new heterojunction photocatalysts have been developed by researchers. Some of them are the p-n heterojunction which is obtained by coupling a p-type semiconductor with an n-type semiconductor with an internal electric field. Due to the presence of an internal electric field, the photogenerated electrons move to the conduction band of the n-type semiconductor and the photogenerated holes transfer to the valence band of the p-type semiconductor, making the spatial of charge carriers much more effective⁹¹. The surface sensitizationis created between the two crystal facets of a semiconductor in order to improve the photocatalytic efficiency which is also cost-effective compared to other semiconductor heterojunctions⁹². The dye photosensitization is a process where the light is absorbed by the dye molecule, and the dye becomes the photosensitizer after which the electron is transferred from the highest occupied molecular orbital to the lowest unoccupied molecular orbital and subsequently to the conduction band of the photocatalyst and the dye sensitizer becomes the cationic radical. The valence band of the photocatalyst is unaffected during the course of the reaction⁹³. Doping is a process of modification of the semiconductor photocatalyst with metals or non-metals which produces new trapping sites for the photogenerated electrons and holes. Doping also leads to an improvement in the optical response of the photocatalyst⁹⁴. The Z-Scheme heterojunction is constructed with two semiconductor photocatalysts with an electron acceptor/donor species. Here, the migration of electron-hole pair takes place from one semiconductor to another through the electron mediator; thus, effective separation of charge carriers is achieved⁹⁵. The carbon/semiconductor heterojunctionis constructed by coupling the carbonaceous materials such as CNTs, graphene, carbon dots etc. with metal oxide photocatalyst. The ultrahigh electron conductivity, high specific surface area, the good mechanical strength of graphene and the intriguing optoelectronic properties and low toxicity level of carbon nanotubes makes them more suitable in combining with other semiconductors. Apart from inorganic materials, organic polymers such as polyaniline and polyethylene glycol have also been coated with the semiconductor metal oxides to improve the photocatalytic activity⁹⁶.

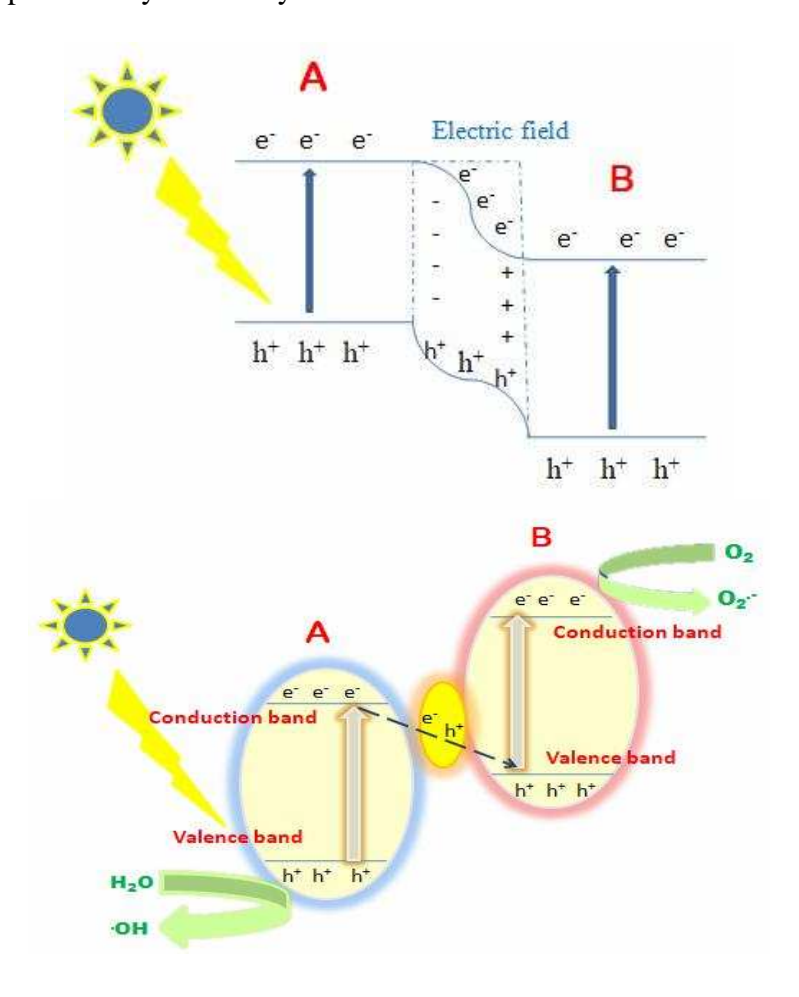


Figure 1.4 Photocatalytic mechanisms operating in p-n heterojunction and z-scheme photocatalysis

1.9. Semiconductor Photocatalysts

During the last ten decades, researchers have turned their attention toward the syntheses of semiconductor metal oxides for their photocatalytic and environmental applications. Among many semiconductor photocatalysts, zinc oxide and titanium dioxide photocatalysts are widely employed in the field of photocatalysis for the abatement of organic pollutants. Some of the interesting properties of zinc oxide material that make it suitable for photocatalytic applications are the low cost, nontoxic nature, thermal and chemical stability and its biocompatibility⁹⁷. Zinc oxide is an n-type semiconductor with a bandgap value of 3.37eV. Zinc oxide has three different phases namely the hexagonal wurtzite phase, zinc blende and rock salt phases. Out of which, only the hexagonal wurtzite phase is stable at room temperature, and hence zinc oxide catalyst in the hexagonal wurtzite phase is synthesized by a wide variety of techniques for photocatalytic applications. Even though both zinc-blende and wurtzite phases of zinc oxide material have tetrahedral geometry, the zinc blende phase of zinc oxide has covalent nature, whereas the wurtzite phase has both covalent and ionic character giving rise to high thermodynamic stability⁹⁸⁻¹⁰⁰. The wide bandgap of zinc oxide material can be tuned to increase its photocatalytic applications. Doping and other surface sensitization processes are employed for this purpose. Hence research is much focused in these years to prepare modified zinc oxide catalyst to increase its photocatalytic response.

Similar to zinc oxide, Titanium dioxide is also an n-type semiconductor with a bandgap of 3.2eV. It has three different phases such as anatase, rutile and brookite¹⁰¹. The phase transformation from the anatase to the rutile to brookite phase is achieved by increasing the temperature from 400 to 1000° C. Thus, the anatase phase of

titanium dioxide catalyst is not stable at higher temperatures. Degussa P-25 (73% anatase and 1% rutile phase), UV-100 (100% anatase) and PC-500 (100% anatase) are some of the well known commercially available titanium dioxide catalysts. Among the commercially available TiO₂ catalyst, Degussa P-25 is reported to be the most active catalyst¹⁰². Due to the non-toxic nature, low cost, size, shape-dependent optoelectronic properties, titanium dioxide catalyst is widely employed by the researchers for environmental remediation purposes.

In recent years bismuth-based materials such as bismuth vanadate, bismuth tungstate, bismuth oxides and bismuth oxyhalides (BiOX), X=Cl, F, Br, I have been investigated by the scientists to obtain a robust catalyst for the degradation of organic pollutants. Among these bismuth photocatalysts, bismuth oxyhalides and their modified forms are synthesized in large numbers due to their non-toxic nature and only a very few harmless reagents are required for its preparation. The Bismuth oxyhalide semiconductor materials have a tetragonal structure. The bismuth atom is surrounded by four oxygen atoms and four halogen atoms producing interlayered slabs of $[Bi_2O_2]^{2+}$ with negative halogen atoms surrounding it. The bismuth oxyfluoride photocatalyst has a bandgap of around 3.6eV and hence do not show any photocatalytic activity under visible light radiation. On the other hand, bismuth oxychloride have a bandgap value between 3.2-3.5 eV which is quite similar to that of zinc oxide and titanium dioxide photocatalysts and thus makes it a suitable photocatalyst for the destruction of dyes and other organic pollutants 103. The metal oxides such as WO₃, CeO₂, Fe₂O₃, CuO, SnO₂, ZrO₂ etc. have been commonly used as the main catalyst as well as co-catalyst for the photocatalytic dye degradation process. However, the metal sulphides and metal selenides are less employed for environmental remediation

due to their toxic and less stable nature. Though a wide variety of metal oxides are used as photocatalysts only a very few catalysts are reported to degrade a wide variety of pollutants¹⁰⁴. So, a semiconductor is said to be photochemically active only when the redox potential of the photogenerated holes is positive and the redox potential of photogenerated electrons is sufficiently negative to generate a superoxide anion radical. Another important property that makes a metal oxide a suitable semiconductor for photocatalytic applications is its bandgap values. Metal oxides with small bandgap values are preferably used as photocatalysts for the degradation of pollutants.

1.9.1. Different methods of synthesizing semiconductor photocatalysts

Semiconductor photocatalysts can be prepared by either the liquid phase method or solid-state method, or via the gas phase method. Some low cost and widely employed techniques adopted for the preparation of semiconductor photocatalysts are discussed below:

1.9.1.1. Sol-gel method: Sol-gel method is one of the wet chemical approaches employed for the synthesis of photocatalysts. In this technique, a precursor is dissolved in a suitable solvent which is later converted into a sol via hydrolysis or alcoholysis process. The formed sol gets transformed into gel after ageing. The obtained wet gelatin can be further thermally treated to obtain the nanopowders. The main advantage of this sol-gel technique is that the synthesis can be done without any special equipment. For example, sharmila devi et al¹⁰⁵ synthesized titanium dioxide nanoparticles vialed sol-gel technique using titanium isopropoxide as the precursor and obtained the TiO₂ nanoparticles by further hydrolysis and calcination process.

1.9.1.2. Precipitation method: In precipitation technique, the precursor salt is dissolved in a suitable solvent. A precipitating agent is added to obtain a precursor precipitate

which is further washed repeatedly with suitable solvent to remove the impurities and it is dried and calcined to obtain the crystalline nanomaterials. For example, Ghorbani et al¹⁰⁶ synthesized zinc oxide nanoparticles of particle size 30±15 nm by chemical precipitation technique using zinc nitrate as the precursor and potassium hydroxide as the precipitating agent.

- **1.9.1.3. Hydrothermal method:** This method provides an advantage of synthesizing single crystals from an aqueous solution of the mixed precursors and chemical reagents in an autoclave vessel that can be operated at a temperature of 600-700°C and at high pressures. For example, Manuja et al¹⁰⁷ synthesized molybdenum disulphide nanoparticles via hydrothermal technique and obtained fine particles of MoS₂ with a crystallite size of 5.5nm.
- **1.9.1.4.** Ultrasound and Microwave-assisted synthesis: Ultrasound or sonochemical technique which, uses a frequency range of 20 kHz to 10MHz, is used to accelerate a chemical reaction. When ultrasound passes through a solution, the growth, formation and implosive collapse of bubbles occurs in the solution. Since the collapse of the bubbles occurin less than a nanosecond, very high temperatures (5000-25000 K), pressure > 1000 atm, and cooling rates > 10⁹ K/s) are developed resulting in chemical reactions. For example, bismuth oxide nanoplates were synthesized by Martinez et al¹⁰⁸ by ultrasound-assisted chemical precipitation method. Microwave heating which operates at a frequency of 2.45GHz, has proved to be an efficient heating source for the production of nanomaterials. The size and shape of the nanoparticles can be controlled by fine tuning of the heating time and microwave power¹⁰⁹.
- **1.9.1.5. Ball milling method:** Ball milling is a top-down approach to synthesize the nanomaterials in the absence of a solvent. Here, a mechanical miller is used to reduce

the particle size and mix the particles into a new phase. The ball milling followed by thermal treatment gives the particles of nanosize. The kinetics of the reaction depends on the energy from the balls to the powder during the milling process and it is used for large scale production of nanomaterials. Numan salah et al¹¹⁰ synthesized nanosized zinc oxide particles from its microcrystalline powder by high energy ball milling technique.

1.9.1.6. Chemical vapour deposition: CVD is a well-known chemical method to produce thin films on a solid substrate by vapourizing the gaseous precursors at a high temperature and under vacuum condition. This technique is widely employed to produce two dimensional materials of uniform thickness and of high purity. Tran Manh Cuong et al¹¹¹ prepared Fe doped TiO₂ nanoparticles by the chemical vapour deposition technique. Another simple and effective technique to prepare the thin films includes the solution casting method in which the polymer is dissolved in a suitable solvent and the desired nanoparticles are added to the solution and finally, poured onto the suitable substrates such as glass or steel plates or to aluminium foil sheets and finally the solvent is evaporated by thermal treatment to obtain composite films. Cuilin et al¹¹² synthesized PLGA functionalized Multiwalled carbon nanotubes by solution casting technique.

Similarly, spray pyrolysis is a techniquethat can be utilized for the preparation of thin films by spraying a precursor salt solution using an atomizer to generate small droplets (aerosol) onto a heated surface and then decomposeto give the final product. Wallace et al¹¹³ synthesized zinc oxide photocatalyst by spray pyrolysis technique.

1.9.1.7. Physical vapour deposition techniques: PVD is a technique used to deposit thin films on a substrate by evaporating the solid substance under vacuum condition.

Organic as well as inorganic materials such as metals, metal oxides and alloys can be deposited by the physical vapour deposition technique. Some of the common physical vapour deposition techniques employed for depositing thin films include the sputtering process, electron beam evaporation technique, pulsed lase deposition technique, spin coating and dip coating technique^{114,115}.

1.9.2. Various Applications of Semiconductor Photocatalysts

Photocatalysis is one of the robust techniques that can be effectively utilized for solving major environmental issues such as air pollution, wastewater remediation, soil pollution etc. Since semiconductor photocatalysts potentially make use of the sunlight source, they are employed for a wide variety of applications.

1.9.2.1. Semiconductor Photocatalysts for the treatment of polluted air

Deterioriation in the quality of the air has alerted scientists and researchers to solve this issue by adopting various technologies. Ruixiang Li et al¹¹⁶ in their review article, threw a light on the photocatalytic efficiency of the titanium dioxide catalyst to treat the polluted air. When TiO₂ semiconductor photocatalyst is mixed with paints or concrete, it can oxidize NO to nitric acid. The formed nitric acid can react with the components of the photocatalyst surface to give nitrate ions which are washed away by the rainwater. Similarly, the photocatalytic degradation of formaldehyde in the air by TiO₂/diatomite composite and the degradation of toluene by bismuth loaded titanium dioxide photocatalyst reported in the literature showed that semiconductors and modified semiconductor photocatalysts are an effective alternative to treat the polluted air.

1.9.2.2. Semiconductor photocatalysts for the remediation of wastewater

Water being a vital source for all living beings, is continuously polluted by dumping a huge amount of chemicals, heavy metals and dyes from the textile, pharmaceutical and mining industries. Zinc oxide and titanium dioxide semiconductors are well-known photocatalysts for the treatment of polluted wastewaters. However, in recent years, the ZnO and TiO2 catalysts have been modified in many ways to improve their photocatalytic efficiency under sunlight. Je et al¹¹⁷ reported 96% degradation of Rhodamine B dye using carbon modified titanium dioxide microspheres and He et al 118 showed that manganese doped TiO₂ was useful for the treatment of tannery effluent. Both the studies confirmed that a faster degradation rate could be achieved using a modified semiconductor photocatalyst compared to bare catalysts. Similarly, bismuthbased compounds such as BiOBr microspheres 119 and BiOCl/Bi₂O₃ composites 120 are efficient in the removal of pharmacologically active compounds such as ibuprofen, ampicillin and oxytetracycline. With the view of the fatal health problems caused by the discharge of heavy metal ions from the metallurgical and mining industries, researchers have attempted to remove these toxic metals from the polluted water using semiconductor photocatalytic technology. Some of the modified semiconductor photocatalysts which are employed for the removal of the heavy metal ions¹²¹ include TiO₂-ZrO₂ coupled catalyst and Mn₃O₄/ZnO/Mn₃O₄ heterojunction for chromium ion reduction, TiO₂/Alg/FeNPs magnetic beads for the removal of Cr(III), Cu(II) and Pb(II) ions, Fe₂ O₃ /g-C₃N₄ nanocomposites and CuO/g-C₃N₄ heterostructures for Hg removal.

1.9.2.3. Semiconductor photocatalysts for hydrogen production

The clean, energy- efficient and abundant nature of hydrogen makes it an ideal source of fuel for the future. The hydrogen production via solar photocatalytic water

splitting reaction has gained much interest in the recent years. The main advantage of hydrogen production via solar photocatalytic water-splitting reaction is the ability to achieve separate hydrogen and oxygen evolution during the reaction and low process cost. It is reported that after modifying the semiconductor photocatalyst by metal loading and Z-scheme heterojunctions an improvement in the photocatalytic water splitting reaction is achieved due to the effect band gap tuning and separation of charge carriers¹²².

1.9.2.4. Semiconductor photocatalysts for N₂ and CO₂ reduction

The photoreduction of carbon dioxide into fuel sources such as carbon monoxide, methane and methanol can solve environmental related issues such as green house effect. Zhang et al¹²³ reported efficient photoreduction of CO₂ to CH₄ under a solar simulator using Bismuth oxylodide photocatalyst. The photoreduction of nitrogen to ammonia generally consumes a large amount of fossil fuels and releases CO₂ however in recent years; the use of semiconductor photocatalytic technology has become a green alternative. Li et al¹²⁴ reported the photocatalytic reduction of nitrogen to ammonia using Bismuth oxybromide nanosheets.

1.9.2.5. Semiconductor photocatalysts for solar cell applications

The ever increasing demand for energy and the depleting energy resources such as fossil fuels have stimulated researchers to seek for an alternate and green source of energy for today's world. The conversion of solar energy into electrical energy using semiconductor photocatalysts has gained much interest among the researchers. The first-generation solar cells based on the expensive silicon wafers are later replaced by semiconductor thin films which offer the advantage of cost-effectiveness. However the conversion efficiency is reported to be very low. Hence,

the modified semiconductors such as quantum dots/semiconductors, organic solar cells and dye-sensitized solar cells are in recent developments to achieve greater energy conversion efficiency^{125,126}.

1.9.2.6. Semiconductor photocatalysts for selective organic reactions

In recent years, semiconductor photocatalysts have been widely modified and utilized to obtain a high yield of industrially important organic compounds. Some selective organic transformations using semiconductor photocatalysts¹²⁷ include reduction of nitrobenzene to aniline using titanium dioxide photocatalyst, Ag loaded TiO₂ photocatalyst is used for the reduction of thio-organic compounds such as bis(2-dipyridyl)disulfide and also for the photo-oxidation of hydrogen sulphide, phenol is an important intermediate in the production of biphenyls, phenolic resins, salicylic acid can be obtained from the starting material benzene using Degussa P-25 TiO₂ photocatalyst.

1.9.2.7. Semiconductor photocatalysts for medical applications

Semiconductor materials capped with biocompatible polymers such as polyethylene glycol, polyaniline, polylactic acid and metals such as copper, silver, gold, zinc, titanium, and recently quantum dots are widely employed as antimicrobial agents as these materials are environmentally friendly due to their non-toxic nature¹²⁸.

1.9.2.8. Semiconductor photocatalysts for Energy and Electronics

The environmental impacts caused due to the emission of greenhouse gases and the use of fossil fuels made the researchers to search for an alternative energy source. Photovoltaic is one such interesting field more studied to efficiently convert and store the solar energy in the form of electrical or chemical energy. Recently, the role of two dimensional and three dimensional semiconductor photocatalysts for solar

fuel generation is highly probed by the researchers due to the simultaneous advantage of degradation of toxic organic pollutants and energy generation¹²⁹.

1.9.2.9. Semiconductor photocatalysts as sensors

In recent years more research is done to understand the applicability of semiconductor metal oxides as sensors. Metal oxides are mainly employed as gas sensors and they are also employed for humidity sensing, electrochemical as well as for biochemical sensing purposes¹³⁰. Sun et al¹³¹ described the application of g-C₃N₄ as a novel non-metal semiconductor-based sensor which is employed in electrochemical sensing of toxic metal ions and in floroscent sensing for the detection of glutathionine.

Some other areas where researchers studied the potential use of semiconductor metal oxides especially ZnO, TiO₂ and their modified forms include antifogging and self-cleaning purposes¹³², as a pigment in paints for indoor and outdoor cleaning, for removal of air pollutants such SO₂, NO₂ and volatile organic carbons¹³³ and they are also employed as composite films as well as surface coatings for food packaging and antimicrobial applications¹³⁴.

BIBLIOGRAPHY

- B.W. Eakins, G.F. Sharman, Volumes of the World's Oceans from ETOPO1, NOAA
 National Geophysical Data Center, Boulder. CO. (2010)
- 2. P.H. Gleick, Water in Crisis: Chapter 2, Oxford University Press (1993)
- 3. United Nations Department of Economic and Social Affairs. Millennium development goals report. United Nations Department of Economic and Social Affairs, New York; (2009)
- 4. WHO/UNICEF. Global Water supply and sanitation assessment report. Geneva and New York: WHO and UNICEF (2000)
- 5. D. Blum, R. Feachem, *International journal of epidemiology* **12** (1983) 357-365
- WHO. Guidelines for Laboratory and Field Testing of Mosquito Larvicides.
 WHO communicable disease control, prevention and eradication. WHO pesticide evaluation scheme (2005) WHO/CDS/WHOPES/GCDPP/2005.13
- 7. L.L. Fei, M.R. Rosenzweig, M.M. Pitt, *Journal of Econometrics***77** (1997) 209-235
- G. Sebastian, P. Gertler, E. Schargrodsky, *Journal of Political Economy*113 (2005) 83-120
- 9. T. Robinson, G. McMullan, R. Marchant, P. Nigam, *Bioresource Technology*77 (2001) 247-255
- 10. G. R. Chatwal, *Synthetic Dyes*. Himalaya Publishing House Pvt. Ltd. (2009)
- K. Venkataraman, Chemistry of synthetic dyes, Vol VI., Reactive dyes,
 ACADEMIC PRESS INC. London Limited. (1972) 52-5201

- 12. H.A. Lubs, The chemistry of synthetic dyes and pigments, REINHOLD PUBLISHING CORPORATION, Waverly Press Inc., Haltimore, Maryland, U.S.A. (1955) 54-12433
- 13. D.J. Naik, H.H. Desai, T.N. Desai, J. Environ. Res. Dev 7 (2013) 1602
- 14. P. Nelliyat, Industrial Growth and Environmental Degradation: A Case Study of Tiruppur Textile Cluster. WORKING PAPER 17/2007, MADRAS SCHOOL OF ECONOMICS, Chennai, Tamil Nadu (2007)
- 15. E. Forgacs, T. Cserháti, G. Oros, *Environment International* **30** (2004) 953-971
- 16. A.A. Vaidya, K.V. Datye, Colourage 14 (1982) 3-10
- 17. Centre for Science and Environment [CSE], 'Not a Non-Issue', *Down to Earth*12 (2004) 19
- 18. A. Shenoy, N. Ahsan, M. Shakeel, *Journal of Basic and Applied Engineering**Research 2 (2015) 678-684
- M.B. Ibrahim, N. Poonam, S. Datel, M. Roger, Bioresource Technology 58 (1996) 217-227
- S. Wijetunga, X.F. Li, C. Jian, Journal of Hazardous Materials 177 (2010)
 792-798
- 21. R.B. Chavan, *Indian journal of textile and fibre research* **26** (2001) 11-21
- W. Przystaś, E.Z. Godlewska, E.G. Sota, Water Air Soil Pollut 223 (2012)
 1581-1592
- 23. M.A. Hubbe, K.R. Beck, W.G. O'Neal, Y.C. Sharma, *Bio Resources* **7** (2012) 2592-2687
- 24. O.J. Hao, H. Kim, P.C. Chiang, Critical Reviews in Environmental Science and Technology **30** (2000) 449-505

- 25. P.I.M. Firmino, M.E.R. Silva, F.J. Cervantes, A.B. Santos, *Bioresource Technology* **101** (2010) 7773-7779
- T. Shiozawa, K. Suyama, K. Nakano, H. Nukaya, H. Sawanishi, A. Oguri, K.
 Wakabayashi, Y. Terao, *Mutation Research* 442 (1999) 105-111
- 27. K.T. Chung, C.E. Cerniglia, *Mutation Research***277** (1992) 201-220
- 28. P.A. Carneiro, G.A. Umbuzeiro, D.P. Oliveira, M.V.B. Zanoni, *Journal of Hazardous Materials* **174** (2010) 694-699
- F.M.D. Chequer, J.P.F. Angeli, E.R.A. Ferraz, M.S. Tsuboy, J.C. Marcarini,
 M.S. Mantovani, D.P. Oliveira, *Mutation Research* 676 (2009) 83-86
- 30. G.A. Umbuzeiro, H. Freeman, S.H. Warren, F. Kummrow, L.D. Claxton, Food and Chemical Toxicology 43 (2005) 49-56
- 31. V.M. Arlt, H. Glatt, E. Muckel, U. Pabel, B.L. Sorg, H.H. Schmeiser, D.H. Phillips, *Carcinogenesis* **23** (2002) 1937-1945
- 32. R.G. Elango, S. Elango, International Journal of Research in Chemistry and Environment **7** (2016) 17-22
- 33. A. Sagle, B. Freeman, B. Future Desalin. Tex **2** (2004)137
- 34. E.O. Ezugbe, S. Rathilal, *MEMBRANES* (2020)
- 35. C.Muro, F. Riera, D.C. Díaz, Membrane separation process in wastewater treatment of food industry. In Food Industrial Processes–Methods and Equipment; In Tech, Rijeka: Rijeka, Croatia, (2012) 253–280
- 36. R. Singh, N. Hankins, Emerging Membrane Technology for Sustainable Water Treatment; Elsevier: Amsterdam, The Netherlands (2016)
- 37. A. Hassanvand, K. Wei, S. Talebi, Q. George, I.D. Chen, S. E. Kentish, Membranes 7 (2017) 54

- 38. H. Smthmann, Makromol. Chem., Macromol. Symp 70 (1993) 363 -377
- 39. A. Dabrowski, Adv Colloid Interface Sci 93 (2001) 135
- 40. M. Asgher, H.N. Bhatti, *Ecol Eng* **38** (2012) 79–85
- 41. C.Y. Yin, M.K. Aroua, W.M.A. Daud, Separation and Purification Technology 52 (2007) 403-415
- 42. P. Bayer, E. Heuer, U. Karl, M. Finkel, Water Research 39(2005)1719–1728
- 43. E. Khoramzadeh, B. Nasernejad, R. Halladj, *J. Taiwan Inst. Chem. Eng.* 44 (2013) 266–269
- 44. E. Pehlivan, T. Altun, S. Parlayici, Food Chem. 135 (2012) 2229–2234
- 45. P.S. Kumar, S. Ramalingam, S.D. Kirupha, A. Murugesan, T. Vidhyadevi, S. Sivanesan, *Chem. Eng. J.***167** (2011) 122–131
- 46. T. Aman, A.A. Kazi, M.U. Sabri, Q. Bano, Colloids Surf. B: Biointerfaces 63 (2008) 116–121
- 47. Y. Ding, D. Jing, H. Gong, L. Zhou, X. Yang, *Bioresour. Technol.* **114** (2012) 20–25
- 48. C. Namasivayam, R. Radhika, S. Suba, *Waste Manag.* **21** (2001) 381–387
- 49. X.Y. Guo, S. Liang, Q.H. Tian, Adv. Mater. Res. 236 (2011) 237–240
- 50. P.K. Malik, *Dyes Pigments* **56** (2003) 239–249
- 51. M.G. Pillai, P. Simha, A. Gugalia, J. Environ. Chem. Eng. 2 (2014) 46–55
- A.K. Chopra, A.K. Sharma, V. Kumar, Archives of Applied Science Research
 3 (2011) 191-206
- 53. S.I. Chaturvedi, *International Journal of Modern Engineering Research* 3 (2013) 93-100
- 54. M.Y. Mollah, *J. Haz. Materials* **114** (2004) 199-210

- O. Sahu, B. Mazumdar, P.K. Chaudhari, *Environ. Sci. Pollut. Res.* 21(2014)
 2397–2413
- 56. X. Chen, Z. Shen, X. Zhu, Y. Fan, W. Wang, *Water* **31** (2003) 127-132
- 57. T.K.F.S. Freitas, V.M. Oliveira, M.T.F. De Souza, H.C.L. Geraldino, V.C. Almeida, S.L. Fávaro, J.C. Garcia, *Ind. Crops Prod.* **76** (2015) 538–544
- 58. C. Zahari, D. Suteu, A.Mureşan, *Environmental Engineering and Management Journal* **11** (2012) 493-509
- 59. M Amini, M. Arami, N.M. Mahmoodi, A. Akbari, *Desalination* **267** (2011) 107–113
- 60. M. Isik, D.T. Sponza, Separation and Purification Technology **60** (2008) 64-72
- 61. K.T. Chung, S.E. Stevens, *Environmental Toxicology and Chemistry* **12** (1993) 2121-2132
- 62. O. Gomaa, H. Kareem, R. Fatahy, *Biodegradation* **23** (2012) 243-251
- A. Ahmad, S.H.M. Setapar, C. Chuong, A. Khatoon, W.A. Wani, R. Kumar,
 M. Rafatullah, RSC Adv. 5 (2015) 30801–30818
- 64. W.H. Glaze, Environ Sci Technol. **21** (1987) 224–30
- 65. A. Gomes, E. Fernandes, J. Lima, J. Biochem. Biophys. Methods 65 (2005) 45–80
- 66. C. Tai, X.X. Gu, H. Zou, Q.H. Guo, *Talanta*, **58** (2002)661–667
- J.G. Montano, L. P'erez-Estrada, I. Oller, M.I. Maldonado, F. Torrades, J. Peral,
 J. Photochem. Photobiol. A: Chem., 195 (2008) 205–214
- 68. M. Pera-Titus, V. Garc´ıa-Molina, M.A. Banos, J. Gimenez, S. Esplugas, *Appl. Catal. B: Environ.*, **47** (2004) 219–256

- 69. R. Munter, Proceedings of the Estonian Academy of Sciences, Chemistry **50** (2001) 59-80
- 70. S.T. Kolaczkowski, P. Plucinski, F.J. Beltran, F.J. Rivas, D.B. Mc Lurgh, Chemical Engineering Journal 73 (1999) 143-160
- 71. S. Caudo, C. Genovese, S. Perathoner, G. Centi, *Microporous and Mesoporous Materials* **107** (2008) 46-57
- 72. H.T. Gomes, S.M. Miranda, M.J. Sampaio, A.M.T. Silva, J.L. Faria, *Catalysis Today* **151** (2010) 153–158
- 73. S. Keav, A. Martin, J. Barbier D. Duprez, *Catalysis Today* **151** (2010) 143–147
- 74. A. Heponiemi, L. Rahikka, U. Lassi, T. Kuokkanen, *Chemical Engineering Transactions* **17** (2009) 209-214
- 75. H. Debellefontaine, M. Chakchouk, J.N. Foussard, D. Tissot, P. Striolo, *Environmental Pollution* **92** (1996) 155-164
- 76. V.S. Mishra, V.V. Mahajani, J.B. Joshi, *Industrial & Engineering Chemistry Research* **34** (1995) 2-48
- 77. C. He, M.A. Asi, Y. Xiaong, D. Shu, X.Z. Li, International Journal of Photoenergy (2009) 7 pages, Article id 634369. https://doi.org/10.1155/2009/634369
- 78. A. Albini, M. Fagnoni, *Chem Sus Chem* **1** (2008) 63
- 79. A. Eibner, *Chem.-Ztg.* **35** (1911) 753-786
- 80. E. Baur, A. Perret, Helv. Chim. Acta 7 (1924) 910
- 81. C. Renz, Helv. Chim. Acta 15 (1932) 1077
- 82. C. Doodeve, J. Kitchener, Trans. Faraday Soc. 34 (1938) 902
- 83. V.N. Filimonov, *Dokl. Akad. Nauk SSSR.* **154** (1964) 922–925
- 84. A. Fujishima, K. Honda, *Nature* **238** (1972) 37–38

- 85. S.N. Frank, A.J. Bard, *J Phys Chem* **81** (1977) 1484–1488
- 86. C.Y. Hsiao, C.L. Lee, D. F. Ollis, *J Catal.* **82** (1983) 418–423
- 87. T. Matsunaga, R. Tomado, T. Nakajima, H. Wake, *FEMS Microbiol Lett* **29** (1985) 211–214
- 88. I. Khan, K. Saeed, N. Ali, I. Khan, B. Zhang, M. Sadiq, *Journal of Environmental Chemical Engineering***8** (2020) 104364
- 89. S.A. Younis, K.H. Kim, *Catalysts* **10** (2020) 1109
- J. Low, J. Yu, M. Jaroniec, S. Wageh, A.A. Al-Ghamdi, *Adv. Mater.* 29 (2017)
 1601694
- 91. W. Zhang, C. Hu, W. Zhai, Z.L. Wang, Y.X. Sun, F.L. Chi, S.L. Ran, X.G. Liu, Y.H. Lv, *Mat. Res.* **19** (2016) 673–679
- 92. Z.D. Wei, Y. Zhao, F.T. Fan, C. Li, Comp. Mater. Sci. 153 (2018) 28–35
- J. L. Wang, L.J. Xu, Critical Reviews in Environmental Science and Technology
 42 (2012) 251-325
- 94. F. Sayilkan, M. Asilturk, P. Tatar, Materials Research Bulletin 43 (2008) 127-134
- 95. H.J. Li, W.G. Tu, Y. Zhou, Z.G. Zou, Adv. Sci. 3 (2016) 12
- 96. R. Leary, A. Westwood, *Carbon* **49** (2011) 741–772
- 97. M. Vaseem, A. Umar, Y.B. Hahn, *Metal oxide nanostructures and their applications* Chapter 4, American Scientific Publishers (2010) 1-36
- 98. H. Morkoc, U. Ozgur, General Properties of ZnO, Zinc Oxide: Fundamentals, Materials and Device Technology, WILEY-VCH Verlag GmbH and Co., Weinheim, (2009) 1–76
- 99. A. Ashrafi, C. Jagadish, J. Appl. Phys. **102** (2007) 071101

- 100. C. Klingshirn, Fundamental Properties of ZnO nanostructures, Chem Phys Chem 8 (2007) 782–803.
- 101. K. Hashimoto, H. Irie, A Fujishima, J. Appl. Phys. 44 (2005) 8269–8285
- 102. M. Huang, J. Yu, B. Li, C. Deng, L. Wang, W. Wu, L. Dong, F. Zhang, M. Fan, J. Alloys Compd. 629 (2015) 55–61
- 103. R. He, S. Cao, P. Zhou, J. Yu, *Chin J Catal* **35** (2014a) 989–1007
- J.H. Pan, H. Dou, Z. Xiong, C. Xu, J. Ma, X. S. Zhao, J. Mater. Chem., 20
 (2010) 4512-4528
- 105. R.S. Devi, R.Venckatesh, R. Sivaraj, International Journal of Innovative

 Research in Science, Engineering and Technology 3 (2014)
- 106. H. R. Ghorbani, F.P. Mehr, H. Pazoki, B.M. Rahmani, *Oriental Journal of Chemistry* **31** (2015) 1219-1221
- 107. M. Manuja, V. Sarath Krishnan, Gijo Jose, *IOP Conf. Series: Materials Science and Engineering* **360** (2018) 012015
- D. Sánchez-Martínezn , I. Juárez-Ramírez, L.M. Torres-Martínez, I. de León-Abarte, Ceramics International, 42 (2016) 2013-20
- 109. E. Aivazoglou, E. Metaxa, E. Hristoforou, AIP Advances 8 (2017) 14 pages
- 110. N. Salah, S.S Habib, Z.H. Khan, A. Memic, A. Azam, E. Alarfaj, N. Zahed, Salim Al-Hamedi, *International Journal of Nanomedicine* **6** (2011) 863–869
- 111. T.M. Cuong, V.A. Tuana, D.T. Phuonga, T.T.K. Hoa, B.H. Linha, M. Anpo,

 Journal of Experimental Nanoscience 7 (2012) 42–52
- 112. C. Lin, Y. Wang, Y. Lai, W. Yang, F. Jiao, H. Zhang, S. Ye, Q. Zhang, *Colloids Surf. B: Biointerfaces* **83** (2011) 367–375

- 113. R. Wallace, A.P. Brown, R. Brydson, *Journal of Materials Science* **48** (2013) 6393 6403
- 114. S.S. Hamdi, *Eng. and Tech. Journal* **34** (2016)
- 115. T. Rohit, Sumit Vyas, K. Shubham, P. Chakrabarti, International conference on device, circuits and communication (2014) doi:10.1109/icdccom.2014. 7024703
- 116. R. Li, T. Li, Q. Zhou, Catalysts 10 (2020) 804
- L.J. Ji, X. Liu, T. Xu, M.D. Gong, S. Zhou, J. Sol Gel Sci. Technol. 93(2020)
 380–390
- X. He, X.C. Wang, B.Z. Cheng, S. Cao, J.F. Zhou, J. Soc. Leather Technol.
 Chem. 103 (2019) 318–322
- 119. H. Tian, Y. Fan, Y. Zhao, L. Liu, RSC Adv 25 (2014) 13061–13070
- B. Priya, P. Raizada, N. Singh, P. Thakut, P. Singh, *J Colloid Interface Sci.* 479 (2016)271–283
- G. Ren, H. Han, Y. Wang, S. Liu, J. Zhao, X. Meng, Z. Li, *Nanomaterials* 11 (2021) 1804
- 122. C.H. Liao, C.W. Huang, C. Jeffrey, S. Wu, Catalysts 2 (2012) 490-516
- 123. G. Zhang, A. Su, J. Qu, Y. Xu, *Mater Res Bull* **55** (2014) 43–47
- 124. H. Li, J. Shang, Z. Ai, L. Zhang, J Am Chem Soc 137 (2015a) 6393–6399
- S. Alhorani, S. Kumar, M. Genwa, P. L. Meena, AIP Conference Proceedings
 2265 (2020) 030632
- 126. M. Kouhnavard, S.Ikeda, N.A.Ludin, N.B.AhmadKhairudin, B.V.Ghaffari, M.A.Mat-Teridi, M.A.Ibrahim, S.Sepeai, K.Sopian, Renewable and Sustainable Energy Reviews 37 (2014) 397–407

- 127. S. Munir, D.D. Dionysiou, S.B. Khan, S.M. Shah, B. Adhikari, A. Shah,

 Journal of Photochemistry and Photobiology B:Biology 148 (2015) 209-222
- 128. X. Peng, Fujin Ai, Li Yan, Enna Ha, Xin Hu, S. He, J. Hu, *Cell Reports Physical Science* **2** (2021) 100436
- 129. S. Sfaelou, P. Lianos, AIMS Materials Science 3 (2016) 270-288
- D. Nunes, A. Pimentel, A. Gonçalves, S. Pereira, R. Branquinho, P. Barquinha,
 E. Fortunato, R. Martins, *Semicond. Sci. Technol.* (2019) in press
 https://doi.org/10.1088/1361-6641/ab011e.
- X. Sun, C. Wang, D. Su, G. Wang, Y. Zhong, Application of Photocatalytic
 Materials in Sensors, Adv. Mater. Technol. (2020) 1900993
- 132. S. Banerjeea, D.D. Dionysiou, C. Suresh Pillai, *Applied Catalysis B:*Environmental 176 (2015) 396–428
- 133. F. Salvadores, M. Reli, O.M. Alfano, Kamila Koc, M.M. Ballari, Frontiers in Chemistry, 8 (2020) 551710
- 134. V.K. Yemmireddy, Y.C. Hung, Comprehensive Reviews in Food Science and Food Safety **16** (2017) 617-63

CHAPTER - II

Review of Literature

CHAPTER - II

REVIEW OF LITERATURE

2.1. Heterogeneous Semiconductor Photocatalysis

In recent years, a considerable amount of research has been carried out to eliminate the micro-organisms, highly toxic and non-biodegradable pollutants from the wastewater by Advanced oxidation process^{1,2}. The advanced oxidation techniques include fenton reactions, photo-fenton like reactions, UV/Ozone, UV/H₂O₂, electrochemical oxidation and heterogeneous catalysis³⁻⁷. The driving force for all these advanced oxidation processes is the generation of reactive oxygen species such as hydroxyl and superoxide anion radicals that initiate the oxidation and reduction reactions⁸. The field of advanced oxidation technology has gained much interest among researchers and industrialists due to the advantages such as the destruction of the pollutants to harmless, biodegradable products, non-selective oxidizing power and the ability to destroy the pathogens in water^{9, 10}.

Among the several advanced oxidation technologies, heterogeneous semiconductor photocatalysis with metal oxides is the most widely reported one for environmental applications due to the possibility of making use of the solar irradiation and applying it to a large scale industrial process¹¹⁻¹³. Solar based photocatalytic technology should be effectively utilized to overcome industrial and environment-related issues. Solar energy, which is a green and sustainable source of energy, can be made use of by the researchers for photocatalytic oxidation of toxic organic pollutants by modifying and tuning the properties of the semiconductor photocatalysts^{14,15}. More often the semiconductor metal oxides are modified to tune its band gap and to achieve

higher photocatalytic efficiency. The recovery and reusability of these photocatalysts makes them suitable for the water treatment process^{16, 17}.

The field of photocatalysis flourished in the past decades because of the extensive research done to obtain low cost, modified semiconductor photocatalysts with high photocatalytic efficiency. Hence, a brief survey of literature is done to find out the photocatalytic efficiency of novel semiconductor metal oxides for the abatement of organic pollutants.

2.2. Semiconductor Photocatalysts for Degradation of Dyes

A wide range of oxide, sulphide, hydroxide and halide based semiconductors are employed for the photocatalytic treatment of dye solutions. Among many semiconductors, a large volume of research is carried out with metal oxide photocatalysts especially using ZnO and TiO₂ catalysts, owing to their stability, narrow bandgap, light absorption property, cost-effectiveness, eco-friendliness and suitable electronic structure having occupied valence band and unoccupied conduction band structures^{18, 19}. Hence, in order to understand the extent of photocatalytic efficiency of these semiconductors, a comprehensive review is done concentrating on the type of pollutants taken for the study, photocatalysts used, synthesis route adopted for the preparation of the photocatalyst, source of light, parameters optimized and finally the percentage degradation achieved.

Doina lutic et al²⁰ synthesized photo-catalytically active Zinc oxide by simple chemical precipitation method using two different precipitating agents such as urea and sodium hydroxide and compared its photocatalytic activity with that of Degussa P-25 titania catalyst. The synthesized zinc oxide photocatalysts were reported to show excellent photocatalytic activity in removing rhodamine 6G dye. The zinc oxide

photocatalyst prepared by the addition of urea gave 94.34% removal of rhodamine 6G dye at pH 10, 30 ppm dye concentration, at a catalyst concentration of 0.3g/L within 90 minutes and the zinc oxide photocatalyst prepared by the addition of sodium hydroxide gave 75.42% removal of rhodamine 6G dye under similar conditions.

Zinc oxide photocatalyst of large surface area of 233.249m²/g was synthesized by Soo-Keun Lee and coworkers²¹ by hydrothermal method using diethylene glycol as a stabilizer and polyethylene glycol 400 as a limiting agent for particle growth. The photocatalytic activity of the synthesized zinc oxide was tested against 0.01mM methylene blue dye solution under a UVB lamp source. The characteristic peak of methylene blue dye solution at 664nm disappeared within 150 minutes at a catalyst concentration of 0.5g/L.

Thangavelselvamani et al²² synthesized bismuth oxide polymorphs and evaluated the photocatalytic performance of the synthesized material for the degradation of four synthetic organic dyes such as rhodamine B, and methyl orange, methylene blue and acid orange 7 under simulated solar illumination. Bismuth oxide polymorphs showed excellent photocatalytic activity towards the degradation of rhodamine B and acid orange 7 dyes compared to methylene blue and methyl orange dyes. The kinetic studies revealed that the photocatalytic degradation of all the dyes followed pseudo first order kinetics, and the generation of hydroxyl radicals during the course of the reaction was confirmed by using terephthalic acid as a probe.

Ke Dai and coworkers²³ investigated the photocatalytic activity of mesoporous titania nanoparticles under UV irradiation. The BET surface area analysis of the synthesized titania nanoparticles was found to be $317.5 \text{ m}^2\text{g}^{-1}$, and the mean particle size of TiO_2 nanoparticles was reported to be 17.6 nm and the crystallite size

calculated from the XRD analysis was 3.1nm. They reported that 1g/L of mesoporous Titania nanoparticles was sufficient to mineralize around 98% of the methyl orange dye after 45 minutes of UV light illumination. The degradation pathway of the methyl orange dye was also discussed by them stating that the degradation proceeded through three intermedial processes such as demethylation, methylation and hydroxylation.

Azita Mohagheghian et al²⁴ reported the photocatalytic degradation of Acid Orange 7 (AO7) by tungsten trioxide nanopowder under UV irradiation. The XRD analysis confirmed the orthorhombic structure of WO₃, and the morphological studies such as SEM and TEM analysis showed that the synthesized tungsten trioxide nanoparticles are moderately spherical in shape with the particle size ranging from 23-65nm. The tungsten trioxide photocatalyst showed 87% removal of 10mg/L acid orange 7 dye solution at a catalyst concentration of 1g/L and pH=3. The use of other oxidizing agents such as hydrogen peroxide, oxalic acid and O₂ purging increased the dye removal efficiency.

A comparative photocatalytic study of six different metal oxides such as cerium oxide, copper oxide, nickel oxide, manganese oxide, tin oxide and zinc oxide was done by Lalitha Gnanasekaran²⁵ and coworkers. Among the six different metal oxides, Zinc oxide showed good photocatalytic activity towards the degradation of methylene blue and methyl orange dyes under UV light within 2 hours. The excellent photocatalytic activity of the zinc oxide photocatalyst was attributed to its small crystallite size and spherical shape. The zinc oxide photocatalyst showed good activity until five repeated cycles.

Surfactant assisted sol-gel method was adopted for the synthesis of TiO₂ photocatalyst²⁶. The HR-TEM analysis carried out by them showed that the synthesized

titanium dioxide nanoparticles are monodispersed, grain shaped with a size less than 10 nm, and from the XRD analysis it was found out that the TiO₂ nanoparticles are highly crystalline in nature and existed in two different phases such as anatase and brookite. The photocatalytic studies conducted by Soon Chang Lee and coworkers showed that the synthesized TiO₂ photocatalyst degraded two azo dyes, namely reactive black 5 and rhodamine B, after 2 hours of UV irradiation.

Photocatalytic activity of various semiconductors such as titanium dioxide (TiO₂), zinc oxide (ZnO), stannic oxide (SnO₂), zinc sulphide (ZnS) and cadmium sulphide (CdS) was evaluated by Kansal et al²⁷ for two commercial dyes such as methyl orange and rhodamine 6G. Among the different synthesized semiconductor photocatalysts, ZnO showed greater photocatalytic activity towards the degradation of methyl orange and rhodamine dyes under UV irradiation. Under UV irradiation 89% of COD reduction was achieved for methyl orange dye within 4 hours, and 75% of COD reduction was achieved for rhodamine dye within 3 hours.

Fahmida Parvin et al 28 investigated the photocatalytic properties of moderately spherical shaped iron oxide nanoparticles for the degradation of Procion blue dye and dissolved organic matter from textile wastewater. The diameter of the Fe₃O₄ nanoparticles ranged from 56-83 nm. About 91% reduction in the fluorescence intensity is reported for procion blue dye using iron oxide nanoparticles under solar irradiation within 40 hours. Similarly, Muhammad Munir Sajid et al 29 investigated the photocatalytic properties of vanadium pentoxide nanoparticles for the degradation of monoazo and diazo dyes. About 99% of methyl orange and congo red dye degradation is reported using vanadium pentoxide nanoparticles within 180 minutes under visible light radiation, which is ascribed to the high surface area and crystalline nature of the V_2O_5 nanoparticles.

Zhang et al³⁰ prepared titanium dioxide photocatalyst by sol-gel technique. An investigation into the photocatalytic activity showed 18% degradation of tetracycline hydrochloride under a 30 W lead emitting diode lamp. Solomon et al³¹ studied the photocatalytic efficiency of one dimensional Fe₃O₄ nanocatalyst. The pollutant chosen for the study was methyl red dye. Using 0.075g/L of nano Fe₃O₄ catalyst, about 50.55% of the methyl red dye degraded within 60 minutes under UV light. Zinc sulphide photocatalyst³² has a bandgap value of 3.6eV. Many researchers have synthesized zinc sulphide due to its non-toxic nature, and the catalyst is reported to show good photocatalytic activity. Jing-Song Hu et al³³ reported the excellent photocatalytic activity of spherical shaped ZnS nanocrystals of 60 nm in size. The zinc sulphide photocatalyst (10mg) degraded the eosin B (5x10⁻⁵M) dye under UV light within 47 minutes which was attributed to the high surface area of the photocatalyst. Copper oxide is one of the good semiconductor photocatalysts with exceptional electrical, mechanical and optical properties with a bandgap value of 1.2eV. Due to its non-toxic nature and easy fabrication process, CuO is employed in various fields 34-36 including electrode materials, gas sensors, semiconductor batteries etc. Scuderi et al³⁷ prepared CuO and Cu₂O nanowires by thermal oxidation of Cu foils and by thermal annealing method. Further investigation into its photocatalytic properties showed that CuO nanowires efficiently degraded the methyl orange dye compared to Cu₂O nanowires. A decreased photocatalytic activity observed in the case of Cu₂O catalyst is attributed to the structural defects.

Although semiconductor metal oxides offer the advantage of mild reaction conditions and the ability to degrade a wide range of dyes³⁸, it is understood from the literature review that some drawbacks that hold back semiconductor metal oxides,

from practical applications are the narrow light absorption ability and easy recombination of photogenerated electrons and holes during the photocatalytic reaction. Hence, in order to overcome this drawback and get improved photocatalytic efficiency with semiconductor metal oxides many alternation strategies are adopted to modify the properties of the photocatalysts. Some of them are discussed below in the following subsections

2.3. COUPLING OF SEMICONDUCTOR PHOTOCATALYSTS

The blending of two semiconductor metal oxides or metal oxide with a metal sulphide photocatalyst is one of the effective strategies adopted by the researchers to improve the photocatalytic efficiency by providing a high surface area for the dye molecules to get adsorbed and it also offers the advantage of the movement of the photogenerated charge carriers from one semiconductor to the conductor band of another semiconductor and thereby effectively separating the photogenerated charge carriers to participate in the photocatalytic reaction ^{39,40}.

Kuzhalosai et al⁴¹ analyzed the photocatalytic properties of SnO₂ loaded ZnO semiconductor photocatalyst under UV-A light. From the X-Ray diffraction studies done by kuzhalosai and group, it was reported that SnO₂-ZnO possessed a hexagonal wurtzite structure with a crystallite size of 6.1 nm and the HR-SEM images showed that the prepared SnO₂-ZnO had a flake-like structures. The bandgap of the synthesized material was reported to be 3.35eV and theSnO₂-ZnO showed superior photocatalytic activity than bare ZnO, pure SnO₂, commercial ZnO, TiO₂-P25 and TiO₂ (Merck). Around 90.9% mineralization of acid orange 10 dye was achieved within 60 minutes using 5g/L of SnO₂-ZnO catalyst under UV-A light.

D. Rajamanickam, P. Dhatshanamurthi and M. Shanthi fabricated SeO₂/TiO₂ nanocomposite photocatalyst via sol-gel technique⁴². The photoluminescence studies carried out by them revealed that there was a decrease in the PL intensity of Se modified TiO₂ photocatalyst, which may be attributed to the suppression of recombination of the photogenerated electron–hole pairs which makes the catalyst more photoactive. The photocatalytic studies carried out by them showed that there was an increase in the percentage degradation of sunset yellow dye in the presence of oxidants such as oxone, potassium bromate and potassium iodate. 5 g L⁻¹ of SeO₂/TiO₂ particles degraded 95% of sunset yellow dye under natural sunlight within 90 minutes.

Lukasz Wolski and Maria Ziolek 43 gave an insight into the mechanistic pathway of methylene blue dye degradation by using Nb₂O₅, ZnO and coupled catalyst ZnNb₂O₆ along with hydrogen peroxide. Among the three catalysts niobium pentoxide is reported to exhibit higher photocatalytic activity compared to zinc oxide and zinc niobate. Lukasz Wolski and Maria Ziolek concluded that the formation of ZnO₂ in the interaction with hydrogen peroxide limited the formation of hydroxyl radicals and the shortening of Nb=O bondlength, ZnNb₂O₆ catalyst prevented the formation of surface peroxo species which inturn decreased the photocatalytic activity of both ZnO and ZnNb₂O₆ catalysts.

Shahram Moradi et al⁴⁴ investigated the effectiveness of additives such as carboxymethyl cellulose, polyvinylpyrrolidone, polyethylene glycol, and hydroxylpropylcellulose in the preparation of ZnO/TiO₂ photocatalyst via sol-gel process. The photocatalytic studies carried out for the methyl orange dye (5ppm) by using different photocatalysts such as ZnO/TiO₂/CMC, ZnO/TiO₂/PEG, ZnO/TiO₂/PVP,

ZnO/TiO₂/HPC showed that ZnO/TiO₂ dispersed in hydroxypropylcellulose (1g L⁻¹) exhibited best degradation efficiency under UV irradiation within 3.5 hours which was attributed to the most uniform particle distribution in the polymer matrix and no agglomeration of the particles had occurred which was evidenced from the SEM micrographs.

Cadmium sulphide coupled with titanium dioxide catalyst immobilized on polycyrlonitrile membranes is employed for the photocatalytic degradation of methylene blue dye under visible light radiation⁴⁵. About 66.29% of the methylene blue dye degradation took place within 120 minutes at 25°C at pH 8.5 using 5% CdS loaded TiO₂ catalyst, which is attributed to the synergistic effect and better charge transfer between CdS and TiO₂ catalyst.

Mohsen Nasirian et al⁴⁶ achieved 62% degradation of methyl orange dye and 46.8% degradation of congo red dye using coupled Fe₂O₃/TiO₂ photocatalyst. It is reported that Fe₂O₃/TiO₂ composite catalyst synthesized via novel UV assisted thermal method increased the lifetime of charge carriers such as electrons and holes and there by increased the photocatalytic efficiency of the catalyst.

Gajendra Kumar Pradhan and K. M. Parida⁴⁷ fabricated Fe₂O₃/CeO₂ mixed photocatalyst and evaluated its photocatalytic activity for the degradation of phenol, methylene blue and congo red dyes. The 50% Fe incorporated cerium oxide is reported to have specific surface area of 94.69 m²/g. It is reported that about 13%, 93% and 100% degradation of phenol, methylene blue and congo red dye is achieved within 4 hours under sunlight using the Fe₂O₃/CeO₂ mixed photocatalyst which is ascribed to the higher surface area and a large number of active sites available on the surface of the catalyst. Similarly, Safi Asim Bin Asif et al⁴⁸ reported the excellent

photodegradation of brilliant cresyl blue dye under solar radiation using Aluminium oxide/Manganese oxide coupled catalyst. The main reactive species involved in the photocatalytic process are reported to be the superoxide anion radicals and hydroxyl radicals.

Weiping Zhang et al⁴⁹ fabricated MoS₂/TiO₂ catalyst through one-step hydrothermal process. The X-ray diffraction studies carried out by them showed three crystalline phases, such as the anatase phase of TiO₂, the ilsemannite phase of Mo₃O₈. H₂O and the molybdenite phase of 3R-MoS₂ are also observed in the XRD pattern of MoS₂/TiO₂ catalyst. The presence of Ti-O-Ti bonds and the characteristic peaks of MoS₂ are confirmed from the fourier transform infrared studies and the spherical morphology of the synthesized Molybdenum disulphide/Titanium dioxide photocatalyst is confirmed from the scanning electron microscopic analysis. It is reported that about 97% of methyl orange dye got degraded within 60 minutes under visible light radiation using MoS₂/TiO₂ catalyst. The high photocatalytic performance of MoS₂/TiO₂ catalyst is attributed to the reduced recombination rates of charge carriers such as electrons and holes. In a similar way, visible light-induced photocatalytic activity of oxides of zinc and bismuth was reported by Gurpreet Kaur et al⁵⁰. It is reported that about 75% and 58% degradation of alizarin red dye is achieved using bismuth oxide and zinc oxide catalysts under visible light radiation.

Pirzada et al⁵¹ prepared TiO₂/ZrO₂ photocatalyst via sol-gel technique followed by calcination at 450°C for 4 hours. The synthesized photocatalyst has a bandgap of 3.22eV, which was investigated for its photocatalytic activity towards the degradation of ponceau BS dye under a 125W mercury lamp and achieved about 24.45% degradation of the dye. Solar light-induced photocatalytic activity⁵² of

CdS/ZnO was evaluated for the degradation of methylene blue dye. The CdS/ZnO photocatalyst prepared by chemical bath deposition technique degraded 54% methylene blue within 240 minutes.

When Wang et al⁵³ used magnetically recoverable Fe₃O₄-ZnO (1g/L) catalyst for the degradation of rhodamine B dye (7mg/L) and found that 99% of the dye degradation took place under 250W UV light within 60 minutes, Chen and coworkers⁵⁴ were able to degrade the same rhodamine B dye (10mg/L), using Fe₃O₄-TiO₂ catalyst (0.2g/L) within 60 minutes under 250W under UV light. The high photocatalytic efficiency of the Fe₃O₄-TiO₂ catalyst is attributed to the superparamagnetic nature and nanporous structure of the catalyst which gives the advantage of the fast transportation of the dye molecule to the surface active sites of the catalyst promoting the photodegradation process.

Ruiz et al⁵⁵ coupled Copper oxide and bismuth vanadate catalysts via a simple impregnation technique and obtained a composite comprising of quasi-spherical and dendrite like particles. The synthesized Cu₂O/BiVO₄ photocatalyst efficiently degraded 89% of methyl orange dye under 54W visible light irradiation within 240 minutes, and similarly, 100% degradation of malachite green dye is achieved using a 2 dimensional CeO₂-CdO material⁵⁶ under UV light source. This multilayered platelet like material is also found to have antimicrobial properties against *Pseudomonas aeruginosa*. It is reported that both holes and hydroxyl radicals played a significant role in the degradation of the malachite dye compared to the superoxide anion radicals.

When Fang and coworkers coupled CdS nanoparticles with Bi_2S_3 nanowires, they were able to achieve 99% degradation of methyl red dye within 40 minutes under UV irradiation. The several hundred nanometers long bismuth sulphide nanowires

supported the triangle shaped cadmium sulphide nanoparticles, and the CdS/Bi_2S_3 heterojunction exhibited enhanced photocatalytic activity due to the high surface area of the product and suppression in the electron-hole recombination⁵⁷.

Kumar Pradhan and coworkers⁵⁸ fabricated mesoporous α -Fe₂O₃/SnO₂ and investigated its photocatalytic activity towards the degradation of malachite green dye. They reported that 2 mol% of Fe₂O₃ catalyst incorporated SnO₂ degraded 86% of the dye under sunlight within 4 hours. The high photocatalytic efficiency of α -Fe₂O₃/SnO₂ is attributed to the effective charge separation.

2.4. METAL DOPED SEMICONDUCTOR PHOTOCATALYSTS

Deposition of precious metal ions on the surface of metal oxide semiconductors is an effective way to capture the excited electrons thereby decreasing the recombination rate of the photogenerated charge carriers and increasing the photocatalytic efficiency. On doping of precious metal ions on the semiconductor surface, there will be continuous movement of electrons from the semiconductor to the metals. A schottky barrier formed at the interface where the semiconductor is in contact with the metals can capture the photogenerated electrons ^{59, 60}.

TiO₂ semiconductor photocatalyst⁶¹ doped with nano gold is reported to be more efficient for the degradation of acid red 88 under visible light irradiation in the presence of some oxidizing agents such as peroxo mono sulfate (PMS), peroxo disulfate (PDS) and hydrogen peroxide (H₂O₂) than pure P-25 titania photocatalyst. The X-ray diffraction analysis revealed that the diffractions that are attributable to the anatase phase of titanium dioxide are spotted without any alterations except in the intensity of the peaks, this may be due to the fact that doping may alter the crystallinity but not the crystal structure, the particle size of the gold doped titanium

dioxide nanoparticles was reported to be between 10-15nm from the TEM analysis. The extent of mineralization of the target pollutant evaluated using total organic carbon (TOC) analysis showed that 48% of acid red 88dye degradation took place in the presence of 0.15mM solution of peroxo mono sulphate and at a catalyst concentration of 1g/L after 4 hours.

Ruby Chauhan, Ashavani Kumar and Ram Pal Chaudhary⁶² investigated the photocatalytic activity of Fe doped ZnS catalyst for the degradation of methylene blue dye under visible and UV irradiation. From the XRD analysis, Ruby chauhan and group confirmed that the Fe doped ZnS nanoparticles existed in the cubic phase and the TEM analysis revealed the cubic morphology of the Fe doped ZnS catalyst with the particle size ranging from 2-5 nm. The photocatalytic studies carried out by them showed that Fe doped ZnS photocatalyst degraded 100% methylene blue dye solution under visible light within 120 minutes, whereas only 56% of methylene blue dye got degraded under UV irradiation within 300 minutes.

Copper-doped and iron-doped zinc oxide⁶³ photocatalyst was synthesized by precipitation decomposition method. The photocatalytic property of the material was tested against methylene blue dye solution in the presence of hydrogen peroxide under visible light irradiation. Fe doped zinc oxide photocatalyst exhibited excellent photocatalytic degradation towards methylene blue dye solution at neutral pH, compared to copper doped zinc oxide and pure zinc oxide photocatalysts.

Silver doped zinc oxide nanocomposite⁶⁴ with a specific surface area of $14.1 \, \mathrm{m}^2 \mathrm{g}^{-1}$ efficiently degraded textile dyes such as methylene blue, methyl orange and textile effluent under visible light irradiation.

Tania Bigdeli and Shahram Moradi Dehaghi utilized zirconium as dopant for titanium dioxide nanoparticles and evaluated its photocatalytic activity in degradation of an azo dye⁶⁵. TiO₂ catalyst doped with 'Zr' degraded congo red (5ppm) within 75minutes under UV irradiation which was attributed to the high surface area of the catalyst.

Mohamad Mohsen Momen et al⁶⁶ prepared WO₃/TiO₂ nanotube films and cobalt coated TiO₂ catalyst via photo-assisted deposition method. Co/WO₃–TiO₂ catalyst exhibited higher photocatalytic activity in the degradation of methylene blue dye compared to undoped and cobalt doped TiO₂ catalyst under visible light radiation which is attributed to the fact that cobalt doping onto the TiO₂ makes it a shallow trap for the separation of photo-induced carriers such as electrons and holes.

Ruby Chauhan et al⁶⁷ prepared manganese doped titanium dioxide photocatalyst via sol-gel route and evaluation of the photocatalytic activity revealed that at pH 6.5 around 88% of 10mg/L of methylene blue dye solution was degraded within 240 minutes under visible light irradiation.

Perillo et al⁶⁸ prepared copper doped zinc oxide nanorods at low temperature via simple chemical precipitation technique. About 99% degradation of methyl orange dye was reported within 120 minutes under sunlight.

Navyashree et al⁶⁹ investigated the photocatalytic performance of Nd³⁺ doped Vanadium pentoxide which possessed orthorhombic structure, and nanorods like shape with an average particle size of 50nm. The photocatalytic experiments carried out by them showed that the synthesized Nd³⁺ doped Vanadium pentoxide catalyst degraded 99% of methylene blue dye under UV light. Similarly, vanadium has been employed as a dopant for the SnO₂ nanoparticles for the photodegradation of rhodamine

B dye 70 . The structural characterization studies carried out by Letifi and co-workers revealed that the synthesized V-SnO₂ nanoparticles possessed a tetragonal shape with an average crystallite size of 10 nm. The UV-DRS studies carried out by them showed a redshift in the absorption by increasing the concentration of vanadium dopant. It is reported that about 95% Rhodamine B dye degradation took place within 150 minutes under UV light which was attributed to the more active sites available on the vanadium doped tin oxide catalyst surface. Hong Hu et al 71 fabricated heterostructured gold/bismuth oxide photocatalyst for the degradation of Rhodamine 6G. The X-ray diffraction studies carried out by them showed that the synthesized Au/Bi₂O₃ photocatalyst is a mixture of both α phase and β phase bismuth oxide particles and the morphological studies carried out by them showed that the synthesized particles possessed a nanoflower like morphology with its size ranging from 2-3.5 μ m. The synthesized Au/ Bi₂O₃ photocatalyst is reported to degrade 100% of the Rhodamine 6G dye within 40 minutes under CHF-XM-500WXe lamp illumination.

Khalil et al⁷² investigated the photocatalytic disinfection property of Pd doped ZnO catalyst against E.Coli under UV light and reported that 100% removal of the bacteria is possible with a catalyst loading of 10 mg/L within 10 minutes. Similarly, one dimensional silver doped ZnO photocatlyst⁷³ was reported to be effective in 58% removal of phenol (20mg/L) under 1500W UV light source within 60 minutes.

Jing-Ling Luo et al⁷⁴ studied the photocatalytic properties of Al doped TiO₂ photocatalyst. The Al-TiO₂ photocatalyst is prepared via modified acrylamide sol-gel route using three different aluminium salts such as aluminium chloride, aluminium nitrate and aluminium sulphate. Among the three different types of Al doped titanium dioxide photocatalyst, Al(NO₃)₃. 9H₂O incorporated titanium dioxide photocatalyst

exhibited 98% degradation of acid orange dye under UV light irradiation for one hour. The high photocatalytic activity observed for aluminium nitrate doped TiO₂ photocatalyst compared to aluminium chloride, aluminium sulphate and commercial Degussa P25 catalysts is attributed to the high surface and narrowed band gap of the photocatalyst. Similar to the findings of the Luo and group, Zada and coworkers⁷⁵ also reported high photocatalytic efficiency of Ag doped TiO₂ photocatalyst compared to the commercial Degussa P25 catalyst.

WO₃ is a semiconductor photocatalyst with a bandgap of approximately 2.8 eV. The excellent properties of the WO₃ catalyst include thermal stability, mechanical strength, non-toxic nature and inertness to chemical reaction etc., made researchers utilize it for water treatment applications⁷⁶⁻⁷⁸. This visible light photocatalyst is used as the main as well as a co-catalyst for photocatalytic studies. Recently Xinying Zhu et al⁷⁹ investigated the photocatalytic properties of La doped WO₃ catalyst and found that it is effective in the degradation of rhodamine B dye under a 1000W xenon lamp irradiation within 10 hours. Compared to undoped tungsten trioxide photocatalyst 'La' doped WO₃ catalyst showed higher photocatalytic activity which is attributed to the more surface area obtained for the doped tungsten trioxide photocatalyst and as well as due to the decrease in the electron-hole recombination process. Similarly, Shanthi et al⁸⁰ reported excellent photocatalytic activity of Ni doped WO₃ catalyst for the degradation of Alizarin red dye under UV light, they also reported that Zn doped WO₃ degraded 97% of methylene blue dye under UV light source within 240 minutes⁸¹.

Wu and Chen⁸² synthesized vanadium doped titanium dioxide catalyst by solgel technique to investigate the effect of doping the vanadium metal onto the TiO₂ catalyst. From the X-ray absorption analysis carried out by them it is observed that

vanadium metal is highly dispersed on the titanium dioxide catalyst giving high surface area, increased particle growth, and enhanced red shift in the UV-Visible absorption spectra which gave high photocatalytic degradtion of the methylene blue and crystal violet dyes compared to the pure titanium dioxide catalyst.

F.B.Li and X.Z.Li⁸³ prepared platinum deposited titanium dioxide photocatalyst via photoreduction method to investigate its photocatalytic properties against methyl orange and methylene blue dyes. They reported that the 'Pt' incorporated TiO₂ photocatalyst showed enhanced visible light absorption compared to pure TiO₂ photocatalyst and degraded 82% methylene blue and 85% methyl orange dyes under mercury lamp which is ascribed to the hindrance in recombination rate of electronhole pairs. Similarly Lee et al⁸⁴ reported the high photocatalytic efficiency of Ag doped titanium dioxide photocatalyst in the reduction of nitrophenol compared to pure TiO₂ photocatalyst.

Lead Sulphide which has a small bandgap energy value of 0.78eV, great charge mobility and high dielectric constant^{85,86}. Suganya et al⁸⁷ improved the photocatalytic efficiency of PbS catalyst by silver ion doping for the degradation of methyl orange under visible light absorption. The Ag/PbS also exhibited good antifungal activity against A.terreus fungus which might be due to the increased formation of reactive oxygen species.

Although precious metal deposits on the surface of semiconductor photocatalysts improves the catalytic efficiency by separation of electron-hole pairs, the thermal instability, the price and affordability of precious metals such as Ag, Au, Pt, Pd, Ru etc. makes it less suitable for large scale application of technology for wastewater remediation ^{88,89}.

2.5. CODOPED AND TRIDOPED SEMICONDUCTOR PHOTOCATALYSTS

When doping of the metal ions into the semiconductor metal oxide photocatalysts provides the advantage of narrowing the bandgap of the materials and suppression in the electron-hole recombination⁹⁰, the non-metal ion doping also offers certain advantages which includes the increased adsorption of the contaminants to the metal oxide surface, enhanced conductivity of TiO₂ photocatalysts⁹¹ etc. An improved interfacial charge transfer can be achieved by codoping a metal ion and a non metal ion to a metal oxide photocatalyst^{92,93}.

Saravanan et al⁹⁴ prepared binary (ZnO/CdO, ZnO/Ag) and ternary ZnO/Ag/CdO nanocomposite via thermal decomposition technique. It was reported that the synthesized ZnO/Ag/CdO nanocomposite possessed a cubic as well as hexagonal wurtzite structure. The BET surface area studies and diffuse reflectance studies showed that there was an increase in the surface area and a decrease in the bandgap of the zinc oxide catalyst by the addition of silver and cadmium oxide particles. The photocatalytic studies carried out by them showed that the ternary ZnO/Ag/CdO nanocomposite degraded more than 90% of methylene blue, methyl orange dyes and industrial textile effluent within 210 minutes under visible light irradiation. The complete mineralization of the pollutants was confirmed by Saravanan and group from the TOC and COD analysis.

A hybrid structured bismuth and gold codoped zinc oxide composite with a surface area of 28.2 (m² g⁻¹) was synthesized by precipitation-decomposition technique⁹⁵. It was reported that 98.7% mineralization of acid red 18 dye was achieved by using 4gL⁻¹ of Bi–Au–ZnO catalyst at pH11 under natural sunlight.

When the photocatalytic activity of the Mn, Mo, La loaded TiO₂ /Activated carbon was evaluated for azo dye and real textile effluent Jorfi et al⁹⁶ found that the catalyst exhibited a high adsorption ability in the visible region and the synthesized photocatalyst showed a reasonable degradation efficiency of 84% for the removal of Reactive red 198 dye at pH 3 with a catalyst loading of 2g L⁻¹ for a dye concentration of 20 mg L⁻¹. The structural and morphological characterization carried out by them showed that the synthesized photocatalyst was of anatase phase with spherical shaped particles of size ranging from 7-11nm, and it possessed a very high surface area of 97.525 m² g⁻¹.

Andrade neto et al⁹⁷ prepared cobalt and manganese codoped zinc oxide photocatalyst via sonochemical method, the co-doping of cobalt and manganese onto zinc oxide photocatalyst decreased the crystallite size of zinc oxide catalyst, whereas an increase in the surface area of zinc oxide photocatalyst along with the change in the morphology from nanoplates like structure to moderately small spherical shaped particles was reported by Andrade neto and co-workers. Compared to cobalt doped zinc oxide, manganese doped zinc oxide and bare zinc oxide photocatalysts, cobalt and manganese codoped zinc oxide photocatalyst exhibited greater photocatalytic activity in the degradation of methylene blue dye and the Co²⁺ and Mn²⁺ codoped ZnO catalyst also exhibited excellent antimicrobial properties.

Abderrahim El Mragui et al 98 prepared a series of monodoped and codoped titanium dioxide based nanomaterials and its photocatalytic activity was evaluated under both UV and visible radiations. The XRD studies carried out by them showed that both monodoped and codoped TiO_2 photocatalyst existed in the anatase phase and the substitution of the Ti^{4+} ions by Co^{2+}/Co^{3+} , Ni^{2+} , P^{5+} or Mo^{6+} and the existence of

Mn²⁺ on the surface of the TiO₂ photocatalyst is confirmed from the X-ray photoelectron spectroscopy studies. It was reported that under UV radiation, bare titanium dioxide nanoparticles exhibited excellent photocatalytic activity in the degradation of methyl orange dye whereas under visible light radiation the best photocatalytic activity was shown by 1% cobalt doped TiO₂ followed by 30% P, Mo codoped TiO₂, 30% P,W-TiO₂ codoped TiO₂, bare TiO₂, 1% Ni-TiO₂ and 1% Mn-TiO₂.

Iron, cerium and nitrogen tridoped titanium dioxide photocatalyst⁹⁹ was utilized by Layegh Khaledi Maki and coworkers for the removal of organic dye direct blue 15 under LED radiation. Fe-Ce-N tridoped TiO₂ photocatalyst degraded direct blue 15 dye within 60 minutes at slightly acidic pH under an LED light which was attributed to the presence of several dopants and their synergistic effect in producing reactive hydroxyl species for the degradation of organic pollutants.

Photocatalytic applications of cadmium and indium codoped titanium dioxide nanoparticles were investigated by Dongliang Liu et al¹⁰⁰. Cd/In codoped TiO₂ photocatalyst calcined at 700° C degraded 99% of methylene blue dye within 30 minutes under visible radiation, which might be due to the increased surface area.

The rare earth metals such as ytterbium, erbium and cerium have been employed as dopants for the titanium dioxide catalyst in the photodegradation of Rhodamine B dyes and phenolic compounds¹⁰¹.

Bianca-Maria Bresolin et al., prepared Cs₃ Bi₂ I₉ perovskite material as a visible-light catalyst for the photocatalytic degradation of Rhodamine B dye in an aqueous solution¹⁰². The perovskite material is reported to degrade 93% of Rhodamine dye within 180 minutes under visible light radiation, whereas without the catalyst, only a negligible amount of dye degraded, and the catalyst retained its photocatalytic activity for three consecutive cycles.

Yoki Yulizar et al¹⁰³ reported La₂ CuO₄ decorated ZnO nanoparticle fabrication using *Strobilanthes Crispus (B.)* leaves extract and evaluated its photocatalytic activity towards the degradation of malachite green dye under visible light illumination. The X-ray diffraction studies carried out by them showed that the La₂ CuO₄ – ZnO nanocomposite possessed both the hexagonal wurtzite phase of zinc oxide nanoparticles and orthorhombic perovskite structure of La₂ CuO₄. The TEM images of the La₂ CuO₄ – ZnO nanocomposite showed that the particles are agglomerated with both hexagonal as well as spherical shapes. About 91% of malachite green dye degradation within 120 minutes under visible light radiation was reported using La₂ CuO₄ – ZnO nanocomposite and catalyst exhibited recyclability for three cycles of the photocatalytic experiment.

Guanjie Xing et al¹⁰⁴ prepared ZnO/NaTaO₃ composite via a simple hydrothermal synthesis method. It is reported that the ZnO/NaTaO₃ composite exhibited excellent photocatalytic degradation of methylene blue dye under visible light radiation, which was attributed to the reduction in the effective charge carrier recombination process induced by the synergistic effect between ZnO and NaTaO₃.

Umair Alam et al¹⁰⁵ synthesized ytterbium and vanadium codoped zinc oxide photocatalyst via sol-gel method which was reported to be effective in the degradation of Rhodamine B and methylene blue dyes and also in the degradation of 4-nitrophenol under visible light radiation. Similarly, when Jila Talat-Mehrabadand and coworkers¹⁰⁶ investigated the photocatalytic activity of silver and magnesium codoped titanium dioxide catalyst, it is reported that compared to the undoped and monodoped TiO₂ catalyst Ag and Mg codoped TiO₂ catalyst exhibited excellent photocatalytic activity in the degradation of acid red 27 dye and about 66% mineralization of AR 27 dye took place within 20 minutes under visible light radiation.

Co-doping of 'Ag and 'C' to titanium dioxide photocatalyst¹⁰⁷ resulted in an alteration in the ratio of anatase to rutile phase. Even though codoping Titanium dioxide with silver and carbon resulted in low band gap energy values, the greatest photocatalytic activity in the degradation of methyl orange dye under visible light radiation was reported for carbon doped TiO₂ photocatalyst compared to the bare TiO₂, silver doped TiO₂ photocatalysts and Ag, C codoped TiO₂ photocatalyst which was attributed to the high surface area and pore volume available for the adsorption of the dye onto the photocatalyst.

Kamini Gupta et al¹⁰⁸ investigated the photocatalytic degradation of aqueous methylene blue dye by using undoped titanium dioxide, nitrogen doped, niobium doped and nitrogen and niobium codoped titanium dioxide nanoparticles under visible light radiation. Mehala Kunnamareddy et al¹⁰⁹ codoped titanium dioxide catalyst with nickel and sulphur and investigated its photocatalytic activity in the degradation of methylene blue dye under visible light radiation. About 85% of 30mg/L of methylene blue dye solution was decolourized within 180 minutes using Ni, S-TiO₂ catalyst which is attributed to the decrease in crystallite size and low bandgap energy values for the codoped titanium dioxide photocatalyst compared pure and monodoped catalysts. The main reactive species such as holes and superoxide anion radicals are reported to play a vital role in the degradation of the organic dye.

Alex T. Kuvarega, Rui W. M. Krause and Bhekie B. Mamba reported that codoping of titanium dioxide catalyst with nitrogen and palladium¹¹⁰ impacted a redshift in the absorption band edge. The Nitrogen and palladium codoped titanium dioxide catalyst degraded eosin yellow dye entirely within three hours under visible light radiation whereas under similar conditions pure TiO₂ catalyst was reported to degrade only 18.2% of eosin yellow dye.

Tungsten and fluorine codoped titanium dioxide nanoparticle¹¹¹ is evaluated for its photocatalytic activity towards the degradation of methylene blue dye under visible light radiation.

Ming-Yang Xing et al¹¹² explained the synergistic effects of boron and nitrogen codoped TiO₂ catalyst for its enhanced photocatalytic performance in the degradation of methyl orange dye under visible light radiation. It was reported that the enhanced photocatalytic activity of the codoped titanium dioxide catalysts is due to the synergistic effect of Ti-B-N-Ti together with Ti-N-B-O structure on the surface of the catalyst rather than the Ti-N-B-O structure only. Similarly, Ying Wang et al¹¹³ investigated the photocatalytic performance of bismuth and sulphur codoped TiO₂ catalyst. Ying Wang and coworkers reported the complete degradation of indigo carmine dye within 40 minutes under visible light radiation, which was attributed to the high specific surface area, oxygen vacancies and acidic sites on the surface of the Bi-S-TiO₂ photocatalyst compared to the bare titanium dioxide catalyst.

Yi Xie et al¹¹⁴ reported that silver loaded S, N doped titanium dioxide catalyst exhibited higher photocatalytic activity towards the degradation of methyl orange dye compared to that of the sulphur and nitrogen codoped TiO₂ catalyst. The high photocatalytic performance of Ag-S-N- TiO₂ catalyst is attributed to the decreased size of silver nanoparticles and the high adsorption capability of the Methyl orange dye on the surface of the Ag-S-N- TiO₂ catalyst.

Visible light-driven photocatalytic activity of carbon, nitrogen and sulphur tridoped titanium dioxide photocatalyst¹¹⁵ was evaluated for the degradation of antibiotics such as tetracycline, ciprofloxacin and chloramphenicol and also for the dyes such as rhodamine-B, methylene blue, and organe red.

Aritra Biswas, Atanu Chakraborty, and Nikhil R. Jana investigated the photocatalytic properties of nitrogen and fluorine codoped titanium dioxide photocatalyst ¹¹⁶. The codoping of nitrogen and fluorine onto titanium dioxide catalyst caused a change in its morphology from rod shaped to spherical shape. The XRD studies carried out by them confirmed the tetragonal phase and the UV-Visible absorption studies showed a redshift in the absorption band edge. Aritra Biswas et al also confirmed the generation of reactive oxygen species OH using terphthalic acid as a probe and the N,F-TiO₂ photocatalyst also showed excellent photocatalytic activity towards the degradation of bisphenol A and the cell viability assay performed by them proved that the N,F-TiO₂ photocatalyst under visible light radiation induced cell death via generation of reaction oxygen species. Similarly, Daimei Chen et al ¹¹⁷ prepared carbon and nitrogen codoped titanium dioxide nanoparticles and evaluated its photocatalytic activity towards the degradation of methylene blue dye under visible light radiation.

Fang Li et al¹¹⁸ studied the photocatalytic activity of fluorine, boron and sulphur tridoped titanium dioxide catalyst. About 44.6% of acid naphthol red dye decolourized within 55 minutes under visible light radiation attributed to the decreased crystallite size and greater surface area of the F-B-S tridoped TiO₂ compared to the undoped Titanium dioxide photocatalyst.

Sajid Ali Ansari and Moo Hwan Cho employed melamine¹¹⁹ as a source of carbon to modify the zinc oxide semiconductor photocatalyst. The X-ray diffraction studies carried out by them showed that there is no change in the hexagonal phase of both undoped and carbon doped ZnO photocatalyst and they confirmed the spherical morphology of the carbon-doped zinc oxide from the SEM and TEM micrographs. Carbon doped zinc oxide catalyst was reported to exhibit good photocatalytic activity in the degradation of Rhodamine B dyes under visible light radiation.

Zinc oxide semiconductor photocatalyst is also modified by incorporating the ionic liquid Cetyl trimethyl ammonium bromide (CTAB)¹²⁰ and its photocatalytic property is evaluated for the degradation of methyl green dye under visible light radiation. Other organic compounds which were employed as a source of carbon include urea¹²¹ doped zinc oxide semiconductor by Xinyu Zhang et al., for the photocatalytic degradation of methylene blue dye, Yijun Yang et al used oleyl amine 122 as source of carbon for doping Titanium dioxide catalyst for hydrogen production, Halimi et al used acetyl acetone¹²³ as a source of carbon for preparing doped titanium dioxide catalyst at low temperature via electrospraying technique. Saba Habibi and Masoud Jamshidi prepared carbon doped titanium dioxide photocatalyst using microcrystalline cellulose¹²⁴ as a source of carbon via sol-gel method for the photocatalytic degradation of methylene blue dye under visible light radiation, Seungho cho and coworkers prepared carbon doped zinc oxide photocatalyst using vitamin C¹²⁵ as a carbon source and obtained polycrystalline nanostructures of zinc oxide material with crystallite size of 7 nm. The prepared carbon doped ZnO catalyst exhibited visible light absorption bands that redshifted relative to UV absorption band exhibited by the pure zinc oxide nanoparticles. The carbon doped ZnO catalyst degraded orange II dye efficiently under visible light radiation.

Guosheng Wu et al¹²⁶ synthesized carbon doped titanium dioxide catalyst using titanium n-butoxide as a common source for both titanium and carbon. The C-doped TiO₂ catalyst existed in both spherical as well as tubular forms. The photocurrent of carbon doped TiO₂ catalyst is reported to be much higher compared to the commercial Degussa P-25 catalyst. Yiseul Park et al¹²⁷ prepared carbon doped TiO₂ catalyst without using an external source. The carbon in the titanium precursor was incorporated into the TiO₂ lattices through a controlled calcinations process.

Carbon, Nitrogen, boron and Fluorine doped TiO₂ catalyst is evaluated for its photocatalytic activity¹²⁸. The XRD studies carried out by them showed that there is no change in the phase and crystalline nature of the doped and undoped TiO₂ samples. However they reported an increase in the crystallite size of doped CNBF/TiO₂ catalyst at higher calcination temperatures. The BET surface area analysis carried out by them showed that there was a decrease in surface area of the CNBF doped TiO₂ catalyst. The complete decolourization of congo red is reported within 2 hours under UV and solar radiation.

Nitrogen-doped titanium dioxide catalyst is evaluated for its photocatalytic activity by Jiwei Zhang et al¹²⁹. The more photocatalytic activity is reported for the nitrogen doped anatase phase TiO₂ catalyst rather than the rutile phased nitrogen doped TiO₂ catalyst.

Weiwen Wang et al¹³⁰ reported an improvement in the photocatalytic efficiency of boron, carbon and nitrogen doped titanium dioxide catalyst by the addition of silver nanoparticles to the photocatalyst. They also explained that the intervention of the silver nanoparticles to the tridoped titanium dioxide catalyst changed the P-N interface heterojunction from (211)/(101) to the (211)/(101)/Ag Z-scheme interface heterojunction, and the photocatalytic experiments carried out by them showed that 94% of methylene blue dye degradation is achieved by the addition of 0.005% of silver to the B-C-N tridoped TiO₂ catalyst.

Investigation of the magnetic and photocatalytic properties of the carbon quantum dots modified bismuth oxide catalyst was carried out by Shelja Sharma et al 131 . They reported the template free facile synthesis of α -Bi $_2$ O $_3$ /C-dots via sonochemical approach. The X-ray diffraction studies carried out by them confirmed the monoclinic

phase of bismuth oxide catalyst with a crystallite size of 28.75 nm. The photoluminescence and UV-DRS spectrum of the α -Bi₂O₃/C-dots showed good optical properties with a bandgap of 2.49 eV. The α -Bi₂O₃/C-dots photocatalyst showed about 66% reduction in the total organic carbon content of indigo carmine dye after the degradation process and it is also reported to be effective in the degradation of levofloxacin. Aruna devi et al¹³² observed improvement in the photocatalytic activity of monoclinic copper oxide photocatalyst after doping with cadmium and barium ions and reported that the Cd, Ba-CuO photocatalyst prepared via co-precipitation technique degraded 77% of congo red within 180 minutes under 300W xeno lamp irradiation and this was attributed to the reduction in band gap energy value (1.6 eV) of the photocatalyst. WO₃ is one of the semiconductor metal oxides with good absorption ability and narrowed bandgap^{133,134}.

However its photocatalytic activity is comparatively less to that of zinc oxide and titanium dioxide photocatalysts. Hence to improve its photocatalytic efficiency more research is carried out by the process of coupling it with other metal oxide photocatalysts. Recently Priya et al¹³⁵ investigated the photocatalytic activity of WO₃ photocatalyst by coupling it with BiFeWO₆ catalyst via simple co-precipitation and hydrothermal methods and found that the composite is efficient in the degradation of rhodamine B dye under visible light irradiation. A similar technique is adopted by Malathi and coworkers¹³⁶ to fabricate and investigate the photocatalytic activity of BiFeWO₆/BiOI composite. They observed that the synthesized BiFeWO₆/BiOI photocatalyst is efficient in the degradation of rhodamine B dye under visible light irradiation. BiFeO₃/BiOI is another similar photocatalytically active composite material¹³⁷ which showed 100% degradation of rhodamine B dye and 71% degradation of

bisphenol A under visible light irriadiation. Chao wang et al¹³⁸ attempted to couple the visible light active Ag₃PO₄ nanocrystals with WO₃ nanosheets and found that Ag₃PO₄/WO₃ hybrid photocatalyst showed higher degradation for methylene blue dye compared to bare Ag₃PO₄ and WO₃ catalysts which is accounted to the extended visible light absorption and effective separation of photoinduced charge carriers. Although the technique of codoping has improved the catalytic efficiency of the semiconductor metal oxide photocatalysts, there are also some limitations such as short term efficiency of the non-metal ion-doped catalysts, formation of oxygen vacancies, multistep experimental process and moreover, the improvement in the catalytic efficiency is highly dependent on the type and concentration of the dopants chosen which needs to be taken into consideration while modifying the photocatalysts ¹³⁹⁻¹⁴².

2.6. DYE SENSITIZED SEMICONDUCTOR PHOTOCATALYSTS

One of the most interesting ways of fabricating semiconductor metal oxides with the more visible light response is to use organic dyes or complexes of ruthenium, rhodium or platinum metal complexes as sensitizers and improve the photocatalytic ability of the semiconductors. Recently, Azadeh Haghighatzadeh¹⁴³ did a comparative analysis of the optical and photocatalytic properties of the chlorophyll and curcumin sensitized titanium dioxide nanoparticles. The optical properties of the sensitized and unsensitized titanium di oxide nanoparticles are studied by UV-Visible diffuse reflectance spectroscopy. The titanium dioxide nanoparticles absorbed in the UV region whereas a redshift in the absorption badge was observed for the dye a sensitized titanium dioxide nanoparticle which was attributed to the photon absorption by the chlorophyll and curcumin pigments on the TiO₂ surface which resulted in high photocatalytic activity.

Jennyfer Diaz-Angulo et al¹⁴⁴ observed an improvement in the photon absorption by sensitizing the titanium dioxide nanoparticles with two different dyes such as Eosin Y and Rhodamine B. About 70.9% of acetaminophen and 83.4% of diclofenac were degraded by using Eosin Y sensitized titanium dioxide nanoparticles whereas only 53% and 34.6% of acetaminophen and diclofenac got degraded in the presence of Rhodamine B sensitized titanium di oxide nanoparticles which were attributed to the anionic nature of Eosn Y dye.

Chitiphon Chuaicham¹⁴⁵ and group investigated the photocatalytic performance of sepiolite for the degradation of several organic dyes and found out that the photocatalytic activity of spent sepiolite after the adsorption of rhodamine B dye increased about twice as much as with pristine sepiolite which indicated that the dyesensitization process could increase the photocatalytic performance of a catalyst. The radical scavenger test carried out using the reagents such as isopropyl alcohol (IPA), benzoquinone (BQ), and potassium iodide (KI) for trapping the h^+ , \bullet O₂ and \bullet OH confirmed that O₂ was the main oxidant species in the photocatalytic degradation of rhodamine B dye over sepiolite under visible light irradiation.

A natural dye anthocyanin extracted from mangosteen peel, was successfully employed as a sensitizer for TiO₂ nanoparticles¹⁴⁶. Md. Ashraful Islam Molla et al¹⁴⁷ experimented with a self dye sensitization technique on the photocatalysts such as zinc oxide and titanium dioxide for the degradation of Orange II and Methyl Orange dyes under the LED and fluorescent light irradiation.

Sukanya Krishnan and Amritanshu Shriwastav¹⁴⁸ investigated the application of chlorophyll as a natural dye sensitizer for the photocatalytic degradation of methylene blue dye under blue LED illumination. About 85% degradation of 20 ppm methylene

blue dye solution was achieved with 2.5 g L⁻¹ of 0.1 wt% chlorophyll/TiO₂, at pH 6, within 2 hours of visible blue LED irradiation.

Titanium dioxide powders modified by quinizarin and zinc protoporphyrin as sensitizers¹⁴⁹ were employed for the photocatalytic degradation of phenol and methyl orange dye under visible light radiation. The enhanced rate of photocatalytic dye degradation by using quinizarin and zinc protoporphyrin dyes as sensitizers is attributed to a double sensitization phenomenon.

ZnO photocatalyst sensitized with methyl red dye¹⁵⁰ improved the rate of degradation of phenol under visible light irradiation. Chlorophyll, β -carotene and N-719 powder were employed as sensitizers¹⁵¹ for titanium dioxide nanotubes. Chlorophyll sensitized titanium dioxide nanotubes showed much higher photocatalytic activity in the degradation of methylene blue dye under visible light compared to that of β -carotene and synthetic N-719 powder. This is attributed to the light harvesting nature and transference of energy between the chlorophyll dye and the TiO₂ substrate.

Anthocyanin extracted from red raddish is used as a template in the synthesis of mesoporous titanium dioxide nanoparticles for the degradation of phenols and dyes under visible light light radiation¹⁵². The dye sensitized TiO₂ degraded 20% methyl thionine chloride, 34.9% of rhodamine B, 56.2% of gentain violet, 54% phenol and 65% of 2,4-dichlorophenol respectively. Eventhough the process of photosensitization has improved the photocataltyic performance of the semiconductor catalysts via effective separation of photogenerated charge carriers and by adsorption of the contaminants to the surface of the metal oxides^{153,154}, a major concern in implementing the technology to a large scale is the desorption of the sensitizers to the aqueous suspension during the repeated cycles of photocatalytic process, toxicity level of the sensitizers used and competitive adsorption of the co-existing species¹⁵⁵⁻¹⁵⁷.

2.7. SUPPORTED SEMICONDUCTOR PHOTOCATALYSTS

Preparation of the semiconductors in an immobilized or supported form to make it suitable for wide-scale practical implementation has become a prior concern among researchers ^{158,159}. Immobilization of the semiconductor metal oxides on different supports such as glass plates, glass beads, stainless steel, polymeric materials, activated carbon, clays etc., offers a great advantage of cost effective separation of the photocatalysts from the wastewater after treatment ¹⁶⁰⁻¹⁶⁴.

S. Sohrabnezhad, M.A. Zanjanchi and M. Razavi identified that Ag/AgCl dispersed in montmorillonite matrix¹⁶⁵ exhibited good photocatalytic activity under visible light radiation. Results of the photocatalytic experiments showed that both visible light and a photocatalyst, are essential for the effective degradation of methylene blue.

Jurate Virkutyte and Rajender S. Varma prepared an eco-friendly and effective iron oxide-pillared montmorillonite composite ¹⁶⁶ for environmental decontamination. The photocatalytic activity of the composite was tested against the degradation of dichlorophenol (DCP) and the results obtained showed that 85% mineralization of dichlorophenol took place in 2.5 hours in the presence of peroxomonosulphate whereas in the presence of other oxidizing agents such as hydrogen peroxide and peracetic acid only 50% and 70% degradation of DCP took place within 3.5 hours respectively.

Synthetic polymers such as polyethylene terphthalate and polystyrene were employed as templates for titanium dioxide and zinc oxide semiconductor photocatalysts¹⁶⁷. Two azo dyes such as acid brown 83 and direct blue1 showed good adsorption towards polymer supported titanium dioxide photocatalyst compared to that of the supported zinc oxide semiconductor photocatalyst. Kinetics studies

revealed that the photodegradation of the dyes were not influenced by the polymeric supports and the reaction followed pseudo-first order kinetics.

Wan Izhan Nawawi Wan Ismail et al¹⁶⁸ prepared immobilized titanium dioxide photocatalyst by coating the titanium dioxide solution onto double sided adhesive tapes supported on glass plates. Immobilized TiO₂/DSAT successfully degraded the cationic methylene blue and anionic reactive red 4 dyes.

Nawi et al¹⁶⁹ investigated the photocatalytic activity of titanium dioxide powder mixed with epoxidized natural rubber-50 (ENR50)/polyvinyl chloride under a fluoroscent lamp for the degradation of methylene blue dye. Mehdi Taghdiri investigated the photocatalytic activity of magnetically recoverable and reusable polyoxometalate coated activated carbon nanoparticles¹⁷⁰. The MAC-HMT-STA nanocomposite selectively adsorbed and degraded methylene blue dye from the binary mixture of methylene blue/rhodamine B and also from the binary mixture of methyl orange/methylene blue. This selective adsorption of methylene blue dye towards MAC-HMT-STA nanocomposite is attributed to the fact that the surface of the composite is negatively charged which has more affinity towards the cationic dyes.

Paul Henri Allé et al¹⁷¹ prepared Titanium dioxide nanoparticles supported on silicon carbide via dip coating process and investigated its photocatalytic activity towards the degradation of rhodamine B dye.

TiO₂ coated polystyrene beads with high mechanical and thermal stability was investigated for its photocatalytic activity¹⁷². The photocatalytic activity of TiO₂ coated polystyrene beads towards the degradation of methylene blue dye remained reasonably high even after 10 successive cycles.

A plasmonic photocatalyst Gold/TiO₂ supported on floating porous Polydimethylsiloxane Sponge was investigated for its photocatalytic activity towards the degradation of Rhodamine B dye under ultra-violet and visible dyes¹⁷³. Chin Mei Ling et al¹⁷⁴ successfully synthesized Titanium dioxide nanoparticles via sol-gel method and immobilized it by coating the TiO₂ powder onto to two glass reactor tubes such as tubular photocatalytic reactor with the recirculation mode and the batch photocatalytic reactor. The effect of air purging and the use of hydrogen peroxide as an oxidant increased the rate of the photocatalytic degradation process.

Fabrication of reduced graphene oxide /Titanate hybrids was done by incorporating the titanium dioxide nanoparticles into the graphene oxide layers by solvothermal treatment 175 for the degradation of methylene blue dye.

S. Razak, M.A. Nawi and K. Haitham successfully synthesized TiO₂/ PANI composite by using epoxidized natural rubber and polyvinyl chloride as adhesives¹⁷⁶. The immobilized TiO₂/ PANI/ENR/PVC composite decolourized 85% of reactive red4 dye under visible light within 60 minutes. This was attributed to the electron donor ability of the conjugated polyaniline polymer upon visible light excitation.

Zhang et al¹⁷⁷ prepared TiO₂/Zeolite composite via hydrolysis deposition and calcination crystallization method for the abatement of pollutants such as Phenol, methyl orange (MO) and rhodamine B (RB) dyes. About 54%, 80% and 84% degradation of phenol, MO and RB dyes were achieved within 360 minutes time under UV irradiation. The photodegradation ability of BiFeO/reduced graphene oxide composite prepared by hydrothermal method is investigated by basith et al¹⁷⁸ and reported that 62% degradation of rhodamine B dye is achieved within 240 minutes under 500W mercury-xenon lamp irradiation.

When J. E.Lee and his group¹⁷⁹ was able to degrade 81% of the methylene blue dye using a three dimensional Au/ZnO/graphene oxide composite under under UV irradiation within 240 minutes, a similar type of three dimensional Au/ZnO/graphene oxide immobilized photocatalyst was fabricated by She et al¹⁸⁰ and investigated its photodegradation ability towards rhodamine B dye.

Jiang et al¹⁸¹ reported that TiO_2 -GO (0.5g/L) photocatalyst degraded 90% of methyl orange dye under 20W UV light source. Similarly using TiO_2 -GO (1g/L) photocatalyst¹⁸² only 62% degradation of methyl orange dye is achieved under visible light within 180 minutes. Rong et al¹⁸³ used titanium dioxide/graphene oxide photocatalyst (0.8g/L) for the degradation of methylene blue dye (10mg/L) and achieved 98% degradation of the dye within 100 minutes under visible light. Wang and coworkers¹⁸⁴ reported the degradation of methylene blue using Sulphur/titanium dioxide/graphene oxide photocatalyst under simulated solar light. A decreased band gap obtained via sulphur doping, movement of the photogenerated charge carriers to the graphene oxide and adsorption of the dye molecules to surface of graphene oxide through π - π interactions increased the photocatalytic efficiency.

Graphitic carbon nitride (g-C₃N₄) is another important member of the semiconductor family with a bandgap of 2.7 eV. Although this three dimensional material is non-toxic and easily processable, the absence of interlayer hybridization of the electronic states has restricted the charge mobility in g-C₃N₄ and hence it has low photocatalytic efficiency^{185, 186}. In order to overcome this limitation researchers began to modify the pure g-C₃N₄ by coupling with metal oxides. For example, Purohit and Coworkers¹⁸⁷ were able to degrade the 68 % of methylene blue dye (10mg/L) under simulated sunlight within 70 minutes using an inorganic-organic hybrid three dimensional

material namely $BiVO_4/g-C_3N_4$ however, when Xin and $Meng^{188}$ attempted to degrade the same methylene blue dye using pure $g-C_3N_4$ only 66% dye degradtion took place within 5 hours under simulated sunlight. Similarly, Zhu et al 189 achieved 88% degradation of tetracycline using $g-C_3N_4$ /Ag/Fe $_3O_4$ within 90 minutes under 300W visible light irradiation and Mousavi et al 190 prepared a visible light driven magnetically separable $g-C_3N_4$ /Fe $_3O_4$ /BiOI photocatalyst and observed that the prepared composite showed higher photocatlytic activity in the degradation of methylene blue, rhodamine B and methyl orange dyes compared to pure $g-C_3N_4$ catalyst.

The higher photocatlytic activity shown by the composite compared to pure $g\text{-}C_3N_4$ catalyst is attributed to the high surface area and efficient separation of electron-hole pairs. Preparation of biocomposites by integrating the metal oxides with low cost, non-toxic and biodegradable polymers such as chitosan, polymethylmethacrylide, polyaniline, polymeric fibres etc. to obtain high surface area¹⁹¹⁻¹⁹⁴ are also considered to be a fruitful area of research. Among Cu^0 , Co^0 , Ni^0 and Ag^0 metals incorporated chitosan/ TiO_2 catalysts, Fayaz Ali et al¹⁹⁵ observed that Cu-Chitosan/ TiO_2 showed excellent photocatalytic activity in the degradation of methyl orange, congo red, methylene blue and acridine orange dyes. The catalyst is also reported to show good photocatalytic efficiency in the reduction of phenols which is attributed to the morphology of Cu-CS/ TiO_2 catalyst and the active sites available on the surface of chitosan.

Similarly, (TiO₂/COS)-on-[Fe₃O₄/PVA–PHB/PCL] fibrous material¹⁹⁶ degraded methylene blue dye within 90 minutes under UV light and the intermolecular interaction of polyaniline providing more electrons to the conduction band of zinc

oxide led to the effective degradtion of methyl orange and methylene blue dyes under visible light irradiation ¹⁹⁷. Zinc Oxide photocatalyst supported on polymethyl methyacrylate fibres is also reported to show excellent degradation of methylene blue dye and phenol under UV light ¹⁹⁸.

From a broad review of literature it is understood that the photocatalysts in the slurry or dispersed forms are reported to give higher photocatalytic efficiency compared to that on the immobilized forms due to the large surface area, homogeneous dispersity of the particles and more contact of the contaminants with the surface active sites of the semiconductor photocatalysts. It is also observed that a lot of research is done by doping and intergrating different metal oxides such as ZnO, TiO₂ as well as bismuth and tungsten oxides to obtain new modified photocatalysts with higher photocatalytic activity. Hence, the present work focuses in synthesis, characterization and evaluation of the photocatalytic activity of the metal doped semiconductors towards various synthetic organic dyes and it is also planned to evaluate catalytic efficiency of the best doped photocatalysts for effluent treatment.

BIBLIOGRAPHY

- N.M. Julkapli, S. Bagheri, S.B.A. Hamid, Scientific World Journal (2014)
 Article ID 692307, 25 pages
- 2. R. Dewil, D. Mantzavinos, I. Poulios, M. A. Rodrigo, *Journal of Environmental Management* **195** (2017) 93-99
- 3. B. Ponnusami, K. Muthu Kumar, *J. Environ. Chem. Eng.* **2** (2014) 557–572
- S.V. Srinivasan, T. Rema, K. Chitra, K. Sri Balakameswari, R. Suthanthararajan,
 B. Uma Maheswari, *Desalination* 235 (2009) 88–92
- 5. G. Boczkaj, A. Fernandes, *Chemical Engineering Journal* **320** (2017) 608-633
- 6. F.C. Moreiraa, A.R. Boaventura, E. Brillas, V.J.P. Vilar, *Applied Catalysis B:*Environmental **202** (2017) 217–261
- 7. S. Ahmed, M.G. Rasul, R. Brown, M.A. Hashi, *Journal of Environmental Management* **92** (2011) 311-330
- 8. X. Du, Y. Zhang, I. Hussain, S. Huang, W. Huang, Chemical Engineering

 Journal 313 (2016), 1023-1032
- 9. M. Rochkind, S. Pasternak, Y. Paz, *Molecules* **20** (2015) 88-110
- 10. S. Wacławek, V.T. Vinod Padil, M. Cernik, Ecol Chem Eng. 25 (2018) 9-34.
- 11. Adesina, Catalysis Surveys from Asia 8 (2004) 265-273
- 12. G. Al-Sayyed, J.C. D'Oliveira, P. Pichat, Journal of Photochemistry and Photobiology A: Chemistry **58** (1991) 99-114
- 13. A. Arques, A.M. Amat, A. Garcia-Ripoll, R. Vicente, *Journal of Hazardous Materials* **146** (2007) 447- 452
- L.G. Devi, B.N. Murthy, Central European Journal of Chemistry 7 (2009)
 118-129

- J.R. Bolton, K.G. Bircher, W. Tumas, C.A. Tolman, Pure Applied Chemistry73 (2001) 627- 637
- J. Liqiang, W. Dejun, W. Baiqi, L. Shudan, X. Baifu, F. Honggang, S. Jiazhong,
 Journal of Molecular Catalysis A: Chemical 244 (2006) 193-200
- 17. I.I.K. Kim, H.J. Ha, S.K. Lee, J.K. Lee, *Korean Journal of Chemical Engineering*22 (2005) 382-386
- 18. G. Kiriakidis, V. Binas, *J. Korean Phys. Soc.* **65** (2014) 297–302
- 19. S. Shen, C.Kronawitter, G. Kiriakidis, *J.Materiomics*. **3** (2017) 1–2
- D. Lutic, C.C. Pastravanu, I. Cretescu, I. Poulios, C.D. Stan, *International Journal of Photoenergy* (2012) 475131
- 21. S.K. Lee, A.Y. Kim, J.Y. Lee, S. H. Ko, S. W. Kim, *Bull Korean Chem Soc* **35** (2014) 2004-08
- 22. T. Selvamani, S. Anandan, L. Granone, D.W. Bahnemann, M. Ashok kumar, *Materials Chemistry Frontiers* 2 (2018) 1664-1673
- 23. K. Dai, H. Chen, T. Peng, D. Ke, H. Yi, Chemosphere 69 (2007) 1361–1367
- A. Mohagheghian, S.A. Karimi, J.K. Yang, M.S. Siboni, J. Adv. Oxid. Technol.18 (2015) 61-68
- G. Lalitha, R. Hemamalini, R. Saravanan, K. Ravichandran, F. Gracia, S. Agarwal, V.K. Gupta, *Journal of Photochemistry & Photobiology, B: Biology* 173 (2017) 43–49
- 26. S.C. Lee, H.U. Lee, S.M. Lee, G. Lee, W.G. Hong, J. Lee, H.J. Kim, *Materials Letters* **79** (2012) 91-94
- 27. S.K. Kansal, M. Singh, D. Sud, *Journal of Hazardous Materials* **141** (2007) 581–590

- 28. F. Parvin, O. K. Nayna, S.M. Tareq, S.Y. Rikta, A.K. Kamal, *Applied Water Science* **8** (2018) 73
- 29. M.M. Sajid, N.A. Shad, Y. Javed, S. B. Khan, Z. Zhang, N. Amin, H. Zhaia, Surfaces and Interfaces 19 (2020) 100502
- T. Zhang, Y. Liu, Y. Rao, X. Li, D. Yuan, S. Tang, Q. Zhao, Chem. Eng. J.
 384 (2020) 123350
- 31. R.V. Solomon, I. S. Lydia, J. P. Merlin, P. Venuvanalingam, *J. Iran. Chem. Soc.*, **9** (2012) 101–109
- 32. A. Henglein, M. Gutierrez, C.H. Fischer, Ber. Bunsenges. Phys. Chem. 88 (1984) 170–175
- 33. J.S. Hu, L.L. Ren, Y.G. Guo, H.P. Liang, A.M. Cao, L.J. Wan, C.L. Bai, *Angew. Chem. Int. Ed.* **44** (2005) 1269 –1273
- 34. J. Singh, G. Kaur, M. Rawat, J. Bioelectron. Nanotechnol. 1 (2016) 1–9
- D.P. Volanti, D. Keyson, L.S. Cavalcante, A.Z. Simoes, M.R. Joya, E. Longo,
 J.A.Varela, P.S. Pizani, A.G. Souza, J. Alloys Compd. 459 (2008) 537–542
- 36. C.C. Vidyasagar, Y. Arthoba Naik, T.G. Venkatesha, R. Viswanatha, *Nano Micro Lett.* **4** (2012) 73–77
- V. Scuderi, G. Amiard, S. Boninelli, S. Scalese, M. Miritello, P.M. Sberna, G. Impellizzeri, V. Privitera, *Materials Science in Semiconductor Processing* 42 (2016) 89-93
- 38. F. Zhang, X. Wang, H. Liu, C. Liu, Y. Wan, Y. Long, Z. Cai, *Appl. Sci.* **9** (2019) 2489
- 39. M.G. Kang, H.E. Han, K.J. Kim, *J. Photochem. Photobiol. A* **125** (1999) 119–125

- 40. A. Arabzadeh, A. Salimi, J. Colloid Interface Sci. 479 (2016) 43–54
- 41. V. Kuzhalosai, B. Subash, A. Senthilraja, P. Dhatshanamurthi, M. Shanthi, Spectrochimica Acta Part A: Molecular and Biomolecular Spectroscopy 115 (2013) 876–882
- 42. D. Rajamanickam, P. Dhatshanamurthi, M. Shanthi, *Spectrochimica Acta Part A: Molecular and Biomolecular Spectroscopy* **138** (2015) 489–498
- 43. L. Wolski, M. Ziolek, Applied Catalysis B: Environmental 224 (2018) 634-647
- 44. S. Moradi, P.A. Azar, S.R. Farshid, S.A. Khorrami, M.H. Givianrad, *International Journal of Chemical Engineering* (2012), Article ID 215373, 5 pages
- 45. P. Nyamukamba, M.J. Moloto, H. Mungondori, *Journal of Nanotechnology* (2019) Article ID 5135618, 10 pages
- 46. M. Nasirian, C.F. Bustillo-Lecompte, M. Mehrvar, *Journal of Environmental Management* **196** (2017) 487- 498
- 47. G.K. Pradhan, K. M. Parida, International Journal of Engineering, Science and Technology 2 (2010) 53-65
- 48. S.A.B. Asif, S.B. Khan, A.M. Asiri, *Nanoscale Research Letters* **10** (2015) 355
- 49. W. Zhang, X. Xiao, L. Zheng and C. Wan, *The Canadian Journal of Chemical Engineering* **93** (2015) 1594-1602
- K. Gurpreet, S. Seema, K. Kirandeep, B. Priti, Water Environment Research
 92 (2020) 1376-1387
- B.M. Pirzada, N.A. Mir, N. Qutub, O. Mehraj, S. Sabir, M. Muneer, *Mater. Sci. Eng. B* 193 (2015) 137–145
- 52. S. Velanganni, S. Pravinraj, P. Immanuel, R. Thiruneelakandan, *Phys. B:*Condens. Matter **534** (2018) 56–62

- 53. J. Wang, J. Yang, X. Li, D. Wang, B. Wei, H. Song, X. Li, S. Fu, *Phys. E Low-dimensional Syst. Nanostructures* **75** (2016) 66–71
- 54. Y. Chen, T. Yuan, F. Wang, J. Hu, W. Tu, *J. Mater. Sci. Mater. Electron.*, **27** (2016) 9983-9988
- E. Aguilera-Ruiz, U.M. García-Pérez, M. De La Garza-Galván, P. Zambrano-Robledo, B. Bermúdez-Reyes, J. Peral, Appl. Surf. Sci., 328 (2015) 361–367
- C. Maria Magdalane, K. Kaviyarasu, J. Judith Vijaya, C. Jayakumar, M.
 Maaza, B. Jeyaraj, J. Photochem. Photobiol. B Biol., 169 (2017) 110–123
- Z. Fang, Y. Liu, Y. Fan, Y. Ni, X. Wei, K. Tang, J. Shen, Y. Chen, J. Phys.
 Chem. C 115 (2011) 13968–13976
- 58. G.K. Pradhan, K. Hemalata Reddy, K.M. Parida, *Catalysis Today* **224** (2014) 171–179
- N. Jaffrezicrenault, P. Pichat, A. Foissy, R. Mercier, *J. Phys. Chem.* 12 (1986)
 2733–2738
- 60. J. Yin, Z. Zou, J. Ye, J. Phys. Chem. B 34 (2003) 14265–14269
- P.S. Sathish Kumar, R. Sivakumar, S. Anandan, J. Madhavan, P. Maruthamuthu,
 M. Ashok kumar, Water Research 42 (2008) 4878 4884
- 62. C. Ruby, Ashavani Kumar, R.P. Chaudhary, Spectrochimica Acta Part A:

 Molecular and Biomolecular Spectroscopy **113** (2013) 250–256
- 63. H. Reza Mardani, M. Forouzani, M. Ziari, P. Biparva, Spectrochimica Acta Part A: Molecular and Biomolecular Spectroscopy **141** (2015) 27–33
- 64. R. Saravanan, N. Karthikeyan, V.K. Gupta, E. Thirumal, P. Thangadurai, V. Narayanan, A. Stephen, *Materials Science and Engineering C* **33** (2013) 2235–2244

- 65. Tania Bigdeli, S. Moradi Dehaghi, Emerging Science Journal 2 (2018) 157-164
- 66. M. Mohsen Momenin, Yousef Ghaye, Ceramics International **42** (2016) 7014-7022
- 67. C. Ruby, Ashavani Kumar, Ram Pal Chaudhary, Spectrochimica Acta Part A:

 Molecular and Biomolecular Spectroscopy 98 (2012) 256–264
- 68. P.M. Perillo, M.N. Atia, *Materials Today Communications* **17** (2018) 562
- 69. G. Navyashree, K. Hareesh, D.V. Sunitha, H. Nagabhushana, G. Nagaraju, *Mater. Res. Express* **5** (2018) 095007
- 70. H. Letifi, Y. Litaiem, D. Dridi, S. Ammar, R. Chtourou, *Advances in Condensed Matter Physics* (2019) Article ID 2157428, 11 pages
- 71. Hong Hu, Chang long Xiao, Xiao cheng Lin, Kun Chen, Haitao Li, Xinyi Zhang, *Journal of Experimental Nanoscience*, **12** (2017) 33–44
- 72. A. Khalil, M. A. Gondal, M. A. Dastageer, *Appl. Catal. A Gen.*, **402** (2011) 162–167
- 73. C. G. Silva, J. L. Faria, Chem. Eng. J., 318 (2016) 95-102
- 74. S. Luo, W. Wang, C. Liu, J. Tian, X. Wu, W. Zu, X. Zhou, X. Yuan, X. Xiang, Sci. Rep., 7 (2017) 8108
- I. Zada, W. Zhang, W. Zheng, Y. Zhu, Z. Zhang, J. Zhang, M. Imtiaz, W. Abbas,
 D. Zhang, Sci. Rep., 7 (2017) 1–9
- M.B. Tahir, G. Nabi, M. Rafique, N.R. Khalid, *Int. J. Environ Sci. Tec.* 14 (2017) 2519–2542
- 77. C. Wang, X. Li, C. Feng, Y. Sun, G. Lu, Sensor Actuat B-Chem. **210** (2015) 75–81

- 78. G. Zerjav, M.S. Arshad, P. Djinovic, J. Zavasnik, A. Pintar, *Appl. Catal. B-Environ.* **209** (2017) 273–284
- 79. X. Zhu, P. Zhang, B. Li, Q. Hu, W. Su, L. Dong, F. Wang, *J. Mater. Sci.: Mater. Electron.* **28** (2017) 12158–12167
- 80. K. Santhi, C. Rani, S. Karuppuchamy, *Journal of Materials Science: Materials in Electronics* **27** (2016) 5033–5038
- 81. K. Shanthi, C. Rani, R. Dilip Kumar, S. Karuppuchamy, *Journal of Materials Science Materials in Electronics* 26 (2015)
- 82. C. Jeffrey, S. Wu, C.H Chen, *Journal of Photochemistry and Photobiology A:*Chemistry **163** (2004) 509–515
- 83. F.B. Li, X.Z. Li, Chemosphere **48** (2002) 1103–1111
- 84. Man Sig Lee, Seong-Soo Hong, Madjid Mohseni, *Journal of Molecular Catalysis A: Chemical* **242** (2005) 135–140
- 85. W.W. Scanlon, *Phys. Rev.* **109** (1958) 47
- 86. A.V. Borhade, B.K. Uphade, *Chalcogenide Lett.* **9** (2012) 299–306
- 87. M. Suganya, A. R. Balu, D. Prabha, S. Anitha, S. Balamurugan, J. Srivind, J. Mater. Sci.: Mater. Electron. 29 (2018) 4312–4319
- 88. V. Subramanian, E.E. Wolf, P.V. Kamat, *Langmuir* **19** (2003) 469–474
- 89. K. Wilke, H.D. Breuer, *J. Photochem. Photobiol. A* **121** (1999) 49–53
- 90. I. Bannat, K. Wessels, T. Oekermann, J. Rathousky, D. Bahnemann, M. Wark, *Chem. Mater.* **21** (2009) 1645-1653
- 91. J. Zhang, Y. Wu, M. Xing, S.A.K. Leghari, S. Sajjad, *Energy Environ. Sci.* 3 (2010) 715-726

- 92. F. Dong, H.Q. Wang, Z.B. Wu, J.F. Qiu, *J. Colloid Interface Sci.* **343** (2010) 200-208
- V. Gombac, L. De Rogatis, A. Gasparotto, G. Vicario, T. Montini, D. Barreca,
 G. Balducci, P. Fornasiero, E. Tondello, M. Graziani, *Chem. Phys.* 339 (2007)
 111-123
- 94. R. Saravanan, M. Mansoob Khan, V.K. Gupta, E. Mosquera, F. Gracia, V. Narayanan, A. Stephen, *Journal of Colloid and Interface Science* **452** (2015) 126–133
- 95. A. Senthilraja, B. Subash, P. Dhatshanamurthi, M. Swaminathan, M. Shanthi, Spectrochimica Acta Part A: Molecular and Biomolecular Spectroscopy 138 (2015) 31–37
- 96. S. Jorfi, S. Mirali, A. Mostoufi, M. Ahmadi, *Chem. Biochem. Eng. Q.*, **32** (2018) 215–227
- 97. N.F. Andrade Neto, Y.G. Oliveira, M.R.D. Bomio, F.V. Motta, *Journal of Electronic Materials* **48** (2019) 5900-5905
- 98. Abderrahim El Mragui, O. Zegaoui, I. Daou, Joaquim Carlos Gomes Esteves da Silva, *Environmental Science and Pollution Research* (2019) https://doi.org/10.1007/s11356-019-04754-6
- 99. L.K. Makia, A. Maleki, R. Rezaee, H. Daraei, K. Yetilmezsoyc, *Environmental Technology & Innovation* **15** (2019) 100411
- 100. D.L. Liu, P. Huang, Y. Liu, Z. Wu, D. Li, J. Guo, T. Wua, *Dalton Transactions*47 (2018) 6177-6183
- 101. D.S. Paeng, B. Huy, N.T. Kim Phuong, V.D. Dao, Y. Lee, *J Chem Technol Biotechnol* (2019), DOI 10.1002/jctb.6292

- 102. B.M. Bresolin, C. Günnemann, D.W. Bahnemann, M. Sillanpaa, *Nanomaterials*10 (2020) 763
- Y. Yulizara, D.O. B. Apriandanua, R.I. Ashnaa, Chemical Physics Letters 755
 (2020) 137749
- 104. G. Xing, C. Tang, B. Zhang, L. Zhao, Y. Su, X. Wang, Journal of Alloys and Compounds 647 (2015) 287-294
- 105. U. Alama, A. Khan, W. Raza, A. Khan, D. Bahnemann, M. Muneer, *Catalysis Today* 284 (2017) 169–178
- 106. J.T. Mehrabad, M. Khosravi, Nasser Modirshahla, M.A. Behnajady, *Desalination and Water Treatment* 57 (2015) 10451-10461
- 107. P. Nyamukamba, L. Tichagwa, S. Mamphweli, L.Petrik, *International Journal of Photoenergy* (2017) Article ID 3079276, 9 pages https://doi.org/ 10.1155/2017/3079276
- 108. G. Kamini, A. Pandey, R.P. Singh, Mater. Res. Express 4 (2017) 125504
- 109. Mehala Kunnama reddy, R. Ranjith, S. Megala, R. Ramesh, D. Barathi, *Journal of Inorganic and Organometallic Polymers and Materials* **31** (2021) 2615-2626
- T. Alex Kuvarega, W. M. Rui Krause, B.B. Mamba, J. Phys. Chem. C 115 (2011)
 22110–22120
- B. Singaram, J. Jeyaram, R. Rajendran, P. Arumugam, K. Varadharajan, *Ionics* 25 (2019) 773-784
- M.Y. Xing, W.K. Li, Y.M. Wu, J.L. Zhang, X.Q. Gong, J. Phys. Chem. C 115
 (2011) 7858–7865
- Y. Wang, Y. Wang, Y. Meng, H. Ding, Y. Shan, X. Zhao, X. Tang, J. Phys.
 Chem. C 112 (2008) 6620-6626

- 114. Y. Xie, J. Kum, X. Zhao, S.O. Cho, Semicond. Sci. Technol. 26 (2011) 085037
- 115. N.T. Lan, V.H. Anh, H.D. An, N.P. Hung, D.N. Nhiem, B.V. Thang, P.K. Lieu, D.Q. Khieu, *Journal of Nanomaterials* (2020), Article ID 1523164, 14 pages
- A. Biswas, A. Chakraborty, N.R. Jana, ACS Appl. Mater. Interfaces 10 (2018)
 1976–1986
- D. Chen, Z. Jiang, J. Geng, Q. Wang, D. Yang, Ind. Eng. Chem. Res. 46
 (2007) 2741-2746
- 118. F. Li, X. Yin, M. Yao, J. Li, J Nanopart Res 13 (2011) 4839–4846
- 119. S.A. Ansari, M.H. Cho, New J. Chem., **41** (2017) 9314-9320
- 120. A.B. Lavand, Y.S. Malghe, *International Journal of Photochemistry* (2015)Article ID 790153, 9 pages
- X. Zhang, J. Qin, R. Hao, L. Wang, Xi Shen, R. Yu, S. Limpanart, M. Ma, R.
 Liu, J. Phys. Chem. C 119 (2015) 20544–20554
- Y. Yang, Dawei Ni, Ye Yao, Y. Zhong, Ying Ma, J. Yao, RSC Adv., 5 (2015)
 93635-93643
- 123. S.U. Halimi, S. Abd Hashib, N. F. Abu Bakar, S. N. Ismail, M. Nazli Naim, N. Abd Rahman, J. Krishnan, IOP Conf. Series: Materials Science and Engineering 358 (2018) 012048
- 124. S. Habibi, M. Jamshidi, Environmental Technology 41 (2019) 3233-3247
- 125. S.Cho, J.W. Jang, J.S. Lee, K.H. Lee, Cryst Eng Comm 12 (2010) 3929–3935
- 126. G. Wu, T. Nishikawa, B. Ohtani, A. Chen, *Chem. Mater.* **19** (2007) 4530-4537
- 127. Y.Park, W. Kim, H. Park, T. Tachikawa, T. Majima, W. Choi, *Applied Catalysis*B: Environmental **91** (2009) 355–361

- 128. R. Ramakrishnan, S. Kalaivani, J. Amala Infant Joice, T. Sivakumar, *Applied Surface Science* **258** (2012) 2515–2521
- 129. J. Zhang, J. Zhang, Z. Jin, Z. Wu, Z. Zhang, Surface Review and Letters 16 (2009) 563–567
- 130. W. Wang, H. Zhao, P. Pan, K. Xue, Z. Zhang, J. Duan, *Ceramics International*,47 (2020) 6094-6104
- 131. S. Sharma, S.K. Mehta, A.O. Ibahdon, S.K. Kansal, *Journal of Colloid and Interface Science* **533** (2018) 227-237
- 132. R. Arunadevi, B. Kavitha, M. Rajarajan, A. Suganthi, A. Jeyamurugan, *Surf. Interfaces* **10** (2018) 32–44
- 133. B. Ahmed, S. Kumar, A.K. Ojha, P. Donfack, A. Materny, *Spectrochim. Acta Part A Mol. Biomol. Spectrosc.* **175** (2017) 250–261
- 134. S.G. Kumar, K.K. Rao, Appl. Surf. Sci. **355** (2015) 939–958
- 135. A. Malathi, P. Arunachalam, A.N. Grace, J. Madhavan, A.M. Mayouf, Applied Surface Science 412 (2017) 85-95
- 136. A. Priya, P. Arunachalam, A. Selvi, J. Madhavan, Abdullah M. Al-Mayouf, Colloids and surfaces 45 (2018) 83-91
- A. Malathi, Prabhakarn Arunachalam, V.S. Kirankumar, J. Madhavan, Abdullah
 M. Al-Mayouf, Optical Materials 84 (2018) 227–235
- 138. C. Wang, M. Wu, M. Yan, H. Shen, F. Cai, Bo Hu, W. Shi, *Ceramics International* 41 (2015) 6784-6792
- 139. U.I. Gaya, A.H. Abdullah, J. Photochem. Photobiol. C 9 (2008) 1-12
- 140. Z.Q. He, T.M. Hong, J.M. Chen, S. Song, Sep. Purif. Technol. 96 (2012) 50-57

- 141. Q. Li, QY.W. Li, P.G. Wu, R.C. Xie, J.K. Shang, J.K., Adv. Mater. **20** (2008) 3717
- 142. F. Dong, H.Q. Wang, Z.B. Wu, Z.B., J. Phys. Chem. C 113 (2009) 16717-16723
- 143. A. Azadehhaghighatzadeh, Bull. Mater. Sci. (2020) 43-52
- 144. J.D. Angulo, I.G. Bonilla, C.J. Tohapanta, M. Mueses, M. Pinzona, F.M. Martinez, *Photochemical & Photobiological Sciences* 18 (2019) 897
- 145. C. Chuaicham, R. Pawar, K. Sasaki, Catalysts 9 (2019) 235
- 146. M. Ghosh, P. Chowdhury, Ajay K. Ray, Catalysts 10 (2020) 917
- 147. Md. A.I. Molla, M. Furukawa, I. Tateishi, H. Katsumata, T. Suzuki, S. Kaneco, ChemEngineering 1 (2017) 8
- 148. S. Krishnan, A. Shriwastav, Journal of Environmental Chemical Engineering9 (2020) 104699
- J.J. Murcia, E.G. Ávila-Martínez, H. Rojas, J. Cubillos, S. Ivanova, A. Penkova,O.H. Laguna, *Nanomaterials* 9 (2019) 517
- 150. A. Wynona, Nimpoeno, H.O. Lintang, L. Yuliati, The 14th Joint Conference on Chemistry AIP Conf. Proc. 2237 (2019) 020048-1–020048-7
- 151. J.J Samuel, F.K. Yam, *Mater.Res.Express* **7** (2020) 015051
- 152. Z. Yan, W. Gong, Y. Chen, D. Duan, J. Li, W. Wang, J. Wang, *International Journal of Photoenergy* (2014) Article ID 968298, 10 pages
- T. Zoltan, M.C. Rosales, C. Yadarola, C. J. Environ. Chem. Eng. 4 (2016)
 3967–3980
- 154. X. Zhao, X. Liu, M. Yu, C. Wang, J. Li, Dyes Pigments 136 (2017) 648–656
- 155. F. Chen, Z. Deng, X.Z. Li, J. Zhang, J. Zhao, *Chem. Phys. Lett.* **415** (2005) 85-88

- 156. F. Chen, W.W. Zou, W.W. Qu, J.L. Zhang, Catal. Commun. 10 (2009) 1510-1513
- 157. O.V. Makarova, T. Rajh, M.C. Thurnauer, *Environ. Sci. Technol.* **34** (2000) 4797-4803
- G. Mascolo, R. Comparelli, M.L. Curri, G. Lovecchio, A. Lopez, A. Agostiano,
 J. Hazard. Mater. 142 (2007) 130-137
- 159. N. Martyanov, J. Klabunde, J. Catal. 225 (2004) 408-416
- 160. H.I. Cho, H.J. Park, G.Y. Kim, *J. Environ. Sci. Health, Part A* **40** (2005) 1033-1044
- T.T. Lim, P.S. Yap, M. Srinivasan, A.G. Fane, Crit. Rev. Environ. Sci. Technol. 41 (2011) 1173-1230
- 162. G. Williams, B. Seger, P.V. Kamat, ACS Nano 2 (2008) 1487-1491
- 163. T.A. Gad-Allah, S. Kato, S. Satokawa, T. Kojima, *Solid State Sci.* **9** (2007) 737-743
- 164. N. Nakayama, T. Hayashi, *Polym. Degrad. Stab.* **92** (2007) 1255-1264
- 165. Sh. Sohrabnezhad, M.A. Zanjanchi, M. Razav, *Spectrochimica Acta Part A: Molecular and Biomolecular Spectroscopy* **130** (2014) 129–135
- 166. J. Virkutyte, R.S. Varma, ACS Sustainable Chem. Eng. 2 (2014) 1545–1550
- 167. C. Sandoval, G. Molina, P.V. Jentszch, J. Perez, F. Munoz, *Journal of Advanced Oxidation Technologies* **20** (2017)
- 168. W.N.W. Ismail, S.K. Ain, R. Zaharudin, A. H. Jawad, M.A.M. Ishak, K. Ismai L, S. Sahid, *International Journal of Photoenergy* (2015) Article ID 232741, 6 pages
- 169. M.A. Nawi, Y.S. Ngoh, S.M. Zain, *International Journal of Photoenergy* (2012) Article ID 859294, 12 pages

- 170. M. Taghdiri, *International Journal of Photoenergy* (2017) Article ID 8575096,15 pages
- 171. P.H. Allé, G.D. Fanou, D. Robert, K. Adouby, P. Drogui, *Applied Water Science* **10** (2020) 207
- 172. M.E. Fabiyi, R.L. Skelton, *Journal of Photochemistry and Photobiology A:*Chemistry 132 (2000) 121–128
- 173. S.Y. Lee, D. Kang, S. Jeong, H. Tung Do, J.H. Kim, ACS Omega 5 (2020) 4233-4241
- 174. C.M. Ling, A.R. Mohamed, S. Bhatia, *Chemosphere* **57** (2004) 547-554
- 175. T. D. N. Phan, V. Hun Pham, E.J. kim, E. Suok Oh, S.H. Hur, J.S. Chung, B. Lee, E.W. Shin, *Applied surface surface* **258** (2012) 4551-4557
- 176. S. Razak, M.A. Nawi, K. Haitham, Applied Surface Science 319 (2014) 90-98
- 177. G. Zhang, A. Song, Y. Duan, S. Zheng, *Microporous Mesoporous Mater.* **255** (2018) 61–68
- 178. M.A. Basith, R. Ahsan, RI. Zarin, M.A. Jalil, Sci. Rep. 8 (2018) 1–11
- J.E. Lee, N.T. Khoa, S.W. Kim, E. J. Kim, S.H. Hahn, *Mater. Chem. Phys.*,
 164 (2015) 29–35
- P. She, S. Yin, Q. He, X. Zhang, K. Xu, Y. Shang, X. Men, S. Zeng, H. Sun,
 Z. Liu, *Electrochim. Acta* 246 (2017) 35–42
- G. Jiang, Z. Lin, C. Chen, L. Zhu, Q. Chang, N. Wang, W. Wei, H. Tang,
 Carbon 49 (2011) 2693–2701
- 182. N.R. Khalid, E. Ahmed, Z. Hong, L. Sana, M. Ahmed, *Curr. Appl. Phys.*, **13** (2013) 659–663
- 183. X. Rong, F. Qiu, C. Zhang, L. Fu, Y. Wang, and D. Yang, *Ceram. Int.* **41** (2015) 2502–251

- 184. W. Wang, Z. Wang, J. Liu, Z. Luo, S. L. Suib, P. He, Sci. Rep. 7 (2017) 1–9
- 185. Y. Cui, J. Huang, X. Fu, X. Wang, Catal. Sci. Technol., 2 (2012) 1396
- Q. Zhang, H. Wang, Z. Li, C. Geng, J. Leng, ACS Appl. Mater. Interfaces 9
 (2017) 1738–21746
- 187. B. Purohit, S. Kumawat, A. Dixit, Mater. Res. Express 5 (2018) 7
- 188. G. Xin, Y. Meng, J. Chem., (2013) 1–5
- Z. Zhu, Z. Lu, D. Wang, X. Tang, Y. Yan, W. Shi, Y. Wang, N. Gao, X. Yao,
 H. Dong, Appl. Catal. B Environ. 182 (2016) 115–122
- 190. M. Mousavi, A. Habibi-Yangjeh, J. Colloid Interface Sci. 465 (2016) 83–92
- 191. R.J. White, R. Luque, V.L. Budarin, J.H. Clark, D.J. Macquarrie, *Methods and applications*. *Chemical Society Reviews* **38** (2009) 481–494
- 192. T. Kamal, S.B. Khan, A.M. Asiri, Cellulose 23 (2016) 1911–1923
- 193. S. Haider, Applied Surface Science **387** (2016) 1154–1161
- I. Ahmad, T. Kamal, T., S.B. Khan, A.M. Asiri, Cellulose 23 (2016) 3577–
 3588
- 195. F. Ali, S.B. Khan, T. Kamal, K.A. AlamrY, A.M. Asiri, *Scientific Reports* **8** (2018) 6260
- 196. E. Korina, O. Stoilova, N. Manolova, I. Rashkov, J. Environ. Chem. Eng. 6 (2018)2075–2084
- R. Saravanan, E. Sacari, F. Gracia, M. M. Khan, E. Mosquera, V. K. Gupta, J.
 Mol. Liq. 221 (2016) 1029–1033
- 198. A. Di Mauro, M. Cantarella, G. Nicotra, G. Pellegrino, A. Gulino, M. V. Brundo, V. Privitera, G. Impellizzeri, *Sci. Rep.* **7** (2017) 1–12

CHAPTER - III

Aim and Scope

CHAPTER – III AIM AND SCOPE

3.1. NEED FOR THE PRESENT INVESTIGATION

Water, as a great natural resource, is central to all aspects of life. The extensive deterioration of the freshwater sources has put severe pressure on the government and public sectors. The quality of the ground water has come down to such an extent that it affects the ecology of our system has risen as a societal issue. Billions of people from all over the world come across water scarcity problems and are left without access to clean and safe drinking water¹⁻³. When the life of the common man and the environment is threatened, the industrial sector also faces much struggle to manage the water resources for the maintenance and technical operations. India's textile and manufacturing industries have paid a significant contribution to the export worldwide, and it has boosted the country's economy. The rapid growth in population, industrial sector and the ever-growing demand for natural resources have placed unprecedented pressure on the government and individuals⁴. In today's world, we are witnessing the conflict for water sources among various users. It is mainly due to the challenges such as poor water management practices, over abstraction of the water from the ground and surface levels and the issue of water crisis is worsened due to pollution caused by the effluent discharge^{5,6}.

The polluted water with high alkalinity, turbidity, TDS and intense colour are not only unsuitable for consumption but also poses severe heath issues and increases the fatality rate among humans and aquatic life⁷. This raised a growing concern among the environmentalist, researchers, as well as to the people who run the textile

and manufacturing sectors. Eventually, they began to rely on the treatment process such as coagulation, membrane filtration, sedimentation, biological processes such as using microbes and physical methods including evaporation, adsorption and the like. Even though effluent treatment by membrane filtration and biological processes arose as a worthy topic of research, the expenditure to feed the microbes, fouling and coggling of the membrane filters, and generation of the secondary pollutants are some of the issues which further needs to be addressed. Many of the conventional treatment techniques are found to be inefficient in attaining the maximum pollutant removal. This is mainly due to the recalcitrant nature of the organic pollutants. Hence the necessity for new advanced technologies and novel processes to abate pollutants arose as a topic of urgent need among the scientific community.

A survey of literature shows that in the past few decades, research is much focused on the advanced oxidation technologies such as fenton and photo-fenton like reactions, UV/H₂O₂, ozonation, wet catalytic air oxidation, electrochemical processes, catalysis using semiconductor metal oxides, sonochemical and microwave methods. All these oxidation technologies are similar but not the same and are predominantly based on the generation of reactive oxygen species such as hydroxyl and superoxide anion radicals for the degradation of pollutants¹⁰. The Advanced oxidation processes (AOP) are considered to be versatile technologies due to the ability to generate reactive oxygen species via different pathways and the organic pollutants are degraded to less-toxic intermediates or non toxic products. In view of the advantages of these AOP techniques, researchers are motivated to make use of the AOP technologies for the treatment of various pollutants such as dyes, pesticides, nitro compounds, phenols etc.

Among various advanced oxidation technologies, the heterogeneous semiconductor photocatalysis is an efficient process¹¹ for the degradation of the toxic pollutants due to the factors such as

- Non-toxic nature of the semiconductor metal oxides.
- > The cost of production of metal oxide photocatalysts is meager.
- > Semiconductor metal oxide photocatalysts are recyclable and reusable without much loss in photocatalytic activity.
- ➤ Properties of the metal oxide photocatalysts are easily tunable.
- > Strong oxidizing ability of the reactive oxygen species.
- The photocatalytic reaction can be performed at normal temperature.
- > It can make use of the sunlight as a natural source of energy.

The major steps involved in the heterogeneous photocatalytic process are:

- (i) Photon induced generation of e⁻- h⁺ pairs.
- (ii) Separation of the e⁻- h⁺ pairs to the valence and conduction bands of the material.
- (iii) The reaction of the $e^ h^+$ pairs with the surface adsorbed O_2 molecules and hydroxyl ions.
- (iv) Generation of reactive radical species such as 'OH and O_2 '.
- (v) Degradation of the toxic pollutants.

Even though light-induced photocatalytic process can give possible solutions to water pollution problems, there is still space for improvement in the solar-powered photocatalytic technology. The photodegradation ability of the heterogeneous semiconductors under direct sunlight is still low because of the fast recombination of the electron-hole pairs, which further results in low quantum yield and photocatalytic

activity¹². In order to make use of the solar photocatalytic technology efficiently a series of modification strategies are adopted by the researchers. Some of the recently adopted methods that we encountered during our literature review include the process such as coupling of the semiconductors, doping of metals and non-metals to the metal oxide semiconductors, codoping and tri-doping, doping a combination of metal and a non-metal, dye sensitization, modifying the semiconductors by quantum dots, preparation of supported semiconductors using carbon nanofibres, carbon nanotubes, graphene oxide, clay materials etc.

When photocatalyst modification techniques such as coupling, noble metal incorporation and dye sensitization gave the advantage of enhancing the electron-hole pair separation, broadening the range of visible light response of the photocatalyst, there are also some limitations associated with these techniques, such as the formation of oxygen vacancies in the case of non-metal doping, introduction of defects and dopant concentration dependency in the case of metal doped photocatalysts, multistep experimental process for codoping, use of expensive noble metals and the use of supports for photocatalysts leads to a major concern of decreased surface area, remobilization of the photocatalysts from the surface of the supports and less photocatalytic activity of the immobilized catalyst compared to dispersed form of catalysts are some major concerns which hinder the application of modified photocatalyst for commercial scale 13,14. Apart from the modification strategies, there are also some other factors that needs to be taken into consideration to obtain good photocatalytic activity such as the preparation methods adopted for the synthesis of photocatalysts, pH of the solution medium, dosage of the catalyst, intensity of light source, concentration of the pollutant, time taken for the degradation process, type of oxidants, surface charge properties photocatalysts etc.

However, there is still scope for the improvement and possibility of achieving a suitable modified photocatalyst via low cost metal doping process. The ability to increase the activity of the metal doped photocatalyst lies in the choice of the dopant and its concentration and from literature survey it is understood that only scarce attempts are made to check the applicability of the doped photocatalysts for real industrial effluents. Hence it is planned to prepare photocatalysts by precipitation method which is a simple, safe and cost effective technique and to evaluate its photocatalytic activity for the degradation of some synthetic organic dyes. Further attempts are made to modify the photocatalyst by finding suitable dopants and to check the utility of best doped photocatalysts for the treatment of industrial effluent.

3.2. AIM AND SCOPE OF THE PRESENT RESEARCH WORK

The present study aims

To degrade the synthetic organic dyes such as methylene blue, indigo carmine, crystal violet, basic yellow 2, acid red 94, congo red and acid green 1 dyes using reusable metal oxide nanophotocatalysts by effective air purging under sunlight.

To extent the potential of new nanophotocatalysts for the treatment of industrial effluent.

To study the antimicrobial property of the photocatalysts against various microorganisms.

The scope of the research programme includes

- Synthetic organic dyes which have industrial applications
- Synthesis of semiconductor photocatalysts which are suitable for the degradation of the selected organic dyes

- Characterization of synthesized photocatalysts in terms of their crystalline nature, morphology, optical response and surface properties
- Self-photolysis of the dyes
- Optimization of parameters such as pH, catalyst weight, initial dye concentration,
 weight percent of dopant and time for completion of degradation
- Kinetics of photocatalytic degradation of dyes
- Studies on the role of radical quenchers, the extent of mineralization, the reusability of the photocatalysts, the mechanism for photocatalytic degradation, total organic carbon analysis, physico-chemical parameters of the effluents, and the antimicrobial activity of the synthesized composite photocatalyst.

3.3. OBJECTIVES OF THE PRESENT WORK

The objective of the present work is:

- (i) To synthesize photocatalytically active semiconductor metal oxides such as zinc oxide, titanium dioxide and bismuth oxychloride by simple chemical precipitation method
- (ii) To study the optical and morphological properties of the synthesized photocatalysts using the analytical techniques such as:
 - X-Ray Diffraction analysis to understand the crystallinity of the synthesized photocatalysts.
 - Field Emission Scanning Electron Microscopic Analysis to study the surface properties of the synthesized photocatalysts.
 - Energy Dispersive X-Ray Analysis to determine the major elemental composition of the synthesized photocatalysts.

- High Resolution Transmission Electron Microscopic Analysis is taken to gain more insight into the morphology, crystallinity and particle size of the synthesized photocatalysts.
- Fourier Transform Infra Red spectroscopy is taken to confirm the formation of metal oxide and metal-metal bonds in the synthesized photocatalysts.
- UV-Visible Diffuse Reflectance Spectroscopy Analysis is done to calculate the band gap values of the synthesized photocatalysts.
- Nitrogen Adsorption Desorption Isotherm is taken for the synthesized photocatalysts to understand the porous nature and to determine the specific surface area.
- (iii) To carry out preliminary photocatalytic experiments under different conditions to understand the effects of adsorption process, magnetic stirring and air oxidation.
- (iv) To determine the optimum pH of the dye solutions using suitable photocatalysts.
- (v) To optimize the weight of the synthesized photocatalysts for the required quantity of dye solution.
- (vi) To fix the initial concentration of the dye solution with respect to optimized pH condition and catalyst dosage.
- (vii) To enhance the photocatalytic decolourization process by incorporating different dopants such as aluminium fluoride and strontium silicate to the metal oxide.
- (viii) To determine the correct weight percent of the dopants in the metal oxide to achieve maximum photocatalytic decolourization efficiency.
- (ix) To carry out the kinetic studies for the photocatalytic dye degradation by Langmuir-Hinshelwood kinetic model.

- (x) To study the effect of radical quenchers and understand the effect of different oxidizing species involved in the photocatalytic process.
- (xi) To find out the percentage degradation of the dye solution by carrying out the total organic carbon analysis.
- (xii) To check the reusability of the photocatalysts to make it cost effective.
- (xiii) To propose a suitable mechanism for the photocatalytic dye degradation process.
- (xiv) To compare the percentage decolourization given by different doped and undoped photocatalysts and to use the best photocatalysts for effluent treatment.
- (xv) To study the disinfection properties of the photocatalysts against different microorganisms and to propose a suitable mechanism.

BIBLIOGRAPHY

- Barua, K. Hubacek, International Journal of Global Environmental Issues 9
 (2009) 50-68
- 2. R. Bertelsen, India Struggles with Textile Water pollution (2012) http://blog.airdye.com/goodforbusiness/2011/12/05/india-struggles-with-textile-waterpollution/
- 3. United Nations World Water Assessment Programme (UN WWAP). (2003).
 United Nations World Water Assessment Programme. The 1st UN World Water Development Report: Water for People, Water for Life.
 URL. http://www.unesco.org/water/wwap/wwdr/wwdr1/.
- 4. Maity, Chakraborty, *Indian Journal of Applied Economics* **8** (1999) 99-119
- 5. K.K. Sivakumar, C. Balamurugan, D. Ramakrishnan, L.H. Bhai, *Rasayan Journal Chemistry* **4** (2011) 264-269
- 6. M. Mondal, G. Biswas, R. Bhattacharya, *International Journal of Environmental Sciences* **6** (2015) 467-471
- 7. K. Rajeswari, R. Subashkumar, K. Vijayaraman, *Journal of Microbiology and Biotechnology Research* **3** (2013) 37-41
- 8. K. Padmaja, J. Cherukuri, M. Anji Reddy, *International Journal of Innovative Research in Science, Engineering and Technology* **3** (2014) 9375-9385.
- 9. P. Rajasulochana, V. Preethy, *Resource-Efficient Technologies* 2 (2016) 175-184
- L. Bilinska, M. Gmurek, S. Ledakowicz, J. Adv. Oxid. Technol. 18 (2015)
 185-194
- L. Gomathi Devi, B. Narasimha Murthy, S. Girish Kumar, Chemosphere 76
 (2009) 1163–1166

- 12. A. Kumar, G. Pandey, *Material Sci & Eng Int J* **1** (2017) 00018
- 13. M.N. Chong, B. Jin, C.W.K. Chow, C. Saint, Water research 44 (2010) 2997-3027
- 14. A.R. Ribeiro, O.C. Nunes, M.F.R. Pereira, A.M.T. Silva, *Environ. Int.* **75** (2015) 33–51

CHAPTER - IV

Materials and Methods

CHAPTER - IV

MATERIALS AND METHODS

This chapter gives information regarding the dyes chosen for the study, chemicals and reagents used for the synthesis of the photocatalysts. Also, various instrumental techniques used for the characterization of the photocatalyst, procedure for the photocatalytic experiments, antimicrobial activity and the physico-chemical analysis of the textile effluent are discussed in the following sub-sections.

4.1. DYES CHOSEN FOR THE STUDY

(i) Methylene Blue

Chemical Structure:

Other Names : Urelene Blue, Provay Blue, Basic Blue.

C.I. No. : 52015

Chemical Classification : Thiazine dye

 $Molecular \ Formula \qquad \qquad : \qquad C_{16}H_{18}ClN_3S$

Molar mass : $319.85 \text{ g mol}^{-1}$

Absorption wavelength λ_{max} : 663nm

Application:

Methylene blue is a water soluble cationic dye. The most common application of dye is that it can be used for colouring paper, temporary hair colourant and mainly it is used on soft vegetable fibers such as jute, flax and hemp. It dyes silk and wool. Only, to a lesser extent it is used on paper, leather and mordant cotton.

(ii) Indigo Carmine

Other Names : Indigotine, Brilliant indigo 4G, Acid Blue 74.

C.I. No. : 3015

Chemical Classification : Indigoid dye

 $Molecular \ Formula \qquad \qquad : \qquad C_{16} \ H_8 \ N_2 N a_2 O_8 S_2$

Molar mass : $466.36 \text{ g mol}^{-1}$

Absorption wavelength λ_{max} : 610 nm

Application

Indigo carmine is one of the anionic dyes used commonly as a textile colouring agent and as an additive in pharmaceutical tablets and capsules. Indigoid dyes are mainly used for cotton and cellulosic fibres. These dyes are not suitable for wool and silk because the fibres are damaged in alkaline medium. They have low affinity for synthetic fibres.

(iii) Crystal Violet

Other Names : Gelatin violet, methyl violet 10 B, Aniline violet.

C.I. No. : 42555

Chemical Classification : Triphenylmethane dye

 $Molecular \ Formula \qquad \qquad : \qquad C_{25}H_{30}ClN_3$

Molar mass : $407.99 \text{ g mol}^{-1}$

Absorption wavelength λ_{max} : 590 nm

Application:

Crystal violet dye is a cationic water soluble dye. It is used as a textile dye which can be directly applied to protein fibres like wool and silk as well as for paper dyeing. It is also used as a component of navy blue dye and black inks for printing purposes. It is also used to colour the products in fertilizers, antifreezers, detergents and also for leather dyeing.

(iv)Basic yellow 2

Other Names : Auramine O, Aizen auramine, Canary Yellow.

C.I. No. : 41000

Chemical Classification : Diarylmethane dye

 $\label{eq:molecular Formula} \qquad \qquad : \qquad C_{17}H_{22}ClN_3$

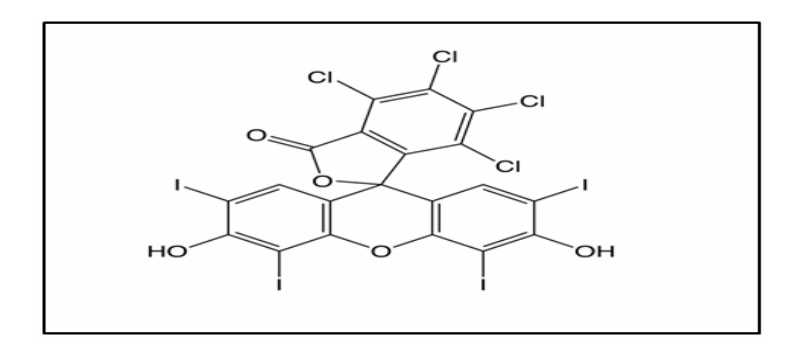
Molar mass : $303.83 \text{ g mol}^{-1}$

Absorption wavelength λ_{max} : 432 nm

Application:

Basic yellow 2 is a cationic water soluble dye. The dye is used as a fluorescent stain and also for staining acid-fast bacteria. It is extensively used for dyeing paper, silk, leather and jute.

(v) Acid Red 94



Other Names : Rose bengal

C.I. No. : 45440

Chemical Classification : Xanthane dye

 $Molecular\ Formula \qquad \qquad : \qquad C_{20}H_4Cl_4I_4O_5$

Molar mass : $973.67 \text{ g mol}^{-1}$

Absorption wavelength λ_{max} : 559 nm

Application:

Acid red 94 is an anionic water soluble dye. It is a photosensitive dye widely used in textile, medicinal and photochemical industries. The dye is generally used for paper dyeing, it is also used for dyeing wool, silk and cotton mordanted with tannin where brilliant shades of fluorescein effects are required on the materials.

(vi) Congo Red

Other Names : Brilliant congo, Cosmos red, Cotton red B.

C.I. No. : 22120

Chemical Classification : Azo dye

Molecular Formula : $C_{32}H_{22}N_6Na_2O_6S_2$

Molar mass : 696.665 g mol⁻¹

Absorption wavelength λ_{max} : 338nm, 497 nm

Application:

Congo red dye is an anionic water soluble dye. The congo red dye is used to dye cotton, in histology to stain tissues as well as an acid-base indicator.

(vii) Acid green 1

Other Names : Naphthol green B, Acid green PXC.

C.I. No. : 10020

Chemical Classification : Nitroso dye

Molecular Formula : $C_{30}H_{15}$ FeN₃Na₃O₁₅S₃

Molar mass : 878.46 g mol⁻¹

Absorption wavelength λ_{max} : 715 nm

Application:

Acid green 1 dye is an anionic dye. The dye shows excellent absorption and excellent light fastness. It is mainly used to dye wool, silk and nylon fabric dyeing, printing and it is also used for leather dyeing.

4.2. CHEMICALS REQUIRED

Zinc acetate dihydrate, Titanium tetrachloride, Bismuth nitrate pentahydrate from Sisco Research Laboratory Chemicals Pvt. Ltd., Aluminium Fluoride, Aluminium silicate, Sodium hydroxide and Ethanol (99.9%) from Merck, Potassium chloride, Ammonium hydroxide, Isopropanol, Ethylene diammine tetra acetic acid, Ascorbic acid and Sodium sulphate from Qualigens were procured and used as such.

Synthetic organic dyes such as Methylene blue, Congo red, Indigo carmine, Crystal violet are purchased from S.D. Fine chemicals, Rose Bengal, Basic yellow 2, Acid green 1 from SRL Chemicals, India of analytical grade were purchased and used. All the reagents of analytical grade were obtained and used without any further purification.

4.3. SYNTHESIS OF PHOTOCATALYSTS

Detailed procedure followed to synthesize the metal doped as well as undoped photocatalysts are discussed in the following sub-sections

4.3.1 Synthesis of Aluminium fluoride doped ZnO and Strontium silicate doped ZnO Photocatalysts

Simple chemical precipitation-decomposition method was adopted for the synthesis of modified zinc oxide photocatalysts. About 2g of zinc acetate dihydrate salt is dissolved in 50 mL of double distilled water and 2 weight percent of aluminium fluoride salt is added to the precursor and the solution is left for magnetic stirring under room temperature for about 30 minutes. To this dopant containing precursor salt solution about 4mL of 0.8M sodium hydroxide solution is added dropwise and 2mL of absolute ethanol is added along the sides of the beaker and the magnetic stirring is continued for about another 60 minutes. A thick white precipitate of zinc hydroxide obtained is centrifuged, washed thrice with double distilled water and it is dried in a hot air oven at 80° C for 6 hours. The dried mass is taken in a silica crucible and further calcined in a muffle furnace at 400° C for 3 hours with a heating rate of 20 min⁻¹ to attain its decomposition temperature. The muffle furnace is allowed to cool down to room temperature and the obtained zinc oxide powder is grinded well using a motor pestle. The fine powders of zinc oxide photocatalyst containing 2 weight percent of aluminium fluoride salt is stored in the refrigerator for further

characterization and photocatalytic studies. Similarly 0.5, 1 and 3 weight percent of aluminium fluoride containing zinc oxide photocatalyst is prepared following the same procedure.

In a similar way, the different weight percent (0.5, 1, 2 and 3 wt %) of strontium silicate containing zinc oxide photocatalyst is prepared following the above procedure. The bare zinc oxide photocatalyst is prepared without the addition of aluminium fluoride and Strontium silicate dopants by chemical precipitation method¹.

4.3.2 Synthesis of Aluminium fluoride doped TiO_2 and Strontium silicate doped TiO_2 Photocatalysts

Aluminium fluoride/TiO₂ and Strontium silicate/TiO₂ Photocatalysts are also prepared by simple precipitation-decomposition method. For synthesizing aluminium fluoride doped titanium dioxide photocatalyst, about 50 mL of double distilled water is added to 9.5 mL of titanium tetrachloride solution under ice cold condition. The solution is left as such to attain the room temperature and it is magnetically stirred for 15 minutes. Then one weight percent of aluminium fluoride salt is added to the precursor solution. A well mixed solution of the precursor and dopant is obtained by continuing the magnetic stirring for about another half an hour. To this combined solution 2 mL of 0.8M sodium hydroxide solution is added dropwise and the temperature in the magnetic stirrer is raised to 60°C and the magnetic stirring is continued for 60 minutes. The thick white precipitate of AlF₃-Ti(OH)₄ obtained is left for digestion for about 30 minutes and the supernatant solution is decanted. The precipitate is washed with double distilled water and the process of digestion and decantation is repeated for three times. The precipitate is then dried in a hot air oven at 80°C for 6 hours. The dried mass of AlF₃-Ti(OH)₄ is further transferred to a silica

crucible and calcined in a muffle furnace at 400°C for 3 hours to obtain one weight percent aaluminium fluoride doped TiO₂ photocatalyst. The photocatalyst is grinded well to a fine powder using a motor pestle and it is stored in the refrigerator for further characterization and photocatalytic studies. Similarly, the remaining TiO₂ photocatalysts with 0.5, 2 and 3 weight percents of aluminium fluoride dopant is prepared by adopting the same procedure.

In a similar way, different weight percent of strontium silicate (0.5, 1, 2 and 3 wt %) containing titanium dioxide photocatalyst is prepared by adopting the above procedure. The bare Titanium dioxide photocatalyst is prepared without the addition of aluminium fluoride and strontium silicate dopants by chemical precipitation method².

4.3.3. Synthesis of Aluminium fluoride doped BiOCl and Strontium silicate doped BiOCl Photocatalysts

Different weight percent of aluminium fluoride doped bismuth oxychloride photocatalyst is prepared by chemical precipitation method in an acidic medium. About 4.85g of bismuth nitrate pentahydrate salt is dissolved in approximately 100mL of double distilled water by heating it at 40°C for about 20 minutes and then the solution is magnetically stirred for about half an hour at room temperature. 3 weight percent of aluminium fluoride powder is added to the precursor salt solution and the magnetic stirring is continued for about another half an hour. To this dopant combined bismuth nitrate precursor salt solution, 50 mL of 0.2M potassium chloride solution is added in a dropwise manner along the sides of the beaker and after the complete addition of potassium chloride solution, 1mL of 25% aqueous ammonium hydroxide is also added and the magnetic stirring is continued for about 7 hours. The beaker with

the precipitated solution is left undisturbed for 60 minutes and then the supernatant liquid is carefully decanted and the precipitate obtained is washed several times with double distilled water and dried in a hot air oven at 120°C for 5 hours. The dried mass is then transferred into a silica crucible and taken to the muffle furnace, calcined at 600°C for 3 hours to obtain crystalline aluminium fluoride doped BiOCl photocatalyst. Similarly the other weight percent (0.5, 1, 2 and 4 wt %) of aluminium fluoride doped BiOCl photocatalyst is prepared by following the same procedure.

In a similar way, different weight percent (0.5, 1, 2, 3 and 4 wt %) of strontium silicate containing bismuth oxychloride photocatalyst is prepared by following the above procedure except that instead of aluminium fluoride, strontium silicate powder is added to the precursor salt solution. The bare bismuth oxychloride photocatalyst is prepared without the addition of aluminium fluoride and strontium silicate dopants by following the procedure³.

4.4. CHARACTERIZATION TECHNIQUES

The analytical instruments used for the characterization of synthesized photocatalysts are discussed below in detail

4.4.1. X-Ray Diffraction Studies

Determination of the phase purity, crystalline or amorphous nature and the crystallite size of all the synthesized photocatalysts were obtained using Powder X-Ray diffractometer (PANalytical X' Pert Pro) using Cu-K α radiation of wavelength 1.54nm, operating at 40 kV and a current of 40mA. The diffractograms were recorded in the 2 θ range of 10 to 100° in steps of 0.02° with count time of 20 s at each point.

The average crystallite sizes of the synthesized photocatalysts are determined using Debye-Scherrer equation (2.1)

D =
$$K\lambda/\beta$$
 Cos θeq.(4.1)

where D is the crystallite size,

K is the constant (0.89),

 λ is the wavelength of radiation (1.54 nm),

β is the full width at half maximum of the diffraction peak,

 θ is the diffraction angle.

4.4.2. Field Emission-Scanning Electron Microscopic Analysis

In Field Emission Scanning electron microscopic analysis, the beam of electrons move across the surface of the mounted sample, collects scattered electrons and provides us a depth profiling of the shape and orientation of the materials taken for the study. Morphological studies of the synthesized bare and metal containing photocatalysts are carried out using FE-SEM (Quanta, FEG 200 F) under different magnifications ranging from 500nm to 10µm.

4.4.3. Energy Dispersive X-Ray Analysis

The elemental compositions of the synthesized photocatalysts were studied using energy dispersive x-ray analysis using FE-SEM (Quanta, FEG 200F) equipped with EDS, a nano manipulation system. The synthesized photocatalysts in the dry powdered form is loaded onto the stub using conductive carbon tapes, the specimen is analyzed for one minute and detected using Si (Li) detector, which gives rise to information pertaining to the elemental composition in the range of ppm-0.1%.

4.4.4. Transmission Electron Microscopic Analysis

A more insight into the surface topography such as shape, size, orientation and selected area diffraction patterns for the synthesized photocatalysts were obtained using HR-TEM (JEOL, JEM 2100F), accelerating potential (120/200kV) under different magnifications ranging from 2 nm to 0.2µm. For HRTEM analysis powdered samples of the catalyst were dispersed in ethanol. The alcoholic solution containing the powdered catalyst was sonicated for 15 minutes, a drop of the solution placed on copper grid was analyzed and the images were recorded.

4.4.5. UV-Diffuse Reflectance Spectrum

The optical response and the bandgap measurements of the synthesized photocatalysts were studied using Shimadzu UV2600 model diffuse reflectance spectrophotometer equipped with an integrating sphere. The powdered photocatalysts were dispersed in a water medium with barium sulphate as an internal standard and a quartz cell with thickness of 5mm is used for the study. The spectra is recorded at room temperature in the range of 200-800nm.

4.4.6. Fourier Transform Infra Red Spectroscopy Studies

Fourier transform infra red spectroscopic technique is used for the identification of metal-metal bonds and metal-oxygen bonds in the synthesized photocatalysts. FTIR spectrum of the powder photocatalysts were recorded using Perkin Elmer 1600 FTIR spectrophotometer using IR grade KBr. About 70 mg of KBr mixed with 10 mg of the sample is made into a pellet using a hydraulic press. The pellet is scanned 60 times at a resolution of 4 cm⁻¹ to record the FTIR spectra in the range of 4000-400 cm⁻¹.

4.4.7. BET-Surface area Analysis

The specific surface area of all the synthesized photocatalysts were determined using Quantachrome instruments, Autosorb IQ Series. For performing the surface area measurements, the samples were degassed at a pressure of 10⁻⁵ torr and a mixture of Helium and Nitrogen (30:70) gas was passed through the degassed samples at liquid nitrogen temperature 77 K as the adsorbate. The specific surface areas of the catalysts were determined from the linear portion of the BET plot.

4.4.8. Double Beam UV-Visible spectrophotometer

UV-Visible spectroscopy is an important technique to evaluate the decrease in the absorption wavelength of the dye solution during photocatalytic reactions. At appropriate time intervals, the dye solution is collected, suitably diluted, and the centrifuged solution is subjected to spectrophotometric analysis using Double Beam UV-Visible (HITACHI U-2910) model spectrophotometer.

4.4.9. Total Organic Carbon Analyzer

The total organic carbon content in the samples before and after the photocatalytic dye degradation process is measured using the Total organic carbon analyzer (TOC-L CPN SHIMADZU) model. The TOC analyzer is such a versatile instrument that it has a detection limit ranging from 4 ppb to 30,000 ppm level.

To measure the total organic carbon content in the prepared dye samples, first the inorganic carbon content in the samples are removed by the acid purging method. For this 2N HCl is purged into the sample in the presence of air. The acid addition ratio with respect to the sample is 2%. The solution is then allowed to flow through the combustion tube packed with the platinum catalyst maintained at 700°C. In this

way, the inorganic carbon in the sample is removed and the sample is then completely oxidized to CO₂. The oxygen used as a carrier gas will be regulated at a flow rate of 150 mL min⁻¹, which carries the combustion products from the combustion tube to the dehumidifier, halogen scrubber and finally detected by the non dispersive infra red (NDIR) detector, which measures the carbon dioxide content. The peak areas given as output signal by the NDIR detector will be processed by the data processing unit. Since, these peak areas correspond to the total carbon content in the sample, the total carbon measured in this method will be referred to as the total organic carbon.

Other equipment used for the photocatalytic experiments include the digital pH meter (ELICO- LI 10T) model for measuring the pH of the solution and a digital Lux meter [Luxtron Lx-101] model is used to measure light intensity.

4.5. Photocatalytic studies

4.5.1. Preparation of the stock solution

Stock solutions of synthetic organic dyes, namely methylene blue, indigo carmine, crystal violet, congo red, basic yellow 2, rose bengal and acid green 1 are prepared by dissolving 0.01g of the respective dyes in 1000 mL of double distilled water and the standard flask is wrapped with a silver foil and stored in a dark place so as to avoid the sunlight penetration. Required quantities of the dye solution are withdrawn from the bulk for each photocatalytic experiment.

4.5.2. Photocatalytic degradation of dyes

For each photocatalytic experiment, 50 mL of the dye solution is withdrawn from the bulk and an appropriate amount of the catalyst is added to it. The solutions are magnetically stirred in the dark for 15 minutes to attain the adsorption-desorption

equilibrium and then it is exposed to sunlight. The dye solutions are continuously mixed by pumping to provide aeration. The capacity of the aerator is 3W and the air supplied is approximately 2.5L/min. At appropriate time intervals, 1-2 mL of the dye solution is withdrawn and centrifuged to remove the catalyst. The solutions are then suitably diluted and the absorbance of the dye solution at specific wavelengths is recorded using a UV-Visible spectrophotometer. All the photocatalytic experiments were carried out on sunny days and the intensity of the light is measured using a digital lux meter (Luxtron Lx-101). The pH studies are carried out by adjusting the pH of the dye solution using 0.1 N NaOH and HCl.

The percentage decolourization is calculated using the formula

$$\frac{C_o - C}{C_o} \times 100$$
eq.(4.2)

Where C_o is the initial concentration of the dye solution and C is the concentration of the dye solution at time 't'.

4.6. Collection and storage of the Dye effluent

To investigate the potential of the best photocatalyst for effluent treatment, the effluent released form dyeing industries was collected from Tiruppur district, Tamil Nadu, India. As Tiruppur is a hub of textile and garment industries and since it has a large number of dyeing units located close to the rivers Noyyal and Amaravathi, this area was chosen for the collection of the effluent. The sample was collected in a clean polythene can of five litre capacity and after bringing it to the laboratory, it was filtered through a whatmann filter paper to remove the suspended particles if any and the filtered sample was stored in a plastic bottle leaving 2.5 cm space above to facilitate mixing via shaking. The effluent collected in this way was stored at room

temperature and later on it was subjected to photocatalytic studies. The physicochemical parameters of the collected dye effluent were analyzed by following standard APHA procedure⁴.

4.7. Antimicrobial studies

4.7.1. Collection of test pathogens

The antibacterial and antifungal activity of samples were exhibited against one gram positive bacterial strains *Staphylococcus aureus* (MTCC 25923) and two gram negative bacterial strains *Escherichia coli* (MTCC 25922), *Pseudomonas aeruginosa* (MTCC 27853) and for fungal culture used in the study are *Candida albicans* (MTCC 282), *Candida auris* (MTCC 3956) *Aspergillus flavus* (MTCC 237) were prepared as test organisms. All the bacterial strains were purchased from the Microbial Type Culture and Collection (MTCC) at Chandigarh, India and the fungal strains from National Chemical Laboratory (NCL), Pune, Maharashtra, India.

4.7.2. Determination of antibacterial activity by disc diffusion method

The disc diffusion method was used to evaluate the antibacterial activity of the samples^{5,6}. Ten ml of Mueller-Hilton agar medium was poured into sterile petri dishes (diameter 60 mm) and inoculated with test organism. Sterile filter paper dics loaded with various concentrations of sample of 60, 80 and 100 µg/ml were placed on the top of Mueller-Hilton agar plates. Amoxicillin was used as the standard. The plates were incubated at 37 °C for 24 hours and the zone of inhibition was recorded in millimeter and the experiment was repeated twice.

4.7.3. Determination of antifungal activity by disc diffusion method

Disc diffusion method⁷ was carried out in order to test the antifungal activity of samples against test pathogens. In petri dishes (60 mm) filled with Sabouraud's dextrose agar (SDA) and seeded with a 0.3 ml of test organism, a sterile filter paper disc (diameter 6 mm, whatmann paper no.3) was placed. The sterile disc was impregnated with 10 μ l of samples at varying concentration of 60, 80 and 100 μ g/ml respectively. The zones of growth inhibition around the disc were measured after 24 hrs of incubation at 37°C while, Fluconazole was used as a standard.

BIBLIOGRAPHY

- N. Yahya, S. N. S. Zahari, A. Ramli, N. M. Mohamad, P. Puspitasari, N. L.
 Che Zul, AIP Conference Proceedings 1136 (2009) 401-405
- 2. P.B. Rathod, K.R. Nemade, S.A. Waghule, *International Journal of Chemical and Physical Sciences* **4** (2015) 491-495
- I.D. Sharma, G.K. Tripathi, V. K. Sharma, S.N. Tripathi, R. Kurchania, C. Kant,
 A. K. Sharma, K.K. Saini, Cogent Chemistry 1 (2015)1076371
- E.W. Rice, R.B. Baird, A.D. Eaton, Standard Methods for the Examination of Water and Wastewater, 23rd Edition, American Public Health Association, American Water Works Association, Water Environment Federation, (2017)
- 5. EUCAST. "Antimicrobial susceptibility testing: EUCAST disk diffusion method". www.eucast.org. EUCAST. Retrieved March 16, 2021
- C. Valgas, S.M. De Souza, E.F.A. Smânia. *Braz. J. Microbiol.* 38 (2007) 369–380
- 7. M.S. Ali-Shtayeh, G.S.I. Abu. *Mycoses*. **42** (1999) 665–672

CHAPTER - V

Results and Discussion

CHAPTER - V

RESULTS AND DISCUSSION

5.1. CHARACTERIZATION AND PHOTOCATALYTIC STUDIES OF ZINC OXIDE, ALUMINIUM FLUORIDE DOPED ZINC OXIDE AND STRONTIUM SILICATE DOPED ZINC OXIDE

5.1.1. X-Ray Diffraction Studies

Powder X-Ray Diffraction (P-XRD) technique was used to study the crystalline nature and phase identification of the synthesized materials. For the present study, the intensity of diffracted beam was recorded at different 2θ values. The P-XRD patterns of bare zinc oxide, aluminium fluoride doped zinc oxide and strontium silicate doped zinc oxide photocatalysts are shown in figure 5.1.1 A-C. The sharp peaks observed in the diffractograms obtained from the synthesized photocatalysts indicate that they are highly crystalline in nature. In the figure 5.1.1 A, the diffraction peaks at 2θ values 31.75, 34.41, 36.24, 47.51, 56.55 and 62.80 correspond to the crystal planes (100), (002), (101), (102), (110) and (103), respectively, and confirm the hexagonal wurtzite phase of the synthesized zinc oxide photocatalyst¹. These observations are in accordance with the values reported in the literature [standard JCPDS (36-1451)]. No additional diffraction peaks arising out of any impurity is observed in the P-XRD pattern of the bare ZnO catalyst. Similar diffraction patterns are also observed for the aluminium fluoride and strontium silicate doped zinc oxide photocatalysts as shown in figures 5.1.1 B and C. No observable peaks due to the doping of aluminium fluoride and strontium silicate in the zinc oxide photocatalyst is visible in the P-XRD

pattern. This may be due to the incorporation of very small amount of the dopants into the lattice of ZnO photocatalyst. However, a decrease in the peak intensities in the P-XRD pattern as well as a decrease in the crystallite size is observed for the AlF₃ doped and SrSiO₃ doped zinc oxide photocatalysts compared to the undoped zinc oxide photocatalyst. This may be due to the fact that the electron density of the dopant atom is different from that of the surrounding atoms, thus the introduction of the dopants or obstacles prevents the growth of crystallite and limits the size of particles². The calculated average crystalline size of bare zinc oxide photocatalyst, aluminium fluoride doped zinc oxide catalyst and strontium silicate doped zinc oxide catalyst, are 35 nm, 25 nm and 18.2 nm, respectively.

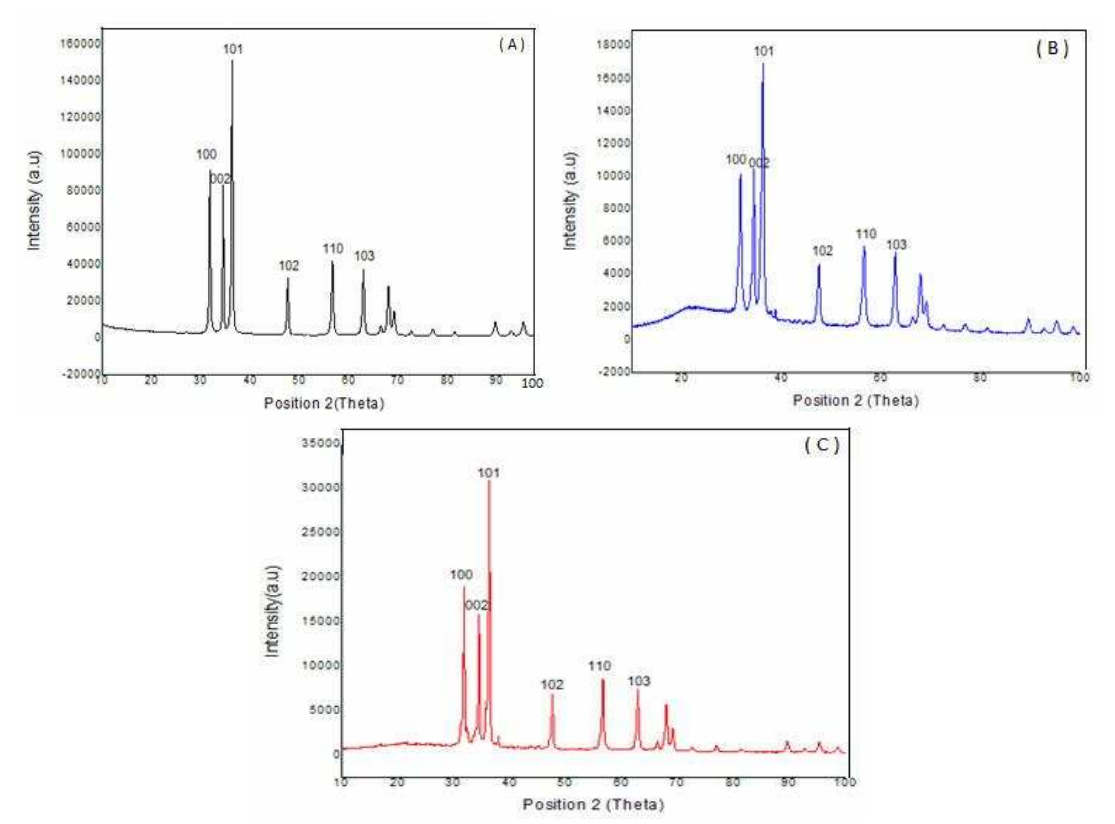


Figure 5.1.1 X-Ray diffraction pattern of the synthesized (A) undoped zinc oxide photocatalyst (B) 2 wt% AlF₃ doped zinc oxide photocatalyst and (C) 2wt% SrSiO₃ doped zinc oxide photocatalyst.

5.1.2. HR-SEM Analysis

High resolution scanning electron microscopy is one of the vital techniques to understand the surface morphology (texture), crystalline nature and orientation of the particles making up the sample. The SEM images of doped and undoped zinc oxide photocatalysts are shown in the figure 5.1.2 A-C. From the SEM images it is observed that the synthesized zinc oxide photocatalyst possess a moderately rod-like structure, even though the particles are observed to be highly agglomerated. The crystalline nature of both the bare and metal doped zinc oxide photocatalyst is evidenced from the SEM micrographs. The morphology of the aluminium fluoride doped and strontium silicate doped zinc oxide catalyst is found to be different from that of the bare photocatalyst. The morphology of aluminium fluoride doped zinc oxide catalyst and strontium silicate doped zinc oxide catalyst is observed to be a cluster of rod shaped particles.

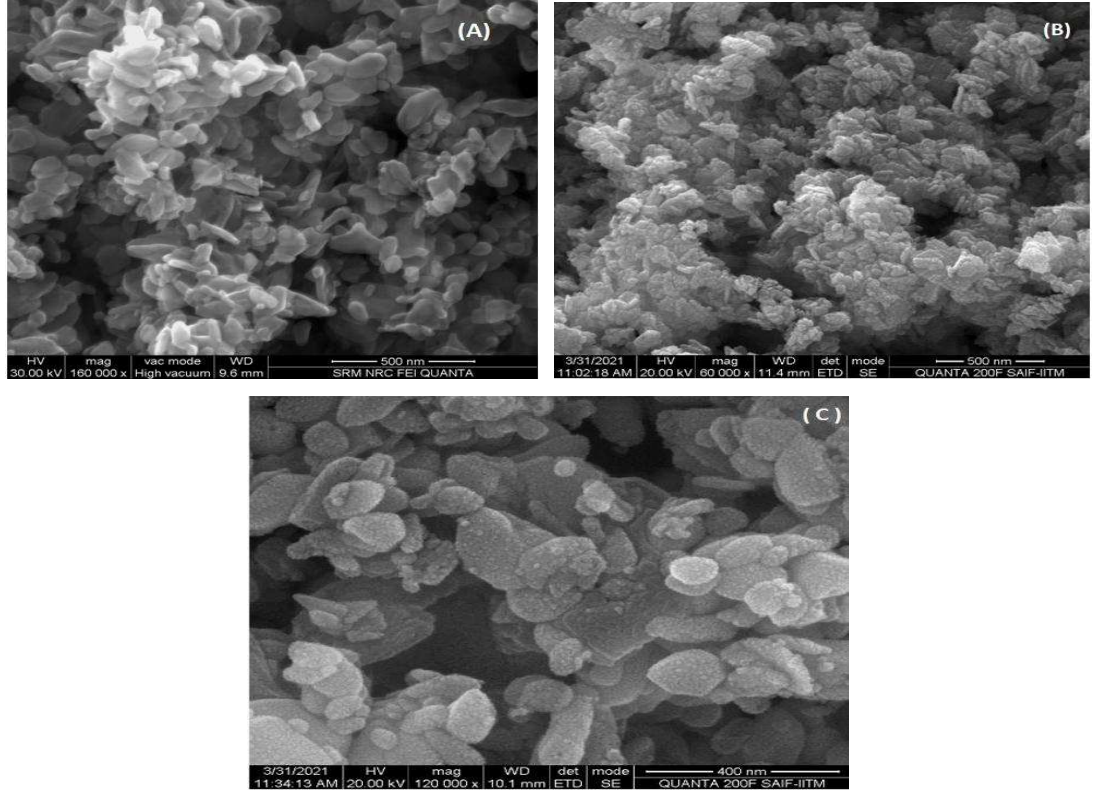


Figure 5.1.2 shows the HR-SEM images of (A) bare zinc oxide photocatalyst (B) 2 wt% AlF₃ doped zinc oxide photocatalyst and (C) 2 wt% SrSiO₃ doped zinc oxide photocatalyst.

5.1.3. Energy Dispersive X-Ray Analysis

The energy dispersive X-ray (EDAX) analysis is routinely used to determine the major elemental composition of nanomaterials and nanocomposites. The EDAX spectrum of the undoped as well as aluminium fluoride and strontium silicate doped zinc oxide photocatalysts are shown in figure 5.1.3 A-C. The EDAX spectrum of the bare zinc oxide photocatalyst shows the presence of the elements viz., zinc and oxygen without any other impurities. Similarly in the EDAX spectrum of the aluminium fluoride doped zinc oxide photocatalyst, the presence of elements such as zinc, oxygen, aluminium and fluorine are confirmed and in the synthesized strontium silicate doped zinc oxide photocatalyst, the presence of elements such as zinc, oxygen, strontium and silicon are observed without any other impurities.

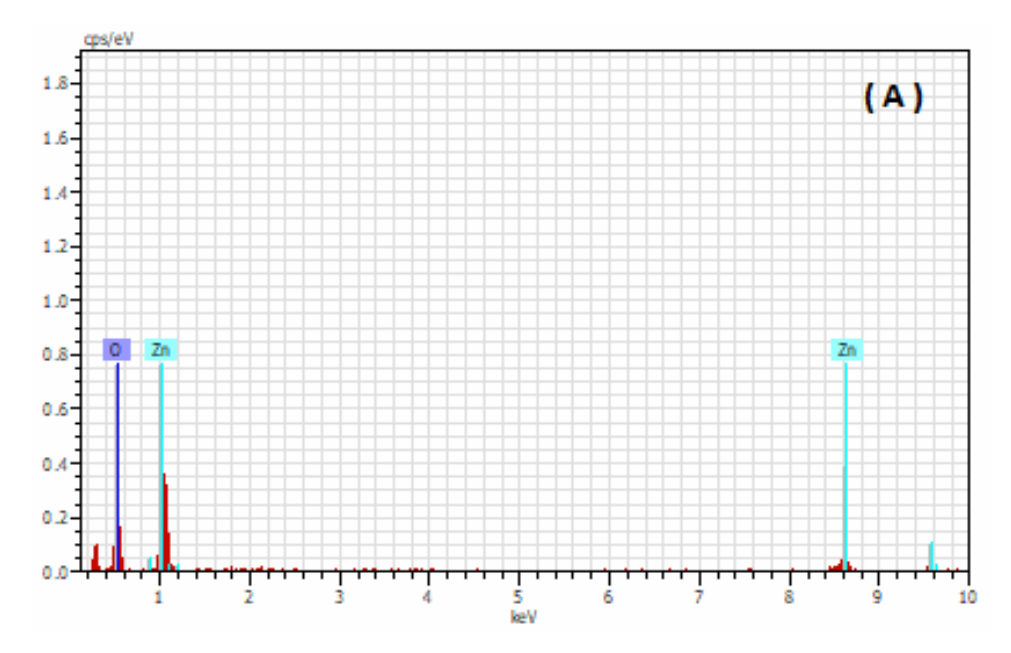


Figure 5.1.3 A shows the EDAX image of bare zinc oxide photocatalyst.

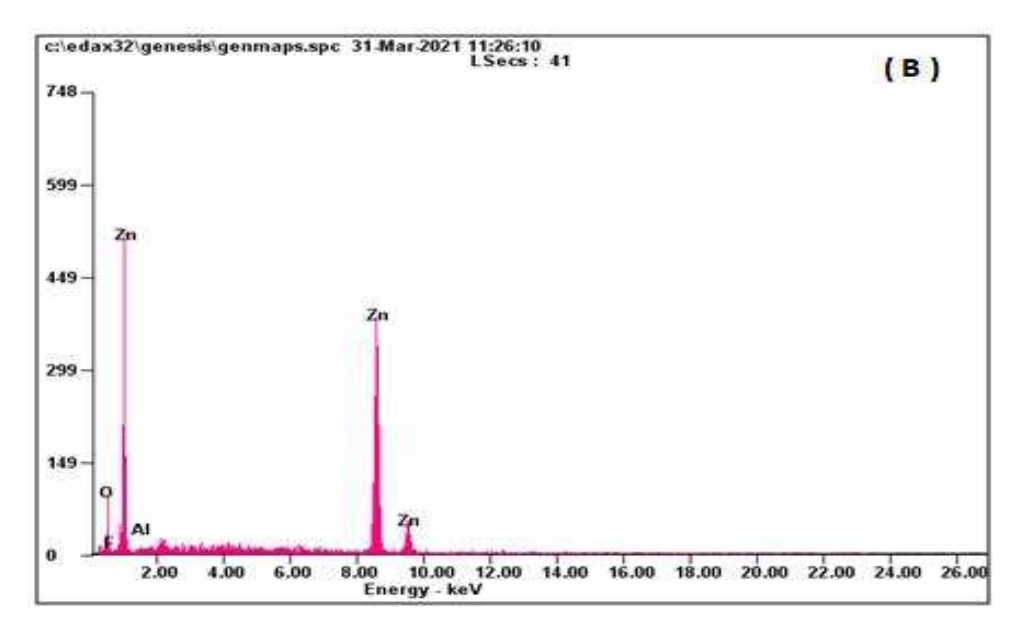


Figure 5.1.3 B shows the EDAX image of 2 wt% aluminium fluoride doped zinc oxide photocatalyst.

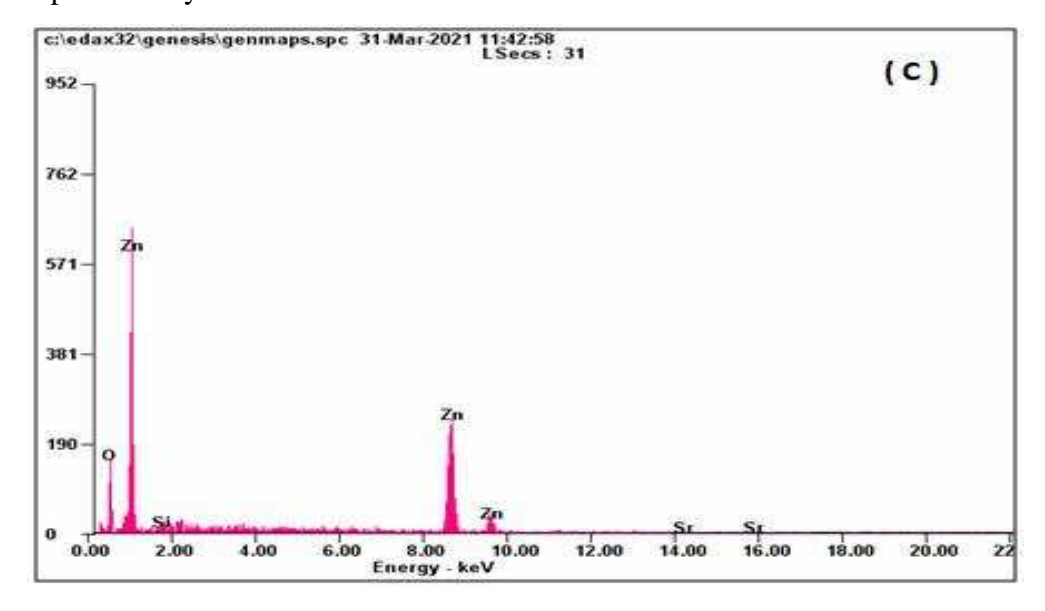


Figure 5.1.3C shows the EDAX image of 2 wt% strontium silicate doped zinc oxide photocatalyst.

5.1.4. Transmission Electron Microscopic Analysis

To gain more insight about the surface morphology and crystallinity of the synthesized photocatalysts a high resolution transmission electron microscopic (TEM) analysis is carried out. The obtained TEM image as well as the Selected Area Electron Diffraction of the bare zinc oxide photocatalyst is shown in figure 5.1.4 A-C. From

the TEM images, it is observed that the synthesized undoped zinc oxide photocatalyst posses a rod-like structure and the particles are found to be highly agglomerated binding to each other. The selected area electron diffraction obtained with the ring-like pattern and dark spots in it, confirms the crystalline nature of the synthesized photocatalyst. Similarly, the TEM images and SAED pattern of the synthesized aluminium fluoride and strontium silicate doped zinc oxide photocatalysts are shown in figures 5.1.4 D-F and 5.1.4 G-I respectively. From the TEM images of the AlF₃ and SrSiO₃ doped zinc oxide photocatalyst it is observed that the synthesized photocatalysts are polymorphic with many rod-like structures in it. The SAED image obtained with ring-like pattern again confirms that the crystallinity in the prepared samples is still retained even after the process of doping.

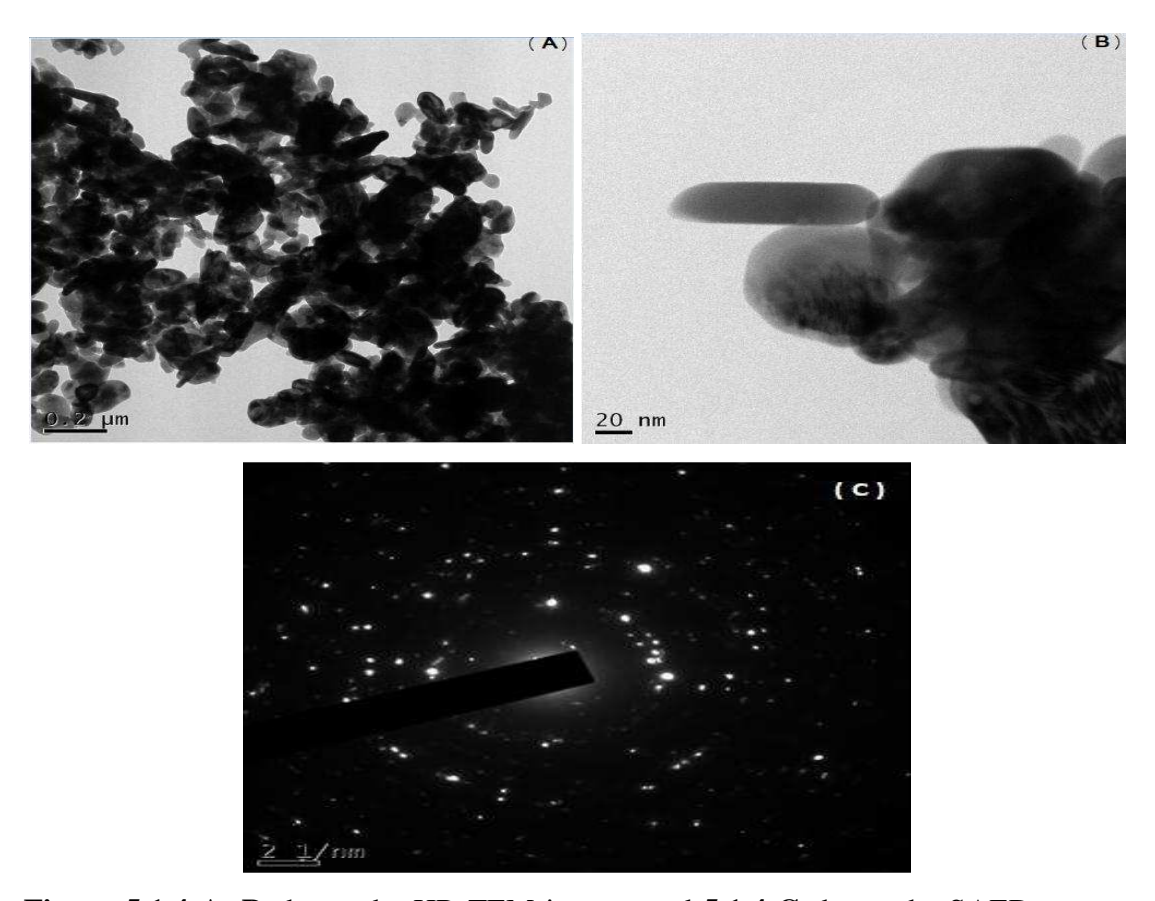


Figure 5.1.4 A, B shows the HR-TEM images and **5.1.4 C** shows the SAED pattern of the undoped ZnO photocatalyst.

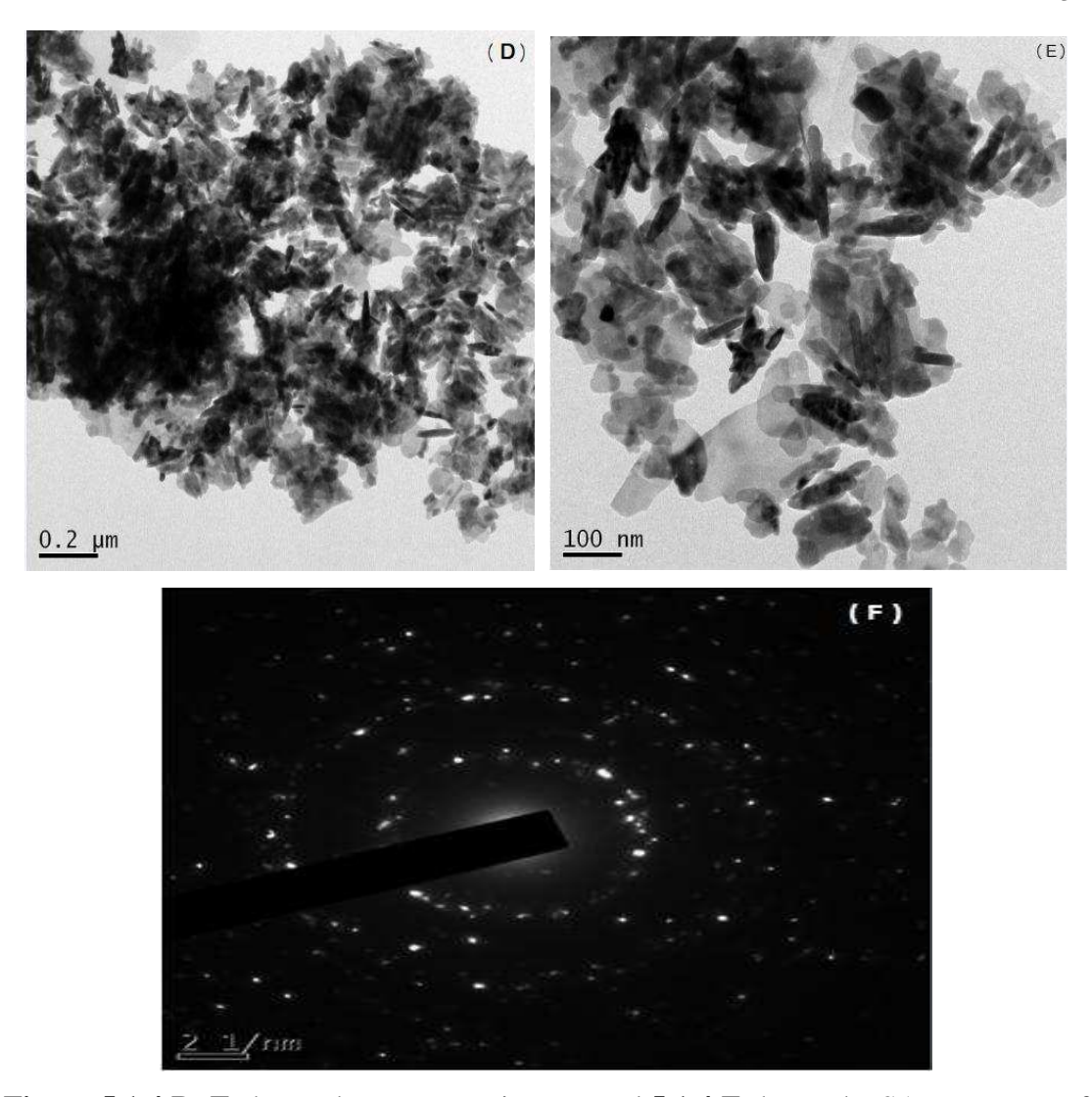


Figure 5.1.4 D, E shows the HR-TEM images and **5.1.4 F** shows the SAED pattern of the 2 wt% AlF₃ doped ZnO photocatalyst.

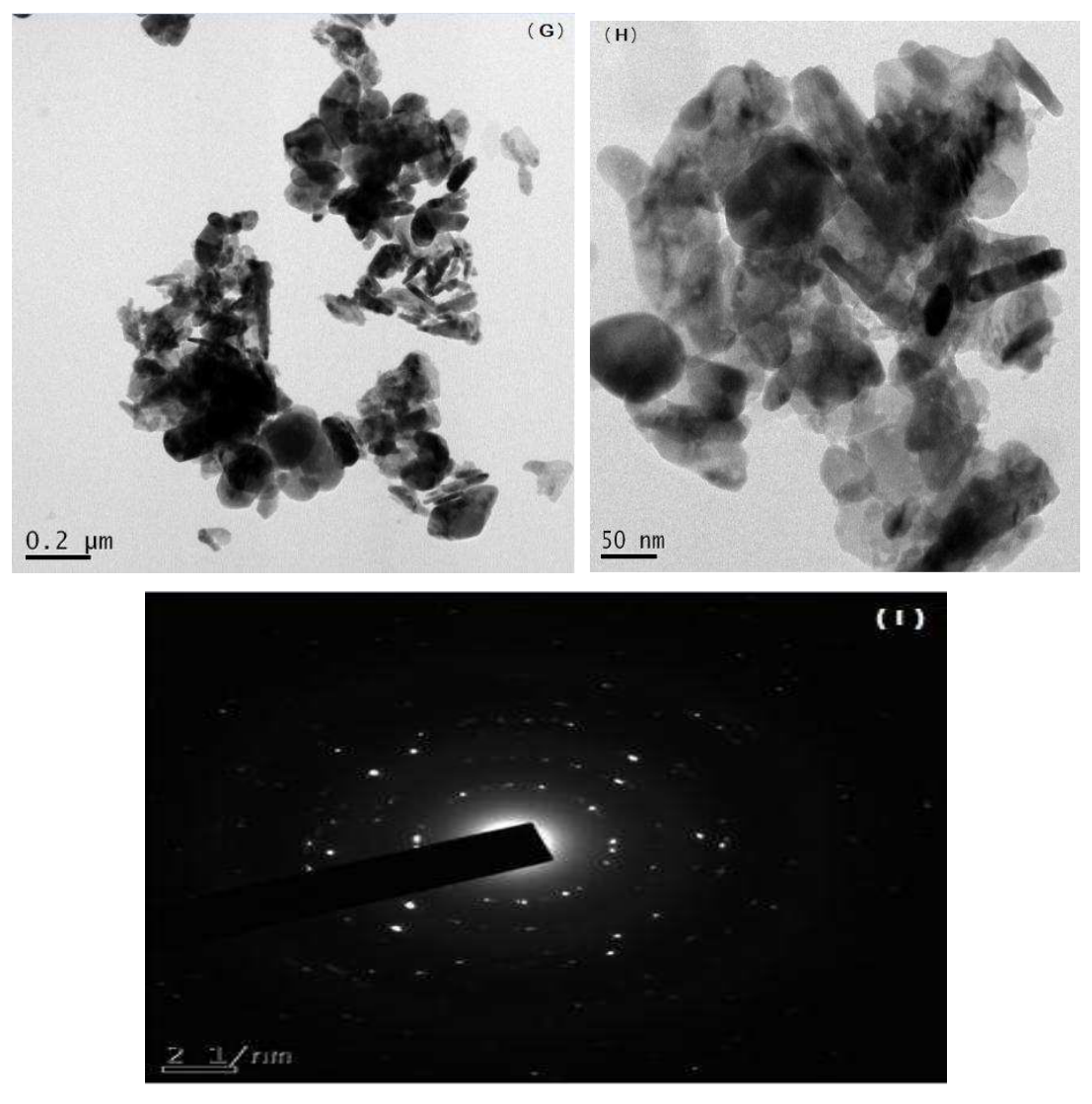


Figure 5.1.4 G, H shows the HR-TEM images and **5.1.4 I** shows the SAED pattern of the 2 wt% SrSiO₃ doped ZnO photocatalyst.

5.1.5. UV-Visible Diffuse Reflectance Spectroscopy Studies

Diffuse reflectance is an optical phenomenon that is used to obtain molecular spectroscopic information from the reflectance of dull surface textured powder samples³. The main advantage of this technique is that the spectra can be obtained with a minimum quantity of the sample preparation.

The optical band gap values of all the synthesized photocatalysts is determined using the following equation

$$E_{g} = \frac{hC}{\lambda} = \frac{1240}{\lambda}$$
eq.(5.1)

where E_g is the bandgap in eV and λ is the cut off wavelength from the absorption spectrum. Figure 5.1.5 A-C shows the DRS-UV-Visible absorption spectra of bare zinc oxide, aluminium fluoride and strontium silicate doped zinc oxide photocatalysts. The calculated band gap values for the ZnO, AlF3 doped ZnO and SrSiO3 doped ZnO photocatalysts are 3.12 eV, 3.02 eV and 3.08 eV, respectively. A decrease in the bandgap values is observed for the doped zinc oxide photocatalysts compared to the undoped zinc oxide catalyst. This decrease in the bandgap energy paves the way for efficient separation of the charge carriers, making the catalyst more photocatalytically active⁴.

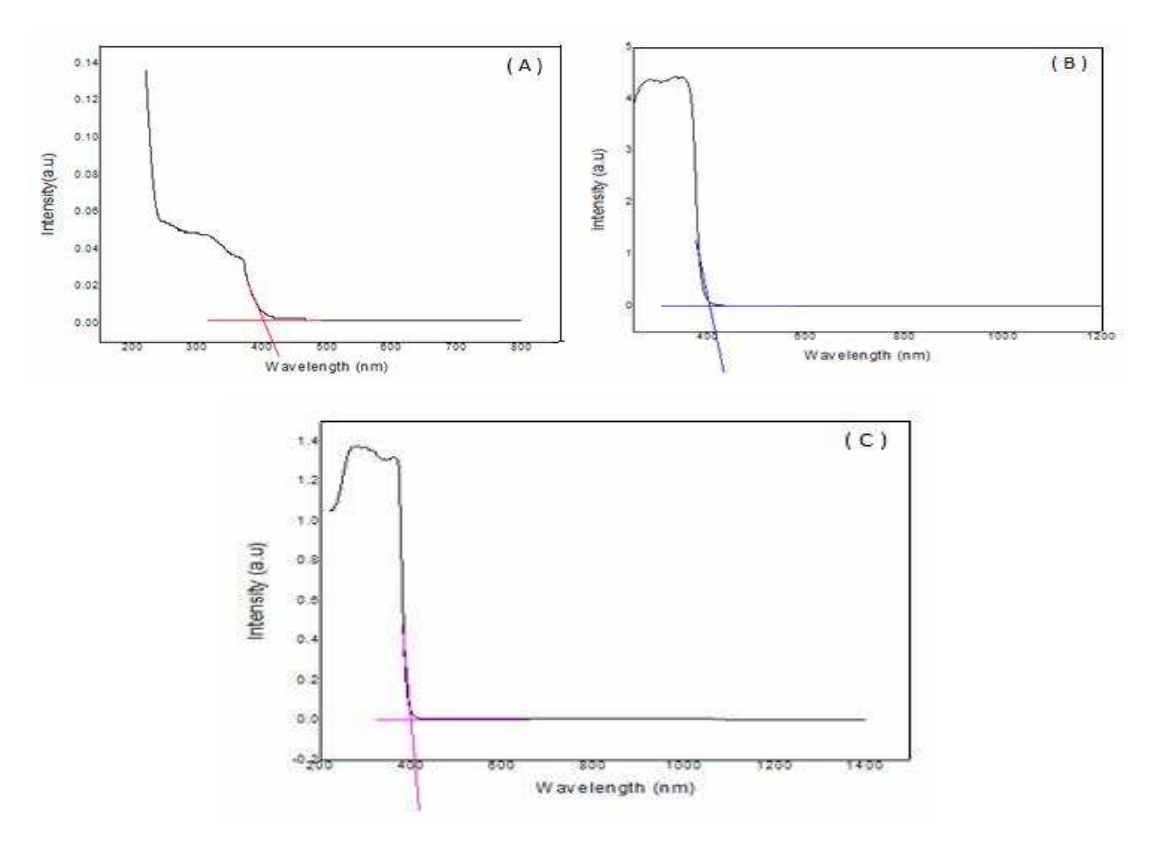


Figure 5.1.5 shows the DRS-UV-Visible absorption spectra for (A) bare ZnO photocatalyst (B) 2 wt% AlF₃ doped ZnO photocatalyst and (C) 2 wt% SrSiO₃ doped ZnO photocatalyst.

5.1.6. Fourier Transform Infra-Red Spectroscopy Studies

Fourier transform infrared spectroscopy is one of the most important spectroscopic tools for the identification of functional groups present in a sample. The main advantage of infrared spectrometers is that the spectrum of any solid, liquid or gas sample can be easily obtained. The physical property of the matter to absorb, transmit or reflect the infra red radiation is made use of to obtain the spectrum. The percentage transmittance is plotted against the wavenumber and the analysis of the shape, position and intensity of the bands in the spectrum provides useful information about the existence of the metal-oxygen bonds in the synthesized material. The FTIR spectra of bare and aluminium fluoride and strontium silicate doped zinc oxide photocatalysts are shown

in figure 5.1.6 A-C. The peak around 3400 cm⁻¹ and the peaks in the range 1400-1600 cm⁻¹ are attributed to the stretching and bending vibrations of the of OH goups which might be due to the presence of water molecules adsorbed on the surface of the photocatalysts. In both undoped and AlF₃ and SrSiO₃ doped ZnO photocatalyst, the bands below 900 cm⁻¹ are due to the crystal lattice vibrations of the inorganic Zn-O-Zn framework in the synthesized materials⁵.

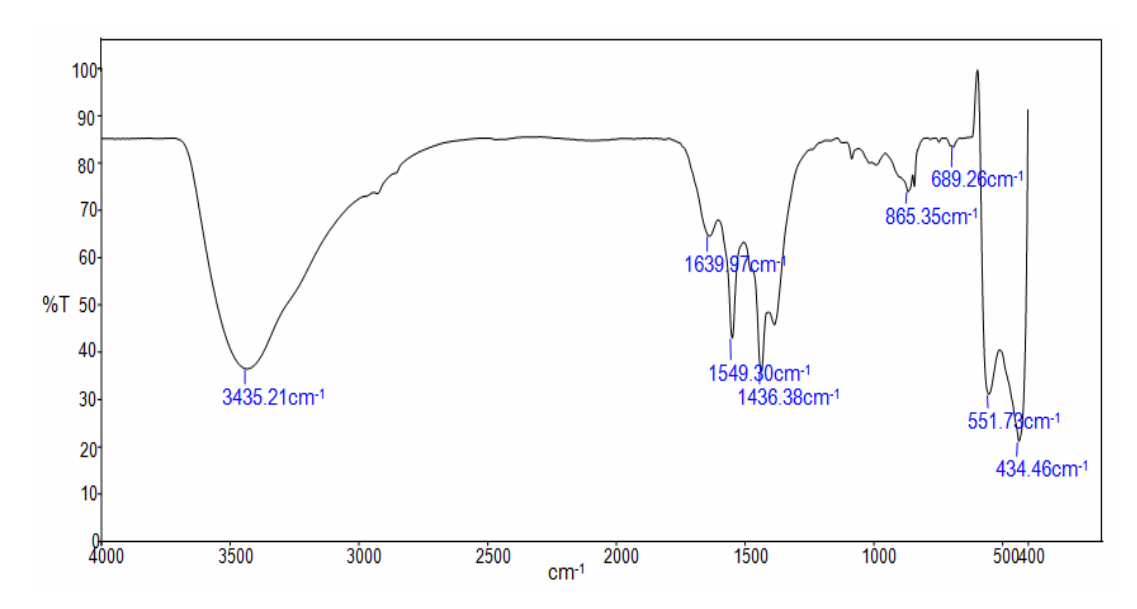


Figure 5.1.6 A FTIR spectrum of the synthesized bare Zinc Oxide photocatalyst.

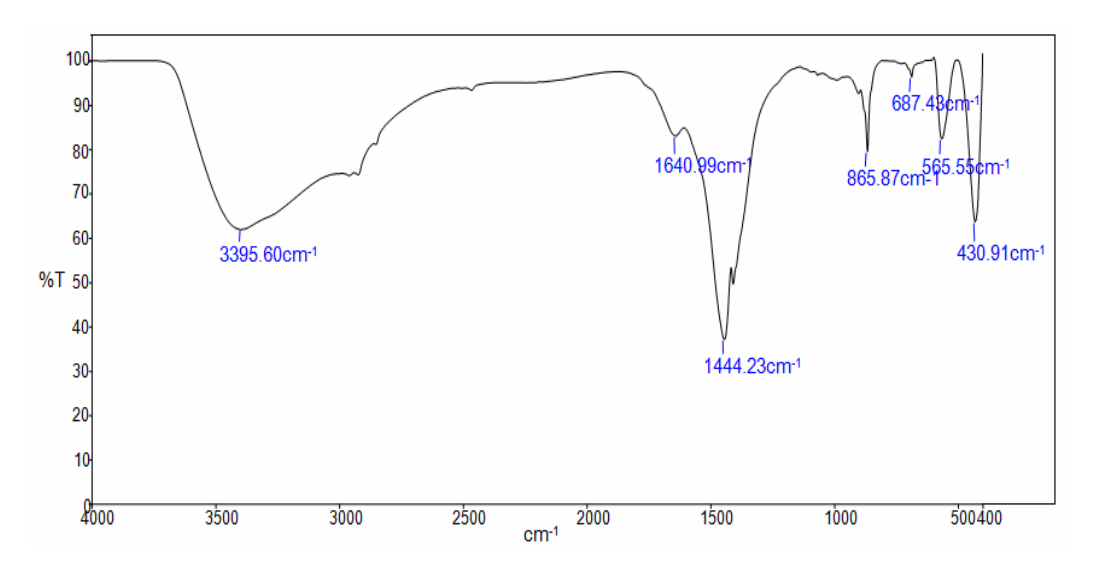


Figure 5.1.6 B FTIR spectrum of the synthesized 2 wt% AlF₃ doped Zinc Oxide photocatalyst.

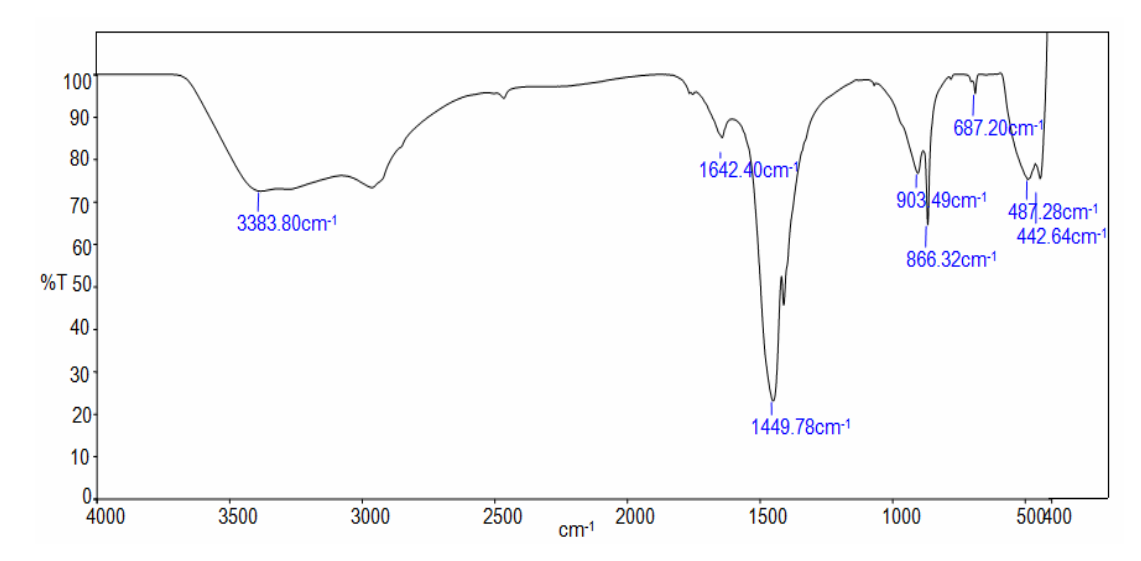


Figure 5.1.6 C FTIR spectrum of the synthesized 2 wt% SrSiO₃ doped zinc oxide photocatalyst.

5.1.7. BET Surface Area Analysis

The Brunauer-Emmett-Teller method is widely employed to determine the specific surface area of the catalysts. The determination of the internal surface area is based on the nitrogen adsorption-desorption isotherm using liquid N₂, at 77K and a relative pressure in the range of 0.05-0.3 bar. The samples taken for the analysis are initially evacuated at a temperature of 250 °C followed by cooling at 77K using liquid nitrogen. Then the partial pressure of nitrogen is increased above the samples until it reaches a near saturation pressure and some quantity of the N₂ gas will be adsorbed by the samples. After stabilization of the equilibrated pressure, the amount of nitrogen adsorbed at equilibrated pressure is recorded to develop a complete adsorption isotherm. The desorption isotherm is recorded by a step-wise reduction in the pressure until a low pressure over the samples is achieved^{6, 7}.

The surface area of the catalyst is determined from the following equation

$$S = V_m N_A / (m \times 22400)$$
eq.(5.2)

Where V_{m} is the volume of gas adsorbed,

 N_A is the Avogadro number $(6.023 \times 10^{23} \text{ molecule/mol})$

m is the weight of the adsorbent after degassing

The Nitrogen adsorption-desorption isotherms of the synthesized bare ZnO, aluminium fluoride doped zinc oxide photocatalyst and strontium silicate doped zinc oxide photocatalysts are shown in figure 5.1.7 A-C. The surface area, pore volume and pore radius of the synthesized ZnO, AlF₃ doped ZnO and SrSiO₃ doped ZnO photocatalysts are given in table 5.1.7. The surface area is an important factor that can be correlated to the activity of the catalyst. The specific surface area of the bare zinc oxide photocatalyst is 19.593 m²/g and that of the aluminium fluoride and strontium silicate doped zinc oxide photocatalysts are 24.117m²/g and 33.768m²/g, respectively. The increased surface area of the modified zinc oxide catalysts can be attributed to the reduced crystallite size of the particles, as evidenced by the XRD analysis of the samples (Figure 5.1.1). The smaller the size of the particles, the more would be the surface area of the material. Similar results were reported by Ketema Worku et al while investigating the photocatalytic activity of Cr doped zinc oxide catalysts.

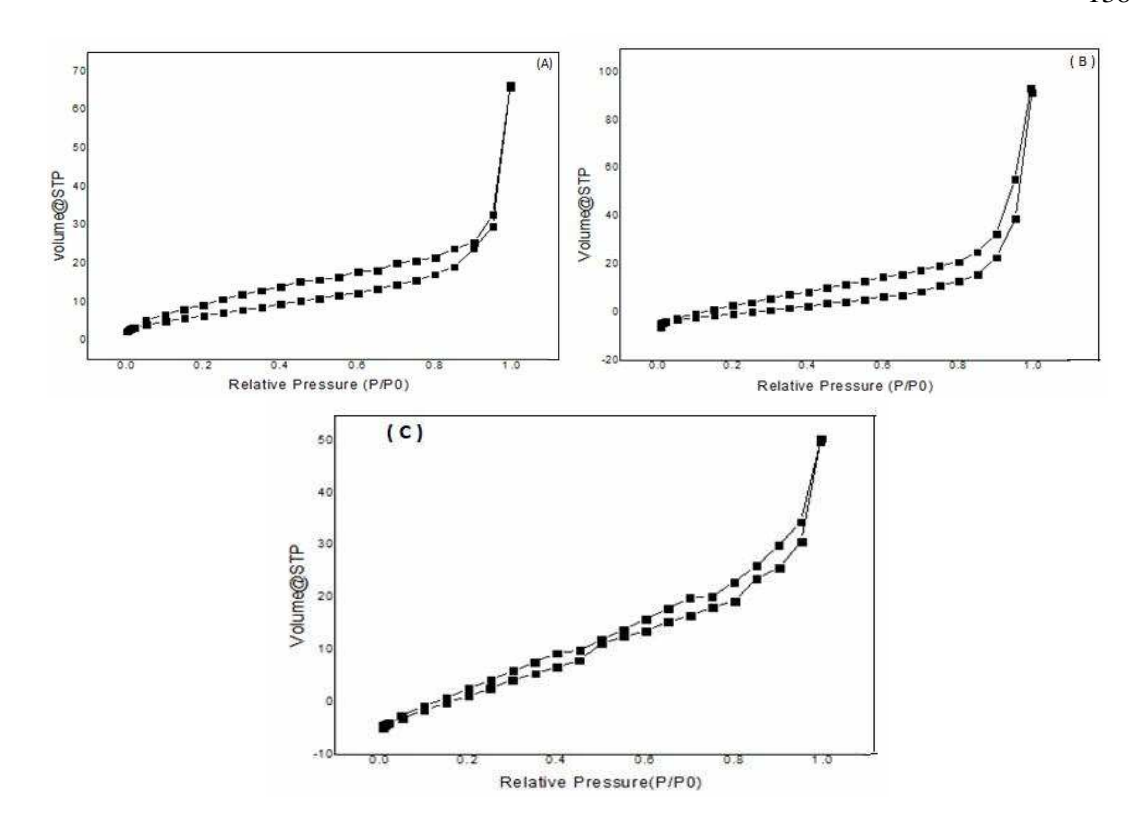


Figure 5.1.7 N_2 adsorption-desorption isotherms of the synthesized (A) undoped ZnO photocatalyst (B) 2 wt% AlF₃ doped ZnO photocatalyst and (C) 2 wt% SrSiO₃ doped ZnO photocatalyst.

Table 5.1.7 Surface area, Pore volume and Pore radius of bare-ZnO, AlF₃ -ZnO and SrSiO₃ -ZnO photocatalysts.

Photocatalysts	Surface area (m²/g)	Pore Volume (cc/g)	Pore Radius (Å)
ZnO	19.593	0.099	15.279
Aluminium Fluoride-ZnO	24.117	0.151	17.048
Strontium silicate-ZnO	33.768	0.086	19.29

5.1.8. Photocatalytic Studies

Most of the dyes are prone to bleaching in the presence of sunlight. Hence, it is essential to understand to what extent the process of self-photolysis of the dye takes place in the absence of the catalyst. Similarly, the uses of aerators to provide air supply and to mix the reaction mixture by continuous stirring are other two important factors that contribute to the dye degradation process to a certain extent. In the present study, the effect of bubbling air into the reaction mixture is evaluated for the photocatalytic degradation of methylene blue, indigo carmine and crystal violet dyes using zinc oxide photocatalyst, and the data are shown in figures 5.1.18 A-C. A maximum of 19, 21 and 23 % degradation of methylene blue, indigo and crystal violet dyes are achieved using zinc oxide photocatalyst and by providing air supply at room temperature. Similarly, under room temperature in the absence of air supply using zinc oxide catalyst, a maximum of 12, 14 and 16% degradation of methylene blue, indigo carmine and crystal violet dyes are achieved. However, when the dye solutions are exposed to sunlight along with the air supply in the absence of the zinc oxide catalyst about 4, 10 and 8% degradation of methylene blue, indigo and crystal violet dyes are achieved within 180 minutes which clearly shows that zinc oxide catalyst, air purging and a light source are the essential components required for the effective degradation of dyes. The increase in the efficiency of dye degradation process observed by using zinc oxide catalyst along with the air supply can be attributed to three main reasons:

(i) Ability of the dyes to get adsorbed on the surface of ZnO catalyst.

- (ii) Ability of the photoexcited conduction band electrons of zinc oxide catalyst to form reactive oxygen species such as O_2 . OH radicals enhance the dye degradation process.
- (iii) Similarly, the dissolution of more air or oxygen into the solution and the turbulent motion caused by agitation enables the dye molecules to reach the catalyst at a faster rate, which in turn, promotes the photocatalytic activity ^{9, 10}.

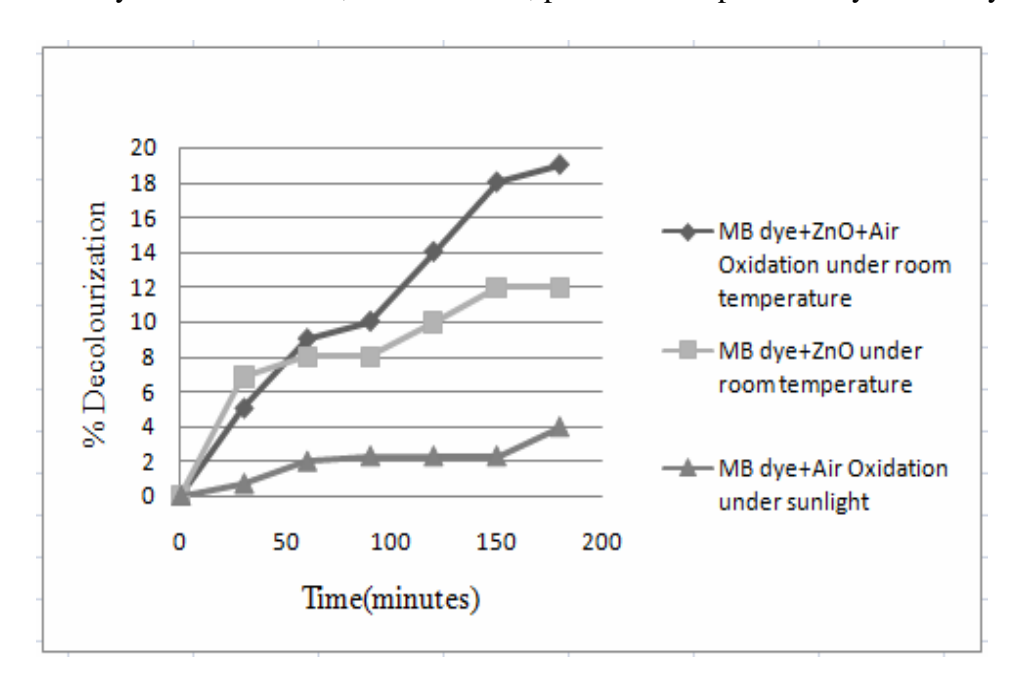


Figure 5.1.8 A Primary analysis of methylene blue dye solution using zinc oxide photocatalyst.

(**Reaction conditions:** Methylene blue dye solution (Conc. 3.12×10^{-5} mol/L; volume = 50 mL), ZnO catalyst = 25 mg/50 mL, without pH adjustment, air supply $\cong 2.5 \text{L/min}$, $I_{solar} = 687 \times 100 \pm 100 \, \text{lux.}$)

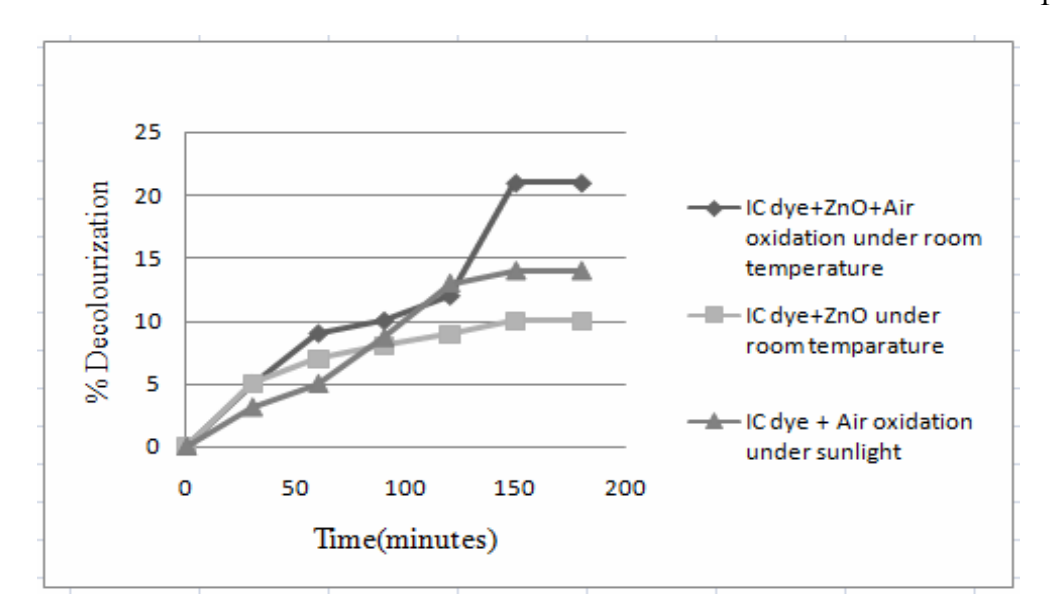


Figure 5.1.8 B Primary analysis of indigo carmine dye solution using zinc oxide photocatalyst.

(**Reaction conditions:** Indigo carmine dye solution (Conc. 2.14×10^{-5} mol/L; volume = 50mL), ZnO catalyst = 25mg/50mL, without pH adjustment, air supply $\cong 2.5$ L/min, sunlight (I_{lux}) = 634 ×100 ±100 lux.)

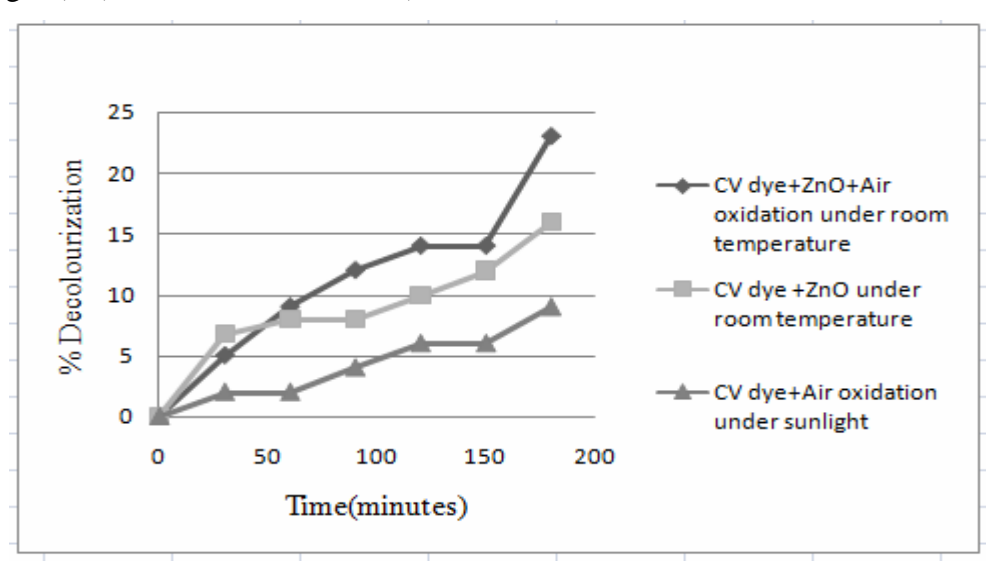


Figure 5.1.8 C Primary analysis of crystal violet dye solution using zinc oxide photocatalyst.

(**Reaction conditions:** Crystal violet dye solution (Conc. 2.45×10^{-5} mol/L; volume=50mL), ZnO catalyst = 25mg/50mL, without pH adjustment, air supply $\cong 2.5$ L/min, sunlight (I_{lux}) = $682 \times 100 \pm 100$ lux.)

5.1.9. Effect of pH on the photocatalytic dye decolourization process

The pH of a solution is one of the important parameters that affect the surface charge properties of a catalyst, charge of dye molecules and adsorption of dye molecules onto the surface of a catalyst. Deterioration in the photocatalytic activity of zinc oxide catalyst can be evidenced at extreme pH levels due to the following reactions:

$$ZnO + 2H^{+} \rightarrow Zn^{2+} + H_{2}O$$
 eq.(5.3)

$$ZnO + H_2O + 2OH^- \rightarrow Zn(OH)_4^{2-}$$
 eq.(5.4)

The pH levels are optimized to achieve an effective degradation of dyes. The variation in the pH levels from 2 to 12 for degradation of 3.12x10⁻⁵ mol/L of methylene blue using zinc oxide catalyst showed that the maximum degradation of the dye took place at pH 6.5. This can be attributed to the decomposition of zinc oxide catalyst at acidic pH levels affecting the generation of reactive species under solar radiation¹¹. Similarly, for the degradation of indigo carmine the maximum dye degradation took place at pH 10 above which a decrease in the efficiency of dye degradation is evidenced. This is due to the fact that the excess of hydroxyl radicals in the solution competes with the anionic indigo carmine dye for the surface active sites of zinc oxide catalyst¹². The zero point charge of a photocatalyst is another important factor that needs to be correlated to account for the higher photocatalytic activity at different acidic and alkaline pH levels. The point of zero charge can be defined as the pH at which the net surface charge of the adsorbent equals zero. Zinc oxide catalyst has a ZPC of 9.0; the surface of the catalyst will be positive below this pH and has a negative charge above this pH according to the following equations¹³

$$ZnOH + H^{+} \rightarrow ZnOH_{2}^{+}$$
 eq.(5.5)
 $ZnOH + OH^{-} \rightarrow ZnO^{-} + H_{2}O$ eq.(5.6)

The maximum degradation of cationic crystal violet dye is observed at alkaline pH 10. This can be due to the fact that at pH 10 the surface of the zinc oxide catalyst will be negatively charged, and hence the cationic crystal violet dye gets adsorbed to the surface of the ZnO catalyst¹⁴. Thus, degradation of crystal violet dye takes place more efficiently at alkaline pH levels compared to that under acidic conditions.

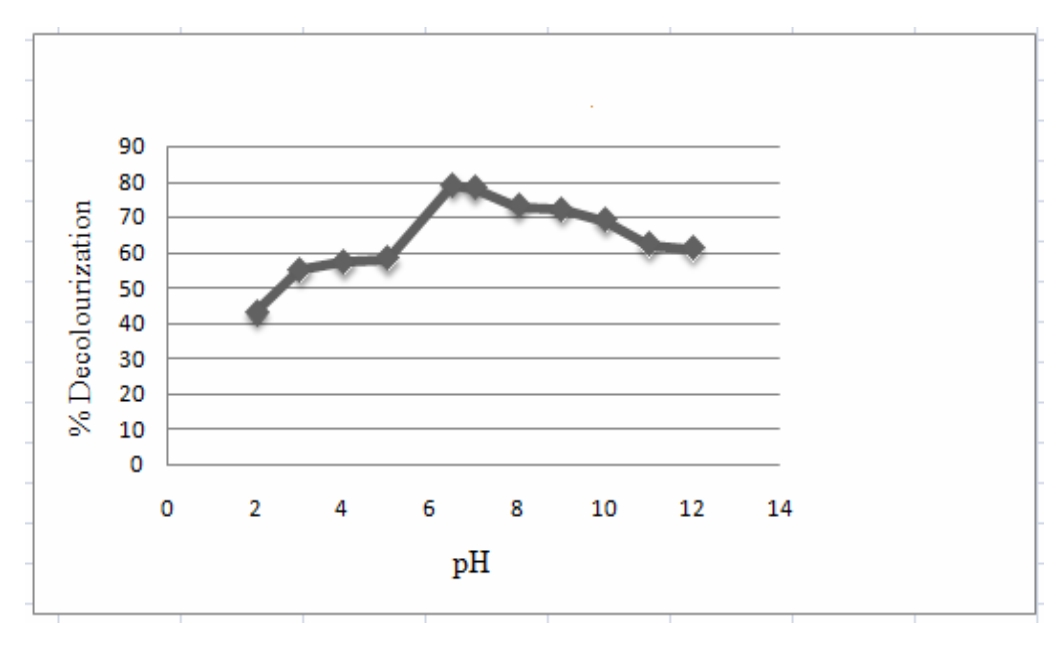


Figure 5.1.9 A Effect of pH on the photocatalytic decolourization of methylene blue dye using zinc oxide catalyst.

(**Reaction conditions:** Methylene blue dye solution (Conc. 3.12×10^{-5} mol/L; volume = 50mL), ZnO catalyst = 25mg/50mL, pH variation = 2-12, air supply $\cong 2.5$ L/min, sunlight (I_{lux}) = 667 $\times 100 \pm 100$ lux, time=30 minutes)

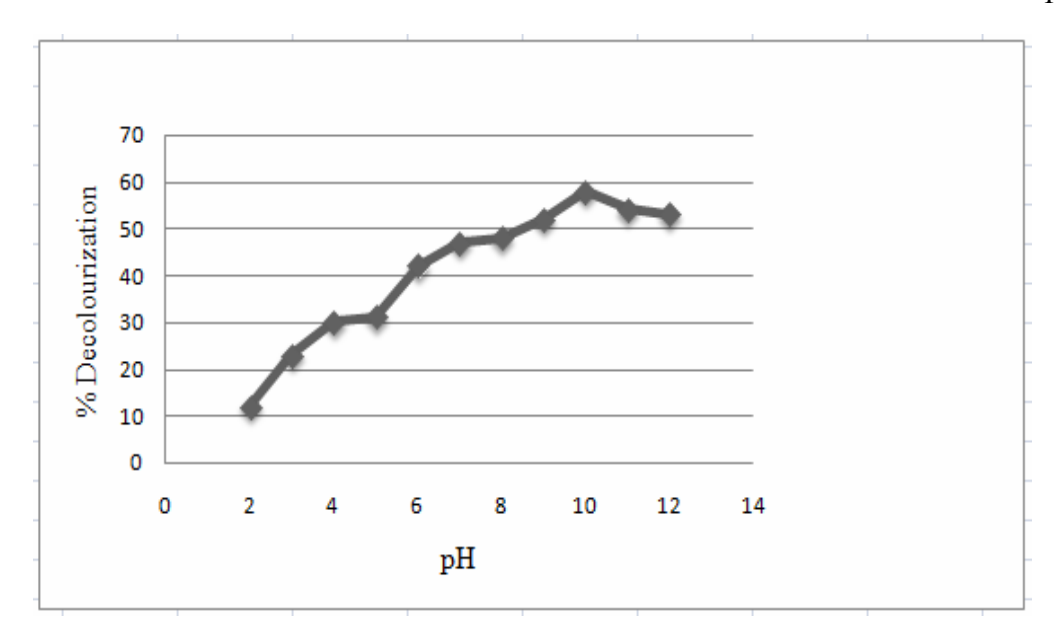


Figure 5.1.9 B Effect of pH on the photocatalytic decolourization of indigo carmine dye using zinc oxide catalyst.

(**Reaction conditions:** Indigo carmine dye solution (Conc. 2.14×10^{-5} mol/L; volume = 50mL), ZnO catalyst = 25mg/50mL, pH variation = 2-12, air supply $\cong 2.5$ L/min, sunlight (I_{lux}) = $689 \times 100 \pm 100$ lux, time=30 minutes)

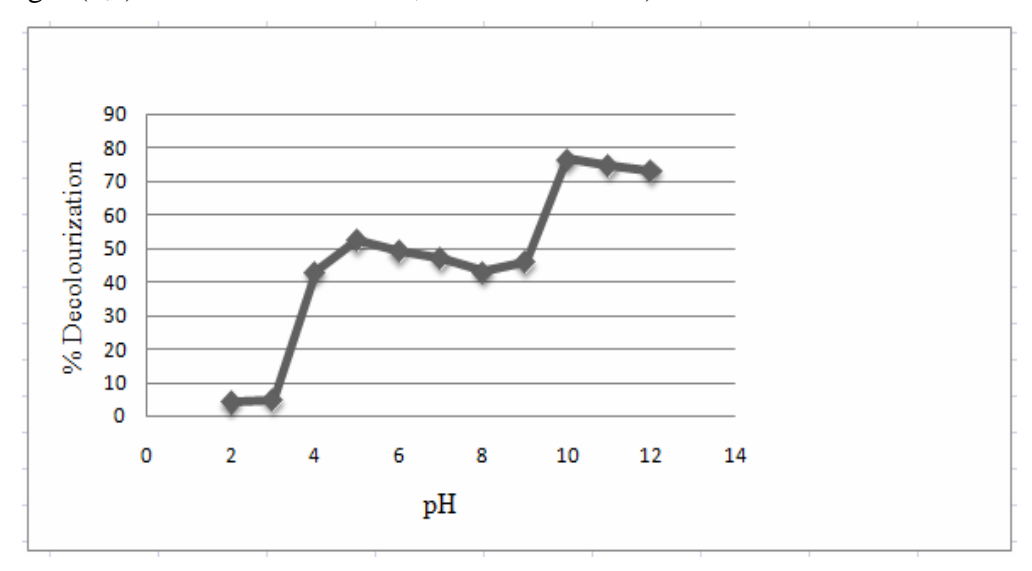


Figure 5.1.9 C Effect of pH on the photocatalytic decolourization of crystal violet dye using zinc oxide catalyst.

(**Reaction conditions:** Crystal violet dye solution (Conc. 2.45×10^{-5} mol/L; volume = 50mL), ZnO catalyst = 25mg/50mL, pH variation = 2-12, air supply $\cong 2.5$ L/min, sunlight (I_{lux}) = $659 \times 100 \pm 100$ lux, time=30 minutes)

5.1.10. Effect of Catalyst Concentration

The level of catalyst dosage is an important factor that needs to be optimized to achieve maximum photocatalytic degradation efficiency. Figures 5.1.10 A-C shows the photocatalytic degradation of methylene blue, indigo carmine and crystal violet dyes by various amounts of the catalyst at optimized pH levels. From the experimental study, it is observed that the degradation of the dyes increases till a catalyst dosage of 25mg and beyond which a decrease in the efficiency of photocatalytic degradation process is noted. This may be due to the fact that initially, on increasing the catalyst dosage, the corresponding dye adsorption capacity to the catalyst surface increases, and the number of surface actives sites of the catalyst available for the dye molecule also increases, leading to the formation of the reactive species such as hydroxyl and superoxide anion radicals that brings an increase in the photocatalytic dye degradation efficiency. However, when the catalyst dosage crosses the optimum level, it can hinder the rate of the photocatalytic dye degradation process which occurs due to the agglomeration of the catalyst particles, and an increased level of the catalyst in the dye solution blocks the penetration of the sunlight path and scattering of the light also leads to a decrease in the photocatalytic efficiency^{15, 16}.

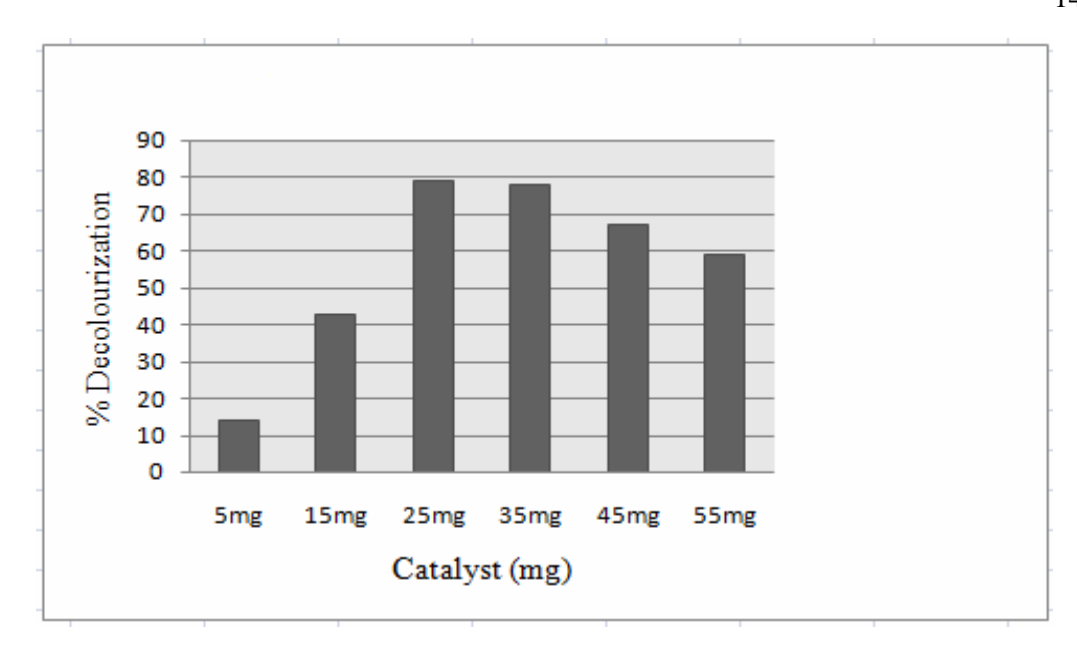


Figure 5.1.10 A Effect of zinc oxide catalyst concentration on the photocatalytic decolourization of methylene blue dye.

(**Reaction conditions:** Methylene blue dye solution (Conc. 3.12×10^{-5} mol/L; volume =50mL), catalyst weight = 5mg- 55mg, pH = 6.5, air supply $\cong 2.5$ L/min, sunlight (I_{lux}) = $623 \times 100 \pm 100$ lux, time=30 minutes)

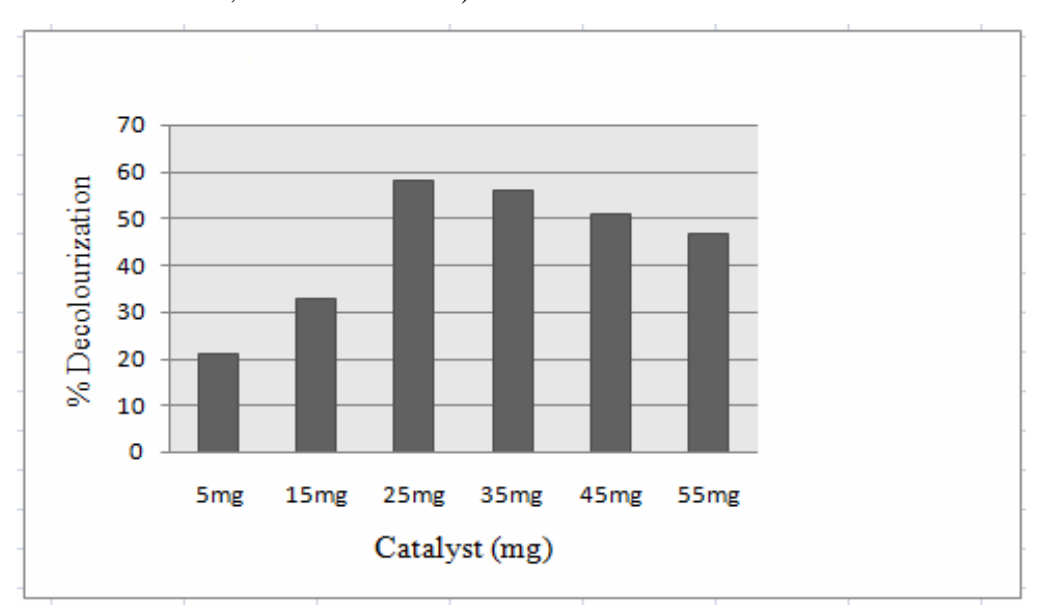


Figure 5.1.10 B Effect of zinc oxide catalyst concentration on the photocatalytic decolourization of indigo carmine dye.

(**Reaction conditions:** Indigo carmine dye solution (Conc. 2.14×10^{-5} mol/L; volume =50mL), catalyst weight = 5mg- 55mg, pH = 10, air supply $\cong 2.5$ L/min, sunlight (I_{lux}) = $692 \times 100 \pm 100$ lux, time=30 minutes)

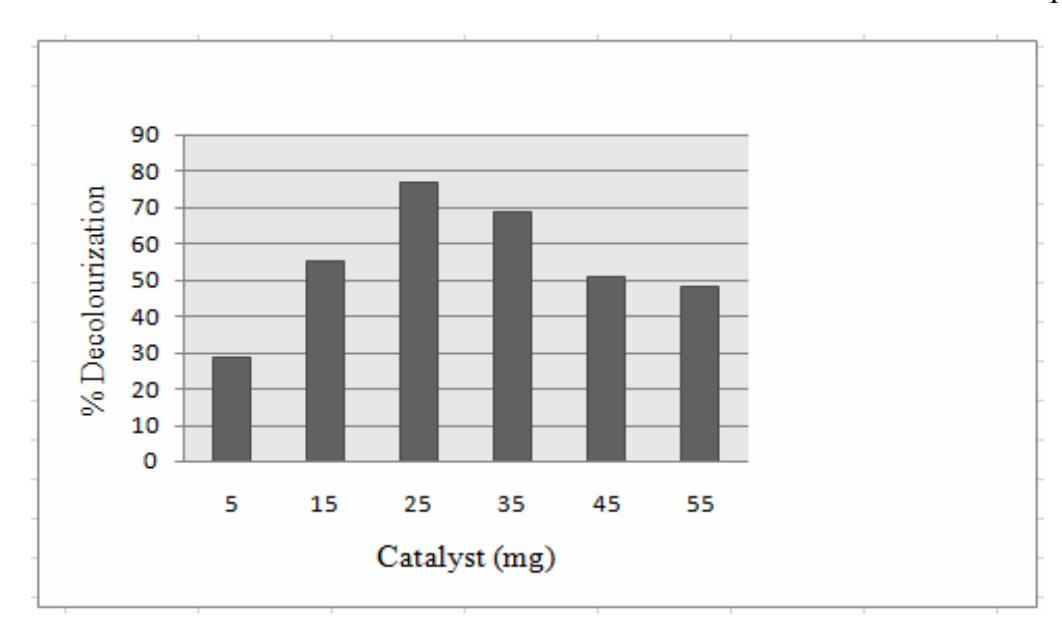


Figure 5.1.10 C Effect of zinc oxide catalyst concentration on the photocatalytic decolourization of crystal violet dye.

(**Reaction conditions:** Crystal violet dye solution (Conc. 2.45×10^{-5} mol/L; volume = 50mL), catalyst weight = 5mg- 55mg, pH = 10, air supply $\cong 2.5$ L/min, sunlight (I_{lux}) = $667 \times 100 \pm 100$ lux, Time=30 minutes)

5.1.11. Effect of Initial Dye Concentration

The study of initial dye concentration in the photocatalytic degradation process is an essential factor from the application point of view. The effect of initial dye concentration is studied by varying the concentration from 3.12×10⁻⁵M to 1.56×10⁻⁴M for methylene blue and from 2.14×10⁻⁵M to 1.07×10⁻⁴M for indigo carmine, and from 2.42×10⁻⁵M to 1.22×10⁻⁴M for crystal violet under optimized pH and catalyst concentration as shown in figure 5.1.11 A-C. The maximum degradation of methylene blue was achieved at a concentration of 3.12×10⁻⁵M. For indigo carmine, it was 2.14×10⁻⁵M and for crystal violet it was 7.35×10⁻⁵M. About 99% of methylene blue degradation took place within 90 minutes when 3.12×10⁻⁵M methylene blue was treated with 25mg of zinc oxide catalyst at pH 6.5, beyond which a decrease in the

photocatalytic degradation process was evidenced. Similarly, 99% of indigo carmine degradation was achieved within 60 minutes using 2.14×10⁻⁵M dye and at 25mg of zinc oxide catalyst at pH 10. About 96% degradation of crystal violet degradation was achieved within 50 minutes using 7.35×10⁻⁵M dye and 25mg of zinc oxide catalyst at pH 10. For all three dyes, a decrease in photocatalytic degradation is observed at higher dye concentrations. This can be attributed to the fact that on increasing the dye concentration, the photon absorption by the dye molecules also increase. However, after crossing the optimized limits, a decrease in the dye degradation is observed. This might be due to the fact that at increased dye concentration levels, the penetration of the photons to the catalyst surface is precluded, which in turn affects the generation of reactive species such as hydroxyl and superoxide anion radicals leading to a decrease in the photocatalytic dye degradation process^{17,18}.

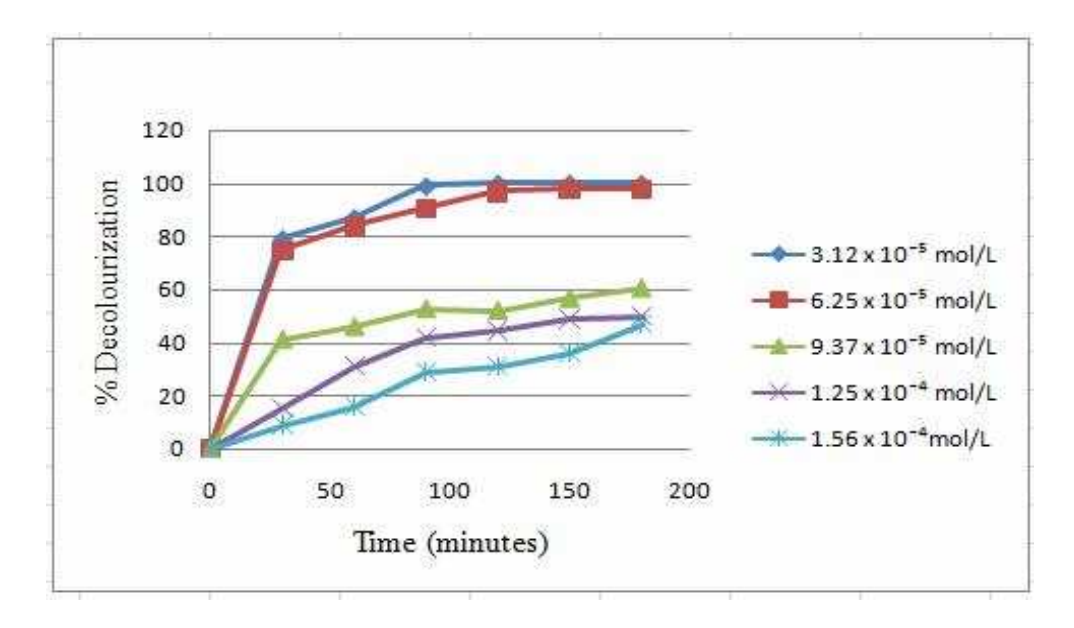


Figure 5.1.11 A Effect of initial concentration of methylene blue on photocatalytic decolourization using ZnO catalyst.

(**Reaction conditions:** Methylene blue dye concentration varied from 3.12×10^{-5} mol/L – 1.56×10^{-4} mol/L, volume of dye solution =50mL, catalyst concentration = 25mg, pH= 6.5, air supply $\cong 2.5$ L/min, sunlight (I_{lux}) = 698 $\times 100 \pm 100$ lux)

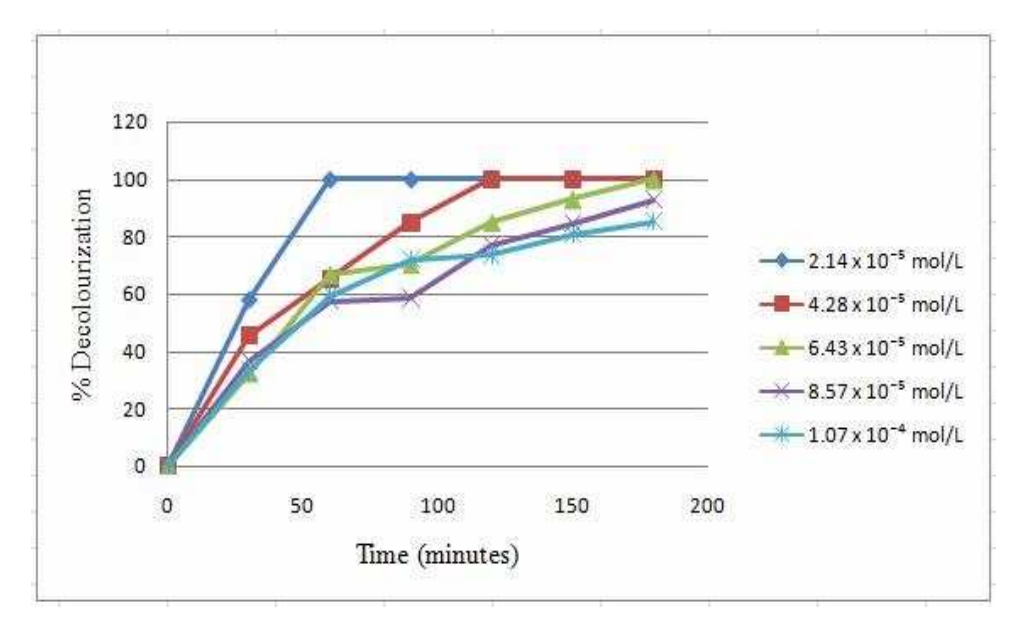


Figure 5.1.11 B Effect of initial concentration of indigo carmine on photocatalytic decolourization using ZnO catalyst.

(Reaction conditions: Indigo carmine dye concentration varied from 2.14×10^{-5} mol/L -1.07×10^{-4} mol/L, volume of dye solution =50mL, catalyst concentration=25mg, pH= 10, air supply $\cong 2.5$ L/min, sunlight (I_{lux}) = $728\times100\pm100$ lux)

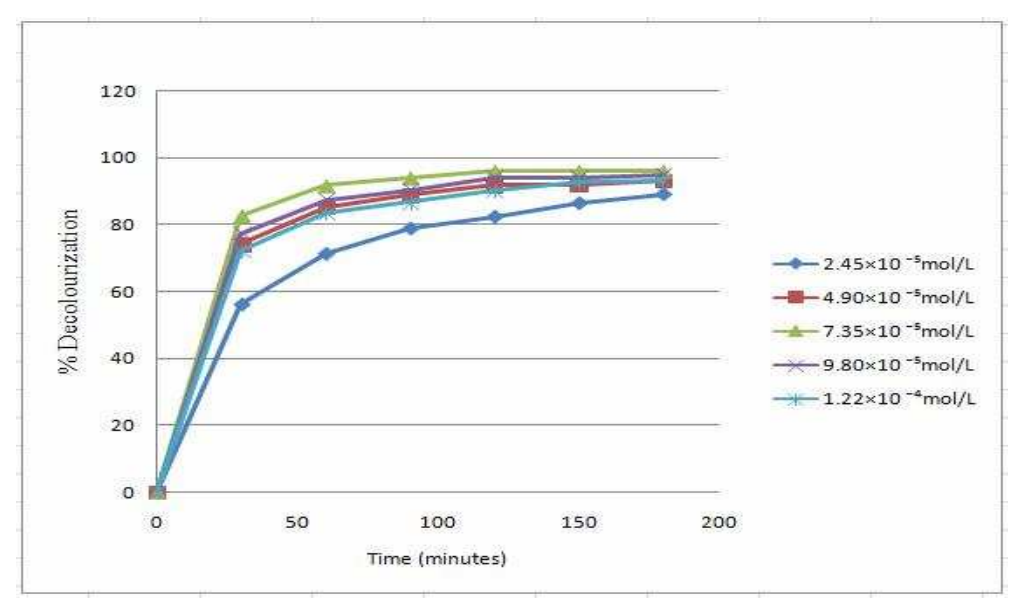


Figure 5.1.11C Effect of initial concentration of crystal violet on the photocatalytic decolourization using ZnO catalyst.

(Reaction conditions: Crystal violet dye concentration varied from 2.45×10^{-5} mol/L -1.22×10^{-4} mol/L, volume of dye solution =50mL, catalyst concentration=25mg, pH= 10, air supply $\cong 2.5$ L/min, sunlight (I_{lux}) = $682\times100\pm100$ lux)

5.1.12. Effect of Addition of Aluminium Fluoride and Strontium Silicate to ZnO Photocatalyst

Even though pure zinc oxide photocatalyst is reported to degrade many synthetic organic dyes, its photocatalytic efficiency is limited by a few factors such as the electron-hole recombination taking place at a faster rate, wide bandgap energy, inefficient transport of the charge carrier to the surface reaction sites of zinc oxide photocatalyst and decomposition of zinc oxide photocatalyst in highly acidic conditions ¹⁹. In order to overcome these limitations and gain high photocatalytic efficiency, researchers began to modify the semiconductors via doping and coupling techniques. Introduction of the foreign materials to zinc oxide lattices and coupling of two semiconductor oxides to obtain a material with different structural and functional properties have gained popularity in recent years due to the fascinating catalytic applications of these photoactive materials.

In the present work, the zinc oxide catalyst is modified by the addition of aluminium fluoride or strontium silicate at different weight percentages (0.5-3%) to obtain surface doped zinc oxide material with increased photocatalytic activity. From the experimental studies carried out, it is observed that the time taken for the degradation of three dyes (methylene blue, indigo carmine and crystal violet) is decreased while using zinc oxide catalyst modified with AlF₃ and SrSiO₃. About 99% degradation of methylene blue (3.12×10⁻⁵M) under optimized conditions: catalyst weight 25mg/50mL; pH 6.5; conversion time 30 minutes; 2wt% of AlF₃ doped zinc oxide photocatalyst. Similarly, 2wt % of SrSiO₃ doped ZnO catalyst degraded methylene blue (3.12×10⁻⁵M) within 60 minutes as shown in figures 5.1.12 A, B.

Indigo carmine dye $(2.14\times10^{-5}\text{M})$ degradation reached 99% within 30 minutes while using 2wt% of AlF₃ doped zinc oxide photocatalyst under the optimized conditions. Similarly, 2wt % of SrSiO₃ doped ZnO catalyst degraded 99% of indigo carmine dye $(2.14\times10^{-5}\text{M})$ within 40 minutes, as shown in figures 5.1.12 C, D.

For crystal violet dye (7.35×10⁻⁵M), a maximum degradation of 98% was achieved within 25 minutes using 2wt% of AlF₃ doped zinc oxide photocatalyst under optimized conditions. However, 2wt % of SrSiO₃ doped ZnO catalyst degraded only 76% of the dye within 60 minutes as shown in figures 5.1.12 E, F. For all the three dyes the photocatalytic efficiency of doped zinc oxide catalysts follows a similar trend i.e. compared to time taken to degrade the dyes by pure ZnO, the time taken by doped zinc oxide photocatalysts are very less. This can be attributed to the fact that introduction of impurity atoms to pure zinc oxide catalyst creates new energy levels above the valence band and below the conduction band, thereby decreasing the band gap energy. These dopants act as trapping centers for the charge carriers and they also facilitate the migration of the electrons and holes to the surface reaction sites of zinc oxide catalyst, increasing the photonic efficiency in generating reactive radical species for the degradation of these synthetic organic dyes in the aqueous solution²⁰. Similarly, the decrease in the photocatalytic activity after reaching a certain dopant concentration for the degradation of the three dyes might be due to the fact that the trapping centres created by the introduction of the dopants to pure zinc oxide catalyst may sometimes act as recombination centres for the electrons and holes which might lead to the decrease in their photocatalytic efficiency.

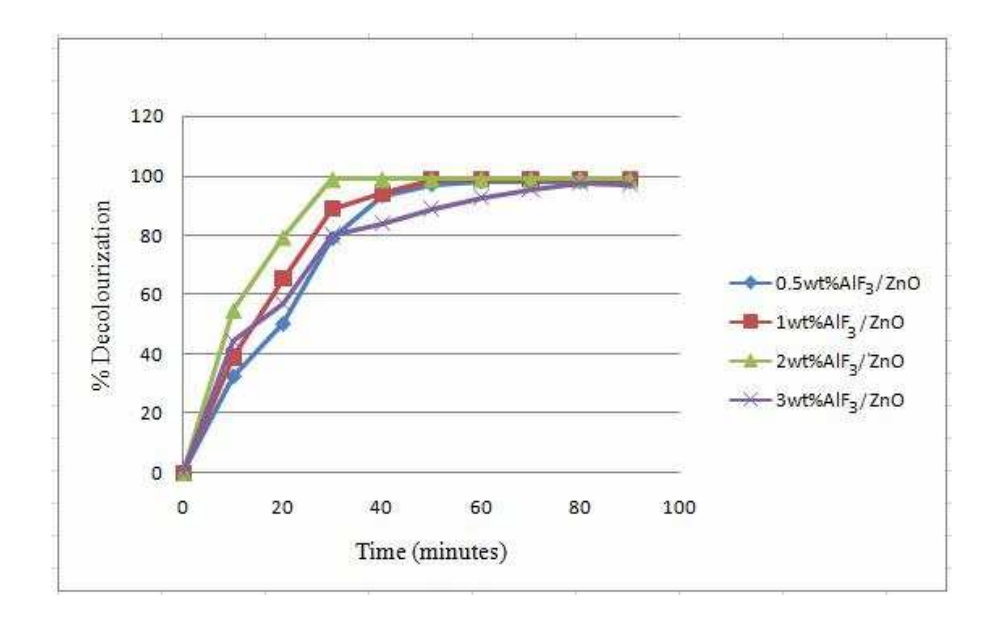


Figure 5.1.12 A Photocatalytic decolourization of methylene blue using different weight percents of aluminium fluoride doped ZnO catalyst.

(Reaction conditions: Methylene blue dye concentration = 3.12×10^{-5} mol/L, volume of dye solution =50mL, weight percent of AlF varied from (0.5-3 wt %), AlF₃/ZnO catalyst weight =25mg, pH= 6.5, air supply $\cong 2.5$ L/min, sunlight (I_{lux}) = $657 \times 100 \pm 100$ lux)

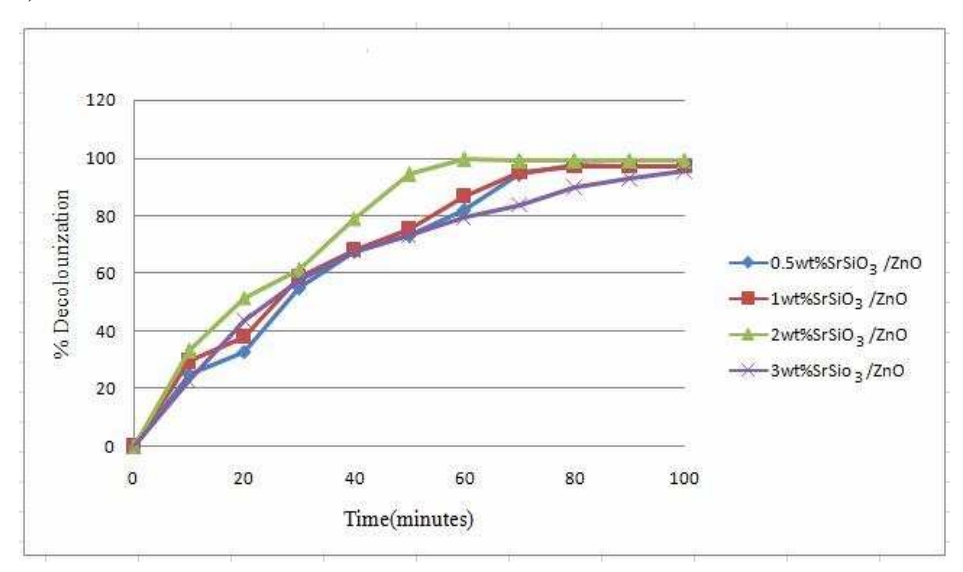


Figure 5.1.12 B Photocatalytic decolourization of methylene blue using different weight percents of strontium silicate doped ZnO catalyst.

(Reaction conditions: Methylene blue dye concentration = $3.12 \times 10^{-5} \text{mol/L}$, volume of dye solution =50 mL, weight percent of SrSi varied from (0.5-3 wt %), SrSiO₃/ZnO catalyst weight =25 mg, pH= 6.5, air supply $\cong 2.5 \text{L/min}$, Sunlight (I_{lux}) = $657 \times 100 \pm 100 \text{ lux}$)

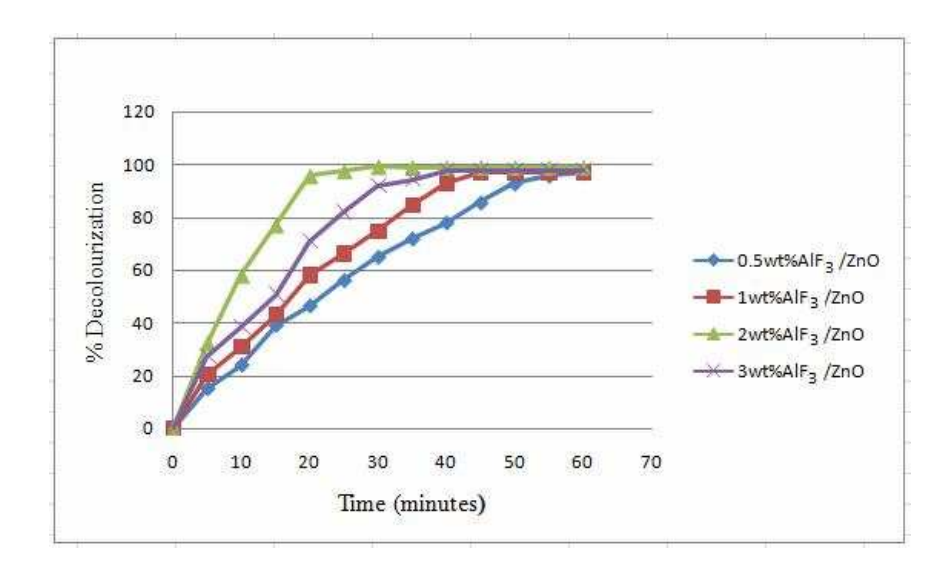


Figure 5.1.12 C Photocatalytic decolourization of indigo carmine using different weight percents of aluminium fluoride doped ZnO catalyst.

(Reaction conditions: Indigo carmine dye concentration = $2.14 \times 10^{-5} \text{mol/L}$, volume of dye solution =50 mL, weight percents of AlF₃ varied from (0.5-3 wt %), AlF₃/ZnO catalyst weight =25 mg, pH= 10, air supply $\cong 2.5 \text{L/min}$, sunlight (I_{lux}) = $689 \times 100 \pm 100 \text{ lux}$)

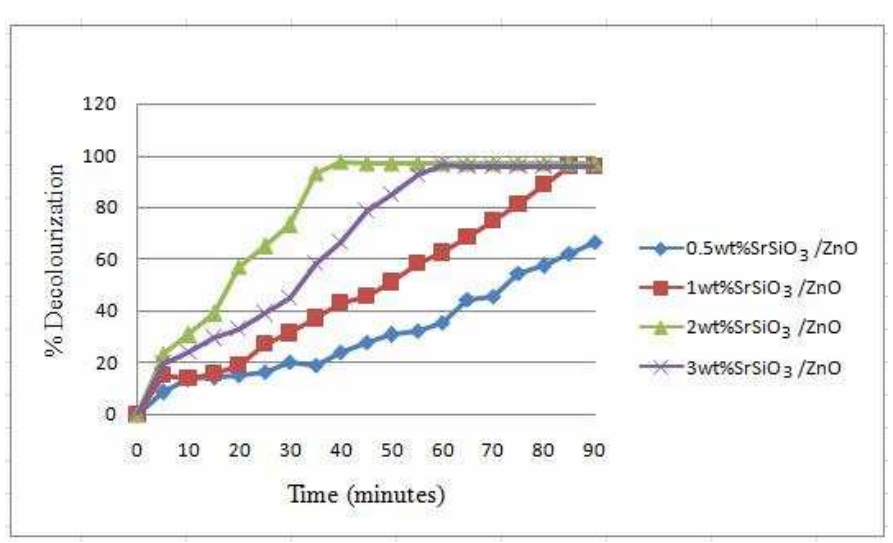


Figure 5.1.12 D Photocatalytic decolourization of indigo carmine dye using different weight percents of strontium silicate doped ZnO catalyst.

(Reaction conditions: Indigo carmine dye concentration = $2.14 \times 10^{-5} \text{mol/L}$, volume of dye solution =50 mL, weight percent of SrSiO_3 varied from (0.5-3 wt %), $\text{SrSiO}_3/\text{ZnO}$ catalyst weight =25 mg, pH=10, air supply $\cong 2.5 \text{L/min}$, sunlight (I_{lux}) = $689 \times 100 \pm 100 \text{ lux}$)

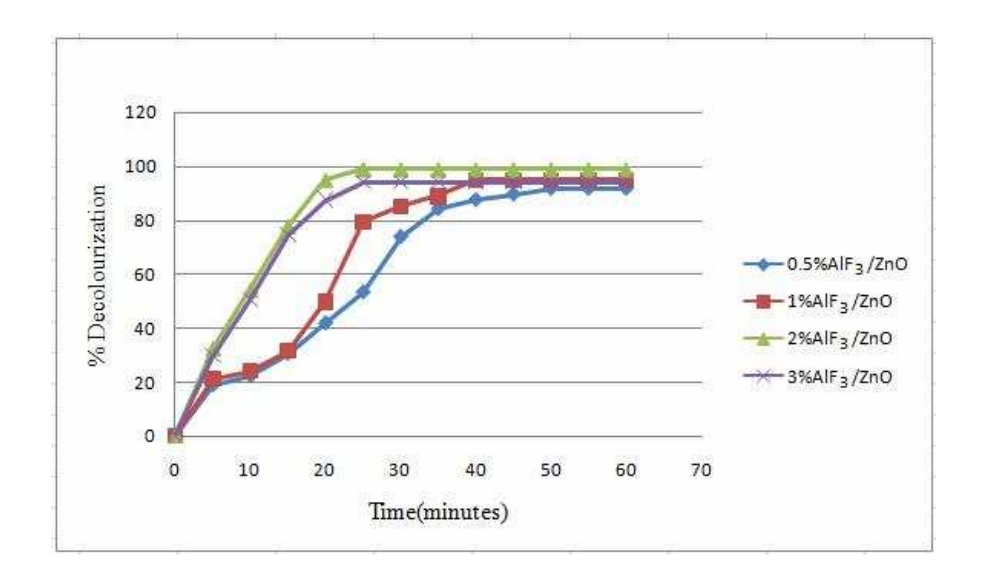


Figure 5.1.12 E Photocatalytic decolourization of crystal violet using different weight percents of aluminium fluoride doped ZnO catalyst.

(Reaction conditions: Crystal violet dye concentration = $7.35 \times 10^{-5} \text{mol/L}$, volume of dye solution = 50 mL, weight percent of AlF₃ varied from (0.5-3 wt %), AlF₃/ZnO catalyst weight = 25 mg, pH= 10, air supply $\cong 2.5 \text{L/min}$, sunlight (I_{lux}) = $723 \times 100 \pm 100 \text{ lux}$)

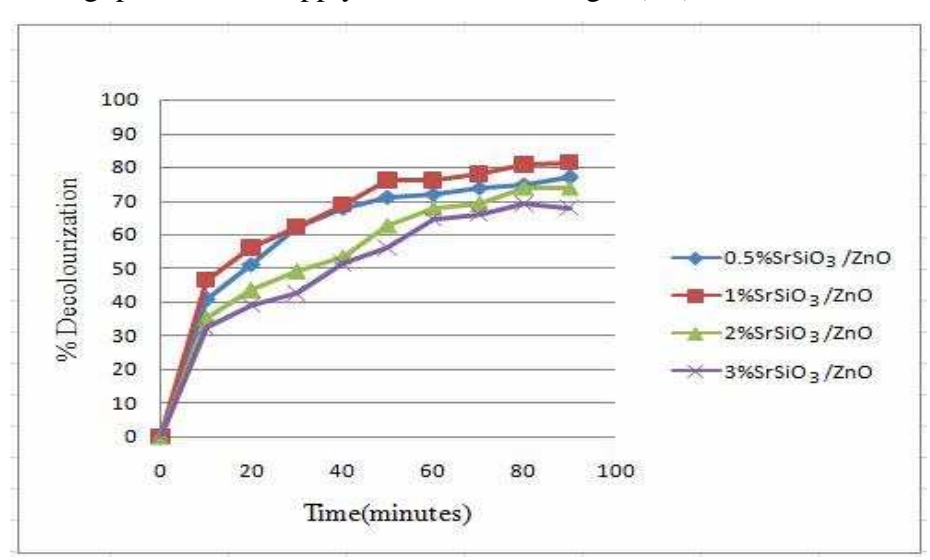


Figure 5.1.12 F Photocatalytic decolourization of crystal violet using different weight percents of strontium silicate doped ZnO catalyst.

(Reaction conditions: Crystal violet dye concentration = $7.35 \times 10^{-5} \text{mol/L}$, volume of dye solution =50 mL, weight percent of SrSiO_3 varied from (0.5-3 wt %), $\text{SrSiO}_3/\text{ZnO}$ catalyst weight =25 mg, pH= 10, air supply $\cong 2.5 \text{L/min}$, sunlight (I_{lux}) = $723 \times 100 \pm 100 \text{ lux}$)

5.1.13. Kinetic Studies

The kinetics of the degradation rate of many organic pollutants such as dyes, pesticides, nitro compounds, phenols etc. are studied by Langmuir–Hinshelwood kinetic model ²¹⁻²³. The main assumptions of the Langmuir–Hinshelwood kinetic model include: (1) at equilibrium the number of surface adsorption sites for the adsorbate is fixed and only one adsorbate can bind at each surface site, (2) the energy of the adsorbed species is the same at any site and is not affected by the adsorbed species on the adjacent site, and (3) the rate of surface adsorption of any species is larger than the rate of any subsequent chemical reaction.

The rate of Langmuir-Hinshelwood expression that explains the kinetics of heterogeneous photocatalytic systems is given by

$$r = -\frac{dc}{dt} = \frac{kr \ KC}{1 + KC} \qquad \qquad \text{eq.}(5.7)$$

where r is the rate of reaction that changes with time, C is the equilibrium concentration of the solution, K is the equilibrium constant for adsorption, and k_r is the limiting rate constant of the reaction at maximum surface coverage. For a highly diluted solution, the term KC becomes less than one, the numerator can be neglected, and the rate can be modelled by the apparent first order kinetics as shown in the following equation

$$r = -\frac{dc}{dt} = kr \ KC = k_{app}C \qquad \qquad \text{eq.}(5.8)$$

Integrating the above equation in the limits $C=C_0$ at t=0, the following equation is deduced

$$In\frac{C_t}{C_0} = -kt \qquad \qquad \text{eq.}(5.9)$$

$$In\frac{C_0}{C} = kt$$
eq.(5.10)

where C_0 is the initial concentration of the dye solution and C is the concentration of the dye solution at a time 't'.

In order to determine the rate and order of the photocatalytic decolourisation of synthetic dyes, namely, methylene blue (3.12x10⁻⁵M), indigo carmine (2.14x10⁻⁵M), and crystal violet (7.35x10⁻⁵M), the dyes were treated with different weight percents of (0.5-3%) aluminium fluoride or strontium silicate doped zinc oxide photocatalyst at optimized pH, and the plots of ln C₀/C vs 't' in minutes are shown in figures 5.1.13.1 A, B, 5.1.13. 2 A, B and 5.1.13.3 A, B. The R² values obtained for decolourization of methylene blue using 0.5-3 wt % of AlF₃ doped ZnO photocatalysts are 0.977, 0.985, 0.946, 0.937 and the rate constant values are 6.70x10⁻², 9.50x10⁻², 2.23x10⁻¹ and 2.40x10⁻² min⁻¹. Similarly, R² values obtained for decolourization of methylene blue using 0.5-3 wt % of SrSiO₃ doped ZnO photocatalysts are 0.994, 0.966, 0.948, 0.984 and the rate constant values are 2.80x10⁻², 3.20x10⁻², 9.80x10⁻² and 6.40x10⁻² min⁻¹ and for bare ZnO catalyst the R² value and rate constant value is 0.948 and 4.90x10⁻² min⁻².

For the photocatalytic decolourization of indigo carmine using 0.5-3 wt % of AlF₃ doped ZnO photocatalysts the R² values obtained are 0.972, 0.987, 0.994, 0.993 and the rate constant values are 6.50×10^{-2} , 8.40×10^{-2} , 2.06×10^{-1} and 1.16×10^{-2} min⁻¹. Similarly, R² values obtained for decolourization of indigo carmine using 0.5-3 wt % of SrSiO₃ doped ZnO photocatalysts are 0.976, 0.977, 0.961, 0.964 and the rate constant values are 6.00×10^{-2} , 1.60×10^{-2} , 1.22×10^{-1} and 6.50×10^{-2} min⁻¹ and for bare ZnO catalyst the R² value and rate constant value is 0.922 and 1.70×10^{-2} min⁻¹. Similarly for the photocatalytic decolourization of crystal violet using 0.5-3 wt % of AlF₃ doped ZnO photocatalysts the R² values obtained are 0.982, 0.976, 0.983, 0.950

and the rate constant values are 7.50×10^{-2} , 1.03×10^{-1} , 2.71×10^{-1} and 1.76×10^{-1} min⁻¹. Similarly, R^2 values obtained for decolourization of indigo carmine using 0.5-3 wt % of $SrSiO_3$ doped ZnO photocatalysts are 0.959, 0.992, 0.982, 0.995 and the rate constant values are 1.60×10^{-2} , 1.76×10^{-2} , 1.89×10^{-2} and 2.00×10^{-2} min⁻¹ and for bare ZnO catalyst the R^2 value and rate constant value is 0.935 and 4.80×10^{-2} min⁻¹. For all the three dyes the plots of $In C_0/C vs$ 't' showed a linear variation of % decolourization with respect to time, and the R^2 values obtained are close to unity. This clearly shows that the photocatalytic decolourisation of the dyes with respect to different weight percents of AlF_3 and $SrSiO_3$ doped and undoped ZnO photocatalyst followed pseudofirst order kinetics.

Aluminium fluoride doped zinc oxide photocatalyst showed higher rate constant values compared to strontium silicate doped and undoped zinc oxide photocatalyst for the decolourization of methylene blue, indigo carmine and crystal violet dyes. Among different weight percent (0.5-3%) of Aluminium fluoride doped zinc oxide photocatalyst, 2wt% showed higher rate constant and the decrease in the rate constant value observed in the case of 3 wt% AlF₃ doped ZnO photocatalyst may be due to the higher coverage of aluminium atoms on the catalytically active surface of zinc oxide photocatalyst. Similar results have been reported by A.N.Rao and coworkers for the photocatalytic degradation of direct yellow12 dye using zinc oxide photocatalyst.

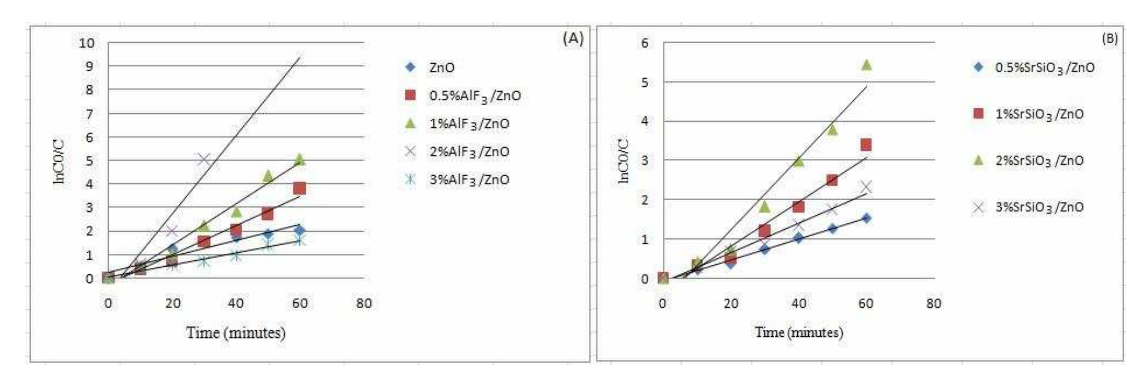


Fig. 5.1.13.1 shows the plot of $\ln C_0/C vs$ 't' for the photocatalytic decolourization of methylene blue using (A) undoped ZnO and (0.5-3 wt%) AlF₃ doped ZnO and (B) using (0.5-3 wt %) SrSiO₃ doped ZnO photocatalyst.

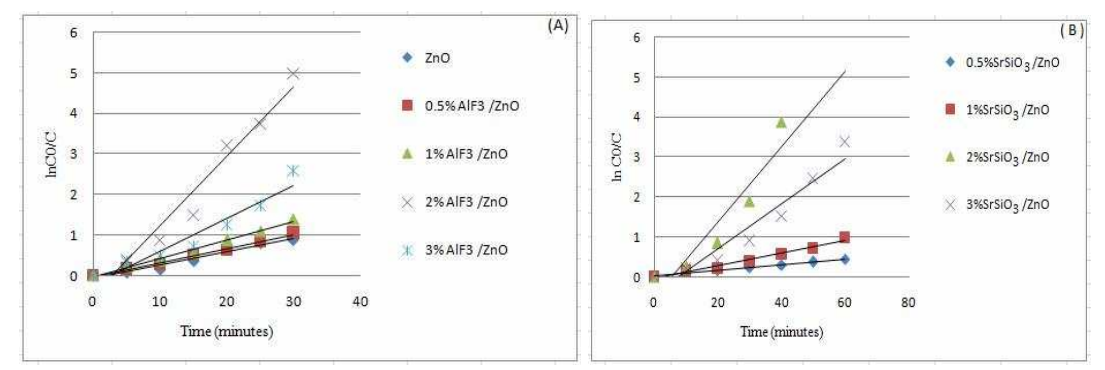


Fig. 5.1.13.2 shows the plot of $\ln C_0/C vs$ 't' for the photocatalytic decolourization of indigo carmine using (A) undoped ZnO and (0.5-3 wt%) AlF₃ doped ZnO and (B) using (0.5-3 wt %) SrSiO₃ doped ZnO photocatalyst.

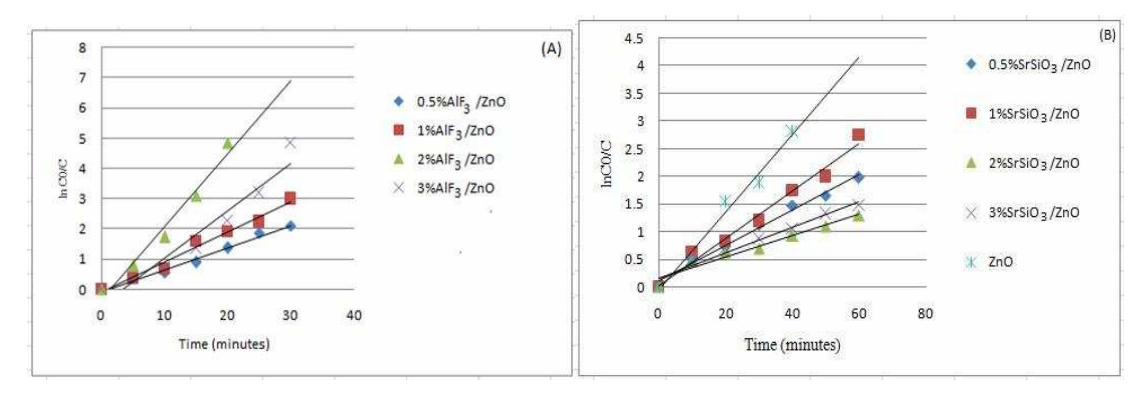


Fig. 5.1.13.3 shows the plot of $\ln C_0/C vs$ 't' for the photocatalytic decolourization of crystal violet using (A) undoped ZnO and (0.5-3 wt%) AlF₃ doped ZnO and (B) using (0.5-3 wt%) SrSiO₃ doped ZnO photocatalyst.

5.1.14. UV-Visible Spectroscopic Analysis

The photocatalytic decolourization of all three dyes, namely, methylene blue, indigo carmine and crystal violet, with respect to time over AlF₃/ZnO and SrSiO₃/ZnO photocatalysts are analyzed with the help of UV-Visible spectrophotometer, and the spectra are shown in figures 5.1.14.1 A, B -5.1.14.3 A, B.

The main characteristic peak of the methylene blue is observed at 663nm in the UV-Visible absorption spectra. The maximum decolourization of the methylene blue is observed from the change in the colour of the dye from blue to colourless within 30 minutes when AlF₃/ZnO photocatalyst is used. However, using SrSiO₃/ZnO photocatalyst the maximum decolourization of the dye is achieved only at 60 minutes and the decrease in the intensity of the colour of the dye is visualized during the course of the reaction as shown in the insets to figures 5.2.14.1 A, B. The presence of conjugated aryl rings in methylene blue constitute the chromophoric group, and the dimethylamine (-NCH₃)₂ moiety acts as the auxochrome, which enhances the colour of the dye. During the photocatalytic process, the continuous decrease in the intensity of the peak at 663nm and the absence of any other peak in the absorption spectra, confirm the complete destruction of the chromophoric group, and this strongly suggests that at the end of the photocatalytic treatment the fragment of the dye do not contain any chromophores.

The indigo carmine dye that belongs to the indigoid class, shows a characteristic absorption peak at 610nm. The decrease in the intensity of the peak observed during the photocatalytic treatment while using AlF₃/ZnO as photocatalysts is shown in figure 5.1.14.2 A, and that observed with SrSiO₃/ZnO photocatalysts is shown in figure 5.1.14.2 B. The maximum decolourization of indigo carmine is

achieved within 30 minutes with AlF₃/TiO₂ photocatalyst and in the case of SrSiO₃/ZnO photocatalyst the time taken to achieve complete decolourization is 40 minutes. A change in colour of the dye from blue to colourless occurs during the course of the reaction, which indicates that the chromophoric enedione structure (O=C-C=C-C=O) as well as the auxochromic -NH groups of the dye are completely destroyed by the photocatalytic treatment.

The crystal violet dye has a prominent absorption peak at 590 nm. The decrease intensity at 590 nm in the absorption spectra of crystal violet was continuously monitored, and the data are shown in the figures 5.1.14.3 A and B. The inset in the figures clearly shows the decrease in the intensity of violet colour at different time intervals. A prominent peak observed for crystal violet at 590 nm in the visible region is due to the presence of the highly conjugated triaryl ring structure of the dye, and also due to the presence of the auxochromic group $-N(CH_3)_2$, which is responsible for enhancing the color of the dye. The disappearance of the prominent absorption peak after the photocatalytic treatment for 30 minutes clearly shows that the chromophoric and auxochromic groups that are responsible for the violet colour of the dye are completely destroyed at the end of the reaction. The absence of new absorption peaks during the course of the reaction as well as at the end of the reaction is a clear indication that the fragmented intermediates do not contain any chromophoric groups.

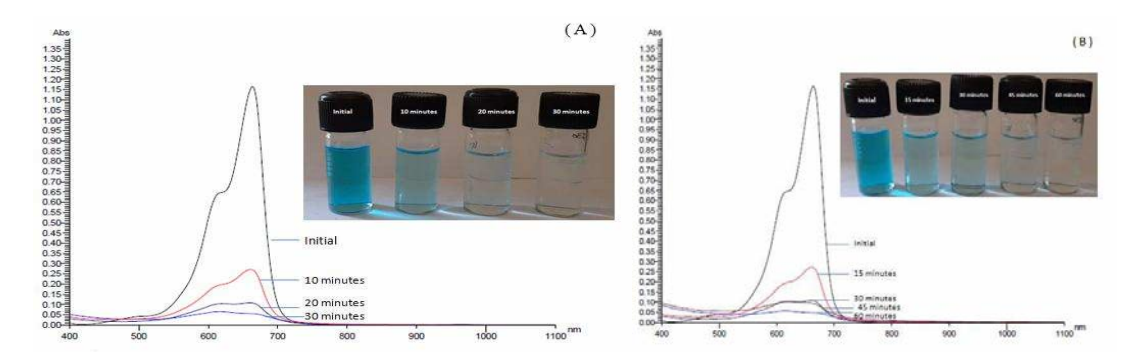


Figure 5.1.14.1 UV-Visible absorption spectra showing the decolourization of methylene blue in the presence of (A) AlF₃/ZnO photocatalyst and (B) SrSiO₃/ZnO photocatalysts.

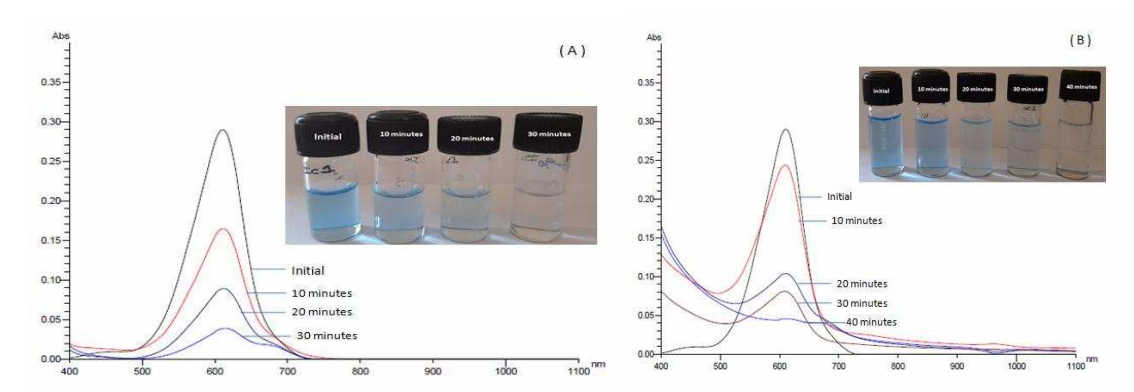


Figure 5.1.14.2 UV-Visible absorption spectra showing the decolourization of indigo carmine in the presence of (A) AlF₃/ZnO and (B) SrSiO₃/ZnO photocatalysts.

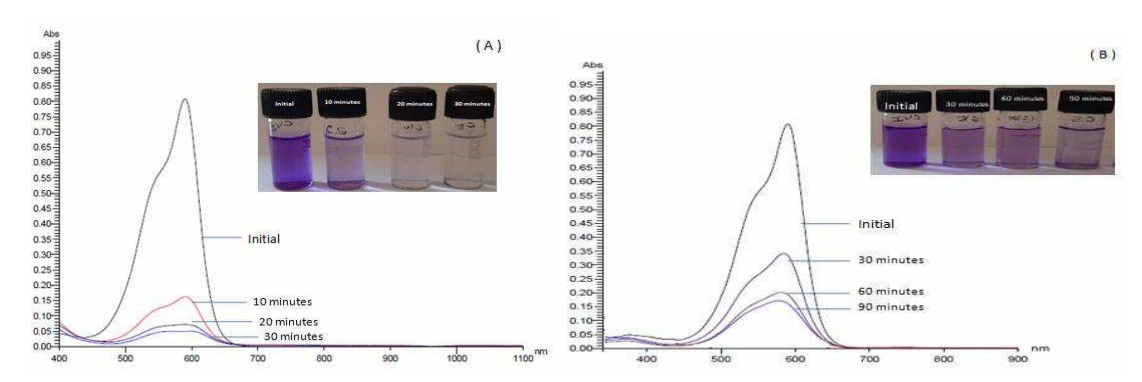


Figure 5.1.14.3 UV-Visible absorption spectra showing the decolourization of crystal violet in the presence of (A) AlF₃/ZnO and (B) SrSiO₃/ZnO photocatalysts.

5.1.15. Comparison of the Degradation Efficiencies of the Photocatalysts

The degradation efficiencies of undoped zinc oxide and different weight percents (0.5-3%) of aluminium fluoride and strontium silicate doped zinc oxide photocatalysts are compared for three synthetic dyes; namely, methylene blue, indigo carmine and crystal violet dye and the values are shown in table 5.1.15.

For methylene blue dye degradation at optimum conditions [dye concentration (3.12x10⁻⁵M), pH 6.5, catalyst weight 25mg/50mL] under solar radiation for 30 minutes, the degradation efficiencies of different photocatalysts are shown below:

 $2\% AlF_3/ZnO > 1\% \ AlF_3/ZnO > 3\% \ AlF_3/ZnO > 0.5\% AlF_3/ZnO > ZnO > 2\%$ $SrSiO_3/ZnO > 1\% \ SrSiO_3/ZnO > 3\% \ SrSiO_3/ZnO > 0.5\% \ SrSiO_3/ZnO$

For indigo carmine dye degradation at optimum conditions [dye concentration $(2.14 \times 10^{-5} \mathrm{M})$, pH 10, catalyst weight $25 \mathrm{mg}/50 \mathrm{mL}$] under solar radiation for 30 minutes, the degradation efficiencies of different photocatalysts are shown below: $2\% \mathrm{AlF_3/ZnO} > 3\% \mathrm{AlF_3/ZnO} > 1\% \mathrm{AlF_3/ZnO} > 0.5\% \mathrm{AlF_3/ZnO} > 2\% \mathrm{SrSiO_3/ZnO} > 3\% \mathrm{SrSiO_3/ZnO} > 1\% \mathrm{AlF_3/ZnO} > 0.5\% \mathrm{SrSiO_3/ZnO}$

For crystal violet dye degradation at optimum conditions [dye concentration (7.35x10⁻⁵M), pH 10, catalyst weight 25mg/50mL] under solar radiation for 30 minutes, the degradation efficiencies of different photocatalysts are shown below:

 $2\% AlF_3/ZnO > 1\% \ AlF_3/ZnO > 0.5\% \ AlF_3/ZnO > 3\% AlF_3/ZnO > ZnO > 1\%$ $SrSiO_3/ZnO > 0.5\% \ SrSiO_3/ZnO > 2\% \ SrSiO_3/ZnO > 3\% \ SrSiO_3/ZnO$

The comparative analysis, shows that aluminium fluoride doped zinc oxide photocatalysts are generally more efficient in degrading the three synthetic dyes compared to strontium silicate modified zinc oxide and bare zinc oxide photocatalysts.

The degradation efficiencies of the photocatalysts depend upon many factors such as the ability of the dye to get adsorbed on the photocatalyst, structure and concentration of the dyes and absorption of light by photocatalysts. In the overall process, the complete degradation of the three dyes is achieved with 2wt% AlF₃/ZnO within a short span of time under sunlight compared to strontium silicate and undoped zinc oxide photocatalysts.

Table 5.1.15 Comparison of the efficiencies (in terms of % decolourization) of doped and undoped zinc oxide photocatalysts towards methylene blue, indigo carmine and crystal violet.

Photocatalyst	Methylene blue (Optimized conditions: pH=6.5, catalyst weight= 25 mg/50mL, Dye concentration= 3.12x10 ⁻⁵ mol/L), Time=30 minutes.	Indigo carmine (Optimized conditions: pH=10, catalyst weight= 25 mg/50mL, Dye concentration= 2.14x10 ⁻⁵ mol/L), Time=30 minutes.	Crystal violet (Optimized conditions: pH=10, catalyst weight= 25 mg/50mL, Dye concentration= 7.35x10 ⁻⁵ mol/L), Time=30 minutes.
Bare ZnO	79	58	85
0.5% AlF ₃ /ZnO	78.8	65	93.5
1% AlF ₃ /ZnO	89	75	95
2 % AlF ₃ /ZnO	98	99	99
3 % AlF ₃ /ZnO	80.2	92.4	87.5
0.5%SrSiO ₃ /ZnO	54.9	23	60.2
1% SrSiO ₃ /ZnO	58.7	34	62
2% SrSiO ₃ /ZnO	61.2	73.5	56.5
3 % SrSiO ₃ /ZnO	57.5	45.6	54

5.1.16. Effect of Radical Quenchers

The involvement of reactive species such as h^+ , OH, O_2 and e^- during the photocatalytic process are investigated by the addition of radical quenchers such as EDTA, isopropyl alcohol, ascorbic acid and sodium sulphate^{25, 26}. For analysing the effect of radical scavenging activity, 1mM solution of the radical quenchers such as EDTA, isopropyl alcohol, ascorbic acid and sodium sulphate are added to the dye solution at optimized pH, catalyst and dye concentration. A blank experiment is also carried out without the addition of quenchers under identical conditions. For the photocatalytic degradation of methylene blue using the most active 2 wt%-AlF₃/ZnO catalyst about 99% degradation of methylene blue dye is achieved in the absence of any quencher. However, around 50% decrease in the degradation efficiency is noticed after the addition of EDTA, isopropyl alcohol, ascorbic acid and sodium sulphate, respectively. The obtained results clearly show that all these reactive species (h^+ , OH, O₂ and e) have actively participated in the photocatalytic process. A similar result was reported by S. Ramanathan and coworkers where the participation of all the reactive species such as h^+ , OH, O_2 is confirmed from the radical scavenging assay for the degradation of methylene green using CRGO/SnO₂ photocatalyst²⁷.

In the photocatalytic degradation of indigo carmine maximum degradation is achieved in the absence of any quencher. About 32%, 13%, 46% and 37% degradation is achieved by the addition of EDTA, isopropyl alcohol, ascorbic acid and sodium sulphate, respectively. The obtained result clearly shows that the involvement of the reactive species in the photocatalytic process follows the order 'OH > h^+ > e^- > O_2 . In the photocatalytic degradation of crystal violet using 2 wt%- AlF₃/ZnO catalyst, about 99% degradation is achieved in the absence of any quencher, and about

43%, 55%, 46% and 57% degradation is achieved by the addition of EDTA, isopropyl alcohol, ascorbic acid and sodium sulphate, respectively. These results clearly show that the involvement of the reactive species in the photocatalytic process follows the order O_2 : $> h^+ > OH > e^-$. In a similar study on the radical scavenging activity carried out by Islam molla and co-workers, it was found that superoxide anion radical and holes were the main reactive oxidative species formed during the photocatalytic degradation of rhodamine B and orange II dyes²⁸.

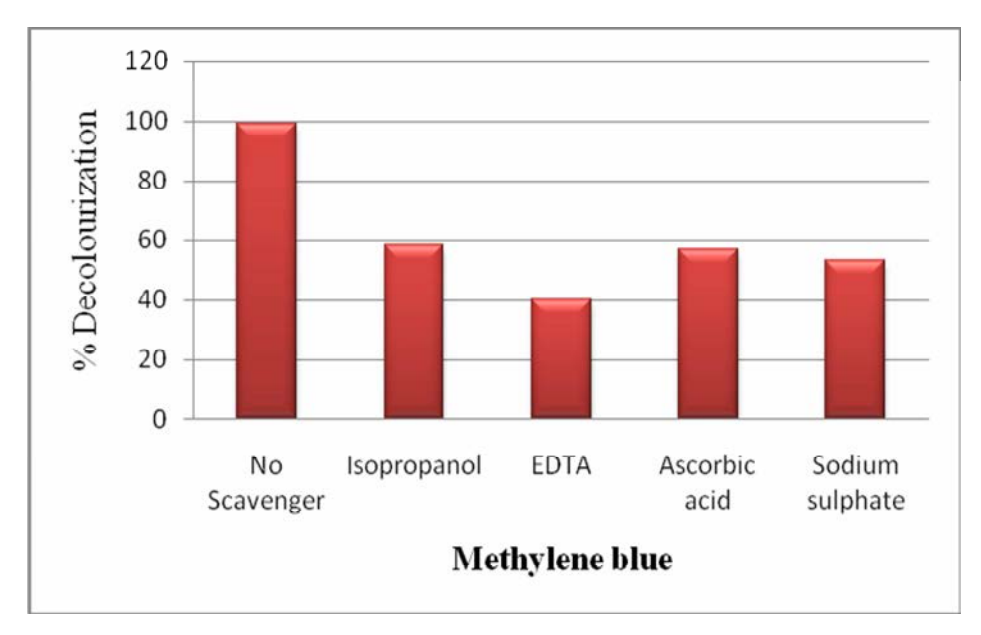


Figure 5.1.16.1 Effect of radical scavengers on the photocatalytic degradation of methylene blue using 2wt% AlF₃/ZnO photocatalyst under optimized conditions

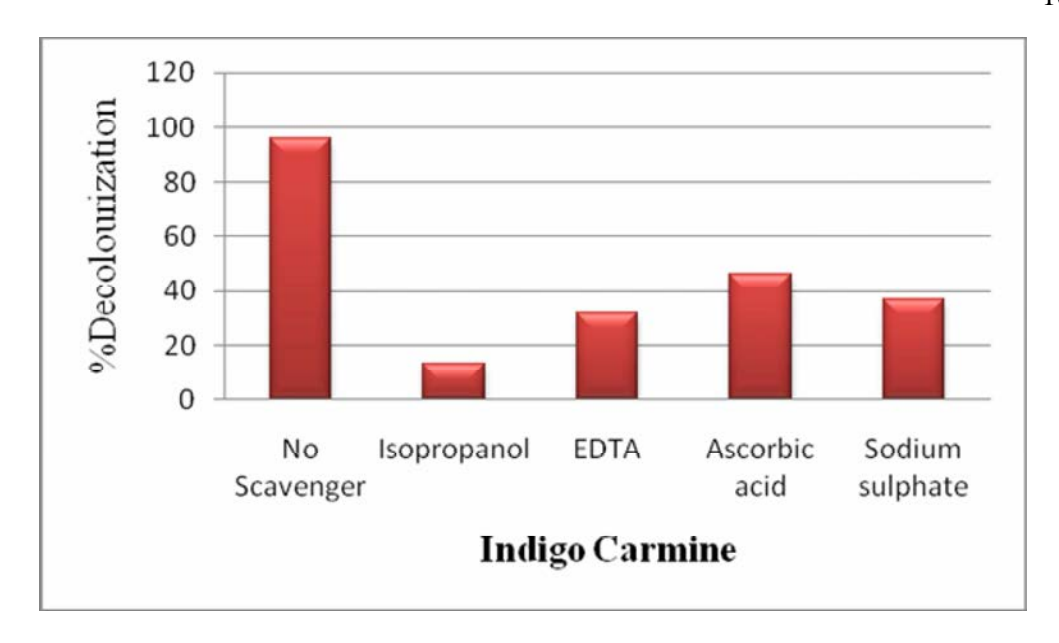


Figure 5.1.16.2 Effect of radical scavengers on the photocatalytic degradation of indigo carmine using (2 wt%)AlF₃/ZnO photocatalyst under optimized conditions

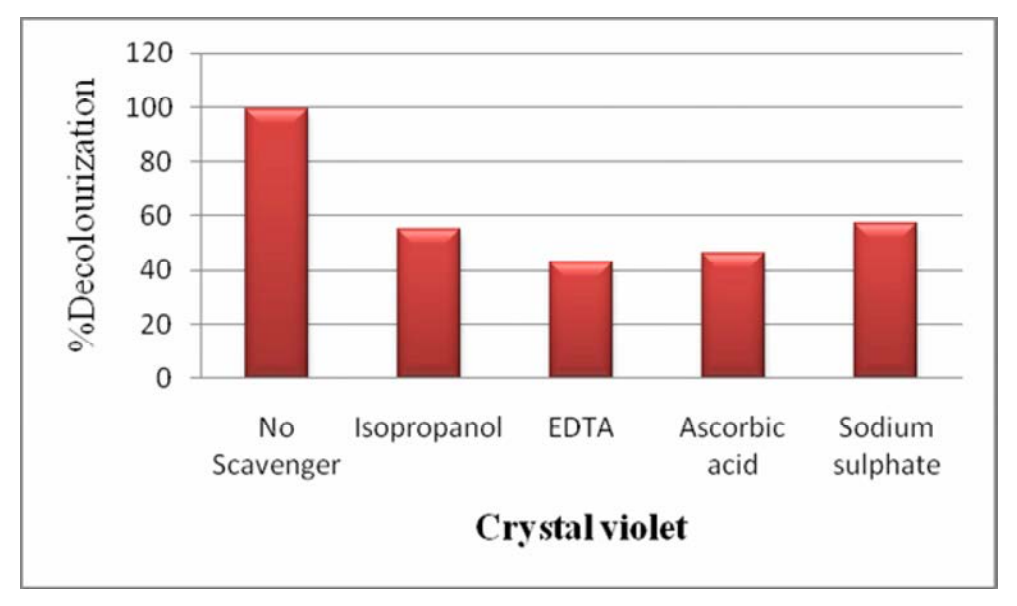


Figure 5.1.16.3 Effect of radical scavengers on the photocatalytic degradation of crystal violet using (2wt%)AlF₃/ZnO photocatalyst under optimized conditions

5.1.17. Mineralization Studies

Total Organic Carbon Analyzer (TOCA) is an instrument used to determine the amount of organic carbon present in the samples. The extents of mineralization of the organic dyes in aqueous samples are determined with the TOCA instrument. The total organic carbon content present in the dye samples before and after the photocatalytic treatment process is determined, and the difference between the values gives the percentage degradation of the dyes. In the present work, the synthetic organic dyes such as methylene blue, indigo carmine and crystal violet before and after photocatalytic treatment using AlF₃/ZnO photocatalyst under sunlight at optimum conditions were subjected to TOCA. About 82.5, 83 and 77 percent mineralization of methylene blue, indigo carmine and crystal violet were achieved, respectively, after the photocatalytic treatment as shown in figure 5.1.17. The percentage mineralization of all the dyes was found to be less compared to the percentage decolourization values calculated from the analysis using UV-Visible spectrophotometer. From the obtained results, it is understood that after the photocatalytic process all the three dye molecules have been converted into more off CO₂, mineral acids and some other organic intermediates, which do not have a chromophoric group to be detected by the spectrophotometer.

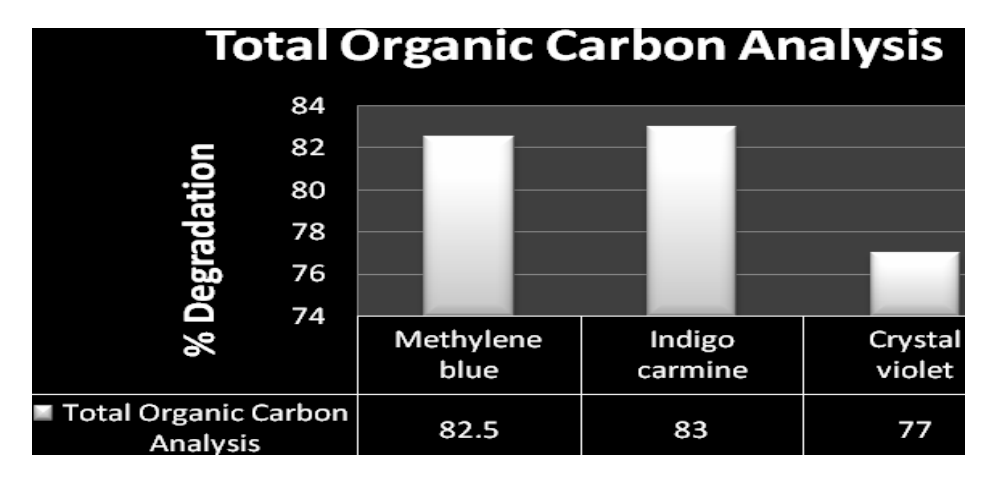


Figure 5.1.17 shows the percentage removal of total organic carbon in the aqueous solution of methylene blue, indigo carmine and crystal violet using 2wt% AlF₃/ZnO photocatalyst under optimized conditions

5.1.18. Reusability Studies

In photocatalysis, the reusability of the catalyst is checked because the recyclability of the catalyst is as important as its efficiency to degrade the pollutants. The possible reuse of the photocatalyst for more number of cycles brings a significant reduction in the overall cost of the photocatalytic treatment. In the present work, the reusability of the most active catalyst 2 wt % AlF₃/ZnO in the degradation of methylene blue, indigo carmine and crystal violet under sunlight is evaluated by reusing the catalyst for four more runs. After each cycle, the catalyst is separated from the dye solution by centrifugation, dried and again treated with the fresh dye solution. The percentage decolourization of the dyes achieved using 2wt % AlF/ZnO after each cycle is plotted and shown in figures 5.1.18A-C. The results of reusability studies, showed that after the five cycles of reuse of the zinc oxide photocatalyst, only a neglible decrease in the catalystic efficiency is observed which might be due to the little loss of the catalyst during washing. Another possible reason for the decrease in the photocatalytic activity after repeated runs could be due to chemisorption of the

dye or intermediates to the catalyst surface, which would reduce the photocatalytic efficiency of the catalyst.

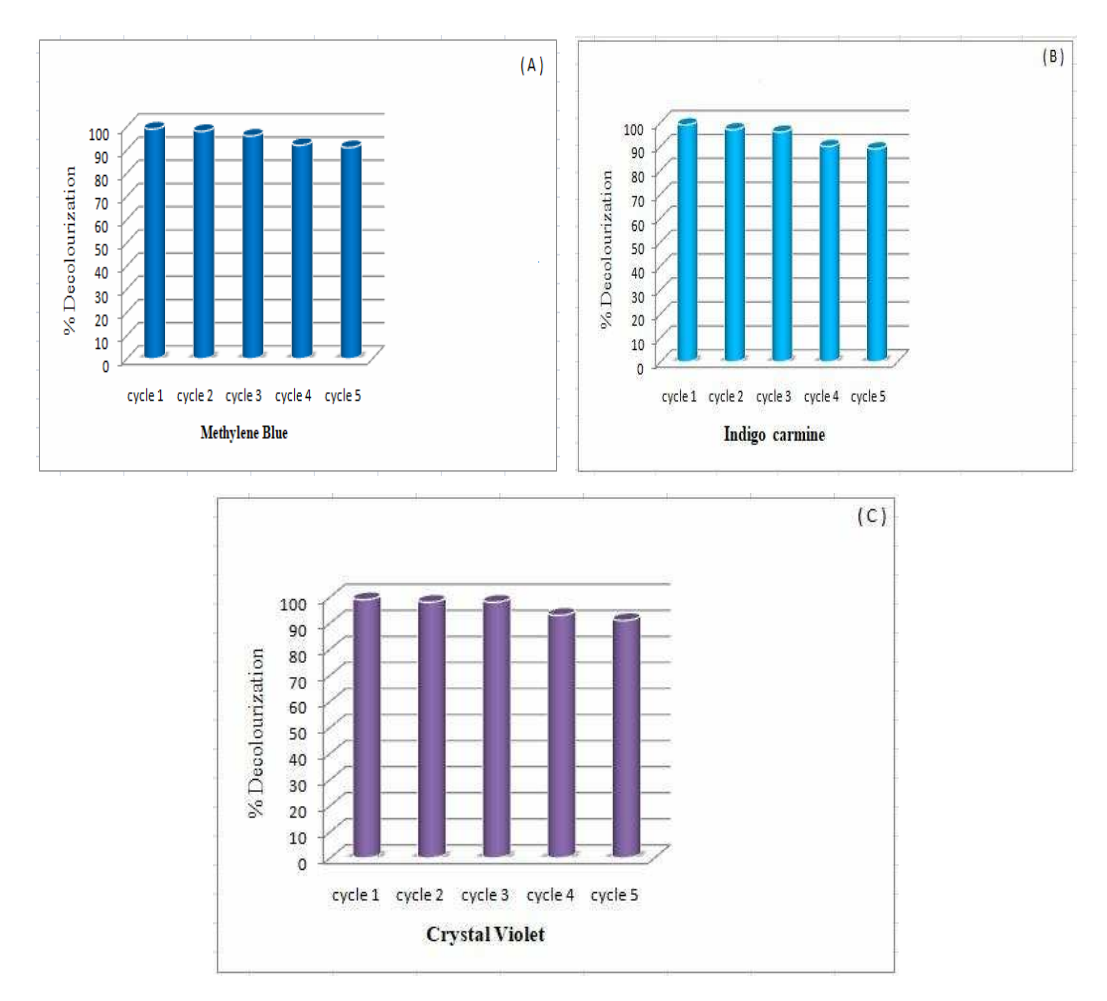


Figure 5.1.18 shows the reusability of the most active 2wt% AlF₃/ZnO catalyst for the photocatalytic degradation of (A) methylene blue (B) indigo carmine and (C) crystal violet dyes

5.1.19. Proposed Mechanism

Zinc oxide semiconductor has unique optoelectric properties. It shows good photocatalytic performance. Under sunlight radiation, the electrons in the valence band of ZnO photocatalyst is excited to generate electron hole pairs and the redox reactions are initiated as shown below

The photocatalytic degradation of the organic pollutants takes place through various free radical reactions giving a large number of intermediates which on subsequent oxidation, leads to the formation of non-toxic products such as CO₂, H₂O and mineral acids. Hence, the participation of the photogenerated electrons and holes in the photocatalytic reaction is essential to achieve an effective oxidation process. However, in a bare zinc oxide photocatalytic system, the recombination of the electrons and holes takes place at a faster rate, and hence the generation of the reactive species such as hydroxyl and superoxide anion radicals is hindered. In view of these facts, doping of the bare zinc oxide photocatalyst with metals such as 'Al' and 'Sr' was done for the present work. Doping creates additional energy levels that are above the valence band edge and below the conduction band edge of ZnO photocatalyst, acting as both electron and hole traps.

From the photocatalytic studies, it was observed that the doping of aluminium fluoride salt to the zinc oxide photocatalyst led to faster degradation of all the three organic dyes. On the other hand, doping of strontium silicate to zinc oxide photocatalyst also degraded the dyes methylene blue and indigo carmine at a faster rate compared to bare ZnO photocatalyst. However the photocatalytic activity was comparatively less to that of 'Al' doped ZnO photocatalyst. In the case of crystal violet dye, the degradation process using 'Sr' doped ZnO photocatalyst took more time compared to both bare ZnO and 'Al' doped ZnO photocatalysts.

The lower photocatalytic activity of strontium silicate doped-ZnO photocatalyst can be ascribed to the following reasons:

Strontium silicate used as a dopant distorts the lattice sites, creates defects and occupies the photocatalytically active sites of zinc oxide photocatalyst thereby reducing the number of active sites available for the photocatalytic reaction.

Addition of excess amount of strontium silicate dopant to zinc oxide sites might have resulted in recombination centers for the photogenerated electron-hole pairs resulting in a decreased photocatalytic activity. Similarly, Gupta et al²⁹ and He et al³⁰ reported that doping of excess amount of transition metal ions such as cobalt can decrease the photocatalytic activity of zinc oxide photocatalyst because the intra bandgap impurity levels created as a consequence of Co²⁺ doping can act as recombination centers for the photogenerated electrons and holes.

The higher photocatalytic activity of aluminium fluoride doped zinc oxide photocatalyst compared to the undoped and SrSiO₃ doped ZnO photocatalysts can be attributed to the fact that the introduction of 'Al' to ZnO catalyst may act as trapping centers for the photogenerated electrons and holes. The additional energy states created by the introduction of Al³⁺ ions to the zinc oxide lattices lead to a reduction in

the bandgap values, and Al^{3+} ions trap the photogenerated electrons and holes to form less stable Al^{2+}/Al^{4+} ions, which further react with the surface adsorbed O_2 and hydroxyl ions to form the reactive species such as hydroxyl and superoxide anion radicals. Girish kumar et al^{31} reported that doping can cause a decrease in the bandgap of ZnO photocatalyst and Faraz et al^{32} reported that introduction of Sm^{3+} as dopant to zinc oxide can inhibit the recombination between electrons and holes. The plausible mechanism is depicted as given below:

The superoxide anion radical and hydroxyl radicals generated in situ are highly reactive species that trigger the degradation of dyes

$$Dye^{+} + O_{2}^{-} \rightarrow Degradation products$$
 eq.(5.24)

$$Dye^{.+} + OH \rightarrow Degradation \ products \qquad \qquad eq.(5.25)$$

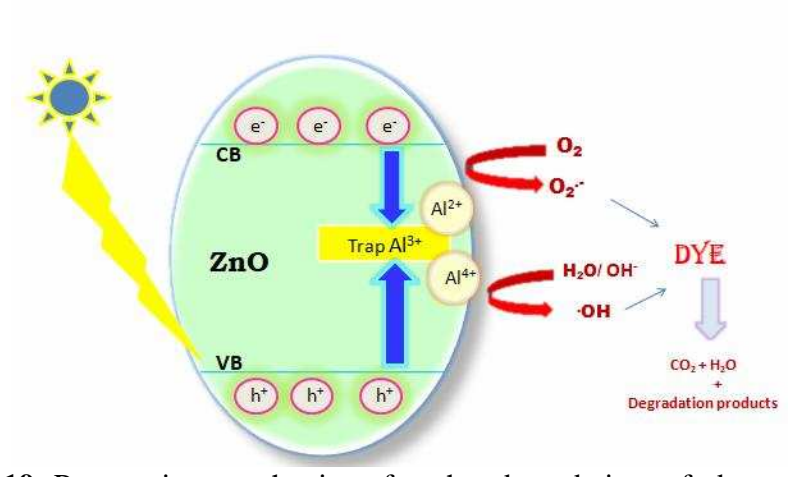


Figure 5.1.19 Perspective mechanism for the degradation of dyes mediated by AlF₃/ZnO catalyst under sunlight.

5.2. CHARACTERIZATION AND PHOTOCATALYTIC STUDIES OF TITANIUM DIOXIDE, ALUMINIUM FLUORIDE DOPED TITANIUM DIOXIDE AND STRONTIUM SILICATE DOPED TITANIUM DIOXIDE

5.2.1. X-Ray Diffraction Studies

The crystallinity and the phase identification of the synthesized neat titanium dioxide, aluminium fluoride and strontium silicate doped titanium dioxide photocatalysts were determined using the powder x-ray diffraction technique, and the recorded diffraction patterns of the synthesized materials are shown in figure 5.2.1A-C. From the powder-XRD pattern obtained for the bare titanium dioxide photocatalyst, it is seen that the diffraction peaks at 2θ values 25.12° , 37.02° , 48.07° , 67.52° , 70.28° , 75.05°, corresponding respectively to the crystal planes (101), (004), (200), (204), (220), (215) represent the anatase phase, which is in accordance with the standard JCPDS [21-1272]. The peaks at 20 values 27.44°, 36.10°, 53.82°, 55.04° corresponding to the crystal planes (110), (103), (105), (211) represents the rutile phase. Peaks at 2θ values 31.69°, 45.42° corresponding to the crystal planes (121) and (032) shows presence of brookite phase in the synthesized TiO₂ photocatalyst^{33,34}. Similar diffraction peaks were also obtained for the aluminium fluoride and strontium silicate doped titanium dioxide photocatalyst except that in the bare TiO₂ photocatalyst and aluminium fluoride doped TiO₂ photocatalyst, the crystal plane (101) corresponding to the $2\theta = 25.12^{\circ}$ value is found with a maximum intensity which indicates that anatase is the main crystal phase of the synthesized materials with some rutile and brookite crystals formed in it. On the other hand, in the powder XRD pattern obtained for the strontium silicate doped TiO₂ photocatalyst the crystal plane (121) corresponding to the $2\theta = 31^{\circ}$ value is found with maximum intensity indicating that brookite is the

main phase in the synthesized SrSiO₃ doped TiO₂ photocatalyst, whereas the anatase and rutile phases of the titanium dioxide photocatalyst are found with decreased intensity. The calculated percentage of anatase, rutile and brookite phases in the synthesized undoped TiO₂ photocatalyst is, respectively, 53.51%, 25.65% and 20.82%. Similarly the aluminium fluoride doped titanium dioxide photocatalyst consists of 31.59% of anatase phase, 26.02% of the rutile phase and 42.38% of the brookite phase, and the strontium silicate doped titanium dioxide photocatalyst consists of 19.67% of the anatase phase, 16.5% of the rutile phase and 63.88% of the brookite phase. Hence, it can be concluded that all the three synthesized titanium dioxide photocatalysts posses anatase, rutile and brookite phases with some variations in the main crystal growth planes. The crystallite size calculated from the Debye Scherrer's equation for neat TiO₂ photocatalyst, AlF₃- TiO₂ photocatalyst and SrSiO₃-TiO₂ photocatalyst are 20.2 nm, 16.8 nm and 17.85 nm, respectively.

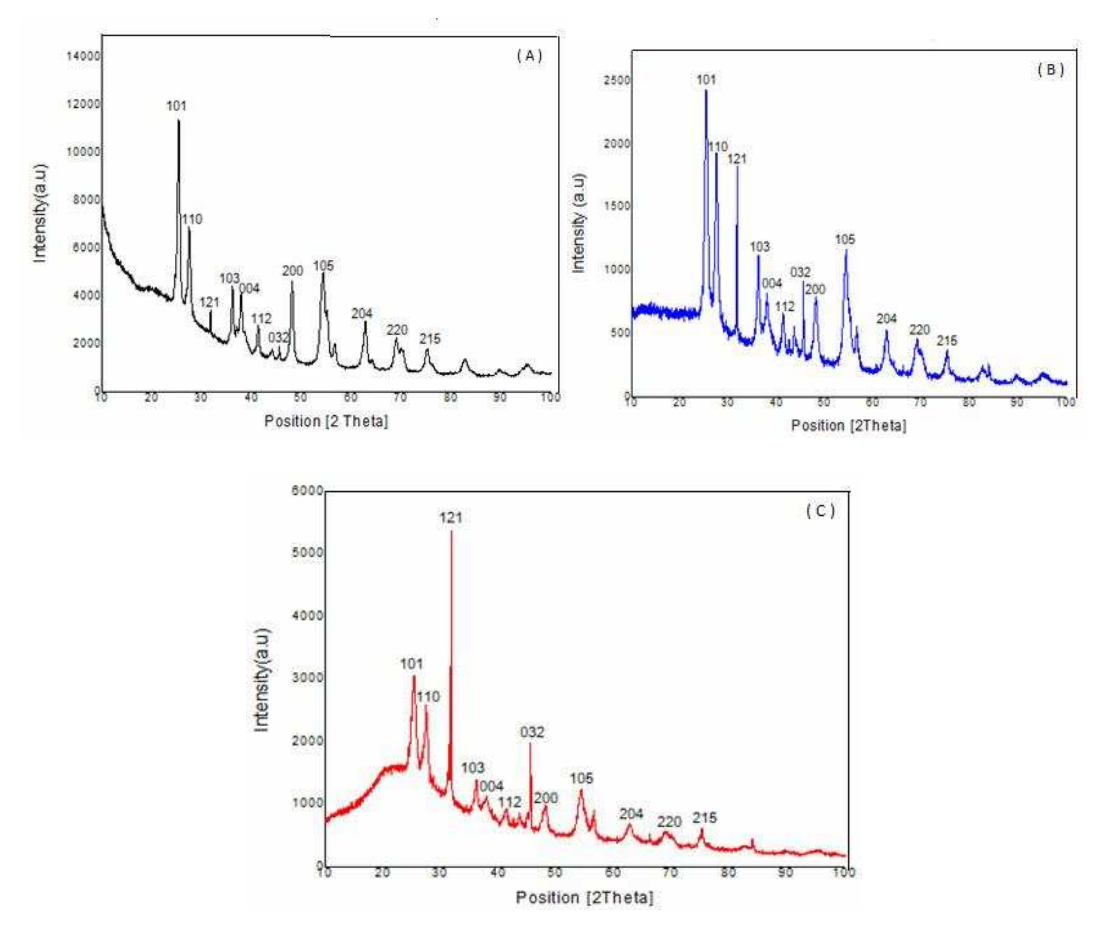


Figure 5.2.1 X-Ray diffraction pattern of the synthesized (A) undoped Titanium dioxide photocatalyst (B) 1 wt% AlF₃ doped Titanium dioxide photocatalyst and (C) 1wt% SrSiO₃ doped Titanium dioxide photocatalyst.

5.2.2. HR-SEM Analysis

The surface morphology of a catalyst plays a significant role in determining its photocatalytic activity. The difference in morphologies of the synthesized neat as well as aluminium fluoride and strontium silicate doped titanium dioxide photocatalysts are shown in figure 5.2.2 A-C. From the scanning electron microscopic analysis, it is observed that the synthesized undoped titanium dioxide photocatalyst posseses a moderately spherical shape. These moderately spherical shaped particles are highly aggregated in such a way that they are bound to each other forming clusters. The HR-SEM image of the aluminium fluoride doped titanium dioxide photocatalyst shows

the formation of moderately spherical shaped particles which are self assembled into a chain like structure. Whereas in the strontium silicate doped titanium dioxide photocatalyst, shows a non-homogeneous dispersion of cluster of TiO₂ particles. All the synthesized titanium dioxide photocatalysts are crystalline in nature, which is evidenced by their SEM micrographs.

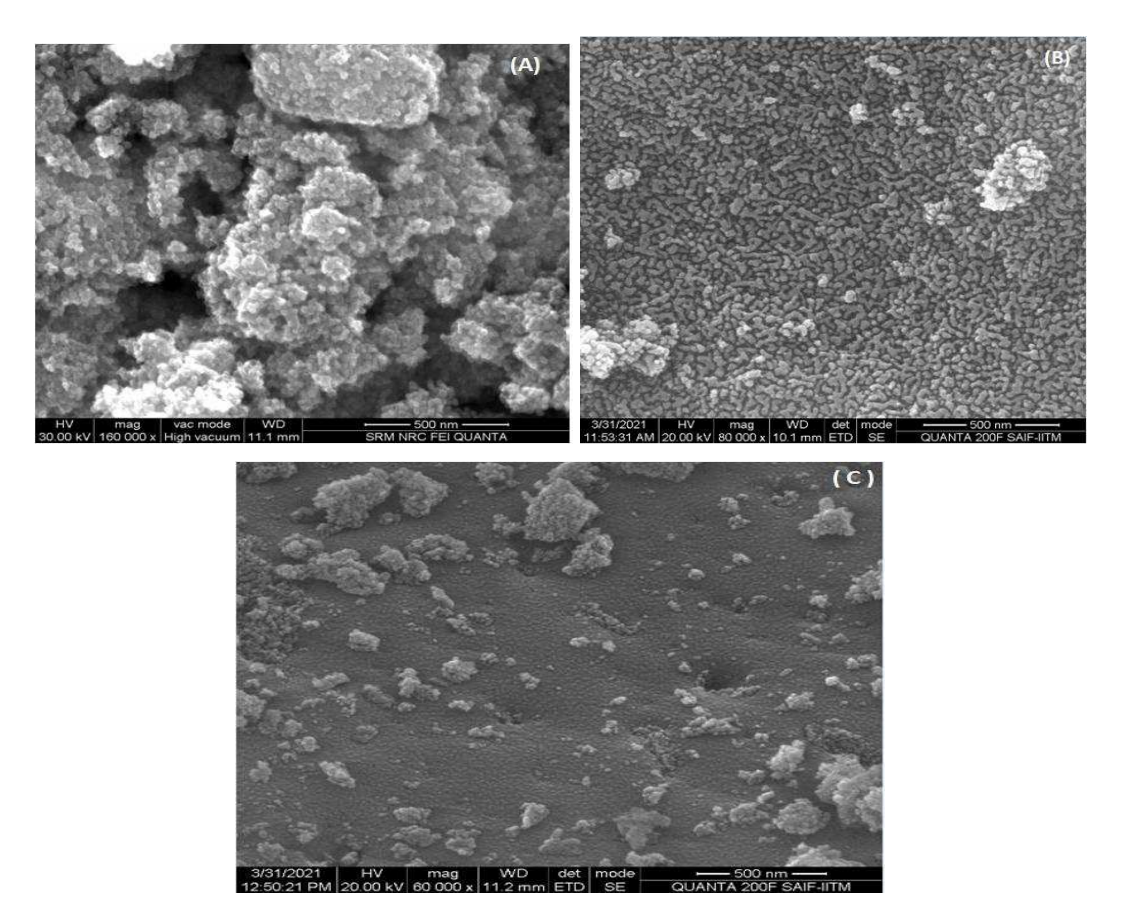


Figure 5.2.2 shows the HR-SEM image of the synthesized (A) undoped titanium dioxide photocatalyst (B) 1 wt% AlF₃ doped titanium dioxide photocatalyst and (C) 1 wt% SrSiO₃ doped titanium dioxide photocatalyst.

5.2.3. Energy Dispersive X-Ray Analysis

The elemental composition of the synthesized neat as well as doped titanium dioxide photocatalysts can be determined from the energy dispersive x-ray analysis. The EDAX spectra of the synthesized undoped TiO₂ catalyst as well as aluminium fluoride and strontium silicate doped TiO₂ photocatalysts are shown in figures 5.2.3 A-C. It is evidenced from the EDAX spectrum of the undoped titanium dioxide photocatalyst the presence of the elements such as titanium and oxygen is present in the major composition without any other impurities. The presence of the elements such as titanium, oxygen, aluminium, fluorine and chlorine are confirmed from the EDAX spectrum of AlF₃ doped TiO₂ photocatalyst. The presence of weak peak of chlorine in the EDAX spectrum could have from the titanium tetrachloride precursor solution of the synthesized titanium dioxide photocatalyst. Similarly, in the EDAX spectrum of the Strontium silicate doped TiO₂ photocatalyst is shown in figure 5.2.3 C, the presence of major peaks of titanium and oxygen are observed along with less intense peaks of strontium and silicon.

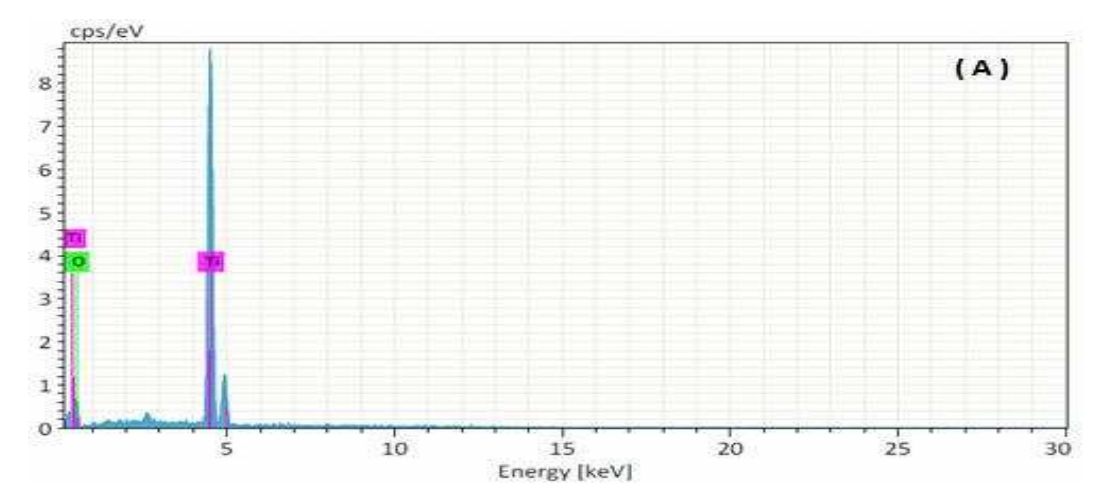


Figure 5.2.3 A shows the EDAX image of the synthesized undoped Titanium dioxide photocatalyst.

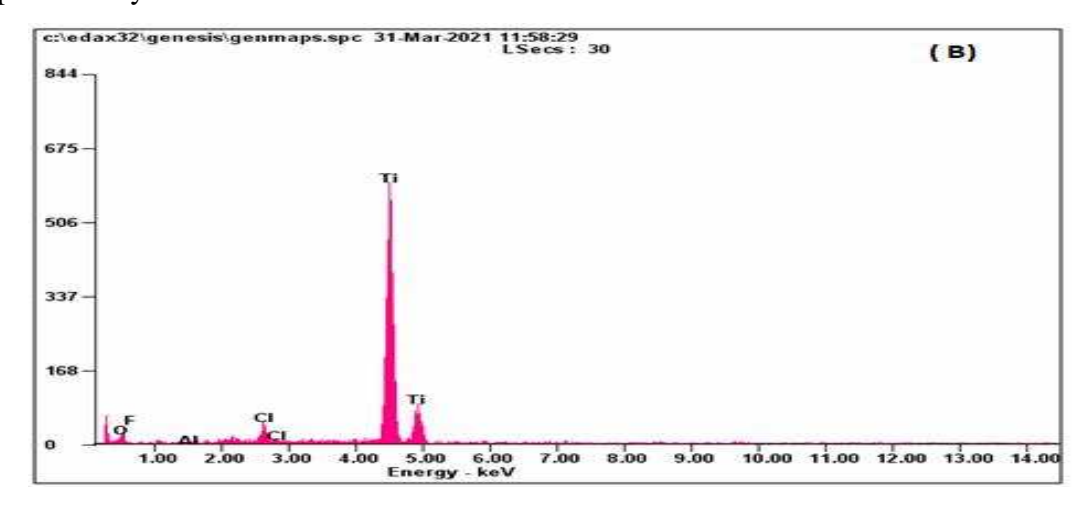


Figure 5.2.3 B shows the EDAX image of the synthesized 1 wt% Aluminium fluoride doped Titanium dioxide photocatalyst.

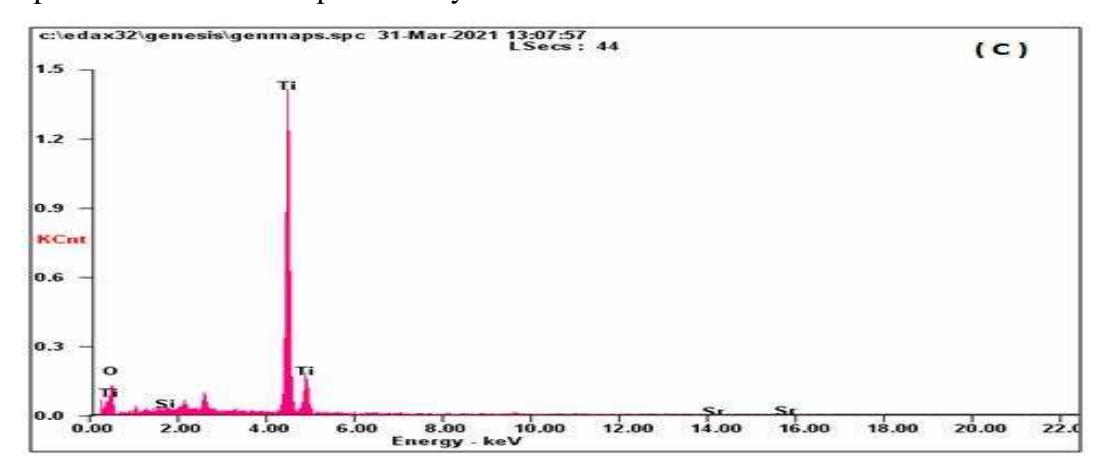


Figure 5.2.3 C shows the EDAX image of the synthesized 1 wt% Strontium silicate doped Titanium dioxide photocatalyst.

5.2.4. Transmission Electron Microscopic Analysis

The transmission electron microscopic analysis provides us images to understand the morphological as well as crystallographic nature of the samples. The TEM images of the synthesized bare titanium dioxide photocatalyst is shown in figure 5.2.4 A-C, and the TEM images of the aluminium fluoride and strontium silicate doped titanium dioxide photocatalysts are shown in figures 5.2.4 D-F and 5.2.4 G-I respectively. From the TEM images it is observed that the synthesized undoped titanium dioxide catalyst is moderately spherical in shape and the AlF₃ and SrSiO₃ doped TiO₂ photocatalyst also possess moderately spherical shaped particles which are highly aggregated. The Selected area electron diffraction obtained for all the synthesized doped as well as undoped titanium dioxide photocatalyst shows a ring like pattern with dark spots in it confirming the crystalline nature of the photocatalysts supporting the XRD data. The TEM images obtained for the doped and undoped TiO₂ photocatalysts are consistent to that of the SEM micrographs.

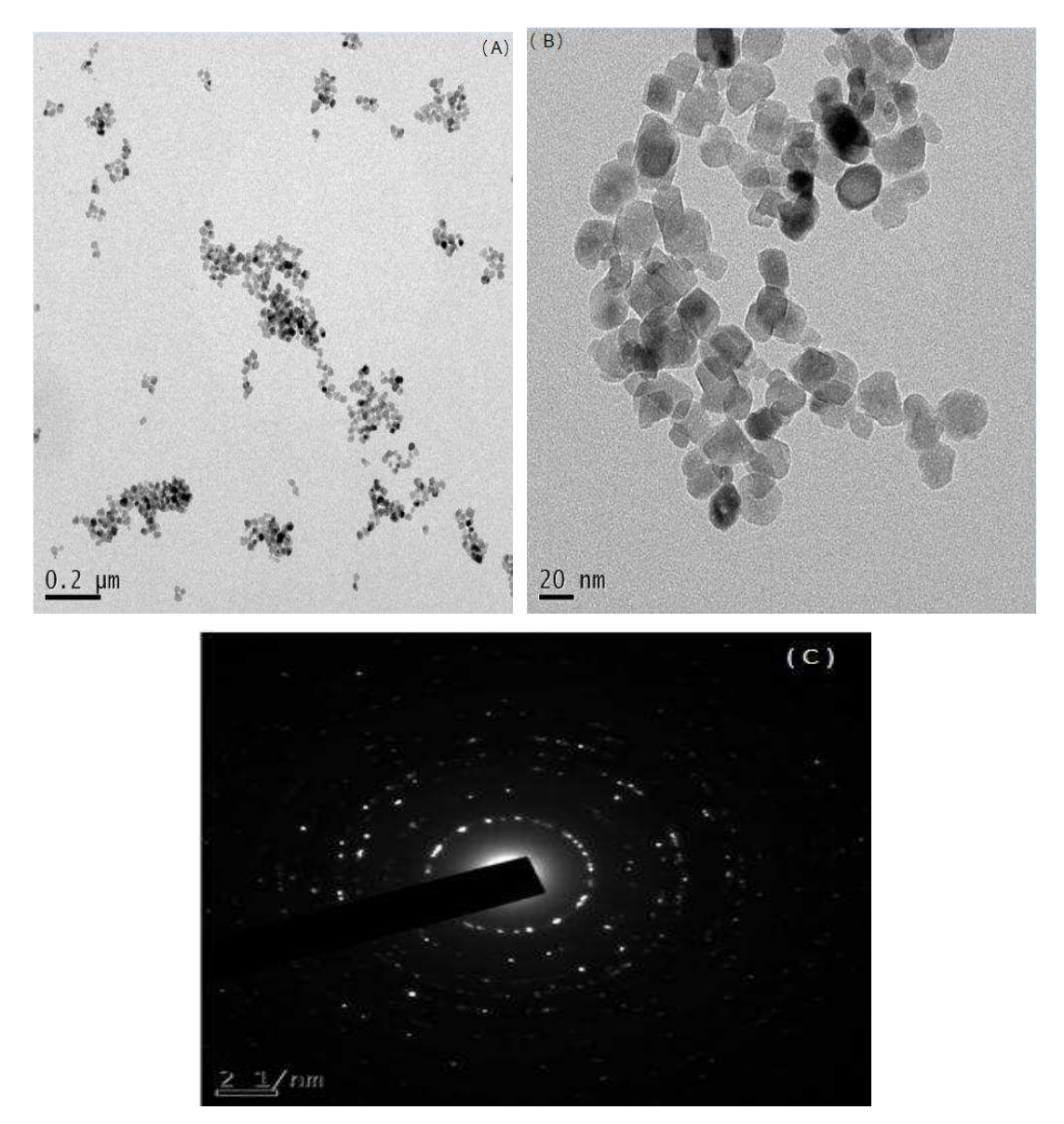


Figure 5.2.4 A, B HR-TEM images and (C) SAED Pattern of the undoped TiO_2 photocatalyst.

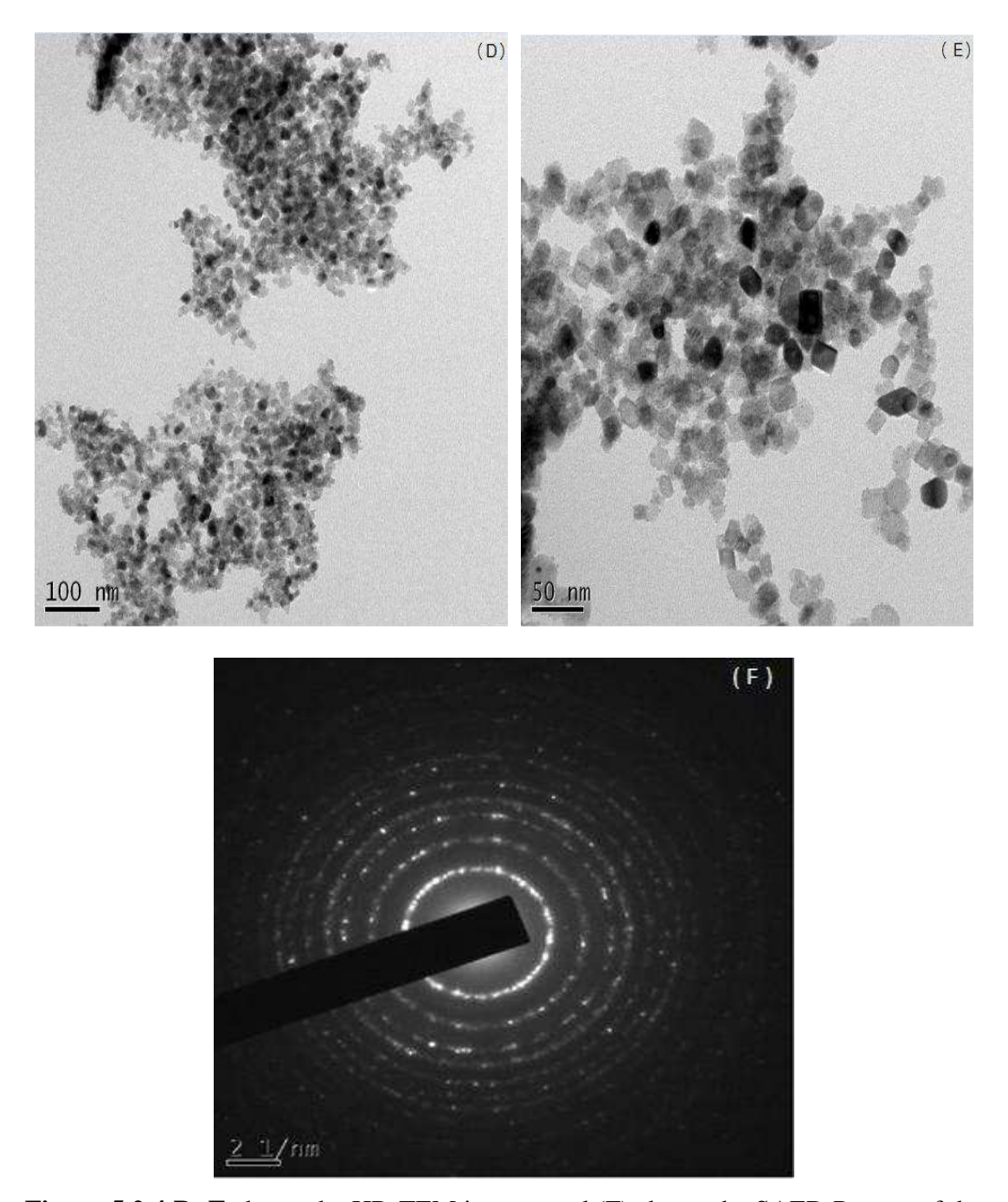


Figure 5.2.4 D, E shows the HR-TEM images and (F) shows the SAED Pattern of the AlF_3 (1%) doped TiO_2 photocatalyst.

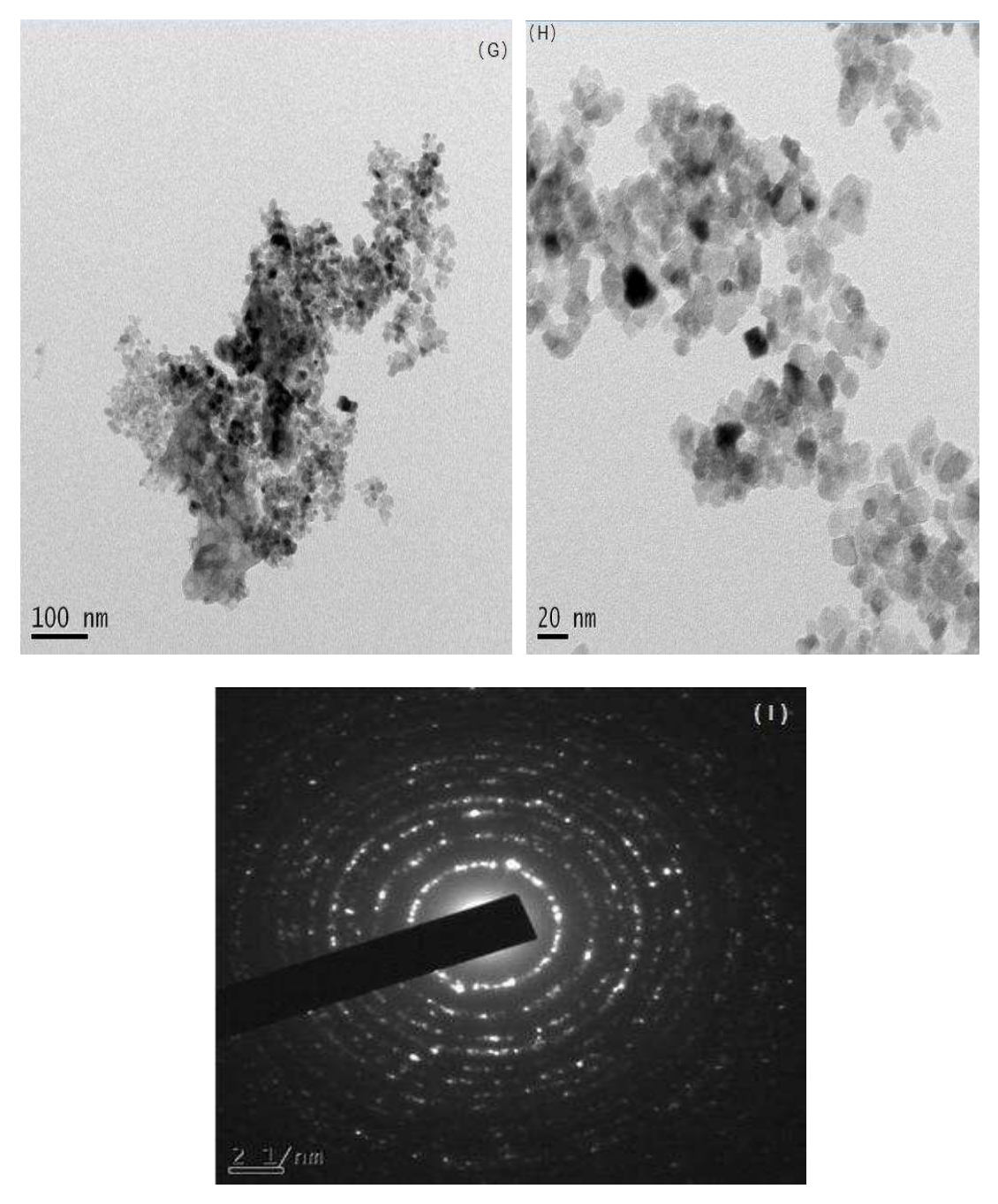


Figure 5.2.4 G, H shows the HR-TEM images and (I) shows the SAED Pattern of the $SrSiO_3$ (2%) doped TiO_2 photocatalyst.

5.2.5. UV-Visible Diffuse Reflectance Spectroscopy Studies

Diffuse reflectance spectroscopy is a widely employed technique to obtain the remission characteristics of opaque solid samples that absorb in the UV or Visible region. The optical response of the photocatalysts is used to determine their bandgap energy values. The DRS-UV-Visible absorption spectra of the synthesized undoped and aluminium fluoride and strontium silicate doped titanium dioxide photocatalysts are shown in figures 5.1.5 A-C. The calculated bandgap values for the synthesized bare TiO₂, 1wt % AlF₃ doped TiO₂ and 1wt % SrSiO₃ doped TiO₂ photocatalysts are 3.01 eV, 2.96 eV and 3.03 eV respectively.

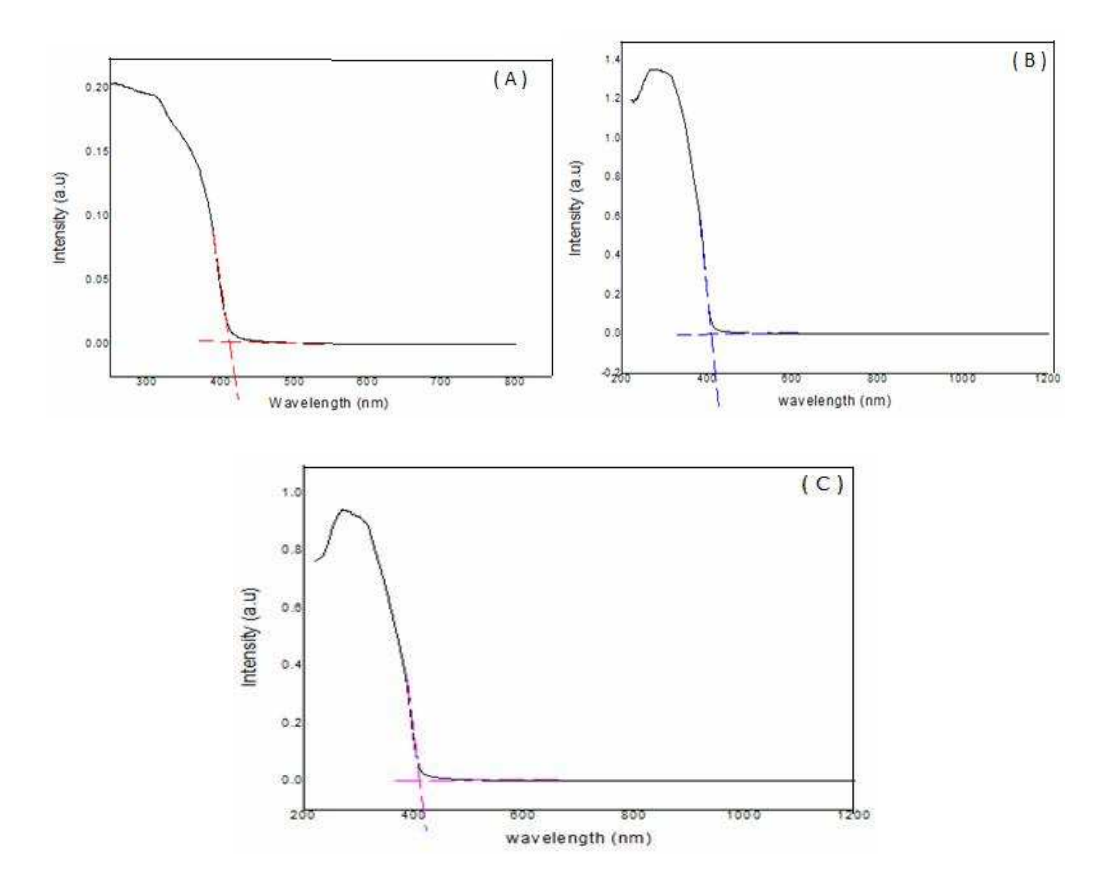
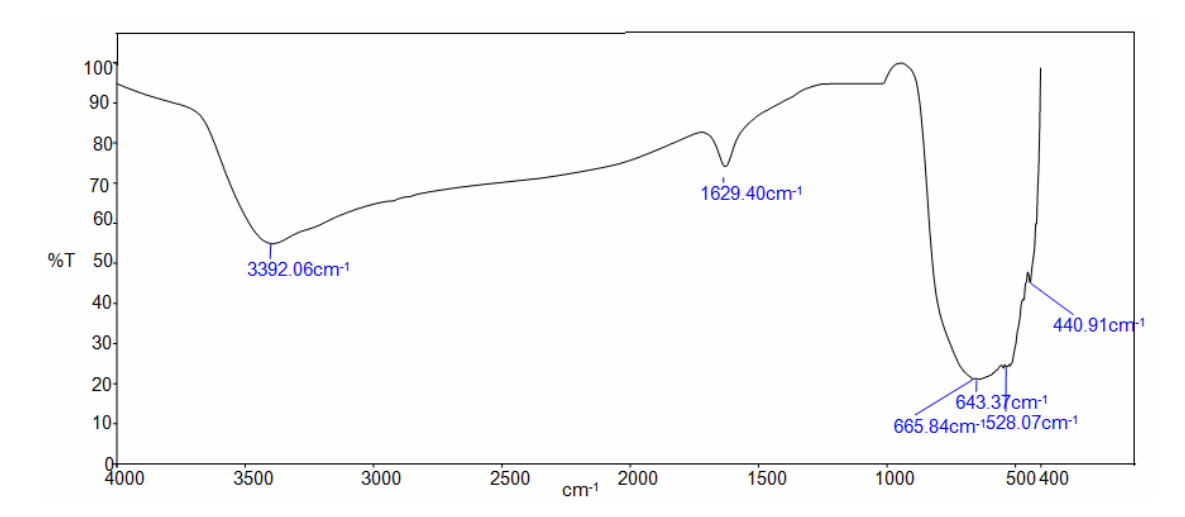


Figure 5.2.5 shows the DRS-UV-Visible absorption spectra for (A) undoped TiO₂ photocatalyst (B) 1 wt% AlF₃ doped TiO₂ photocatalyst and (C) 1 wt% SrSiO₃ doped TiO₂ photocatalyst.

5.2.6. Fourier Transform Infra-Red Spectroscopy Studies

In the earlier days the IR technique was found to be useful in obtaining qualitative as well as quantitative information pertaining to the organic samples alone. However, in recent years due to the advent of long-wavelength instrumentation, it has been found to be equally useful for the analysis of inorganic materials. The FTIR spectra of bare titanium dioxide photocatalyst and aluminium fluoride and strontium silicate doped titanium dioxide catalysts are shown in figures 5.1.6A, B and C. The peaks at around 3400 cm⁻¹ and 1400-1600 cm⁻¹ observed in the bare as well as doped TiO₂ photocatalysts correspond to the stretching and bending vibrations of -OH groups which might be due to the adsorbed water molecules on the surface of the photocatalyst. The bands below 950cm⁻¹ in both the doped and undoped titanium dioxide photocatalysts corresponds to the vibrational modes of Ti-O-Ti bonds³⁵⁻³⁷.



 $\textbf{Figure 5.2.6} \ \textbf{A} \ \textbf{FTIR} \ \textbf{spectrum of the synthesized bare Titanium dioxide photocatalyst}.$

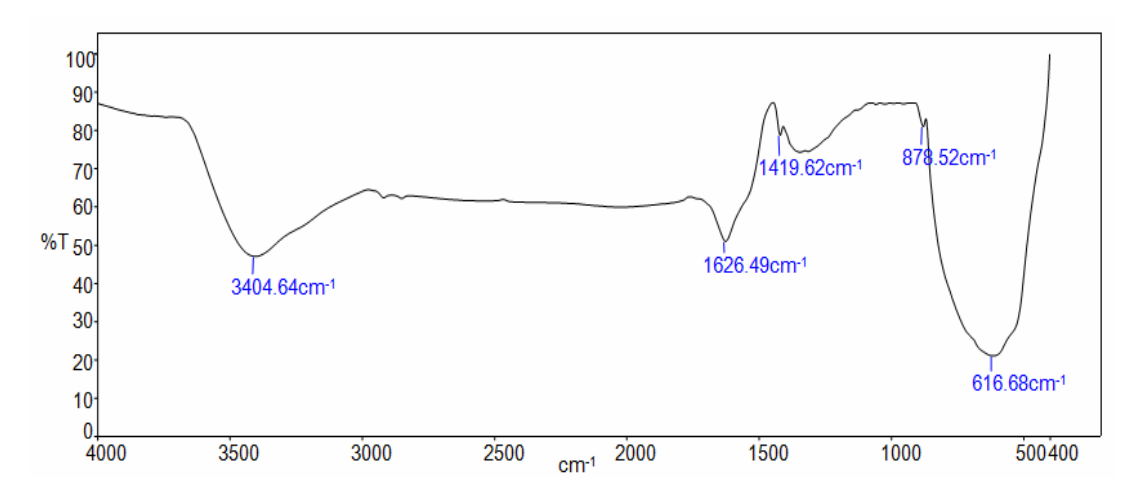


Figure 5.2.6 B FTIR spectrum of the synthesized 1 wt% AlF₃ doped Titanium dioxide photocatalyst.

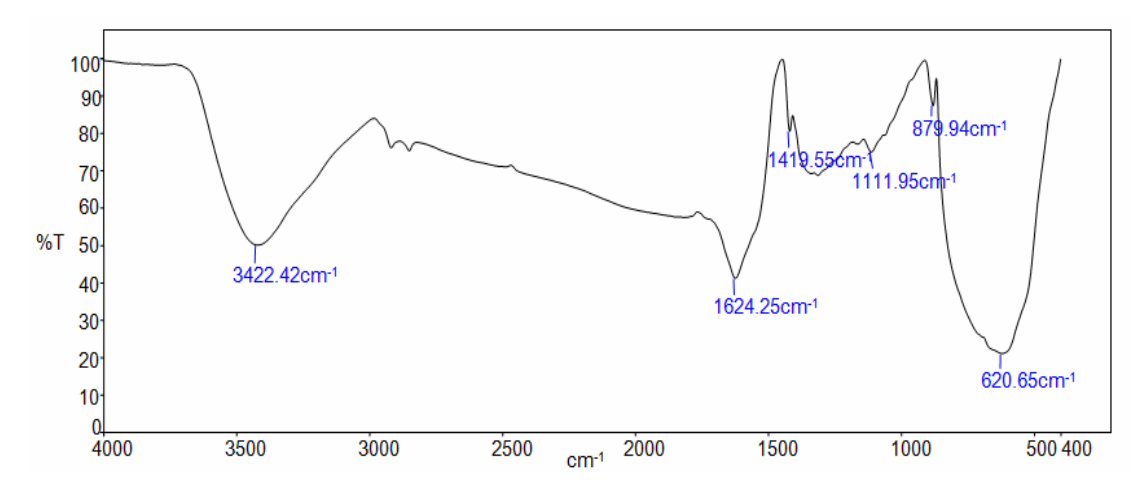


Figure 5.2.6 C FTIR spectrum of the synthesized 1 wt% $SrSiO_3$ doped Titanium dioxide photocatalyst.

5.2.7. BET Surface Area Analysis

The Brunauer-Emmett-Teller (BET) surface area analysis is a facile technique employed to study the surface adsorption characteristics of the solid samples. The nitrogen adsorption-desorption isotherms of the synthesized titanium dioxide, aluminium fluoride doped titanium dioxide and strontium silicate doped titanium dioxide photocatalysts are shown in figure 5.2.7 A-C. The specific surface area of the bare titanium dioxide photocatalyst is $61.006 \text{ m}^2/\text{g}$ and that of the aluminium fluoride and strontium silicate doped titanium dioxide photocatalysts are $62.092 \text{ m}^2/\text{g}$ and $78.295 \text{ m}^2/\text{g}$ respectively.

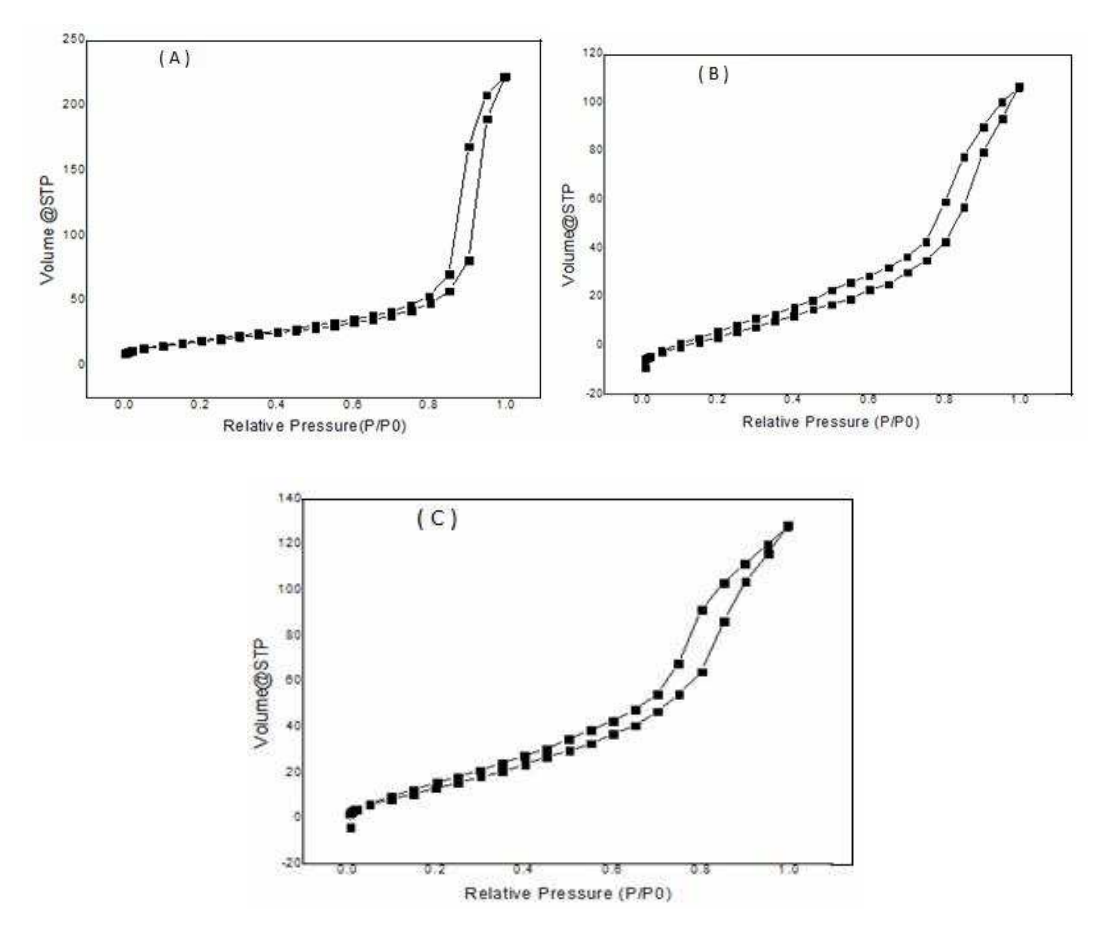


Figure 5.2.7 N₂ adsorption-desorption isotherm of the synthesized (A) TiO₂ photocatalyst (B) 1 wt% AlF₃ doped TiO₂ photocatalyst and (C) 1 wt% SrSiO₃ doped TiO₂ photocatalyst.

Table 5.2.7 shows the surface area, Pore volume and Pore radius of bare-TiO₂, AlF₃-TiO₂ and SrSiO₃-TiO₂, photocatalysts.

Photocatalysts	Surface area (m²/g)	Pore Volume (cc/g)	Pore Radius (Å)
TiO ₂	61.006	0.339	151.669
Aluminium Fluoride- TiO ₂	62.092	0.178	17.065
Strontium silicate- TiO ₂	78.295	0.203	17.081

5.2.8. Photocatalytic Studies

The effects of aeration, stirring of the reaction mixture, and the extent of adsorption are a few factors that need to be taken into consideration to achieve an overall enhancement in the photocatalytic dye degradation process. Hence in the present study a preliminary analysis of decolourization of basic yellow 2, congo red and Acid red 94 dyes are studied under varying conditions as shown in figure 5.2.8(A-C). About 13, 18 and 16% decolourization of basic yellow 2, congo red and Acid red 94 dyes are achieved by effective air purging in the presence of titanium dioxide catalyst at room temperature. Similarly 9, 12 and 12% decolourization of basic yellow 2, congo red and Acid red 94 dyes are achieved in the presence of titanium dioxide catalyst at room temperature without air purging. However, under sunlight in the absence of TiO₂ catalyst about 4, 7 and 5% decolourization of basic yellow 2, congo red and Acid red 94 dyes are achieved by purging air into the reaction mixture. From the experimental studies carried out it is understood that the use of a photocatalyst and effective air purging into the reaction mixture, and a light source are essential for the photocatalytic dye decolourization process. Similarly it is also reported that the presence of dissolved oxygen in the reaction does not affect the adsorption of the dye molecules on the surface of TiO₂ catalyst³⁸ and the oxygen dissolved in the solution acts an electron acceptor in the photocatalytic reaction enhancing the decolourization process³⁹.

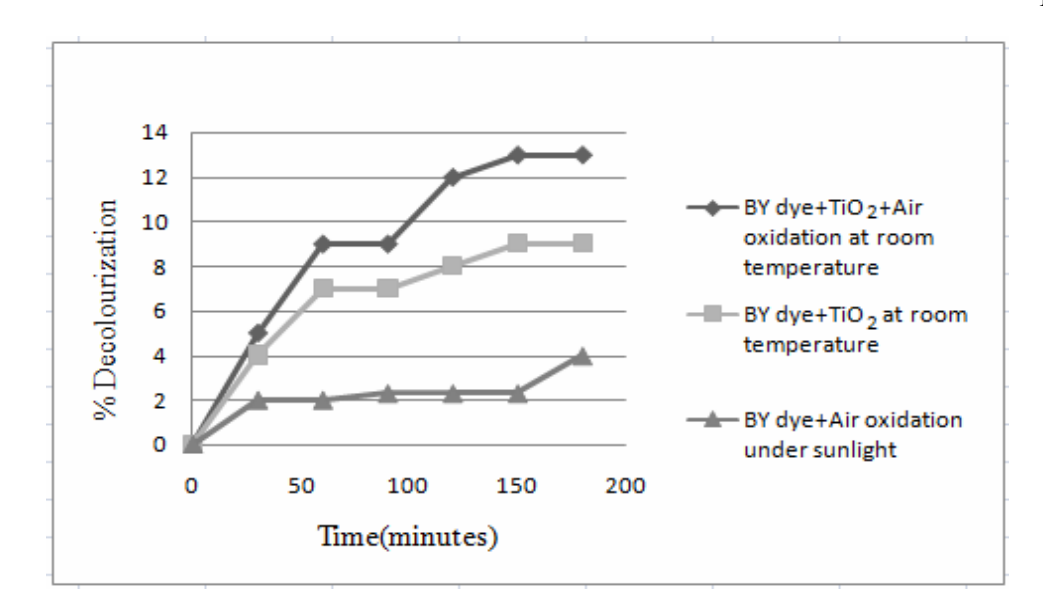


Figure 5.2.8 A Primary analysis of basic yellow 2 dye solution using titanium dioxide photocatalyst.

(**Reaction conditions:** Basic yellow 2 dye solution (Conc. 3.29×10^{-5} mol/L; volume = 50mL), TiO₂ catalyst = 25mg/50mL, without pH adjustment, air supply $\cong 2.5$ L/min, $I_{solar} = 726 \times 100 \pm 100$ lux.)

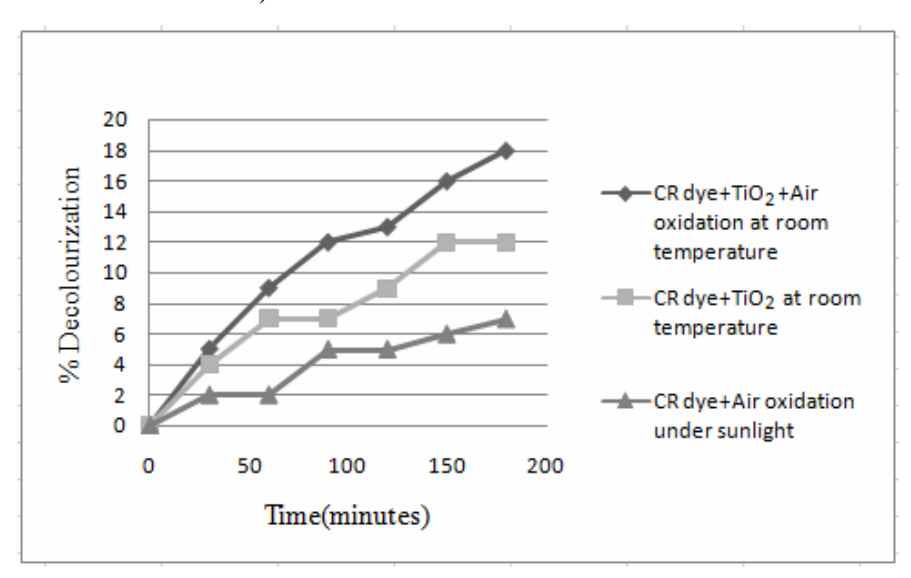


Figure 5.2.8 B Primary analysis of congo red dye solution using titanium dioxide photocatalyst.

(**Reaction conditions:** Congo red dye solution (Conc. 1.43×10^{-5} mol/L; volume = 50 mL), TiO_2 catalyst = 25 mg/50 mL, without pH adjustment, air supply $\cong 2.5 \text{L/min}$, $I_{solar} = 798 \times 100 \pm 100 \text{ lux.}$)

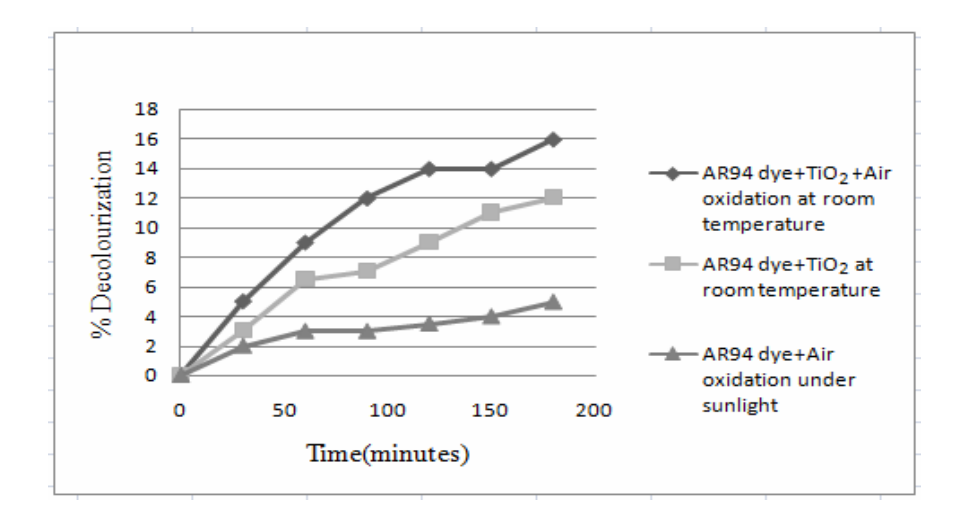


Figure 5.2.8 C Primary analysis of acid red 94 dye solution using titanium dioxide photocatalyst.

(**Reaction conditions:** Acid red 94 dye solution (Conc. 1.96×10^{-5} mol/L; volume = 50mL), TiO_2 catalyst = 25mg/50mL, without pH adjustment, air supply $\cong 2.5\text{L/min}$, $I_{solar} = 756 \times 100 \pm 100$ lux.)

5.2.9. Effect of pH on the photocatalytic dye decolourization process

The pH optimization is an important factor to achieve maximum efficiency in the photocatalytic dye degradation process. The pH of the solution not only affects the generation of hydroxyl radicals but also the surface charge properties of a photocatalyst, as well as the sorption and desorption of the dye molecules onto the photocatalyst surface. The zero point charge of TiO₂ catalyst is nearly 6.5. Above this pH level, the surface of the TiO₂ catalyst is negatively charged and below this pH level it is positively charged. The protonation and deprotonation on the surface of titanium dioxide catalyst under acidic or alkaline conditions can take place according to the following equations⁴⁰

$$TiOH + H^+ \rightarrow TiOH_2^+$$
 eq.(5.26)

$$TiOH + OH^{-} \rightarrow TiO^{-} + H_{2}O$$
eq.(5.27)

The maximum degradation of basic yellow 2 dye is observed at alkaline pH, this is due to the fact that the cationic basic yellow 2 dye gets attracted to the negatively charged surface of titanium dioxide catalyst above pH level 6.5 and similarly, the anionic acid red 94 dye shows a maximum dye decolourization under acidic conditions, this is due to the fact that the anionic acid red dye gets attracted to the positively charged surface of titanium dioxide catalyst below pH level 6.5. A similar trend is observed for the congo red dye degradation, the maximum dye degradation took place at neutral pH 7.5, whereas under acidic and alkaline pH levels, the dye degradation efficiency of titanium dioxide catalyst was comparatively less. This can be attributed to the fact that at acidic and neutral pH levels, the surface of the titanium dioxide catalyst is positively charged and attracts the anionic congo red dye to its surface, however at alkaline pH levels the surface of TiO₂ catalyst becomes negatively charged and the repels the anionic congo red dye. The variation of pH levels for basic yellow 2, acid red 94 and congo red dyes using titanium dioxide catalyst are shown in the following figures 5.2.9A-C respectively.

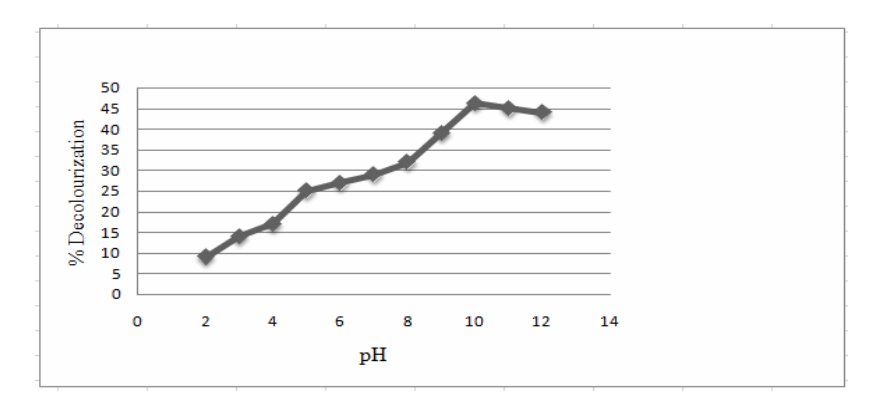


Figure 5.2.9 A Effect of pH on the photocatalytic decolourization of basic yellow 2 using titanium dioxide catalyst.

(**Reaction conditions:** Basic yellow 2 dye solution (Conc. 3.29×10^{-5} mol/L; volume = 50mL), TiO₂ catalyst = 25mg/50mL, pH variation = 2-12, air supply $\cong 2.5$ L/min, $I_{solar} = 778 \times 100 \pm 100$ lux, Time=30 minutes)

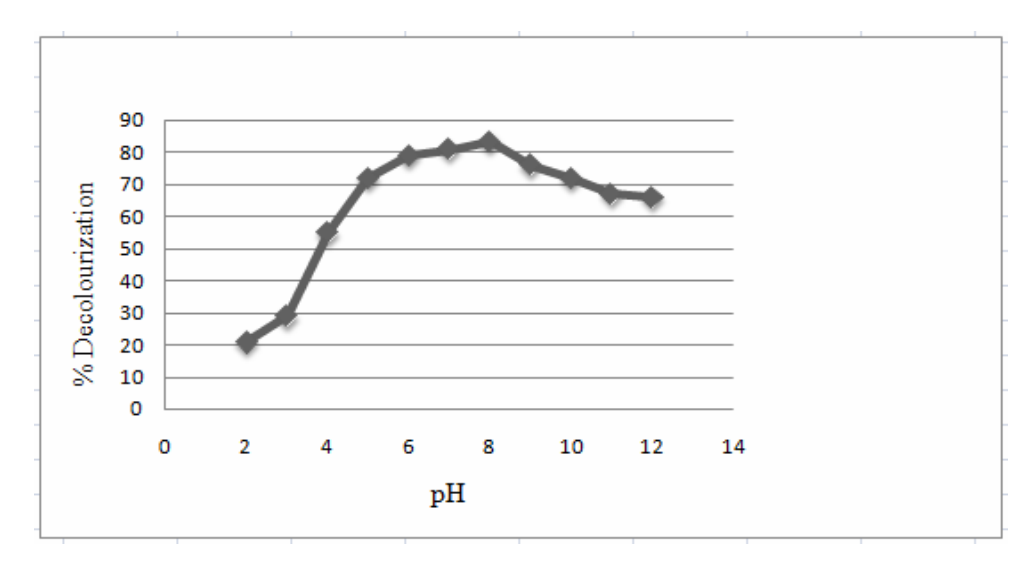


Figure 5.2.9 B Effect of pH on the photocatalytic decolourization of congo red dye using titanium dioxide catalyst.

(**Reaction conditions:** Congo red dye solution (Conc. 1.43×10^{-5} mol/L; volume =50mL), TiO₂ catalyst = 25mg/50mL, pH variation = 2-12, air supply \cong 2.5L/min, $I_{solar} = 829 \times 100 \pm 100$ lux, Time=30 minutes)

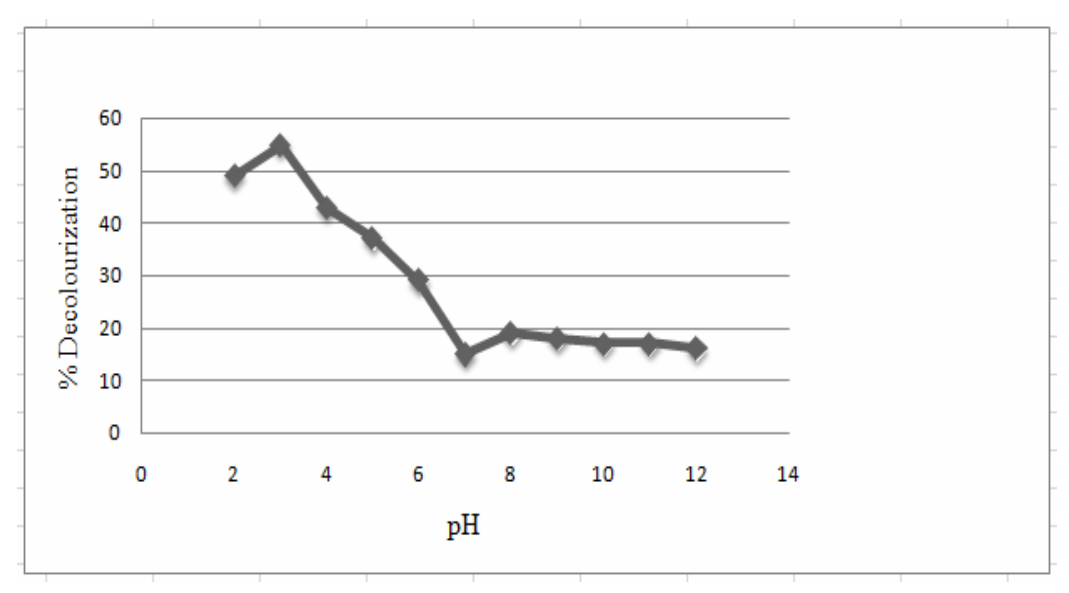


Figure 5.2.9 C Effect of pH on the photocatalytic decolourization of acid red 94 dye using titanium dioxide catalyst.

(**Reaction conditions:** Acid red 94 dye solution (Conc. 1.96×10^{-5} mol/L; volume = 50mL), TiO_2 catalyst = 25mg/50mL, pH variation = 2-12, air supply $\cong 2.5\text{L/min}$, $I_{\text{solar}} = 689 \times 100 \pm 100$ lux, Time=30 minutes)

5.2.10. Effect of Catalyst Concentration

The weight of the photocatalyst is an important factor that needs to be optimized to achieve maximum degradation of the dyes. The optimum level of titanium dioxide catalyst for the photodegradation of the three synthetic dyes namely basic yellow 2, acid red 94 and congo red is found out from the experimental studies as shown in figure 5.2.10A-C. For basic yellow 2 dye solution (3.29x10⁻⁵M), 25mg of TiO₂ photocatalyst showed maximum degradation efficiency at an optimum pH 10, similarly for acid red 94 dye (1.96x10⁻⁵M) maximum dye degradation efficiency was achieved using 15mg of titanium dioxide catalyst at an optimum pH 3 and 25 mg of TiO₂ catalyst showed maximum degradation efficiency for congo red dye (1.43x10⁻⁵M) at an optimum pH 7.5 beyond which a decrease in the photocatalytic degradation efficiency is noted. From the experimental studies it is observed that a similar trend is followed for the degradation of all the three dyes. Initially an increase in the degradation efficiency is observed by the increasing the TiO₂ catalyst dosage beyond a certain limit the addition of the catalyst to the reaction mixture only showed a decrease the photocatalytic degradation process. This is due to the fact that on increasing the catalyst dosage the number of surface area for the dye molecule absorption is high and the increase in the active sites for the generation of reactive species such as hydroxyl and superoxide anion radicals also contributes to the increased photodegradation process. Similarly, a decrease in the photodegradation process is evidenced beyond the addition of a certain limit of catalyst dosage this is due to the reason that increased suspension of the catalyst particles in the reaction mixture blocks the sunlight penetration and the particles tend to agglomerate and hence surface area of the particles gets decreased thereby causing a decrease in the photocatalytic efficiency⁴¹⁻⁴³.

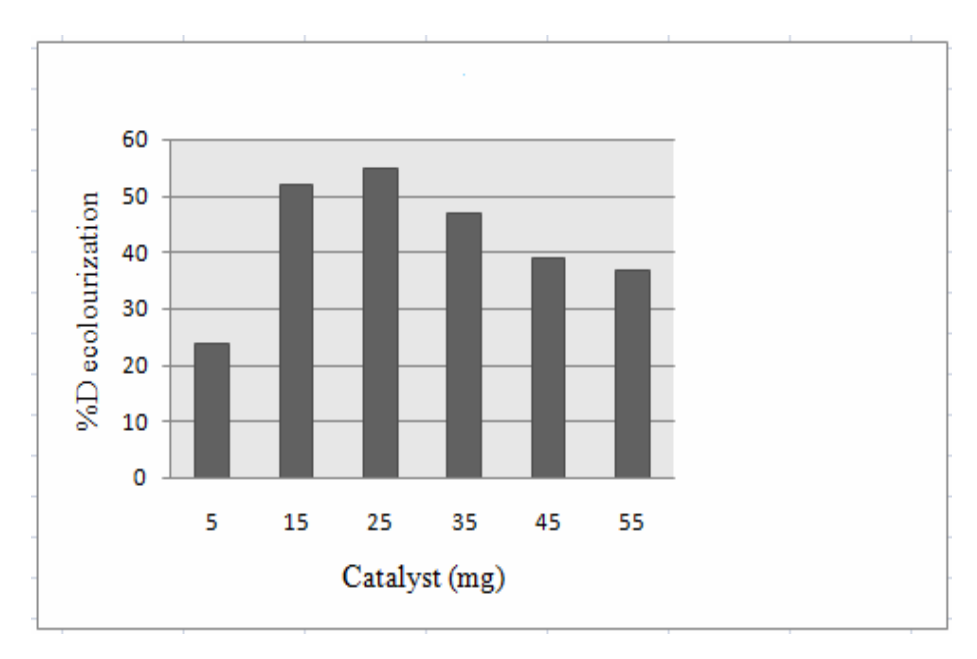


Figure 5.2.10 A Effect of Titanium dioxide catalyst concentration on the photocatalytic decolourization of Basic yellow 2 dye.

(**Reaction conditions:** Basic yellow 2 dye solution (Conc. 3.29×10^{-5} mol/L; volume = 50mL), catalyst weight = 5mg-55mg, pH = 10, air supply $\cong 2.5$ L/min, $I_{solar} = 683 \times 100 \pm 100$ lux, Time=30 minutes)

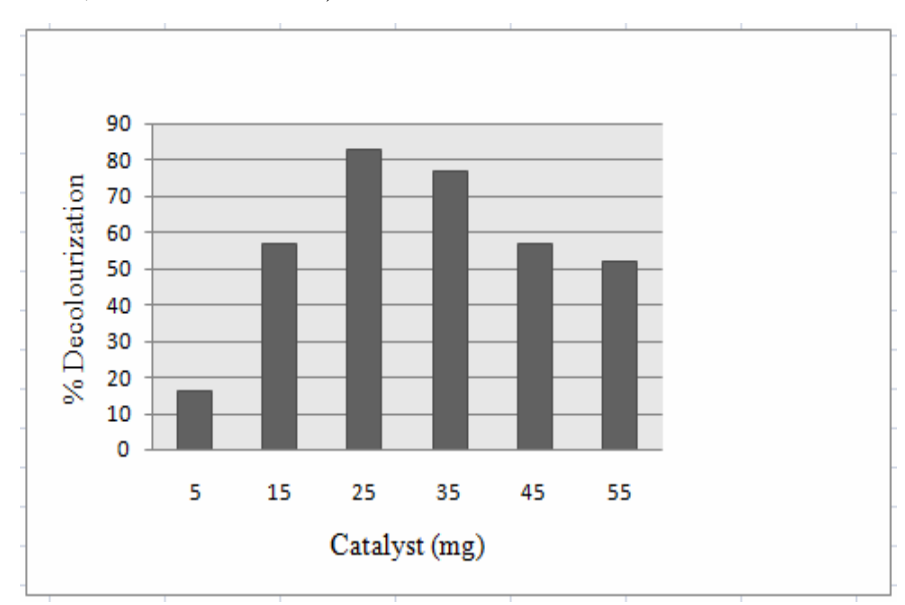


Figure 5.2.10 B Effect of titanium dioxide catalyst concentration on the photocatalytic decolourization of congo red dye.

(**Reaction conditions:** Congo red dye solution (Conc. 1.43×10^{-5} mol/L; volume = 50mL), catalyst weight = 5mg-55mg, pH = 8, air supply $\cong 2.5$ L/min, $I_{solar} = 786 \times 100$ ± 100 lux, Time=30 minutes)

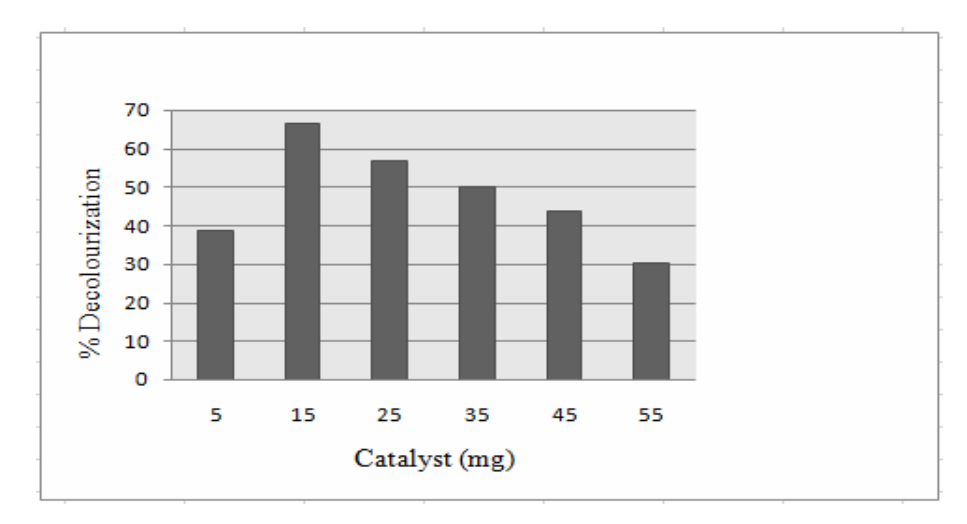


Figure 5.2.10 C Effect of titanium dioxide catalyst concentration on the photocatalytic decolourization of acid red 94 dye.

(**Reaction conditions:** Acid red 94 dye solution (Conc. 1.96×10^{-5} mol/L; volume = 50mL), catalyst weight = 5mg-55mg, pH = 3, air supply $\cong 2.5$ L/min, $I_{solar} = 857 \times 100$ ± 100 lux, Time=30 minutes)

5.2.11. Effect of Initial dye concentration

The rate of photocatalytic degradation depends on the nature and concentration of the pollutant. Maximum photocatalytic dye degradation percentage can be achieved by fixing an optimum dye concentration. The effect of initial dye concentration is studied by varying the concentration of basic yellow 2 dye from 3.29x10⁻⁵M to 1.64x10⁻⁴M at an optimized pH level 10 and a catalyst dosage of 25mg. Similarly, the acid red 94 dye concentration is varied from 1.96x10⁻⁵M to 4.91x10⁻⁵M at an optimized pH level 3 with a catalyst concentration of 15mg, and the concentration of the congo red dye is varied from 1.43x10⁻⁵M to 7.17x10⁻⁵M at optimized pH level 7.5 with a catalyst concentration of 25mg as shown in figure 5.2.11A-C. About 89% of basic yellow dye degradation was achieved for a concentration of 9.87x10⁻⁵M, 98% degradation for 3.93x10⁻⁵M acid red 94 dye and 96% of dye degradation took place for 1.43x10⁻⁵M of congo red dye beyond which a decrease in the photocatalytic

degradation process is evidenced which is attributed to the fact that at for an initial dye concentration the number surface active sites of TiO₂ catalyst will be sufficient for the photodegradation process. However, with an increase in the concentration of the dye, the number of the surface active sites of the TiO₂ catalyst available for the dye molecules remain the same and the adsorption of the dye molecules to the catalyst surface will be less leading to a decrease in the photocatalytic activity⁴⁴. Another reason for the decrease in the photocatalytic degradation process is that on increasing the concentration of the dye solution, the path length of the photons entering the solution gets decreased and hence penetration of the sunlight to the catalyst surface is also hindered which in turn leads to a decrease in the photocatalytic activity⁴⁵.

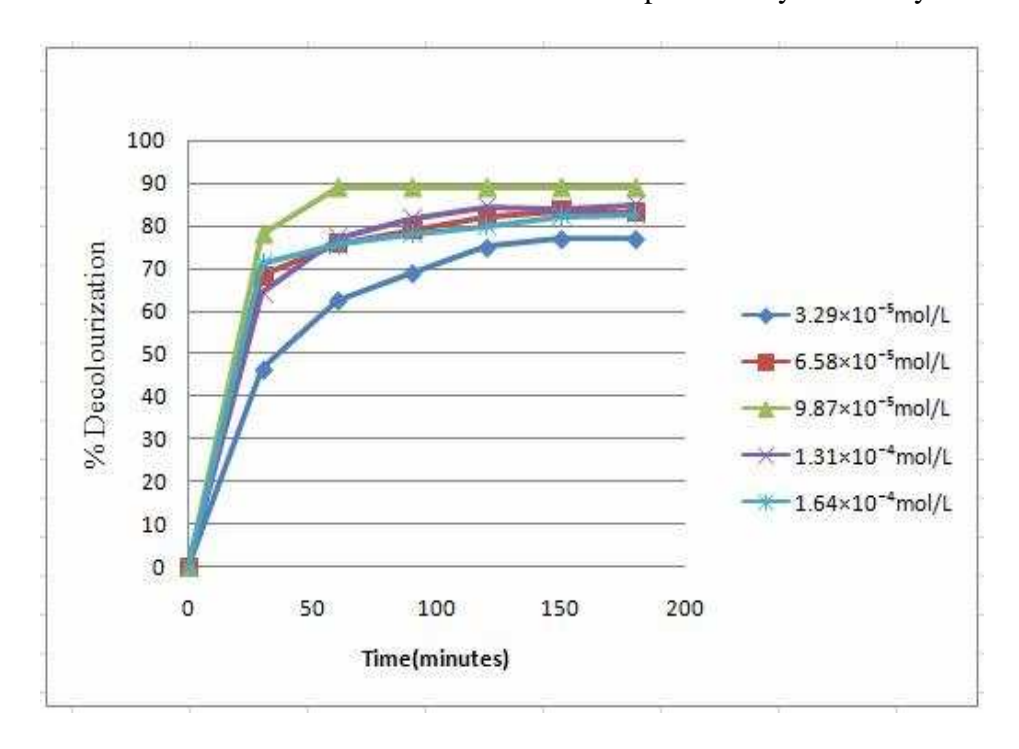


Figure 5.2.11A Effect of initial concentration of basic yellow 2 on the photocatalytic decolourization using ZnO catalyst.

(Reaction conditions: Basic yellow 2 dye concentration varied from $3.29 \times 10^{-5} \text{mol/L} - 1.64 \times 10^{-4} \text{mol/L}$, volume of dye solution =50mL, catalyst concentration = 25mg, pH= 10, air supply $\cong 2.5 \text{L/min}$, $I_{\text{solar}} = 837 \times 100 \pm 100 \text{ lux}$)

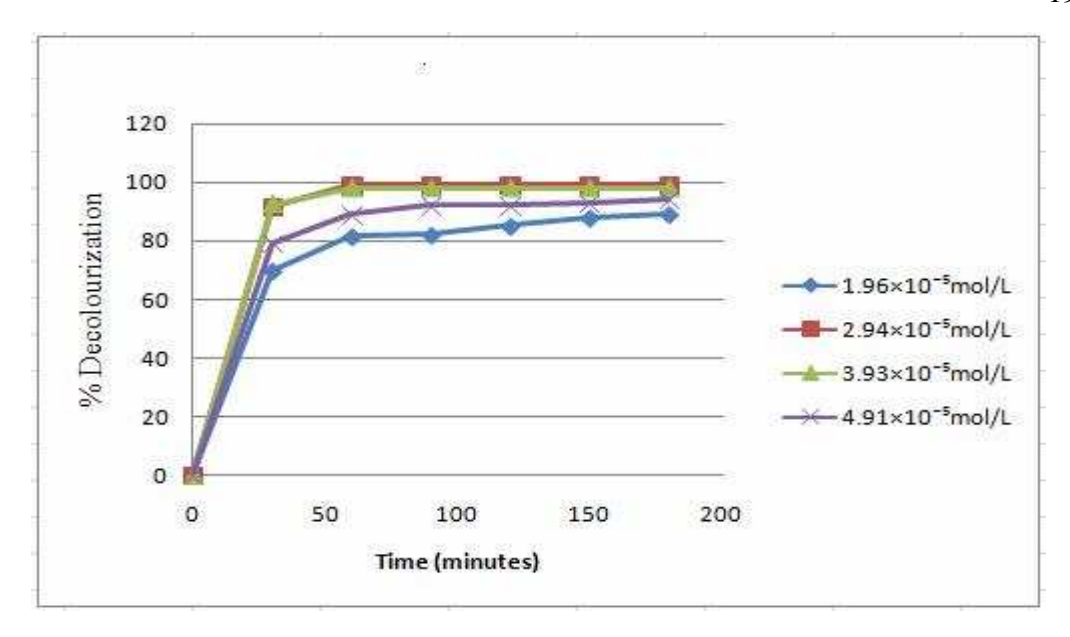


Figure 5.2.11B Effect of initial concentration of acid Red 94 on the photocatalytic decolourization using TiO₂ catalyst.

(Reaction conditions: Acid red 94 dye concentration varied from $1.96 \times 10^{-5} \text{mol/L} - 4.91 \times 10^{-5} \text{mol/L}$, volume of dye solution =50mL, catalyst concentration=15mg, pH= 3, air supply $\cong 2.5 \text{L/min}$, $I_{\text{solar}} = 667 \times 100 \pm 100 \text{ lux}$)

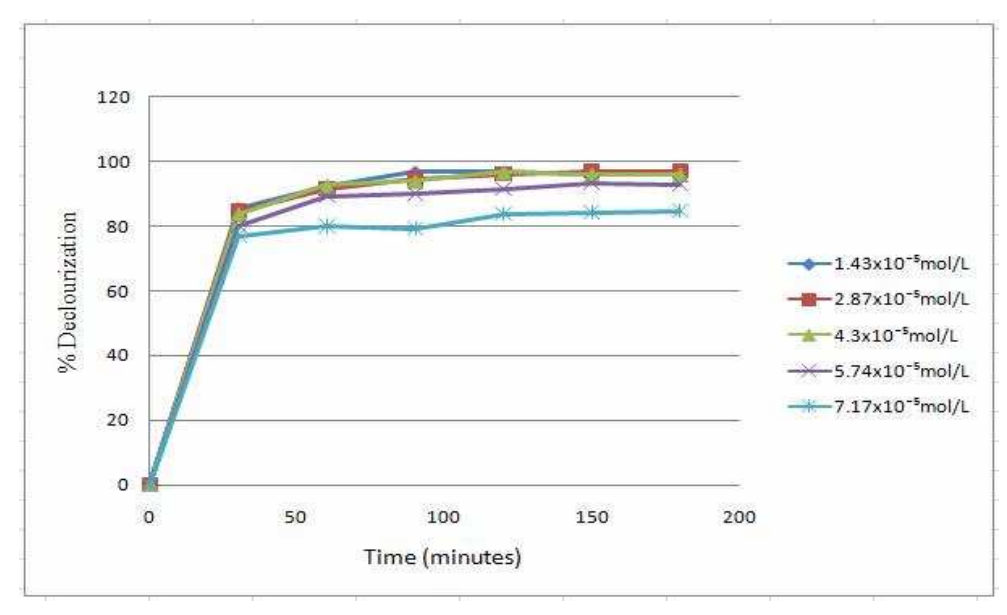


Figure 5.2.11C Effect of initial concentration of congo red on the photocatalytic decolourization using TiO₂ catalys.t

(Reaction conditions: Congo red dye concentration varied from $1.43 \times 10^{-5} \text{mol/L} - 7.17 \times 10^{-5} \text{mol/L}$, volume of dye solution =50mL, catalyst concentration=25mg, pH= 7.5, air supply $\cong 2.5 \text{L/min}$, $I_{\text{solar}} = 693 \times 100 \pm 100 \text{ lux}$)

5.2.12. Effect of Addition of Aluminium Fluoride and Strontium Silicate to TiO₂ Photocatalyst

Titanium dioxide is a promising photocatalyst with strong oxidation capacity and excellent stable physical and chemical properties. Since the synthesis methods of titanium dioxide photocatalyst are very simple and the need of only mild reaction conditions for the synthesis of titanium dioxide catalyst has made its usage very common for photocatalytic applications. Even though pure titanium dioxide photocatalyst is reported to degrade many synthetic organic dyes, the rapid recombination of the electron-hole pairs and the wide bandgap energies of titanium dioxide have limited its practical applications. Another important reason for the limitation of employing TiO₂ for photocatalytic applications is the agglomeration of the titanium dioxide particles which leads to a decrease in the catalytic activity of the TiO₂ catalyst. In order to overcome these limitations, researchers began to modify titanium dioxide catalyst by introducing different cations such as cobalt, molybdenum, nickel etc., and anions such as nitrogen, fluorine, sulphur to the lattices of titanium dioxide catalyst to decrease the band gap energy and reduce the rate of recombination of charge carriers. Coupling of TiO₂ photocatalyst with different other semiconductors such as Fe₂O₃, CuO, ZnO, MgO, and SnO₂ is also done to improve the photocatalytic performance of titanium dioxide catalyst⁴⁶.

Activated carbon derived from biomass and reduced graphene oxides are carbon based supports that are used for TiO₂ photocatalyst. The titanium dioxide photocatalyst modified with erythrosin and phthalocyanine as sensitizers are also reported to show good photocatalytic activity. Preparation of the composites with precious metals such as Ni/Pd/TiO₂, Pt/TiO₂, Ag/C/TiO₂, Au/TiO₂ are also found to show good photocatalytic activity towards the degradation of many organic dyes

however, the preparation of such precious metal doped photocatalysts is not found to be cost effective for a large scale treatment of the effluents.

In the present work, the Titanium dioxide catalyst is modified by the addition of aluminium fluoride and strontium silicate salts by varying the weight percent from (0.5-3%) to obtain the titanium dioxide material with photocatalytic activity greater than that of pure TiO₂ material. From the experimental studies carried out it is observed that the time taken for the degradation of the three dyes namely basic yellow 2, Acid red 94 and Congo red has decreased using titanium dioxide catalyst modified with AlF₃ and SrSiO₃ salts. About 90% degradation of basic yellow 2 dye (9.87x10⁻⁵M) under optimized conditions catalyst weight 25mg/50mL, pH 10 was achieved within 25 minutes using 1wt% AlF₃ doped Titanium dioxide photocatalyst. However, 1wt % SrSiO₃/TiO₂ catalyst degraded only 58% of basic yellow 2 dye (9.87x10⁻⁵M) within 60 minutes as shown in figures 5.2.12 A, B.

Acid red 94 dye (3.93x10⁻⁵M) degradation reached 99% within 30 minutes using 1wt% AlF₃ doped titanium dioxide photocatalyst under optimized conditions catalyst weight 15mg/50mL, pH 3 and similarly, 1wt % SrSiO₃/TiO₂ catalyst degraded only 39% of acid red 94 dye (3.93x10⁻⁵M) within 60 minutes as shown in figures 5.2.12 C, D.

For congo red dye (1.43x10⁻⁵M) a maximum degradation of 96% was achieved within 30 minutes using 1wt% AlF₃ doped titanium dioxide photocatalyst under optimized conditions catalyst weight 25mg/50mL, pH 7.5 and similarly, 1wt % SrSiO₃/TiO₂ catalyst degraded 95% of the dye within 30 minutes as shown in figures 5.2.12 E, F. For all the three dyes the photocatalytic efficiency using AlF₃ doped titanium dioxide catalyst follows a similar trend i.e. compared to the pure TiO₂ the time taken by the Aluminium fluoride doped titanium dioxide photocatalysts to

degrade the dye is very less. This can be attributed to the fact that introduction of the impurity atoms to the pure titanium dioxide catalyst creates new energy levels above the valence band and below the conduction band there decreasing the band gap energy and these dopants act as trapping centers for the charge carriers and they also facilitate the migration of the electron and holes to the surface reaction sites of titanium dioxide catalyst increasing the photonic efficiency in generating reactive radical species for the degradation of these synthetic organic dyes from the aqueous solution ⁴⁷⁻⁵⁰. Similarly, the decrease in the photocatalytic activity after reaching a certain dopant concentration for the degradation of the three dyes namely basic yellow 2, acid red 94 and congo red might be due to the fact that the trapping centres created by the introduction of the dopants to the pure titanium dioxide catalyst may sometimes act as recombination centres for the electrons and holes which might lead to the decrease in their photocatalytic efficiency.

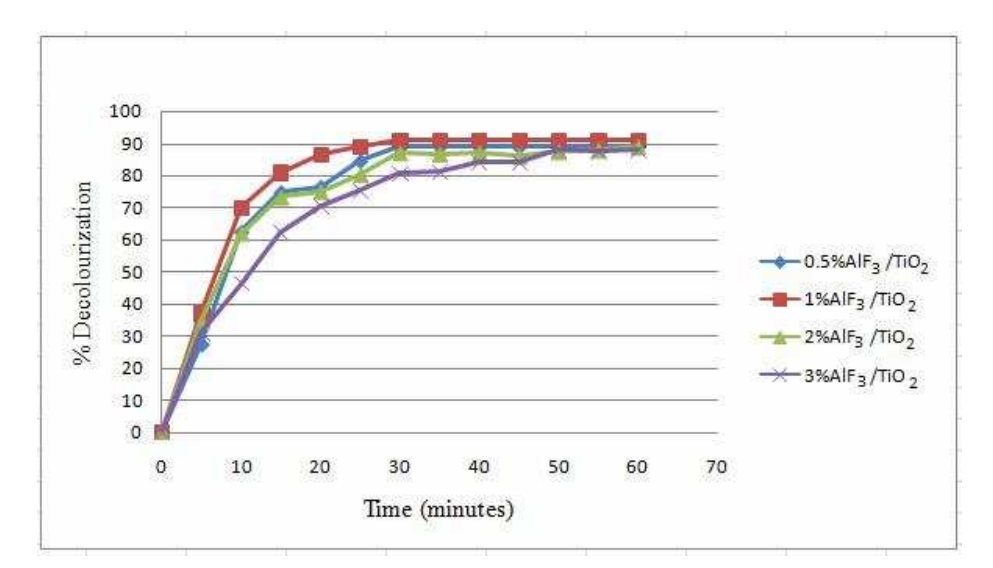


Figure 5.2.12 A Photocatalytic decolourization of basic yellow 2 using different weight percents of aluminium fluoride doped TiO₂ catalyst.

(Reaction conditions: Basic yellow 2 dye concentration = $9.87 \times 10^{-5} \text{mol/L}$, volume of dye solution =50 mL, weight percent of AlF₃ varied from (0.5-3 wt %), AlF₃/TiO₂ catalyst weight =25 mg, pH= 10, air supply $\cong 2.5 \text{L/min}$, $I_{\text{solar}} = 787 \times 100 \pm 100 \text{ lux}$)

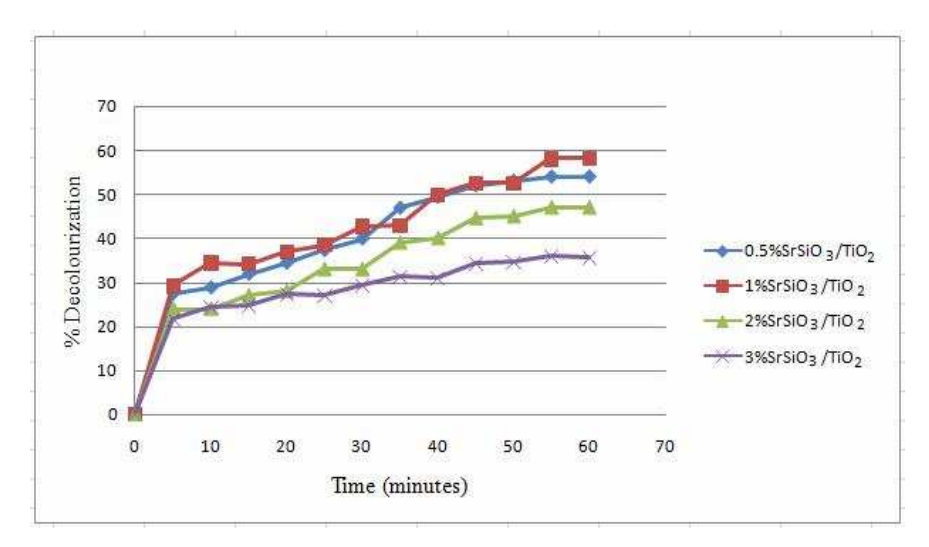


Figure 5.2.12 B Photocatalytic decolourization of basic yellow 2 using different weight percents of strontium silicate doped TiO₂ catalyst.

(Reaction conditions: Basic yellow 2 dye concentration = $9.87 \times 10^{-5} \text{mol/L}$, volume of dye solution =50 mL, weight percent of SrSiO_3 varied from (0.5-3 wt %), $\text{SrSiO}_3/\text{TiO}_2$ catalyst weight =25 mg, pH= 10, air supply $\cong 2.5 \text{L/min}$, $I_{\text{solar}} = 787 \times 100 \pm 100 \text{ lux}$)

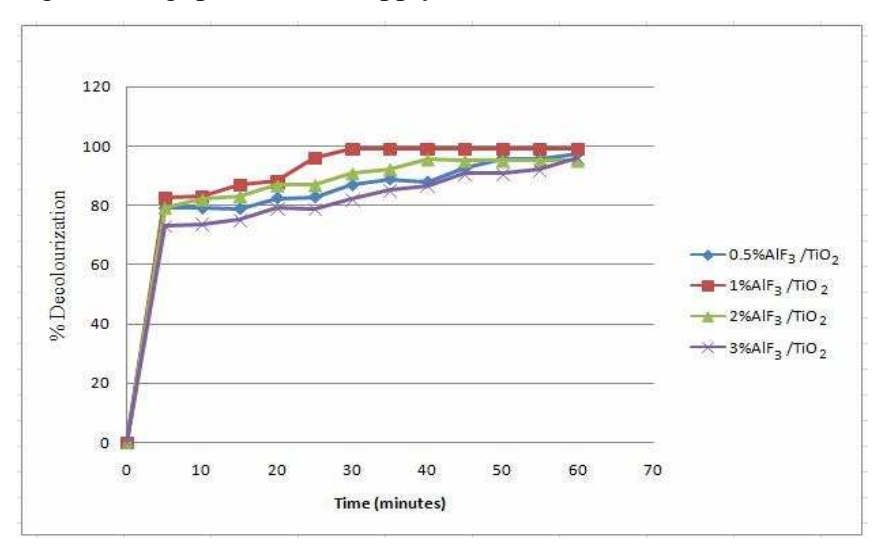


Figure 5.2.12 C Photocatalytic decolourization of acid red 94 using different weight percents of aluminium fluoride doped TiO₂ catalyst.

(Reaction conditions: Acid red 94 dye concentration = $3.93 \times 10^{-5} \text{mol/L}$, volume of dye solution =50 mL, weight percent of AlF₃ varied from (0.5-3 wt %), AlF₃/TiO₂ catalyst weight =15 mg, pH= 3, air supply $\cong 2.5 \text{L/min}$, $I_{\text{solar}} = 793 \times 100 \pm 100 \text{ lux}$)

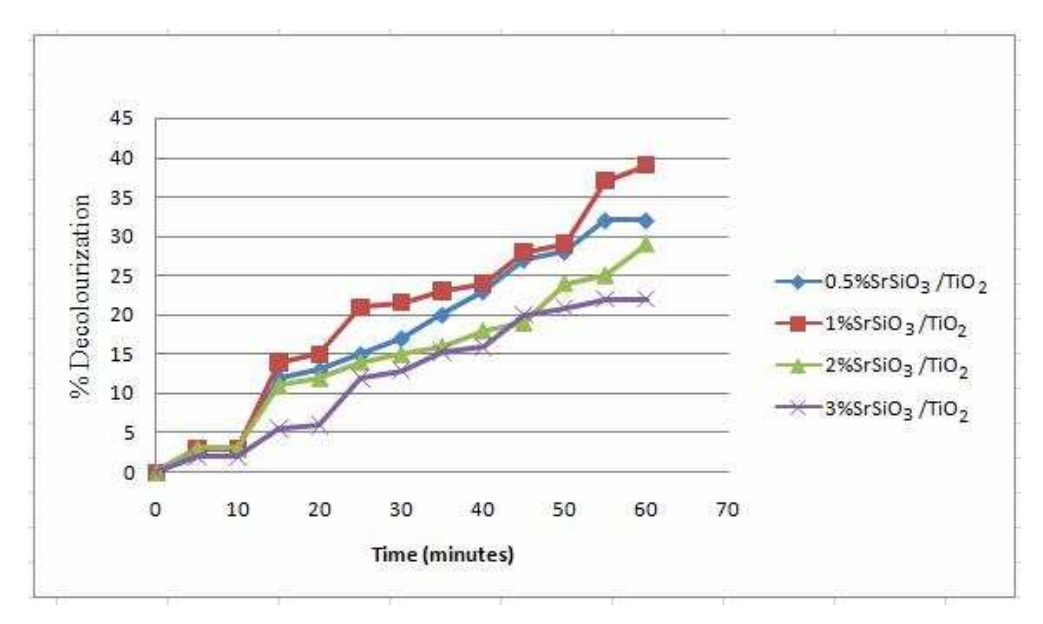


Figure 5.2.12 D Photocatalytic decolourization of acid red 94 using different weight percents of strontium silicate doped TiO₂ catalyst.

(Reaction conditions: Acid red 94 dye concentration = $3.93 \times 10^{-5} \text{mol/L}$, volume of dye solution =50 mL, weight percent of AlF₃ varied from (0.5-3 wt %), SrSiO₃/TiO₂ catalyst weight =15 mg, pH= 3, air supply $\cong 2.5 \text{L/min}$, $I_{\text{solar}} = 793 \times 100 \pm 100 \text{ lux}$)

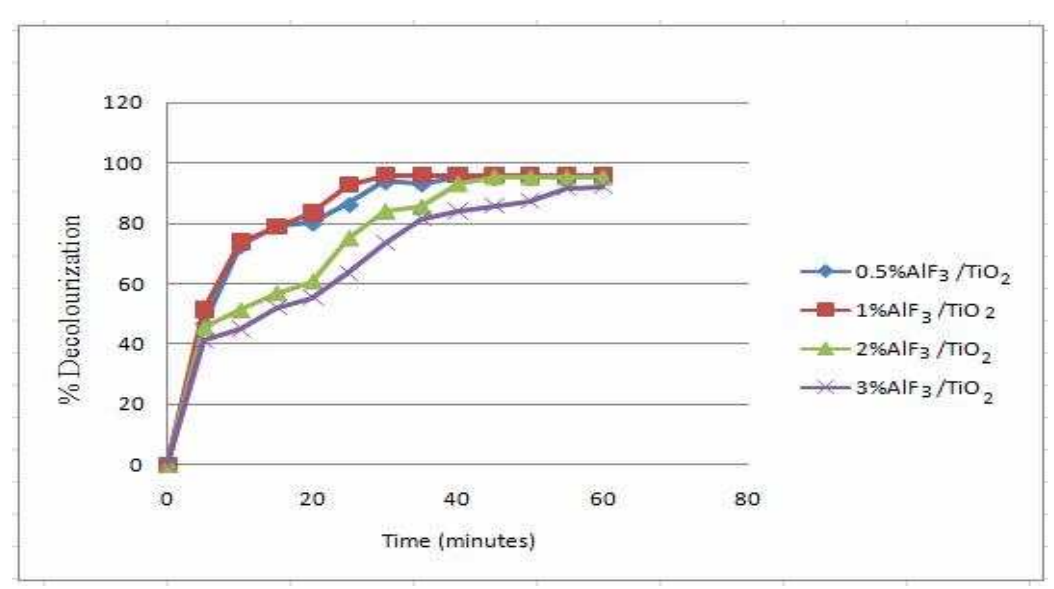


Figure 5.2.12 E Photocatalytic decolourization of congo red using different weight percents of aluminium fluoride doped TiO₂ catalyst.

(Reaction conditions: Congo red dye concentration =1.43x10⁻⁵mol/L, volume of dye solution =50mL, weight percent of AlF₃ varied from (0.5-3 wt %), AlF₃/TiO₂ catalyst weight =25mg, pH=7.5, air supply \cong 2.5L/min, I_{solar} = 772 × 100 \pm 100 lux)

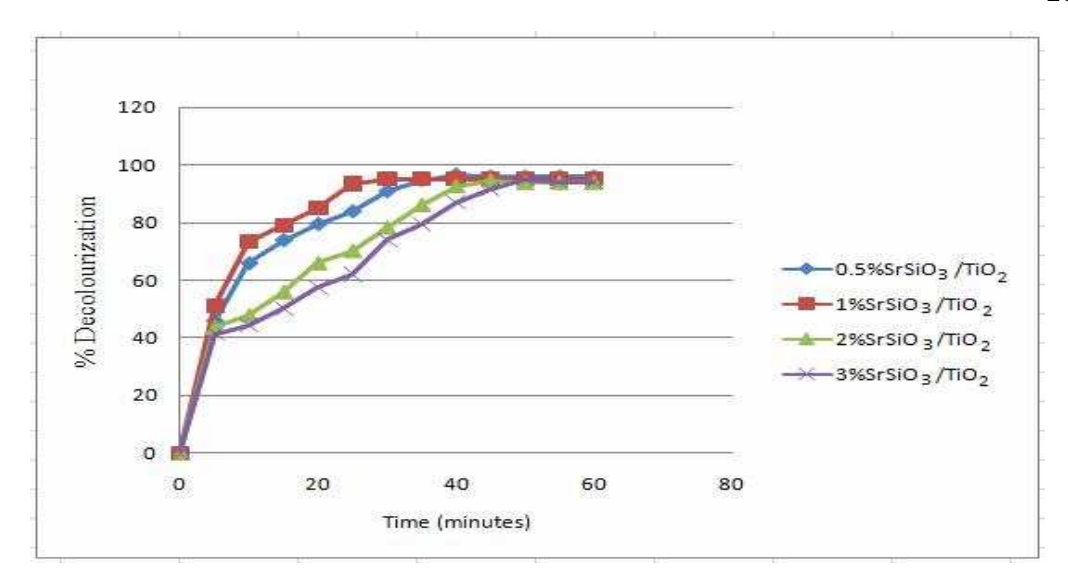


Figure 5.2.12 F Photocatalytic decolourization of congo red using different weight percents of strontium silicate doped TiO₂ catalyst.

(Reaction conditions: Congo red dye concentration =1.43x10⁻⁵mol/L, volume of dye solution =50mL, weight percent of SrSiO₃ varied from (0.5-3 wt %), SrSiO₃/TiO₂ catalyst weight =25mg, pH=7.5, air supply \cong 2.5L/min, I_{solar} = 772 × 100 \pm 100 lux)

5.2.13. Kinetic Studies

Langmuir-Hinshelwood kinetic model is widely employed to understand the rate of photocatalytic dye degradation process. The kinetics of photocatalytic dye degradation is depicted using the following first order equation

$$\ln\left(\frac{C_0}{C}\right) = k_{app}t \qquad \qquad \text{eq.}(5.28)$$

where k_{app} is the pseudo-first order rate constant (min⁻¹), C_o is the initial concentration of the dye solution, C is the concentration of the dye solution at time 't', respectively. A plot of $\ln C_o/C$ vs 't' is shown in figures 5.2.13.1 A, B, 5.2.13.2 A, B and 5.2.13.3A, B for the photocatalytic decolourization of three dyes namely basic yellow 2 (9.87x10⁻⁵M), acid red 94 dye (3.93x10⁻⁵M) and congo red dye (1.43x10⁻⁵M) under optimized conditions.

The R^2 values obtained for decolourization of basic yellow 2 using 0.5-3 wt % of AlF₃ doped TiO₂ photocatalysts are 0.978, 0.982, 0.981, 0.990 and the rate constant values are 7.20×10^{-2} , 8.10×10^{-2} , 6.0×10^{-2} and 5.20×10^{-2} min⁻¹. Similarly, R^2 values obtained for decolourization of methylene blue using 0.5-3 wt % of SrSiO₃ doped TiO₂ photocatalysts are 0.976, 0.989, 0.990, 0.991 and the rate constant values are 1.0×10^{-2} , 8.0×10^{-3} , 9.0×10^{-3} and 3.0×10^{-3} min⁻¹ and for bare TiO₂ catalyst the R^2 value and rate constant value is 0.984 and 2.20×10^{-2} min⁻¹.

For the photocatalytic decolourization of acid red 94 using 0.5-3 wt % of AlF₃ doped TiO₂ photocatalysts the R² values obtained are 0.956, 0.977, 0.946, 0.932 and the rate constant values are 6.90×10^{-2} , 1.50×10^{-1} , 4.40×10^{-2} and 3.70×10^{-2} min⁻¹. Similarly, R² values obtained for decolourization of acid red 94 using 0.5-3 wt % of SrSiO₃ doped TiO₂ photocatalysts are 0.983, 0.963, 0.990, 0.986 and the rate constant values are 6.0×10^{-3} , 8.0×10^{-3} , 9.70×10^{-3} and 9.0×10^{-3} min⁻¹ and for bare TiO₂ catalyst the R² value and rate constant value is 0.958 and 2.43x10⁻² min⁻¹. Similarly for the photocatalytic decolourization of congo red using 0.5-3 wt % of AlF₃ doped TiO₂ photocatalysts the R² values obtained are 0.949, 0.978, 0.969, 0.925 and the rate constant values are 7.40×10^{-2} , 9.80×10^{-1} , 4.60×10^{-1} and 3.0×10^{-1} min⁻¹. Similarly, R^2 values obtained for decolourization of congo red using 0.5-3 wt % of SrSiO₃ doped TiO₂ photocatalysts are 0.966, 0.960, 0.904, 0.865 and the rate constant values are 6.90×10^{-2} , 9.60×10^{-2} , 3.70x10⁻² and 3.90x10⁻² min⁻¹ and for bare TiO₂ catalyst the R² value and rate constant value is 0.988 and 5.90×10^{-2} min⁻¹. The linear fit between $\ln C_0/C$ versus time (minutes) obtained for all the plots along with the R² values close to unity supports the conclusion that the photocatalytic decolourization of the three dyes followed pseudofirst order kinetics with respect to the different weight percent (0.5-3%) of AlF_3 and $SrSiO_3$ doped TiO_2 catalysts.

Aluminium fluoride doped titanium dioxide photocatalyst showed higher rate constant values compared to strontium silicate doped and undoped titanium dioxide photocatalyst for the decolourization of basic yellow 2, acid red 94 and congo red dyes. Among different weight percent (0.5-3%) of aluminium fluoride doped titanium dioxide photocatalyst, 1wt% showed higher rate constant and the decrease in the rate constant value observed in the case of 2 wt% and 3wt% AlF₃ doped TiO₂ photocatalyst may be due to the higher coverage of aluminium atoms on the catalytically active surface of titanium dioxide photocatalyst. The difference in the rate constant values obtained between doped and undoped TiO₂ photocatalyst clearly explains the advantage of doping of aluminium fluoride (or) strontium silicate over titanium dioxide.

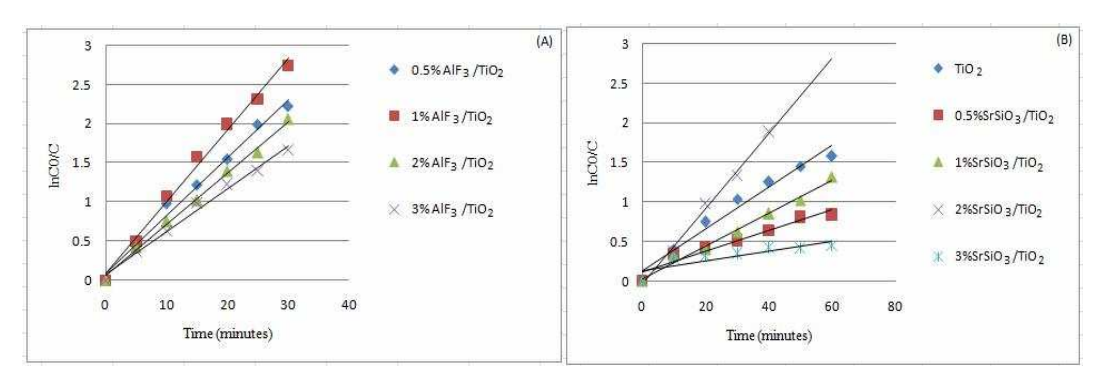


Fig. 5.2.13.1 shows the plot of $\ln C_0/C vs$ 't' for the photocatalytic decolourization of basic yellow 2 using (A) (0.5-3 wt%) AlF₃ doped TiO₂ and (B) using undoped TiO₂ and (0.5-3 wt%) SrSiO₃ doped TiO₂ photocatalyst.

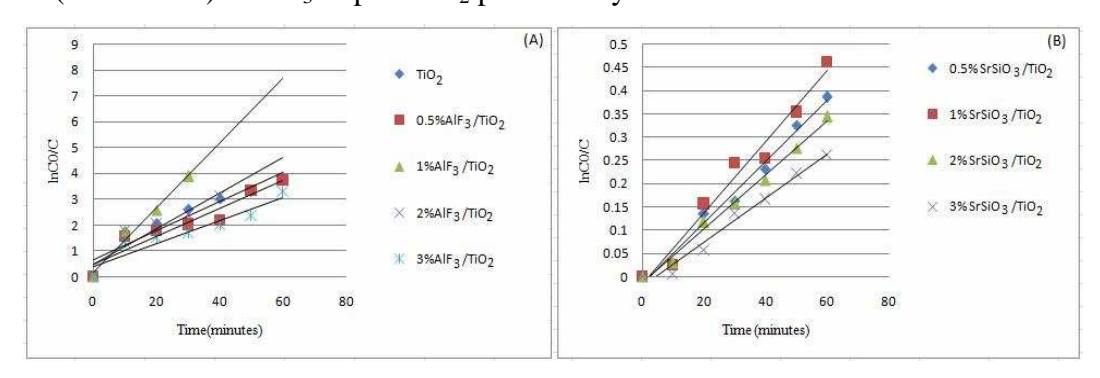


Fig. 5.2.13.2 shows the plot of $\ln C_0/C vs$ 't' for the photocatalytic decolourization of acid red 94 using (A) undoped TiO_2 and (0.5-3 wt%) AlF₃ doped TiO_2 and (B) using (0.5-3 wt%) SrSiO₃ doped TiO_2 photocatalyst.

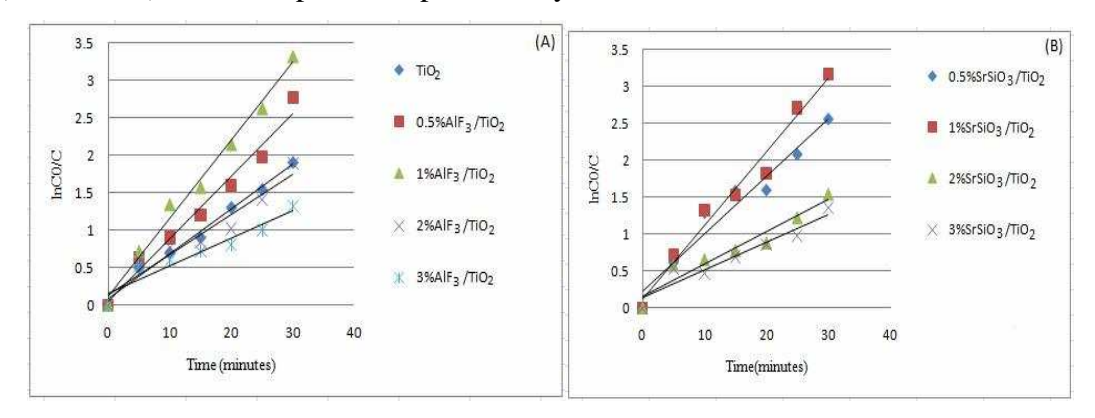


Fig. 5.2.13.3 shows the plot of $\ln C_0/C vs$ 't' for the photocatalytic decolourization of congo red using (A) undoped TiO_2 and (0.5-3 wt%) AlF₃ doped TiO_2 and (B) using (0.5-3 wt%) SrSiO₃ doped TiO_2 photocatalyst.

5.2.14. UV-Visible Spectroscopic Analysis

The photocatalytic decolourization of all the three dyes, namely basic yellow 2, acid red 94 and congo red with respect to time over AlF₃/TiO₂ and SrSiO₃/TiO₂ photocatalysts are analyzed with the help of UV-Visible spectrophotometer and the spectra are shown in figures 5.2.14.1A, B-5.2.14.3A,B.

The main characteristic peak of the basic yellow dye is observed at 432nm in the UV-Visible absorption spectra. About 89% decolourization of the dye is observed by the change in the colour of the dye from yellow to colourless within 30 minutes using the AlF₃/TiO₂ photocatalyst whereas even after the photocatalytic treatment for 60 minutes using SrSiO₃/TiO₂ photocatalyst, only a slight change in the yellow color of the dye is visualized during the course of the reaction as shown in the insets to figures 5.2.14.1A, B. The highly conjugated diaryl system connected by a methane is the chromophoric group and the dimethylamine (-NCH₃)₂ in the structure of the basic yellow dye is the auxochrome which enhances the colour of the dye. During the photocatalytic process the continuous decrease in the intensity of peak at 432nm and the absence of any other peak in the absorption spectra confirms the complete destruction of the chromophoric group and this strongly suggests that after the end of the photocatalytic treatment the fragment of the dye do not contain any chromophores.

The acid red 94 dye which belongs to xanthene class shows a characteristic absorption peak at 559nm. The decrease in the intensity of the peak observed during the photocatalytic treatment with using AlF₃/TiO₂ photocatalysts is shown in figure 5.2.14.2 A and using SrSiO₃/TiO₂ photocatalysts is shown in the figure 5.2.14.2 B. The maximum decolourization of AR 94 dye is achieved within 30 minutes using AlF₃/TiO₂ photocatalyst whereas only 23% dye decolourization took place using

SrSiO₃/TiO₂ photocatalyst. A change in colour of the dye from pink to colourless occurs during the course of the reaction indicates that the chromophoric quinoid structure of the dye as well as the auxochromic hydroxyl groups of the dye is completely destroyed by the photocatalytic treatment.

The congo red dye has two prominent absorption peaks at 338nm and 497nm respectively. The decrease in the absorption spectra of the main peak for the congo red dye at 497nm is contiunously monitored and shown in the figures 5.2.14.3A and B, and the inset to figures clearly shows the decrease in the intensity of the red colour of the dye at different time intervals. A prominent peak observed for the congo red dye at 497nm in the visible region is due to the presence of the azo chromophoric group and the peak at 338nm is due to the aromatic benzene ring. The disappearance of absorption peak after the photocatalytic treatment clearly shows that the chromophoric and auxochromic groups responsible for the red colour of the congo red dye is completely destroyed at the end of the reaction. The absence of new absorption peaks during the course of the reaction as well as at the end of the reaction is a clear indication that the fragmented intermediate species does not contain any chromophoric groups.

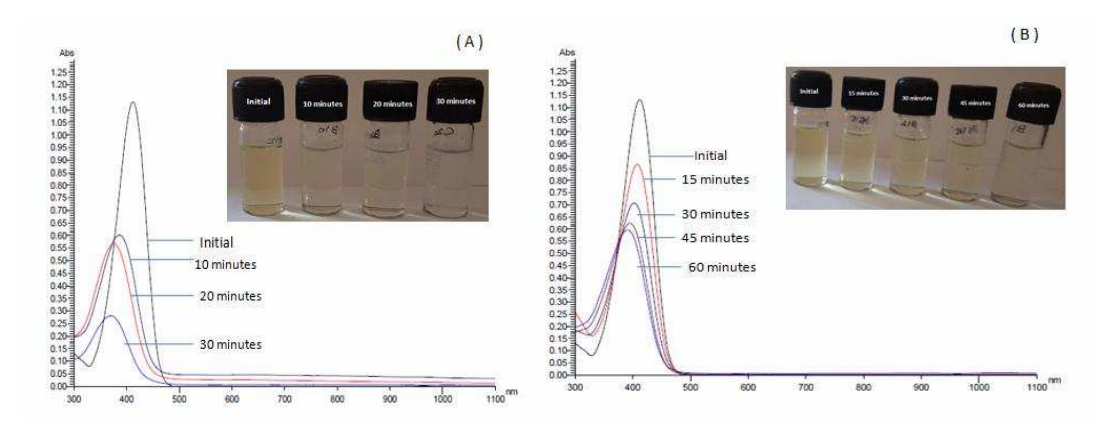


Figure 5.2.14.1 UV-Visible absorption spectra showing the decolourization of basic yellow 2 in the presence of (A) AlF₃/TiO₂ and (B) SrSiO₃/TiO₂ photocatalysts.

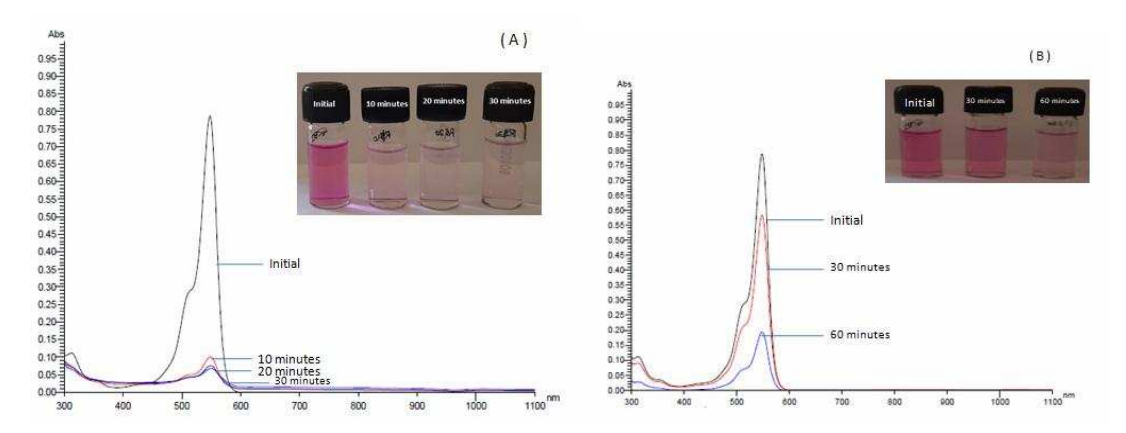


Figure 5.2.14.2 UV-Visible absorption spectra showing the decolourization of acid red 94 in the presence of (A) AlF₃/TiO₂ and (B) SrSiO₃/TiO₂ photocatalysts.

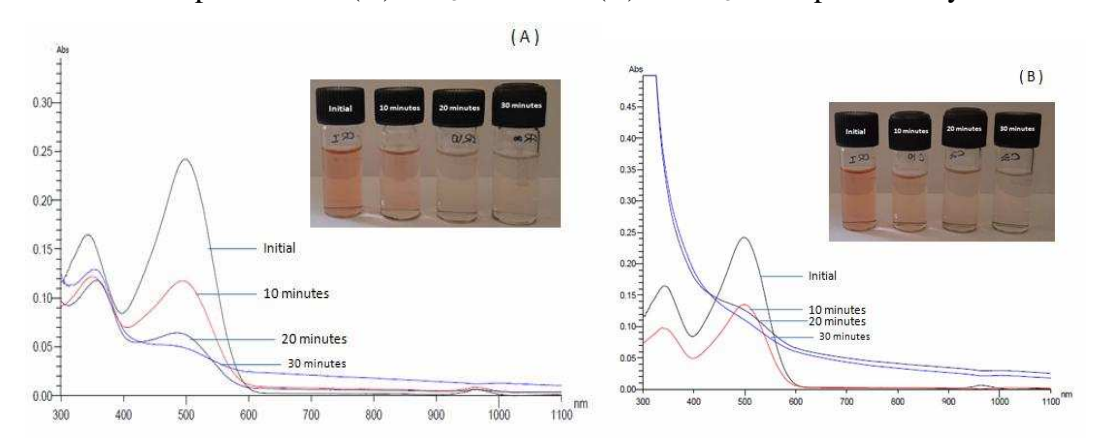


Figure 5.2.14.3 UV-Visible absorption spectra showing the decolourization of congo red in the presence of (A) AlF₃/TiO₂ (B) SrSiO₃/TiO₂ photocatalysts.

5.2.15. Comparison of the Efficiencies of Different Photocatalysts

The degradation efficiencies of bare titanium dioxide and different weight percents (0.5-3%) of aluminium fluoride and strontium silicate doped titanium dioxide photocatalysts are compared for three synthetic dyes, namely, basic yellow 2, acid red 94 and congo red dyes and the values are shown in table 5.2.15.

For basic yellow 2 dye degradation at optimum conditions [dye concentration (9.87x10⁻⁵M, pH 10, catalyst weight 25mg/50mL)] under solar radiation for 30 minutes, the degradation efficiencies of different photocatalysts are shown below:

 $1\% AlF_3/TiO_2 > 2\% \ AlF_3/TiO_2 > 0.5\% \ AlF_3/TiO_2 > 3\% AlF_3/TiO_2 > TiO_2 > 2\% \ SrSiO_3/TiO_2 > 1\% \ SrSiO_3/TiO_2 > 0.5\% \ SrSiO_3/TiO_2 > 3\% \ SrSiO_3/TiO_2$

For acid red 94 dye degradation at optimum conditions [dye concentration (3.93x10⁻⁵M, pH 3, catalyst weight 15mg/50mL)] under solar radiation for 30 minutes, the degradation efficiencies of different photocatalysts are shown below:

 $1\% AlF_3/TiO_2 > TiO_2 > 3\% \ AlF_3/TiO_2 > 2\% \ AlF_3/TiO_2 > 0.5\% AlF_3/TiO_2 > 1\%$ $SrSiO_3/TiO_2 > 0.5\% \ SrSiO_3/TiO_2 > 2\% \ SrSiO_3/TiO_2 > 3\% \ SrSiO_3/TiO_2$

For congo red dye degradation at optimum conditions [dye concentration (1.43x10⁻⁵M, pH 7.5, catalyst weight 25mg/50mL)] under solar radiation for 30 minutes, the degradation efficiencies of different photocatalysts are shown below:

 $1\% AlF_3/TiO_2 > 1\% \ SrSiO_3/TiO_2 > 0.5\% \ AlF_3/TiO_2 > 0.5\% \ SrSiO_3/TiO_2 >$ $TiO_2 > 2\% \ AlF_3/TiO_2 > 2\% \ SrSiO_3/TiO_2 > 3\% AlF_3/TiO_2 = 3\% \ SrSiO_3/TiO_2$

From the comparative analysis, it is observed that different weight of aluminium fluoride doped titanium dioxide photocatalysts are generally more efficient in degradading the three synthetic dye namely basic yellow 2, acid red 94 and congo red compared to different weight percent of (0.5-3 wt%) strontium silicate modified titanium dioxide as well as bare titanium dioxide photocatalysts.

The degradation efficiencies of the photocatalysts depend upon many factors such as the ability of the dye to get adsorbed on the photocatalyst, structure and concentration of the dyes and absorption of light by photocatalysts. In the overall process, the complete degradation of the three dyes namely basic yellow 2, acid red 94 and congo red is achieved with 1wt% AlF₃/TiO₂ within a short span of time under sunlight compared to strontium silicate and undoped titanium dioxide photocatalysts.

Table 5.2.15 Comparison of the efficiencies (in terms of % decolourization) of doped and undoped titanium dioxide photocatalysts towards basic yellow 2, acid red 94 and congo red.

	D ' 11 A	4 1 104	C 1
Photocatalyst	Basic yellow 2 (Optimized conditions: pH=10, catalyst weight= 25 mg/50mL, Dye concentration= 9.87x10 ⁻⁵ mol/L), Time=30 minutes.	Acid red 94 (Optimized conditions: pH=3, catalyst weight= 15 mg/50mL, Dye concentration= 3.93x10 ⁻⁵ mol/L), Time=30 minutes.	Congo red (Optimized conditions: pH=7.5, catalyst weight= 25 mg/50mL, Dye concentration= 1.43x10 ⁻⁵ mol/L), Time=30 minutes.
Bare TiO ₂	78	92	85.3
0.5% AlF ₃ / TiO ₂	88	89	93.7
1% AlF ₃ / TiO ₂	90.9	99	96
2 % AlF ₃ / TiO ₂	87.8	90.8	83.8
3 % AlF ₃ /TiO ₂	80	82	74
0.5%SrSiO ₃ / TiO ₂	40	15	92
1% SrSiO ₃ / TiO ₂	43	23	95
2%SrSiO ₃ / TiO ₂	47	14	78.4
3 %SrSiO ₃ / TiO ₂	32	12	74

5.2.16. Effect of Free radical scavenging activity

The formation of reactive species such as h^+ , OH, O_2^- and e^- during the photocatalytic process is investigated by the addition of radical quenchers such as EDTA, isopropyl alcohol, ascorbic acid and sodium sulphate. For investigating the effect of radical scavenging activity, 1mM solution of the radical quenchers such as EDTA, isopropyl alcohol, ascorbic acid and sodium sulphate are added to the dye solution at optimized pH, catalyst and dye concentration. A blank experiment is also carried out without the addition of quenchers under identical conditions. For the photocatalytic degradation of basic yellow 2 using the most active 1 wt%-AlF₃/TiO₂ catalyst about 89% degradation of the dye is achieved in the absence of any quencher. However, only about 20%, 30%, 23% and 22% degradation is achieved by the addition of EDTA, isopropyl alcohol, ascorbic acid and sodium sulphate, respectively and for the photocatalytic degradation of acid red 94 dye using the most active 1 wt%-AlF₃/TiO₂ catalyst about 99% degradation is achieved in the absence of any quencher and about 45%, 58%, 51% and 52% degradation is achieved by the addition of quenchers such as EDTA, isopropyl alcohol, ascorbic acid and sodium sulphate respectively. The obtained results clearly show that all the reactive species such as h^+ , 'OH, O₂' and e has actively participated in the photocatalytic degradation of basic yellow 2 and acid red 94 dyes. Similarly, Zehigoud et al⁵¹ reported the active role played by the reactive species such as h^+ , OH, O_2 and e^- using CHCl₃ and MeOH as scavengers for electronic holes, isopropanol for OH and potassium dichromate as a scavenger for superoxide anion radicals in the photocatalytic degradation of reactive green dye using CuO/TiO₂ photocatalyst.

In the photocatalytic degradation of congo red using the most active 1wt% AlF₃/TiO₂ catalyst about 94% degradation dye is achieved in the absence of any quencher. About 37%, 36%, 49.5% and 26% degradation is achieved by the addition of EDTA, isopropyl alcohol, ascorbic acid and sodium sulphate, respectively. The obtained result clearly shows that the hydroxyl radical is the main reactive species in the photocatalytic degradation of congo red dye compared to the holes and electrons. However, the participation of the superoxide anion radicals in the photocatalytic process is found to be less significant. Similarly, Bhagwat et al⁵² reported the photocatalytic degradation of congo red dye using ZnTiO₃/TiO₂ catalyst and their investigation of the radical scavenging activity during the photocatalytic process showed that the hydroxyl radicals are the main reactive species for the degradation of the congo red dye.

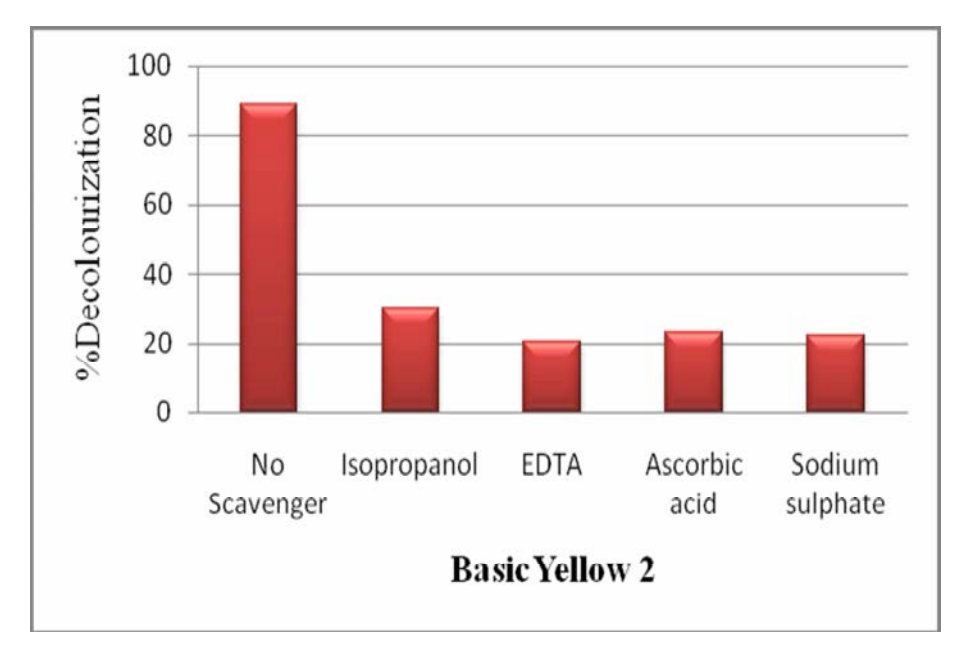


Figure 5.2.16.1 Effect of radical scavengers on the photocatalytic degradation of basic yellow 2 using 1wt% AlF₃/TiO₂ photocatalyst under optimized conditions.

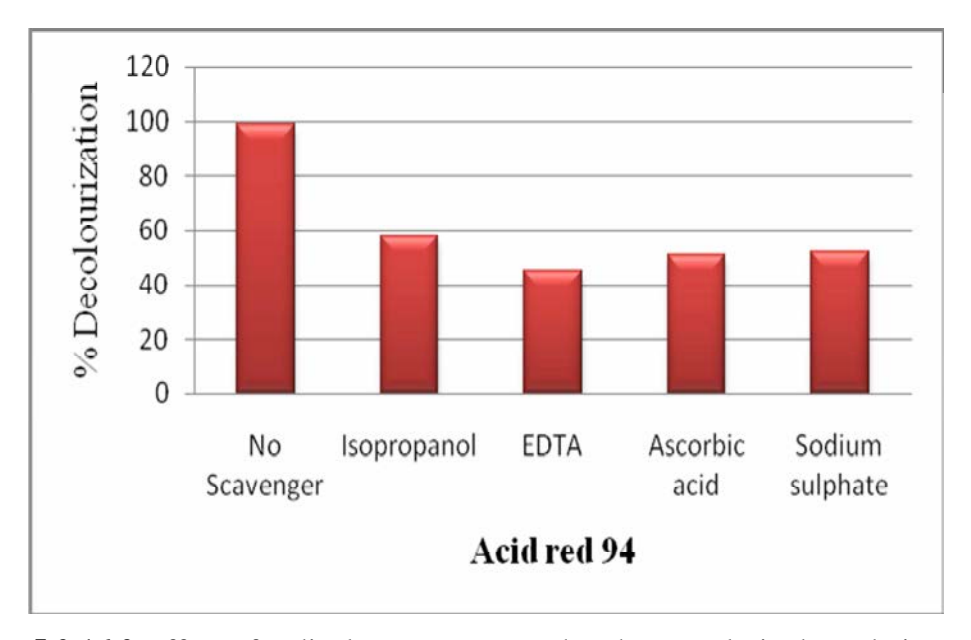


Figure 5.2.16.2 Effect of radical scavengers on the photocatalytic degradation of acid red 94 using 1wt% AlF₃/TiO₂ photocatalyst under optimized conditions.

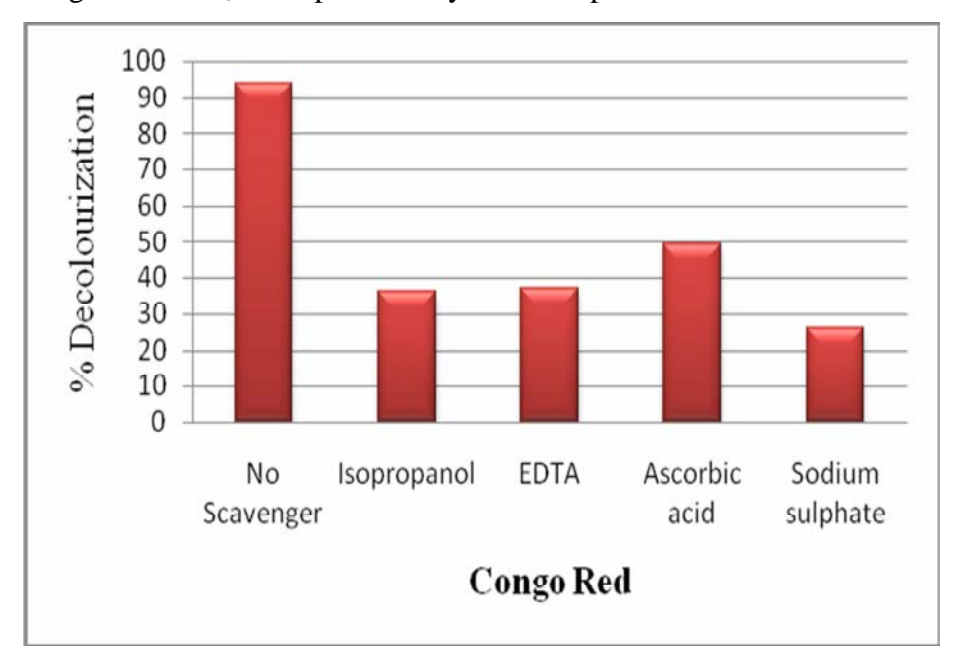


Figure 5.2.16.3 Effect of radical scavengers on the photocatalytic degradation of congo red using 1wt% AlF₃/TiO₂ photocatalyst under optimized conditions.

5.2.17. Mineralization Studies

Total organic carbon analysis is a versatile technique used to study the extent of mineralization of the organic pollutants. In the present study, to analyze the extent of degradation of the dyes the samples of three dyes namely basic yellow 2, acid red 94 and congo red are collected before and after photocatalytic treatment with 1 wt % AlF₃/TiO₂ photocatalyst under optimized conditions and it is subjected to TOC analysis. About 64.9, 76.7 and 72% degradation of basic yellow 2, acid red 94 and congo red dyes are achieved respectively. The percentage degradation values obtained from the TOC analysis is less compared to the decolourization values calculated from the spectrophotometric measurements which indicate that even though the destruction of the chromophoric group of the dyes is achieved within 30 minutes of photocatalytic treatment under sunlight the complete mineralization of dye molecule into CO₂, H₂O and mineral acids might take longer time.

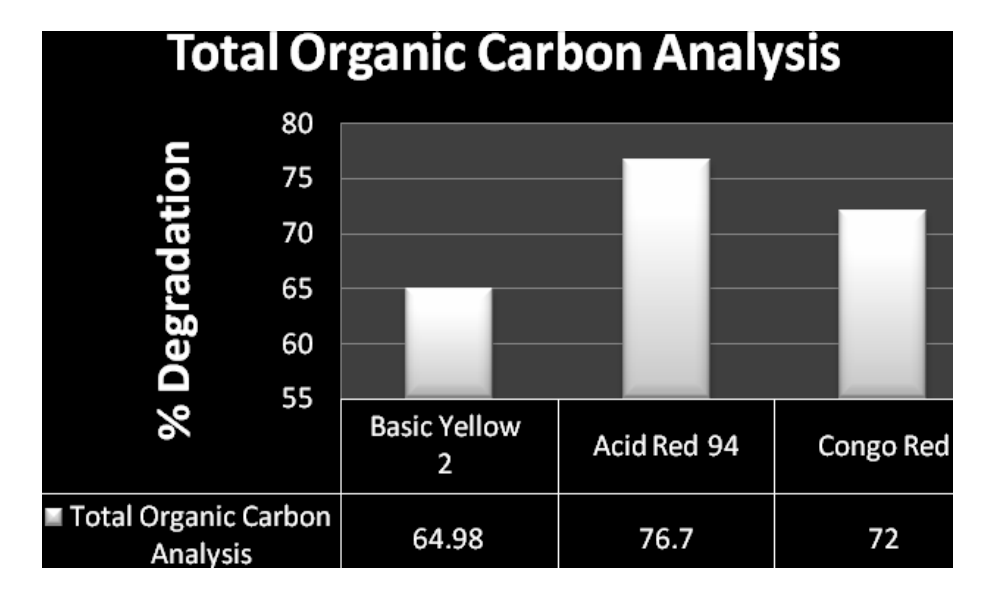


Figure 5.2.17 shows the percentage removal of total organic carbon in the aqueous solution of basic yellow 2, acid red 94 and congo red dyes using 1wt% AlF₃/TiO₂ photocatalyst under optimized conditions.

5.2.18. Reusability Studies

The recovery and reuse of a catalyst is very important in a photocatalytic reaction as it can significantly reduce the operational cost of the effluent treatment process. In order to evaluate the reusability of the most active catalyst 1wt% AlF₃/TiO₂ the catalyst is recovered by centrifugation, washed repeatedly with distilled water and dried in the hot air oven and then it is further subjected to the photocatalytic treatment with fresh dye solution. After each cycle, the absorbance of the dyes namely basic yellow 2, acid red 94 and congo red dye in recorded from the spectrophotometer and the percentage decolourization is calculated and the graphs are plotted as shown in figure 5.2.18 A-C. From the experimental studies it is noted that even after the 5th cycle only a negligible loss in the catalytic activity is found which suggests that the aluminium fluoride doped titanium dioxide catalyst can be efficiently reused multiple times without much loss in the photocatalytic activity.

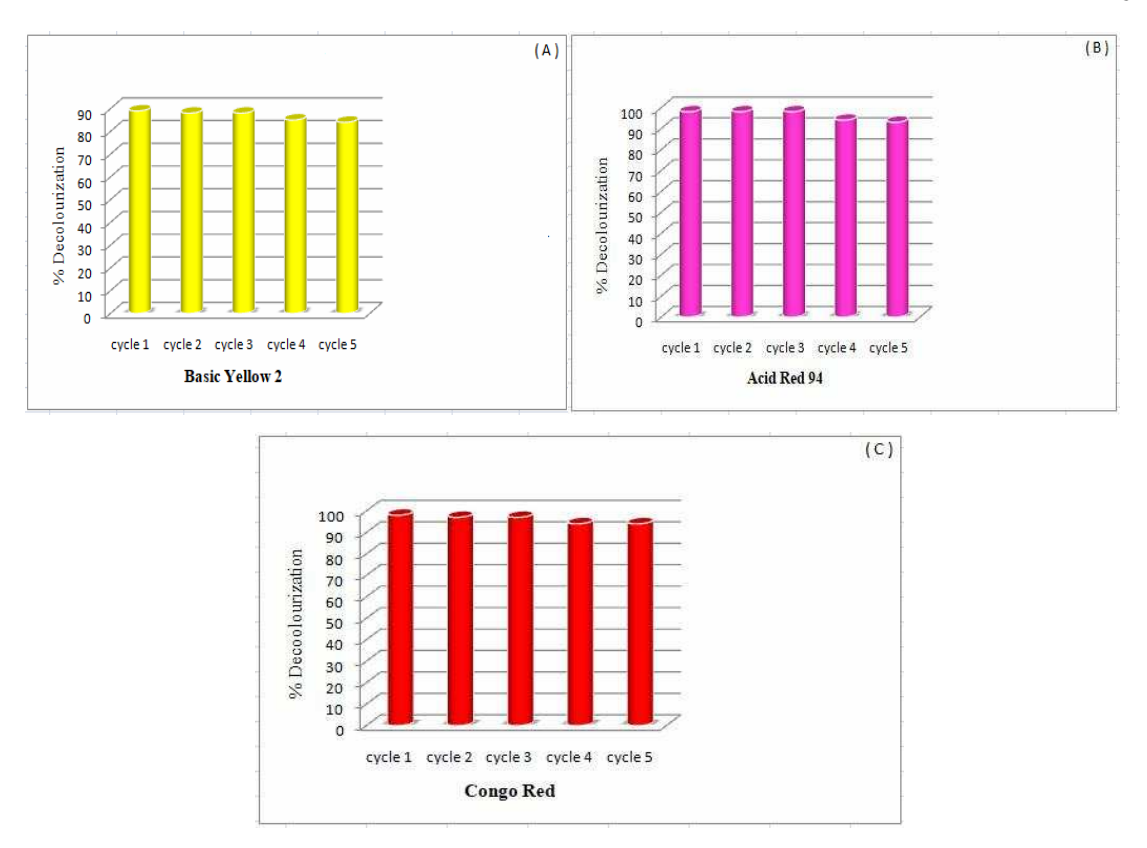


Figure 5.2.18 shows the reusability of the most active 1wt% AlF₃/TiO₂ catalyst for the photocatalytic degradation of (A) basic yellow 2 (B) acid red 94 and (C) congo red dyes.

5.2.19. Proposed Mechanism

Titanium dioxide photocatalyst have fascinating opto-electronic properties⁵³ and are used in the light-induced photochemical reactions. When titanium dioxide is irradiated with the light of energy greater than or equal to its bandgap energy, the electrons are excited from the valence band to the conduction band of the TiO₂ material. The excited electrons initiate the reduction reactions on the catalyst surface and the holes in the valence band participate in the oxidations reactions, however when these electrons and holes are not involved in the photocatalytic reaction they recombine and dissipate energy in the form of heat. The mechanism of redox reactions in the TiO₂ photocatalytic system by light absorption is shown below

The photocatalytic degradation of the organic pollutants takes place through various free radical reactions giving large number of intermediates which on subsequent oxidation leads to the formation of non-toxic products such as CO₂, H₂O and mineral acids. Hence, the participation of the photogenerated electrons and holes in the photocatalytic reaction is essential to achieve an effective oxidation process⁵⁴. However, in a bare titanium dioxide photocatalytic system the recombination of the electrons and holes takes place at a faster rate, and hence the generations of the reactive species such as hydroxyl and superoxide anion radicals are hindered. In view of these facts, doping of the bare titanium dioxide photocatalyst with metals such as 'Al' and 'Sr' was done for the present work. Doping creates additional energy levels that is above the valence band edge and below the conduction band edge of TiO₂ photocatalyst acting as both electron and hole traps.

From the photocatalytic studies, it was observed that the doping of aluminium fluoride salt to the titanium dioxide photocatalyst led to faster degradation of the synthetic organic dyes. On the other hand, strontium silicate doped titanium dioxide photocatalyst took more time for the photocatalytic decolourization of the dyes.

The lower photocatalytic activity of strontium silicate doped-TiO₂ photocatalyst can be ascribed to the following reasons:

Strontium silicate used as a dopant distorts the lattice sites, creates defects and occupies the photocatalytically active sites of titanium dioxide photocatalyst thereby reducing the number of active sites available for the photocatalytic reaction.

Addition of excess amount of strontium silicate dopant to titanium dioxide sites might have resulted in recombination centers for the photogenerated electronhole pairs resulting in a decreased photocatalytic activity⁵⁵.

The higher photocatalytic activity of aluminium fluoride doped titanium dioxide photocatalyst compared to the undoped and $SrSiO_3$ doped TiO_2 photocatalysts can be attributed to the fact that the introduction of 'Al' to TiO_2 catalyst may act as trapping centers for the photogenerated electrons and holes⁵⁶. The additional energy states created by the introduction of Al^{3+} ions to the titanium dioxide lattices lead to a reduction in the bandgap values, and Al^{3+} ions trap the photogenerated electrons and holes to form less stable Al^{2+}/Al^{4+} ions which further react with the surface adsorbed O_2 and hydroxyl ions to form the reactive species such as hydroxyl and superoxide anion radicals. The plausible mechanism is depicted as given below:

The superoxide anion radical and hydroxyl radicals generated in situ are highly reactive species that triger the degradation of dyes.

$$Dye^{.+} + O_2^{.-} \rightarrow Degradation products \qquad \qquad eq.(5.42)$$

$$Dye^{-+} + OH \rightarrow Degradation products$$
 eq.(5.43)

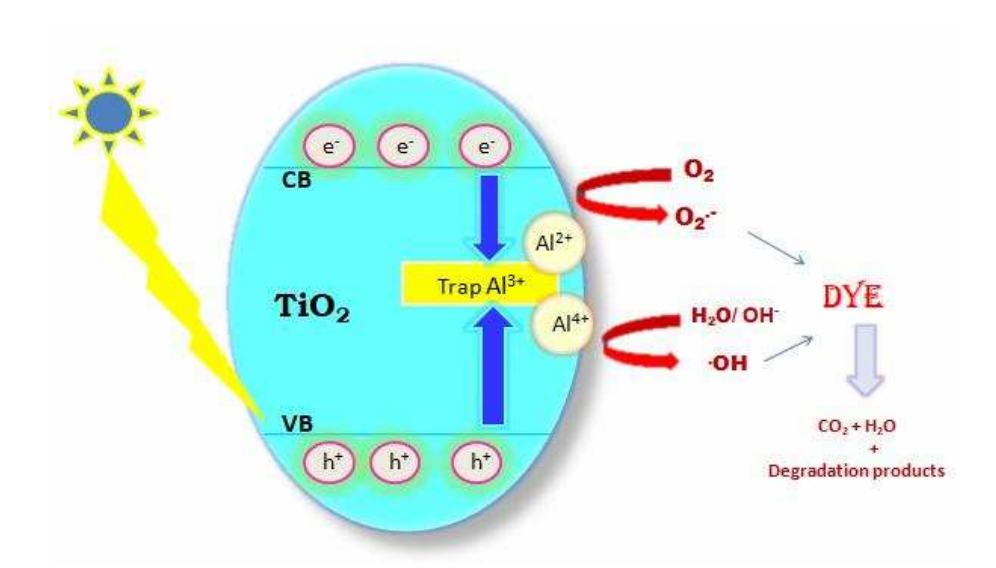


Figure 5.2.19 Perspective mechanism for the degradation of dyes mediated by 1 wt % AlF₃/TiO₂ catalyst under sunlight.

5.3. CHARACTERIZATION AND PHOTOCATALYTIC STUDIES OF BISMUTH OXYCHLORIDE, ALUMINIUM FLUORIDE DOPED BISMUTH OXYCHLORIDE AND STRONTIUM SILICATE DOPED BISMUTH OXYCHLORIDE CATALYSTS

5.3.1. X-Ray Diffraction Studies

The phase and crystallinity of the synthesized bismuth oxychloride, aluminium fluoride doped bismuth oxychloride and strontium silicate doped bismuth oxychloride photocatalysts were determined using the powder X-ray diffraction (P-XRD) technique. The X-Ray diffraction peaks of the undoped bismuth oxychloride photocatalysts obtained at the 2θ values 12.0, 24.1, 25.98, 32.47, 33.43, 36.52, 41.82, 46.67, 49.67, 54.13, 55.08, 58.58, 60.60, 68.02, 74.96, 77.45 corresponding to the crystal planes 001, 002, 101, 110, 102, 003, 112, 200, 113, 104, 212, 220, 213, 214 and 006 which is in accordance with the [standard JCPDS (85-0861)] confirms the tetragonal phase of the pure bismuth oxychloride photocatalyst⁵⁷. Similar diffraction patterns were observed for the aluminium fluoride and strontium silicate doped bismuth oxychloride

photocatalysts. The X-Ray diffraction pattern for the undoped BiOCl, AlF₃ 3wt% and SrSiO₃ 3wt% doped BiOCl photocatalysts are shown in figure 5.1.3 A-C. No additional peaks with observable intensity due to the doping of aluminium fluoride and strontium silicate are recorded in XRD spectrum, which might be due to the very low concentration of the dopants on the bismuth oxychloride photocatalyst. The sharp and intense peaks observed in the XRD pattern indicate that the synthesized photocatalysts are crystalline in nature. The average crystallite size of the synthesized bismuth oxychloride photocatalyst calculated according to the debye-scherrer's equation is found to be 14.7 nm and for the aluminium fluoride and strontium silicate doped bismuth oxychloride photocatalysts it is 22.2 and 22.12 nm respectively.

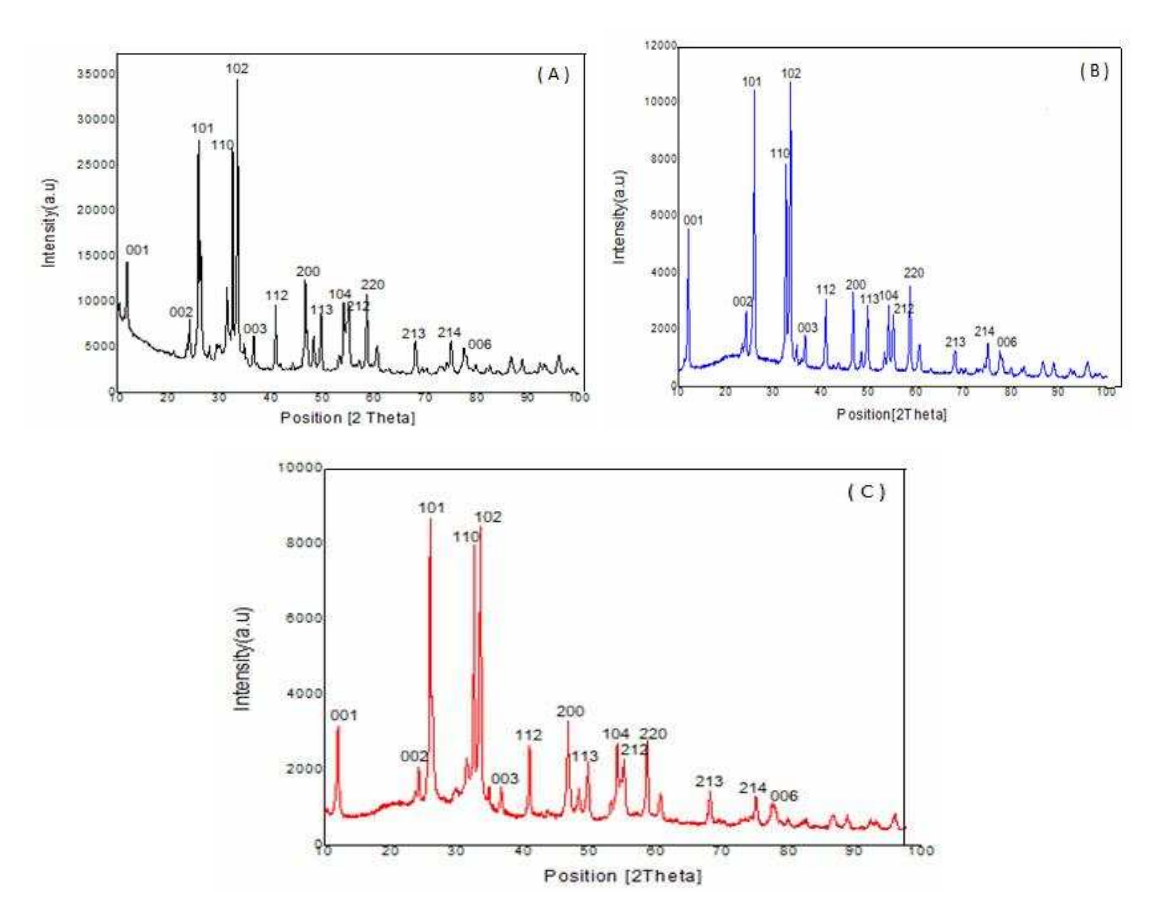


Figure 5.3.1 X-Ray diffraction pattern of the synthesized (A) undoped bismuth oxychloride photocatalyst (B) 3 wt% AlF₃ doped bismuth oxychloride photocatalyst and (C) 3 wt% SrSiO₃ doped bismuth oxychloride photocatalyst.

5.3.2. HR-SEM Analysis

To obtain information about the morphology of the synthesized bismuth oxychloride and aluminium fluoride and strontium silicate doped bismuth oxychloride photocatalysts, the catalysts are subjected to high resolution scanning electron microscopic analysis and the corresponding images are shown in figure 5.3.2 A-C. The selected area FE-SEM micrographs of all three photocatalysts bare BiOCl, 3 wt% AlF₃ doped BiOCl and 3 wt% SrSiO₃ doped BiOCl under different magnifications shows that the synthesized photocatalysts posses a flake like structure.

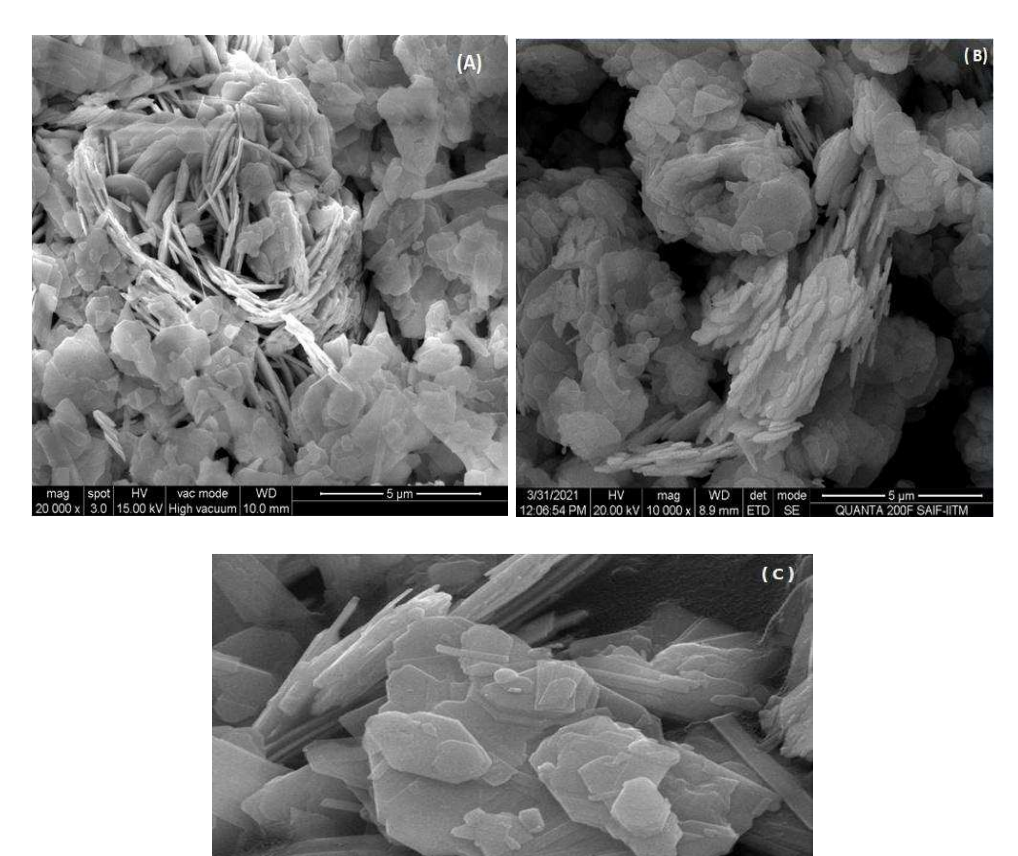


Figure 5.3.2 shows the HR-SEM image of the synthesized (A) bare bismuth oxychloride photocatalyst (B) 3 wt% AlF₃ doped bismuth oxychloride photocatalyst and (C) 3 wt% SrSiO₃ doped bismuth oxychloride photocatalyst.

5.3.3. Energy Dispersive X-Ray Analysis

Energy dispersive X-Ray (EDAX) analysis is a non-destructive analytical technique that can be used to determine the major elemental composition in the synthesized material. The EDAX spectrum of the synthesized undoped bismuth oxychloride photocatalyst, 3 wt% aluminium fluoride and 3wt% strontium silicate doped bismuth oxychloride photocatalysts are shown in figure 5.3.3A-C. The presence of the elements such as bismuth, oxygen and chlorine are evidenced from the EDAX spectrum of the synthesized bare bismuth oxychloride photocatalyst. Similarly, the peaks of the elements such as bismuth, oxygen, chlorine, aluminium and fluorine are observed in the EDAX spectrum of the synthesized AlF₃-BiOCl photocatalyst. Similarly, the presence of the elements such as bismuth, oxygen, chlorine, strontium and silicon are observed in the EDAX spectrum of the synthesized SrSiO₃-BiOCl photocatalyst.

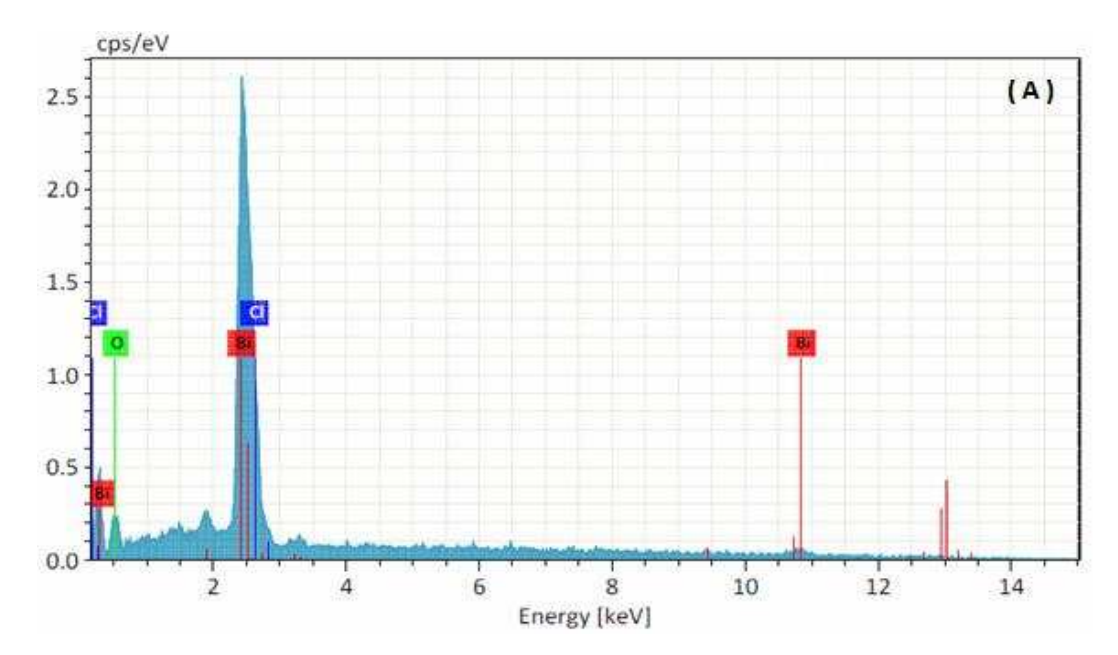


Figure 5.3.3 A shows the EDAX image of the synthesized undoped bismuth oxychloride photocatalyst.

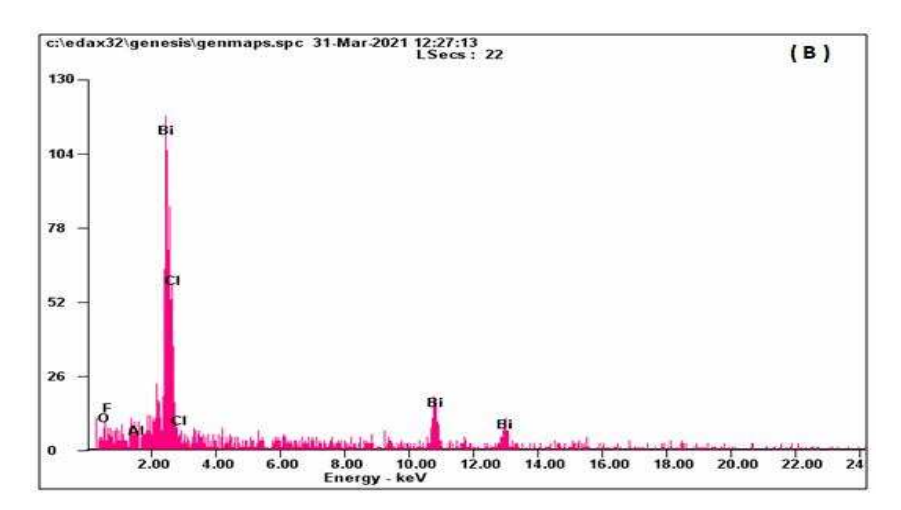


Figure 5.3.3 B shows the EDAX image of the synthesized aluminium fluoride doped bismuth oxychloride photocatalyst.

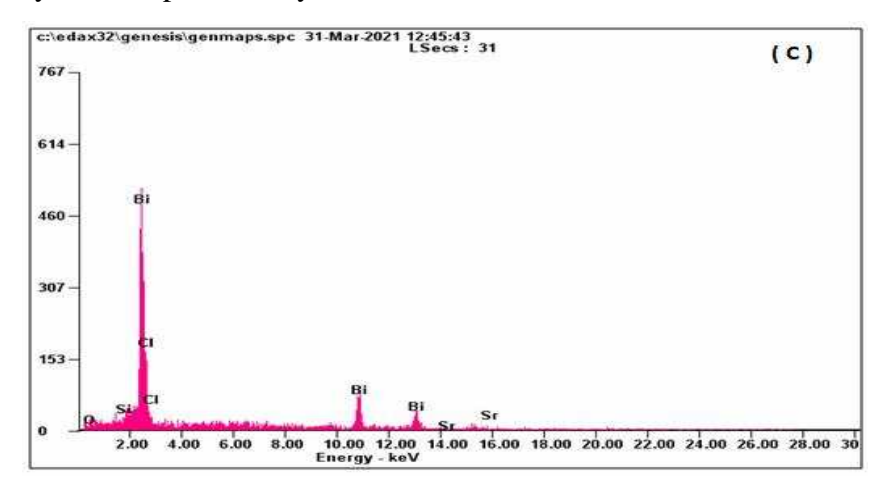


Figure 5.3.3 C shows the EDAX image of the synthesized strontium silicate doped bismuth oxychloride photocatalyst.

5.3.4. Transmission Electron Microscopic Analysis

The TEM images of the synthesized bare bismuth oxychloride photocatalyst and aluminium fluoride and strontium silicate doped bismuth oxychloride photocatalysts are shown in figures 5.3.4 A-I. From the TEM micrographs it is observed that the synthesized bare bismuth oxychloride photocatalyst possess flake-like structures, this observation is similar to that observation made from the SEM micrographs. The selected area electron diffraction pattern of the doped as well as undoped bismuth oxychloride photocatalyst shows a well arranged pattern with dark spots in it,

indicating that the synthesized bismuth oxychloride based photocatalysts are crystalline in nature which supports the data obtained from the XRD results.

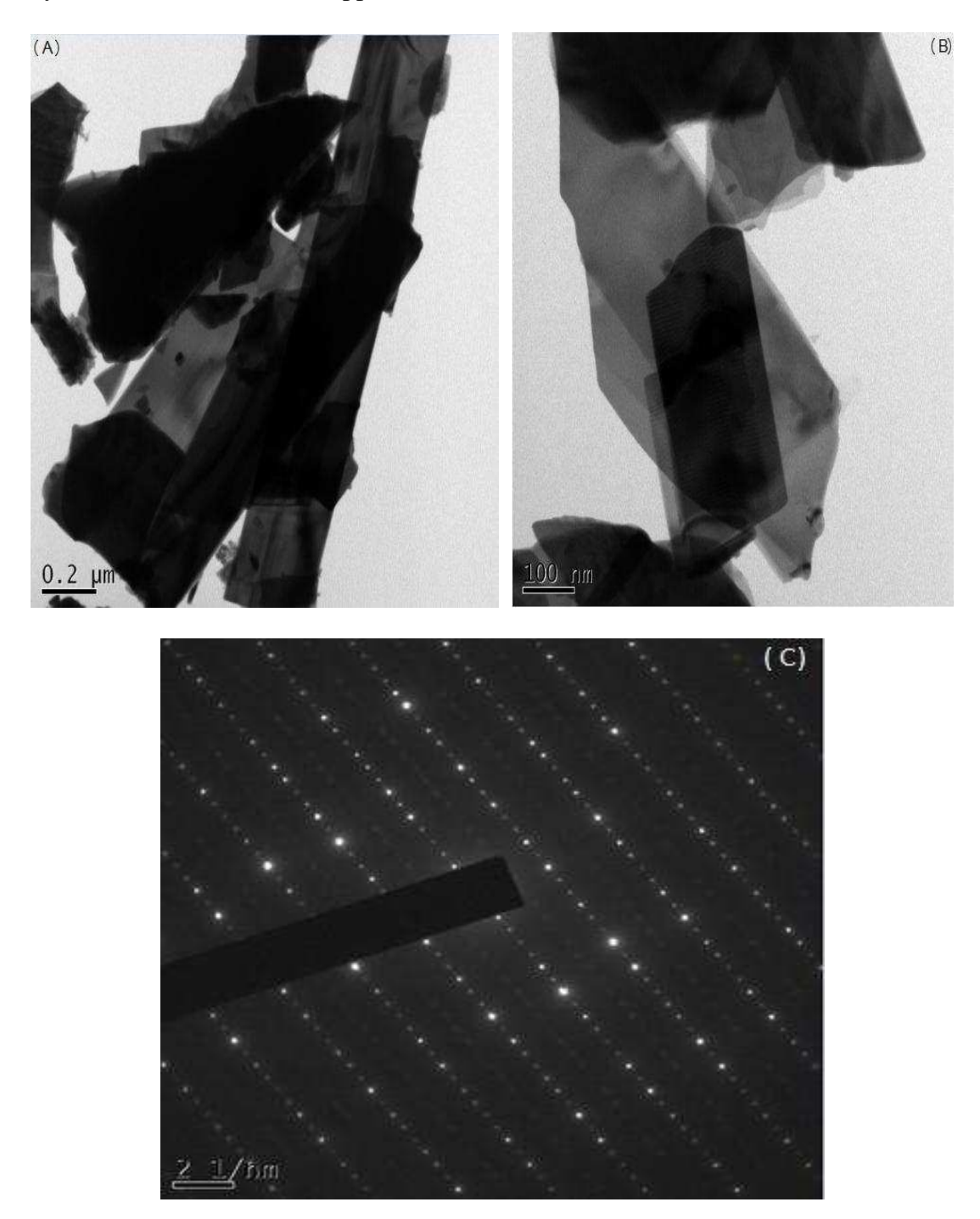


Figure 5.3.4 A, B HR-TEM images and (C) SAED pattern of the undoped Bismuth oxychloride photocatalyst.

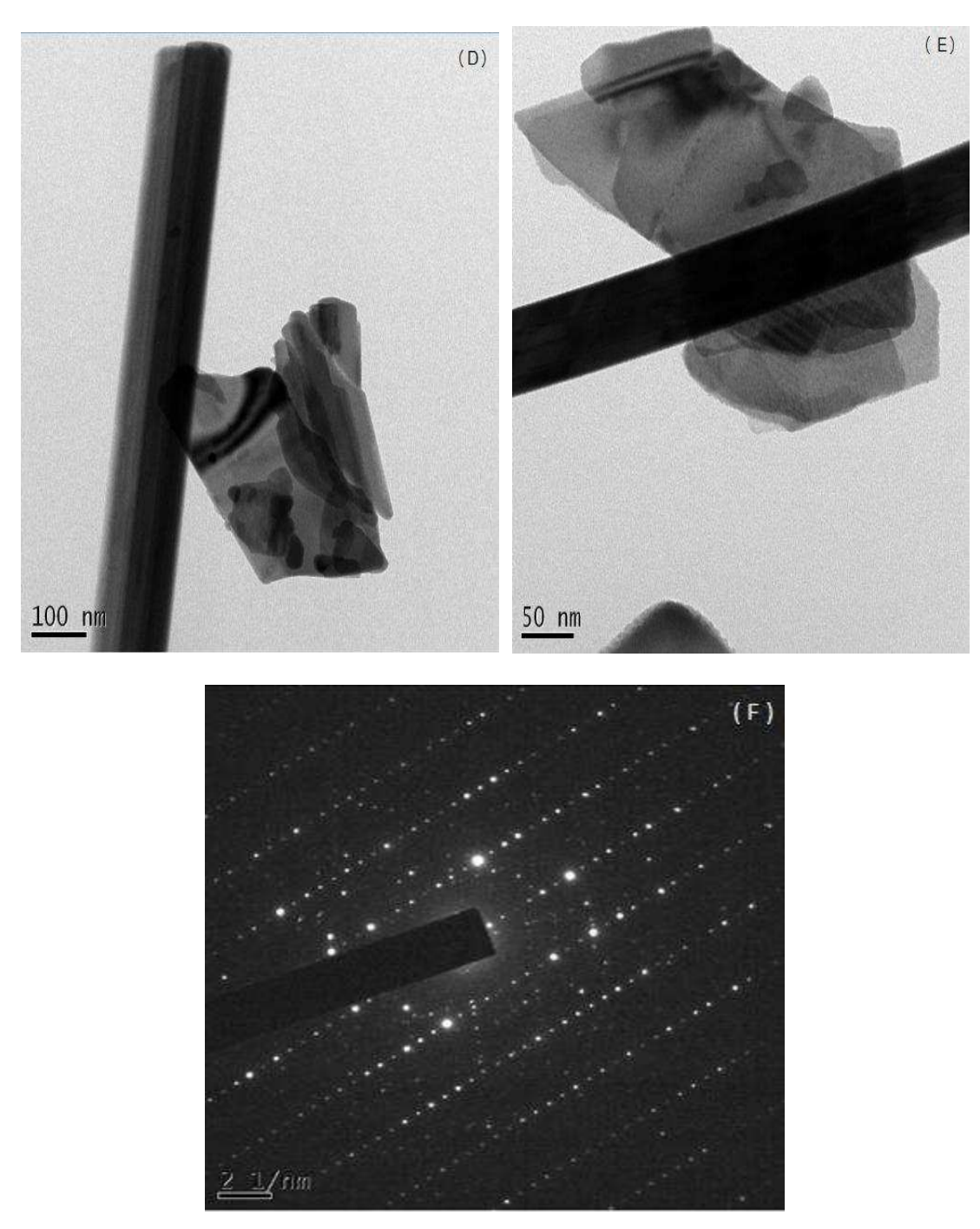


Figure 5.2.4 D, E shows the HR-TEM images and (F) shows the SAED pattern of the 3 wt % AlF_3 doped BiOCl photocatalyst.

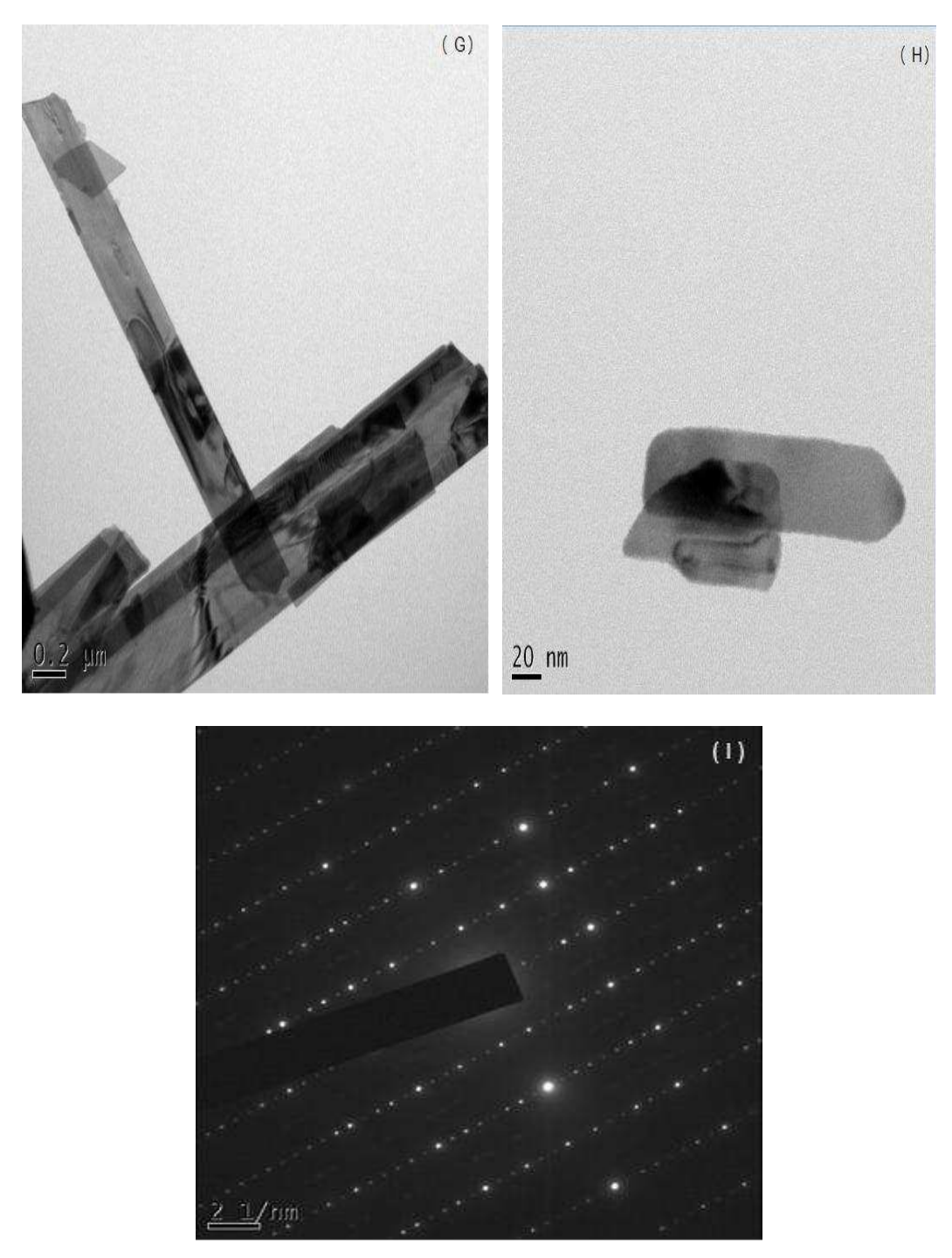


Figure 5.3.4 G, H shows the HR-TEM images and (I) shows the SAED pattern of the 3wt% SrSiO₃ doped BiOCl photocatalyst.

5.3.5. UV-Visible Diffuse Reflectance Spectroscopy Studies

Diffuse Reflectance Spectroscopy is a powerful analytical technique that utilizes the UV, visible or near Infra-red light as the probe to study the spectral characteristics of opaque solid samples. In the case of diffuse reflection, the light incident on the rough surfaced samples is reflected in all the directions. From the percentage reflectance, the absorbance and transmittance values can be calculated and the bandgap energy values are obtained from the cut-off wavelength in the absorption spectra. The DRS-UV-Visible absorption spectra of the synthesized undoped and aluminium fluoride and strontium silicate doped bismuth oxychloride photocatalysts are shown in figures 5.3.5 A-C. The calculated bandgap values for the synthesized bare BiOCl, 3wt% AlF₃ doped BiOCl and 3 wt% SrSiO₃ doped BiOCl photocatalysts are 3.12 eV, 3.02 eV and 3.03 eV respectively.

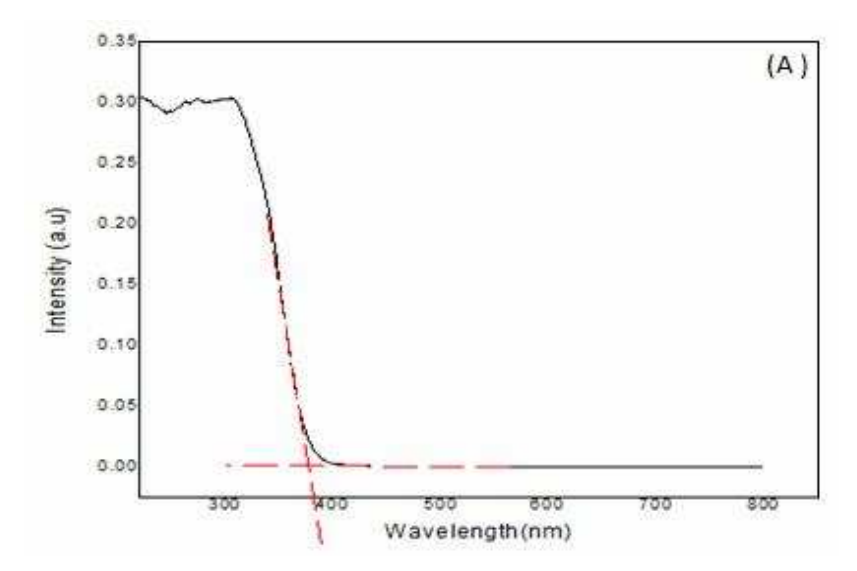


Figure 5.3.5 A shows the DRS-UV-Visible absorption spectra for bare BiOCl photocatalyst.

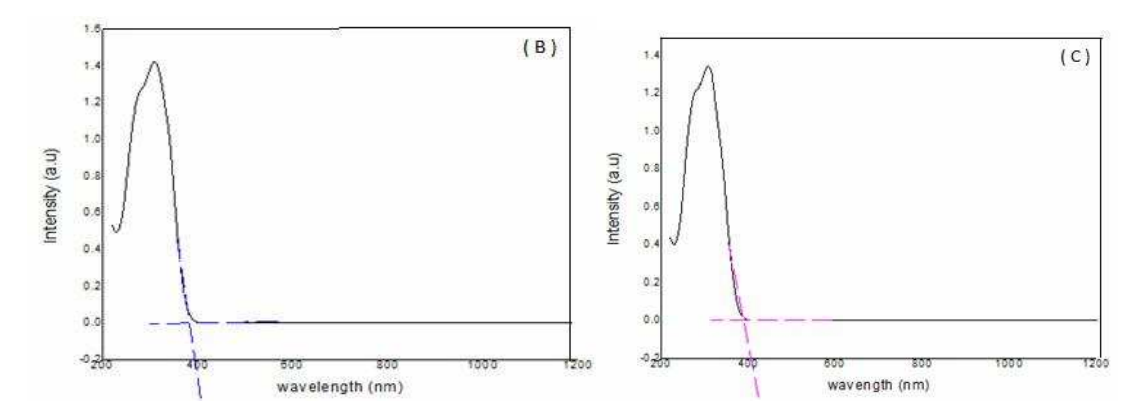


Figure 5.3.5 B shows the DRS-UV-Visible absorption spectra for 3 wt% AlF₃ doped BiOCl photocatalyst and **5.3.5 C** shows the DRS-UV-Visible absorption spectra for 3 wt% SrSiO₃ doped BiOCl photocatalyst.

5.3.6. Fourier Transform Infra-Red Spectroscopy Studies

Infra-Red Spectroscopy is a widely employed technique by the chemists for the identification of functional groups. Simple IR spectra are obtained for the compounds with high purity and less IR active bonds. The FTIR spectrum of the synthesized bare bismuth oxychloride photocatalyst as well as aluminium fluoride and strontium silicate doped bismuth oxychloride photocatalysts are shown in figure 5.3.6 A, B and C. In all the three BiOCl photocatalysts the peaks at around 3400cm⁻¹ and 1400-1600cm⁻¹ corresponds to the stretching and bending vibrations of the hydroxyl groups indicating the presence of adsorbed water molecules on the surface of the catalysts. The weak band at around 1100 cm⁻¹ observed in the BiOCl catalysts might be due to the O-Cl stretching. The bands below 950 cm⁻¹ confirm the characteristic framework vibrations of Bi-O bonds in the bare as well as doped bismuth oxychloride photocatalysts⁵⁸⁻⁶⁰.

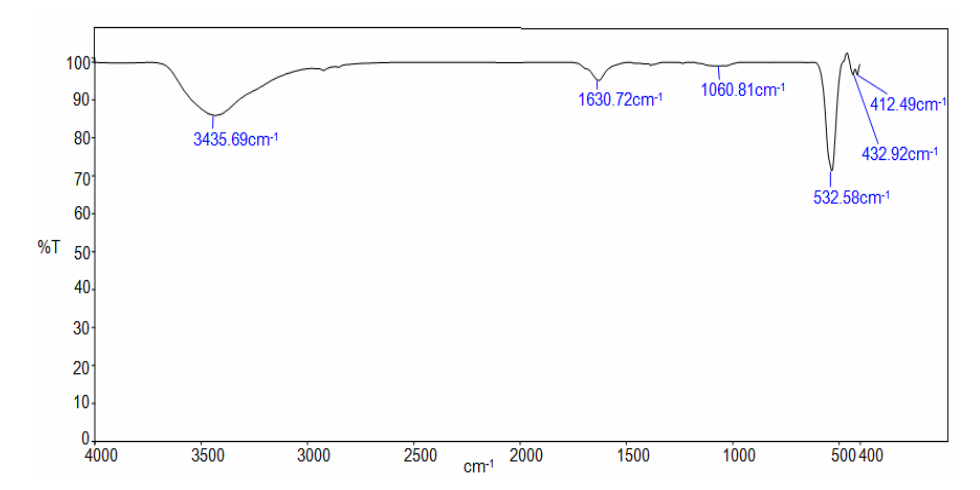


Figure 5.3.6 A FTIR spectrum of the synthesized bare bismuth oxychloride photocatalyst.

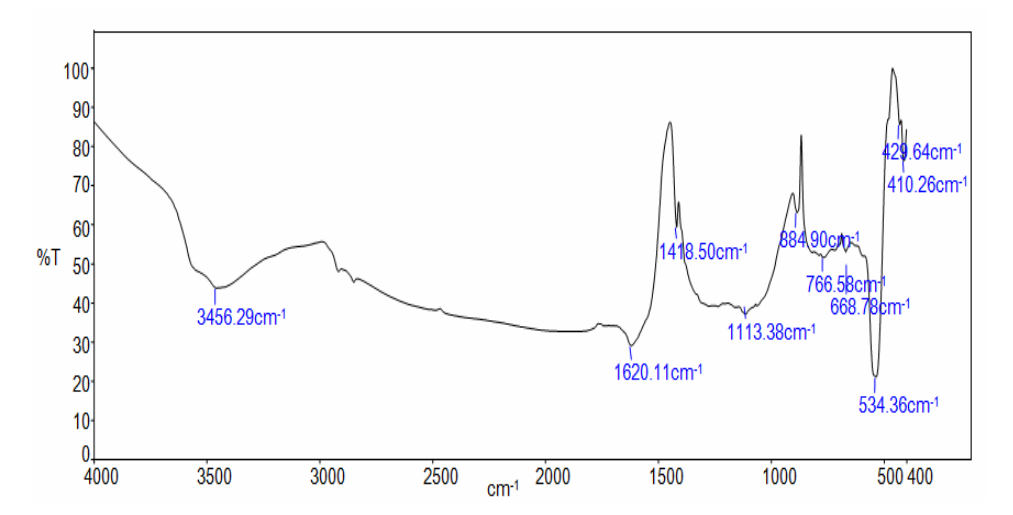


Figure 5.3.6 B FTIR spectrum of the synthesized 3wt% AlF₃/BiOCl photocatalyst.

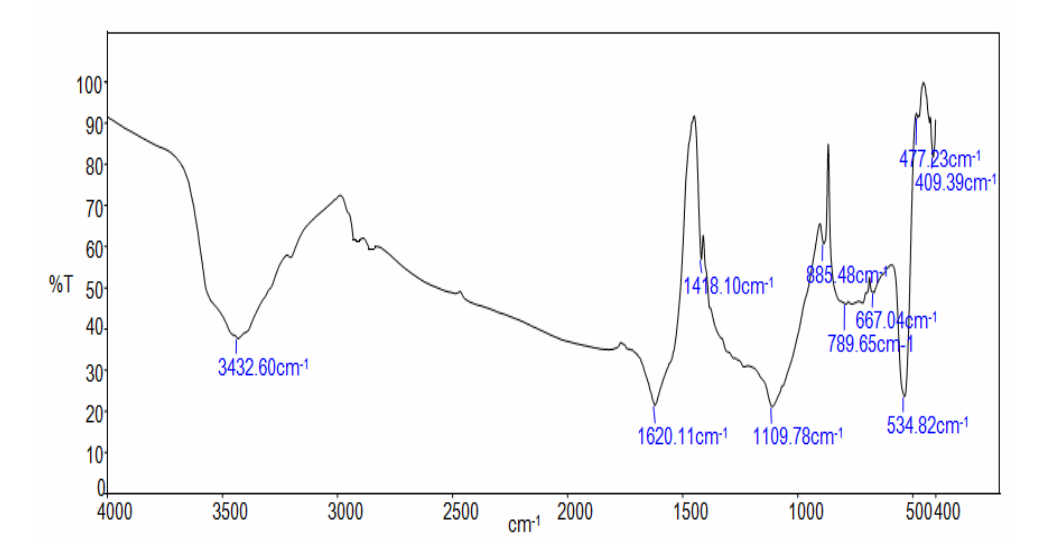


Figure 5.3.6 C FTIR spectrum of the synthesized 3wt% SrSiO₃/BiOCl photocatalyst.

5.3.7. BET Surface Area Analysis

The specific surface area of solid samples can be determined by gas adsorption analysis where an inert gas such as nitrogen or a mixture of nitrogen and helium is used as the adsorbate. Brunauer-Emmett-Teller (BET) surface area is a multi-point measurement method which describes the relationship between the numbers of the gas molecules adsorbed at a given relative pressure. The observations are generally referred to as the physical adsorption or physisorption. The nitrogen adsorption-desorption isotherms of the synthesized Bismuth oxychloride, aluminium fluoride doped bismuth oxychloride and strontium silicate doped bismuth oxychloride photocatalysts are shown in figure 5.3.7 A-C. The N₂ adsorption-desorption isotherms of all the synthesized bismuth oxychloride photocatalysts indicate a stepwise multilayer adsorption which is found to be the characteristics of aggregates of plate like particles having slit like pores. The specific surface area of the bare bismuth oxychloride photocatalyst is 18.726 m²/g and that of the aluminium fluoride and strontium silicate doped titanium dioxide photocatalysts are 14.837m²/g and 20.577m²/g respectively. The surface area of Al incorporated BiOCl is decreased which might be due to the partial blockage of pores in the structures of the bismuth oxychloride photocatalyst.

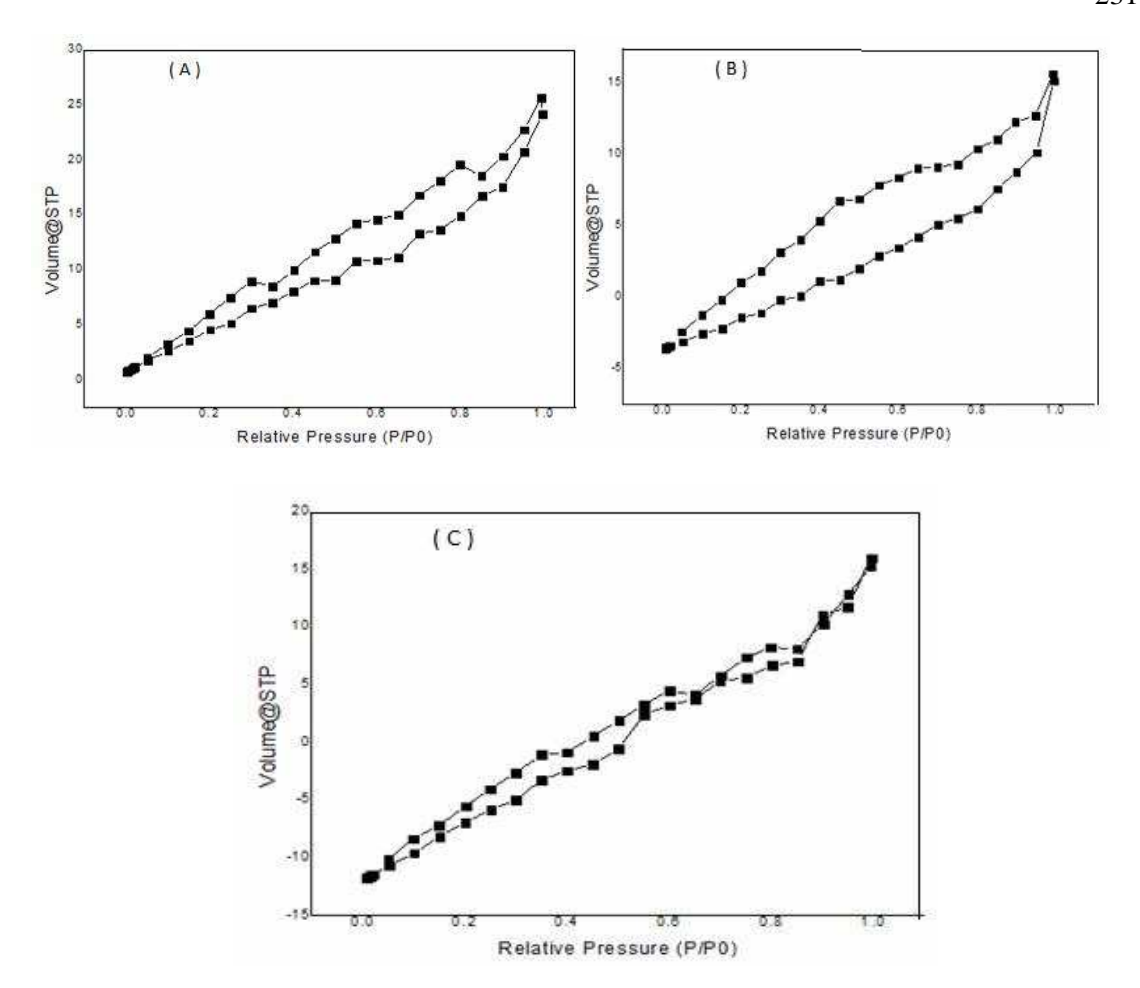


Figure 5.3.7 N_2 adsorption-desorption isotherm of the synthesized (A) BiOCl photocatalyst (B) 3 wt% AlF₃ doped BiOCl photocatalyst and (C) 3 wt% SrSiO₃ doped BiOCl photocatalyst.

Table 5.3.7 Surface area, pore volume and pore radius of bare-BiOCl, AlF₃-BiOCl and SrSiO₃-BiOCl photocatalysts.

Photocatalysts	Surface area (m²/g)	Pore Volume (cc/g)	Pore Radius (Å)
BiOCl	18.726	0.036	21.527
Aluminium Fluoride- BiOCl	14.837	0.030	15.280
Strontium silicate- BiOCl	20.577	0.039	21.548

5.3.8. Photocatalytic Studies

The effects of aeration, stirring of the reaction mixture and the extent of adsorption are a few factors that need to be taken into consideration to achieve an overall enhancement in the photocatalytic dye degradation process. Hence in the present study a preliminary analysis of decolourization of acid green 1 dye was studied under varying conditions as shown in figure 5.3.8 A. About 13 % decolourization of the dye is achieved by effective air purging in the presence of bismuth oxychloride catalyst at room temperature. Similarly 9% decolourization of acid green 1 dye is achieved in the presence of bismuth oxychloride catalyst at room temperature without air purging. However, under sunlight in the absence of BiOCl catalyst about 4% decolourization of the dye is achieved by purging air into the reaction mixture. From the experimental studies carried out it is understood that the use of a photocatalyst and effective air purging into the reaction mixture in the presence of sunlight is essential for the photocatalytic dye decolourization process.

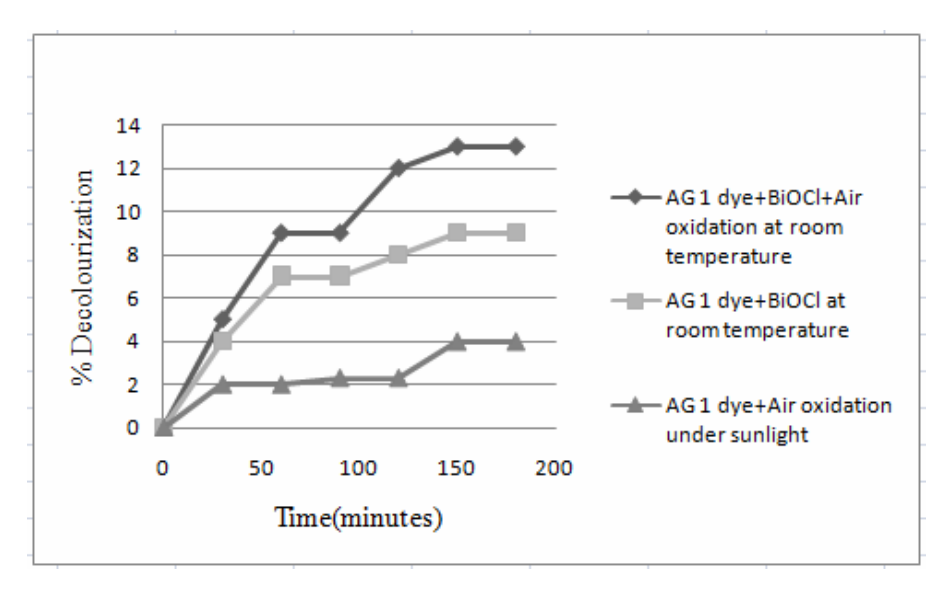


Figure 5.3.8 Primary analysis of acid green 1 dye solution using bismuth oxychloride photocatalyst.

(**Reaction conditions:** Acid green 1 dye solution (Conc. 1.13×10^{-5} mol/L; volume = 50mL), BiOCl catalyst = 25mg/50mL, without pH adjustment, air supply $\cong 2.5$ L/min, $I_{solar} = 699 \times 100 \pm 100$ lux.)

5.3.9. Effect of pH on the photocatalytic dye decolourization process

The solution pH is one of the most significant parameter that determines the electrostatic interaction between the catalyst and the substrates during the photocatalytic dye degradation process. The zero point charge of bismuth oxychloride catalyst is 4 below which the surface of the catalyst becomes positively charged and above this pH level the surface of the bismuth oxychloride catalyst is negatively charged. The maximum degradation of acid green 1 dye is observed at pH 5 this may be due to the fact that under acidic conditions the surface of bismuth oxychloride catalyst has a positive charge and attracts the anionic acid green 1 dye. However under extreme pH conditions, a large decrease in the dye degradation is observed this might be due to the fact that the three SO₃ groups of the acid green dye strongly adsorbs to the positively charged surface of bismuth oxychloride catalyst thus preventing the interaction of the light source with the catalyst and hence decrease in the photocatalytic dye degradation is observed similarly, at high alkaline pH levels the electrostatic repulsion taking place between the negatively charged surface of BiOCl catalyst and the SO₃ groups of the acid green dye leads to a decrease in the photocatalytic degradation process. The photocatalytic degradation of acid green 1 dye using bismuth oxychloride catalyst at various pH levels ranging from 2 to 12 is shown in figure 5.3.9 respectively.

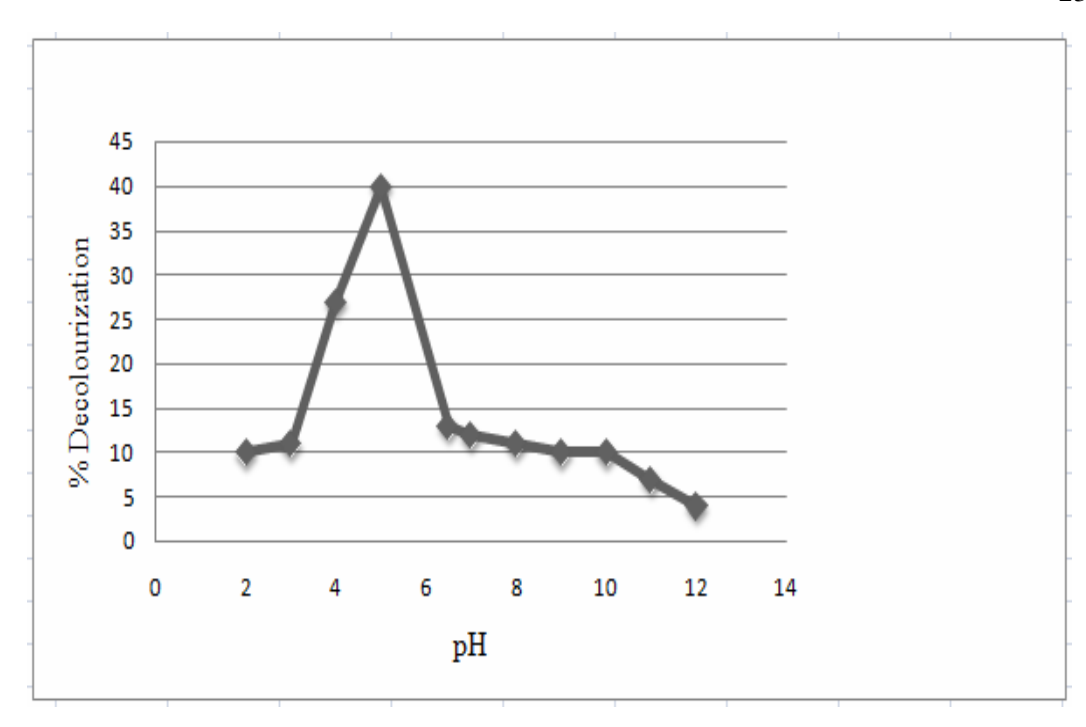


Figure 5.3.9 Effect of pH on the photocatalytic decolourization of acid green 1 using bismuth oxychloride catalyst.

(**Reaction conditions:** Acid green 1 dye solution (Conc. 1.13×10^{-5} mol/L; volume =50mL), BiOCl catalyst = 25mg/50mL, pH variation = 2-12, air supply $\cong 2.5$ L/min, $I_{solar} = 757 \times 100 \pm 100$ lux, Time=30 minutes)

5.3.10. Effect of Catalyst Concentration

Initially, the overall rate and removal efficiency in a photocatalytic process is directly proportional to the amount of catalyst however beyond a certain limiting value the reaction rate is independent of the catalyst concentration. Therefore, the excessive use of the photocatalyst will only decrease the rate of degradation process and it also increases the overall cost of treatment process. Hence, optimizing the catalyst dosage is necessary to achieve good photocatalytic efficiency. The optimum level of bismuth oxychloride catalyst for the photodegradation of the acid green 1 dye is found out from the experimental studies as shown in figure 5.3.10. For acid green 1 dye solution (2.27x10⁻⁵M), 15mg of BiOCl photocatalyst showed maximum degradation efficiency

at slightly acidic pH 5, beyond which a decrease in the photocatalytic degradation efficiency is noted. From the experimental studies it is observed that initially by increasing the catalyst dosage the degradation efficiency also increases, it then limits and finally decreases at high dosage. Initially on increasing the catalyst dosage dye adsorption capacity to the catalyst surface increases and the number of surface actives sites of the catalyst available for the dye molecule also increases, leading to a faster degradation of the dye molecules⁶¹. Similarly, a decrease in the photodegradation process is evidenced beyond the addition of a certain limit of catalyst dosage this is due to the reason that the turbidity of the dye solution increases at higher catalyst dosage levels thereby increasing the light scattering and reducing the penetration of the light source into the reaction mixture⁶².

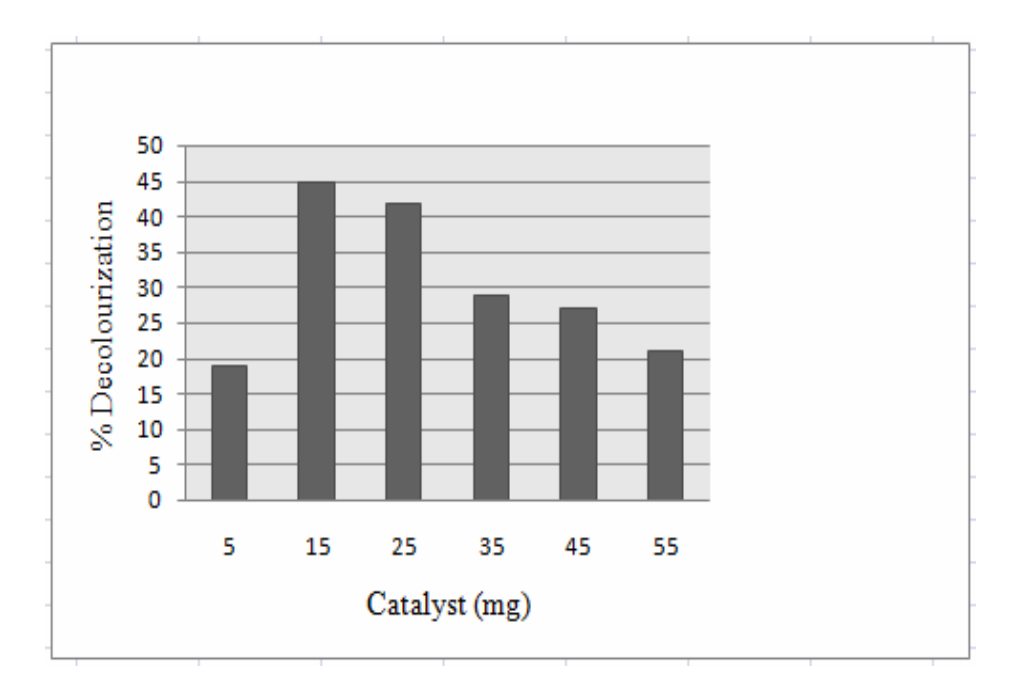


Figure 5.3.10 Effect of bismuth oxychloride catalyst concentration on the photocatalytic decolourization of acid green 1 dye.

(Reaction conditions: Acid green 1 dye solution (Conc. 1.13×10^5 mol/L; volume = 50mL), catalyst weight = 5mg-55mg, pH = 5, air supply $\cong 2.5$ L/min, $I_{solar} = 723 \times 100 \pm 100$ lux, Time=30 minutes)

5.3.11. Effect of Initial dye concentration

The rate of dye degradation strongly depends on the interaction of the dye molecules with the photocatalyst and the abundance or the concentration of the dye molecules with respect to the catalyst particles is an important factor that is to be optimized to achieve an effective degradation of the dyes. The concentration of acid green 1 dye is optimized by carrying out the photocatalytic dye degradation at different dye concentrations ranging from 1.13x10⁻⁵M to 5.69x10⁻⁵M at an optimized pH level of 5 with a catalyst dosage of 15mg. About 75% degradation of acid green 1 dye is observed at a concentration of 2.27x10⁻⁵M under optimized catalyst and pH levels within 180 minutes as shown in figure 5.3.11. A decrease in the photocatalytic degradation of the dye is observed beyond a concentration level of 2.27x10⁻⁵M this is due to the fact that on increasing the concentration of the dye solution, the number of dye molecules competing for the surface active sites of the catalyst also increases. Hence, the presence of excessive amount of dye in the water decreases the overall efficiency of the photocatalytic process⁶³. Similarly, the increase in the dye concentration beyond the optimal limit will act as a blocking surface between the incident photons and the catalyst surface which leads to a decrease in the generation of reactive species such hydroxyl and superoxide anion radicals and hence, the rate of photocatalytic dye degradation also decreases⁶⁴.

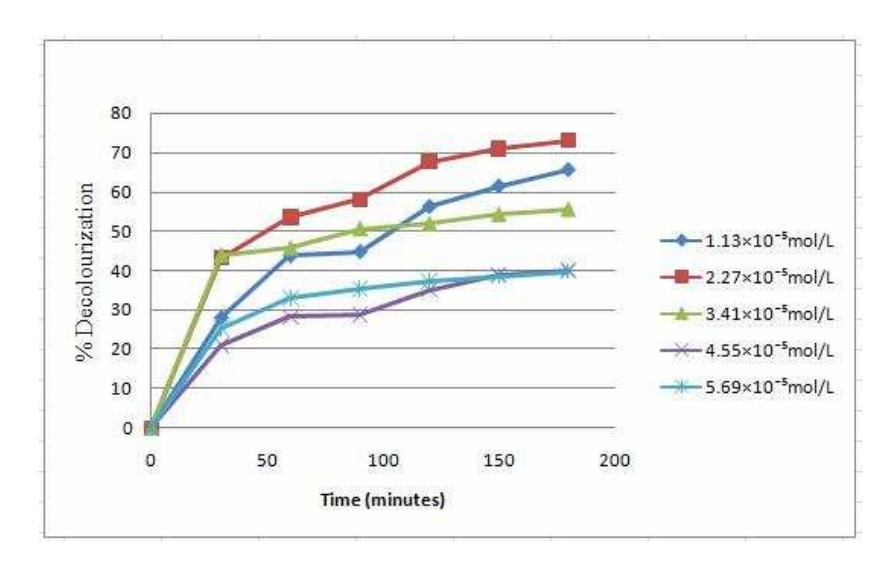


Figure 5.3.11 Effect of initial concentration of acid green 1 on photocatalytic decolourization using BiOCl catalyst.

(Reaction conditions: Acid green 1 dye concentration varied from $1.13 \times 10^{-5} \text{mol/L} - 5.69 \times 10^{-5} \text{mol/L}$, volume of dye solution =50mL, catalyst concentration=15mg, pH= 5, air supply $\cong 2.5 \text{L/min}$, $I_{\text{solar}} = 857 \times 100 \pm 100 \text{ lux}$)

5.3.12. Effect of Addition of Aluminium Fluoride and Strontium silicate to BiOCl photocatalyst

In recent years bismuth related materials have gained much interest among the environmental chemists due to their stable chemical and optical properties, easy synthesis and non-toxic nature. For example, Pan et al⁶⁵ reported the photocatalytic degradation of bisphenol A using BiOI catalyst, Cheng et al⁶⁶ illustrated the photocatalytic efficiency of visible light responsive 3D-BiOBr hollowspheres for the removal of toxic chromium metal ion from water and Gondal et al⁶⁷ reported the photocatalytic decolourization of Rhodamine 6G dye under monochromatic pulsed laser light using BiOCl photocatalyst. Similarly other bismuth related materials such as BiVO₄, BiPO₄, Bi₃NbO₇, (BiO)₂CO₃, β- and α-Bi₂O₃ are reported to show excellent photocatalytic activity towards the degradation of toxic organic pollutants.

Fascinating photocatalytic applications of layer structured bismuth materials made researchers to explore more potentiality of the bismuth based photocatalysts by enhancing the photon absorption properties, separation of the electron-hole pairs and narrowing of the band gap energies. Researchers explored the photocatalytic performance of many unprecedented bismuth based materials with low cost to cope up with the industrial needs. Some of them are Graphene-Bi₂MoO₆ for the photocatalytic degradation of reactive brilliant red X-3B under visible light radiation, C₃N₄/BiPO₄ and bismuth oxyiodide-TiO₂ composites are used for the removal of methylene blue, bismuth sulphide-bismuth oxyiodide composite for the breakdown of methyl orange, Ag/AgCl/BiOCl composite photocatalyst for the degradation of Rhodamine B dye under visible light radiation, F-doped Bi₂WO₆ photocatalyst for the degradation of rhodamine B under simulative sunlight, Co- doped BiVO₄ photocatalyst for the degradation of methylene blue dye under visible light radiation, Al-BiOBr photocatalyst for the degradation of methyl orange dye under visible light radiation, $\mathrm{Sm}^{\mathrm{3+}}$ and $\mathrm{Eu}^{\mathrm{3+}}$ doped β-Bi₂O₃ photocatalyst for the degradation of methylene blue and Rhodamine B dyes under solar and simulated solar irradiation⁶⁸.

From the literature sources it is understood that very scarce attempts have been made to modify bismuth oxychloride photocatalyst with aluminium fluoride and strontium silicate. Hence, in the present work, bismuth oxychloride photocatalyst is modified by adding different weight percent (0.5-3%) of aluminium fluoride and strontium silicate salts, and evaluated its photocatalytic activity towards the degradation of acid green 1 dye as shown in figure 5.3.12 A, B. From the experimental studies carried out it is observed that the time taken for the degradation of the acid green 1 dye using AlF₃/BiOCl photocatalyst as well as SrSiO₃/BiOCl photocatalyst is very less compared to that with bare bismuth oxychloride photocatalyst.

About 80% degradation of acid green 1 dye (2.27x10⁻⁵M) under optimized conditions catalyst weight 15mg/50mL, pH 5 was achieved within 90 minutes using 3wt% AlF₃ doped bismuth oxychloride photocatalyst and similarly, 3wt % SrSiO₃/BiOCl catalyst degraded 74% of acid green 1 dye (2.27x10⁻⁵M) within 90 minutes respectively.

Compared to the pure bismuth oxychloride and strontium silicate/BiOCl photocatalyst the time taken by the aluminium fluoride doped bismuth oxychloride photocatalysts to degrade the dye is very less this can be attributed to the fact that introduction of the impurity atoms to the pure bismuth oxychloride catalyst creates new energy levels above the valence band and below the conduction band there decreasing the band gap energy and these dopants act as trapping centers for the charge carriers and they also facilitate the migration of the electron and holes to the surface reaction sites of bismuth oxychloride catalyst increasing the photonic efficiency in generating reactive radical species for the degradation of these synthetic organic dyes from the aqueous solution. Similarly, the decrease in the photocatalytic activity after reaching a certain dopant concentration for the degradation of the acid green 1 dye might be due to the fact that the trapping centres created by the introduction of the dopants to the pure BiOCl photocatalyst may sometimes act as recombination centres for the electrons and holes which might lead to the decrease in their photocatalytic efficiency.

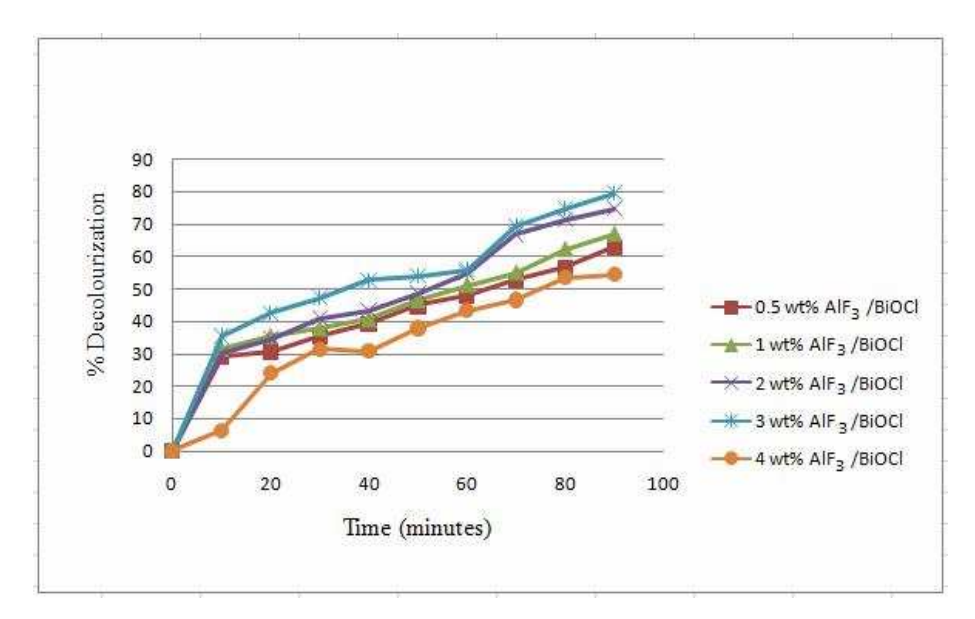


Figure 5.3.12 A Photocatalytic decolourization of acid green 1 dye using different weight percent of aluminium fluoride doped BiOCl catalyst.

(Reaction conditions: Acid green 1 dye concentration = $2.27 \times 10^{-5} \text{mol/L}$, volume of dye solution =50 mL, weight percent of AlF₃ varied from (0.5-4 wt %), AlF₃/BiOCl catalyst weight =15 mg, pH=5, air supply $\cong 2.5 \text{L/min}$, $I_{\text{solar}} = 728 \times 100 \pm 100 \text{lux}$)

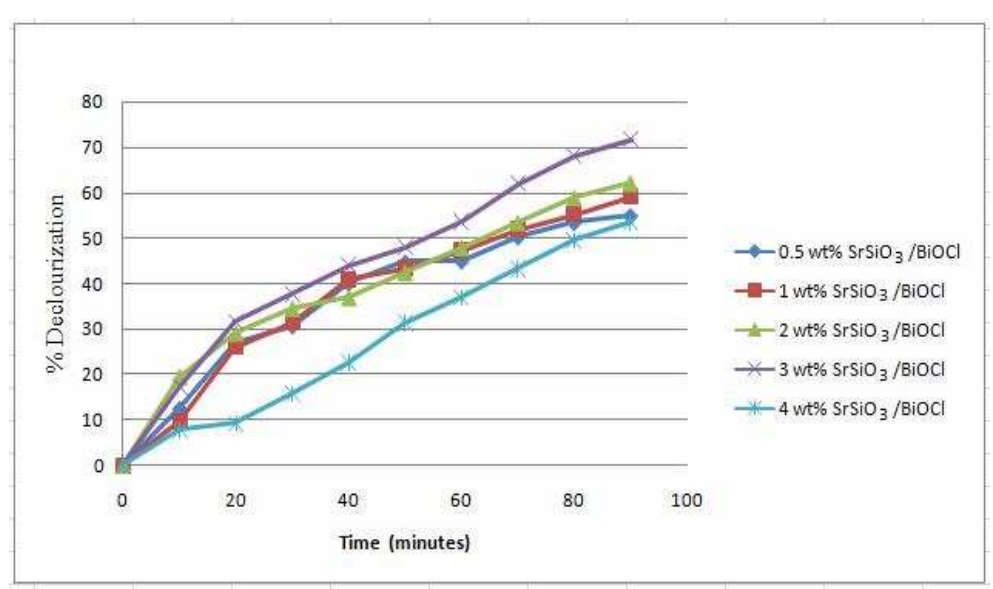


Figure 5.3.12 B Photocatalytic decolourization of acid green 1 dye using different weight percent of Strontium silicate doped BiOCl catalyst.

(Reaction conditions: Acid green 1 dye concentration = 2.27×10^{-5} mol/L, volume of dye solution =50mL, weight percent of SrSiO₃ varied from (0.5-4 wt %), SrSiO₃/BiOCl catalyst weight =15mg, pH=5, air supply $\cong 2.5$ L/min, $I_{solar} = 728 \times 100 \pm 100$ lux)

5.3.13. Kinetic Studies

For the photocatalytic degradation of acid green 1 dye (2.27x10⁻⁵M) studied at optimized pH level 5 using aluminium fluoride and strontium silicate (0.5-4%) doped bismuth oxychloride catalysts, the rate and order of the reaction is studied by Langmuir-Hinshelwood kinetic model using the expression $\ln (C_0/C)$ versus time 't'. The R² values obtained for decolourization of acid green 1 using 0.5-4 wt % of AlF₃ doped BiOCl photocatalysts are 0.996, 0.983, 0.966, 0.978, 0.981 and the rate constant values are 9.22×10^{-3} , 1.16×10^{-2} , 4.60×10^{-2} , 9.78×10^{-2} and 6.80×10^{-2} min⁻¹. Similarly, R² values obtained for decolourization of acid green 1 using 0.5-4 wt % of SrSiO₃ doped BiOCl photocatalysts are 0.987, 0.976, 0.985, 0.963, 0.982 and the rate constant values are 8.90×10^{-3} , 9.60×10^{-3} , 1.0×10^{-2} , 8.75×10^{-2} and 5.30×10^{-2} min⁻¹ and for bare BiOCl catalyst the R² value and rate constant value is 0.946 and 8.60x10⁻³ min⁻¹. Recently, S. Seddigi et al⁶⁹ investigated the kinetics of photocatalytic degradation of synthetic organic dyes such as methylene blue and methyl orange by Langmuir-Hinshelwood kinetic model, the plot of $-\ln(C/C_0)$ vs 't' made by them showed that the reaction followed first order kinetics with respect to the catalyst concentration. In the present work, a linear fit obtained between $\ln (C_0/C)$ versus time 't' and the R^2 values close to unity reveals that the photocatalytic degradation of acid green dye using different weight percent of AlF₃ and SrSiO₃-loaded BiOCl photocatalysts followed pseudo-first order kinetics.

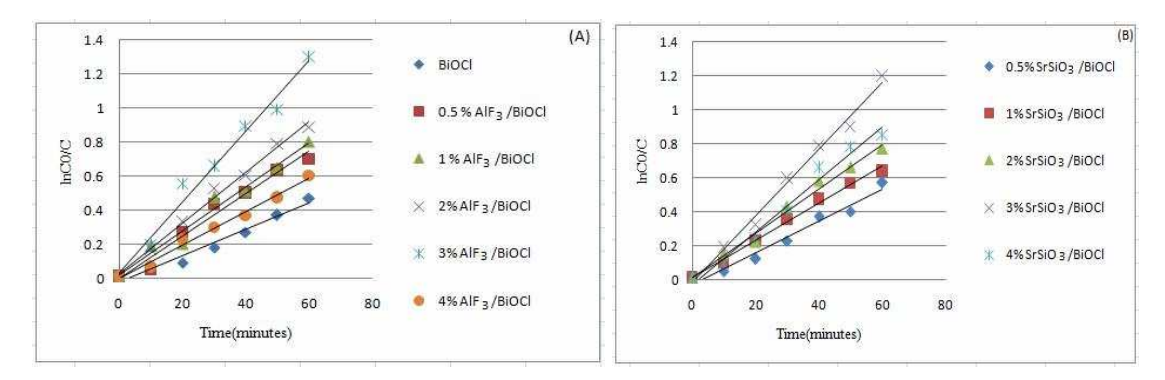


Fig. 5.3.13 shows the plot of $\ln C_0/C vs't'$ for the photocatalytic decolourization of acid green 1 using (A) undoped BiOCl and (0.5-4 wt%) AlF₃ doped BiOCl and (B) using (0.5-4 wt %) SrSiO₃ doped BiOCl photocatalyst.

5.3.14. UV-Visible Spectroscopic Analysis

The UV-Visible absorption studies is carried out for the photocatalytic degradation of the acid green 1 dye using AIF₃/BiOCl and SrSiO₃/BiOCl photocatalysts to understand the extent of destruction of the chromophoric groups present in the dye. The most prominent absorption peak of the acid green 1 dye observed at around 715nm decreases continuously during the course of the reaction as shown in figures 5.3.14 A, B and the inset shows the change in the colour of the dye from green to colourless which is due to the destruction of the chromophoric nitroso group present in the dye. With the increase in the reaction time, the decrease in the intensity of the peak at 715 nm of the dye is monitored with the help of UV-Visible spectrophotometer and it is observed that a maximum decrease in the intensity of the peak is reached within 90 minutes during the photocatalytic treatment using AIF₃/BiOCl catalyst which implies that the aluminium fluoride incorporated bismuth oxychloride catalyst is effective in the destruction of the nitroso dye (Acid green 1) indicating that the fragment of the dye do not contain any chromophoric groups which is evidenced from the UV-Visible absorption studies.

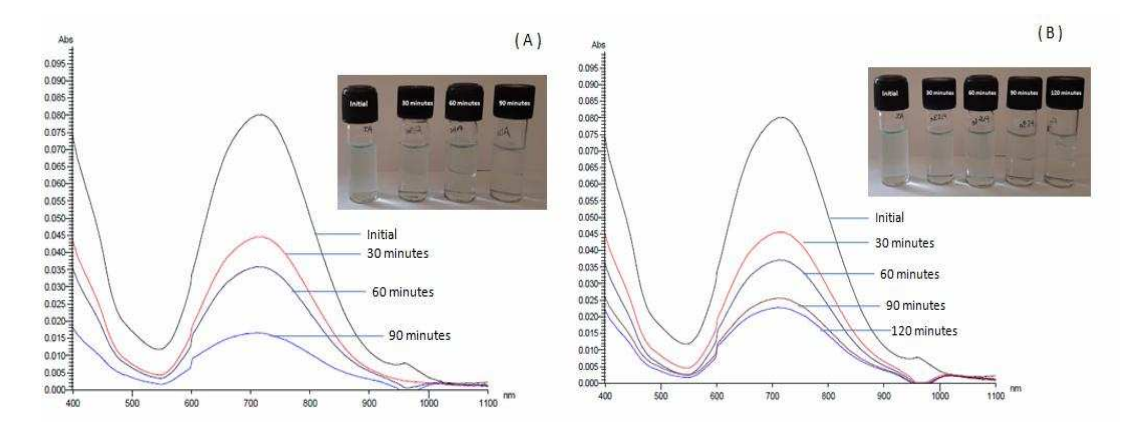


Figure 5.3.14 UV-Visible absorption spectra showing the decolourization of acid green 1 in the presence of (A) AlF₃/BiOCl and (B) SrSiO₃/BiOCl photocatalysts.

5.3.15. Comparison of the Efficiencies of Different Photocatalysts

The degradation efficiencies (in terms of % decolourization) of bare bismuth oxychloride and different weight percents (0.5-4 wt%) of aluminium fluoride and strontium silicate doped bismuth oxychloride photocatalysts is compared for the synthetic dye acid green 1 and the values are shown in table 5.3.15.

For acid green 1 dye degradation at optimum conditions such as dye concentration (2.27x10⁻⁵M, pH 5, catalyst weight 15mg/50mL) under solar radiation for 90 minutes, the degradation efficiencies of different photocatalysts are shown below:

 $3\%AlF_3/BiOCl > 2\% AlF_3/BiOCl > 3\% SrSiO_3/BiOCl > 1\% AlF_3/BiOCl > 0.5\%AlF_3/BiOCl = 2\% SrSiO_3/BiOCl > 1\% SrSiO_3/BiOCl > BiOCl > 0.5\% SrSiO_3/BiOCl > 4\% AlF_3/BiOCl <math>\approx$ 4% SrSiO_3/BiOCl

From the comparative analysis, it is observed that aluminium fluoride doped bismuth oxychloride photocatalyst are generally more efficient in degradading the acid green 1 dye compared to bare bismuth oxychloride photocatalyst and strontium silicate doped bismuth oxychloride photocatalyst.

The degradation efficiencies of the photocatalysts depend upon many factors such as the ability of the dye to get adsorbed on the photocatalyst, structure and concentration of the dyes and absorption of light by photocatalysts. In the overall process, a maximum of 80% degradation of the acid green 1 is achieved with 3 wt% AlF₃/BiOCl photocatalyst within 90 minutes of time under sunlight compared to strontium silicate and undoped bismuth oxychloride photocatalysts.

Table 5.3.15 Comparison of the efficiencies (in terms of % decolourization) of doped and undoped bismuth oxychloride oxide photocatalysts towards acid green 1.

Photocatalysts	Acid green 1 dye (Optimized conditions: pH=5, Catalyst weight=15mg/50mL, Initial dye concentration= (2.27x10 ⁻⁵ mol/L), Time=90 minutes.)	
Bare BiOCl	58	
0.5% AlF ₃ /BiOCl	62	
1% AlF ₃ /BiOCl	67	
2% AlF ₃ /BiOCl	74.8	
3% AlF ₃ /BiOCl	80	
4% AlF ₃ /BiOCl	54	
0.5% SrSiO ₃ /BiOCl	55	
1% SrSiO ₃ /BiOCl	59	
2% SrSiO ₃ /BiOCl	62	
3% SrSiO ₃ /BiOCl	71.6	
4% SrSiO ₃ /BiOCl	53.5	

5.3.16. Effect of Free radical scavenging activity

In order to understand the involvement of reactive species and mechanism of photocatalytic degradation process an indirect chemical probe method was adopted with scavengers of various possible active species. The generation of reactive species such as h^+ , OH, O_2 and e^- during the photocatalytic process is investigated by the addition of radical quenchers such as EDTA, isopropyl alcohol, ascorbic acid and sodium sulphate. For investigating the effect of radical scavenging activity, 1mM solution of the radical quenchers such as EDTA, isopropyl alcohol, ascorbic acid and sodium sulphate are added to the dye solutions at optimized pH, catalyst and dye concentrations and a blank experiment is also carried out without the addition of quenchers under identical conditions. For the photocatalytic degradation of acid green 1 dye using the most active 3 wt%-AlF₃/BiOCl catalyst about 80% degradation of the dye is achieved in the absence of any quencher and about 32%, 58%, 29% and 47% degradation is achieved by the addition of quenchers such as EDTA, isopropyl alcohol, ascorbic acid and sodium sulphate respectively. The experimental results clearly shows that compared to electrons and hydroxyl radicals, the involvement of holes and superoxide anion radical species are significant during the photocatalytic process. Similarly Pingmuang et al⁷⁰ reported that the addition of benzoquinone as a superoxide anion radical scavenger completely quenched the degradation reaction of methylene blue and Rhodamine B dyes using BiVO₄ catalyst.

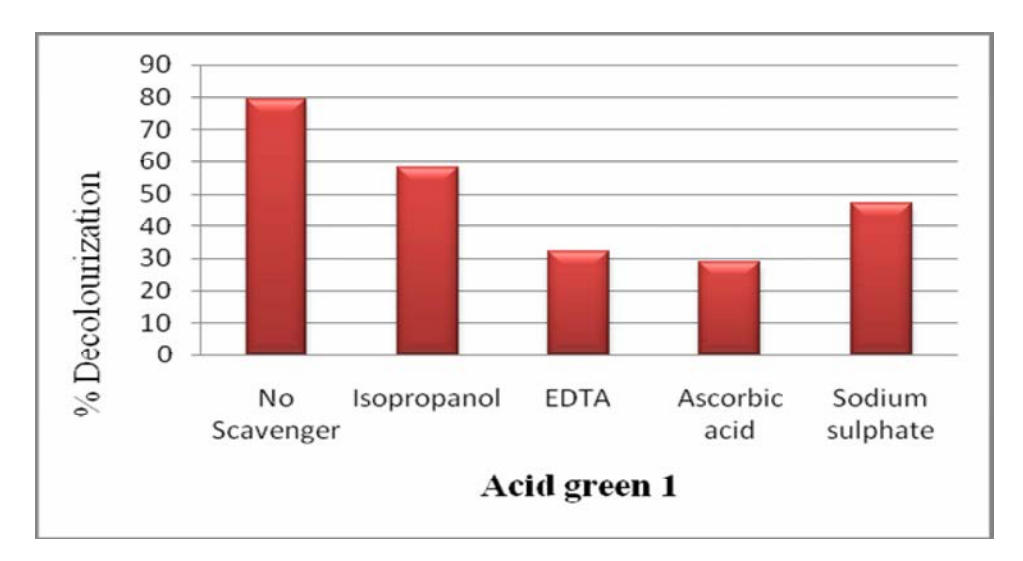


Figure 5.3.16 Effect of radical scavengers for the photocatalytic degradation of acid green 1 dye using 3wt % AlF₃/BiOCl photocatalyst under optimized conditions.

5.3.17. Mineralization Studies

Only 10-20 % reduction in the total organic carbon content level is achieved by conventional water treatment methods⁷¹. Advanced oxidation process such as heterogeneous photocatalysis using semiconductors, is a great technology that degrades the toxic organic pollutants to harmless mineralized products. In order to confirm the degradation of acid green 1 dye (2.27x10⁻⁵), total organic carbon measurements is carried out for the aqueous dye sample before and after the photocatalytic treatment with 3 wt % AlF₃/BiOCl at optimum pH and catalyst concentration under sunlight. About 52.7% degradation of the acid green 1 dye is achieved after 90 minutes of sunlight irradiation whereas from the spectrophotometric measurement it is observed that 79% decolourization of the acid green 1 dye is achieved. The results obtained suggest that the complete mineralization of dye molecule into CO₂, H₂O and mineral acids might take longer time.

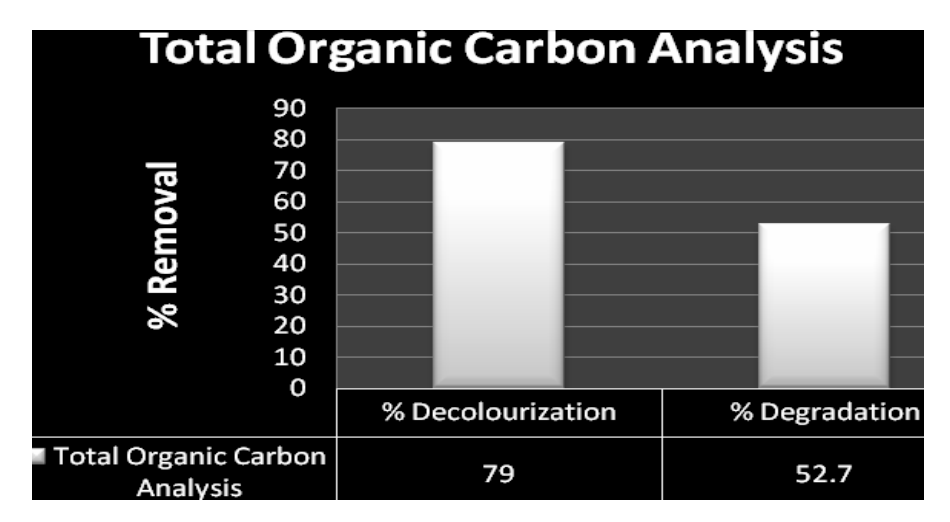


Figure 5.3.17 shows the percentage removal of total organic carbon in the aqueous solution of acid green 1 dye using 3wt% AlF₃/BiOCl photocatalyst under optimized conditions.

5.3.18. Reusability Studies

Evaluation of the recyclability and reusability of the photocatalyst is significant for large scale effluent treatment process⁷². Hence, in the present work the reusability of the most active catalyst 3 wt% AIF₃/BiOCl is checked against acid green 1 dye. The photocatalyst is recovered by centrifugation, dried and reused with fresh dye solutions and the absorbance is recorded using UV-Visible spectrophotometer. From the reusability studies, it is observed that the only a negligible decrease of 5 % loss in photocatalytic activity occurred until three cycles. However, in the 4th and 5th runs a significant loss of photocatalytic activity occurred from 79 to 48% which suggests that the aluminium fluoride loaded bismuth oxychloride photocatalyst can be efficiently reused for three repeated cycles.

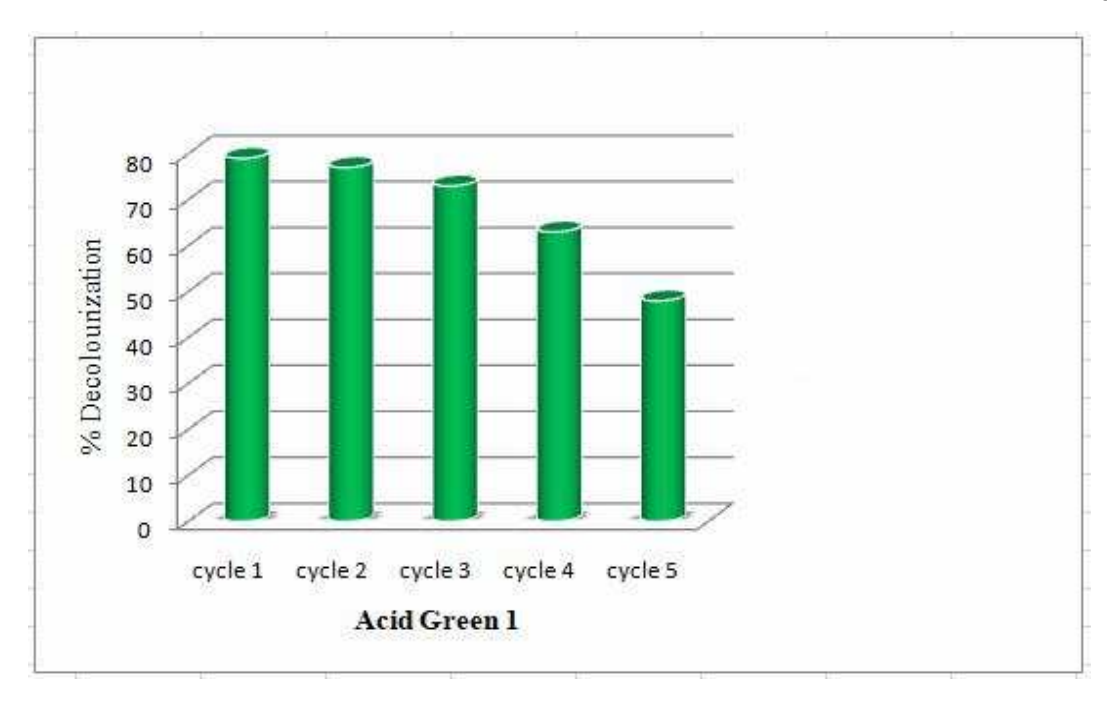


Figure 5.3.18 shows the reusability of the most active 3 wt % AlF₃/BiOCl catalyst for the photocatalytic degradation of acid green 1 dye.

5.3.19. Proposed Mechanism

Bismuth oxychloride is a layered semiconductor photocatalyst with unique photoelectric properties and is found to show good photocatalytic performance⁷³. Under sunlight radiation, the electrons in the valence band of BiOCl photocatalyst is excited to generate electron hole pairs and the redox reactions are initiated as shown below

excited to generate electron note pairs and the redox reactions are initiated as shown below				
$BiOCl + hv \rightarrow BiOCl (h^{+}_{VB} + e^{-}_{CB})$	eq.(5.35)			
BiOCl (h^+_{VB}) + $H_2O \rightarrow BiOCl + H^+ + ^-OH$	eq.(5.36)			
BiOCl (h^+_{VB}) + $^-OH \rightarrow$ BiOCl + ^+OH	eq.(5.37)			
BiOCl (e^{-}_{CB}) + O ₂ \rightarrow BiOCl + O ₂ .	eq.(5.38)			
O_2 · $+ H^+ \rightarrow HO_2$ ·	eq.(5.39)			
HO_2 + H^+ + BiOCl (e^{CB}) \rightarrow H_2O_2 + BiOCl	eq.(5.40)			
$H_2O_2 + BiOCl (e^{CB}) \rightarrow OH + OH + BiOCl$	eq.(5.41)			
Dye + 'OH/O ₂ ' \rightarrow Degradation products	eq.(5.42)			

The fast recombination of the photogenerated electrons and holes in the BiOCl photocatalyst has limited its practical applications in water treatment process. Hence, in order to overcome this limitation and enhance the sunlight absorption ability, numerous studies and modifications on the BiOCl photocatalyst is carried out in recent years. Some of the common methods adopted for the modification of BiOCl photocatalyst include ion doping, coupling, photosensitization, noble metal deposition etc. Among various methods adopted doping of metal ions was reported to be effective in enhancing the light absorption ability and accelerating the separation of electron hole pairs in the bismuth oxychloride photocatalyst⁷⁴.

In view of these facts, doping of the bare BiOCl photocatalyst with metals such as 'Al' and 'Sr' was done for the present work. Doping creates additional energy levels that is above the valence band edge and below the conduction band edge of BiOCl photocatalyst acting as both electron and hole traps.

From the photocatalytic studies, it was observed that the doping of aluminium fluoride salt to the bismuth oxychloride photocatalyst led to a faster degradation of the synthetic dye acid green 1 compared to strontium silicate modified BiOCl and undoped BiOCl photocatalysts.

The lower photocatalytic activity of strontium silicate doped-BiOCl photocatalyst can be ascribed to the following reasons:

Strontium silicate used as a dopant distorts the lattice sites, creates defects and occupies the photocatalytically active sites of bismuth oxychloride photocatalyst thereby reducing the number of active sites available for the photocatalytic reaction.

Addition of excess amount of strontium silicate dopant to bismuth oxychloride sites might have resulted in recombination centers for the photogenerated electron-hole pairs resulting in a decreased photocatalytic activity.

The higher photocatalytic activity of aluminium fluoride doped bismuth oxychloride photocatalyst compared to the undoped and SrSiO₃ doped BiOCl photocatalysts can be attributed to the fact that the introduction of 'Al' to the BiOCl catalyst may act as trapping centers for the photogenerated electrons and holes. The additional energy states created by the introduction of Al³⁺ ions to the [Bi₂O₂]Cl lattices lead to a reduction in the bandgap values, and Al³⁺ ions trap the photogenerated electrons and holes to form less stable Al²⁺/Al⁴⁺ ions which further react with the surface adsorbed O₂ and hydroxyl ions to form the reactive species such as hydroxyl and superoxide anion radicals. The plausible mechanism is depicted as given below:

The superoxide anion radical and hydroxyl radicals generated in situ are highly reactive species that triger the degradation of dyes.

$$Dye^{-+} + O_2^{--} \rightarrow Degradation products$$
 eq.(5.48)

$$Dye^{+} + OH \rightarrow Degradation products$$
 eq.(5.49)

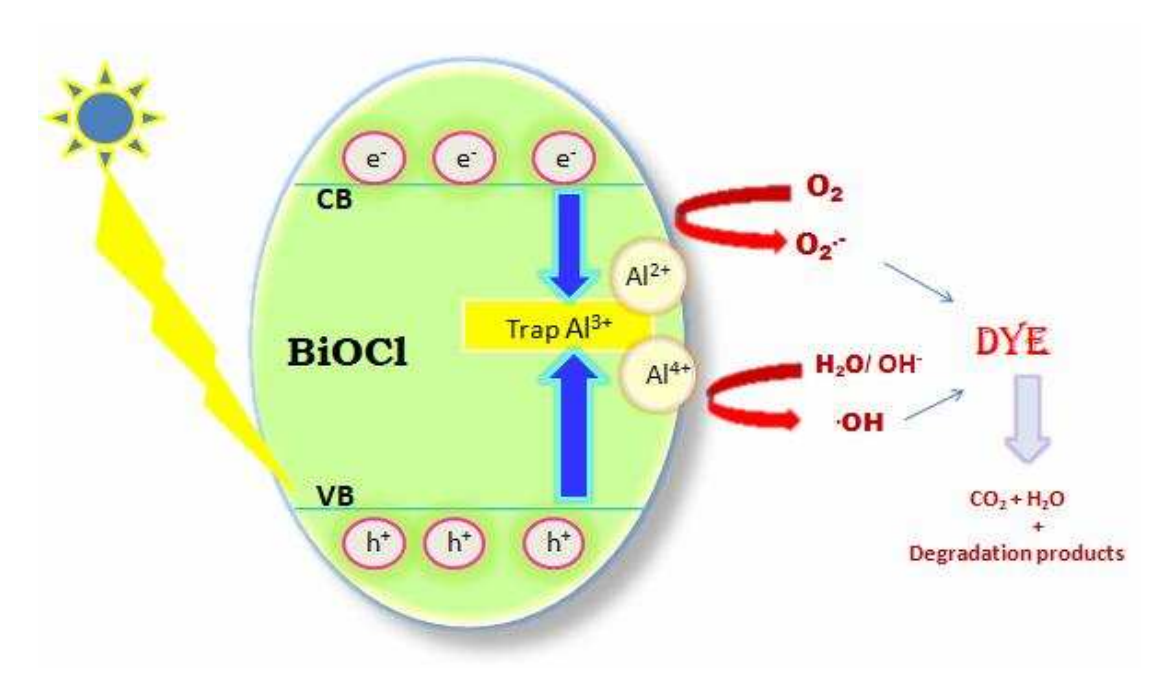


Figure 5.3.19 Perspective mechanism for the degradation of dye mediated by AlF₃/BiOCl catalyst under sunlight.

Similarly, Cao et al⁷⁵ reported that the doping of 'Mn' to BiOCl photocatalyst has improved the light absorption ability and separation of electron hole pairs which in turn increased the photocatalytic performance of the BiOCl catalyst. Recently Sheng et al⁷⁶ reported the synergistic effect of Cd²⁺ and Fe²⁺ reduced the band gap energy level of bismuth oxybromide photocatalyst and the introduction of impurity energy levels by Cd²⁺ and Fe²⁺ doping enhanced the electronic transitions and utilization of the electrons and holes in the photocatalytic redox reactions.

5.4. EFFLUENT TREATMENT AND ANTIMICROBIAL ACTIVITY OF 2%AlF₃-ZnO/1%AlF₃-TiO₂/3%AlF₃-BiOCl PHOTOCATALYST

The best photocatalysts among the aluminium fluoride and strontium silicate doped ZnO, aluminium fluoride and strontium silicate doped TiO₂ as well as aluminium fluoride and strontium silicate doped BiOCl were identified from the photocatalytic study. In order to understand the practical utility of these photocatalysts, the synthesized photocatalysts 2wt%AlF₃-ZnO/1wt%AlF₃-TiO₂/3wt% AlF₃-BiOCl were mixed in equal weight ratios(1:1:1) and used for the treatment of the collected effluent. The antimicrobial property of the synthesized 2wt%AlF₃-ZnO/1wt%AlF₃-TiO₂/3wt%AlF₃-BiOCl composite photocatalyst and the mechanism of antimicrobial action are studied and the details are discussed below in the following sub-sections

5.4.1. Effluent Treatment

The effluent released from the dyeing house is highly polluted and is visible with unacceptable color, high biological oxygen demand, chemical oxygen demand, dissolved solids, surfactants and traces of metals. The toxic organic contaminants present in the released wastewater is highly resistant to chemical, physical and biological degradation process and persist in the environment for a long period of time giving rise to several health issues and unnecessary damage to environment. The major cause for the visibility of the intense color in the released wastewater is the incomplete fixing of the dyes to the fabric. The amount of dye lost during the process of dyeing depends upon the application method, type and quality of the fabric used and upon the depth of the shades required as per the demand. In order to control water pollution our government has set forth general standards for the release of wastewater from the industries. The permissible limit for the discharge of wastewater is given below in table 5.4.1.

Table 5.4.1 Permissible limits for the discharge of wastewaters according to Indian Standards

Parameters	Discharge of wastewater into inland surface	Discharge of wastewater into Sewers	Discharge of wastewater for irrigation
Colour (Hazen units)	25	300	-
Odour	unobjectionable	unobjectionable	unobjectionable
Suspended solids(mg/L), max	100	600	200
Total dissolved solids (mg/L), max	2100	2100	1000
рН	5.5-9.0	5.5-9.0	5.5-9.0
Temperature (°C)	40	45	Shall not exceed 5°C above the receiving water temperature
Oil and grease (mg/L), max	10	20	10
Total residual chlorine (mg/L), max	1.0	-	-
Total nitrogen (mg/L), max	100	-	-
Biological oxygen demand (mg/L), max	30	350	100
Chemical oxygen demand (mg/L), max	250	-	-
Sulphide (mg/L), max	2.0	-	-
Fluorides (mg/L), max	2.0	15	-
Cadmium (mg/L), max	2.0	1.0	-
Mercury (mg/L), max	0.01	0.01	-
Nitrates(mg/L), max	10	-	-
Phenolic compounds (mg/L), max	1.0	5.0	
Iron (mg/L), max			
Arsenic (mg/L), max	0.2	0.2	0.2
Lead(mg/L), max	0.1	1.0	-
Zinc(mg/L), max	5.0	15	-
Selenium (mg/L), max	0.05	0.05	-

Total chromium (mg/L), max	2.0	2.0	-	
Copper (mg/L), max	3.0	3.0	-	
Nickel(mg/L), max	3.0	3.0	1	
Dissolved phosphates (mg/L), max	5.0	-	-	
Manganese (mg/L), max	2	2	-	
Vanadium (mg/L), max	0.2	0.2	-	
Free ammonia (mg/L), max	5.0	-	-	
Ammonical nitrogen (mg/L), max	50	50	-	
Bio-assay test	90% survival of fish after 96 hours in 100% effluent	90% survival of fish after 96 hours in 100% effluent	90% survival of fish after 96 hours in 100% effluent	
Radioactive materials (a) Alpha emitters micro curie (mg/L), max	10 ⁻⁷	10 ⁻⁷	10 ⁻⁶	
(b) Beta emitters micro curie (mg/L), max	10-6	10 ⁻⁶	10-7	

Very scarce attempts have been made by the researchers to check the applicability of the mixed photocatalysts for the treatment of real textile effluent. Recently, Khan et al 77 investigated the catalytic applicability of ZnO and TiO $_2$ photocatalysts and hydrogen peroxide for the effluent collected from Gul Ahamed industry in Karachi and reported that titanium dioxide showed efficient decolorization of the effluent (95%) compared to ZnO photocatalyst (64%) under UV irradiation within 150 minutes. Similarly, Nogueira et al 78 reported the photocatalytic treatment of mining and kraft pulp mill effluents using TiO $_2$ – Fe $_2$ O $_3$ /H $_2$ O $_2$ /UV and achieved 93%, 63% and 89% removal of color, aromatic compounds and chemical oxygen demand respectively.

In the present work the efficiency of the synthesized 2wt%AlF₃-ZnO/1wt%AlF₃-TiO₂/3wt% AlF₃-BiOCl photocatalyst is tested against the effluent under sunlight. As Tiruppur (Tamil Nadu, India) has a large cluster of dyeing units and is a hub of textile and manufacturing industries, this place was chosen for the sample collection. The colour of the collected effluent was deep green to black and in order to achieve efficient degradation, the collected effluent is initially filtered, diluted the effluent with water in the ratio (1:9) and subjected to photocatalytic degradation process. The decolourization of the effluent before and after the photocatalytic treatment is monitored using the UV-Visible Spectrophotometer shown in the following figure.

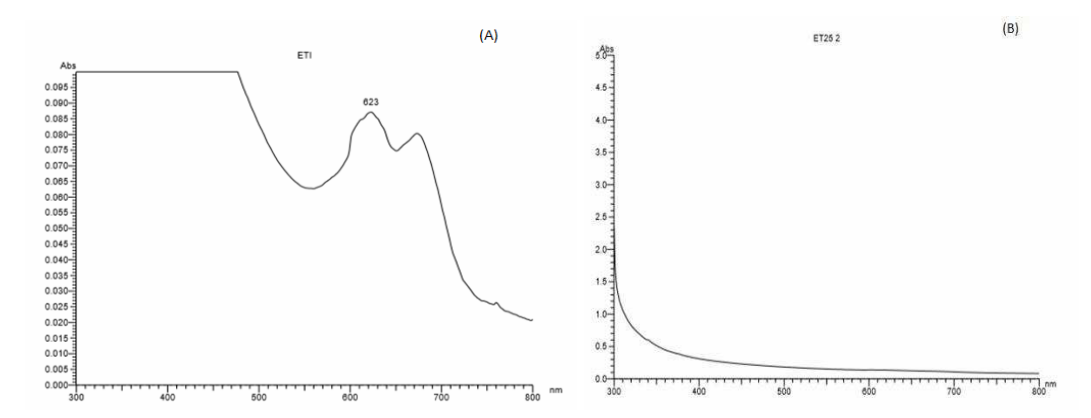


Figure 5.4.1 (A) UV-Visible absorption spectrum of the diluted effluent before the photocatalytic tretament (B) UV-Visible absorption spectrum of the effluent after the photocatalytic tretament

From the UV-Visible spectral studies, it is observed that the effluent before the photocatalytic treatment shows peaks at 623 nm, 292 nm and 244 nm. After the treatment of the effluent with 2wt%AlF₃-ZnO/1wt%AlF₃-TiO₂/3wt% AlF₃-BiOCl composite photocatalyst under direct sunlight with effective air purging it is observed the peak at 623 nm in the UV-Visible absorption spectrum completely disappeared however, the peaks at 292, 244 nm and the presence of peak at 273 nm shows that

although a drastic decrease in the colour of the effluent is achieved after the photocatalytic treatment, colorless pollutants still remain in the effluent and hence, a thorough analysis of the physico-chemical parameters of the effluent before and after the photocatalytic treatment is done to understand the extent of removal of the pollutants from the wastewater.

5.4.2. Analysis of the physico-chemical parameters of the Effluent

Colour

The intense color observed in the water resources located nearby manufacturing, textile, dyeing and printing units are due to the discharge of unfixed dyes, lignin, tannins, organic and inorganic chemicals. The humic and fulvic acids present in the water sources gives color and further the iron content in the water bodies increases the intensity of the color due to the formation of soluble ferric humates. Here, the collected effluent was deep green in color (550 Hazen units) which significantly reduced to < 1.0 Hazen units after the photocatalytic treatment.

Odor

Odor is an important parameter that affects the quality and aesthetics of the drinking water sources. Most organic and some inorganic chemicals that are discharged from the municipal and industrial areas, decayed vegetable matters and associated pathogens are a major cause for the unacceptable odor of the water. The odor of the effluent after the photocatalytic treatment is agreeable.

Turbidity

Clarity of the water source is an important determinant that needs to be evaluated before human consumption. The main reason for turbid water is due to contamination by dissolved organic and inorganic particulates. The turbidity measurements

of the samples are made in terms of Nephelometric turbidity units. The turbidity of the effluent before the photocatalytic treatment is found to be 128 NTU which has reduced to 116 NTU after the photocatalytic treatment process.

Electrical conductivity

The electrical conductivity depends on the mobility and concentration of the ions present in the water. The electrical conductivity of the effluent was 4394 Micromhos cm⁻¹ which decreased to 1523 Micromhos cm⁻¹ after the photocatalytic treatment process.

Total dissolved solids

The presences of high level of solid content in the water induces unfavorable physico-chemical reactions and are considered to be of inferior platability. Water sources with greater than 500mg/L of TDS are unsuitable for drinking purposes. The TDS of the effluent was 2636mg/L which reduced to 914mg/L after the photocatalytic treatment process.

Total suspended solids

Analyses of the solid content in the water and wastewater samples are important because the high concentration of suspended solids may be aesthetically unsatisfactory for bathing and other domestic purposes. The TSS of the effluent was 38mg/L which reduced to 29mg/L after the photocatalytic treatment process.

pН

The intensity of acidity or basicity of a solution is characterized by pH or hydrogen ion activity. The pH measurement is one of the important parameter required for every phase of water supply and especially in the wastewater treatment process. The pH at 25°C for the effluent was 8.12 which decreased to 7.5 after the photocatalytic treatment process.

Alkalinity

The alkalinity is referred to as the acid neutralizing capacity of the water. Total alkalinity is an important parameter that needs to be checked whether it is suitable for irrigation and domestic purposes. The alkalinity measured as CaCO₃ in the effluent was 829 mg/L which drastically reduced to 378 mg/L after the photocatalytic treatment process.

Total Hardness

The hardness of the water can be defined as the sum of the concentration of calcium and magnesium ions. The total hardness of a sample can vary from zero to hundreds of milligrams per liter depending upon the source. The total hardness of the effluent was calculated to be 460 mg/L which after the photocatalytic treatment process was below the detection limit.

Chlorides

The presence of chlorine is high in wastewater compared to freshwater sources and its presence in the wastewater is detected as Cl⁻ ion. The concentration of chlorine in water resources becomes high due to the discharge of polluted wastewaters from the industries and leads to increased salty taste depends on the chemical composition of the water. The major issues of increased level of chloride in water are inhibition of plant growth, strains metallic pipelines. The chloride concentration in the effluent was 650 mg/L before the photocatalytic treatment and it significantly decreased to 165 mg/L after the treatment.

Fluorides

The excess amount of fluorine content in the water may lead to fluorosis. The concentration of F of ion in the effluent was 1.88 mg/L which reduced to 1.41 mg/L after the photocatalytic treatment process

Sulphate content

When the concentration of sulphate exceeds a level of 250mg/L in water it may bring a laxative effect on combination with calcium and magnesium ions. Bacterial attack causes reduction of sulphate to form hydrogen sulphide gas. The excessive discharge of sulphate is from sewage treatment plants, run off from agricultural lands, tanneries, textile mills as well as from paper and pulp industries. About 393mg/L of sulphate is estimated as SO₄²⁻ ions in the effluent which significantly reduced to 136mg/L after the photocatalytic treatment.

Iron content

Iron is an essential constituent of drinking water however the level of iron content in the drinking sources may increase due to the discharge from the industrial sectors which further causes stains in the utensils and leads to objectionable taste and color to the food. However, the increased level of iron content in portable water may cause severe health issues such as nausea, vomiting, diarrhea, stomach pain and even damage the liver and pancreas. The concentration of iron in the effluent is 0.41 mg/L which has reduced to 0.29 mg/L after the photocatalytic treatment.

Nitrates and Nitrites

Only trace quantities of nitrate is present in surface water but may attain high levels in ground water and the consumption of nitrate containing water can lead to methemoglobinemia in infants. The amount of nitrate estimated as NO_3^- in the effluent was found to be 25 mg/L which reduced to 21 mg/L after the photocatalytic treatment. Similarly, the amount of nitrite estimated as NO_2^- in the effluent was found to be 0.094 mg/L which reduced to 0.082 mg/L after the photocatalytic treatment.

Chemical oxygen demand

Chemical oxygen demand analysis refers to the determination of equivalent amount of oxygen required to chemically oxidize the organic matter in the wastewater. The chemical oxygen demand for the effluent before photocatalytic treatment was 265 mg/L which reduced to 132mg/L after the photocatalytic treatment process.

Biological oxygen demand

BOD refers to the amount of molecular oxygen required to biochemically oxidize the organic matter present in wastewaters. The biological oxygen demand for the effluent before photocatalytic treatment was 21 mg/L which reduced to 10mg/L after the photocatalytic treatment process.

Total organic carbon

TOC analysis refers to the measurement of the organic carbon content present in the wastewater released from the textile, dyeing and printing units. The total organic level in the drinking water varies from <1.0 to > 25mg/L and in the wastewater it can be above 100mg/L. The total organic carbon content in the effluent was 120mg/L which drastically reduced to 60mg/L after the photocatalytic treatment.

Table 5.4.2 Results of the Physico-chemical analysis of the effluent before and after the photocatalytic treatment

S. No.	Parameters	Before the photocatalytic treatment	After the photocatalytic treatment
1.	Colour (Hazen units)	550	<1.0
2.	Odour	Agreeable	Agreeable
3.	Electrical conductivity (Micromhos/cm)	4394	1523
4.	Turbidity (NTU)	128	116
5.	pH value	8.12	7.56
6.	Total suspended solids (mg/L)	38	29
7.	Total dissolved solids (mg/L)	2636	914
8.	Total hardness (mg/L)	460	<1.0
9.	Total alkalinity (mg/L)	829	378
10.	Chlorides (mg/L)	650	165
11.	Sulphates (mg/L)	393	136
12.	Total iron (mg/L)	0.41	0.29
13.	Fluorides (mg/L)	1.88	1.41
14.	Nitrates(mg/L)	25	21
15.	Nitrites(mg/L)	0.094	0.082
16.	Chemical oxygen demand (mg/L)	265	132
17.	Biological oxygen demand (mg/L)	21	10
18.	Total organic carbon (mg/L)	120	60

5.4.3. In Vitro Antimicrobial Assay of the synthesized 2 wt %AlF₃-ZnO/1 wt % AlF₃-TiO₂/3 wt % AlF₃-BiOCl composite

The formulation, development and widespread use of antibiotics has led to the growth of new multidrug resistant microbial strains and therefore a safety concern about the health standards has considerably increased over the past decades. The increasing concern for food safety and human health standards made the scientists all over the world to explore new antimicrobial substances with no side effects. The non-toxic nature, chemically stability and strong oxidizing power by free radical generation of the Ag, TiO₂ and ZnO nanomaterials made the scientists to test the antimicrobial properties of these materials against a wide range of gram positive and gram negative bacteria. The positive results obtained stimulated many researchers to synthesize and investigate the antimicrobial properties of many more new inorganic materials.

5.4.4. Antimicrobial activity of nanocomposites

Recently Lalabadi et al⁷⁹ reported that ZnO/TiO₂/4A Zeolite composite synthesized by hydrothermal method showed good antibacterial activity against gram positive and gram negative bacteria. Similarly, different concentrations of Ag/TiO₂ and Cu²⁺/TiO₂ composites⁸⁰ used to inhibit the growth *E. coli* C600, *S. cerevisiae* W303 strains and *Arabidopsis thaliana* Col-0 strain showed that among Ag/TiO₂ and Cu²⁺/TiO₂, silver doped TiO₂ significantly reduced the growth of *E.Coli*. According to the recent review articles⁸¹⁻⁸³, ZnO/Graphene oxide, Ag/ZnO, Fe₂O₃/TiO₂, Au/TiO₂, CuO, Mn₂O₃, Ce-TiO₂, Bi₂O₃, PVP coated Bismuth nanoparticles are some promising materials which showed good antimicrobial activity. The combination of UV light, laser technology along with the antibiotics such as amoxicillin is found to show a synergic effect in the growth inhibition on bacteria such as Escherichia coli, Pseudomonas

aeruginosa, Proteus vulgaris, and Staphylococcus aureus. A single nanomaterial prepared via different routes is reported to show varying level of inhibitory action against the microbes. The principle factors differentiating the antimicrobial potential of the nanomaterials include their size, shape, crystal growth and moreover the interaction of these materials with the pathogens. In recent years, a large number of research articles reported the photocatalytic antimicrobial action against various pathogens.

Some of the advantages of the photocatalytic disinfection are

- The use of atmospheric oxygen by the catalysts replaces the role of toxic and hazardous chemicals.
- Photocatalysts used are less expensive and reusable.
- Power supply and any maintenance related to it can be eliminated as the catalysts has the ability to make use of solar radiation.
- The photocatalytic technique is simple, easily adoptable and can be operated not only in cities but also in remote and rural areas.
- Complete destruction of the microorganisms is possible.

The most common microorganisms used for the microbial studies include *Escherichia coli, Staphylococcus aureus, Enterococcus faecalis, Streptococcus Faecalis, Bacillus subtilis, Acinetobacter baumannii, Mycobacterium tuberculosis, Pseudomonas aeruginosa, Candida albicans,* and *Aspergillus niger*. Several studies reported that the diffusion of the positively charged metal ions into microbes and the reactive oxygen species formed caused the oxidation and cell destruction of the microbes.

5.4.5 Antibacterial studies of 2wt%AlF₃-ZnO/1wt%AlF₃-TiO₂/3wt%AlF₃-BiOCl photocatalyst

The disc diffusion method is carried out to assess the antibacterial activity of the 2wt% AlF₃-ZnO/1wt% AlF₃-TiO₂/3wt% AlF₃-BiOCl photocatalyst. The concentration

of the photocatalyst is varied from 60 to 100μg/ml to find out the maximum zone of inhibition that can be achieved with minimal catalyst concentration shown in figure 5.4.5 and the results are tabulated in table. For the bacteria *S. aureus*, the zone of inhibition increased from 3mm to 5mm on increasing the catalyst concentration from 60μg/ml to100μg/ml and a similar trend is observed in the case of other bacteria *P. aeruginosa* and *E. Coli* the maximum zone of inhibition observed is 7mm and 6mm respectively for 100μg/ml of catalyst concentration. Amoxicillin is used as a standard for the antibacterial activity and the zone of inhibitions observed are 9mm, 8mm and 9mm for *S. aureus*, *P. aeruginosa* and *E. Coli* respectively. Among the three different types of bacteria *S. aureus*, *P. aeruginosa* and *E. Coli*, the maximum antibacterial action using 2 wt%AlF₃-ZnO/1wt% AlF₃-TiO₂/3wt% AlF₃-BiOCl composite catalyst is observed against *P. aeruginosa* which might be due to difference in the membrane structures of the bacteria. Overall the synthesized 2wt%AlF₃-ZnO/1wt%AlF₃-TiO₂/3wt%AlF₃-BiOCl catalyst showed good antibacterial efficacy.

Table-5.4.5 Results of *in vitro* Antibacterial activity of 2wt% AlF₃-ZnO/1wt%AlF₃-TiO₂/ 3 wt%AlF₃-BiOCl catalyst

Samples	Concentrations (µg/ml)	Organisms/Zone of inhibition (mm)			
		Samples			
		Staphylo- -coccus aureus	Pseudomonas aeruginosa	Escherichia coli	
2wt%AlF ₃ ZnO/ 1wt%AlF ₃ TiO ₂ / 3wt%AlF ₃ - BiOCl catalyst	60	3	5	4	
	80	4	6	5	
	100	5	7	6	
Ethanol	10 μl/disc	0	0	0	
Standard (Std) (Amoxicillin)	10 μl/disc	9	8	9	

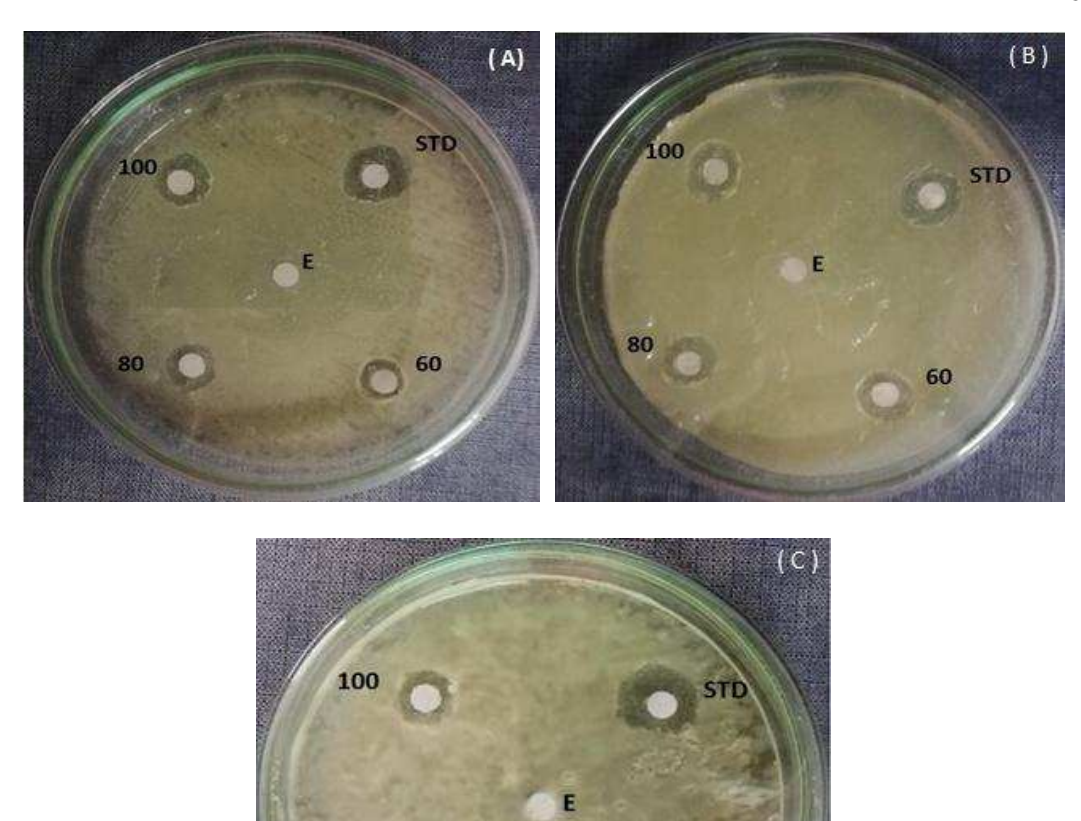


Fig. 5.4.5 Antibacterial disc diffusion assay of 2wt%AlF₃-ZnO/1wt%AlF₃-TiO₂/3wt% AlF₃-BiOCl composite towards (A) *Staphylococcus aureus* (B) *Pseudomonas aeruginosa* and (C) *Escherichia coli* respectively

5.4.6. Antifungal studies of 2wt%AlF₃-ZnO/ 1wt%AlF₃-TiO₂/3wt%AlF₃-BiOCl photocatalyst

The disc diffusion method is carried out to assess the antifungal activity of the 2wt%AlF₃-ZnO/1 wt%AlF₃-TiO₂/3wt%AlF₃-BiOCl composite. The concentration of the photocatalyst is varied from 60 to 100µg/ml to find out the maximum zone of inhibition that can be achieved with minimal catalyst concentration shown in figure 5.4.6 and the results are tabulated in table. For the fungi *Aspergillus flavus*, the zone

of inhibition increased from 3mm to 6mm on increasing the catalyst concentration from 60μg/ml to100μg/ml and a similar trend is observed in the case of other fungi *Candida auris* and *Candida albicans* the maximum zone of inhibition observed is 6mm and 5mm respectively for 100μg/ml of catalyst concentration. Fluconazole is used as a standard for the antifungal activity and the zone of inhibitions observed are 8mm, 7mm and 7mm for *Aspergillus flavus*, *Candida auris* and *Candida albicans* respectively. The zone of inhibition observed of all the three different types of fungi *Aspergillus flavus*, *Candida auris* and *Candida albicans* is found to be more or less the same using 2wt%AlF₃-ZnO/1wt%AlF₃-TiO₂/3wt%AlF₃-BiOCl composite catalyst and it is concluded that the synthesized 2wt%AlF₃-ZnO/1wt%AlF₃-TiO₂/3wt%AlF₃-TiO₂/3wt%AlF₃-BiOCl catalyst showed good antifungicidal activity.

Table-5.4.6: Results of *in vitro* Antifungal activity of 2wt%AlF₃-ZnO/1wt%AlF₃-TiO₂/3wt %AlF₃-BiOCl composite

Samples	Concentrations (µg/ml)	Organisms/Zone of inhibition (mm)			
		Samples			
		Aspergillus flavus	Candida auris	Candida albicans	
2 wt % AlF ₃ - ZnO/ 1 wt % AlF ₃ -TiO ₂ / 3 wt % AlF ₃ - BiOCl	60	3	4	3	
	80	5	5	4	
	100	6	6	5	
Ethanol	10 μl/disc	0	0	0	
Standard (Std) (Fluconazole)	10 μl/disc	8	7	7	

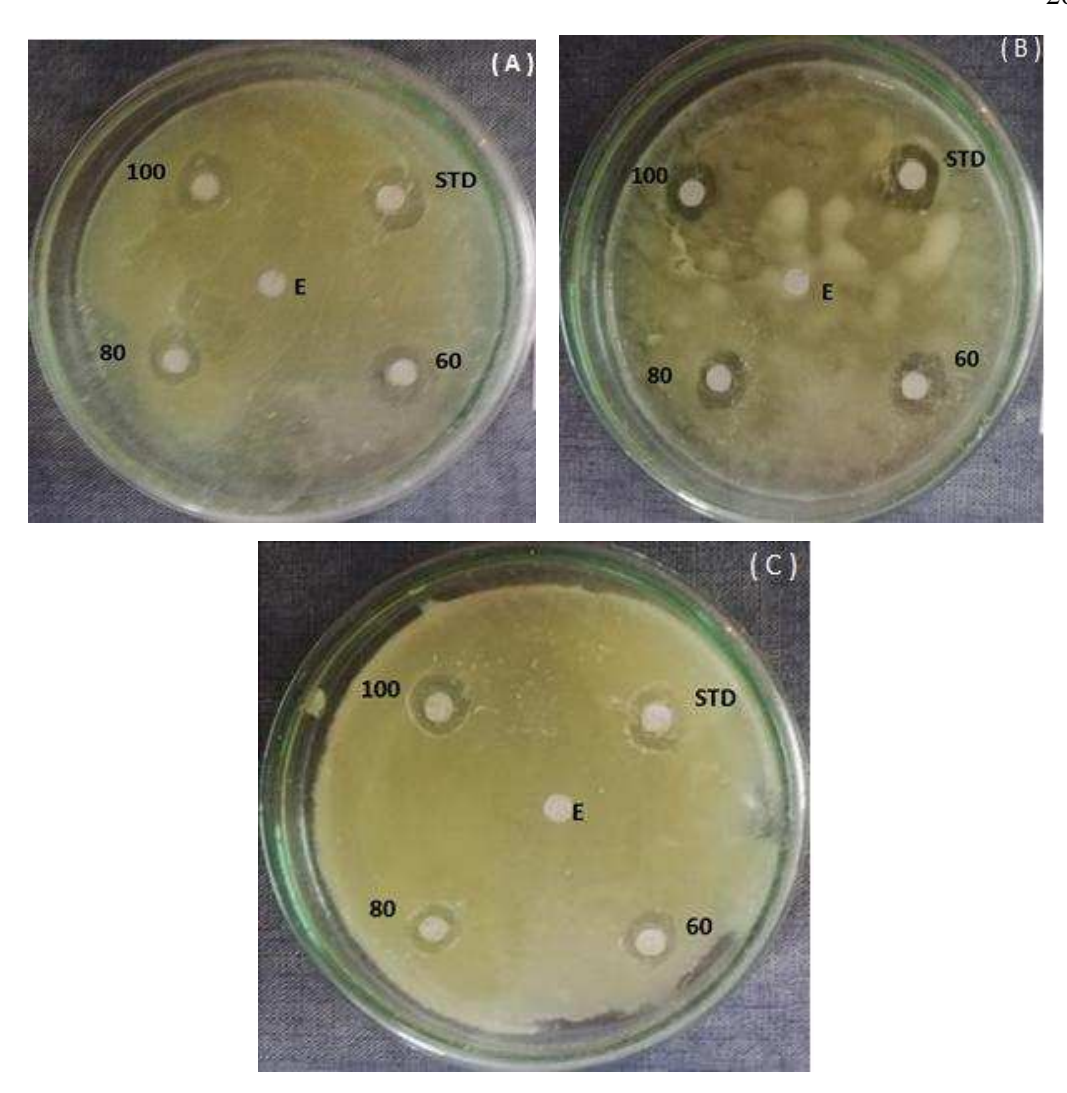


Fig. 5.4.6 Antifungal disc diffusion assay of 2wt%AlF₃-ZnO/1wt%AlF₃-TiO₂/3wt%AlF₃-BiOCl composite towards (A) *Aspergillus flavus* (B) *Candida vulgaris* and (C) *Candida albicans* respectively

5.4.7. Mechanism of antimicrobial activity

The exact mechanism behind the antimicrobial action caused by the photocatalytic materials is still not clear. Based on the literature reports a probable mechanism for the deactivation of the microbes is given below

- (i) Formation of the Reactive Oxygen Species (ROS)
 - The lethality caused to the microbes by ZnO, TiO₂, BiOCl catalysts are due to the production of the reactive oxygen species such as (OH, H₂O₂, O₂²-) and their oxidative reactivity.

- The photogenerated charge carriers react with the water molecules to produce H⁺ and ⁻OH ions.
- The microbe and nanoparticles mixture containing oxygen molecules, yield superoxide anion which further react with H⁺ ions to produce HO₂·
- The HO₂ radicals further react with H⁺ ions to produce hydrogen peroxide molecules.
- The superoxide and hydroxyl ions cannot penetrate into the cell wall of the microbes due to the negative charges carried by them and they are found only in the outer surface of the microbes, however the hydrogen peroxide molecules which are capable of passing through the cell wall of the microbes, destruct the cell components and finally triggers cell death⁸⁴.

Many studies reported that the antimicrobial activity also took place even under dark conditions. Recently Hirota et al⁸⁵ tested ZnO nanoparticles towards E. Coli and found that the antimicrobial action took under dark condition producing superoxide species.

(ii) Another important factor causing destruction of the microbes is the release of the metal ions and internalization of the metal ions, the small size of the particles makes its easily permeable to the cell wall and cell membrane enabling intracellular oxidative damage

The cell wall of a microorganism is its first defensive barrier. The cell wall of yeast or fungi is composed of chitin and polysaccharides, in case of gram positive bacteria it is composed of peptidoglycan and teichoic acid and for gram negative bacteria it is formed of a thin layer of peptidoglycan and a secondary lipid layer of lipopolysaccharides and lipoproteins. During the oxidative damage the cell wall of the

organism gets ruptured initially and depending upon the composition of the cell wall for each organism the activity of the ROS will slightly vary. For example, in fungi, the 'OH radicals are captured by the sugar subunits of polysaccharides and the cleavage of the polysaccharides chain lead to the exposition of the cell membrane and in case of gram negative bacteria such as E. Coli per-oxidation leads to the destruction of cell wall. The cell membrane being the second most inner protective layer is mainly composed of phospholipids. Oxidation of the cell membrane by reactive oxygen species leads to loss of membrane integrity, leakage of cellular content. Due to the oxidative damage of the cell membrane, the respiratory chain of the organism also gets affected. The double membrane mitochondria are a natural source of reactive oxygen species in aerobic metabolism. The presence of the nanoparticles increases the production of ROS and a small dysregulation in the electron transfer process of the mitochondrial respiratory chain can attenuate the cell damage. The reactive oxygen species such as hydroxyl radicals can attack the sugar phosphate groups leading to the breakage of the nucleobase strand and can cause damage at the molecular level affecting the regulatory metabolism such as transcription, replication and cell division. The intrusion of the metal ions to the microorganisms can significantly lower the activity of the iron transfer protein and inhibit the uptake of inorganic phosphates thereby inhibiting the cell growth and survival. The metal ions and reactive oxygen species not only cause damage to the cell components but also affect the pathway of cell signaling molecules that binds the lipopolysaccharides and also inhibits the microbial aggregation and biofilm formation⁸⁶.

So it is concluded that the presence of nanoparticles increases the formation of reactive oxygen species which causes oxidative damage to the microorganisms and responsible for the antimicrobial action.

BIBLIOGRAPHY

- 1. S.Z. Kang, T. Wu, X. Li, J. Mu, Colloids and Surfaces A: Physicochem and Eng Aspects 369 (2010) 268–271
- S. Suwanboon, P. Amornpitoksuk, A. Sukolrat, Ceramics International 37 (2011) 1359–1365
- 3. J. P. Blitz, Techniques in Analytical Chemistry Series. chapter 5, ISBN 0-471-12359-5 © John Wiley & Sons, Inc. (1998)
- S. Yi, J. Cui, S. Li, L. Zhang, D. Wang, Y. Lin, Appl. Surf. Sci. 319 (2014)
 230-236
- 5. M. Shadpour, M. Maryam, Bull. Mater. Sci 35 (2012) 333
- 6. Sing, S.W. Kenneth, *Advances in Colloid and Interface Science* **76–77**(1998) 3–11
- 7. F. Rouquerol, J. Rouquerol, S.W. Kenneth, Sing. P. Llewellyn, G. Maurin, Adsorption by Powders and Porous Materials, Principles, Methodology and Applications 2nd Edition. Amsterdam. NL: Academic Press/ Elsevier Ltd. pp. 263–267(2014)
- A.K. Worku, D.W. Ayele, N.G. Habtu, G.A. Melas, T.A. Yemata, N.Y. Mekonnen,
 M.A. Teshager, SN Applied Sciences 3 (2021) 699
- 9. M.S. Nasrollahzadeh, M. Hadavifar, S.S. Ghasemi, M.A. Chamjangali, *Appl. Water Sci.* **8** (2018) 104
- J. Nishio, M. Tokumura, H.T. Znad, Y. Kawase, J. Hazard. Mater. 138
 (2006) 106–115
- 11. S. Lakshmi, R. Renganathan, S.J. Fujita, *Photochem. Photobiol. A: Chem.* **88** (1995)163-167

- 12. G. Thennarasu, A. Sivasamy, *Ecotoxicology and Environmental Safety* **134** (2016) 412-420
- 13. M.O. Fatehah, H.A. Aziz, S. Stoll, J. Colloid Sci. Biotechnol. 3 (2014) 75–84
- 14. R. Comparelli, E. Fanizza, M. Curri, P. Cozzoli, G. Mascolo, A. Agostiano, *Appl. Catal. B* **60** (2005) 1–11
- 15. M.A. Behnajady, Y. Tohidi, *Desalination Water Treatment* **53** (2015) 1335–1341
- 16. N.K. Singh, S. Saha, A. Pal, Desalination Water Treatment 53 (2015) 501–514
- 17. B. Subash, B. Krishnakumar, M. Swaminathan, M. Shanthi, *Langmuir* **29** (2013) 939–949
- 18. A.M. Abdelsamad, T.A. Gad-Allah, F.A. Mahmoud, M.I. Badawy, *J. Water Process Eng.* **25** (2018) 88–95
- L.V. Trandafilović, D.J. Jovanović, X. Zhang, S. Ptasińska, M. Dramićanin,
 Appl. Catal. B 203 (2017) 740–752
- 20. G.K. Weldegebrieal, Inorganic Chemistry Communications 120 (2020) 108140
- 21. R.W. Matthews, Journal of Catalysis 111 (1988) 264–272
- 22. G. Mills, M.R. Hoffmann, Environ. Sci. Technol. 27 (1993)1681–1689
- 23. N. Serpone, *J. Adv. Oxid. Technol.* **10** (2007)
- 24. A.N. Rao, B. Sivasankar, V. Sadasivam, *Journal of Molecular Catalysis A:*Chemical **306** (2009) 77–81
- 25. Y.H. Chiu, T.M. Chang, C. Chen, M. Sone, Y. Hsu, Catalysts 9 (2019) 430
- A. Pavanello, A. Blasco, P.F. Johnston, M.A. Miranda, M.L. Marin, *Catalysts* 10 (2020) 774

- 27. S. Ramanathan, N. Radhika, D. Padmanabhan, A. Durairaj, S.P. Selvin, S. Lydia, S. Kavitha, S. Vasanthkumar, ACS Omega, (2019) http://pubs.acs.org/journal/acsodf
- Md. Ashraful Islam Molla, I. Tateishi, M. Furukawa, H. Katsumata, T. Suzuki,
 S. Kaneco, *Open Journal of Inorganic Non-metallic Materials* 7 (2017) 1-7
- 29. A. Gupta, N.K. Verma, H.S. Bhatti, J. Low Temp. Phys. 147 (2007)49–57
- 30. R. He, R.K. Hocking, T. Tsuzuki, J. Aus. Ceram. Soc. 49 (2013)76–81
- 31. S. Girish Kumar, R. Kavitha, C. Sushma, *Interface Science and Technology* **31** (2020) 285-312
- 32. M. Faraz, F.K. Naqvi, M. Shakir, N. Khare, New J. Chem **42** (2018) 2295-2305
- D. Reyes-Coronado, G. Rodr´ıguez-Gattorno, M.E. Espinosa-Pesqueira, C.
 Cab, R.D. Coss, G. Oskam, *Nanotechnology* 19 (2008)145605
- 34. H. Lin, L. Li, M. Zhao, X. Huang, X. Chen, G. Li, R. Yu, *Journal of the American Chemical Society* **134** (2012) 8328-8331
- 35. T. Bezrodna, G. Puchkovska, V. Shimanovska, J. Baran, *Molecular Crystals and Liquid Crystals* **413**(2004) 71-80
- 36. A.Z. Simoes, F. Moura, T.B. Onofre, M.A. Ramirez, J.A. Varela, E. Longo, *Journal of Alloys and Compounds* **508** (2010) 620-624
- 37. O. Liang, X. Shen, F. Song, M. Liu, Journal of Material Science and Technology 27 (2011) 996–1000
- 38. S. Liu, N. Jaffrezic, C. Guillard, *Applied Surface Science* **255** (2008) 2704–2709.

- B. Pal, R. Kaur, I.S. Grover, Journal of Industrial and Engineering Chemistry
 33 (2016) 178–184
- 40. M. Kosmulski, Journal of Colloid Interface Science 298 (2006) 730-741
- 41. K. Saeed, I. Khan, T. Gul, M. Sadiq, Appl. Water Sci. 7 (2017)3841–3848
- 42. M.S. Nasrollahzadeh, M. Hadavifar, S.S. Ghasemi, M.A. Chamjangali, *Appl. Water Sci.* **8** (2018)
- 43. U.G. Akpan, B.H. Hameed, *J. Hazard. Mater.* **170** (2009) 520–529
- 44. N. Daneshvar, D. Salari, A.R. Khataee, *J. Photochem. Photobiol. A: Chem.*157 (2003) 111–116
- 45. K.M. Reza, A.S.W. Kurny, F. Gulshan, Appl. Water Sci. 7 (2017) 1569–1578
- 46. R. Li, T. Li, Q. Zhou, Catalysts 10 (2020) 804
- 47. S. Ahadi, N.S. Moalej, S. Sheibani, *Solid State Sci.* **96** (2019)
- 48. J.H. Zhang, D. Fu, S.Q. Wang, R.L. Hao, Y.X. Xie, *J. Ind. Eng. Chem.* **80** (2019) 23–32
- M.A.M. Khan, R. Siwach, S. Kumar, A.N. Alhazaa, Opt. Laser Technol. 118
 (2019) 170–178
- 50. V. Bhatia, A. Dhir, J. Environ. Chem. Eng. 4 (2016) 1267–1273
- 51. H. Zeghioud, A.A. Assadi, N. Khellaf, H. Djelal, A. Amrane, S. Rtimi,

 Materials 12 (2019) 412
- U. O. Bhagwat, J.J. Wu, A.M. Asiri, S. Anandan, *Chemistry Select* 4 (2019) 6106 –6112
- 53. J. Ovenstone, J. Mater. Sci. 36 (2001) 1325
- 54. J.G. Yu, X.J. Zhao, J.C.Du, W.M. Chen, J. Sol-Gel Sci. Technol. 17 (2000) 163
- 55. A. Kudo, R. Niishiro, A. Iwase, H. Kato, *Chemical Physics* **339** (2007) 104-110

- J. Schneider, M. Matsuoka, M. Takeuchi, J. Zhang, Y. Horiuchi, M. Anpo,
 D.W. Bahnemann, *Chem. Rev.* 114 (2014) 9919–9986
- 57. I.D. Sharma, G.K. Tripathi, V.K. Sharma, S.N. Tripathi, R. Kurchania, C. Kant, A. K. Sharma, K.K. Saini, *Cogent Chemistry* **1** (2015) 1076371
- 58. T. Xie, L. Xu, C. Liu, J. Yang, M. Wang, *Dalton Trans.*, **43** (2014) 2211–2220
- V. Fruth, M. Popa, D. Berger, C.M. Ionica, M. Jitianu, J. Eur. Ceram. Soc., 24
 (2004) 1295–1299
- J. Song, C. Mao, H. Niu, Y. Shen, S. Zhang, Cryst. Eng. Comm., 12 (2010)
 3875–3881
- 61. W.C. Xu, J.Z. Fang, X.M. Zhu, Z.Q. Fang, C.P. Cen, *Mater. Res. Bull.* **72** (2015) 229–234
- 62. M. Yan, Y.L.Wu, Y. Yan, X. Yan, F.F. Zhu, Y.Q. Hua, W.D. Shi, *ACS Sustainable Chem. Eng.* **4** (2016) 757–766
- 63. A. Gnanaprakasam, V.M. Sivakumar, M. Thirumarimurugan, *Asia-Pac. J. Chem. Eng.* (2017) Published online in Wiley Online Library (wileyonlinelibrary.com) DOI: 10.1002/apj.2112, pp.1-9
- 64. A. Gnanaprakasam, V.M. Sivakumar, M. Thirumarimurugan, *Indian J. Mat. Sci.* (2015) Article ID 601827, pp. 16
- 65. M.L. Pan, H. Zhang, G. Gao, L. Liu, W. Chen, *Environ Sci Technol.* **49** (2015) 6240–6248
- H. Cheng, B. Huang, Z. Wang, X. Qin, X. Zhang, Y. Dai, Chem. Eur. J. 17
 (2011) 8039-40
- 67. M. Gondal, X. Chang, Z. Yamani, *Chem. Eng. J.* **165** (2010) 250
- 68. H. Zhao, F. Tian, R. Wang, R. Chen, Reviews in Advanced Sciences and Engineering, 3 (2014) 1–25

- 69. Z.S. Seddigi, M.A. Gondal, U. Baig, S.A. Ahmed, M.A. Abdulaziz, E.Y. Danish, M. M. Khaled, A. Lais, *PLOS ONE* (2017) DOI:10.1371/journal. pone.0172218
- K. Pingmuang, J. Chen, W. Kangwansupamonkon, G. Wallace, S. Phanichphant,
 A. Nattesta, *Scientific reports* 7 (2017) 8929
- 71. G.S. Wang, S.T. Hsieh, C.S. Hong, *Water Research* **34** (2000) 3882–3887
- 72. J. Tucher, C. Streb, Beilstein Journal of Nanotechnology 5 (2014) 711-716
- 73. Y. Li, H. Jiang, X. Wang, X. Hong, B. Liang, RSC Adv. 11 (2021) 26855
- L. Zhang, F. Liu, X. Xiao, X. Zuo, J. Nano Environ. Sci. Pollut. Res. 26
 (2019) 28871–28883
- 75. J.Y. Cao, J.J. Li, W. Chu, W.L. Cen, *Chem. Eng. J.* **400** (2020) 125813–125824
- H. Sheng, W. Wang, R. Dai, J. Ning, L. Zhang, Q. Wu, F. Zhang, J. Yan, W.
 Zhang, Nanomaterials 11 (2021) 423
- 77. W.Z. Khan, I. Najee, S. Ishtiaque, *International Journal of Engineering and Science* 5 (2016) 61-70
- 78. V. Nogueira, I. Lopes, T.A.P. Rocha-Santos, F. Gonçalves, R. Pereira, *Environ Technol.* **39** (2018) 1586-1596
- 79. M.A. Lalabadi, A. Ehsani, B. Divband, M.A. Sani, *Scientific Reports* **9** (2019) 17439
- 80. C.G. Piña, I.E. Medina-Ramírez, P. Guzmán, R.R. Martínez, J.F. Morales-Domínguez, I.R. Franchini, *International Journal of Photoenergy* (2016) Article ID 8060847, 14 pages

- 81. A. Sirelkhatim, S. Mahmud, A. Seeni, N. Haida, M. Kaus, L.C. Ann, S. Khadijah, M. Bakhori, H. Hasan, D. Mohamad, *Nano-Micro Lett.* (2015) DOI 10.1007/s40820-015-0040-x,
- 82. C.L. Dicastillo, M.G. Correa, F.B. Martínez, C. Streitt, M.J. Galotto, *Intech Open* (2020) DOI: http://dx.doi.org/10.5772/intechopen.90891
- 83. L.D. Geoffrion, D. Medina-Cruz, M. Kusper, S. Elsaidi, F. Watanabe, P. Parajuli, A. Ponce, T. Ba Hoang, T. Brintlinger, T.J. Webster, G. Guisbiers, Nanoscale Adv., 3 (2021) 4106
- 84. J. Sawai, E.Kawada, F. Kanou, H. Igarashi, A. Hashimoto, T. Kokugan, M. Shimizu, *J. Chem. Eng. Jpn.* **29** (1996) 627–633
- 85. K. Hirota, M. Sugimoto, M. Kato, K. Tsukagoshi, T. Tanigawa, H. Sugimoto, *Ceramics International* **36** (2010) 497–506
- 86. A. Sirelkhatim, S. Mahmud, A. Seeni, N.H. Mohamad Kaus, L.C. Ann. S.K. Mohd Bakhori, H. Hasan, D. Mohamad, *Nano-Micro Lett.* (2015) DOI 10.1007/s40820-015-0040-x

CHAPTER - VI

Summary and Conclusion

CHAPTER - VI

SUMMARY AND CONCLUSION

6.1. SUMMARY OF THE PRESENT RESEARCH WORK

Heterogeneous semiconductor photocatalysis is one of the recently employed techniques and an active area of research for the degradation of synthetic organic dyes in aqueous solutions. During the process of photocatalysis, the toxic non-biodegradable pollutants are converted into easily degradable and harmless products. Among many semiconductor metal oxide and metal sulphide photocatalysts, the most frequently used photocatalysts are zinc oxide and titanium dioxide. Recently, bismuth based semiconductor oxides are also employed for environmental remediation purposes. All the three photocatalysts ZnO, TiO₂ and BiOCl are well known for their fascinating structural properties and are reported to be non-toxic with strong oxidizing ability and thus employed for the degradation of wide range of synthetic organic dyes, pesticides, phenols and nitro compounds. These photocatalysts are found to have similar band gap value of ~3.2 eV and are less active in the visible region. Similarly, the fast recombination of the photogenerated charge carriers during the photocatalytic process results in low photocatalytic efficiency of these materials. To overcome this limitation, present research work, modification of these three semiconductors is done by doping these materials with non-toxic and low-cost metal salts such as aluminium fluoride and strontium silicate. Their optical, structural and morphological characteristics were studied using different analytical techniques such as X-Ray diffraction studies, field emission scanning electron microscopy, energy dispersive X-ray analysis, high resolution transmission electron microscopy, fourier transform infra red spectroscopy,

UV-Visible diffuse reflectance spectroscopy and nitrogen adsorption-desorption isotherm. For the present study, ZnO, TiO₂, BiOCl, AlF₃/ZnO, SrSiO₃/ZnO, AlF₃/TiO₂, SrSiO₃/TiO₂, AlF₃/BiOCl and SrSiO₃/BiOCl photocatalysts were synthesized. The photocatalytic activities of the doped and undoped zinc oxide catalysts were evaluated for the degradation of three synthetic organic dyes, namely, methylene blue, indigo carmine and crystal violet under direct sunlight. Similarly, the photodegradation studies of basic yellow 2, acid red 94 and congo red was carried out using doped and undoped titanium dioxide photocatalysts. For the degradation of acid green 1, doped and undoped bismuth oxychloride photocatalysts were utilized. The operational parameters such as effect of pH, catalyst concentration and initial concentration of the dye were optimized for efficient degradation of dyes under sunlight. The kinetic studies were carried out for the decolourization of the dyes using different weight percent of doped photocatalysts to understand the order and rate of the reaction. The extent of mineralization was studied by carrying out the total organic carbon analysis before and after the photocatalytic treatment process. On comparing the efficiencies of the different doped and undoped photocatalysts with respect to time, it was found that aluminium fluoride doped zinc oxide, titanium dioxide and bismuth oxychloride photocatalysts were the more efficient, compared to the undoped and strontium silicate doped photocatalysts. The effect of radical scavengers was also studied using the most active aluminium fluoride doped photocatalysts for all dye solutions to understand which radical species plays the most active role in the photocatalytic degradation and by which mechanism. The recovery and reusability of the most active catalysts was carried out to understand the stability of these synthesized photocatalysts under direct sunlight. To test the efficacy of the synthesized photocatalysts on real environmental

samples, textile effluent was collected and the physico-chemical characteristics of the effluent containing high dye content was analyzed. The photocatalytic activity of AlF₃ doped photocatalyst on the textile effluent was evaluated. The composite photocatalyst was also tested against different pathogens to understand the photocatalytic disinfection properties and its underlying mechanism.

6.2. CONCLUSIONS DRAWN FROM THE PRESENT RESEARCH WORK

- Simple chemical precipitation method was adopted for the synthesis of undoped and doped ZnO, TiO₂ and BiOCl photocatalysts.
- From the X-Ray diffraction studies it could be concluded that the synthesized materials were highly crystalline. All the ZnO based catalysts possessed hexagonal wurtzite phase, the TiO₂ catalysts possessed anatase, rutile and brookite phases, the BiOCl catalysts possessed tetragonal phase.
- The determined average crystallite sizes of the undoped and doped photocatalysts are in nanometer dimension.
- From the field emission scanning electron microscopy analyses it is observed that the bare zinc oxide photocatalysts, AlF₃/ZnO and SrSiO₃/ZnO photocatalysts have moderately rod like structure, undoped TiO₂, AlF₃ doped TiO₂ and SrSiO₃ doped TiO₂ photocatalysts show moderately spherical shape. A moderately flake like structure is seen in the case of BiOCl photocatalysts and the formed particles are agglomerated.
- The Energy dispersive X-ray analysis showed that the synthesized ZnO based photocatalysts are composed of elements such as Zn, O, Al, F, Sr and Si depending upon the composition of the catalyst chosen for the study. Similarly, Ti, O, Al, F, Sr and Si elements were observed in the EDAX spectrum of TiO₂

based catalysts. As expected Bi, O, Cl, Al, F, Sr and Si were observed from the BiOCl based photocatalysts. All the synthesized photocatalysts are obtained with good purity.

- The TEM images show that the synthesized ZnO based photocatalysts show moderately rod like structure and are agglomerated which is consistent with the FESEM results. TiO₂ based photocatalysts show moderately spherical shape. Similarly, the TEM images of BiOCl show that the synthesized photocatalysts are in flake like structure.
- Further the SAED pattern obtained along with the TEM images of all photocatalysts shows clear, well distinguished circular pattern supporting the XRD data that both doped as well as undoped ZnO, TiO₂ and BiOCl catalysts are crystalline in nature.
- The band gap values of photocatalysts doped with AlF₃ and SrSiO₃ have decreased. Thus, it can be concluded from the UV-DRS results that the process of doping can decrease the band gap values of the photocatalysts.
- The FTIR spectrum confirms the presence of metal-oxygen bonds in all the three types of doped as well as undoped ZnO, TiO₂ and BiOCl photocatalysts.
- The nitrogen adsorption-desorption isotherm analyses of all the synthesized photocatalysts clearly revealed that there is an increase in the surface area of the doped catalysts compared to undoped catalysts, which indicate that more surface active area will be available for the dye molecules to get adsorbed.
- From the primary photocatalytic studies carried out it is understood that ZnO,
 TiO₂ and BiOCl catalysts were more effective, only when air was purged into the reaction mixture under sunlight.

- The optimal initial concentrations of the synthetic dyes were in 10⁻⁵M concentration range.
- The optimized catalyst weight for degradation of methylene blue, indigo carmine, crystal violet dye, basic yellow 2, congo red dyes is 25mg/50mL and for acid red 94 and acid green 1 dyes it is 15mg/50mL.
- The optimum pH for the photocatalytic degradation of methylene blue, indigo carmine, crystal violet dye, basic yellow 2, congo red dyes, acid red 94 and acid green 1 dyes are 6.5, 10, 10, 10, 7.5, 3 and 5 respectively.
- The maximum photocatalytic degradation efficiency (decolourization) was observed with 2 wt% dopant in the case of ZnO, 1 wt% dopant in the case of TiO₂ and 3 wt% dopant in the case of BiOCl.
- The kinetics of decolourization of dyes at different weight percents of photocatalysts followed pseudo-first order kinetics.
- From the radical scavenging assay it was concluded that electrons, holes,
 hydroxyl and superoxide anion radicals played an active role in the photocatalytic degradation.
- The disappearance of the prominent absorption bands of the synthetic dyes in the UV-Visible spectra confirmed the destruction of the dyes.
- The TOC analyses revealed ~ 60-80% mineralization of the dyes.
- From the recoverability and reusability studies, we conclude that the most active photocatalysts (doped with 1-3 wt% AlF₃) can be reused for 5 times without significant loss in catalytic efficiency.
- A new composite [2wt%AlF₃-ZnO/1wt%AlF₃-TiO₂/3wt%AlF₃-BiOCl] in 1:1:1 weight ratio chosen for the treatment of the effluent showed a significant

- reduction in the parameters such as color, odour, pH, conductivity, TDS, TSS, hardness, alkalinity, turbidity, BOD, COD, TOC, nitrite, nitrate, iron, chloride, fluoride and sulphate content after the photocatalytic treatment under sunlight.
- It is interesting to note that the composite also showed good antimicrobial activity against different microorganisms such as *S. aureus*, *P. aeruginosa*, *E. Coli*, *Aspergillus flavus*, *Candida auris* and *Candida albicans*.

6.3. SCOPE FOR FURTHER STUDY

- The present photocatalytic degradation study is limited to dyes and to a few microorganisms it can be further extended for the evaluation of drugs, pesticides and many other toxic organic compounds.
- ➤ In the present study, the modification of the semiconductor oxides are done with only two metals, the modification of the metal oxides with multielements, rare metal ions and non-metals can be done and its photocatalytic activity can also be evaluated in future.
- An investigation into the analysis of the degradation products by LCMS study will throw more light on the mechanistic and degradation pathway of the dyes.
- ➤ In the present study powdered photocatalysts are used for the degradation of the dyes which limits the complete recovery of the catalysts and hence more modified forms of the catalyst with different supports can be prepared and evaluated in future.
- ➤ The potentiality of the photocatalysts used in the present study should be evaluated for other reactions such CO₂ reduction, water splitting reactions and as the ZnO, TiO₂ photocatalysts have good optoelectronic properties the potential

- of these catalyst as well as their modified forms can be evaluated for sensor applications.
- As sunlight being one most abundant natural resource, design and development of reactors to make use of the technology under direct sunlight should be initiated this will be useful for many small scale and large scale industries in India that will ultimately lead to the efficient recycling of the dyeing effluent.

List of Paper Publications

LIST OF PAPER PUBLICATIONS

- 1. **Preeja Thattil P.,** Vinotha S. and Leema Rose A.*, Photodegradation of Thiazine and indigoid dyes using zinc oxide nanocatalyst coupled with air oxidation under sunlight, *Research Journal of Chemistry and Environment*, January 2020, vol.24(1), pp.24-33.
- S. Vinotha, Preeja. P. Thattil and A. Leema Rose*, Degradation of Methylene blue dye using dimethyl dioxirane as the oxidizing agent, International Journal of Scientific and Technology Research, March2020, vol.9(3), pp.6761-6764.
- 3. **Preeja. P. Thattil** and A. Leema Rose*, Photocatalytic removal of xanthene and diaryl methane dyes by air oxidation using TiO₂ nanospheres under sunlight, *International Journal of Scientific and Technology Research*, April 2020, vol.9(4), pp.3357-3363.
- 4. **Preeja. P. Thattil** and A. Leema Rose*, Enhanced removal of crystal violet dye using zinc oxide nanorods and air oxidation under sunlight radiation, *Rasayan Journal of Chemistry*, April-June 2020, vol.13(2), pp.1166-1173.
- 5. **Preeja. P. Thattil** and A. Leema Rose*, High Photocatalytic Performance of Modified Bismuth Oxychloride Semiconductor under Sunlight, *Oriental Journal of Chemistry*, 2021, vol. 37(4), pp. 770-778.
- 6. A. Leema Rose*, B. Shabushree and **Preeja P. Thattil,** Structural Characterization, Antimicrobial and Antioxidant Assay of Biogenically Synthesized Maghemite (γ-Fe₂O₃) Nanoparticles, *Journal of Pharmaceutical Research International*, 2021, 33(43B), pp.32-41.
- 7. **Preeja. P. Thattil** and A. Leema Rose*, Fabrication and Structural Characterization of SrSiO₃/TiO₂ Photocatalyst for the Degradation of Congo Red Dye under Sunlight, *Rasayan Journal Of Chemistry*, Vol. 15, No. 1, 2022.

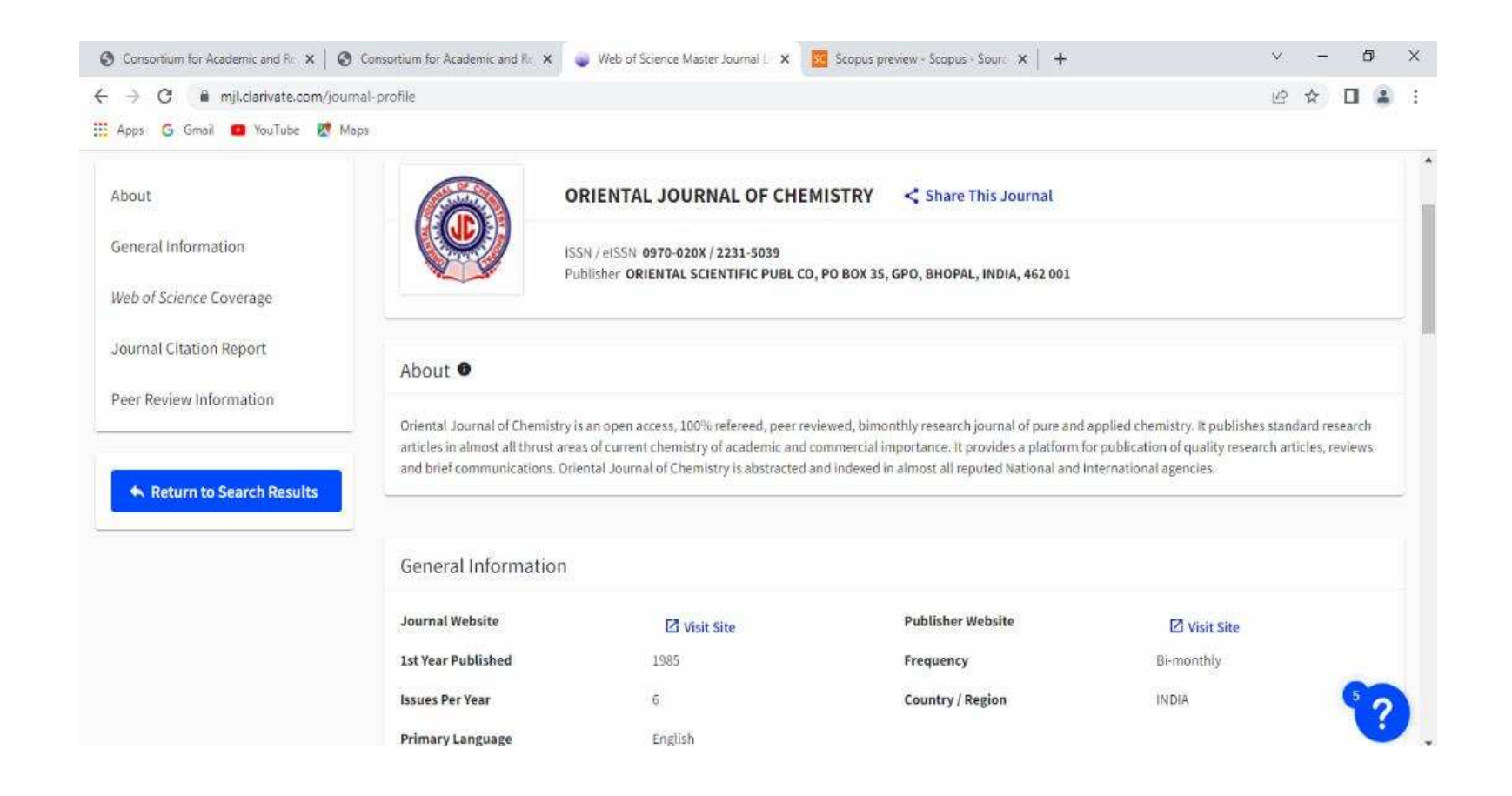
List of Paper Presentations

LIST OF PAPER PRESENTATIONS

Papers Presented in National and International Conferences

- 1. "Photodegradation of thiazine and indigoid dyes using ZnO nanocatalyst coupled with air oxidation under solar irradiation", Preeja. P. Thattil and Dr. A. Leema Rose in National conference on Nano National Summit-Current Trends and Future Perpectives, Holy Cross College (Autonoumous), Affiliated to Bharathidasan University, Tiruchirappalli, 9th and 10th January 2019.
- "Titanium dioxide nanocatalyst for photocatalytic degradation of acid red dye under solar radiation", Preeja. P. Thattil and Dr. A. Leema Rose in International conference on Frontier Areas in Chemical Technologies, Alagappa University, Karaikudi, 25th and 26th July 2019.
- 3. "Titanium dioxide nanocatalyst for photocatalytic degradation of basic yellow 2 dye under solar irradiation", Preeja. P. Thattil and Dr. A. Leema Rose in International conference on New Vistas in Material Science, Seethalakshmi Aachi College for Women, Affiliated to Alagappa University, Sivagangai district, 12th September 2019.
- 4. "Photocatalytic degradation of triaryl methane dye using ZnO nanocatalyst under solar irradiation", Preeja. P. Thattil and Dr. A. Leema Rose in National Seminar on Recent Trends in Chemistry, Jayaraj Annapackiam College for Women (Autonomous), Affiliated to Mother Teresa Women's University, Theni district, 10th December 2019.
- 5. Participated in the International Virtual Conference on "Modern Instrumentation and Characterization Techniques in Applied Sciences", organized by MIET Kumaon Haldwani & Department of Chemistry, H.N.B Govt. P. G. College,

- Khatima, Uttarakhand in Collaboration with USERC DST Dehradun & Department of Chemistry, R.H. Govt. P.G. College, Kashipur, Uttarakhand, India, 5-6 July 2020.
- 6. Participated in the National Virtual Conference on "Recent Advances in Analytical Techniques" organized by Department of Chemistry & ADDP Shri Varshney College Aligarh, Dr. B. R. Ambedkar University Agra, Uttar Pradesh, Centre of Bio-Medical Research Lucknow, Uttar Pradesh in Collaboration with Department of Chemistry, R.H. Govt. P.G. College, Kashipur, Uttarakhand, Department of Chemistry, H.N.B Govt. P. G. College, Khatima, Uttarakhand in Collaboration with USERC DST Dehradun, Uttarakhand Govt. India, 16-17 August 2020.
- 7. "Synthesis and Structural Characterization of BiOCl Photocatalyst for the Degradation of Acid green 1 Dye under Sunlight", Preeja. P. Thattil and Dr. A. Leema Rose in International Virtual Conference on Expanding Frontiers in Chemistry, Arul Anandar College (Autonomous), Affiliated to Madurai Kamaraj University, Madurai, 11 & 12th November 2021.
- 8. "Synthesis of maghemite iron oxide nanoparticles and evaluation of their antifungal and antioxidant activities" Preeja. P. Thattil and Dr. A. Leema Rose in International Virtual Conference on Futuristic Aspects of Sensors and Biosensors (IVCFASB-2022), Holy Cross College (Autonomous), Affiliated to Bharathidasan University, Tiruchirappalli, 3 & 4th March 2022.





ORIENTAL JOURNAL OF CHEMISTRY

An International Open Access, Peer Reviewed Research Journal

ISSN: 0970-020 X CODEN: OJCHEG 2021, Vol. 37, No.(4): Pg. 770-778

www.orientjchem.org

High Photocatalytic Performance of Modified Bismuth Oxychloride Semiconductor under Sunlight

PREEJA. P. THATTIL and A. LEEMA ROSE*

Department of Chemistry, Holy Cross College (Autonomous), Affiliated to Bharathidasan University,
Tiruchirappalli-620 002, Tamil Nadu, India.

*Corresponding author E-mail: leemarose25@gmail.com

http://dx.doi.org/10.13005/ojc/370402

(Received: July 08, 2021; Accepted: August 09, 2021)

ABSTRACT

In recent years, the bismuth compounds have gained much interest due to their potential applications in the field of Photocatalysis. In our present work, Bismuth oxychloride Photocatalyst and Aluminium fluoride doped Bismuth oxychloride photocatalyst were synthesized by simple chemical methods using bismuth nitrate pentahydrate as the precursor. The synthesized photocatalysts were characterized by different analytical techniques such as X-ray diffraction analyses, Ultraviolet-Diffuse reflectance spectrum, Field Emission-Scanning Electron Microscopy, Energy dispersive X-ray analyses, Fourier transform infrared spectroscopy studies and BET surface area analysis. The photocatalytic performances of the as-synthesized doped and undoped bismuth oxychloride photocatalyst were tested towards the degradation of Acid green 1 dye. The parameters such as the effect of pH, catalyst concentration and initial dye concentration are optimized, and the kinetic studies are carried out for the photocatalytic dye degradation process. The experimental results showed that about 80% of the Acid green 1 dye got decolourized within 90 min by effective air purging under natural sunlight radiation in the presence of the AlF-BiOCI photocatalyst under optimized conditions.

Keywords: AIF-BiOCl photocatalyst, XRD, HR-SEM, Acid green 1 dye, Air Oxidation, Solar radiation.

INTRODUCTION

Water pollution has become a major environmental concern as it encourages the transmission of many waterborne diseases, especially in developing nations. The paper, textile, leather, printing and dyeing industries which utilize a large amount of coloring materials such as dyes that are non-biodegradable and synthetically stable poisons are released into the nearby water bodies. This release of the effluent

into the nearby water streams are considered to be a serious environmental hazard to both aquatic as well as human life¹. Different water treatment techniques such as Coagulation, flocculation, adsorption, membrane separation, UV/Ozone treatment have been employed for the removal of the organic pollutants from the wastewater²⁻⁵. Among the various water treatment technologies, the development of advanced oxidation process in the past years have gained considerable interest by the researchers due to



the low-cost, eco-friendliness and the potential to completely degrade the organic pollutants into harmless products such as carbon dioxide and water⁶⁻¹⁰. Among many semi-conductor nanocatalysts bismuth-based semiconductors have gained tremendous consideration in the field of photocatalysis for its remarkable action against hazardous pollutants¹¹⁻¹³. Bismuth oxychloride is reported to show excellent photocatalytic activity in the degradation of variety of organic pollutants such as dyes, pesticides, phenols and microbes as it possesses a high chemical stability¹⁴. Many researchers have reported the excellent photocatalytic activity of Bismuth oxychloride photocatalyst which is attributed to the layered structure of [Bi₂O₂]²⁺ monolayer and dual 'Cl' layers¹⁵. However, its large band gap (3.17-3.54 eV) energy values have limited its activity as a photocatalyst towards many pollutants¹⁶. Hence, in order to overcome these limitations many modifications of bismuth oxychloride photocatalyst have been researched by the materials scientists in the recent years. Among which coupling and doping of the BiOCI photocatalyst with other suitable semiconductors are found to be effective in getting better photo-response and also facilitate the separation of photo induced electron-hole pairs which interact with the hydroxyl radicals to provide excellent photodegradation of the contaminants17. Hence, in our present work we have mainly focused on synthesizing a modified bismuth oxychloride photocatalyst via a facile low cost approach using water as the solvent, bismuth nitrate pentahydrate as the precursor, potassium chloride as the source of halogen and Aluminium fluoride as the dopant. The as-synthesized bismuth oxychloride photocatalyst have been employed for the degradation of the textile dye Acid green 1. It is a nitroso dye with the molecular formula (C₃₀H₁₅FeN₃Na₃O₁₅S₃) and Molecular Weight (878.46). The dye shows excellent absorption and excellent light fastness. It is mainly used in solar salt industry and wool, silk and nylon fabric dyeing and printing can also be used for leather dyeing^{18,19}. The chemical structure and UV-Visible absorption spectrum of the Acid green 1 dye is shown in Figure 1.

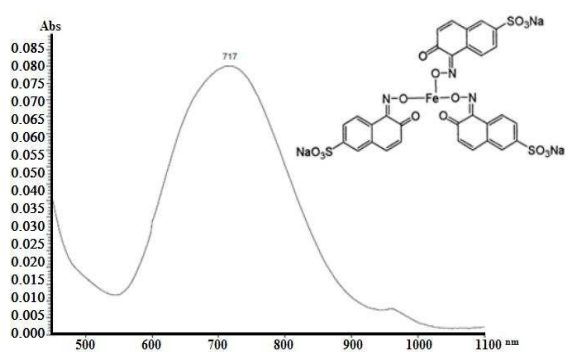


Fig.1. Shows the UV-Visible spectrum and Chemical structure of Acid green 1 dye

EXPERIMENTAL

Materials

All materials used in this experiment are of analytical grade. Bismuth nitrate pentahydrate (M.W. 485.07, purity 98%) and Acid green 1 dye was purchased from S. D. Fine Chemicals., Potassium chloride from Merck and ethanol (99.9%) was purchased from Changshu Hongsheng Fine Chemical Co. Ltd. The solution pH was measured using Elico digital pH meter. The decolourization of dyes was monitored by UV-Visible spectrophotometer (Hitachi-U2910).

Synthesis of AIF-BiOCI Photocatalyst

Bismuth nitrate pentahydrate is used as a precursor to prepare the bismuth oxychloride catalyst. In a typical synthesis, 0.1M bismuth nitrate pentahydrate is dissolved in 100 mL double distilled water. About 3 wt% of Aluminium fluoride salt is added to the precursor solution and it is continuously stirred for about half an hour and this solution is labeled as A. Potassium chloride is used as a source of chlorine which is dissolved in a minimum quantity of double distilled water labeled as solution B. The solution B is added to A and the mixture is stirred continuously for 30 minutes. The pH of the solution is adjusted to 2 using aqueous ammonia solution. The stirring is continued for 7 h and the obtained precipitate is repeatedly washed with double distilled water, dried in a hot air oven followed by calcinations process. 0.5, 1, 2 and 4 wt% of AIF/BiOCI photocatalyst is prepared by adopting the same procedure and bare Bismuth oxychloride catalyst is prepared without the addition of Aluminium fluoride as the dopant.

Characterization

The instrument UV-Spectrophotometer (Hitachi U2910) was used for measuring the decrease in absorbance of the dyes throughout the experiment for all the parameters optimized. The morphological characterizations of the synthesized AIF/BiOCI and BiOCI photocatalyst were investigated by HR-SEM with EDAX (FEI Quanta FEG 200-High Resolution Scanning Electron Microscope). The crystallinity and crystal phase of the as-synthesized photocatalysts were analyzed by X-ray diffraction (XRD, Rigaku) patterns with Cu-k α Radiation (λ = 1.54178 Å) in the range of 20-65 degree is scanned at 40 kV. The UV-DRS are carried out with the help of the instruments UV-Spectrophotometer SHIMADZU/ UV-2600, BET surface area analysis using Quanta chrome instruments, Autosorb IQ series and Fourier transform infrared spectroscopy (Bruker Tensor-27) for the confirmation of the metal-oxide bond in the synthesized photomaterial.

Photocatalytic Degradation Experiments

About 1.13×10⁻⁵ mol/Lof Acid green 1 dye was prepared as the stock solution, from which required volume was withdrawn for each experiment. All the photocatalytic experiments were carried out on sunny days between 11 am to 2 pm. The suspensions were magnetically stirred in the dark for 15 min to attain adsorption-desorption equilibrium between dye and the catalyst. Before exposing the dye solution to sunlight irradiation, the initial absorption peak was recorded. To evaluate the effect of initial dye concentration, the concentration of the dye varied from 1.13×10⁻⁵ mol/L to 5.69×10⁻⁵ mol/L. The experiment was continued for 3 h at appropriate intervals small aliquots of the solution are withdrawn and the decrease in the absorbance is noted. The effect of pH was studied by adjusting the solution using NaOH and HCI. The blank experiments were performed in the dark at room temperature following the above procedure. The percentage decolourization was calculated using the formula

$$\frac{C0-C}{C0} \times 100$$

Where $\rm C_{\scriptscriptstyle 0}$ is the concentration of the dye solution at t=0 and C is the concentration of the dye solution at time t.

RESULTS AND DISCUSSION

X-Ray Diffraction Analysis

The crystalline phase of the synthesized AIF-BiOCI and BiOCI photocatalyst is investigated by using powder X-ray diffraction analysis. The XRD pattern of the synthesized material is shown in Fig. 2a and 2b. The sharp diffraction patterns observed for the synthesized AIF doped BiOCI and bare BiOCI photocatalyst suggests that these photocatalysts are highly crystalline in nature. The diffraction peaks at 20 positions 12.1, 24.2, 26, 32.5, 33.6, 36.7, 41, 46.7, 49.8, 55.2, 58.7, 68.2, 75.1, 77.6 corresponds to the crystal planes (001) (002) (101) (101) (102) (003) (112) (200) (004) (104) (212) (114) (220) (214) and (006) respectively, according to JCPDS card No. 85-0861. As no additional diffraction peaks are observed in the doped BiOCI photocatalyst or no other peaks are observed which might arise from impurity, it is concluded that the synthesized Bismuth oxychloride photocatalyst samples are pure. In the XRD pattern, the peak (102) is found with maximum intensity indicating it to be the preferred growth plane²⁰.

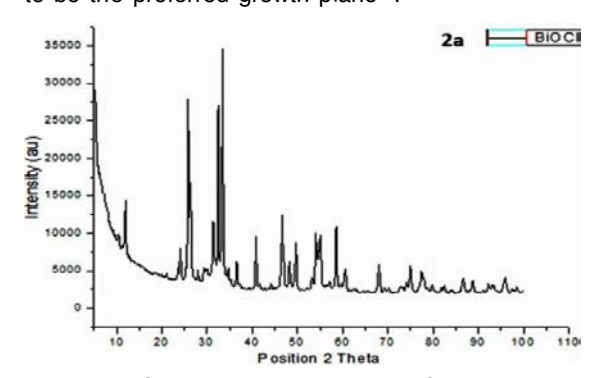


Fig. 2a. Shows the XRD pattern of the Synthesized Bismuth oxychloride photocatalyst

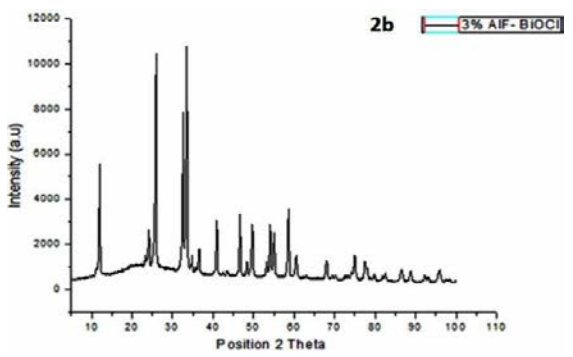


Fig. 2b. shows the XRD pattern of the synthesized AIF doped BiOCI photocatalyst

HR-SEM and **EDAX** Analysis

The morphology of the BiOCI and AIF doped BiOCI photocatalysts are studied from the scanning electron microscopic technique. It is found from the SEM micrographs that the synthesized Bismuth oxychloride photocatalyst possess nanoflake like structure and the width of the nanoflakes ranges from 69.3 to 75.1nm and the AIF-BiOCI photocatalyst also possessed flake-like arrangement which is shown in the SEM images Fig. 3a and 3b. Energy dispersive X-ray analysis is used to determine the major elemental composition in the synthesized materials²¹. Using this technique, the elemental composition of the synthesized materials is obtained with high resolution. The EDAX analysis data confirmed that the elements Bismuth, oxygen and chlorine are present in major composition without any other impurity in the BiOCI photocatalyst and the presence of aluminium, fluorine, Bismuth, oxygen and chlorine in the synthesized AIF-BiOCI photocatalyst is also confirmed from the EDAX data shown in Figure 4a and 4b.

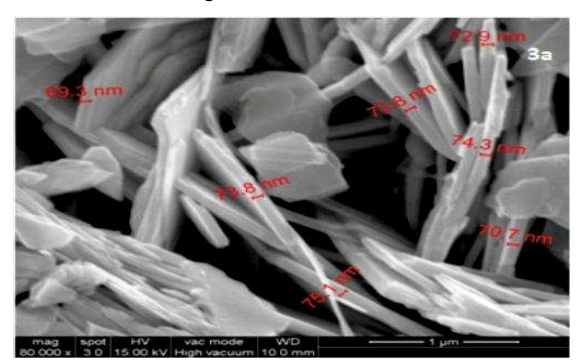


Fig. 3a. shows the FE-SEM images of the synthesized Bismuth oxychloride photocatalyst

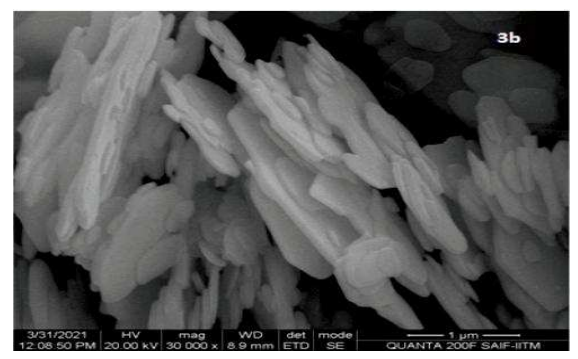


Fig. 3b. Shows the FE-SEM images of the synthesized AIF-BiOCI photocatalyst

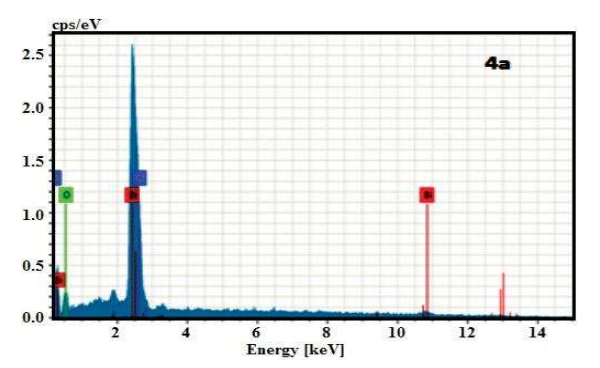


Fig. 4a. Shows the EDAX images of the synthesized Bismuth oxychloride photocatalyst

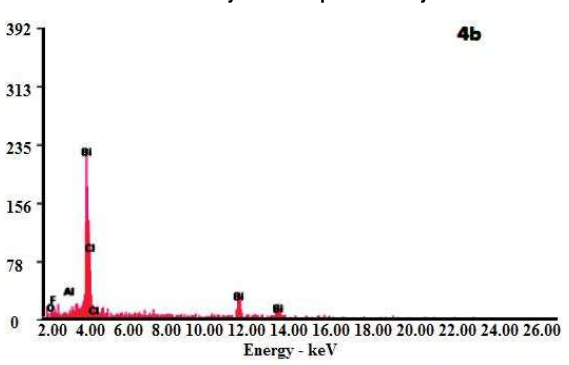


Fig. 4b. Shows the EDAX images of the synthesized AIF-BiOCI photocatalyst

UV-Diffuse reflectance spectrum

The band gap measurements of the synthesized bismuth oxychloride and aluminium fluoride doped bismuth oxychloride photocatalyst is done with the help of UV-Visible diffuse reflectance spectroscopy which paves way to understand whether there are changes in the band gap of the modified semiconducting photomaterial and whether the photomaterial absorbs the UV or Visible radiation²². The band gap of the synthesized AIF-BiOCI and bare BiOCI photocatalyst is calculated using the following relation: $E_a = 1240/\lambda$, where λ is the cut off wavelength and E_a is the band gap energy in electron volts (eV). The band gap energy of the bismuth oxychloride photocatalyst is found to be 3.2ev and the band gap value of the Aluminium fluoride doped bismuth oxychloride photocatalyst is calculated to be 2.86ev.

Fourier Transform Infra-Red spectroscopy

The metal-oxygen bond formation in the synthesized AIF-BiOCl and bare BiOCl photocatalyst is confirmed from the fourier transform infra-red spectroscopy shown in Fig. 6. The band observed at 3435 cm⁻¹ in both AIF-BiOCl and bare BiOCl photocatalyst corresponds to the stretching vibrations of hydroxyl group. The peak at 1630 cm⁻¹ confirms

the bending vibrations of the water molecules which are adsorbed on the surface of the photocatalyst. The broad bands between 412 and 850 cm⁻¹ are due to the framework vibrations of Bi-O bonds. The peak at about 532 cm⁻¹ resulted from the symmetrical stretching vibration of the Bi-O band is a typical peak of BiOCI photocatalyst which is observed in both AIF-BiOCI and bare BiOCI photocatalysts²³⁻²⁵.

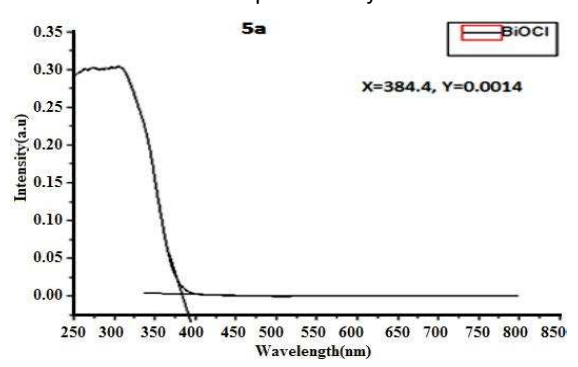


Fig. 5a. shows the UV-DRS plot of the synthesized Bismuth oxychloride photocatalysts

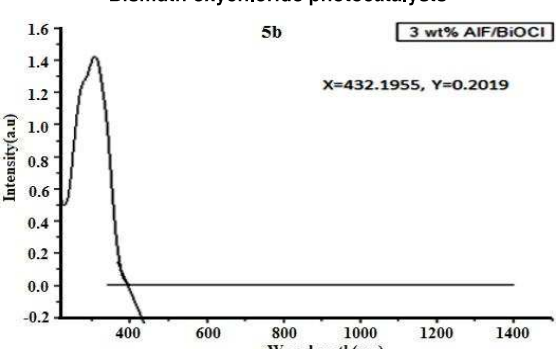


Fig. 5b. shows the UV-DRS plot of the synthesized Bismuth oxychloride and AIF-BiOCI photocatalysts

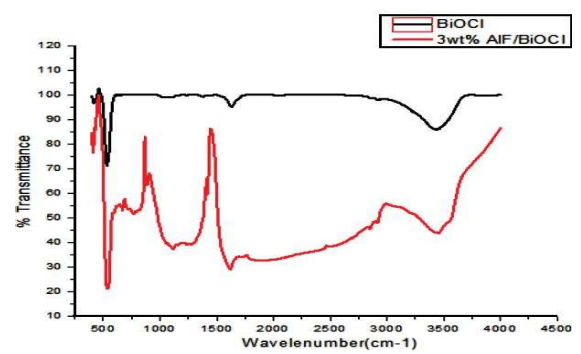


Fig. 6. Shows the FTIR spectrum of the synthesized BiOCl and AIF-BiOCl photocatalyst

BET Surface area measurements

Surface area is a crucial factor for determining the catalytic activity of the bare as well as surface modified photocatalysts^{26,27}. The specific

surface area as well as the BJH pore size distribution of AIF-BiOCI and bare BiOCI photocatalysts are measured by Nitrogen adsorption-desorption isotherms and the plots are shown in Fig. 7a and 7b. The N₂ adsorption-desorption plots for samples BiOCI and AIF/BiOCI (3 wt%) are categorized as type IV isotherms, which proves the existence of pores in between each inter-crossed linked nanoplates^{28,29}. From the BET surface area measurements, it is found that the specific surface area of the bismuth oxychloride photocatalyst is 18.726 m²/g with a pore volume of 0.036 cc/g and the specific surface area of the AIF- Bismuth oxychloride photocatalyst is 14.837 m²/g with a pore volume of 0.030 cc/g.

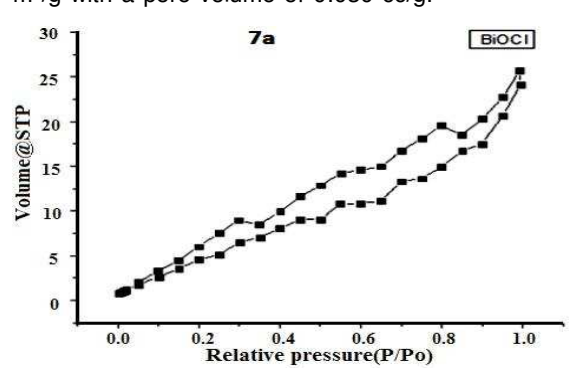


Fig. 7a. Shows the Nitrogen adsorption-desorption isotherms of the synthesized BiOCI photocatalyst

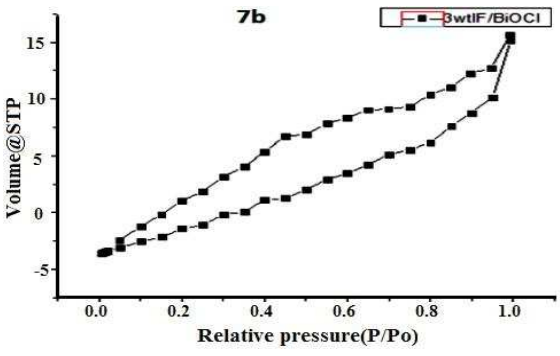


Fig. 7b. shows the Nitrogen adsorption—desorption isotherms of the synthesized AIF-BiOCI photocatalyst

Photocatalytic Degradation studies of Acid green 1 dye Effect of pH

The influence of pH on the photocatalytic decolourization of acid green 1 dye $(1.13\times10^{-5} \text{ mol/L})$ is studied by varying the pH range from 3 to 12 at a catalyst concentration of 15 mg per 50 mL of the dye solution. The maximum decolourization efficiency is observed at pH 5 which is shown in Fig. 8. The higher degradation of anionic acid green 1 dye at acidic pH = 5 is due to its interaction with the H⁺ ions.

On the other hand, in alkaline medium the negatively charged BiOCI catalyst and the anionic acid green 1 dye competes for interaction with hydroxyl ions thereby resulting in low photocatalytic degradation process³⁰.

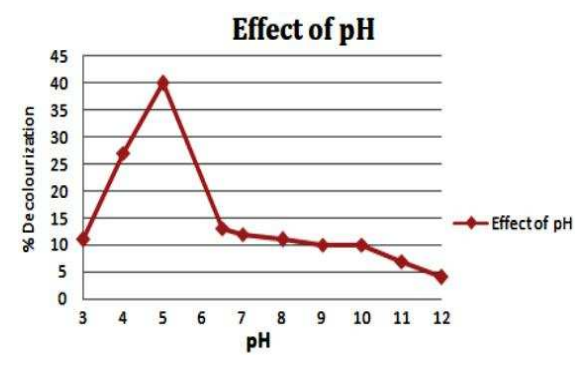


Fig. 8. 1.13x10-5 mol/L of acid green 1 dye solution, 25 mg of BiOCI catalyst, pH varied from 3 to 12, air flow rate = 2.5L/min under sunlight

Effect of Catalyst Concentration

For the effective decolourization of acid green 1 dye the bismuth oxychloride catalyst dosage is optimized by varying the catalyst concentration from 5 mg to 55 mg per 50 mL of the dye solution at optimized pH level 5. The maximum decolourization is observed for 15 mg of the catalyst dosage which is shown in Fig. 9. On increasing the BiOCI catalyst dosage a decrease in the photocatalytic dye decolourization process is observed. This may be due to the fact that on increasing the catalyst dosage the number of active surface area increases for the dye molecules to get adsorbed31 and by adding excess amount of catalyst dosage, turbidity in the dye solution gets increased which in turn decreases the sunlight penetration as a result of which there is a decrease in the dye decolourization process.

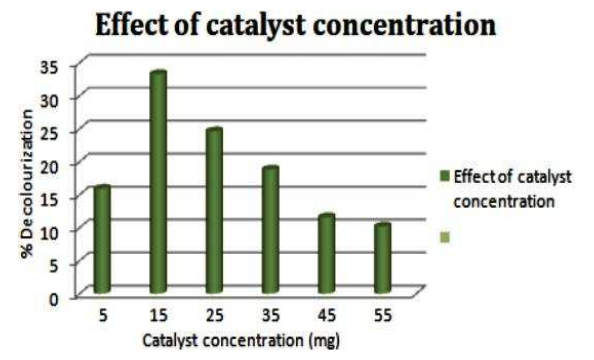


Fig. 9. 1.13x10⁻⁵ mol/L of acid green 1 dye solution, BiOCI catalyst dosage varied from 5 mg to 55 mg, pH = 5, air flow rate = 2.5L/min under sunlight

Effect of initial dye concentration

The initial dye concentration of the acid

green 1 dye is varied in the range 1.13×10-5 mol/L to 5.69×10⁻⁵ mol/L to find out the maximum dye concentration that can be decolourized with bismuth oxychloride photocatalyst (15 mg/50mL of dye solution) at optimized pH level 5. The maximum decolourization of AG1 dye is observed at a concentration of 2.27×10⁻⁵ mol/L which is shown in Fig. 10. The experimental results shows that beyond the concentration level of 2.27×10⁻⁵ mol/L there is a decrease in the dye decolourization process, this may be due to the fact that at higher dye concentration levels the number of active sites of the bismuth oxychloride photocatalyst available for the dye molecules is very less and hence the probability of the dye molecule to react with the hydroxyl ions is less which shows a retardation in the dye decolourization process³².

Effect of Initial Dye Concentration

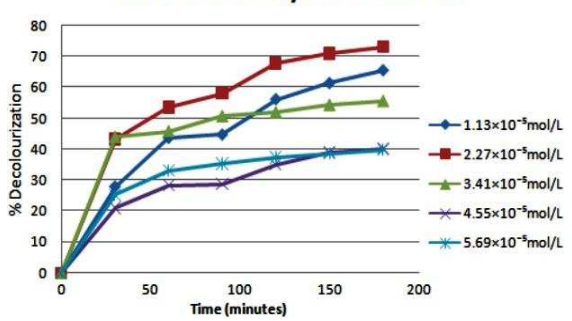


Fig. 10. 15mg of BiOCl catalyst, pH = 5, initial acid green 1 dye concentration varied from 1.13x10-5 mol/L to 5.69x10-5 mol/L, air flow rate = 2.5L/min under sunlight

Effect of Different weight percent of AIF onto BiOCI photocatalyst

The photocatalytic response of both doped and undoped bismuth oxychloride photocatalyst is studied by doping different weight percent (0.5, 1, 2, 3 and 4 wt%) of aluminium fluoride which is shown in Fig. 11. The maximum dye decolourization is observed for 3 wt% of aluminium fluoride doped bismuth oxychloride photocatalyst within 90 min whereas the bare BiOCI photocatalyst degraded AG1 dye only at 180 min under similar experimental conditions and under dark condition in the absence of the sunlight only 18% of the dye got decolourized this may be due to the adsorption of the AG1 dye onto the photocatalyst surface. The faster degradation of AG1 dye with AIF-BiOCI photocatalyst may be attributed to the decrease in size of the catalyst with the surface area. Greater the surface-active sites available, greater will be the photocatalytic activity. A second factor responsible for the increase in photocatalytic degradation is the decrease in the band gap energy values. Generally, in a semiconductor the decrease in the band gap values causes generation of electrons and holes more quickly which further reacts with the hydroxyl radicals to degrade the dye molecules³³.

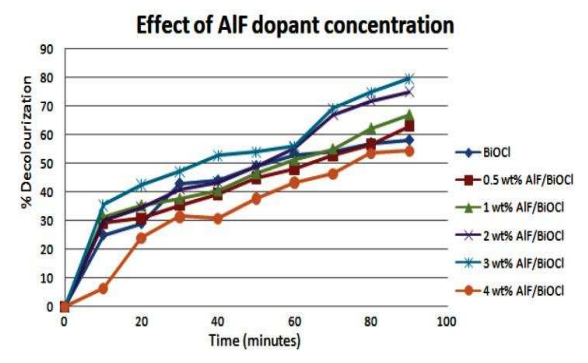


Fig. 11. shows the variation for different weight percent of AIF dopant concentration onto BiOCI catalyst for the photocatalytic decolourization of Acid green 1 dye

Kinetic studies

Langmuir-Hinshelwood (L-H) kinetic model is used here to study the kinetics of doped and undoped heterogeneous semiconductor photocatalyst. This (L-H) kinetic model has been widely used by several authors to find out the order of the reaction in heterogeneous semiconductor photocatalysis³⁴⁻³⁷. The kinetic studies carried out for the photocatalytic degradation of AG1 dye follows pseudo first order kinetics according to the equation.

$ln [C_0]/[C] = kt$

Where k is the pseudo-first-order rate constant (min⁻¹), C_0 is the concentration of dyes (g L⁻¹) at t = 0, C is the concentration of dyes at reaction time t (minute). The linear fit between In $[C_0/C]$ and irradiation time't' for bismuth oxychloride and Aluminium fluoride (0.5, 1, 2 and 3 wt%) doped bismuth oxychloride photocatalyst is shown in Fig. 12. The calculated average R² value for the bare bismuth oxychloride photocatalyst is 0.9514 and for different weight percent of AIF-BiOCI were found to be 0.9196, 0.9629 and 0.9095 respectively.

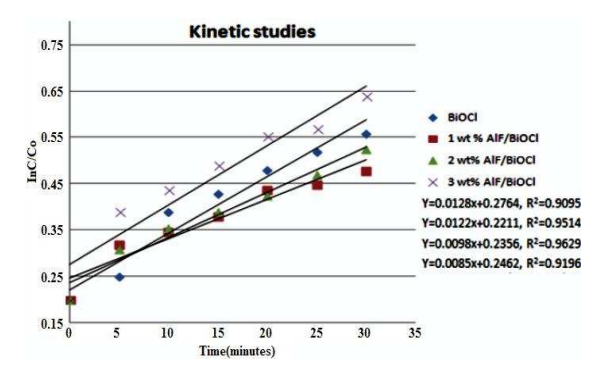


Fig.12. shows the pseudo-first order kinetic plot for the photocatalytic decolourization of Acid green 1 dye using different weight percent (0-3%) of Aluminium fluoride doped Bismuth oxychloride catalyst

CONCLUSION

Aluminium fluoride doped bismuth oxychloride and bare bismuth oxychloride photocatalyst is prepared via simple chemical precipitation technique. The optical and morphological characteristics of the synthesized BiOCI and AIF-BiOCI are studied and compared with the help of spectroscopy techniques such as XRD, FE-SEM, EDAX, FTIR, UV-DRS and BET surface area studies. The crystalline nature and hexagonal wurtzite structure of the synthesized BiOCI and AIF-BiOCI photomaterial is confirmed from the X-ray diffraction studies. The SEM images showed that the synthesized photomaterial possessed a flake-like structure and the major elements such as bismuth, oxygen, aluminium and fluorine in the synthesized photomaterial is confirmed from the EDAX data. The FTIR studies confirmed the metal-oxide bond formation and a decrease in the band gap and surface area of the AIF-BiOCI catalyst compared to that of the bare BiOCl photocatalyst is studied from the UV-DRS and BET surface area analysis. Further the photocatalytic activity carried out for the acid green 1 dye showed that AIF doped bismuth oxychloride photocatalyst degraded the dye within 90 min under sunlight radiation at optimized conditions whereas the bare bismuth oxychloride photocatalyst took more under similar optimized conditions. The photocatalytic reaction followed pseudo-first order kinetics according to Langmuir-Hinshelwood kinetic model. Thus, on concluding, AIF-BiOCI photocatalyst coupled with air oxidation under sunlight has proved to be an efficient photocatalyst for the degradation of the acid green 1 dye in aqueous solution.

ACKNOWLEDGEMENT

The authors sincerely thank Dr. S. Thennarasu, Sr. Principal Scientist, Department of Organic and Bio-Organic Chemistry, Central Leather Research Institute, Chennai, for his valuable suggestions given for the successful completion of the work. We also thank PG and Research

Department of Chemistry, Holy Cross College (Autonomous), Tiruchirappalli, for providing the necessary laboratory facilities.

Conflict of Interest

The authors declare that there is no conflict of interest.

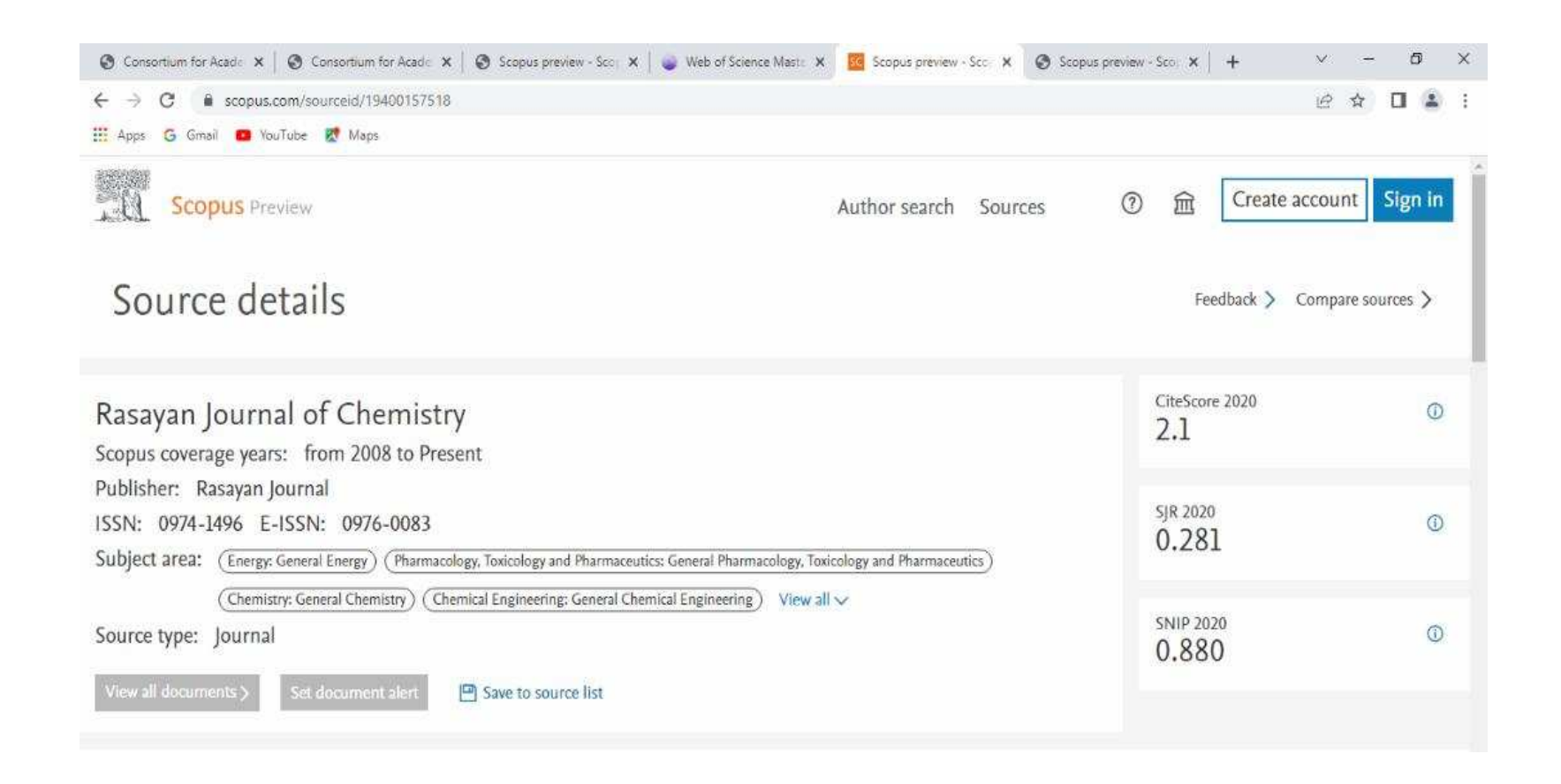
REFERENCES

- 1. Brit., Synthetic Dyes: A look at Environmental & Human Risks., **2008**.
- Matilainen, A.; Vepsäläinen, M.; Sillanpää, M., Natural Organic Matter Removal by Coagulation during Drinking Water Treatment: A Review. Advances in Colloid and Interface Science., 2010, 159(2), 189-97.
- 3. Liu, Y.; Zeng, G.; Tang, T., Highly effective adsorption of cationic and anionic dyes on magnetic Fe/Ni nanoparticles doped bimodal mesoporous carbon, *Journal of Colloid and Interface Science.*, **2015**, *448*, 451–549.
- 4. Khulbe, K.C.; Matsuura, T., Removal of heavy metals and pollutants by membrane adsorption techniques, *Applied Water Science.*, **2018**, *8*,19.
- Laisheng, Li.; Zhu, W.; Zhang, P.; Lu, P., UV/O3-BAC process for removing organic pollutants in secondary effluents, *Desalination.*, 2017, 1-3, 114-124.
- Song, L.; Pang, Y.; Zheng, Y.; Ge, L., Hydrothermal synthesis of novel g-C3N4/BiOCI heterostructure nanodiscs for efficient visible light photodegradation of Rhodamine B, Appl. Phys. A: Mater. Sci. Process., 2017, 123, 500.
- 7. Pu, X.; Zhang, D.; Gao, Y.; Shao, X.; Ding, G.; Li, S.; Zhao, S., One-pot microwave-assisted combustion synthesis of grapheme oxide—TiO₂ hybrids for photodegradation of methyl orange, *J. Alloys Compd.*, **2013**, *551*, 382–388.
- Gao, X.; Zhang, X.; Wang, Y.; Peng, S.; Yue, B.; Fan, C., Rapid synthesis of hierarchical BiOCI microspheres for efficient photocatalytic degradation of carbamazepine under simulated solar irradiation, *Chem. Eng. J.*, 2015, 263, 419–426.
- Zhang, Y.; Zhang, Q.; Shi, Q.; Cai, Z.; Yang, Z., Acid-treated g-C3N4 with improved photocatalytic performance in the reduction of aqueous Cr (VI) under visible-light, Sep. Purif. Technol., 2015, 142, 251–257.
- 10. Yan, S.C.; Li, Z.S.; Zou, Z.G., Photodegradation of rhodamine B and methyl orange over

- boron-doped g-C3N4 under visible light irradiation, *Langmuir.*, **2010**, *26*, 3894–3901.
- Seddigi, Z.S.; Gondal, M.A.; Baig, U.; Ahmed, S.A.; Abdulaziz, M.A.; Danish, E.Y., Facile synthesis of light harvesting semiconductor bismuth oxychloride nano photo-catalysts for efficient removal of hazardous organic pollutants, *PLOS ONE.*, 2017, 12(2),e0172218.
- Shen, K.; Gondal, M.A.; Al-Saadi, A.A.; Liye, L.; Chang, X.; Xu, Q., Visible light induced photodegaradtion of Rhodamine dyes over BiOCl and the vital importance of frontier orbital energy of the dye molecules in the reaction kinetics, *Res. Chem. Intermed.*, 2015, 41, 2753-2766.
- 13. Kang, S.; Pawar, R.C.; Pyo, Y.; Khare, V.; Lee, C.S., Size-controlled BiOCl±RGO composites having enhanced photodegradative properties, *J. Exp. Nanosci.*, **2016**, *11*, 259-275.
- Li, K.; Liang, Y.; Yang, J.; Gao, Q.; Zhu, Y.; Liu, S.; Xu, R.; Wu, X., Controllable synthesis of 001 facet dependent four square BiOCI nanosheets: a high efficiency photocatalyst for degradation of methyl orange, *J. Alloys.* Compd., 2017, 695, 238–249.
- Wen.; Ren, W. L.; Peng, F., Recent advances of bismuth oxychloride photocatalytic material: Property, preparation and performance enhancement, *Journal of Electronic Science* and Technology, 2020, 18(2), 100020.
- Liu, X.; Su, Y.; Zhao, Q.; Du, C.; Liu, Z., Constructing Bi₂₄O₃₁Cl₁₀/BiOCI heterojunction via a simple thermal annealing route for achieving enhanced photocatalytic activity and selectivity, Sci. Rep. Sci., 2016.
- 17. Zhao, H.; Tian, F.; Wang, F.; Chen, R., A Review on Bismuth-Related Nanomaterials for Photocatalysis, *Reviews in Advanced Sciences and Engineering.*, **2014**, *3*, 1–25.
- Raue.; Roderich.; Corbett.; John F., Nitro and Nitroso Dyes, Ullmann's Encyclopedia of Industrial Chemistry., 2000.

- 19. Horobin, R.W.; Kiernan, J.A., Conn's Biological Stains: A Handbook of Dyes, Stains and Fluorochromes for Use in Biology and Medicine, *BIOS Scientific. Publ.*, **2002**, *101*, 102.
- Sharma, I.D.; Tripathi, G.K.; Sharma, V.K.; Tripathi, S.N.; Kurchania, R.; Kant, C.; Sharma, A.K.; Saini, K.K., One-pot synthesis of three bismuth oxyhalides (BiOCl, BiOBr, BiOI) and their photocatalytic properties in three different exposure conditions, *Cogent Chemistry.*, 2015, 1, 1076371.
- Ascencio Aguirre, F.M.; Bazan Diaz, L.; Mendoza Cruz, R.; Vazquez, M.S.; Encinia, O.O.; Rodriguez, A.G.; Becerra, R.H., Chemical synthesis and characterization of bismuth oxychloride BiOCI nanoparticles, Appl. Phys. A., 2017, 123, 155.
- 22. Sharma, K.; Dutta, V.; Sharma, S.; Raizada, P.; Hosseini Bandegharaei A.; Thakur, P.; Singh, P., Recent advances in enhanced photocatalytic activity of bismuth oxyhalides for efficient photocatalysis of organic pollutants in water: A review, *Journal of Industrial and Engineering Chemistry.*, **2019**.
- Xie, T.; Xu, L.; Liu, C.; Yang, J.; Wang, M., Magnetic composite BiOCI-SrFe₁₂O₁₉: a novel p-n type heterojunction with enhanced photocatalytic activity, *Dalton Trans.*, 2014, 43, 2211–2220.
- Fruth, V.; Popa, M.; Berger, D.; Ionica, C.M.; Jitianu, M., Phase investigation in the antimony doped Bi₂O₃ system, *J. Eur. Ceram. Soc.*, 2004, 24, 1295–1299.
- Song, J.; Mao, C.; Niu, H.; Shen, Y.; Zhang, S., Hierarchical structured bismuth oxychlorides: self-assembly from nanoplates to nanoflowers via a solvothermal route and their photocatalytic properties, *Cryst. Eng. Comm.*, 2010, 12, 3875–3881.
- Tian, F.; Xiong, J.; Zhao, H.; Liu, Y.; Xiao, S.; Chen, R., Mannitol-assisted solvothermal synthesis of BiOCI hierarchical nanostructures and their mixed organic dye adsorption capacities, Cryst. Eng. Comm., 2014, 16, 4298–4305.
- 27. Wang, X.; Bi, W.; Zhai, P.; Wang, X.; Li, H.; Mailhot, G.; Dong, W., Adsorption and photocatalytic degradation of pharmaceuticals by BiOCIxIy Nanospheres in aqueous solution, *Appl. Surf. Sci.*, **2016**, *360*, 240–251.
- 28. Di, J.; Xia, J.; Ji, M.; Wang, B.; Yin, S.; Zhang, Q.; Chen, Z.; Li, H., Carbon quantum dots

- modified BiOCI ultrathin nanosheets with enhanced molecular oxygen activation ability for broad spectrum photocatalytic properties and mechanism insight, *ACS Appl. Mater. Interfaces.*, **2015**, *7*, 20111–20123.
- 29. Qiao, R.; Mao, M.; Hu, E.; Zhong, Y.; Ning, J.; Hu, Y., Facile formation of mesoporous BiVO4/Ag/AgCl heterostructured microsperes with enhanced visible-light photoactivity, *Inorg. Chem.*, **2015**, *54*, 9033–9039.
- Rashid, J.; Karim, S.; Kumar, R.; Barakat, M.A.; Akram, B.; Hussain, N.; Bin H.B.; Xu, M., A facile synthesis of bismuth oxychloride graphene oxide composite for visible light photocatalysis of aqueous diclofenac sodium, *Scientific Reports.*, 2020, 10, 14191.
- Grilla, E.; Kagialari, M.N.; Petala, A.; Frontistis, Z.; Mantzavinos, D.; Photocatalytic Degradation of Valsartan by MoS₂/BiOCI Heterojunctions, *Catalysts.*, 2021, 11, 650.
- Seddigil, Z.S.; Gondal, M.A.; Baig, U.; Ahmed, S.A.; Abdulaziz1, M.A., Danish, E.Y.; Khaled, M.M.; Lais, A., Facile synthesis of light harvesting semiconductor bismuth oxychloride nano photo-catalysts for efficient removal of hazardous organic pollutants, PLOS ONE., 2017.
- 33. Li, H.; Li, J.; Zhihui, Ai.; Jia, F.; Zhang, L., Oxygen Vacancy-Mediated Photocatalysis of BiOCI: Reactivity, Selectivity, and Perspectives, *Angew. Chem. Int. Ed.*, **2018**, *57*, 122-138.
- 34. Tanwar, R.; Mandal, U.K., Photocatalytic activity of Ni0.5Zn0.5Fe₂O₄@polyaniline decorated BiOCI for azo dye degradation under visible light-integrated role and degradation kinetics interpretation, *RSC Adv.*, **2019**, *9*, 8977.
- 35. Ramachandran, S.; Sivasamy, A., Synthesis of nanocrystalline bismuth oxide and its visible photocatalytic activity in the degradation of an organic dye, *Inorganic and Nano-Metal Chemistry.*, **2018**.
- Cui, P.; Wang, J.; Wang, Z.; Chen, J.; Xing, X.; Wang, L.; Yu, R., Bismuth oxychloride hollow microspheres with highvisible-light photocatalytic activity, Nano Research., 2015.
- 37. Cao, B.; Dong, P.; Cao, S.; Wang, Y., BiOCl/Ag₃PO₄ Composites with Highly Enhanced Ultraviolet and Visible Light Photocatalytic Performances, *J. Am. Ceram. Soc.*, **2013**, *96*(2), 544–548.







Vol. 13 | No. 2 | 1166 - 1173 | April - June | 2020 ISSN: 0974-1496 | e-ISSN: 0976-0083 | CODEN: RJCABP http://www.rasayanjournal.com

http://www.rasayanjournal.co.in

ENHANCED REMOVAL OF CRYSTAL VIOLET DYE USING ZINC OXIDE NANORODS AND AIR OXIDATION UNDER SUNLIGHT RADIATION

Preeja. P. Thattil and A. Leema Rose

Department of Chemistry, Holy Cross College (Autonomous), Affiliated to Bharathidasan University, Tiruchirappalli-620 002, Tamil Nadu, India. E-mail: leemarose25@gmail.com

ABSTRACT

A simple chemical precipitation method is employed for the synthesis of ZnO nanorods using zinc acetate precursor in basic medium. The synthesized zinc oxide nanoparticles are characterized using x-ray diffraction analysis, transmission electron microscopy, diffuse reflectance spectroscopy, photoluminescence and bet surface area analysis. These zinc oxide nanorods are used for the photocatalytic decolorization of crystal violet dye and the rate enhancement is achieved by air purging under sunlight radiation. Effective dye removal is attained by optimizing the parameters such as the effect of pH, catalyst dosage and initial dye concentration and the nature of the interaction of hydroxyl and superoxide anion radicals with the crystal violet dye is discussed in this paper.

Keywords: ZnO Nanorods, Crystal Violet, Air Oxidation, Solar Radiation.

© RASĀYAN. All rights reserved

INTRODUCTION

A very large amount of dye effluents is being released by various industrial processes such as paper and pulp manufacturing, plastics, dyeing of cloth, leather treatment and printing which have been considerably increased over the last few decades. 1,2 Synthetic organic dyes from the textile industries are mainly non-biodegradable, creating major environmental pollution and health hazards. Crystal violet is one such cationic, triaryl methane dye which is widely used in the preparation of navy blue and black inks for printing purposes. It is also used as a coloring agent for various products such as fertilizers, types of antifreeze, detergents, and leather. The dye is also used as a histological stain³⁻⁵ despite its extensive applications, crystal violet is reported to be persistent in the environment for a long duration and hence it poses a toxic effect to the aquatic and human life and therefore it is regarded to be a biohazard substance. Since this dye molecule is considered to be a toxic agent^{6,7} it has to be eliminated, by converting it into eco-friendly products using a large variety of semiconductor nanoparticles is considered to be a demanding area of research. Many scientific reports suggested the use of semiconductor photocatalyst for the efficient conversion of organic pollutants into relatively harmless products such as minerals, CO₂ and water^{8,9}. ZnO is an n-type semiconductor photocatalyst with a large number of active sites. It has a wide bandgap of 3.2 Ev. 10 Surface and core defects, such as oxygen vacancies, zinc and oxygen interstitials provide active sites for preventing the electron-hole recombination. This, in turn, enhances the generation of superoxide and hydroxyl radicals, which is found to be responsible for the photocatalytic dye degradation process. 11,12 Thus, ZnO is extensively studied as a photocatalyst in water treatment application due to its low cost, favorable optical, electronic and catalytic properties. 13,14 Recently, Nirmalya Tripathy et al., reported the photocatalytic degradation of crystal violet dye under UV irradiation using ZnO nanonails.¹⁵ In 2010, Swaminathan et al. confirmed the photocatalytic degradation of Acid Black 1 dye by cyclic voltammetric measurements and Chemical Oxygen Demand analysis. 16 Srivastava et al., reported the synthesis of zinc oxide semiconductor nanoparticles by electrochemical method for the degradation of nitrobenzene and azo dye.¹⁷ In this paper, we report the photocatalytic degradation of crystal violet dye using zinc oxide nanorods enhanced by air oxidation under sunlight. The



results obtained from the research work showed that about 96% of the crystal violet dye got degraded within 50 minutes by using the only 25mg of zinc oxide nanocatalyst which clearly showed that the synthesized zinc oxide nanorods are promising materials for the removal of other triaryl methane class of compounds.

EXPERIMENTAL

The Zinc acetate Dihydrate salt (M.W. 219.50, purity 98.5%) was purchased from Sisco Research Laboratories Pvt.Ltd., sodium hydroxide from Merck and ethanol (99.9%) was purchased from Changshu Hongsheng Fine Chemical Co. Ltd. The capacity of the air pump used for the experiments is 3W and air supplied is 2.5L/min. Crystal violet dye (molecular formula C25H30ClN3, MW 407.99 and λ max = 590 nm) was obtained from S. D.Fine Chemicals. The chemical structure of the dye is shown in Fig.-1.

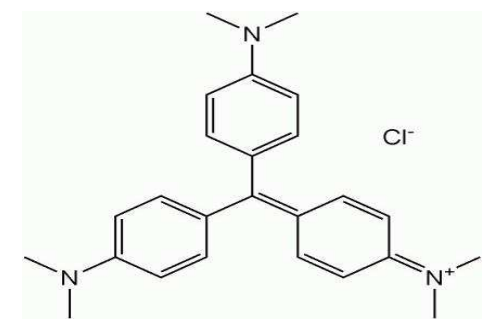


Fig.-1: Chemical Structure of the Crystal Violet Dye.

The morphological characterizations of the synthesized zinc oxide nanoparticles were investigated by scanning electron microscopy (JEOL JSM-7600F FEG-SEM) equipped with energy dispersive spectroscopy (EDS-Bruker), and transmission electron microscopy (TEM CM 200). The crystallinity and crystal phase of the as-synthesized ZnO nanoparticles were analyzed by X-ray diffraction (XRD, Rigaku) patterns with Cu-k α Radiation (λ = 1.54178 Å) at a scan rate of 40 kV. To study the recombination of electron-holes in the photocatalyst, the PL emission spectrum of the sample is measured with Shimadzu/RF6000 and the bandgap of the semiconductor is determined by the diffuse reflectance spectroscopy (Shimadzu/ UV 2600). The surface area and pore volume are determined by the nitrogen adsorption/desorption analyzer.

General Procedure

Synthesis of Zinc Oxide Nanoparticles

Zinc acetate dihydrate is used as a precursor to prepare the zinc oxide nanoparticles. About 0.5g of zinc acetate dihydrate is dissolved in a minimum quantity of double-distilled water. 2mL of ethanol and sodium hydroxide is used as a strong base to precipitate the salt solution. A thick white precipitate is obtained and the mixture is stirred continuously for 30 minutes and then dried in the hot air oven at 100° C for 3 hours and then it is calcined at 450° C.

Photocatalytic Degradation Experiments

The varying stock solutions of crystal violet dye (10mg to 50mg/L) is prepared, from which 50mL was withdrawn for each experiment. All the photocatalytic experiments were carried out on sunny days between 11 am to 2 pm. Before, exposing the dye solution to sunlight irradiation the initial absorption peak was recorded. The reaction was carried out in the open air and the solution was continuously mixed by pumping to provide aeration. The experiment was continued for 3 hours, at appropriate intervals 2mL of the dye solution is withdrawn and centrifuged to separate the catalyst. The effect of pH was studied by adjusting the solution using 0.1N NaOH and 0.1N HCl. The blank experiments were performed in the dark at room temperature following the above procedure. The percentage decolorization was calculated using the formula:

$$\frac{C0-C}{C0} \times 100$$

Where C_0 is the initial concentration of the dye solution and C is the concentration of the dye solution at time t.

RESULTS AND DISCUSSION

Catalyst Characterization

The morphology of the synthesized zinc oxide nanocatalyst is examined by FESEM and TEM analysis.

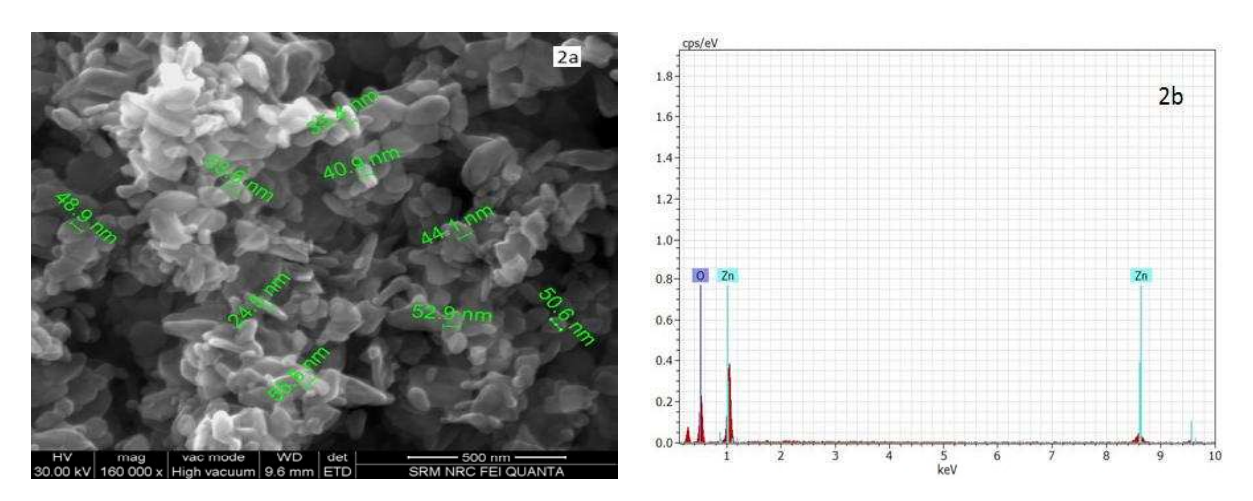


Fig.-2: a and b shows the FE-SEM Images and the EDAX Spectrum of the Synthesized Zinc Oxide Nanoparticles

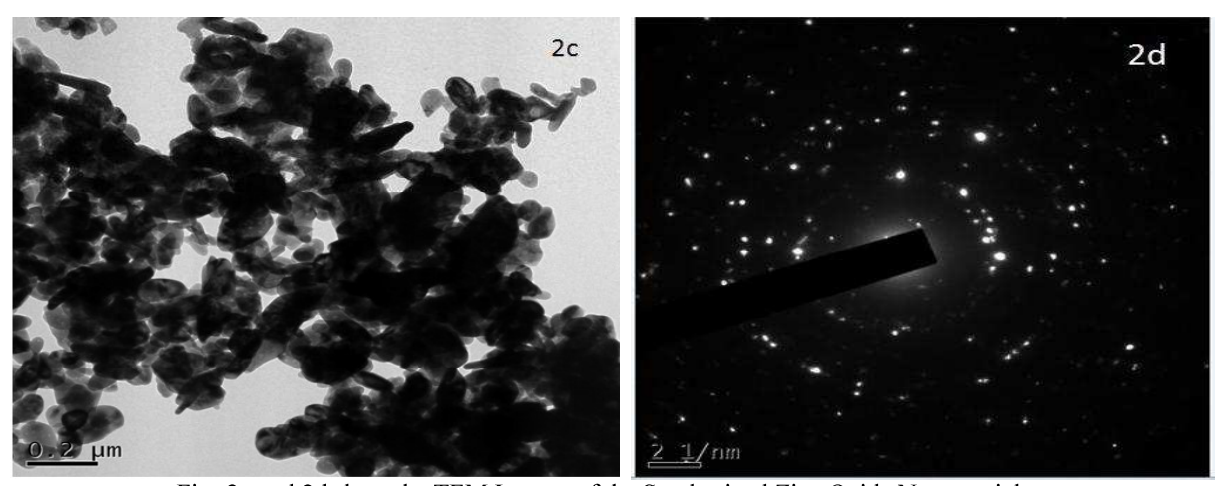


Fig.-2c and 2d show the TEM Images of the Synthesized Zinc Oxide Nanoparticles.

From Figs.-2a and 2c it is found that the synthesized zinc oxide particles posses a moderate rod-like structure with the particle size ranging from 24.5nm to 55.5nm. Additionally, the dark-spotted circles in the SAED pattern indicate the crystalline nature of the zinc oxide nanorods. This result is in agreement with that found to zinc oxide nanoparticles prepared from similar precursors ^{18,19}. The typical EDAX spectrum of the zinc oxide particles in Fig.-2b shows the presence of zinc and oxygen elements in major composition which confirms the successful formation of zinc oxide nanoparticles without any impurities. Further, the crystallinity, band gap value, surface area, optical property, and structural disorders and the defects of the as-synthesized ZnO nanorods were examined by XRD, UV-DRS, nitrogen adsorption-desorption analyzer and room-temperature PL spectrum, respectively.

XRD spectrum of the synthesized zinc oxide nanoparticles shows that all the diffraction peaks were indexed to the hexagonal wurtzite phase of zinc oxide. The diffraction peaks at $2\theta = 31.8$, 34.5, 36.4, 47.6, 56.8, and 63.0 shown in Fig.-3a corresponds to the crystal planes (100), (002), (101), (102), (110), and (103), respectively, which is following the JCPDS file no. 36-1451.²⁰ From the obtained XRD results,

it is found that (101) peak is the most intense one which is also the preferred growth plane of zinc oxide nanoparticles. Bandgap energy (Eg) of the zinc oxide nanocatalyst is obtained using the following relation:

$$Eg = \frac{1240}{\lambda}$$

 $Eg=\frac{1240}{\lambda}$ Where, Eg is the bandgap energy in electron volts (eV) and λ is the wavelength (nm) corresponding to maximum absorption. The Eg of nanocatalyst synthesized using chemical precipitation method was found to be 3.12 eV respectively (as shown in Fig.-3b), which matches well with literature. 21 Room temperature Photoluminescence spectrum of ZnO generally shows three major peaks: the first peak is a UV emission peak around 380 nm, the second peak is a green emission peak around 520nm and the third is a red or orange emission peak around 600 nm.²² PL spectrum of the synthesized zinc oxide nanoparticles was recorded with 254 nm excitation (Fig.-3c). PL emission curve of as formed ZnO nanorods showed a peak at 396 nm which may be due to the electron-hole pair recombination or band to band recombination 23,24 and the broad green emission peak at 523nm correspond to the presence of singly ionized oxygen vacancies.²⁵ The surface area is one of the most important factors that influence the catalytic activity of the semiconductor nanoparticles. The nitrogen adsorption-desorption isotherms of the as-synthesized zinc oxide nanoparticles are shown in Fig.-3d. From the BET surface area measurements, it is found that the specific surface area of the zinc oxide nanocatalyst is 19.593m²/g and its pore volume is 0.099cc/g.

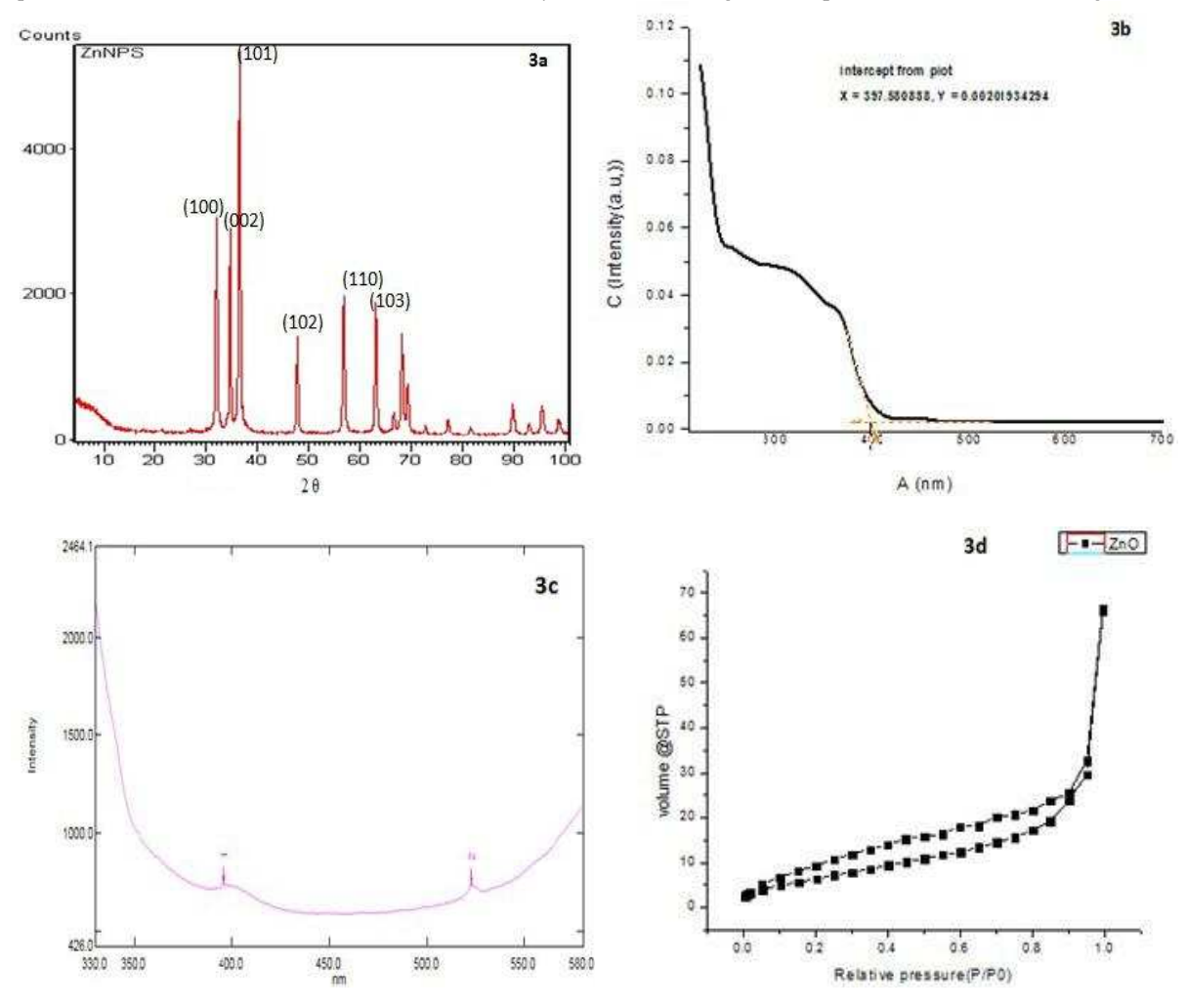


Fig.-3: 3a shows the XRD Pattern of the Synthesized ZnO Nanoparticles, 3b shows the UV-DRS Plot for the Synthesized ZnO Nanoparticles, 3c shows the PL Spectrum of the Synthesized ZnO Nanoparticles and 3d shows the N₂ Adsorption-Desorption Isotherm Pattern of ZnO Nanoparticles

Photocatalytic Degradation of Crystal Violet Dye Effect of pH

The effect of pH in the range of 3–12 and experimental conditions (25mg of ZnO catalyst, 10 mg/L dye concentration) on the overall rate of decolorization is studied. The maximum decolorization efficiency was obtained in alkaline pH=10 shown in Fig.-4. This may be because, in acidic pH values, the photodecomposition of zinc oxide nanoparticles may take place.²⁶ On the other hand, there is an increase in several hydroxyl ions, at higher pH values and it consequently leads to an increase in the photodecolorization process. But when the pH value is so high there is an abundant number of hydroxyl ions around catalyst which compete with dye molecules in adsorption on the surface of photocatalyst; this causes a decrease in photodecolorization efficiency.²⁷

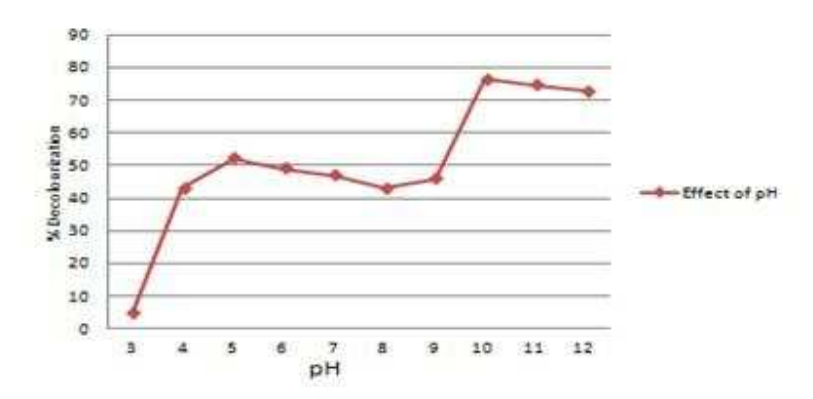


Fig.-4: 0.01g/L Crystal Violet Dye Solution, 25mg of ZnO Catalyst, pH varied from 3 to 12, Airflow Rate = 2.5L/min under Sunlight.

Effect of Catalyst Dosage

The optimum amount of zinc oxide catalyst for the effective decolorization of crystal violet dye is found out by varying the catalyst concentration from 5mg to 55mg for 10mg/L of the dye solution shown in Fig.-5. Initially, by increasing the catalyst concentration till 25mg there is an increase in dye degradation beyond which a decrease in the decolorization rate is observed. This is due to fact that active sites required for the photocatalytic dye decolorization increases by increasing the catalyst concentration and beyond the addition of 25mg of catalyst to the dye solution there is an increase in the turbidity of the suspension and decrease in sunlight penetration occurs as a result of which a decrease in the photodecolorization process is observed.²⁸

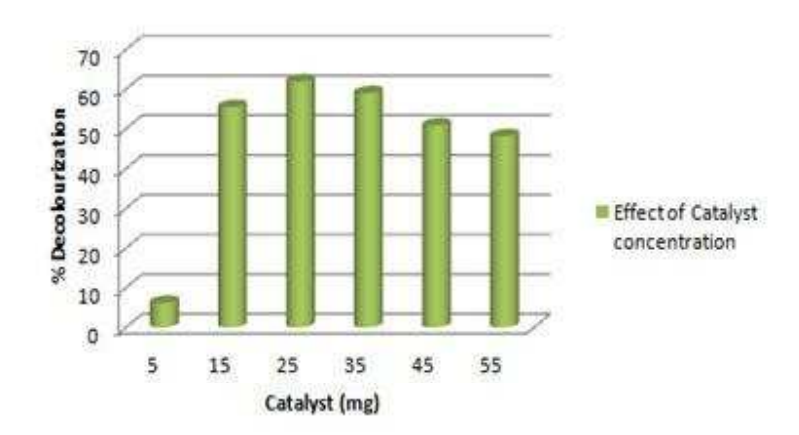


Fig.-5: 0.01g/L Crystal Violet Dye Solution, ZnO Catalyst Dosage Varied from 5mg to 55mg, pH = 10, Air Flow Rate = 2.5L/min under Sunlight.

Effect of Initial Dve Concentration

Only a negligible percentage of the dye gets decolorized in the absence of the catalyst which shows that it is resistant to self photolysis. About 96% of crystal violet dye got degraded within 50 minutes in the presence of ZnO catalyst, air oxidation under solar light at pH=10. From these findings, it is clear that solar light, air oxidation and a semiconductor photocatalyst are needed for the effective degradation of crystal violet dye. The effect of varying initial dye concentrations on the degradation of crystal violet dye with ZnO has been investigated by selecting a concentration range of 10mg/L to 50mg/L under the experimental conditions of catalyst concentration 25mg, pH range 10 and continuous air oxidation which is shown in Fig.-6. The experimental results show that an increase in dye degradation up to 30mg/L of dye solution is observed beyond which there is a decrease in the rate of the degradation process. The formation of hydroxyl radicals and its ability to react with dye molecules decides the rate of the dye degradation process. At higher dye concentrations there is a decrease in the probability of the dye molecules to react with OH radicals and hence a decrease in the dye degradation rate is observed.²⁹

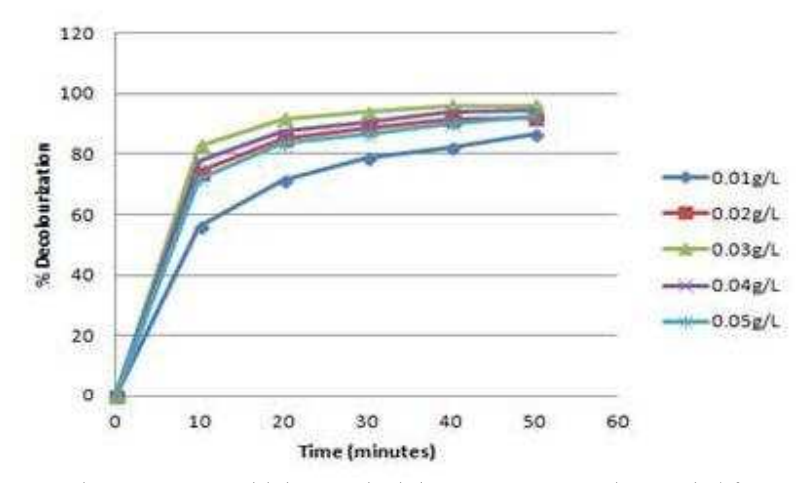


Fig.-6:25mg of ZnO Catalyst, pH = 10, Initial Crystal Violet Dye Concentration Varied from 0.01g/L to 0.05g/L, Air Flow Rate = 2.5L/min under Sunlight.

Degradation Mechanism

Under solar irradiation, the electron gets excited from the valence band of ZnO to the conduction band which leads to the generation of an electron and hole^{30,31}. Then the electron and holes generated take part in the photocatalytic degradation process by producing highly reactive radical species like *hydroxyl* and *superoxide radicals* which react with the dye molecules to give non-hazardous degradation products.

$$ZnO + h\vartheta$$
 \longrightarrow $ZnO(e_{CB} + h^{+}_{VB})$
 $e^{-}+O_{2}$ \longrightarrow O_{2}^{-}
 $O_{2}^{-}+CV$ \longrightarrow Degradation Products of CV
 $h^{+}_{VB}+H_{2}O$ \longrightarrow $H^{+}+OH$
 $h^{+}_{VB}+OH$ \longrightarrow HO
 $HO^{-}+CV$ \longrightarrow Degradation Products of CV

The major products of degradation of crystal violet dye in aqueous solution by advanced oxidation processes were reported by other researchers. According to Huan he et al.,³² the photocatalytic degradation of CV took place by three major processes such as N-de-methylation, destruction of conjugated structure and opening-benzene ring and the major products obtained in the destruction of CV dye was reported to be a series of N-de-methylated products and in the secondary stage organic acids, such as oxalic acid, terephthalic acid, phthalic acid, benzoic acid and 3-hydroxybenzoic acid and so on, were the low molecular intermediates which resulted from the cleavage of the triphenylmethane ring in CV structure. Similar findings were reported by Hongzhe Chen et al.,³³ the intermediates and products formed in the process of degradation of CV dye were mono-, di-, tri-N-de-methylated intermediates

corresponding to the m/z peaks 372, 358, 344 and 330 detected by the LC-MS analysis and he also reported the presence of another peak with m/z of 371 which might be due to the isomerization of CV and this intermediate undergoes a faster degradation than with that of CV, making it hard to be detected and the intermediates with smaller molecular weight were glycol, 2-hydroxypropanoic acid and pyrocatechol.

CONCLUSION

ZnO nanorods were successfully synthesized by a simple chemical precipitation method. Enhanced degradation of crystal violet dye is possible by effective air purging under solar irradiation within a very short period 50 minutes. Thus this simplest, low-cost and effective technique can be employed for the degradation of other triphenylmethane dyes let out from the textile as well as other dyeing industries.

ACKNOWLEDGMENT

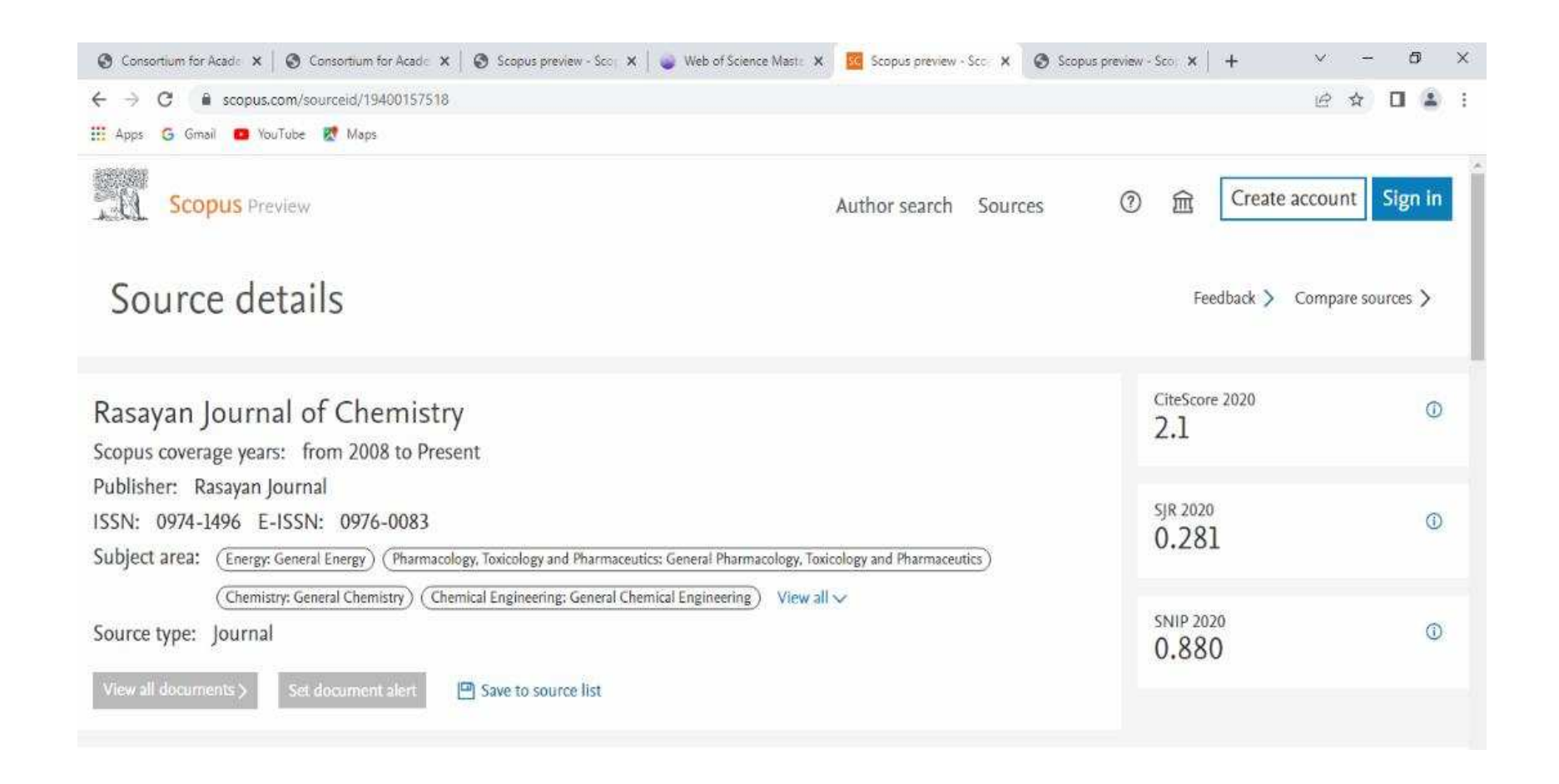
The authors sincerely thank Dr. S. Thennarasu, Sr. Principal Scientist, Department of Organic and Bio-Organic Chemistry, Central Leather Research Institute, Chennai, for his valuable suggestions given for the successful completion of the work. We also thank the PG and Research Department of Chemistry, Holy cross-college, Trichy for providing the necessary laboratory facilities.

REFERENCES

- 1. Mehtap Ejder-Korucu, Ahmet Gurses, Cetin Dogar, Sanjay K. Sharma and Metin Acikyildiz, 2015, Removal of Organic Dyes from Industrial Effluents: An Overview of Physical and Biotechnological Applications, Scrivener Publishing LLC, Beverly, pp.1-34.
- 2. H. Ali, Water Air Soil Pollution, 213, 251(2010), DOI:10.1007/s11270-010-0382-4
- 3. H.C. Thompson Junior, L.G. Rushing, T. Gehring, and R. Lochmann, *Journal of Chromatography B: Biomedical Science Applications*, **723**, 287(1999), **DOI**:10.1016/s0378-4347(98)00536-2
- 4. M. Saquib and M. Muneer, *Dyes Pigments*, **56**, 37(2003), **DOI:**10.1016/S0143-7208(02)00101-8
- 5. C. Sahoo, A.K. Gupta, and A. Pal, *Dyes Pigments*, **66**, 189(2005), **DOI:**10.1016/j.dyepig.2004.09.003
- 6. L.G. Rushing and M.C. Bowman, *Journal of Chromatographic Science*, **18**, 224(1980), **DOI**:10.1093/chromsci/18.5.224
- 7. K.A. Adegoke and O.S. Bello, *Water Resources and Industry*, **12**, 8(2015), **DOI:**10.1016/j.wri.2015.09.002
- 8. Loganathan, A. Sivakumar, B. Murugesan and P. Sivakumar, *Rasayan Journal of Chemistry*, **12(4)**, 1710(2019), **DOI:**10.31788/RJC.2019.1245351
- 9. H. Sutanto, I. Marhaendrajaya, G. W. Jaya, E. Hidayanto, M. Mukholit, S. Wibowo and Y. Wahyono, *Rasayan Journal of Chemistry*, **12(1)**, 138(2019), **DOI:**10.31788/RJC.2019.1215034
- 10. R. Dnyaneshwar Shinde, S. Popat Tambade, G. Manohar Chaskar, and M. Kisan Gadave, *Drinking Water Engineering Science*, **10**, 109(2017), **DOI**:10.5194/dwes-10-109-2017
- 11. S. Girish Kumar and K.S.R. Koteswara Rao, *RSC Advances.*, **5**, 3306(2015), **DOI:**10.1039/C4RA13299H
- 12. A. Janotti and C.G. Van de Walle, *Republican Prog. Physics*, **72**, 126501(2009), **DOI:**10.1088/0034-4885/72/12/126501
- 13. N. P. Diantariani, I. Kartini, A. Kuncaka, and E. T. Wahyuni, *Rasayan Journal of Chemistry*, **13(1)**, 747(2020), **DOI:**10.31788/RJC.2020.1315597
- 14. M. Giruba, J. Christina Rhoda, S. Chellammal and K. Ravichandran, *Rasayan Journal of Chemistry*, **13 (1)**, 439(2020), **DOI:**10.31788/RJC.2020.1315501
- 15. Nirmalya Tripathy, Rafiq Ahmad, Jeong Eun Song, Hyun Park, and Gilson Khang, *AIMS Materials Science*, **4(1)**, 267(2017), **DOI:**10.3934/matersci.2017.1.267
- 16. B. Krishnakumar and M. Swaminathan, *Indian Journal of Chemistry*, **49A**, 1035(2010)
- 17. V. Anand and V. C. Srivastava, *Journal of Scientific and Industrial Research*, **75**, 632(2016), **DOI:** 123456789/35575
- 18. J. C. Qian, Z. X. Chen and L. J. Zhu, Advanced Materials Research, 800, 276(2013),
- 19. W. Shen, Z. Li, H. Wang, Y. Liu, Q. Guoa, and Y. Zhang, *Journal of Hazardous Materials* **152**, 172(2008), **DOI:**10.1016/j.jhazmat.2007.06.082

- 20. L.Y. Yanga, S. Donga, J.H. Suna, J.L. Fenga, Q.H. Wua, S.P. Sunc, *Journal of Hazardous Materials*, **179**, 438(2010), **DOI**: 10.1016/j.jhazmat.2010.03.023
- 21. Abebe Balcha, Om Prakash Yadav and Tania Dey, *Environmental Science Pollution Research*, (2016), **DOI:** 10.1007/s11356-016-7750-6
- 22. Haiping He, Yuxia Wang and youming Zou, *Journal of Physics, D: Applied Physics*, **36**, 2972(2003), **DOI:** 10.1088/0022-3727/36/23/017
- 23. Vinod Kumar, S. Som, Vijay Kumar, Vinay Kumar, O.M. Ntwaeaborwa, E. Coetsee, and H.C.Swart, *Chemical Engineering Journal*, **255**,541(2014), **DOI**: 10.1016/j.cej.2014.06.027
- 24. M. Zhong, G. Shan, Y. Li, G. Wang, and Y. Liu, *Materials Chemistry Physics*, **106**, 305(2007), **DOI**:10.1016/j.matchemphys.2007.06.007
- 25. L. K. Jangir, Y. Kumari, Anil Kumar, Manoj Kumar and K. Awasthi, *Materials Chemistry Frontiers*, **1**, 1413(2017), **DOI:** 10.1039/C7QM00058H
- 26. S. Lakshmi, R. Renganathan, and S.J. Fujita, *Journal of Photochemistry and Photobiology A: Chemistry*, **88**,163(1995), **DOI**:10.1016/1010-6030(94)04030-6
- 27. G. Thennarasu and A. Sivasamy, *Ecotoxicology and Environmental Safety*,**134(2)**, 412(2016), **DOI:**10.1016/j.ecoenv.2015.10.030
- 28. N. Daneshvar, D. Salari and A.R. Khataee, *Journal of Photochemistry and Photobiology A: Chemistry*, **162(2-3)**,317(2004), **DOI:**10.1016/S1010-6030(03)00378-2
- 29. M.A. Behnajady, N. Modirshahla, and R. Hamzavi, *Journal of Hazardous Materials*, **133(1-3)**,226(2006), **DOI**:10.1016/j.jhazmat.2005.10.022
- 30. Azita Mohagheghian, Seyydeh-Amene Karimi, Jae-Kyu Yang, and Mehdi Shirzad-Siboni, *Journal of Advanced Oxidation Technology*, **18**,1 (2015), **DOI:**10.1515/jaots-2015-0108
- 31. S.H. Sohrabnezhad, M.A. Zanjanchi and M. Razavi, *Spectrochimica Acta Part A: Molecular and Biomolecular Spectroscopy*, **130**, 129(2014), **DOI:**10.1016/j.saa.2014.02.188
- 32. H. He, S. Yang, K. Yu, Y. Ju, C. Sun and L. Wang, *Journal of Hazardous Materials*, **173**, 393(2010), **DOI**:10.1016/j.jhazmat.2009.08.084
- 33. H. Chen, S. Yang, J. Chang, K. Yu, D. Li, C. Sun, and A. Li, *Chemosphere*, **89**, 185(2012), **DOI**:10.1016/j.chemosphere.2012.05.050

[RJC-5558/2019]



RASĀYAN J. Chem.



Vol. 15 | No. 1 |651-658| January - March | 2022 ISSN: 0974-1496 | e-ISSN: 0976-0083 | CODEN: RJCABP http://www.rasayanjournal.com http://www.rasayanjournal.co.in

FABRICATION AND STRUCTURAL CHARACTERIZATION OF SrSiO₃/TiO₂ PHOTOCATALYST FOR THE DEGRADATION OF CONGO RED DYE UNDER SUNLIGHT

Preeja P. Thattil and A. Leema Rose[⊠]

PG and Research Department of Chemistry, Holy Cross College (Autonomous), Affiliated to Bharathidasan University, Tiruchirappalli-620 002, Tamil Nadu, India.

□ Corresponding Author: leemarose25@gmail.com

ABSTRACT

Titanium dioxide and strontium silicate-loaded titanium dioxide photocatalysts are prepared via a simple chemical precipitation technique using titanium tetrachloride as the precursor solution in an alkaline medium. Different characterization techniques such as x-ray diffraction analyses, field emission scanning electron microscopic analyses, transmission electron microscopic analyses, energy dispersive x-ray analyses and bet surface area studies are carried out for the synthesized photocatalysts. The enhancement in the photocatalytic activity of the strontium silicate loaded titanium dioxide against the bare titanium dioxide catalyst is investigated using congo red dye as a model pollutant. The parameters such as catalyst concentration, pH and initial dye concentration are optimized to achieve maximum degradation of congo red dye using the modified titanium dioxide photocatalyst. The kinetic studies using the Langmuir-Hinshelwood model are investigated to study the rate and order of the photocatalytic dye degradation process.

Keywords: SrSiO₃/TiO₂Composite, Photodegradation, Congo Red Dye, XRD, HRTEM, Air Oxidation, Solar Radiation.

RASĀYAN J. Chem., Vol. 15, No.1, 2022

INTRODUCTION

Water pollution problems have increased continuously over the past decades due to the extensive development of textile, printing and dyeing units. The unfixed dyes and toxic chemical compounds released into the aquatic system from the textile industries are a major cause of water pollution. ¹⁻³ A wide variety of synthetic dyes used in the textile and dyeing industries are non-biodegradable in nature. When these non-biodegradable dyes are released into the water bodies, they persist in the environment for a long period of time, posing serious health hazards to the aquatic and human life. 4,5 Among the wide variety of dyestuffs, the azo dyes constitute a major class, they are widely employed in the dyeing industries due to the intensity of the colors, fast fixation of the dyes to the fabric. Congo red is one such azo class of dye widely employed in the textile and dyeing industries. Due to the thermal and optical stability of congo red dye, it is not readily degradable. They are highly toxic and are suspected carcinogens that create serious environmental and health concerns. Conventional water treatment techniques such as sedimentation, flocculation, membrane filtration and adsorption are found to be less effective in the removal of toxic synthetic dyes from the environment and under anaerobic conditions the dyes are transformed to aromatic amines which are also potentially carcinogenic in nature. 6-9 Hence, an investigation into the advanced technologies for the abatement of these organic pollutants is widely researched by scientists all over the world. The advanced oxidation processes such as heterogeneous catalysis is a clean and commercially scalable method for the degradation of toxic organic pollutants. ¹⁰Titanium dioxide catalystis one of the best semiconductor photocatalysts widely employed for the removal of azo dyes. However, the wide bandgap of titanium dioxide catalysts (3.2eV) makes it less favorable for photocatalytic process.¹¹⁻¹³ Hence, in recent years researchers have focused on modifying TiO2 catalyst in order to improve its photocatalytic response. Recently, Himanshu Narayan et al., reported the photocatalytic degradation of congo red dye using Nd2+, Er3+ loaded TiO2 photocatalyst. 14Adiyansyah et al., reported a faster photocatalytic activity for the degradation of reactive black 5 dye using sulphurdoped TiO₂ photocatalyst.¹⁵ Similarly, silicon oxide supported TiO₂ photocatalyst also exhibited excellent



photocatalytic activity against the removal of ammonia in aqueous solution within 24 hours. ¹⁶ In our present study, the photocatalytic activity of strontium silicate incorporated TiO₂ photocatalyst prepared via simple chemical precipitation technique is employed for the degradation of congo red dye under natural sunlight.

EXPERIMENTAL

Material and Methods

The titanium tetrachloride solution and sodium hydroxide were purchased from Sisco Research Laboratories Pvt. Ltd. Congo red dye is purchased from S.D. Fine chemicals. The chemical structure of the Congo red dye is shown in Fig.-1.

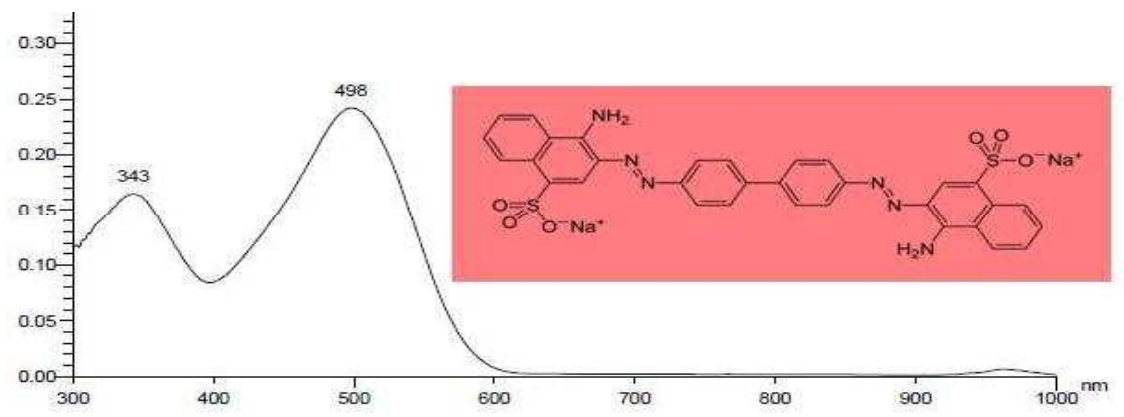


Fig.-1: UV-Visible Absorption Spectrum and Chemical Structure of the Congo Red Dye

Synthesis of SrSiO₃/TiO₂Photocatalyst

Titanium tetrachloride solution (1M) is used as a precursor solution to prepare titanium dioxide nanoparticles. One weight percent of strontium silicate powder is added to the precursor solution and it is magnetically stirred for 30 minutes. Slowly the temperature of the solution is raised to 60° C and sodium hydroxide is added as a precipitating agent and the stirring is continued for another half an hour. The thick white precipitate obtained is washed repeatedly with distilled water and dried in the oven for 6 hours and finally, it is calcined at 400°C to obtain powders of 1wt% SrSiO₃/TiO₂ photocatalyst. Similarly, different weight ratios (0.5, 2 and 3%) of strontium silicate-loaded titanium dioxide photocatalysts are prepared and the bare TiO₂ photocatalyst is prepared without the addition of the strontium silicate.

Photocatalytic Degradation Experiments

The stock solution of congo red dye $(1.43x10^{-5}\text{mol/L})$ is prepared, from which 50mL was withdrawn for each photocatalytic experiment. All the photocatalytic experiments were carried out under sunlightbetween 11 am to 2 pm. The reaction was carried out in the open air and the solution was continuously mixed by aeration. The photocatalytic experiment was carried out for three hours and at different time intervals,approximately 2mL of the dye solution was taken and centrifuged so that it was free from the catalyst. The pH optimization of the solution is done by adjusting the solution to appropriate pH levels using 0.1N NaOH and 0.1N HCl. A similar procedure was carried out at room temperature to get the blank experimental value. The percentage decolorization was calculated using the formula A_0 . A/ A_0 x100 where A_0 is the initial absorbance and A is the absorbance of the solution at a time 't'.

RESULTS AND DISCUSSION

Catalyst Characterization

The morphology of the synthesized titanium dioxide and strontium silicate loaded titanium dioxide photocatalysts was examined by Field Emission-Scanning Electron Microscopy and Transmission Electron Microscopy analysis.

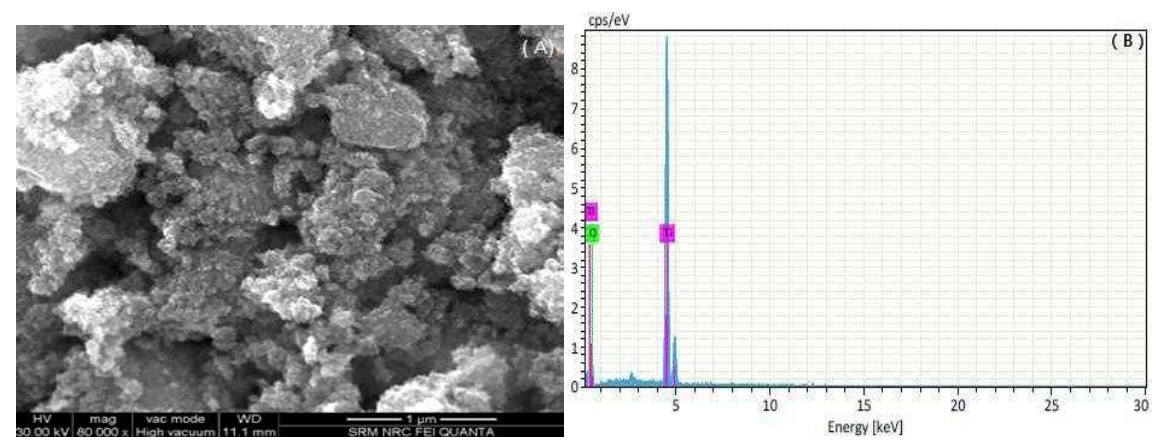


Fig.-2: A and B shows the FE-SEM Image and the EDAX Spectrum of the Synthesized Titanium dioxide photocatalyst

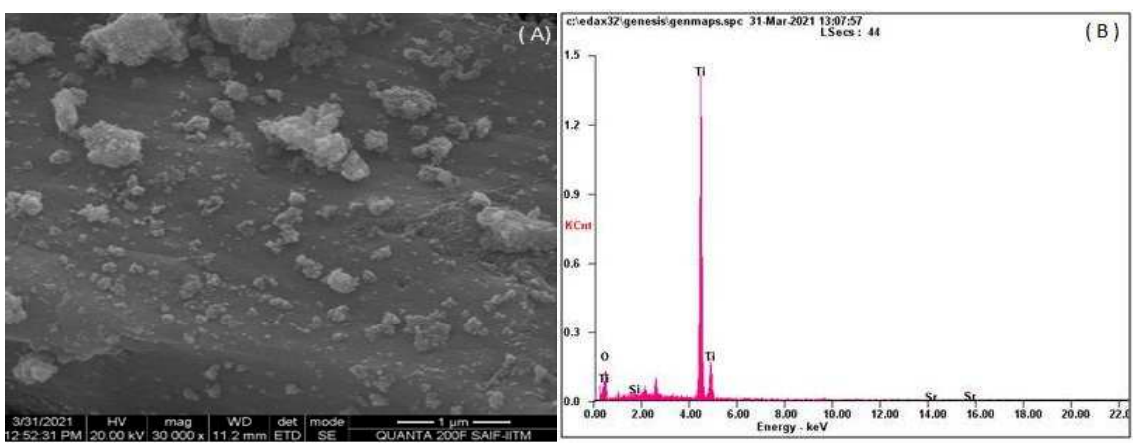


Fig.-3: A and B show the FE-SEM image and the EDAX Spectrum of the synthesized Strontium silicate loaded Titanium dioxide Photocatalyst.

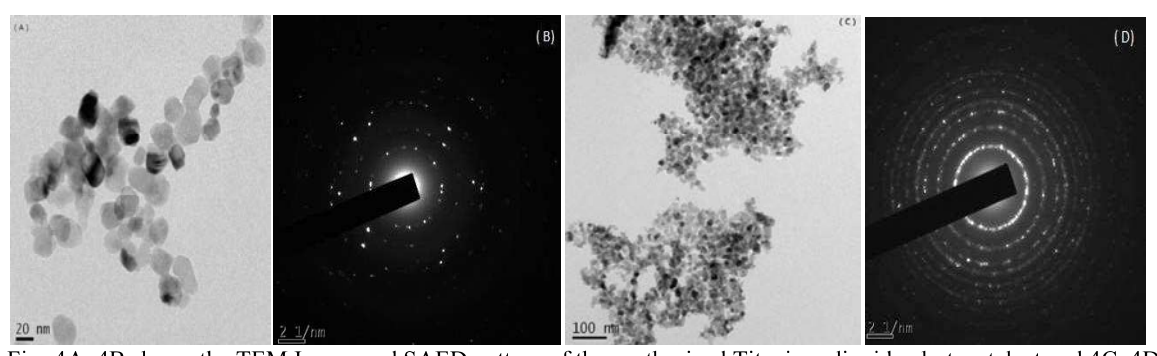


Fig.-4A, 4B shows the TEM Image and SAED pattern of the synthesized Titanium dioxide photocatalyst and 4C, 4D shows the TEM Image and SAED pattern of the strontium silicate loaded titanium dioxide photocatalyst.

From the FE-SEM and TEM images shown in Figs.-2a,3a and 4a,4c it is found that the synthesized bare titaniumdioxide particles and strontium silicate loaded titanium dioxide catalyst are moderatelyspherical in shape with the particle size ranging from 12.5nm to 33.8 nm for the undoped titanium dioxide photocatalyst. Additionally, the rings and dark-spotted circles in the SAED pattern of the synthesized TiO₂ and SrSiO₃/TiO₂ photocatalysts indicate the crystalline nature of the titanium dioxide particles and it also reveals that the crystallinity of titanium dioxide particles is still retained even after modification with

strontium silicate. This result is in agreementwith that found in titaniumdioxide nanoparticles prepared from similar precursors. ^{17,18} The typical EDAXspectrum of the titanium dioxide particles and strontium silicate loaded titanium dioxide particles are shown in Fig.-2b,3bwhich confirms the presence of titanium and oxygen elements in majorcomposition in the synthesized TiO₂ photocatalyst and the presence of titanium and oxygen in major with less intense peaks of strontium and silicon are also detected in the EDAX spectrum for the synthesized SrSiO₃/TiO₂ photocatalyst. This indicates that the synthesized TiO₂ and SrSiO₃/TiO₂ photocatalysts are obtained without any impurities.

Further, the crystallinity and surface area properties of the as-synthesized TiO2 and SrSiO3/TiO2 photocatalysts were examined by XRD and nitrogen adsorption-desorptionanalyzer, respectively.XRD spectrum of the synthesized TiO₂ and SrSiO₃/TiO₂ photocatalysts are shown in Fig.-5a and 5b. The crystal planes (101), (004), (200), (204), (220), (215) represent the anatase phase¹⁹ which is in accordance with the standard JCPDS [21-1272] and the crystal planes (110), (103), (105), (211) representing the rutile phase²⁰ and the crystal planes (121) and (032) representing the brookite phase²¹ are evidenced in the synthesized materials. From the obtained XRD results, it is found that (101) peak representing the anatase is the most intense one, which is also the preferred growth plane of bare titanium dioxidenanoparticles, however, in the strontium silicate loaded titanium dioxide nanoparticles the crystal plane (121) representing the brookite phase is found with maximum intensity indicating it as the preferred growth plane. The sharpness and intensity of all the peaks in both TiO₂ and SrSi/TiO₂ photocatalysts once again confirm the crystalline nature of the synthesized materials. The average crystallite calculated from the debye scherrer's equation for bare titanium dioxide catalystis 20.2 nm and for SrSiO₃/TiO₂ catalysts the crystallite size decreased to 17.85 nm. The catalytic activity of a photocatalyst can be correlated to the surface area of the catalyst; the higher the surface area greater will be the photocatalytic activity. ^{22,23}The nitrogen adsorption-desorption isotherms of the as-synthesized TiO2 and SrSiO3/TiO2 photocatalysts are shown in Fig.-6a and 6b.From the BET surface area measurements, it is found that thespecific surface area of the bare titanium dioxide catalyst is 61.006m²/g and the surface area of the strontium silicate loaded titanium dioxide catalyst increased to 78.295m²/g respectively.

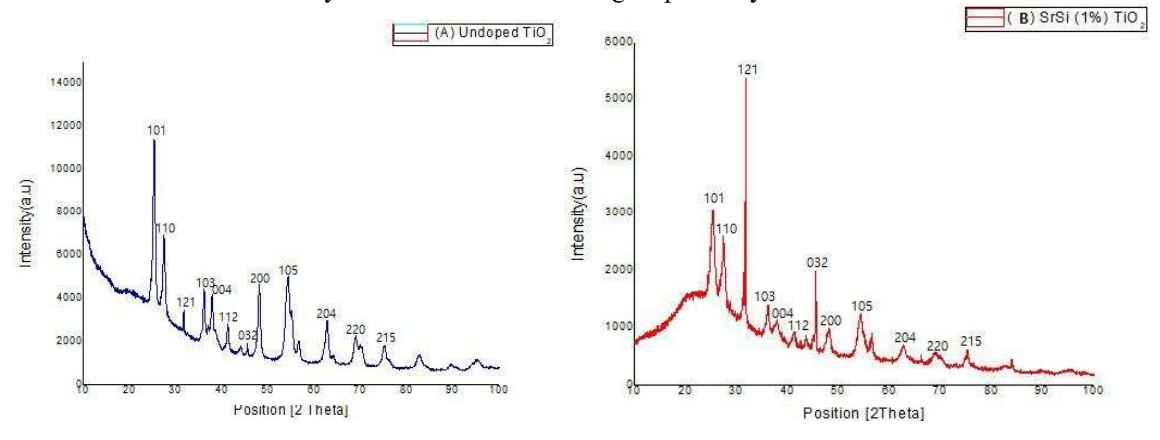


Fig.-5 A and B shows the XRD Pattern of the synthesized Titanium dioxide and the 1% strontium silicate loaded titanium dioxide photocatalyst.

Photocatalytic Degradation of Congo Red Dye Effect of pH

The effect of pH in the range of 4–9 is studied for 10 mg/L(50ml) of congo red dye solution. The maximum decolorization efficiency was observed in neutral pH=7.5 as shown in Fig.-7. In neutral and acidic pH the anionic congo red dye gets easily adsorbed to the positively charged surface of titanium dioxide nanoparticles and hence good decolorization efficiency is achieved at acidic and neutral pH levels however, at alkaline pH levels beyond pH8 the titania catalyst with negatively charged surface repels the anionic congo red dye and thus a decrease in the photocatalytic decolorization of the dye is observed.^{24,25}

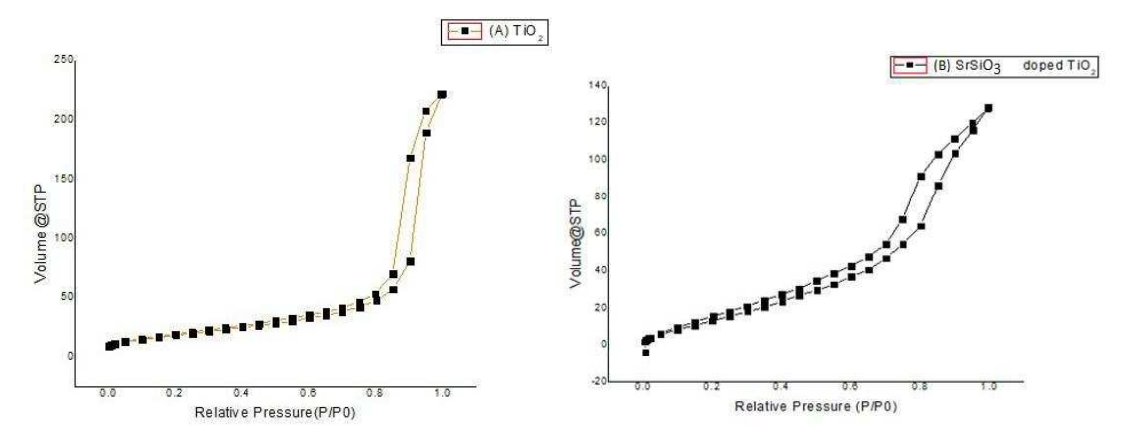


Fig.-6 A and B shows the Nitrogen Adsorption-Desorption isotherm of the synthesized Titanium dioxide and the 1% strontium silicate loaded titanium dioxide photocatalyst. (Figure (B) changed)

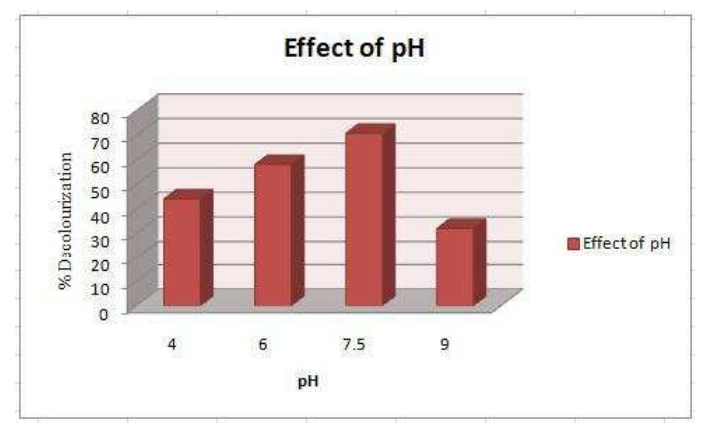


Fig.-7: 0.01g/L Congo Red Dye Solution, 25mg of TiO₂catalyst, pH varied from 4 to 9, airflow rate =2.5L/min under Sunlight.

Effect of Catalyst Dosage

The optimum amount of titanium dioxide catalyst for the effective decolorization of congo red dye is found by varying the weight of TiO₂ catalyst from 15mg to 35mg as shown in Fig.-8. The maximum decolorization of congo red dye is achieved with 25 mg of the titanium dioxide catalyst beyond which a decrease in the decolorization rate is observed. This is due to fact that active sites required for the photocatalytic dye decolorization increase by increasing the catalyst concentration and beyond the addition of a certain amount of the catalyst to the dye solution there will be an increase in the turbidity of the suspension and hence decreases the sunlight penetration. This decrease in sunlight penetration in the dye solution brings about a decrease in the photodecolorization process. ^{26, 27}

To find out the optimum concentration of congo red dye, the concentration of the dye is varied from 10-50mg/L and the maximum dye decolorization efficiency is evaluated using 25mg of bare titanium dioxide at an optimum pH of 7.5 by effective air purging under sunlight. About 94% of 10mg/L of congo red dye got decolorized within 90 minutes. The interaction of the hydroxyl radicals with the dye molecules decreases on increasing the congo red dye concentration and the turbidity of the solution blocks the sunlight penetration path, which also accounts for the photodecolourization of the dye at higher concentrations. Under similar conditions, 95% of dye decolorization took place within 40 minutes using 1% strontium silicate loaded titanium dioxide photocatalyst, whereas under room temperature only

12% of the dye decolorization took place. This clearly shows that the dye is resistant to self-photolysis and that both TiO₂ catalyst and effective air purging under sunlight are essential for efficient photocatalytic decolorization of congo red dye. Further modifying the titanium dioxide catalyst loading different weight percent of strontium silicate has also reduced the time taken for the photocatalytic dye decolorization process.

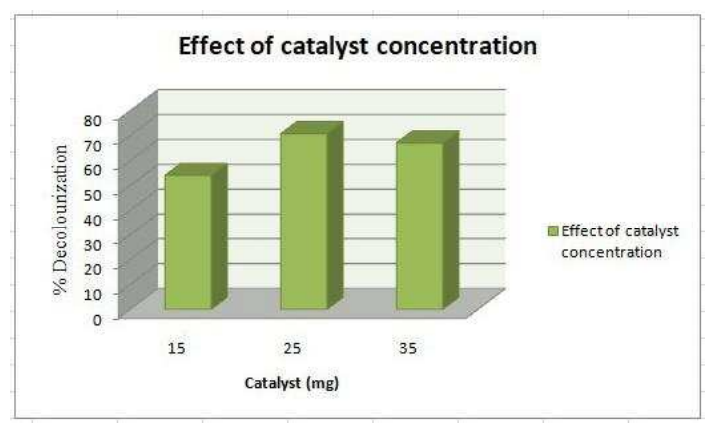


Fig.-8: 0.01g/L Congo Red Dye Solution, TiO₂ catalyst dosage varied from 15mg to 35mg, pH = 7.5, Air Flow Rate = 2.5L/min under Sunlight.

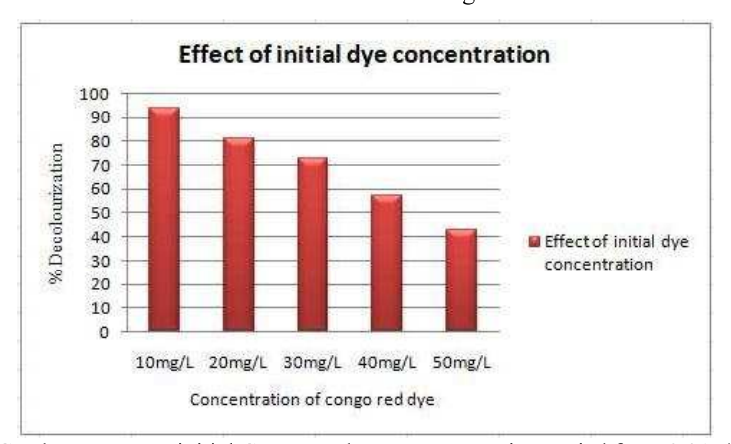


Fig.-9:25mg of TiO_2 Catalyst, pH=7.5, initial Congo Red Dye concentration varied from 0.01g/L to 0.05g/L, airflow rate = 2.5L/min under Sunlight.

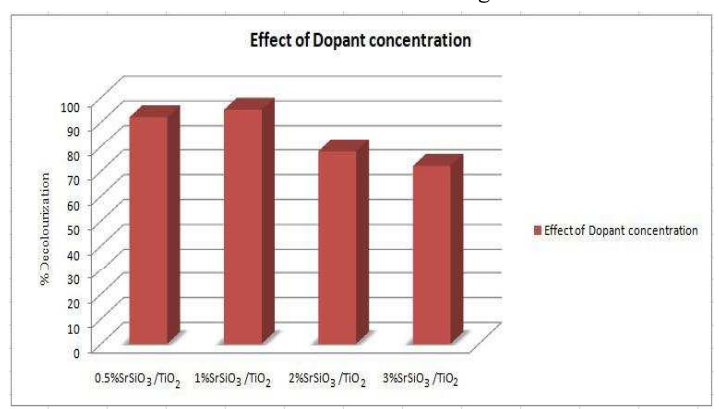


Fig.-10: Initial Congo Red Dye concentration (10mg/L), strontium silicate weight varied from 0.5-3% on TiO₂ catalyst(25mg), pH=7.5, airflow rate = 2.5L/min under Sunlight. (Figure changed)

Kinetic Studies

The kinetics for the degradation of congo red dye using titanium dioxide and strontium silicate loaded TiO₂ photocatalyst is studied by Langmuir Hinshelwood kinetic model. According to the (L-H model), the integrated form of pseudo-first order kinetics³⁰⁻³² is as follows:

 $\ln [C_0]/[C] = kt$

Where, k is the pseudo-first-order rate constant (min⁻¹), C₀ is the initial concentration of dyes (g L⁻¹), C is the concentration of the congo red dye at time 't' (minutes).

The linear fit between ln [C₀/C] and irradiation time 't' under different weight percent of strontium silicate loaded TiO₂ photocatalysts was plotted to understand the pseudo-first-order rate equation. The photocatalytic experiments for degradation of congo red dye solution followed pseudo first order kinetics shown in Fig.-11. The calculated average R² values are 0.966, 0.960, 0.904 and 0.865 for 0.5-3% strontium silicate incorporated titanium dioxide photocatalysts respectively.

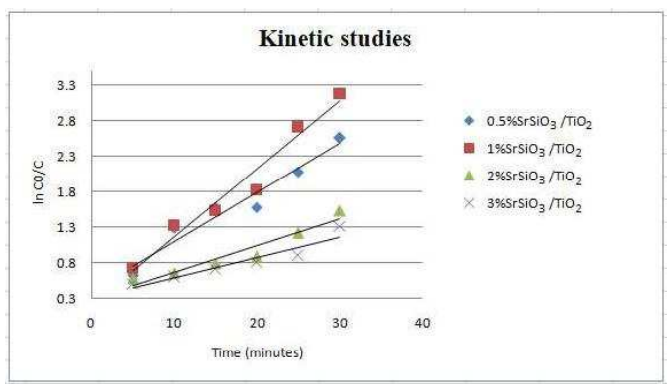


Fig.-11: The Plots of $\ln([C_{\theta}]/[C])$ versus Time for different weight percent of strontium silicate loaded TiO_2 photocatalyst. (Figure changed)

CONCLUSION

SrSiO₃/TiO₂ composite photocatalyst was successfully synthesized by a simple chemical precipitation method. Effective degradation of Congo red dye is achieved by effective air purging under solar irradiation within a very short span of time. Thus, this simplest, low-cost and effective technique can be employed for the degradation of the azo class of dyes from the aqueous solution.

ACKNOWLEDGEMENT

The authors sincerely acknowledge Dr. S. Thennarasu, Sr. Principal Scientist, Department of Organic and Bio-Organic Chemistry, CLRI, Chennai, for his valuable suggestions provided for the completion of the work. We also thank the management and PG and Research Department of Chemistry, Holy cross-college, Trichy for the support and the facilities provided to carry out the research work.

REFERENCES

- 1. A. Riga, K. Soutsas, K. Ntampegliotis, V. Karayannis and G. Papapolymerou, *Desalination*, **211**, 72(2007), https://doi.org/10.1016/j.desal.2006.04.082
- 2. MehtapEjder-Korucu, Ahmet Gurses, Cetin Dogar, Sanjay K. Sharma and MetinAcikyildiz, 2015, Removal of Organic Dyes from Industrial Effluents: An Overview of Physical and Biotechnological Applications, Scrivener Publishing LLC, Beverly, pp.1-34.
- 3. H. Ali, Water Air Soil Pollution, 213, 251(2010), https://doi.org/10.1007/s11270-010-0382-4
- 4. H.Lachheb, E.Puzenat, A.Houas, M.Ksibi, E.Elaloui, C.Guillard and J.M.Herrmann, *Appl. Catal., B*, **39**, 75(2002), https://doi.org/10.1016/j.desal.2005.04.048
- 5. Y.Wang, Water Research, 34(3), 990(2000).

- 6. A. Mittal, V. Thakur and V. Gajbe, *Environmental Science and Pollution Research*, **20(1)**,260(2013), https://doi.org/10.1007/s11356-012-0843-y
- 7. N. Barka, S. Qourzal, A. Assabbane, A. Nounah and Y. Ait-Ichou, *Arabian Journal of Chemistry*, **3(4)**, 279(2010), https://doi.org/10.1016/j.arabjc.2010.06.016
- 8. N. Saibaba KV and R.V. Kandisa, *Rasāyan Journal of Chemistry*, **12(4)**, 2176(2019), https://doi.org/10.31788/RJC.2019.1245478
- 9. M.Stylidi, D.I. Kondarides and X.E. Verkyios, Applied catalysis B. Environmental, 40, 271(2003)
- 10. Y.G.Wang, B.Li, C.L.Zhang, L.F.Cui, S.F.Kang, X.Liand L.H.Zhou, *Appl. Catal. B* **131**, 277(2013), https://doi.org/10.1016/j.jsamd.2018.07.003
- 11. H. Narayan, H. Alemu, L. Macheli, M. Thakurdesai and T. K. Gundu Rao, *Nanotechnology*, **20**, 255601(2009), https://doi.org/10.1088/0957-4484/20/25/255601
- 12. F. Han, V. S. Kambala, M. Srinivasan, D. Rajarathnam and R. Naidu, *Applied Catalysis A: General*, **359**, 25(2009), https://doi.org/10.1016/j.apcata.2009.02.043
- 13. A. G. Agrios, P. J. Pichat, Journal of Applied Electrochemistry, 35, 655(2005).
- 14. Himanshu Narayan and Hailemichael Alemu, *IOP Conf. Series: Journal of Physics: Conference Series*, **82**, 394 (526071879).
- 15. Adiansyah, I. Elisabeth Purba, M. Tarigan, Lisnadiyanti, Yusnaidar and I.P. Mahendra, *Rasayan Journal of Chemistry*, **13(1)**, 757(2020), http://dx.doi.org/10.31788/RJC.2020.1315461
- 16. E.T. Wahyuni, S. Suherman, D. Satyawati, R. Puspita and M. Mudasir, *Rasayan Journal of Chemistry*, **13(1)**, 574(2020), http://dx.doi.org/10.31788/RJC.2020.1315464
- 17. V.P. Muhamedshajudheen, K. Viswanathan, K. Aniatha Rani, A. Uma Maheswari and S. Saravana Kumar, *International Journal of Chemical and Molecular Engineering*, **10(5)**, 2016.
- 18. R. Desai, S. K. Gupta, S.Mishra, P.K. Jha and A. Pratap, *International Journal of Nanoscience*, **10**, 1249(2011), https://doi.org/10.1142/S0219581X11008381
- 19. Y. Han, H. S. Kim and H. Kim, *Journal of Nanomaterials*, **Volume 2012**, Article ID 427453(2012), https://doi.org/10.1155/2012/427453
- 20. R. Kaplan, B. Erjavec, G. Dra zi c, J. Grdadolnik, and A. Pintar, *Applied Catalysis B, Environmental*, (2015), http://dx.doi.org/10.1016/j.apcatb.2015.08.027
- 21. H. Lee, S. C. Lee, J. H. Seo, W. G. Hong, H. Kim, H. J. Yun, H. J. Kim, and J. Lee, *Chemical Engineering Journal*, (2013), http://dx.doi.org/10.1016/j.cej.2013.02.099
- 22. S. C. Lee, H. U. Lee, S. M. Lee, G. Lee, W. G. Hong, J. Lee, and H. J. Kim, *Materials Letters*, 79 191(2012).
- 23. L. Mate jova, Zdene k Mate and Olga Šolcova, *Microporous and Mesoporous Materials*, **154** 187(2012).
- 24. S. Erdemo glu, S. K. Aksub, F. Sayılkan, B. Izgi, M. Asilt urk, H. Sayılkan, F. Frimmel and S, erefG uc, er, *Journal of Hazardous Materials*, **155**, 469(2008).
- 25. N. J. Bejarno-Perez and M. F. Suarez-Herrera, *Ultrasonics Sonochemistry*, **14**, 589(2007), https://doi.org/10.1016/j.ultsonch.2006.09.011
- 26. Y. Ou, J. Lin, S. Fang and D. Liao, Catalysis Communications, 8, 936(2007).
- 27. T. Peng, D. Zhao, K. Dai, W. Shi and K. Hirao, *The Journal of Physical Chemistry B*,**109**, 4947(2005), https://doi.org/10.1021/jp044771r
- 28. S. A. Qaradawi and S. R. Salman, *Journal of Photochemistry and Photobiology A*,**148**, 161(2002), http://dx.doi.org/10.1016/S1010-6030(02)00086-2
- 29. X. W. Zhang, Y. Z. Wang and G. T. Li, *Journal of Molecular Catalysis A: Chemical*, 237, 199(2005), https://doi.org/10.1016/j.molcata.2005.03.043
- 30. Y. Caoa, X. Lia, Z. Biana, A. Fuhrb, D. Zhang, J. Zhu, *Applied Catalysis B: Environmental*, **180**, 551(2016), https://doi.org/10.1016/j.apcatb.2012.09.005
- 31. Ruby Chauhan, Ashavani Kumar, Ram Pal Chaudhary, *Spectrochimica Acta Part A: Molecular and Biomolecular Spectroscopy*, **98**, 256(2012), https://doi.org/10.1016/j.saa.2012.08.009
- 32. S. K. Kansal, M. Singh, D. Sud, *Journal of Hazardous Materials*, **141**, 581(2007), https://doi.org/10.1016/j.jhazmat.2006.07.035

[RJC-6821/2021]



Journal of Pharmaceutical Research International

33(43B): 32-41, 2021; Article no.JPRI.73038

ISSN: 2456-9119

(Past name: British Journal of Pharmaceutical Research, Past ISSN: 2231-2919,

NLM ID: 101631759)

Structural Characterization, Antimicrobial and Antioxidant Assay of Biogenically Synthesized Maghemite (γ-Fe₂O₃) Nanoparticles

A. Leema Rose^{1*}, B. Shabushree¹ and Preeja P. Thattil¹

¹PG and Research Department of Chemistry, Holy Cross College (Autonomous), Trichy-620 002, India.

Authors' contributions

This work was carried out in collaboration among all authors. All authors read and approved the final manuscript.

Article Information

DOI:10.9734/JPRI/2021/v33i43B32522

Editor(s

(1) Dr. Francisco Cruz-Sosa, Metropolitan Autonomous University, México.

Reviewers:

(1) Hamzah Abdulrahman Salman, University of Mashreq, İraq. (2) E. Ugbabe Grace, National Institute for Pharmaceutical Research and Development (NIPRD), Nigeria.

Complete Peer review History: https://www.sdiarticle4.com/review-history/73038

Original Research Article

Received 20 June 2021 Accepted 27 August 2021 Published 08 September 2021

ABSTRACT

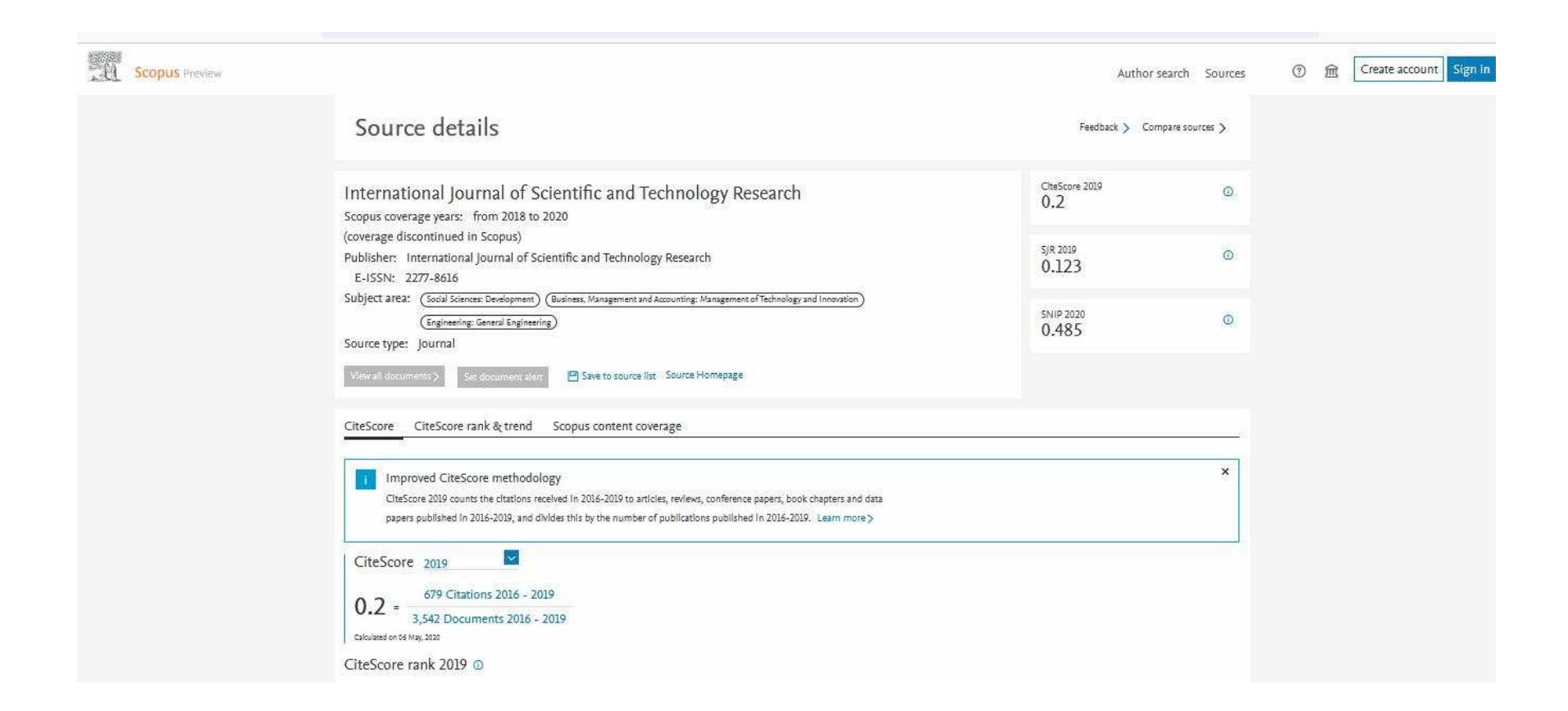
Aims: The present study focused on the optical and morphological characterization, antioxidant and antimicrobial activities of the biogenically synthesized iron oxide nanoparticles.

Methods: The preliminary phytochemical screening was done for the leaf extract of *Annona reticulate L*. The leaf extract and Ferrous Sulphate heptahydrate were used to synthesize the iron oxide nanoparticles under room temperature. The determination of antioxidant activity was done using DPPH free radical scavenging assay and the determination of antimicrobial activity using disc diffusion method.

Results: The UV-visible spectra showed the sharp absorption peak at 278 nm. The Fourier-transform infrared spectroscopy studies revealed the role of phytochemical constituents in the leaf extract for the iron oxide nanoparticles formation. X-ray diffraction pattern showed the presence of γ phase of Fe₂O₃ nanoparticles. Scanning electron microscope analysis showed the moderately spherical morphology of γ -Fe₂O₃ nanoparticles and Energy-dispersive X-ray peaks showed the presence of iron and oxygen in the synthesized nanoparticles. Particle size analysis showed that the synthesized γ -Fe₂O₃possessed an average size of 115.9 nm.

Conclusion: The synthesized γ -Fe₂O₃ nanoparticles have potential antioxidant and antimicrobial activity.

^{*}Corresponding author: E-mail: leemarose25@gmail.com;



Photocatalytic Removal Of Xanthene And Diaryl Methane Dyes By Air Oxidation Using Tio₂ Nanospheres Under Sunlight

Preeja. P. Thattil, A. Leema rose

Abstract \rightarrow Titanium dioxide nanocatalyst was synthesized by simple chemical precipitation method and is characterized by XRD, FE-SEM, EDAX, TEM, BET Surface area analysis, FTIR, UV-DRS and Photoluminescence. The synthesized TiO₂ catalyst is evaluated for its photocatalytic activity towards the degradation of Rose Bengal and basic yellow (Auramine O) dyes under solar irradiation. The parameters such as catalyst dosage, initial dye concentration, pH were optimized for the effective photocatalytic dye degradation. The photodegradation rates of Rose bengal reached 98% within 60 minutes of reaction time and for basic yellow 89% of the dye degradation is achieved within 60 minutes of irradiation and the rate of dye degradation was found to be enhanced by air oxidation using TiO₂ catalyst under sunlight.

Key words: Air oxidation, FE-SEM, Photocatalysis, Solar radiation, TiO2, TEM, XRD.

1 INTRODUCTION

Among different transition metal oxide nanoparticles, titanium dioxide in its anatase phase have notable applications in waste water management [1], [2]. They are proved to be efficient, less expensive, non-toxic, resistance to corrosion and reusable [3]. These properties of titanium dioxide make it possible to use this metal oxide for a wide variety of applications. Parthasarathi and thilagavathi used titanium dioxide nanoparticles for microbial resistance [4]. Juti Rani Deka and Hong Wen Wang [5] synthesized mesoporous TiO2 for the photoanodes in dye sensitized solar Cells. Chang Sheng Guo et al., [6] used TiO₂ microspheres catalysts for bisphenol A Degradation. Julie Joseane Murcia et al., [7] utilized fluorinated and platinized titania for the photocatalytic treatment of dyestuffs and stained wastewater coming from handicrafts factories. Titanium dioxide nanoparticles are prepared by various methods like sol-gel technique, hydrothermal synthesis, chemical vapour deposition, reverse microemulsion method, solid state reaction, solvothermal method, microwave and sonochemical methods [8]. Among all these wide techniques, chemical precipitation method is one of the easiest to yield low temperature, high purity nanoparticles. In the present work, the photocatalytic activity of titanium dioxide nanoparticles is evaluated against two dyes rose Bengal and basic yellow. Rose Bengal (Acid Red 94) falls under the class of xanthene derivatives [9]. It is anionic water soluble and a photosensitive dye widely used in textile, medicinal and photochemical industries [10], [11].

Even though, rose Bengal dye has wide applications, the toxic effects of the dye have also been investigated. Tabery HM studied the Toxic effect of rose bengal dye on the living human corneal epithelium [12]. Lee et al., investigated the In vitro study for staining and toxicity of rose bengal on cultured bovine corneal endothelial cells [13]. Basic yellow O is а diarylmethane dye used fluorescent stain. Basic yellow 2 dye can be used to stain acid-fast bacteria in a way similar to ziehl-neelsen stain. It can also be used as a fluorescent version of Schiff reagent. It is most commonly used dye in cotton, leather, jute and paper Indus tries [14], [15]. However, the excessive exposure to commercially available auramine dyes Induces DNA Damage in Vivo in Liver, Kidney and Bone Marrow Cells [16], [17]. The chemical structures of rose Bengal and basic yellow dyes are shown in the following figure (1a), (1b).

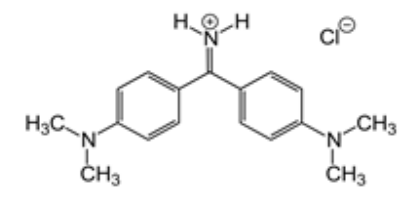


Fig1a. Chemical structure of Basic yellow Auramine O dye.

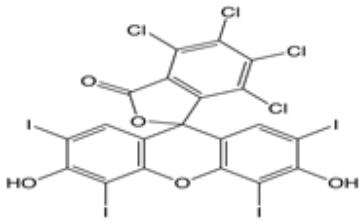


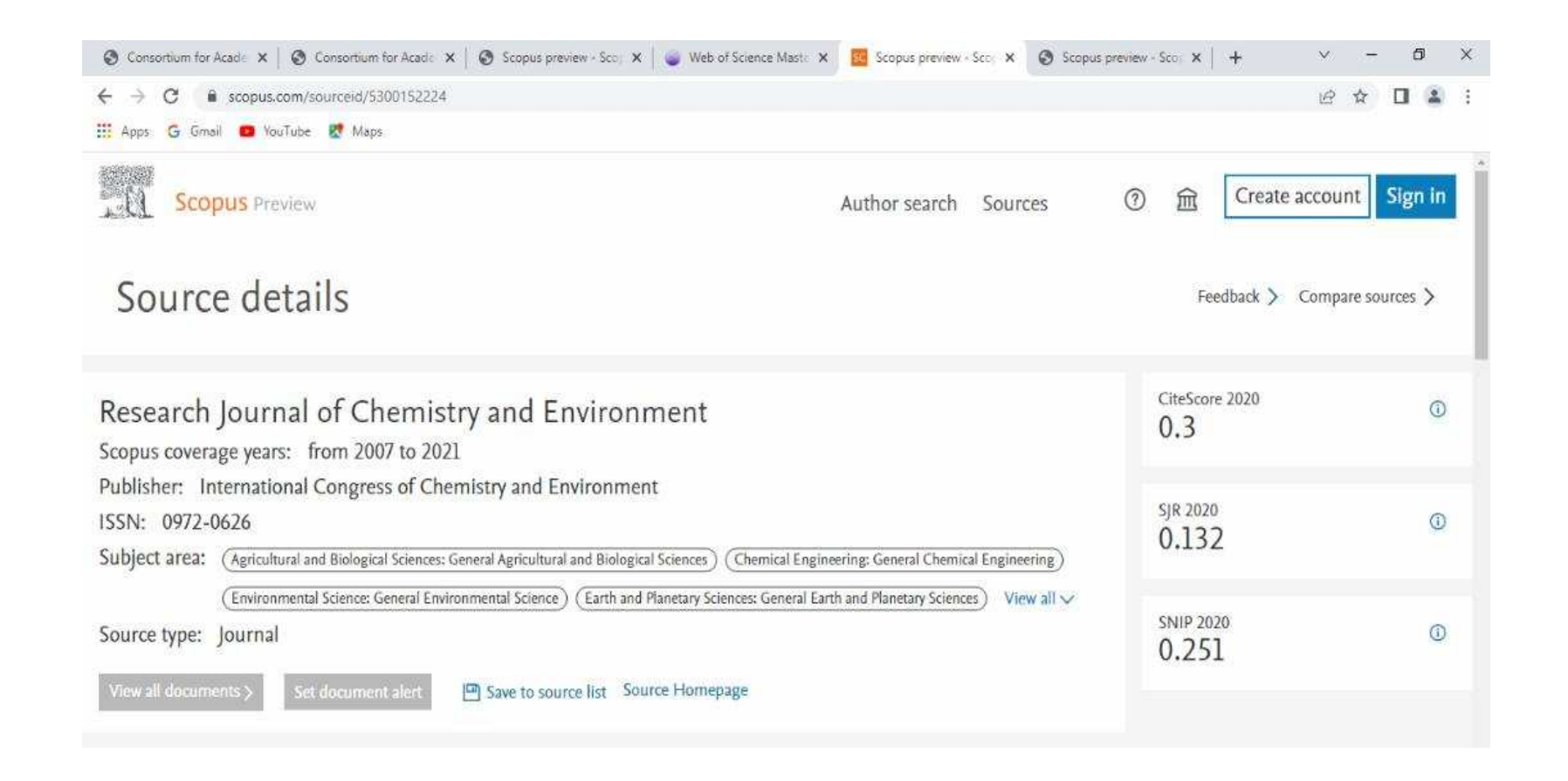
Fig1b. Chemical structure of Rose Bengal dye.

2 PROCEDURE

The Titanium tetrachloride salt (M.W. 189.679g/ml, purity 99%) was purchased from Sisco Research Laboratories Pvt.Ltd., sodium hydroxide from Merck and ethanol (99.9%) was purchased from Changshu Hongsheng Fine Chemical Co. Ltd. The capacity of the air pump used for the

Preeja.P.Thattil is currently pursuing Doctor of Philosophy in Chemistry at Holy Cross College (Autonomous), Affiliated to Bharathidasan University, Tiruchirappalli-620 002, Tamil Nadu, India.

Dr. A. Leema Rose is currently working as an Associate Professor in the PG and Research Department of Chemistry, Holy Cross College (Autonomous), Affiliated to Bharathidasan University, Tiruchirappalli-620 002, Tamil Nadu, India. Corresponding author; Email address: leemarose25@gmail.com Phone: +919965441442



Res. J. Chem. Environ.

Photodegradation of Thiazine and Indigoid Dyes using Zinc Oxide Nanocatalyst coupled with Air Oxidation under Solar Irradiation

Preeja Thattil P., Vinotha S. and Leema Rose A.*

PG and Research Department of Chemistry, Holy Cross College (Autonomous), Bharathidasan University, Tiruchirappalli-620 002, Tamil Nadu, INDIA
*leemarose25@gmail.com

Abstract

Zinc Oxide nanoparticles having an average Crystallite size of 5.6 nm are used as the photocatalyst for the decolourization of methylene blue, a thiazine dye and also for indigo carmine, an Indigoid dye. The combined effect of air oxidation along with zinc oxide nanoparticles enhanced the decolourization process. The operational parameters such as pH, catalyst concentration and the effect of initial dye concentration are optimized.

Keywords: Zinc oxide, Heterogeneous photocatalyst, Thiazine dye, Indigoid dye.

Introduction

A dye or a dyestuff is usually a coloured organic compound or mixture that may be used for imparting colour to a substrate in a reasonably permanent fashion. Synthetic dyes are the organic dyes originally derived from coal-tar derivatives, but currently synthesized from benzene and its derivatives¹. Synthetic dyes quickly replaced the traditional natural dyes because of their low cost. They offered a vast range of new colours and imparted better properties to the dyed materials. However, synthetic dyes retain harmful effects on the environment and human beings. First, synthetic dyes are made up of chemical compounds that can be harmful to humans, especially those who work in their production. Water pollution becomes a major alarming problem in our society when these manufactured synthetic dyes are dumped directly to the water bodies without proper effluent treatment²⁻⁴.

Photocatalysis is a newly emerging clean and cost-effective method for the large-scale treatment of water bodies polluted with dyes and other organic compounds. Zinc oxide is one of the best semiconductor nanoparticles with good photocatalytic efficiency, non-toxic nature, low cost and eco-friendliness⁵⁻¹¹.

However, the wide band gap of zinc oxide nanoparticles (3.37 ev) has limited its applications and they can only be photoexcited in UV region of the electromagnetic spectrum. Since, the UV component reaching the earth surface is only 4 to 5%, the photocatalytic efficiency of zinc oxide nanoparticles is low under sunlight^{12,13}.

Hence, in order to improve the oxidation process, air which is a natural and abundant source of oxygen has been coupled

with the zinc oxide photocatalyst. This present work reports the photocatalytic degradation of two important synthetic dyes methylene blue and indigo carmine. Indigo carmine (3, 30-dioxo-2,20-bisindolyden-5,50-disulfonic acid sodium salt) also known as indigotine I belongs to the indigoid family which is one of the oldest known dyes. It is one of the anionic dyes used commonly as a textile coloring agent and as an additive in pharmaceutical tablets and capsules¹⁴.

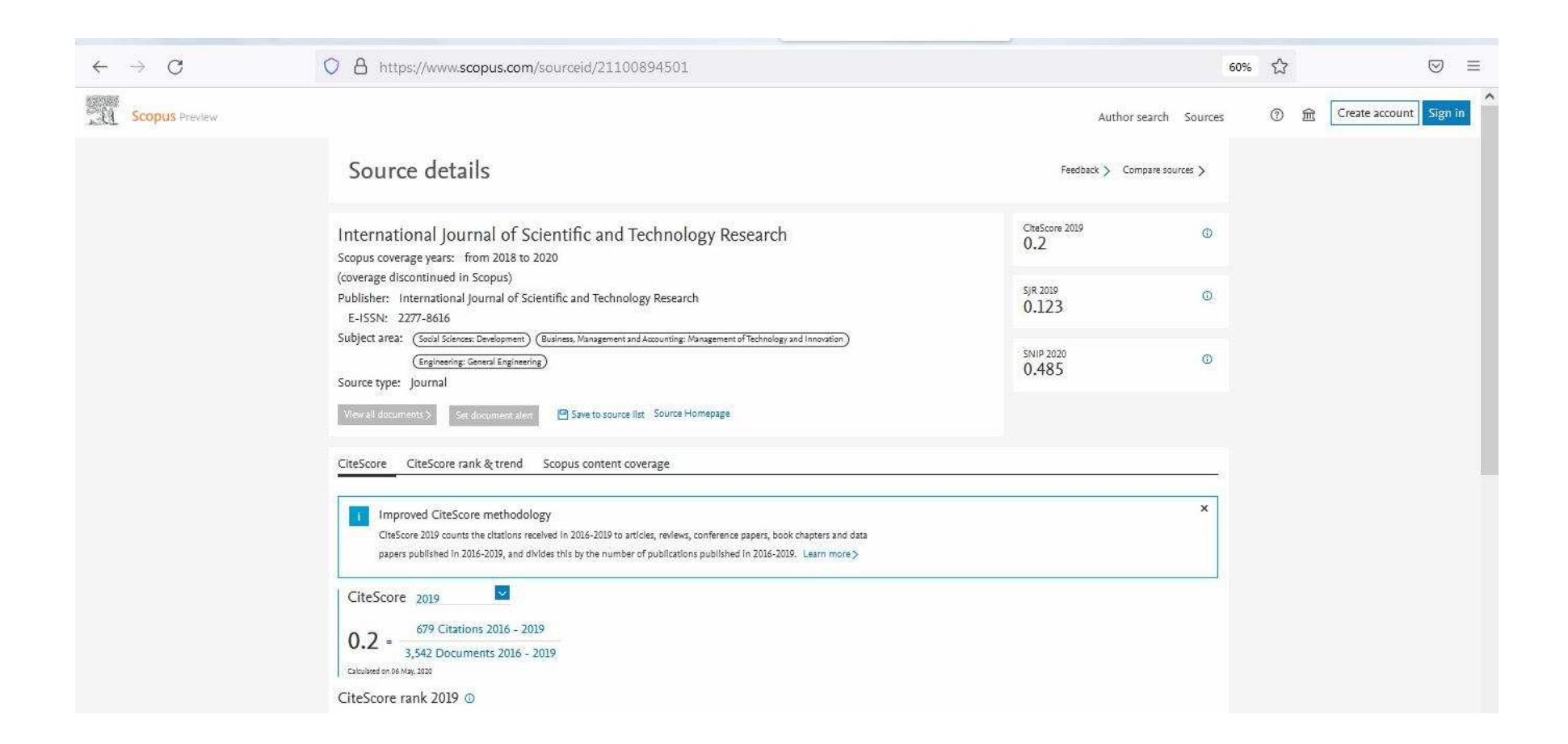
In spite of its application in medical diagnostic purposes, it is a highly toxic indigoid class of dye and causes skin and eye irritations¹⁵. Consumption of this carcinogenic dye leads to reproductive, developmental, neuronal and acute toxicity¹⁶. It is also known to cause mild to severe hypertension and cardiovascular and respiratory effects¹⁷. Methylene blue [3,7-bis(dimethylamino)-phenothiazin-5-iumchloride] finds use as a cationic dye in the textile industry. Thiazine ring system has been the characteristic structure of this dye. It is most commonly used for coloring paper, temporary hair colorant and mainly used on soft vegetable fibers such as jute, flax and hemp.

Only, to a lesser extent it is used on paper, leather and mordanted cotton. It dyes silk and wool but has very poor light fastness on these fibers^{18,19}. The dye, although not considered to be a very toxic dye, can reveal very harmful effects on the living things. After inhaling, symptoms such as difficulties in breathing, diarrhea and nausea can occur in human beings²⁰. The chemical structure of these dyes is shown in figures 1a and 1b.

Material and Methods

All materials in this experiment are of analytical grade and were prepared in the laboratory. Zinc acetate dihydrate salt (M.W. 219.50, purity 98.5%) was purchased from Sisco Research Laboratories Pvt. Ltd., sodium hydroxide from Merck and ethanol (99.9%) was purchased from Changshu Hongsheng Fine Chemical Co. Ltd. The capacity of the air pump used for the experiments is 3W and air supplied is 2.5L/min.

pH of the solution was measured using Elico digital pH meter. Dye used for representing the thiazine dyes is methylene blue and for indigoid dyes, it is indigo carmine due its solubility in water. Both the dyes were purchased from S.D. Fine Chemicals. The decolourization of dyes was monitored by UV-visible spectrophotometer (Hitachi- U 2910).



Degradation of Methylene Blue Dye Using Dimethyl Dioxirane as oxidizing agent

S.Vinotha, Preeja.P.Thattil, A. Leema Rose

Abstract: Dyes produced by the textile, printing and paper industries can end up in waste waters and are therefore a potential source of pollution of rivers and waterways. To overcome this problem many techniques are followed to degrade the dye contaminates in waterways among them AOP (Advance Oxidation Process) is the advanced process. This study reports on the advanced oxidation of methylene blue by means of the combined action of dimethyl dioxirane. The influence of different parameters, such as oxidizing agent concentration, initial dye concentration and pH in the oxidative process has been studied. The degradation of methylene blue dye was evaluated under dark condition at room temperature by using dimethyl dioxirane as oxidizing agentThe effect of pH, effect of oxidizing agent and initial dye concentration on the degradation efficiency of methylene blue was investigated. The results reveal that the optimum oxidation conditions of methylene blue are as follows: pH = 7, oxidizing agent = 500µL and 10 mg/L methylene blue dye concentration. Under these conditions, the removal efficiency of methylene blue was 99.2%.

Keywords: Advance Oxidation Process; Methylene blue; pH; Initial Dye concentration; Dimethyl Dioxirane.

1 INTRODUCTION

One of the most important environmental problems of the textile industry is the generation of large volumes of highly coloured wastewater (Balanosky et al., 2000), the release of which into the ecosystems causes esthetic pollution, eutrophication, and perturbation in aquatic life (Vautier et al., 2001). Despite the fact that the release of colour wastewater into the earth comprises just a little extent of water contamination, the way that colours are obvious at low fixations—combined with ever stricter governments guidelines-is constraining material enterprises to get their waste effluents an undeniably elevated expectation preceding releasing them into the nearby sewage framework or to the rivers (Robinson et al., 2001; Venkata al., 2003). Consequently, colour removal from wastewater is frequently viewed as considerably more significant than the evacuation of solvent lackluster natural substances, a noteworthy reason to the synthetic oxygen request (COD) of the accepting waters (Pal Toor et al., 2006). Conventional treatments have been used to decolorize industrial textile wastewaters, such as adsorption (Faria et al., 2005) chemical coagulation (Sanghi and Bhattacharya, 2005), chemical oxidation processes—some of which utilize Fenton reagent (Perez. et al., 2002), ozone (Alaton et al., 2004), and the combined action of these oxidants or any of them with H_2O_2 (Hassan et al., 2002., Uner et al., 2004), and electrochemical oxidation (Lorimer et al., 2000). Biological processes have been also used to decolorize effluents from the textile industry, and in particular on azo dyes (Shaw et al., 2002),

But they are not always effective in removing colour because of the low biodegradability of textile dyes and so tertiary treatments are needed to decolorize dye effluents before discharge (Van der zee and Villaverde, 2005). Therefore, most biological and physical-chemical treatments have limited applicability, and thus present significant disadvantages for colour removal and so, recently, the application of so-called advanced oxidation processes (AOPs) has been increasingly observed (Ledakowicz et al., 2001; Robinson et al., 2001) mainly applied to decolourize effluents containing azo dyes. These technologies are based on the initial formation of hydroxyl radicals, usually generated by the combined action of UV radiation and diverse oxidants, such as Fenton reagent, O₃, H₂O₂, or a mixture of some of them (Legrini et al., 1993). These radicals further oxidize organic matter, compounds that are recalcitrant to conventional biological and physicalchemical treatments, such as most dyes used in the textile industry. The present paper is focused on the advanced oxidation of methylene blue dye, in order to enhance the efficiency of this AOP by means of addition of low dimethyl dioxirane concentration, aimed at producing a nontoxic colourless effluent in a short period of time. The substrate was a highly coloured aqueous solution of methylene blue whose optical absorbance at 663 nm. The influence of different parameters, such as oxidizing agent concentration, and pH has been studied.

2 EXPERIMENTAL METHODS

2.1 Materials

All the chemicals used for preparation of dimethyl dioxirane are analytical grade reagents with 99% purity. Potassium peroxy monosulfate is obtained from TCI chemicals. Acetone from Pure chems and sodium bicarbonate from Merck. All chemicals are used as such without further purification.

2.2. Preparation of oxidizing agent

Acetone and water were taken in (1:2) ratio and cooled in an ice at 20°C. Sodium bicarbonate and potassium peroxy monosulfate were added in (2:1) ratio with constant stirring. The colour of acetone turned pale yellow, which indicates the formation of dimethyl dioxirane.

Research Scholar, PG & Research Department of Chemistry, Holy Cross College (Autonomous), Affiliated to Bharathidasan University, Trichy-2.

Research supervisor, PG & Research Department of Chemistry, Holy Cross College (Autonomous), Affiliated to Bharathidasan University, Trichy-2.

^{* &}lt;u>Corresponding author</u>:leemarose25@gmail.com Phone 9965441442.